

"Made available under NASA sponsorship  
in the interest of early and wide dis-  
semination of Earth Resources Survey  
Program information without liability  
for any use made to date."

7.8-10069

CR 151612

## MICROWAVE REMOTE SENSING AND ITS APPLICATION TO SOIL MOISTURE DETECTION

By

Richard Wayne Newton

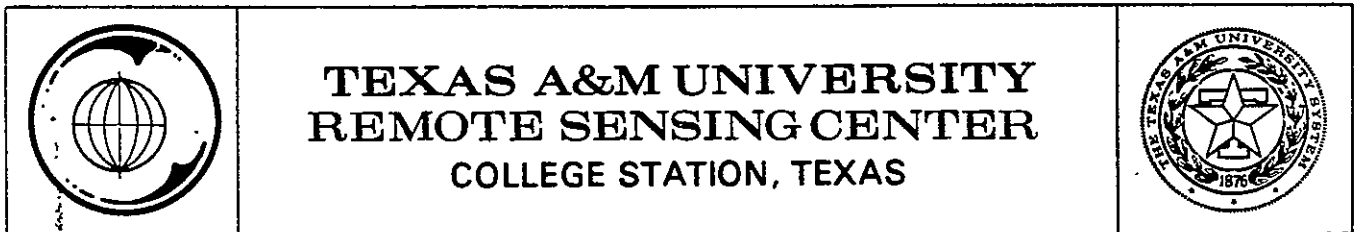
January 1977



Supported by

National Aeronautics and Space Administration

NAS9 - 13904



(E78-10069) MICROWAVE REMOTE SENSING AND  
ITS APPLICATION TO SOIL MOISTURE DETECTION  
(Texas A&M Univ.) 531 F HC A23/MF A01

N78-17442

CSCI 08M

Unclas

G3/43 00069

MICROWAVE REMOTE SENSING AND ITS APPLICATION  
TO SOIL MOISTURE DETECTION

By

Richard Wayne Newton

January 1977

Supported by

National Aeronautics and Space Administration

NAS9-13904

*mepp*

## ABSTRACT

### Microwave Remote Sensing and Its Application to Soil Moisture Detection

Theoretical and experimental studies of the thermal microwave emission from moist soil were performed. The theoretical study was undertaken to provide a physical understanding of the emission from soil and its relationship to soil moisture. It is shown that the soil permittivity is dependent on the soil water matric potential independent of soil texture. Relationships describing the effects of the soil permittivity profile, surface roughness and vegetation cover on the microwave emission from soil are developed. Emission from the soil volume is described using a radiative transfer approach, the effect of surface roughness is modeled using the Kirchhoff approximation and vegetation cover is modeled as a dielectric slab.

Two experimental measurement programs were performed in order to verify the theoretical predictions and demonstrate the feasibility of estimating soil moisture remotely

using passive microwave sensors. Antenna temperature measurements of bare and vegetated, smooth and rough soil surfaces were obtained at 1.4 GHz and 10.6 GHz. These data demonstrate that a uniform surface roughness decreases the antenna temperature sensitivity to soil moisture at both 1.4 GHz and 10.6 GHz, but that the 10.6 GHz wavelength is sensitive to much smaller scales of surface roughness than is the 1.4 GHz wavelength. The effects of a periodic row structure are also demonstrated. It is also shown that uniform vegetation up to 125 cm tall has a minimal effect on the response of 1.4 GHz emission to soil moisture. However, such vegetation effectively masks the soil moisture response at 10.6 GHz.

A technique of estimating the average soil moisture within a surface layer is demonstrated. It is shown that at 1.4 GHz the depth of this surface layer ranges from a few centimeters up to approximately 20 centimeters depending on the soil moisture conditions. At 10.6 GHz this surface layer is never more than 2 centimeters thick. This technique is shown to be effective for a range of uniform surface roughness conditions. However, the soil moisture estimation accuracy decreases with surface roughness. At 1.4 GHz the approximate soil moisture estimation accuracy is shown to be +3% to -6% for a smooth surface, +4% and -5% for a medium rough surface, and +5.5% and -6%



for a rough surface. At 10.6 GHz it was estimated that the surface soil moisture could be measured to within  $\pm 10\%$  for "smooth" and medium rough surfaces, and to within  $\pm 6\%$  for a rough surface.

Since soil moisture can be measured to different depths by using different wavelengths, the surface soil moisture profile can be estimated using a multifrequency system. It is expected that a frequency between 1.4 GHz and 10.6 GHz will yield better estimates of surface soil moisture than 10.6 GHz due to a smaller sensitivity to surface roughness. In addition, the soil moisture estimation technique will apply equally well to soil water matric potential independent of soil texture. This indicates that the feasibility of remotely estimating available water to plants in the near surface, or degree of soil saturation (two parameters that are of interest to agriculturalists and hydrologists) is realizable.

## TABLE OF CONTENTS

<u>Chapter</u>	<u>Page</u>
ABSTRACT . . . . .	i
TABLE OF CONTENTS. . . . .	iv
LIST OF TABLES . . . . .	xi
LIST OF FIGURES. . . . .	xiii
I. INTRODUCTION. . . . .	1
Problem Statement . . . . .	1
Approach. . . . .	2
Scope of the Report . . . . .	4
II. SOIL MOISTURE . . . . .	6
Soil-Water Interaction. . . . .	6
Soil Composition . . . . .	6
Textural Separates. . . . .	7
The Surface of Clay Particles . . . . .	13
Chemical and Mineralogical Make-up of Clay . . . . .	16
Soil Water . . . . .	26
Soil-Water-Plant Interrelationships . . . . .	28
Soil Water Descriptions. . . . .	30
The Energy State of Soil Water . . . . .	34
Soil-Water-Plant Relations . . . . .	37

<u>Chapter</u>	<u>Page</u>
Soil Permittivity . . . . .	43
Soil Moisture Dependence . . . . .	44
Measurement Results . . . . .	44
Comparison to Other L-band Measurements . . . . .	70
Other Effects . . . . .	73
III. MICROWAVE EMISSION . . . . .	77
Mathematical Description of Energy Transfer . . . . .	78
Soil Volume . . . . .	80
Peake's Approach . . . . .	81
Radiative Transfer . . . . .	83
Scattering in the Soil Volume . . . . .	86
Surface Roughness . . . . .	88
Geometrical and Pseudo-Physical Optics Models . . . . .	89
Kirchhoff Solution . . . . .	91
Small Perturbation . . . . .	93
Composite Surface Theory . . . . .	95
Vegetation . . . . .	96
Models of Scattering Coefficients of Vegetation . . . . .	96
Models of Emission of Vegetation . . . . .	98
Microwave Measurements . . . . .	103
Active Microwave Measurements . . . . .	104
Bare Soil . . . . .	104
Vegetation . . . . .	106

<u>Chapter</u>	<u>Page</u>
Passive Airborne Microwave Measurements . . . . .	110
Passive Ground-based Measurements . . .	120
Bare Soil . . . . .	120
Vegetated Soil . . . . .	126
Applicability of Published Measurements . . . . .	127
IV. MODELS . . . . .	128
Introduction . . . . .	128
Soil Volume . . . . .	130
Model Description . . . . .	130
Modeling Options . . . . .	130
Radiative Transfer Equations . . . . .	133
Attenuation Constant . . . . .	143
Power Transmission and Reflection Coefficients . . . . .	149
Equation Interpretation . . . . .	154
Demonstration of the Model . . . . .	157
Comparison to Accepted Procedures . . . . .	157
Calculated Soil Volume Brightness Temperatures . . . . .	158
Surface Roughness . . . . .	172
Model Development . . . . .	172
Peake Approach . . . . .	172
Transmission Scattering . . . . .	173
Differential Transmission Coefficients . . . . .	179

<u>Chapter</u>	<u>Page</u>
Conversion to Scattering Coefficients . . . . .	180
Demonstration of the Model . . . . .	188
Comparison to the Peake Approach . . .	188
Computed Effects of Roughness . . . .	191
Vegetation . . . . .	206
Model Description . . . . .	206
Uniformly Vegetated Surface . . . . .	212
Row Crops . . . . .	216
Model Demonstration . . . . .	224
Uniform Vegetation . . . . .	224
Row Vegetation . . . . .	227
V. MEASUREMENT PROGRAM . . . . .	233
Microwave Signature Acquisition System . . .	233
Background . . . . .	233
MSAS Description . . . . .	234
RF Subsystem . . . . .	240
Receiver Subsystem . . . . .	241
Data Processing Subsystem . . . . .	245
Experiment . . . . .	246
Measurement Program in 1974 . . . . .	246
Measurement Program in 1975 . . . . .	256
Microwave Data Reduction . . . . .	260

<u>Chapter</u>	<u>Page</u>
VI. COMPARISON BETWEEN ANTENNA TEMPERATURE AND BRIGHTNESS TEMPERATURE . . . . .	266
Measured Antenna Temperature . . . . .	267
Power Output of an Antenna . . . . .	267
Apparent Antenna Temperature . . . . .	276
Effects of Beamwidth . . . . .	280
Polarization Mixing . . . . .	281
Like Polarization . . . . .	285
Cross Polarization . . . . .	287
Transmission Angle Averaging . . . . .	291
Atmospheric Radiation . . . . .	292
VII. ANALYSIS OF MEASUREMENTS . . . . .	303
Introduction . . . . .	303
Quantification of Moisture and Temperature Profiles . . . . .	304
Soil Moisture Profile . . . . .	305
Description of Soil Moisture Parameters . . . . .	305
Optimization of the Soil Moisture Description . . . . .	311
Interpretation of the Equivalent Incoherent Soil Moisture . . . . .	316
Soil Temperature Profile . . . . .	329
Data Interpretation and Soil Moisture Correlation . . . . .	331
Smooth Surface Moisture and Angle Dependence . . . . .	332

<u>Chapter</u>	<u>Page</u>
Effects of Roughness . . . . .	346
Uniform Roughness . . . . .	346
Effect of Row Direction . . . . .	366
Effect of Vegetation . . . . .	388
Uniform Vegetation Cover . . . . .	389
Row Vegetation Cover . . . . .	394
Soil Moisture Estimation . . . . .	399
Scope . . . . .	399
Uniform Roughness . . . . .	403
Surface Roughness Prediction . . . . .	407
Soil Moisture Measurement . . . . .	413
Row Structure . . . . .	423
Effect of Vegetation . . . . .	427
VIII. CONCLUSION . . . . .	429
Summary of Results . . . . .	429
Recommendations . . . . .	433
REFERENCES . . . . .	437
APPENDIX A - DIFFERENTIAL TRANSMISSION COEFFICIENTS . . . . .	448
APPENDIX B - CORRECTION OF DATA FOR SELF EMISSION . . . . .	462
The Self Emission Contribution . . . . .	462
Correction Scheme Using Radar Data . . . . .	466
Self Emission at 1.4 GHz . . . . .	471
Self Emission at 10.6 GHz . . . . .	479

ChapterPage

APPENDIX_C - EQUIVALENT SOIL MOISTURE AND -- SOIL TEMPERATURE TABULATIONS .	488
--	-----



## LIST OF TABLES

<u>Table</u>		<u>Page</u>
II-1	The Relation of Surface to Particle Size (after Baver, Gardner and Gardner [1]) . . . . .	14
II-2	Surface Area in Relation to Shape of Particle (after Baver, Gardner, and Gardner [1]) . . . . .	17
II-3	Results of Physical and Chemical Analysis of the Soil Samples Used in the Permittivity Analysis . . . . .	51
II-4	Tabulation of Volumetric Transition Moistures Graphically Obtained from Figures II-18 through II-23 . . . . .	64
II-5	Matric Potential Versus Soil Moisture for Samples 7 and 18, Miller Clay and Sand . . . . .	67
VI-1	Ranges of Sky Brightness Temperature of the Atmosphere: $\theta_z = 0$ deg. (after Paris [40]) . . . . .	296
VI-2	Ranges of Sky Brightness Temperature of the Atmosphere: $\theta_z = 55$ deg. (after Paris [40]) . . . . .	297
VII-1	Data Used to Calculate Correlation Coefficients (Field CS) . . . . .	314
VII-2	Results of the Correlation Analysis . . .	317
VII-3	Separation of Profiles for Regression Analysis . . . . .	325
VII-4	Linear Regression Equations for Soil Profile Categories I, II, and III . . . .	327
VII-5	Linear Regression Fits to the 1974 1.4 GHz Measurements . . . . .	351
VII-6	Roughness Parameter, Q, for Each Surface Preparation . . . . .	357

<u>Table</u>		<u>Page</u>
VII-7	Soil Bulk Density Measurements . . . . .	374
VII-8	Comparison Between 1974 and 1975 Measured Response to Soil Moisture by Weight at a Transmission Angle of 20° . . . . .	377
VII-9	80% Confidence Intervals on the Population Mean at 25% EQSM for $T_{N_h}$ Measured at 1.4 GHz . . . . .	419
B-1	Values of $\sigma^\circ$ Extrapolated from Measurements Reported by Battilvala and Cihlar [106] . . . . .	472
B-2	Parameters Used to Calculate the Self Emitted Noise Power of the L-band System . . . . .	475
B-3	Calculations of the L-band Self Emitted Component; Measurement Set Three . . . . .	480
B-4	Parameters Used to Calculate the Self Emitted Component of the X-band System . . . . .	486
B-5	Calculations of the X-band Self Emitted Component for Measurement Set Three . . . . .	487
C-1	Equivalent Soil Moisture and Soil Temperature Calculations for the 1974 Experiment . . . . .	490
C-2	Equivalent Soil Moisture and Soil Temperature Calculations for the 1975 Experiment . . . . .	495
C-3	Ground Sampling Locations that Correspond to the Antenna Temperature Measurement Sets Made at Each Azimuth Angle . . . . .	500

## LIST OF FIGURES

<u>Figure</u>		<u>Page</u>
II-1	Classification of soil separates < 2.0 mm on the basis of particle size (After Baver, Gardner, and Gardner [1]) . . . . .	9
II-2	Construction of grain-size distribution curve (after Kezdi [2]) . . . . .	11
II-3	USDA soil textural classification triangle . . . . .	12
II-4	The basic tetrahedron and octahedron structures and their graphical representations . . . . .	19
II-5	Diagrammatic sketches of clay mineral structures showing the sheeting effect . . . . .	21
II-6	Graphical representation of the layering of basic mineral sheets that forms interlayer positions for cations . . . .	24
II-7	Typical dehydration curves of different clay minerals (after Kezdi [2]). . . . .	29
II-8	Components of the soil-water complex . .	31
II-9	Matric potential of soil fractions as a function of texture and water content (after Taylor and Ashcroff [10]) . . . .	39
II-10	The availability of water to plants as a function of percentage clay content . . . . .	42
II-11	Relative permittivity of sand as a function of moisture by weight . . . . .	45
II-12	Relative permittivity of sandy clay as a function of moisture by weight . . . .	46
II-13	Relative permittivity of clay loam samples 7 and 18 as a function of moisture by weight . . . . .	47

<u>Figure</u>		<u>Page</u>
II-14	Relative permittivity of clay loam samples 4 and 5 as a function of moisture by weight . . . . .	48
II-15	Relative permittivity of clay as a function of moisture by weight . . . . .	49
II-16	Relative permittivity of Miller clay as a function of moisture by weight . . . . .	50
II-17	Field capacity as a function of transition moisture . . . . .	55
II-18	Relative permittivity of sand as a function of volumetric water content . . . . .	57
II-19	Relative permittivity of samples 14 and 15 as a function of volumetric water content . . . . .	58
II-20	Relative permittivity of samples 7 and 18 as a function of volumetric water content . . . . .	59
II-21	Relative permittivity of samples 4 and 5 as a function of volumetric water content . . . . .	60
II-22	Relative permittivity of sample 13 as a function of volumetric water content . . . . .	61
II-23	Relative permittivity of Miller clay as a function of volumetric water content . . . . .	62
II-24	Permittivity of all soils referenced to the transition moisture . . . . .	65
II-25	Matric potential of Miller clay, samples 7 and 18, and sand assuming equivalence of permittivity versus soil moisture for all soil textures . . . . .	69

<u>Figure</u>		<u>Page</u>
II-26	Results of calculations of relative permittivity for soils of different salt contents (after Carver [27]) . . . .	76
III-1	Graphic illustration of the various contributions to a radiometer measurement . . . . .	79
III-2	Scattering coefficient as a function of effective soil moisture content (after Ulaby et al. [79]) . . . . .	105
III-3	Moisture sensitivity as a function of incident angle (after Ulaby et al. [79]) . . . . .	107
III-4	Angular response (2.75 GHz) for three bare fields with similar soil moisture but different surface roughness (after Ulaby and Batlivala [80]) . . . . .	108
III-5	Angular response (7.25 GHz) for three bare fields with similar soil moisture but different surface roughness (after Ulaby and Batlivala [80]) . . . . .	109
III-6(a)	Scattering coefficient measured at 5.9 GHz for low and high soil moisture conditions (after Ulaby [81]) . . . . .	111
III-6(b)	Scattering coefficient measured at 5.9 GHz for low and high soil moisture conditions (after Ulaby [81]) . . . . .	112
III-7	Plot of 19 GHz measured antenna temperature versus soil moisture for light soils (sandy loam and loam) and heavy soils (clay loam) (after Schmugge et al. [85]) . . . . .	114
III-8	Plot of 19 GHz measured antenna temperature versus soil moisture in top 1 cm expressed as percent field capacity (after Schmugge et al. [85]) . .	116

<u>Figure</u>		<u>Page</u>
III-9	Plot of 1.4 GHz measured antenna temperature versus soil moisture in top 1 cm expressed as a percent of field capacity (after Schmugge et al. [85]) . . . . .	117
III-10	Plot of 1.4 GHz measured antenna temperature versus soil moisture expressed as a percent of field capacity in the top 2.5 cm (after Schmugge et al. [85]) . . . . .	118
III-11	The 21 cm response for dry and overlying wet sand (after Blinn et al. [90]) . . . . .	122
III-12	Plate measurements of moist sand (after Blinn et al. [90]) . . . . .	123
III-13	Antenna temperature versus soil moisture for a smooth bare field (after Lee [91]) . . . . .	124
III-14	Moisture effects for smooth and rough junction sand (after Blinn and Quade [89]) . . . . .	125
IV-1	Soil surface and vegetation surface reference datums . . . . .	131
IV-2	Soil volume geometry used in the radiative transfer model of soil emission . . . . .	134
IV-3	Geometry used to describe the relationship between incident, reflected, and transmitted power density . . . . .	151
IV-4	Percentage contribution of two centimeter soil layers to the total volume emission calculated at 1.4 GHz for uniform soil moisture and temperature profiles . . . .	161
IV-5	Brightness temperature of a soil volume for uniform moisture and nonuniform temperature profiles. Each curve represents both vertical and horizontal polarizations . . . . .	163

<u>Figure</u>		<u>Page</u>
IV-6	Soil temperature profiles used to demonstrate that the emission from a soil volume is not isotropic for nonuniform temperature profiles (Figure IV-5) . . . . .	164
IV-7(a)	The contribution of two centimeter soil layers to the total volume brightness temperature for soil temperature profiles A and B of Figure IV-6 . . . . .	165
IV-7(b)	The contribution of two centimeter soil layers to the total volume brightness temperature for soil temperature profiles A and B of Figure IV-6 . . . . .	166
IV-8	Soil moisture profiles used to demonstrate that the emission from a soil volume is not isotropic for nonuniform moisture profiles . . . . .	168
IV-9	Calculated brightness temperatures of the soil volume for nonuniform soil moisture profiles . . . . .	169
IV-10	The contribution of two centimeter soil layers to the total volume brightness temperature for soil moisture profiles A and B of Figure IV-8 . . . . .	171
IV-11	Geometry used to describe differential transmission coefficients . . . . .	175
IV-12	Geometry used to describe the transmission and reflection of energy at a smooth interface . . . . .	182
IV-13	Geometry used to describe bistatic scattering coefficients . . . . .	185
IV-14	Geometry used to relate the bistatic scattering coefficients in the hemisphere above the soil surface to the bistatic scattering coefficients in the hemisphere below the soil surface . . . . .	190

<u>Figure</u>		<u>Page</u>
IV-15	Calculated horizontally-polarized emission of smooth bare soil as a function of volumetric soil moisture and transmission angle . . . . .	199
IV-16	Calculated vertically polarized emission of smooth bare soil as a function of volumetric soil moisture and transmission angle . . . . .	200
IV-17	Calculated change in emission of smooth bare soil as a function of volumetric soil moisture . . . . .	202
IV-18	Calculated response of smooth bare soil to volumetric soil moisture as a function of transmission angle . . . . .	203
IV-19	Calculated horizontal brightness temperature of bare soil as a function of roughness and transmission angle . . . . .	204
IV-20	Calculated vertical brightness temperature of bare soil as a function of roughness and transmission angle . . . . .	205
IV-21	Calculated brightness temperature of bare soil as a function of roughness and soil moisture . . . . .	207
IV-22	Change in the response of bare soil emission to soil moisture as a function of surface roughness . . . . .	208
IV-23	Geometry for radiation from row vegetation (after Sibley [75]) . . . . .	217
IV-24	Geometry for emission perpendicular to rows (after Sibley [75]) . . . . .	219
IV-25	Geometry for propagation through a row canopy at an arbitrary azimuth angle (after Sibley [75]) . . . . .	220



<u>Figure</u>		<u>Page</u>
IV-26	Geometry used to aid in the explanation of the average distance the soil emission must traverse through a row canopy for arbitrary azimuth and transmission angles . . . . .	221
IV-27	Vertically polarized brightness temperature of a uniform canopy as a function of soil moisture and vegetation density . . . . .	225
IV-28	Vertically polarized brightness temperature of a uniform canopy as a function of soil moisture for three combinations of vegetation and soil temperatures . . . . .	226
IV-29	Moisture content determined from apparent temperature of vegetated soil (after Sibley [75]) . . . . .	228
IV-30	Brightness temperature of row vegetation at 10.6 GHz as a function of soil moisture and transmission angle looking perpendicular to the rows . . . . .	229
IV-31	Brightness temperature of row vegetation at 10.6 GHz as a function of soil moisture and transmission angle looking parallel to the rows . . . . .	230
IV-32	Vertical brightness temperature of row vegetation as a function of transmission and azimuth angles . . . . .	231
IV-33	Horizontal brightness temperature of row vegetation as a function of transmission and azimuth angles . . . . .	232
V-1	Boom truck with the radiometer mounted at the end of the boom (top). Close-up showing details of the radiometer antennas and truss structure (bottom). .	235

<u>Figure</u>		<u>Page</u>
V-2	Van that houses the radiometer control and data processing electronics . . . . .	236
V-3(a)	Block diagram of the MSAS subsystems . . . . .	237
V-3(b)	Block diagram of the MSAS subsystems . . . . .	238
V-4	Block diagram descriptive of the gain modulation technique . . . . .	242
V-5	Layout of the 1974 experimental plots . . . . .	248
V-6	Smooth field used in the 1974 measurements program . . . . .	250
V-7	Medium rough field used in the 1974 measurements program . . . . .	251
V-8	Rough field used in the 1974 measurements program . . . . .	252
V-9	Example of the uniform vegetation covers used in the 1974 measurements program . . . . .	253
V-10	Row planted vegetation used in the 1974 measurements program . . . . .	254
V-11	Layout of the 1975 experimental plots . . . . .	257
V-12	Field layout used in the 1975 measurements program . . . . .	259
V-13	Functional diagram of the MSAS (See text for explanation of symbols) . . . .	261

<u>Figure</u>		<u>Page</u>
VI-1	Geometry used to demonstrate the proper integration of intensity to obtain flux . . . . .	270
VI-2	Representation of an antenna beamwidth . . . . .	272
VI-3	Relationship between the antenna and surface coordinate systems . . . . .	282
VI-4	Relationship between the surface and antenna polarization vectors . . . . .	284
VI-5	Normalized power received in horizontal polarization as a function of transmission angle, $\theta_0$ , for different beamwidths (after Grody [113]) . . . . .	288
VI-6	Comparison of measured antenna temperature to the corresponding apparent temperature . . . . .	289
VI-7	Degradation of measured antenna temperature due to transmission angle averaging . . . . .	293
VI-8	Sky brightness temperature for a standard atmosphere as computed by Paris [114] . . . . .	295
VI-9	Reflected horizontally polarized sky brightness temperature for 35% soil moisture . . . . .	299
VI-10	Reflected vertically polarized sky brightness temperature for 35% soil moisture . . . . .	300
VI-11	Reflected horizontally polarized sky brightness temperature for 10% soil moisture . . . . .	301
VI-12	Reflected vertically polarized sky brightness temperature for 10% soil moisture . . . . .	302

<u>Figure</u>		<u>Page</u>
VII-1	Comparison of calculated soil moisture parameters to the measured soil moisture averaged over depth . . . . .	312
VII-2	Comparison of equivalent incoherent soil moisture calculated at 10.6 GHz to measured soil moisture averaged over depth . . . . .	319
VII-3	Comparison of equivalent incoherent soil moisture calculated at 1.4 GHz to measured soil moisture averaged over depth . . . . .	320
VII-4	Comparison of equivalent incoherent soil moisture ( $m_I$ ) calculated at 1.4 GHz to the depth that corresponds to an average soil moisture equal to $m_I$ . .	322
VII-5	Definition of soil moisture profile type . . . . .	324
VII-6	Linear regression fits and confidence intervals for the data in Figure VII-4 .	328
VII-7	Measured 1.4 GHz emission as a function of soil moisture and transmission angle . . . .	334
VII-8	1.4 GHz antenna temperature measurements of smooth, bare soil at nadir as a function of equivalent incoherent soil moisture . . . . .	335
VII-9	Horizontal 1.4 GHz antenna temperature measurements of smooth, bare soil at 20° as a function of equivalent incoherent soil moisture . . . . .	336
VII-10	Vertical 1.4 GHz antenna temperature measurements of smooth, bare soil at 20° as a function of equivalent incoherent soil moisture . . . . .	337
VII-11	Horizontal 1.4 GHz antenna temperature measurements of smooth, bare soil at 35° as a function of equivalent incoherent soil moisture . . . . .	338

<u>Figure</u>		<u>Page</u>
VII-12	Vertical 1.4 GHz antenna temperature measurements of smooth, bare soil at 35° as a function of equivalent incoherent soil moisture . . . . .	339
VII-13	Horizontal 1.4 GHz antenna temperature measurements of smooth, bare soil at 50° as a function of equivalent incoherent soil moisture . . . . .	340
VII-14	Vertical 1.4 GHz antenna temperature measurements of smooth, bare soil at 50° as a function of equivalent incoherent soil moisture . . . . .	341
VII-15	Sensitivity of 1.4 GHz antenna temperature measurements to soil moisture of smooth, bare soil based on linear regression fits . . . . .	342
VII-16	Calculated brightness temperature of a smooth, bare soil as a function of uniform soil moisture . . . . .	345
VII-17	Sensitivity of antenna temperature measurements to soil moisture for average moistures greater than 25% . . .	347
VII-18	Normalized 1.4 GHz antenna temperature measurements as a function of soil moisture for three surface roughness conditions . . . . .	349
VII-19	Normalized antenna temperatures corresponding to a 35% EQSM. These data were used in conjunction with Figures VII-20 and VII-21 to obtain the Q distributions for each surface . .	353
VII-20	Vertically polarized normalized brightness temperature as a function of transmission angle and Q, calculated for 35% soil moisture . . . . .	355
VII-21	Horizontally polarized normalized brightness temperature as a function of transmission angle and Q, calculated for 35% soil moisture . . . . .	356

<u>Figure</u>		<u>Page</u>
VII-22	Graphical illustration of a physical interpretation of the effect of roughness on the emission from a soil surface . . . . .	359
VII-23	Illustration of the compression in the result of the integration effect (Figure VII-22) of a rough surface as the soil moisture changes from wet to dry . . . . .	360
VII-24	Horizontal 10.6 GHz antenna temperature measurements as a function of soil moisture for three surface conditions . .	362
VII-25	Linear regression fits to 1.4 GHz antenna temperature measurements (@20°) of bare soil as a function of soil moisture for three surface preparations .	363
VII-26	Linear regression fits to 1.4 GHz antenna temperature measurements (@35°) of bare soil as a function of soil moisture for three surface preparations .	364
VII-27	Linear regression fits to 1.4 GHz antenna temperature measurements (@50°) of bare soil as a function of soil moisture for three surface preparations . . . . .	365
VII-28	1.4 GHz antenna temperature measurements made at an azimuth angle of 0° with respect to the row direction, as a function of soil moisture . . . . .	368
VII-29	1.4 GHz antenna temperature measurements made at an azimuth angle of 30° with respect to the row direction, as a function of soil moisture . . . . .	369
VII-30	1.4 GHz antenna temperature measurements made at an azimuth angle of 45° with respect to the row direction, as a function of soil moisture . . . . .	370

<u>Figure</u>		<u>Page</u>
VII-31	1.4 GHz antenna temperature measurements made at an azimuth angle of 60° with respect to the row direction as a function of soil moisture . . . . .	371
VII-32	1.4 GHz antenna temperature measurements made perpendicular to the row direction as a function of soil moisture . . . . .	372
VII-33	Comparison of linear regression fits to 1974 measurements of uniformly rough, bare surfaces to 1975 measurements of row tilled bare surfaces . . . .	376
VII-34	Illustration of how the distribution of transmission angles from which an antenna receives radiation changes as the azimuth angle between the plane of transmission and row direction is varied . . . . .	380
VII-35	1.4 GHz antenna temperature measurements made parallel to the row direction at 20° as a function of soil moisture . . . . .	382
VII-36	1.4 GHz antenna temperature measurements made parallel to the row direction at 35° as a function of soil moisture . . . . .	383
VII-37	1.4 GHz antenna temperature measurements made parallel to the row direction at 50° as a function of soil moisture . . . . .	384
VII-38	10.6 GHz antenna temperature measurements made parallel to the row direction as a function of soil moisture . . . . .	386
VII-39	10.6 GHz antenna temperature measurements made perpendicular to the row direction as a function of soil moisture . . . . .	387

<u>Figure</u>		<u>Page</u>
VII-40	Horizontal 10.6 GHz antenna temperature measurements of a vegetated smooth surface as a function of soil moisture . . . . .	390
VII-41	Comparison of bare and vegetated 1.4 GHz measurements made as a function of soil moisture at a 20° transmission angle . . . . .	391
VII-42	Comparison of bare and vegetated 1.4 GHz measurements made as a function of soil moisture at a 35° transmission angle . . . . .	392
VII-43	Comparison of bare and vegetated 1.4 GHz measurements made as a function of soil moisture at a 50° transmission angle . . . . .	393
VII-44	Comparison of horizontal 1.4 GHz measurements of two uniform vegetation densities . . . . .	395
VII-45	Comparison of vertical 1.4 GHz measurements of two uniform vegetation densities . . . . .	396
VII-46	Comparison between bare and vegetated 10.6 GHz antenna temperature measurements made parallel to the row direction . . . . .	397
VII-47	Comparison between bare and vegetated 10.6 GHz antenna temperature measurements made perpendicular to the row direction . . . . .	398
VII-48	Comparison of bare and vegetated 1.4 GHz measurements of row tilled surfaces made parallel to the rows as a function of soil moisture . . . . .	400
VII-49	Comparison of bare and vegetated 1.4 GHz measurements of row tilled surfaces made perpendicular to the rows as a function of soil moisture . . . . .	401



<u>Figure</u>		<u>Page</u>
VII-50	Horizontal 1.4 GHz antenna temperature measurements as a function of soil moisture for three surface conditions . .	404
VII-51	Comparison of the mean and standard deviation of the 0-1 cm soil moisture measured in fields CS and CM . . . . .	406
VII-52	1.4 GHz antenna temperature measurements made as a function of transmission angle for three surface preparations . . . . .	408
VII-53	Comparison of the effect of soil moisture on the difference between vertical and horizontal normalized antenna temperatures measured at 20° for three rms surface heights . . . .	410
VII-54	Comparison of the effect of soil moisture on the difference between vertical and horizontal normalized antenna temperatures measured at 35° for three rms surface heights . . . .	411
VII-55	Comparison of the effect of soil moisture on the difference between vertical and horizontal normalized antenna temperatures measured at 50° for three rms surface heights . . . .	412
VII-56	The difference between vertical and horizontal antenna temperatures measured at 35° for three rms surface heights . . . . .	414
VII-57	Demonstration of the separability of 1.4 GHz antenna temperature measurements into soil moisture and surface roughness classes . . . . .	417
VII-58	Soil moisture and surface roughness partitions obtained from Figure VII-57 for 1.4 GHz measurements . . . . .	418

<u>Figure</u>		<u>Page</u>
VII-59	10.6 GHz measurements plotted in a manner that demonstrates the separability of soil moisture and surface roughness (as in Figure VII-57) . . . . .	422
VII-60	The difference between predicted brightness temperatures at vertical and horizontal polarization as a function of their average for transmission angles of 30° and 50°. The straight lines are lines of constant moisture in the top layer (after Burke and Paris [32]) . . . . .	425
VII-61	Brightness temperature predictions for field 260A. Arrows mark the vertical and horizontal 10.6 GHz antenna temperature measurements (after Burke and Paris [32]) . . . . .	426
A-1	Geometry used in describing the differential transmission coefficients . . .	449
B-1	1.4 GHz fresh water measurements that demonstrate the effect of self emission near nadir . . . . .	463
B-2	10.6 GHz fresh water measurements that demonstrate the effect of self emission near nadir . . . . .	464
B-3	Calculations of the brightness temperature of smooth bare soil for two extreme moisture conditions . . . . .	465
B-4	Measurements of emission from dry bare soil at 1.4 GHz . . . . .	467
B-5	Measurements of emission from moist bare soil at 1.4 GHz . . . . .	468
B-6	Measurements of emission from wet bare soil at 1.4 GHz . . . . .	469
B-7	Comparison of measurements to calculations of emission from smooth soil . . .	473

<u>Figure</u>		<u>Page</u>
B-8	Relationship between the area "viewed" by an antenna and its beamwidth. . . . .	477
B-9	10.6 GHz measurements of a wet smooth bare field . . . . .	481
B-10	Simplified block diagram of the 10.6 GHz front end. . . . .	483

## CHAPTER I

### INTRODUCTION

#### Problem Statement

During the past few years a considerable effort has been devoted to the development of techniques for obtaining information about the sub-visible surface of a scene. Remote sensors operating in the microwave frequency spectrum produce data that contain subsurface information. The microwave energy that is measured by the sensor interacts to a certain extent with the subsurface medium. As a result, investigations into subsurface phenomenon have been approached in most cases by utilizing sensors operating in the microwave spectrum. Both passive and active microwave sensors have been utilized in these studies. The research reported in this document deals primarily with passive microwave sensors.

The application of microwave sensors that has stirred the majority of interest in the last few years is the remote measurement of soil moisture. This application is felt to be viable since it has been demonstrated by

laboratory measurements that the microwave permittivity of soil is highly dependent on soil moisture. This result indicates the existence of an interaction mechanism between electromagnetic energy and soil moisture. Such a mechanism is required in order for a scene to have a microwave response that is dependent on soil moisture. However, other factors such as inhomogeneities in the soil, the geometry of the surface boundary, and vegetation above the soil interact with the electromagnetic energy and also affect the microwave response of the soil.

This study is an experimental investigation into the interaction of electromagnetic energy in the microwave frequency spectrum with soil to determine the ability, quantitatively, to estimate soil moisture from remote measurements made with microwave sensors. This investigation results in a technique for extracting soil moisture information from data acquired with microwave sensors. The technique is analyzed to demonstrate its limitations and predicted accuracy.

### Approach

In order to determine the ability to estimate soil moisture remotely, it is necessary to understand the

physical phenomena that are responsible for the interaction mechanisms that produce the microwave response of a scene, and to understand the inherent limitations of using this response to estimate soil moisture. The inherent limitations in the ability to estimate soil moisture are a result of the effects of physical scene parameters on the microwave response of the scene. These parameters are soil type, soil inhomogeneities, surface roughness, soil moisture and temperature variation with depth, and vegetation cover.

The investigation of the interaction of electromagnetic energy with the scene is made less complicated experimentally by considering the subsurface, surface, and vegetation separately. It is also advantageous to study each of these scene components separately in order to obtain a physical interpretation of the effect of each on the microwave measurements.

The general approach to this research was to generate physical models that describe the individual effects of each component on the emitted microwave energy of the scene. Combinations of these physical models were then utilized to assess the ability to estimate soil moisture and to determine the optimum techniques of doing so. In addition, ground-based field experiments were performed with passive microwave sensors to measure the effects of each scene component independently under controlled conditions.

Results of these experimental measurements were compared to predictions made with the models.

### Scope of the Report

This report establishes a technique of measuring soil moisture with microwave sensors. Chapter II provides background information on soils, the interaction of water with soils, and the uptake of soil water by plants as well as a reasonably detailed discussion on the effects of soil water on the microwave permittivity of soil. Chapter III completes the background material by providing a review of published thermal microwave measurements of soil-vegetation scenes, as well as modeling techniques that have been used to describe these data. In the review of Chapter III the advantages and disadvantages of these modeling techniques and the limitations of the previously published microwave measurements are discussed.

Chapter IV contains the development of the models used as the basis of this research. These models are evaluated in detail to demonstrate the effects of scene parameters on the microwave response of the soil. Chapter V is a description of measurement programs designed to acquire experimental data appropriate for validating the models described in Chapter IV. In Chapter VI the effects of the sensor system on the true microwave response of a scene

are described. These effects must be considered when comparing model predictions to actual measurements.

In Chapter VII the passive microwave measurements described in Chapter V are analyzed to determine a procedure for estimating soil moisture. Of special importance is the effect of the soil moisture distribution with depth. An analysis is provided to demonstrate to which part of the soil moisture profile a microwave measurement is responsive. In this analysis a parameter is obtained that is related to the average available soil water within an effective skin depth. This parameter describes the response of the microwave measurement to soil moisture. It is used in the remainder of the analysis and is the parameter that is estimated from microwave measurements.

Chapter VIII contains a summary of the results of this report and recommendations for future studies.



## CHAPTER II

### SOIL MOISTURE

The emission or scattering of microwave energy from a soil surface is governed to a large extent by the permittivity of the soil. Soil permittivity is dependent on the moisture content of the soil. As a result, the microwave emission of soil varies with soil moisture. The interaction between soil and soil water is explained as background for an analysis of the mechanism that causes the permittivity of soil to vary with soil moisture. In addition, since soil moisture measurements are utilized in some applications to determine the availability of soil water to vegetation, it is also instructive to discuss the soil-water-plant interrelationship. In order to address all of these topics in a logical manner, Chapter II is divided into three main sections. The first topic is soil and soil-water interaction, the second is soil-water-plant interrelationships, and the third is soil permittivity. The first two sections are tutorial in nature and draw largely from Baver, Gardner, and Gardner [1], Kezdi [2] and Spangler [3].

#### Soil-Water Interaction

##### Soil Composition

Soil is defined as the unconsolidated mineral matter

on the earth's surface that serves as a medium for plant growth [3]. The solid phase of soil consists of organic matter and the product of weathering of parent rocks and the minerals that they contain. Soil is categorized by describing the physical properties that determine the utility of a soil. This is true in either agriculture or civil engineering. A major property used in categorizing soils is the size of the particles making up a soil. The individual or primary soil particles are referred to as textural separates.

Textural separates - The different textural separates in soils are classified into various sized groups. Soil particles are not generally spherical in nature; however, their size distribution is classified on the basis of equivalent diameters. The larger textural separates can be isolated by means of mechanical sieving. In this case the equivalent diameter refers to the diameter of a sphere that will pass through a given size opening. The finest mesh readily available (No. 200 B.S. sieve) has an aperture of approximately 0.08 mm. Textural separates smaller than this must be isolated using sedimentation techniques [2]. In the sedimentation technique, the soil is suspended in water and the velocity with which the particles fall is measured to determine their equivalent diameters. In this case, the equivalent diameter refers to the diameter of a

sphere that has the same density and settling velocity as the soil particles.

Several systems have evolved for classifying textural separates. Figure II-1 contains a comparison of some of these classifications. Both the United States Department of Agriculture (USDA) and the International Society of Soil Science classifications are used by agriculturists. Although these classifications are dissimilar in their definitions of sand and silt size ranges, they both use 0.002 mm ( $2\mu$ ) as the upper size limit of clays. Clay is the key textural separate in these two classifications. The physical and chemical properties of soil are affected to a much greater degree by the clay content of the soil than by the sand and silt content of the soil.

Atterburg [4], who suggested the International classification, established the  $2\mu$  upper limit of clay size based on bacteriological and physical properties. Bacteria cannot move in pores between grains smaller than this size. Also, clay particles finer than  $2\mu$  do not settle from suspensions but remain in a state of Brownian movement for a period of at least 24 hours [1]. Further justification for this definition of clay was provided by mineralogical studies which showed that relatively few unweathered primary minerals existed in fractions smaller than  $2\mu$  [2].

All soils contain a continuum of soil particle sizes however, the distribution of soil particle sizes varies

DA-CE USBR	Fines (silt or clay)						Fine sand		Coarse sand	
FAA	Clay		Silt			Fine sand		Coarse sand		
AASHTO ASTM	1) Colloids	Clay	Silt			Fine sand		Coarse sand		
USDA	Clay		Silt			Very fine sand	Fine sand	Medium sand	Coarse sand	Very coarse sand
ISSS	Clay		Silt		Fine sand			Coarse sand		
0.001 0.002 0.005 0.01 0.02 0.05 0.10 0.20 0.50 1.0 2.0										
Particle Size (mm)										

DA-CE = Department of Army, Corps of Engineers  
 USBR = U.S. Bureau of Reclamation  
 FAA = Federal Aviation Authority  
 AASHTO = American Association of State Highway Officials  
 ASTM = American Society of Testing and Materials  
 USDA = U.S. Department of Agriculture  
 ISSS = International Society of Soil Science  
 Note (1) = Reported with clay

Figure II-1. Classification of soil separates  $\leq 2.0$  mm on the basis of particle size (after Baver, Gardner, and Gardner [1]).

from soil to soil. The most accurate method of characterizing a soil is by its particle size distribution. An example of such a distribution is given in Figure II-2. The particle size distribution is generally integrated (averaged) over some specified particle size intervals, such as those given in Figure II-1. These averages are then ratioed with the integral of the entire particle size distribution, thereby providing the percentage content of each size interval chosen for averaging.

The composition of a soil according to such percentages can be visualized with the aid of a triangular diagram such as shown in Figure II-3. This triangular diagram illustrates soil categories based on the USDA textural separate classification shown in Figure II-1. A point corresponding to clay loam (35% clay, 30% silt, and 35% sand) is marked on the triangle as an example. The USDA soil classification diagramed in Figure II-1 and the resulting triangle of Figure II-3 will be used throughout the remainder of this document.

As pointed out earlier, it is the clay fraction of the soil that is most important in determining the physical and chemical characteristics of soils. This is a result of the fact that these properties are highly associated with the surface activity of the individual soil particles. Clay particles have a layered platelike structure that

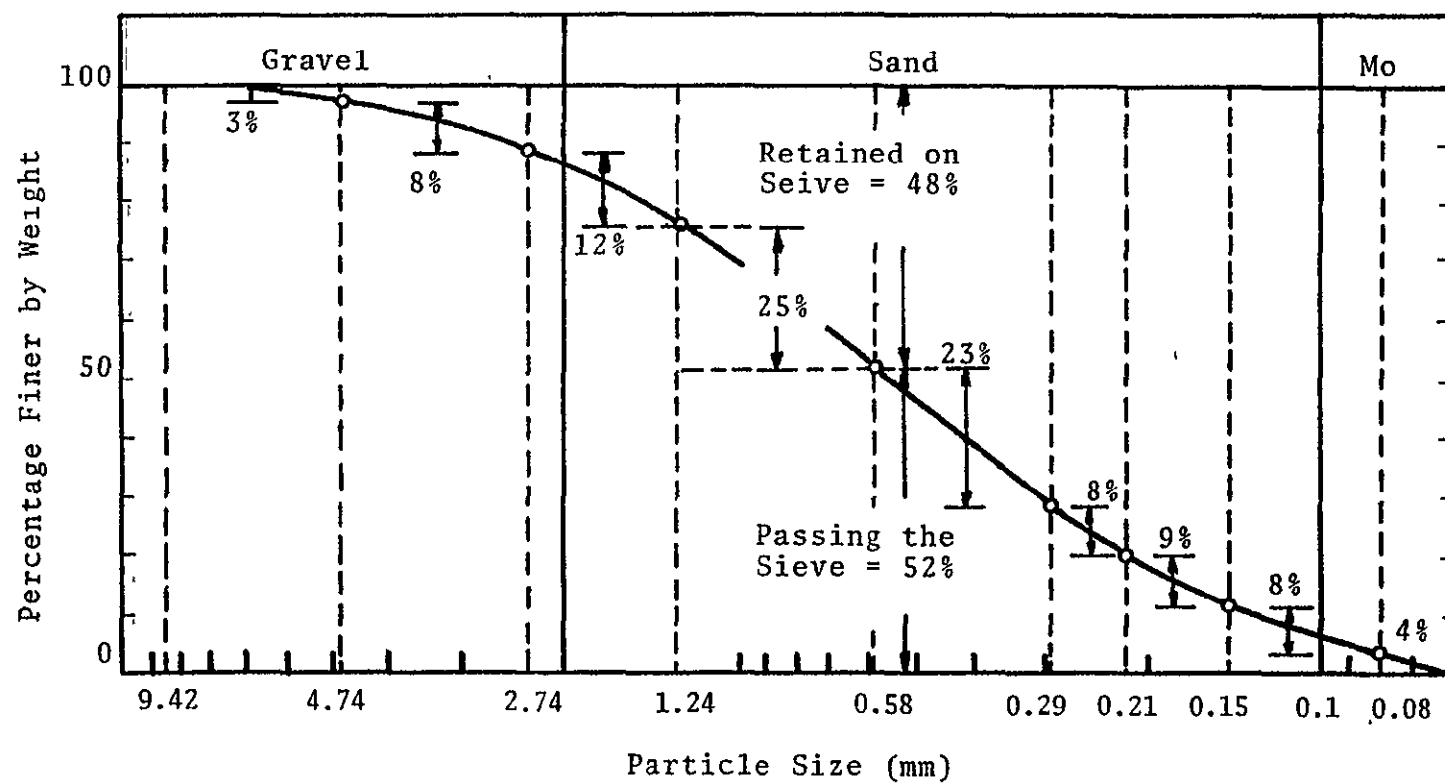


Figure II-2. Construction of grain-size distribution curve (after Kexdi [2]).

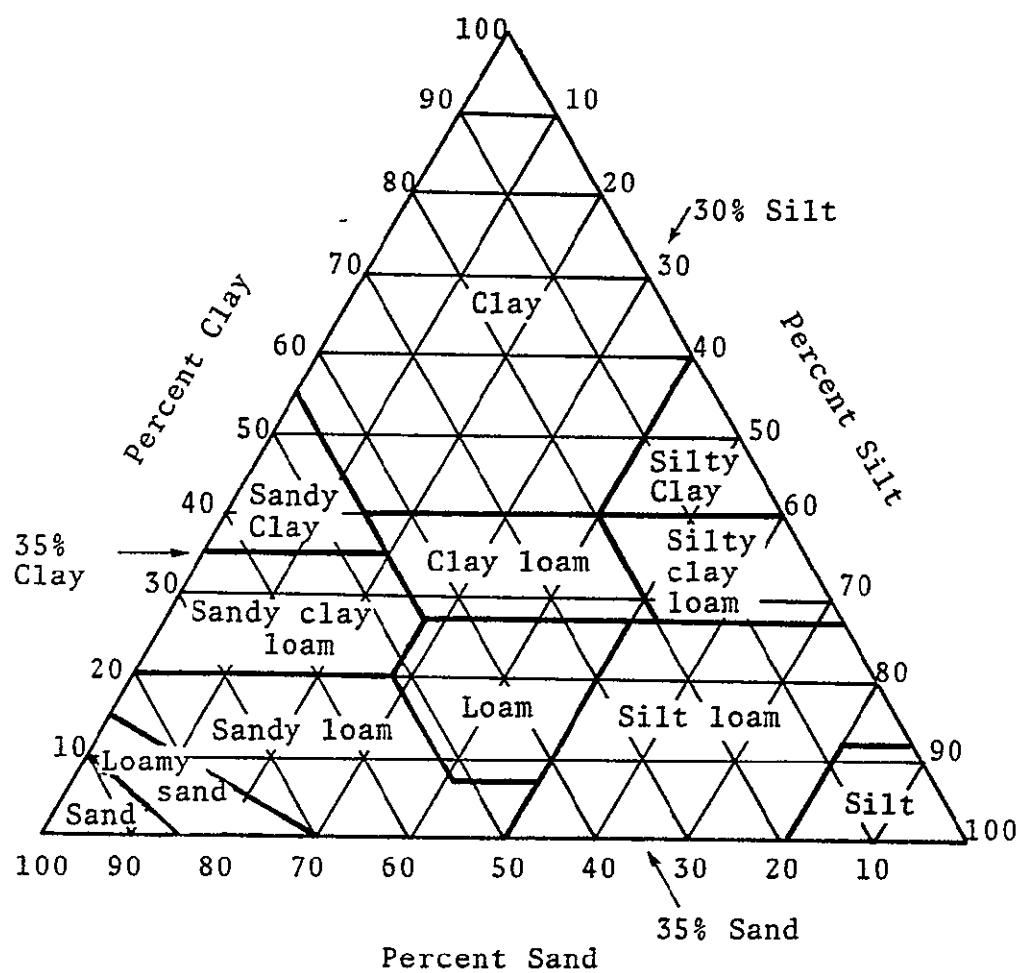


Figure II-3. USDA soil textural classification triangle.

results in very large surface areas per unit weight, much larger than the other textural separates. In addition, clay particles are not electrically neutral, but have negative charges associated with their surfaces. The large surface areas in conjunction with the surface charges allow clay particles to interact with other polar molecules and ions to a greater extent than the other textural separates. Since this interaction takes place on the surface of the clay particles it is termed "surface activity". A more detailed discussion on clay structure is provided in the next two sections.

The surface of clay particles - The extent of surface of a clay is generally expressed in terms of specific surface, square centimeters of surface per gram or per cubic centimeter of dispersed phase where the individual clay particles are separated. The specific surface of a particle is dependent on its size as well as its shape. This can be demonstrated by comparing the specific surfaces of different textural separates utilizing their equivalent diameters and assuming that they are spherical. Table II-1 demonstrates that a very small amount of material ( $\pi/6 \text{ cm}^3$ ) may have a very large surface area for very small individual particles. Note that a given volume of a  $2 \mu$  clay has 50 times the surface area of an equal volume of very fine sand. Colloidal clay ( $100 \text{ m}\mu$ ) has 20 times the surface area of  $2 \mu$  clay and 1000 times the surface area of very fine sand.



TABLE II-1

The Relation of Surface to Particle Size (after Baver, Gardner and Gardner [1])

Diameter of sphere	Textural name	Volume per particle ( $\pi/6$ ) $D^3$	Number of particles in $\frac{\pi}{6}$ cc	Total surface $\pi D^2 \times$ number of particles
1 cm	Gravel	( $\pi/6$ ) $(1)^3$	1	3.14 cm <sup>2</sup> (0.49 in. <sup>2</sup> )
0.1 cm (1 mm)	Coarse sand	( $\pi/6$ ) $(0.1)^3$	$1 \times 10^3$	31.42 cm <sup>2</sup> (4.87 in. <sup>2</sup> )
0.05 cm (500 $\mu$ )	Medium sand	( $\pi/6$ ) $(0.05)^3$	$8 \times 10^3$	62.83 cm <sup>2</sup> (9.74 in. <sup>2</sup> )
0.01 cm (100 $\mu$ )	Very fine sand	( $\pi/6$ ) $(0.01)^3$	$1 \times 10^6$	314.16 cm <sup>2</sup> (48.67 in. <sup>2</sup> )
0.005 cm (50 $\mu$ )	Coarse silt	( $\pi/6$ ) $(0.005)^3$	$8 \times 10^6$	628.32 cm <sup>2</sup> (97.34 in. <sup>2</sup> )
0.002 cm (20 $\mu$ )	Silt	( $\pi/6$ ) $(0.002)^3$	$125 \times 10^6$	1,570.8 cm <sup>2</sup> (1.69 ft <sup>2</sup> )
0.0005 cm (5 $\mu$ )	Fine silt	( $\pi/6$ ) $(0.0005)^3$	$8 \times 10^9$	6,283.2 cm <sup>2</sup> (6.76 ft <sup>2</sup> )
0.0002 cm (2 $\mu$ )	Clay	( $\pi/6$ ) $(0.0002)^3$	$125 \times 10^9$	15,708 cm <sup>2</sup> (16.9 ft <sup>2</sup> )
0.0001 cm (1 $\mu$ )	Clay	( $\pi/6$ ) $(0.0001)^3$	$1 \times 10^{12}$	31,416 cm <sup>2</sup> (33.8 ft <sup>2</sup> )

TABLE II-1 (Continued)

Diameter of sphere	Textural name	Volume per particle ( $\pi/6$ ) $D^3$	Number of particles		Total surface $\pi D^2$ x number of particles
			in $\frac{\pi}{6}$ cc		
0.00005 cm (500 m $\mu$ )	Clay	( $\pi/6$ ) (0.00005) <sup>3</sup>	$8 \times 10^{12}$	62,832	cm <sup>2</sup> (67.6 ft <sup>2</sup> )
0.00002 cm (200 m $\mu$ )	Colloidal Clay	( $\pi/6$ ) (0.00002) <sup>3</sup>	$125 \times 10^{12}$	157,080	cm <sup>2</sup> (169 ft <sup>2</sup> )
0.00001 cm (100 m $\mu$ )	Colloidal Clay	( $\pi/6$ ) (0.00001) <sup>3</sup>	$1 \times 10^{15}$	314,160	cm <sup>2</sup> (338 ft <sup>2</sup> )
0.000005 cm (50 m $\mu$ )	Colloidal Clay	( $\pi/6$ ) (0.000005) <sup>3</sup>	$8 \times 10^{15}$	628,320	cm <sup>2</sup> (676 ft <sup>2</sup> )

In the above examples the shape of the particles was assumed to be spherical. In reality, as will be described in the next section, clay particles have a platelike structure. Spheres have the smallest surface area per unit volume of all geometrical shapes. Platelike structures or disks have the largest. This is demonstrated in Table II-2 in which a  $2\mu$  spherical particle was used as the reference surface. It is seen that the surface area increases dramatically with particle shape. This indicates that if the shape of the particles had been taken into account in Table II-1, there would be an even more dramatic increase in specific surface as the particle size decreased. This results from the fact that clay particles tend to be plate-shaped particles with a thickness that is smaller than the lateral demension.

Chemical and mineralogical makeup of clay - It was mentioned above that clay is the surface active fraction of soil, and it was demonstrated that clay has the largest specific surface area of all the textural separates. As a result, clay has a high degree of physical and chemical activity and is the primary factor in determining the physical properties of the soil. Sand and silt separates contain many primary minerals that have considerable importance from the standpoint of soil development; however, influence on the physical properties of a soil is small.

TABLE II-2  
 Surface Area in Relation to Shape of Particle  
 (after Baver, Gardner, and Gardner [1])

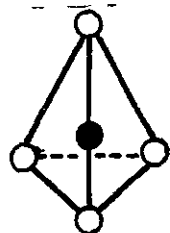
Shape	Radius (cm)	Volume (cm <sup>3</sup> )	Surface (cm <sup>2</sup> )	Increase in surface (percent)
Sphere	$1 \times 10^{-4}$	$4.2 \times 10^{-12}$	$1.26 \times 10^{-7}$	
Disk				
h = $1 \times 10^{-4}$ cm	$1.155 \times 10^{-4}$	$4.2 \times 10^{-12}$	$1.56 \times 10^{-7}$	23.8
h = $5 \times 10^{-5}$ cm	$1.67 \times 10^{-4}$	$4.2 \times 10^{-12}$	$1.84 \times 10^{-7}$	45.8
h = $2 \times 10^{-5}$ cm	$2.58 \times 10^{-4}$	$4.2 \times 10^{-12}$	$4.51 \times 10^{-7}$	257.8
h = $1 \times 10^{-5}$ cm	$3.65 \times 10^{-4}$	$4.2 \times 10^{-12}$	$8.59 \times 10^{-7}$	538.9

The clay mineral structure that causes clay to be highly surface active is discussed in the following paragraphs.

X-ray and petrographic techniques came into use in mineralogical studies of clays in the late 1920's and throughout the 1930's [1]. Through the use of these techniques it was demonstrated that clays are primarily crystalline minerals with the major constituent being silicon, aluminum, ferrous and ferric iron, magnesium, and oxygen atoms, plus hydroxyl groups. There are two basic structural units that are responsible for the various clay structures. One is a silicon tetrahedron (Figure II-4) in which a silicon atom holds oxygen atoms in such a way that they form corners of a tetrahedron. The other structural unit is the aluminum octahedron. In this unit six hydroxyl groups (OH) or oxygen atoms are arranged such that each forms a corner of an octahedron with an aluminum atom in the center holding them together. The details of how these basic structural units interact to form a clay mineral is provided in Baver, Gardner, and Gardner [1]. The general mechanism of the structural combination of these two basic structural units is important to understanding the interaction of clay with water.

In an idealized structure the silicon tetrahedrons link together forming a sheet known as the silica or tetrahedra sheet. In a similar fashion the aluminum octahedrons link together forming an alumina or octahedral

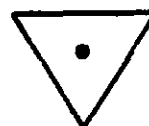
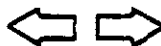
### Basic Silicon Tetrahedron



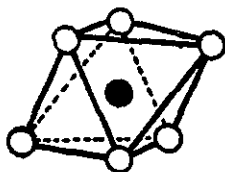
○ - Oxygen

● - Silicon

Represented by



### Basic Aluminum Octahedron



○ - Oxygen or OH

● - Aluminum, magnesium or iron

Represented by

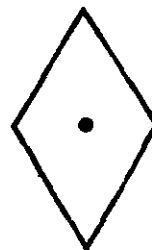


Figure II-4. The basic tetrahedron and octahedron structures and their graphical representations.






sheet. The base of the silica sheet is formed by oxygen atoms and the top and bottom of the alumina sheet are hydroxyl surfaces. These two sheets link together to form a clay mineral that has a platelike structure.

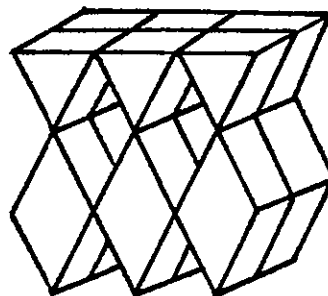
There are two clay mineral structures that can be formed by combining the silica and alumina sheets. A 1:1 lattice structure is formed by an alumina sheet and a silica sheet. A 2:1 lattice structure is formed by a alumina sheet sandwiched between two silica sheets. Schematic representations of these mineral structures are given in Figure II-5, as well as a representation of the linking of the structural units to form a clay.

As noted in Figure II-5, the idealized clay structures are electrostatically neutral and have clear-cut surfaces. This does not generally occur in nature. There can be substitutions in the crystal lattice (isomorphous substitutions) that cause the clay crystal to become negatively charged as well as causing the crystal structure to become expanded out of shape. For example, a trivalent aluminum atom can substitute for the tetravalent silicon atom in the silicon tetrahedron sheet. Similarly, the divalent magnesium and ferrous iron atoms and trivalent ferric iron can substitute for the aluminum atom in the alumina octahedron sheet. Both of these isomorphous substitutions increase the negative charge of the structure.

## 1:1 Mineral








Basic Unit

		<u>Charge</u>
	-6 O	-12
	-4 Si +16	
	-40+20H	-14
	-4 AL +12	
	-6 OH	-6
	<u>+28</u>	<u>-28</u>

Basic Mineral Structure

## 2:1 Mineral

Basic Unit

		<u>Charge</u>
	-6 O	-12
	-4 Si +16	
	-40+20H	-10
	-4 AL +12	
	-40+20H	-10
	-4 Si +16	
	-6 O	-12
	<u>+44</u>	<u>-44</u>

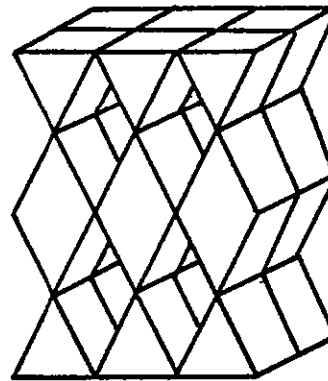
Basic Mineral Structure

Figure II-5. Diagrammatic sketches of clay mineral structures showing the sheeting effect.



This negative charge is generally balanced by an extra cation absorbed to the surface of the clay mineral. Cations that balance negative charges originating from substitutions within the crystal structure are called exchangeable cations. They can be displaced from the planar surfaces of the clay minerals by other cations or water molecules.

Isomorphous substitution of atoms with larger radii than the original atom causes strains in the crystal lattice and results in a nonidealized clay mineral structure. In addition, other physical departures from the ideal structure occur as a result of silica tetrahedra being inverted instead of having the apex pointed at the octahedra sheet. These nonidealized situations cause the planar surfaces of the clay mineral to be rough instead of smooth. Moreover, the edges of the crystal may be beveled and frayed resulting in broken bonds on these edges. These broken bonds also create negative charges that can be balanced by exchangeable cations. The total number of exchangeable cations is referred to as "cation exchange capacity".

The degree to which each of the above mechanisms (isomorphous substitutions and edge effects) contribute to the cation exchange capacity of a clay mineral depends on the type of clay structure under consideration. There are basically three major groups of clay minerals:

- 1) Kaoline (1:1 lattice)

- 2) Hydrous mica; major subgroup is illite (2:1 lattice)
- 3) Montmorillonite (2:1 expanding lattice).

There is little isomorphous substitution in the Kaolin group. The silica and alumina are held together through hydrogen bonding and are held together so tightly that cations or water molecules cannot permeate the interlayer positions between the kaolinite clay mineral layers. As a result, its colloidal properties are determined by the external clay surfaces only, and the surface area per unit weight is small. Since there is little isomorphous substitution, broken bonds on the edges of the clay mineral are primarily responsible for ionic reactions. This, coupled with the small surface area per unit weight, causes the cation exchange capacity to be very low, on the order of 10 milli-equivalents (me) per 100 grams of clay.

Illite, which is a major subgroup of the hydrous mica group, does have isomorphous substitution with the major substitutions occurring in the silica sheets. Non-exchangeable potassium ions balance these charges and hold the structural unit layers very tightly (Figure II-6). Since the unit layers are held tightly together the cation exchange capacity resides on the external surfaces or on the frayed edges of the crystal. The cation exchange capacity is on the order of 20 to 40 me per 100 grams of clay. For the most part, the nonexchangeable potassium ions

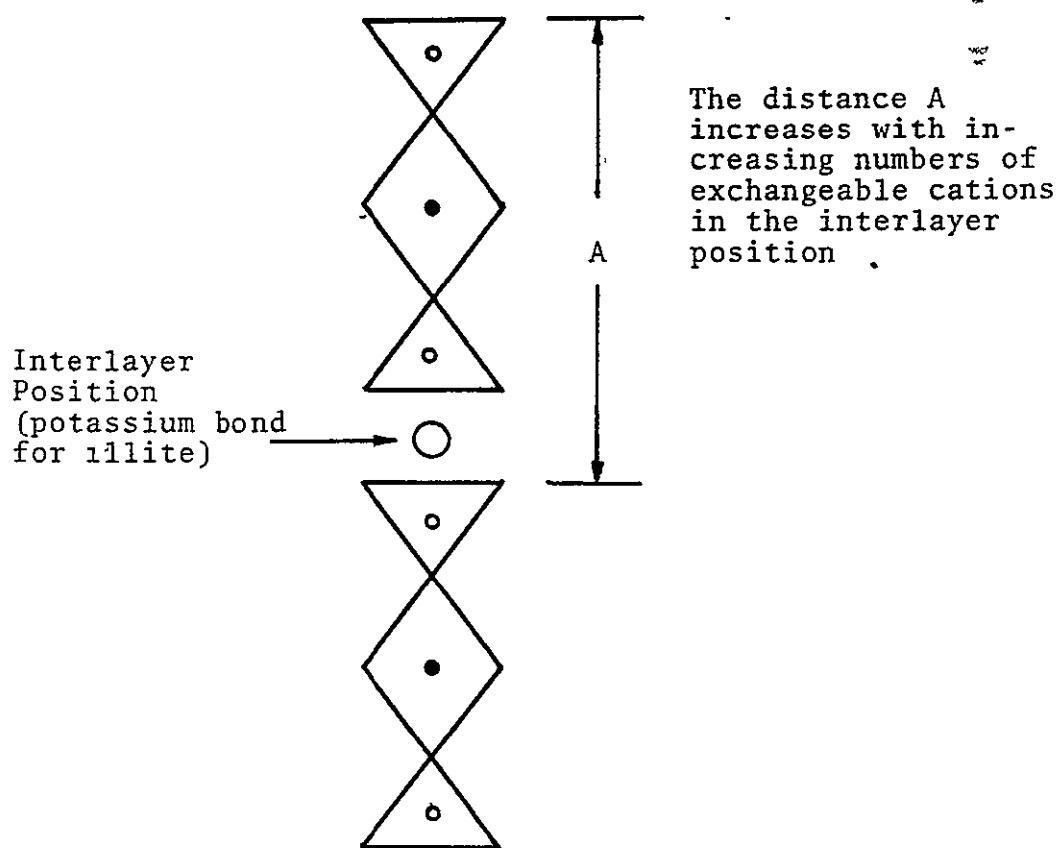


Figure II-6. Graphical representation of the layering of basic mineral sheets that forms interlayer positions for cations.

balances the charge imbalance resulting from the isomorphous substitution and as a result the cation exchange capacity does not reflect the degree of isomorphous substitution.

The montmorillinite group has a 2:1 unit layer structure with isomorphous substitution occurring in both the silica and alumina sheets. The crystal lattice structure can expand and contract depending on the amount of exchangeable cations present between the structural unit layers. Figure II-6 diagrams the expanding lattice structure. Montmorillonite has the highest cation exchange capacity of the three major clay groups. It varies between 80 and 150 me per 100 grams of clay.

The basic crystal lattice makeup of three groups of clays has been discussed as part of the background information for describing the interaction of water with soil. The discussion dealt solely with idealized clay minerals. It should be kept in mind that clay minerals do occur in which the unit layers are not uniformly stacked. These interstratified or mixed-layer clays can have different surface properties which affect the ionic exchange capacity of the clay mineral. However, the major points of the discussion were that clay is the dominating textural separate in determining soil-water interaction phenomena, and that the type of clay mineral structure is also of importance in soil-water interaction.

## Soil Water

From a structural standpoint there are four kinds of soil water: pore water, solvate water, adsorbed water, and structural water [2]. Pore water exhibits the same physical and chemical characteristics as bulk water and is capable of moving within the soil under hydrodynamic forces unless restricted by capillary action or entrapped by air bubbles. Solvate water is subject to polar, electrostatic, and ionic binding forces and forms a hydration shell around the soil grains, presumably not more than 200 molecules thick. Solvate water has a greater density and viscosity than bulk water, however, it can still move under hydrodynamic forces. Adsorbed water is a very thin layer of water of from 1 to 10 molecules (depending on the clay mineral) in thickness attracted to the external surface of clay minerals or held as interlayer water by minerals with expanding lattice structure. Adsorbed water cannot be moved by normal hydrodynamic forces. Structural water is actually hydroxyl groups that constitute part of the crystal lattice. Since this water is part of the soil structure, it is in reality not water and is not driven off unless the crystal lattice is destroyed.

Adsorbed and solvate water result from the fact that the crystal surfaces of clays are polar. As a result, they can attract polar molecules and ions from the environment

around them. Since water molecules are dipolar, they are attracted to the clay particles and to cations that are held by the clay lattice. A portion of the water molecules can enter between the layers of a crystal (interlayer water) such as montmorillonite, the most predominant type of clay. It is this interlayer water that causes clay to swell when wetted. The water molecules immediately around the polar surfaces are arranged in a highly oriented pattern and the electrostatic attractive forces are extremely great. Proceeding outward from the surface, successive layers of water molecules are linked together due to their polar nature to form a chainlike configuration, but their degree of orientation diminishes farther away from the crystal surface. The degree of orientation diminishes with distance from the crystal surface since the electrostatic attractive forces diminish with distance.

This entire complex is termed the adsorption complex, however, only the layer of water a few molecules thick that is tightly bound to the clay lattice is termed adsorbed water. The more loosely bound water molecules are termed solvate water. The type of cations adsorbed on a clay mineral greatly influences the thickness of the adsorbed and solvate layer of water the clay is capable of holding.

All solvate water can be driven off of a soil when it is heated in an oven at moderate temperature. However, adsorbed water cannot be completely driven off at moderate

oven temperatures since it is very tightly bound to the clay crystal lattice. Soil samples are normally dried to a constant weight at an oven temperature in the range of 105°C to 110°C [5]. However, this is an arbitrarily chosen temperature range [6]. Figure II-7 demonstrates the effect of oven temperature on the moisture of three types of clay minerals. Zero percent moisture in Figure II-7 corresponds to complete dehydration at which point all of the adsorbed water has been removed. Since there are no distinguishing features of these hydration curves at 105°C, it is obvious that 105°C is arbitrary and that the amount of adsorbed water left in the soil is a function of clay type.

### Soil-Water-Plant Interrelationships

The interaction of water with soil was described earlier in terms of the interaction of water with the clay particles. In this section techniques of describing the amount of water held in soil will be discussed; the energy state of the water held in the soil will be described in terms of potentials; and finally, the ability of crops to utilize the water in the soil is described in terms of these potential gradients. This discussion is designed to provide insight as to the parameters that are of importance in remotely measuring soil moisture for agricultural purposes.

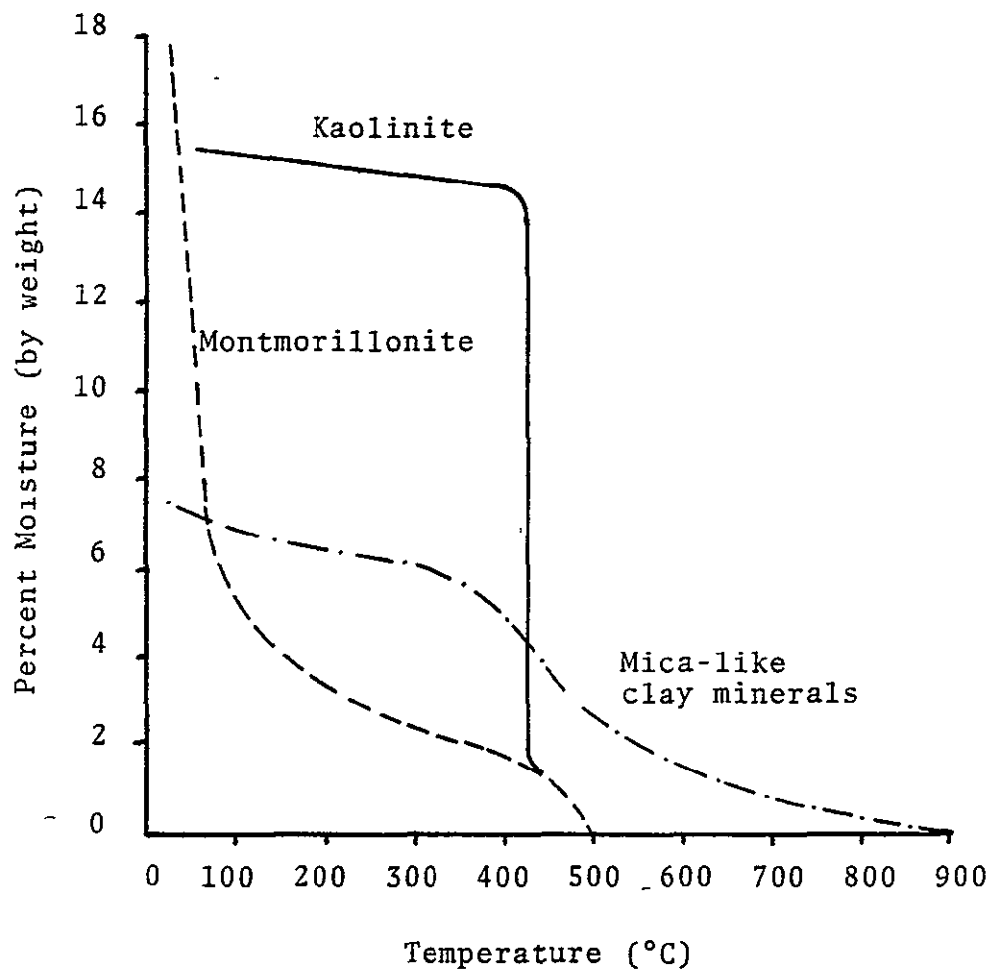


Figure II-7. Typical dehydration curves of different clay minerals (after Kezdi [2]).



## Soil Water Descriptions

There are two methods of describing the amount of water in a soil. One is to measure the water content on a per unit mass basis (gravimetric water content) and the other is to measure it on a per unit volume basis (volumetric water content). The importance of the basis used to measure soil moisture will become apparent in the section on soil permittivity.

Any specified volume of soil can be subdivided into three subvolumes as shown in Figure II-8.

$$V_T = V_a + V_w + V_s \quad (\text{II-1})$$

where

$V_T$  = total volume of soil

$V_a$  = volume of air

$V_w$  = volume of water

$V_s$  = volume of mineral and organic matter.

Obviously, the same equation holds true for the masses of each of the subgroups. The gravimetric water content,  $\theta_m$ , is defined by:

$$\theta_m = \frac{M_w}{M_s} \quad (\text{II-2})$$

where

$M_w$  = mass of water in the total volume

$M_s$  = mass of mineral matter in the total volume

Generally, the soil moisture on a per unit mass basis is

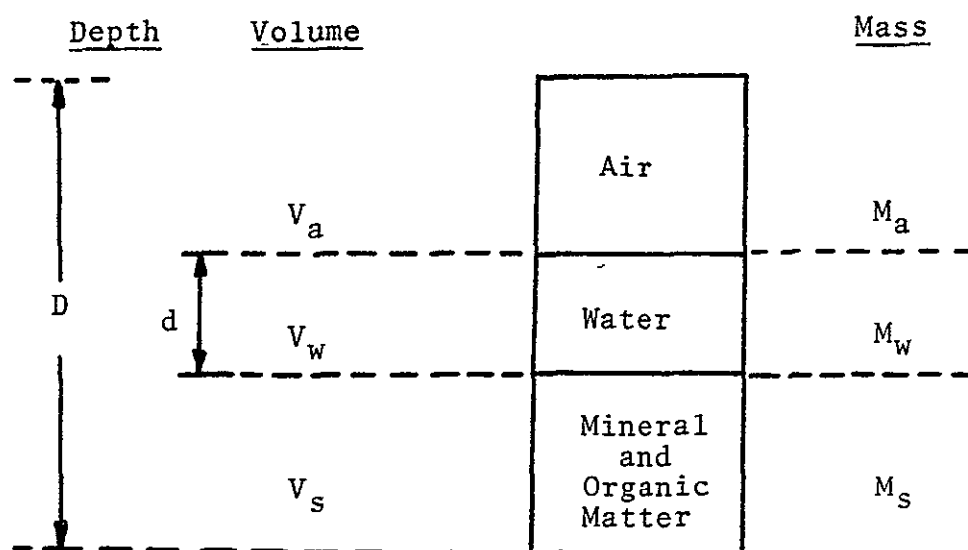


Figure II-8. Components of the soil-water complex.

converted to percentage by multiplying  $\theta_m$  by 100. The mass of water in a soil sample is generally determined by drying the soil sample in an oven. In order for soil moisture measurements to be consistent between soil samples, all of the soil samples should be dried at the same oven temperatures. In conventional ovens 105°C is generally used to dry soil. At this temperature, the absorbed water is not driven off.

When using microwave ovens to dry soil samples, consistency of drying is generally dependent on the experience of the operator. The load voltage standing wave ratio and the temperature of the sample have been shown to be good indicators of exposure time to obtain properly dried samples [7]. In most situations these parameters are not easily measurable. Care must be exercised when using microwave ovens since errors as high as 20% moisture by mass can occur as a result of inconsistency in drying different clay types [8]. However, the ability to utilize microwave ovens for drying soil samples adequately has been demonstrated by Miller et al. [9].

Water content by volume  $\theta_v$ , is defined by

$$\theta_v = \frac{V_w}{V_T} \quad (\text{II-3})$$

$\theta_m$  and  $\theta_v$  can therefore be related by the bulk density,  $\rho_B$ ,

of the soil which is defined as the mass of the soil divided by the total volume.

$$\rho_B = \frac{M_s}{V_a + V_w + V_s} = \frac{M_s}{V_T} \quad (\text{II-4})$$

Since

$$\theta_m = \frac{M_w}{M_s} = \frac{\rho_w V_w}{\rho_B V_T} \quad (\text{II-5})$$

then

$$\theta_m = \frac{\rho_w}{\rho_B} \theta_v \quad (\text{II-6})$$

The bulk density of water is unity by definition. As a result, the water content by volume is simply the water content by weight multiplied by the bulk density

$$\theta_v = \rho_B \theta_m \quad (\text{II-7})$$

The soil moisture by volume is not only a useful parameter from the standpoint of permittivity of soil, but it can also be used to calculate the equivalent depth of water in some specified soil column from which the sample was acquired. The equivalent depth of the water specified by "d" in Figure II-8 could be a useful parameter in the determination of irrigation needs. The equivalent depth is calculated by multiplying the volumetric soil moisture

by  $D$ , the depth of the volume from which the soil sample was acquired, i.e.

$$d = D \rho_s \theta_m \quad (\text{II-8})$$

### The Energy State of Soil-Water

Most processes involving water in soil and plant systems can be described in terms of the potential energy of the water in the soil. Potential energy is measured by the force required to move a body directly against a force field. It is the product of the force times the distance. The potential energy associated with an increment of water can be assessed by the forces acting upon it. Potential energy differences from point to point in isothermal systems determine the direction of flow of water through a soil.

There are several forces that act upon water in soil; for example, the pull of the earth's gravitational field, the attractive forces of the soil surfaces, and weight of unsupported soil acting upon water below that soil. Also, ions that are dissolved in the water attract water molecules and resist their being pulled away.

Each of these forces, plus others not mentioned, give rise to a potential energy. However, some of these separate potentials are combined into a single potential for

convenience. The total water potential is the sum of matric, gravity, pressure, osmotic, and overburden potentials. When water is at rest in the soil its total potential must be zero.

Matric potential is a measure of the attraction of solid soil surfaces for water as well as the attraction of water molecules for each other. It is this potential that gives rise to the unbalanced forces across air-water interfaces that cause the phenomenon of surface tension. The matric potential is historically referred to as capillary potential since it is analogous over a significant part of its range to the situation that exists where water rises in small capillary tubes. However, in a disperse system such as soil, it extends beyond simple capillary phenomena. As the water content of the soil decreases, a point is reached where the water content of the pore spaces between soil particles (which is affected by capillary action) becomes negligible compared to the water held directly on the particle surfaces. Matric potential is defined with respect to some reference water table. Matric potential of water above the reference water table is negative while the matric potential increases to zero at the reference water table and remains zero below the reference water table.

Gravity potential is that potential that arises due to the pull of gravity. Work must be done on water to

raise it to a point above the reference water table where the gravity potential is positive. Below the reference water table, work is done by the water and the gravity potential is negative. For water at equilibrium below the reference water table, the gravity and matric potentials are equal and opposite in sign.

Osmotic potential results from the hydration of ions in the soil solution. The polar nature of water causes water molecules to be attracted to ions in the soil solution. These attractive forces tend to orient water around ions and the osmotic potential refers to the work required to pull water away from these ions. Clay particles suspended in a solution will cause the same phenomenon because of the attraction of clay for water. However, since the clay particle is a solid and is not an ion, this is considered to be a matric effect.

Osmotic potentials are important in dealing with plants. Assuming a plant root can be modeled as a semi-permeable membrane across which water molecules can pass, but salt ions cannot, then osmotic potential can develop across this membrane if there are dissolved ions in the soil water. (Actually, plant membranes selectively pass ions.) The attraction of ions in the soil water to water molecules in the plant root require the plant to develop a larger root potential in order to acquire water from the soil.

Pressure potential is due either to the weight of water at a point under consideration or to gas pressure that is different from that which exists at the reference position. Changes in atmospheric pressure can produce a pressure potential, however, the pressure potential produced in this fashion is generally negligible in comparison to the pressure potential resulting from water weight. The pressure potential at a point beneath the water table is equal and opposite to the gravity potential that is measured from the free water surface. Overburden weight of unsupported soil produces a potential similar to pressure potential except that it is a result of the weight of the soil that is free to move. This potential is termed overburden potential.

#### Soil-Water-Plant Relations

All of the potentials briefly described in the paragraphs above are related to the flow of water through soil. However, the controlling potentials in soil-water-plant relations are the matric potential and the osmotic potential. These potentials describe the energy that is required by the plant to draw water from the soil. Gravity potential also affects the uptake of water by plants since work is required to move water from the root zone to the plant. However, this potential is small in comparison to the matric and osmotic potentials the plant must overcome.



It is quite significant that soil-water potential is a major factor in the ability of a plant to take water from the soil. Its importance lies in the fact that soil of different textures can hold different percentages of soil moisture by weight at the same matric potential. The significance of this to the remote sensing of soil water using microwave sensors will become apparent in the discussion of soil-water-permittivity relationships. It will be demonstrated that the microwave permittivity of soil is dependent not only upon soil moisture by volume (total number of water molecules), but also on the matric potential at which that water is held. This suggests that it may be possible to make a direct measurement of the water available to a plant.

The ability of different soil types to hold different amounts of water at the same matric potential is graphically demonstrated by Figure II-9. Figure II-9 is a plot of gravimetric water content (soil moisture by weight) as a function of matric potential (this assumes pure water so that the osmotic potential is zero). Notice that the matric potential is given in bars of pressure. This arises from the fact that the potential energy of soil water is generally expressed in terms of per unit quantity of water on a volume basis. The units are force-length divided by volume, which is the equivalent unit of pressure.

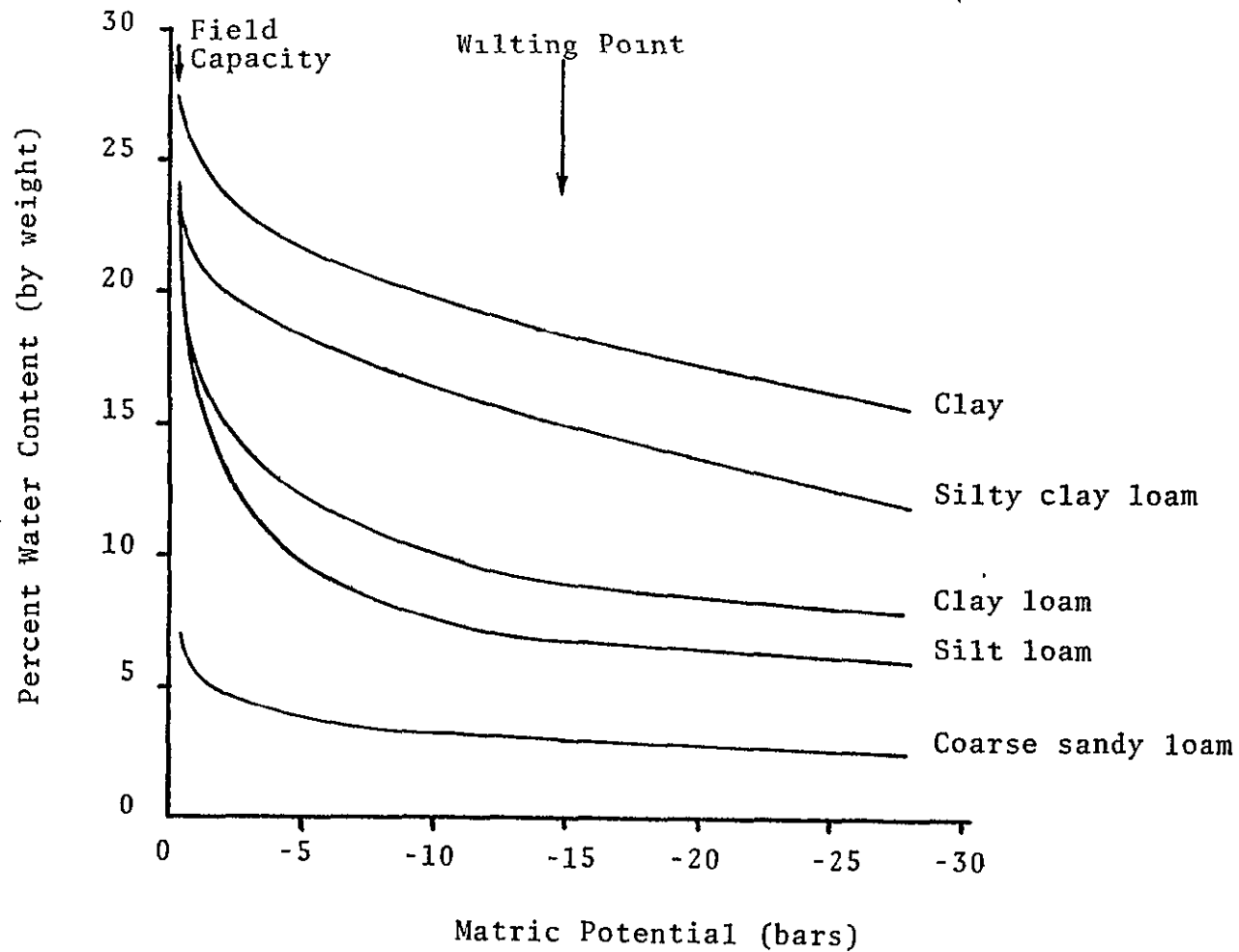


Figure II-9. Matric potential of soil fractions as a function of texture and water content (after Taylor and Ashcroft [10]).

A matric potential of zero bars corresponds to a saturated soil water condition. At this point all of the soil pores are filled with water. The matric potential at which water is held to the soil particles as the soil dries is a function of the specific surface of the soil and the cation exchange capacity. As a result, soils with larger clay contents hold more water than soils with lesser clay contents at the same matric potential. The very steep section of the curves of Figure II-9 correspond to water draining from the large soil pores where there is little effect due to matric potential. As the pores empty, a higher percentage of the remaining water is in contact with the soil surfaces where it is held by higher matric potential forces.

Soil water that is available to the plant can be defined in terms of the field capacity and wilting point of the soil. Field capacity has been defined as the water content of a soil profile, usually in the rooting zone, after the rate of drainage from an initially saturated profile has become negligibly small.

No single criterion exists for determining what is considered to be negligible drainage. As a result, the definition of field capacity is somewhat arbitrary. Generally,  $-1/3$  bar of matric potential is arbitrarily taken to be field capacity [11]. However, soils of different

percentages of textural separates, compaction, stratification, etc., have considerably different drainage characteristics. This means that different fields or even different locations within the same field could be at different matric potentials but could have equivalent "negligible" drainage. This effect could result in very large errors of water retention estimates when field capacity is arbitrarily associated with a particular matric potential such as  $-1/3$  bar. The wilting point of a plant is defined as that water content below which the plant cannot recover from the wilting symptoms. This has been shown to occur at approximately -15 bars [12], however, it is somewhat dependent on plant type and the speed at which the plant was wilted.

The water that is available to a plant is roughly that water content at the field capacity minus the water content at the wilting point. Figure II-10 is a plot of the available water as a function of percentage clay content. This data was obtained from Figure II-9. Figure II-10 demonstrates that from an available water standpoint, loams are the optimum soil for vegetation. It should be noted that moisture is only one ingredient for good vegetation growth. Soil temperature and soil aeration in the root zone are also critical items that cannot be overlooked in agricultural situations.

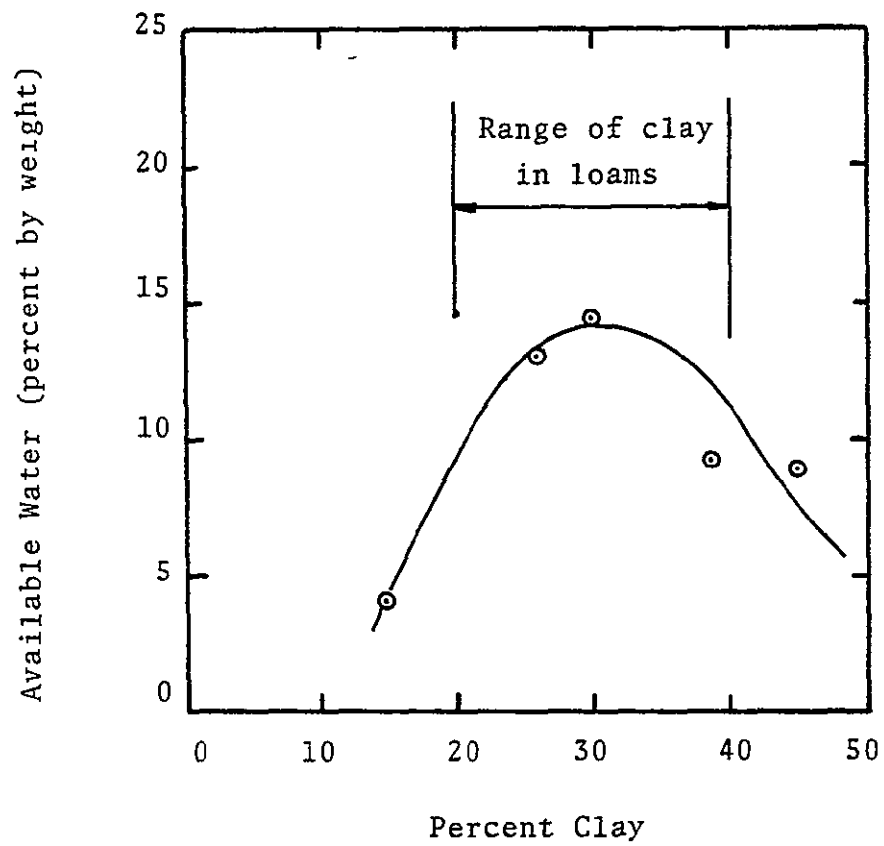


Figure II-10. The availability of water to plants as a function of percentage clay content.

## Soil Permittivity

Quantitative measurements of soil permittivity are of vital importance to the interpretation and basic understanding of the interactions of electromagnetic energy with natural and agricultural terrain. Values of permittivity are a basic input to models describing emission and scattering phenomena at microwave frequencies. As a result, an understanding of the permittivity of soil must be developed before quantitative methods of interpreting microwave measurements can be realized. Microwave measurements are analyzed to determine the effect of changes in the permittivity of the soil. The relationship between soil moisture and soil permittivity provides the soil moisture information available from measurements of the microwave response of soil. Permittivity measurements made at L-band (1.4 GHz) at Texas A&M University [13] will be used to demonstrate the effect of permittivity on moisture content. Following this discussion is a summary of the effects of soil temperature, frequency, and adsorbed cations.

In the following discussion, permittivity is a complex quantity. In the open literature the real part of the permittivity is often referred to as dielectric constant while the imaginary part is related to conductivity. Relative permittivity is the ratio of the real and imaginary part of the permittivity to the dielectric constant of

free space. As a result, relative permittivity is a dimensionless quantity.

### Soil Moisture Dependence

Measurement results - The measurements of soil permittivity at L-band reported by Newton and McClellan [13] were made as a function of soil texture at a constant environmental temperature of about 25°C. Figures II-11 through II-16 contain plots of these measurements as a function of gravimetric moisture content. Table II-3 identifies the soil samples that were used by texture and indicates their respective salt contents. The permittivity of these soils appears to be dependent on soil texture when plotted as a function of percent moisture by weight.

All of the soils described in Figures II-11 through II-16, except the sand sample, have a relatively high clay content (greater than 31%) and as a result have two pronounced regions in the real part,  $\epsilon_r'$ , of the relative permittivity plots. The permittivity of the sand sample has two pronounced regions also, but the region near 0% moisture is smaller than for the samples with higher clay content. Each of the soils measured have the same value of  $\epsilon_r'$  at 0% moisture. In addition, the slope of  $\epsilon_r'$  is the same for all of the soils, approximately 0.144 per percent moisture, from 0% moisture to a "transition" region where

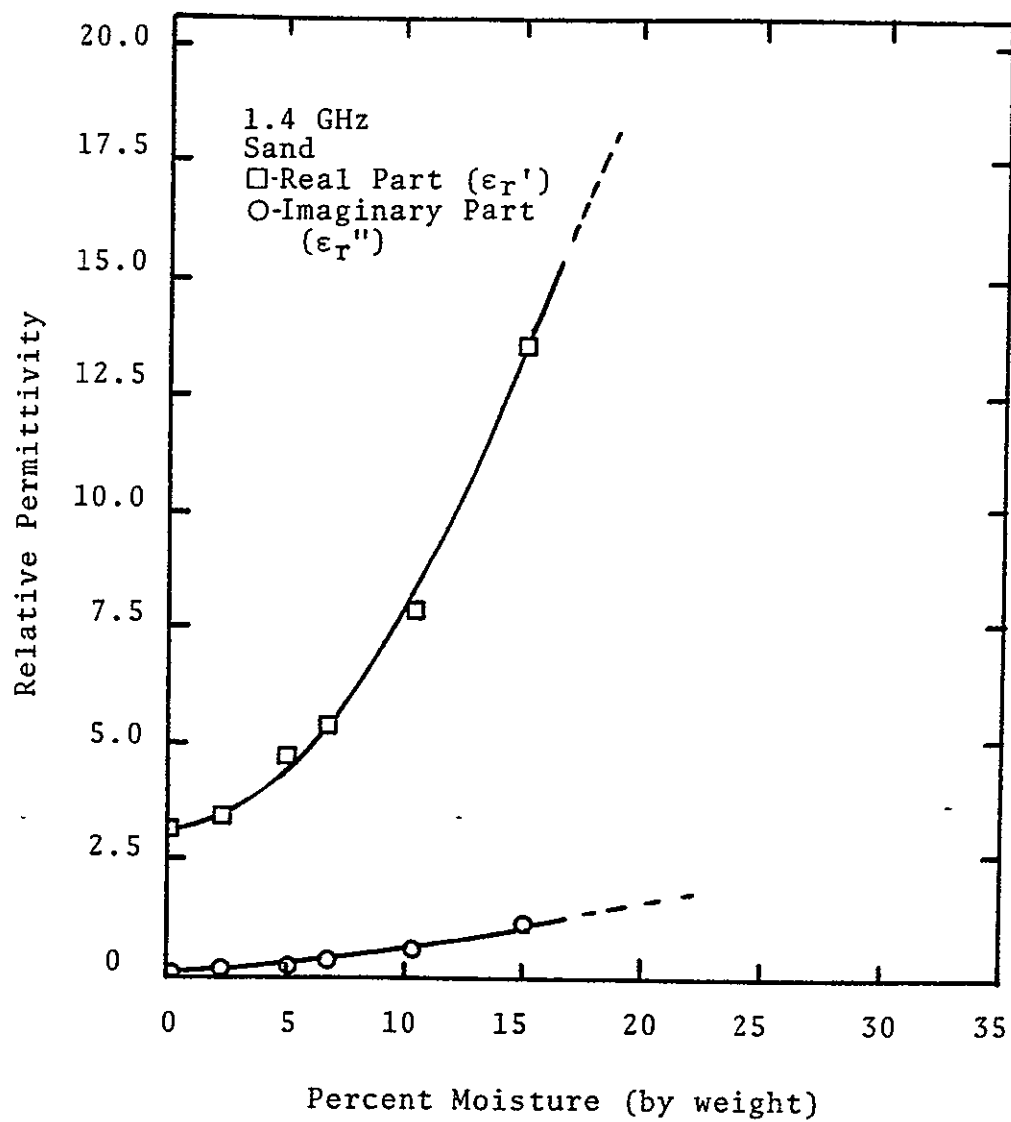


Figure II-11. Relative permittivity of sand as a function of moisture by weight.



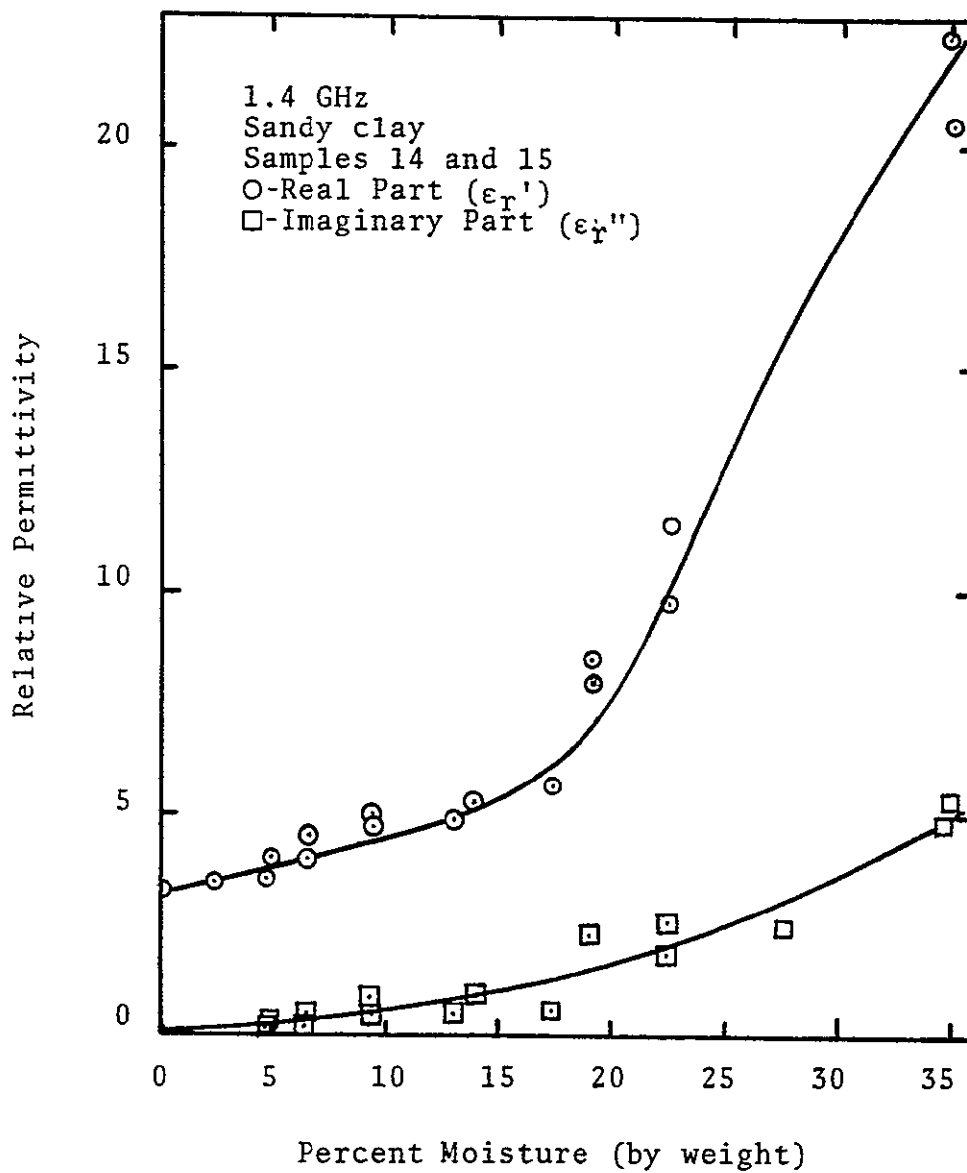


Figure II-12. Relative permittivity of sandy clay as a function of moisture by weight.

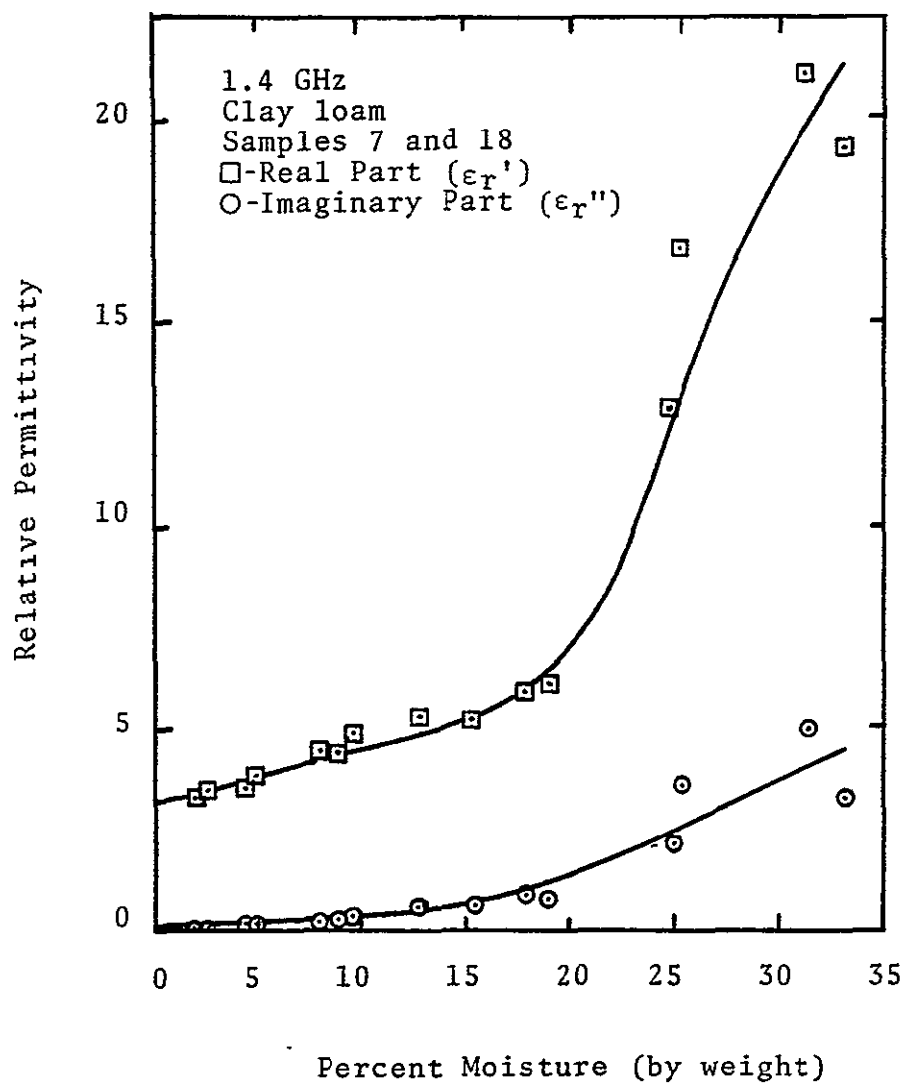


Figure II-13. Relative permittivity of clay loam samples 7 and 18 as a function of moisture by weight.

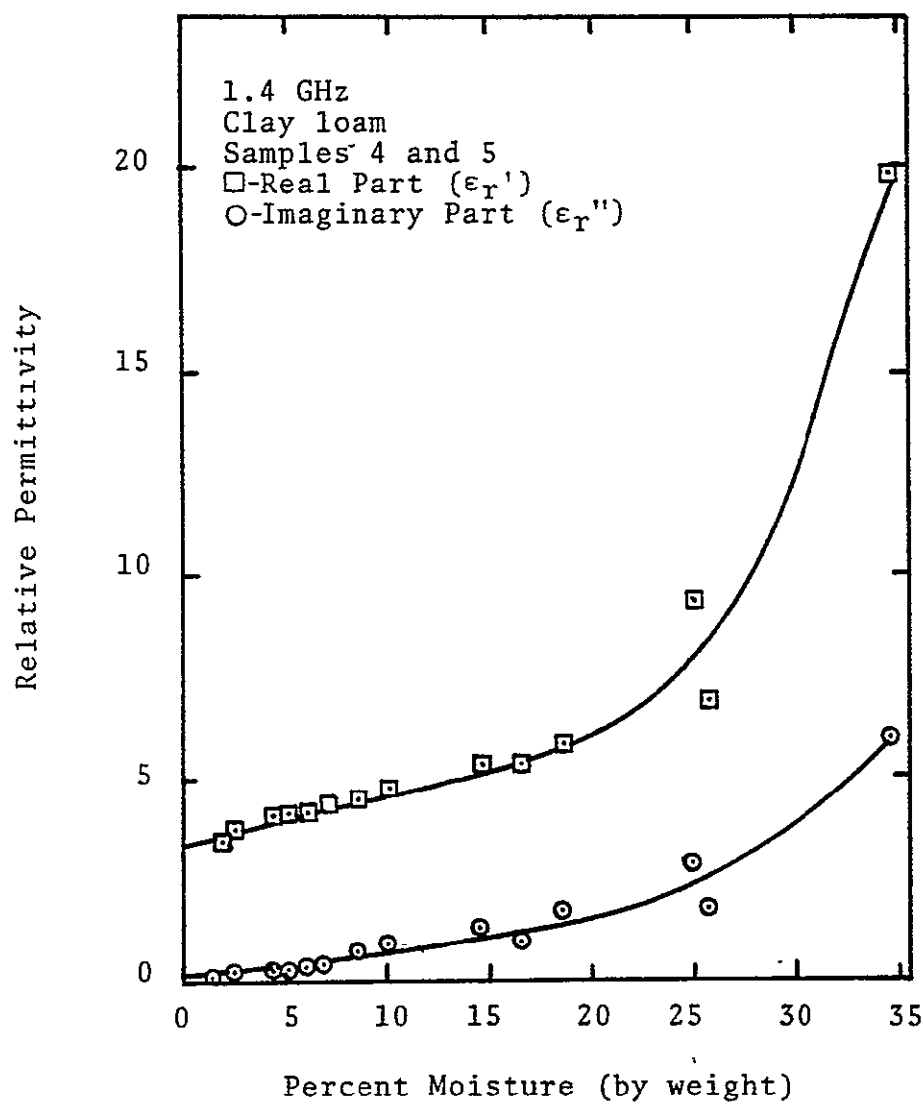


Figure II-14. Relative permittivity of clay loam samples 4 and 5 as a function of moisture by weight.

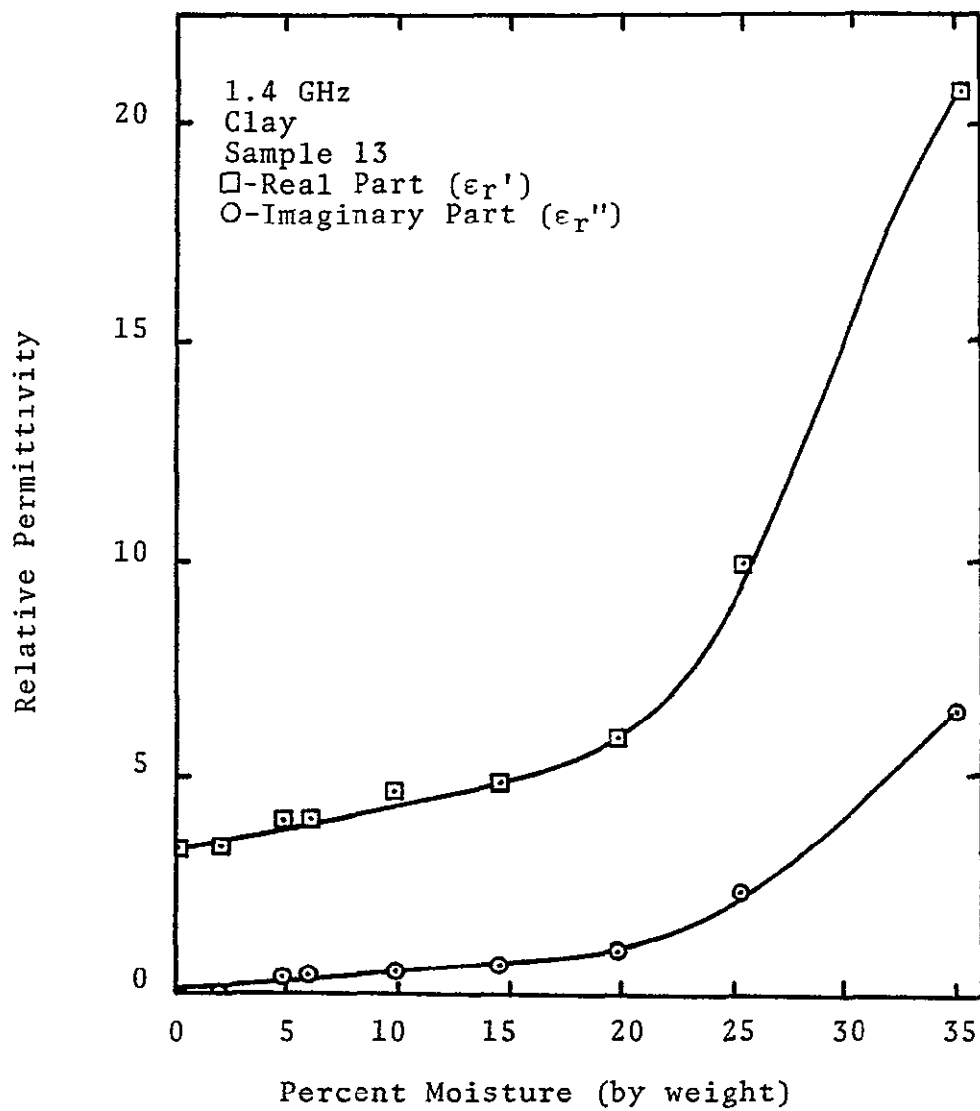


Figure II-15. Relative permittivity of clay as a function of moisture by weight.

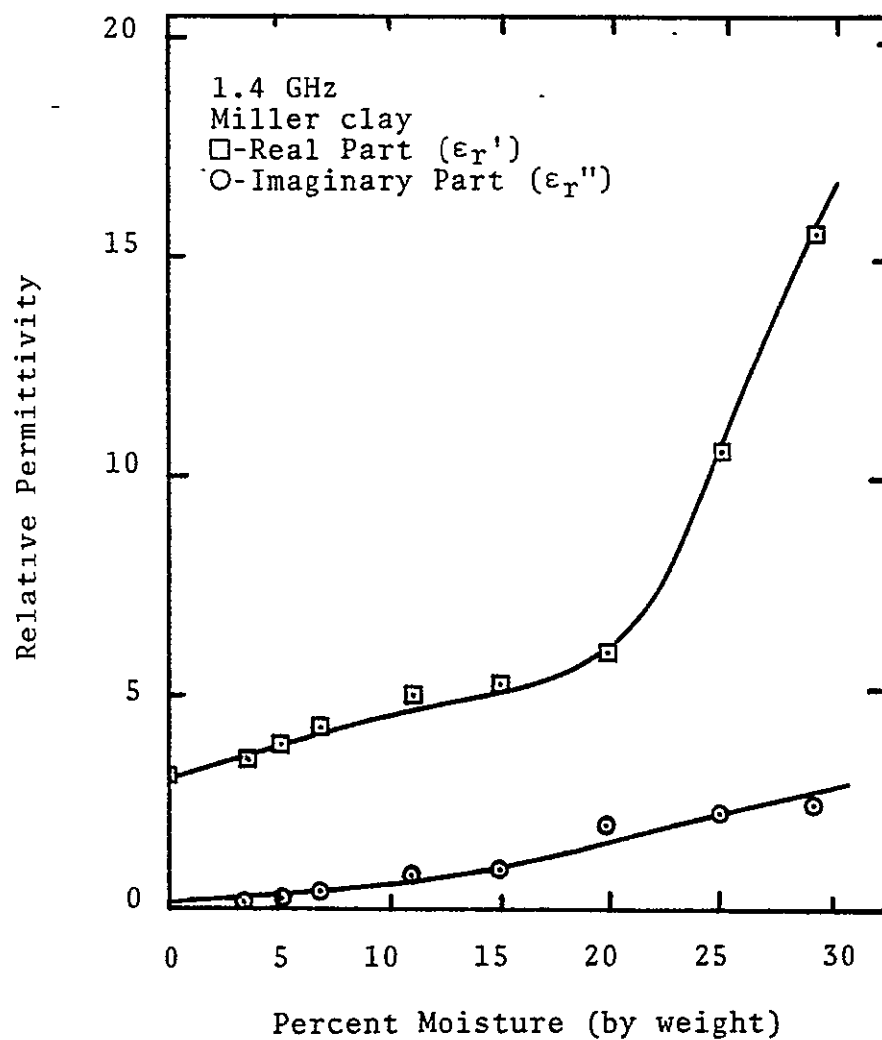


Figure II-16. Relative permittivity of miller clay as a function of moisture by weight.

Table II-3

## Results of Physical and Chemical Analysis of the Soil

## Samples Used in the Permittivity Analysis

Sample	Percentage			Texture*	Salt (ppm)	pH	Reaction Description
	Clay	Silt	Sand				
1	32.0	10.0	58.0	SCL	1523.2	6.6	Neutral
2	26.0	8.0	66.0	SCL	512.0	6.9	Neutral
3	27.2	18.8	54.0	SCL	550.4	7.0	Neutral
4	35.2	28.0	36.8	CL	371.2	7.2	Neutral
5	33.2	24.0	42.8	CL	166.4	7.4	Mildly Alkaline
6	33.2	16.0	50.8	SCL	204.8	7.5	Mildly Alkaline
7	39.0	22.0	39.0	CL	268.8	7.5	Mildly Alkaline
8	26.0	4.0	70.0	SCL	243.2	7.0	Neutral
9	32.0	14.0	54.0	SCL	268.8	7.3	Neutral
10	25.2	10.0	64.8	SCL	332.8	7.3	Neutral
11	26.0	12.0	62.0	SCL	449.2	6.7	Neutral
12	26.0	4.0	70.0	SCL	170.2	7.1	Neutral
13	43.6	12.0	44.4	C	320.0	7.3	Neutral
14	37.6	8.0	54.4	SC	170.2	7.5	Mildly Alkaline
15	41.6	10.0	49.4	SC	640.0	7.4	Mildly Alkaline
16	27.6	8.0	64.4	SCL	358.4	7.5	Mildly Alkaline
17	25.6	8.0	66.4	SCL	268.8	7.8	Mildly Alkaline
18	31.0	36.0	33.0	CL	256.0	7.6	Mildly Alkaline
Miller							
Clay	62	35	3	C			
Sand	7	7	86	S			

\*S-sandy; C-clay; L-loam; based on the USDA textural classification

the slope quickly changes to approximately 1.02 per percent moisture.

The transition region is simply that moisture region within which the permittivity curve has a sharp slope change. The transition moisture is a function of soil texture. Notice that for sand, (Figure II-11) the transition moisture is low, approximately 3%. For heavy clay (Figures II-15 and II-16) it occurs at approximately 20%, while the soils with slightly less clay have a transition moisture that is generally a little less than 20%. The imaginary part of the permittivity,  $\epsilon_r''$ , also changes slope at the transition moisture. This is clearly evident on all plots except Figures II-11 and II-16 which are sand and Miller clay, respectively.

Permittivity of soil has been reported by a number of authors in an effort to explain its dependence on moisture, temperature, and texture. Cihlar and Ulaby [14] provide a comprehensive review of these measurements. Experimental evidence indicates that "dry" soils exhibit practically the same dielectric properties (at a particular frequency) independent of their texture and that it is the water that is added to the soil (as distinguished from structural water) that produces the polarizing characteristics of soils. Wiebe [15] and Lundien [16] have explained the slow increase in the real part of the permittivity for moistures less than the transition moisture to be due to water in the

adsorption complex. Adsorbed water is tightly bound to the clay particles and therefore cannot change positions under the influence of an electric field unless it moves in conjunction with the soil particle to which it is attached. The theory is advanced that the adsorbed water does not contribute to the dielectric properties of the soil independent of the soil particles. This theory fits the data in Figures II-11 through II-16, since  $\epsilon_r'$  is constant for all of the soils at 0% moisture (where there is no solvate water). In addition, it is further theorized that it is the solvate water that produces the dielectric response of soil for moistures below the transition moisture, and the combination of solvate and pore water that produces the dielectric response above the transition moisture.

This theory seems plausible since all of the solvate water has been driven off when a soil is oven dried. As water is added to the soil, the water becomes loosely attracted by the clay particles in the form of solvate water until the capacity of the particular soil type has been reached, at which time any additional water becomes pore water. This is further supported by the fact that solvate water is somewhat mobile, but is attracted by electrostatic forces that can cause the relaxation properties of the solvate water molecules to be different from that of bulk water. In addition, pore water can be



considered to be bulk water since it is essentially unmodified by electrostatic forces.

The above theory indicates that the permittivity of soil is only dependent on the soil texture by the fact that the soil texture determines the amount of water that can be held as solvate water. The transition moisture should then correlate with field capacity since the amount of solvate water a soil can hold and the field capacity of a soil are both dependent on soil texture. Figure II-17 is a plot of field capacity as a function of transition moisture. Field capacity was calculated based on a regression equation generated for the soils of the Phoenix, Arizona area by T. Schmugge of the NASA Goddard Space Flight Center. The correlation between field capacity and transition moisture is obvious. Wilting point defined for a particular crop type can also be correlated in this manner.

Since it is the number of dipole moments (water molecules) that produce the dielectric properties of soil, then the permittivity of soil should be examined as a function of volumetric soil moisture (grams  $\text{H}_2\text{O}/\text{cm}^3$ ). The percent moisture by weight does not indicate the number of water molecules present. The same percentages of moisture by weight do not necessarily correspond to equal amounts of water for different soil types since the bulk

$$\text{Field capacity} = 25.1 - 2.207 (\% \text{ sand}) + 0.221 (\% \text{ clay})$$

- |                       |                     |
|-----------------------|---------------------|
| △-Miller clay         | □-Clay loam (7, 18) |
| ○-Clay (13)           | ▲-Clay loam (4, 5)  |
| ●-Sandy clay (14, 15) | ○-Sand              |

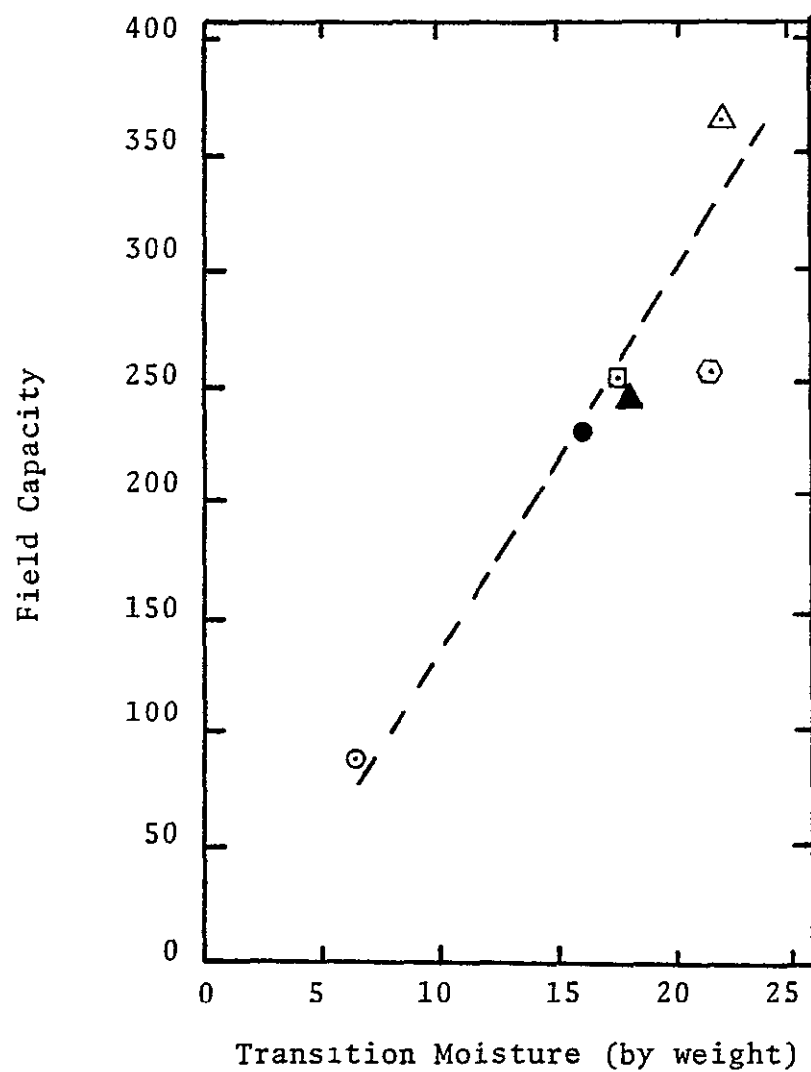


Figure II-17. Field capacity as a function of transition moisture.

density of each could be different. This indicates that the permittivities in Figures II-11 through II-16 should be plotted as a function of volumetric water content thereby removing the effects of bulk density. The moistures corresponding to each permittivity measurements were converted to a volumetric basis using the bulk density of the soil corresponding to each individual measurement. Figures II-18 through II-23 demonstrate the behavior of permittivity as a function of volumetric water content (grams  $H_2O/cm^3$ ). These plots do not show as sharp a break at the transition moistures as do Figures II-11 through II-16. Neglecting the sand sample, it can be seen that the permittivities for moistures less than the transition region are independent of soil type, as expected, and only dependent on the amount of solvate water. The sand sample actually fits this criterion also since its permittivity at zero moisture is equal to the others, but its transition region starts almost immediately since coarse sand holds practically no solvate water.

In addition, based on the theory set forth, it is expected that the permittivity above the transition region will be independent of soil type and only dependent on the amount of pore water present in the soil. This can be seen to hold true by plotting permittivity as a function of volumetric moisture minus volumetric transition moisture

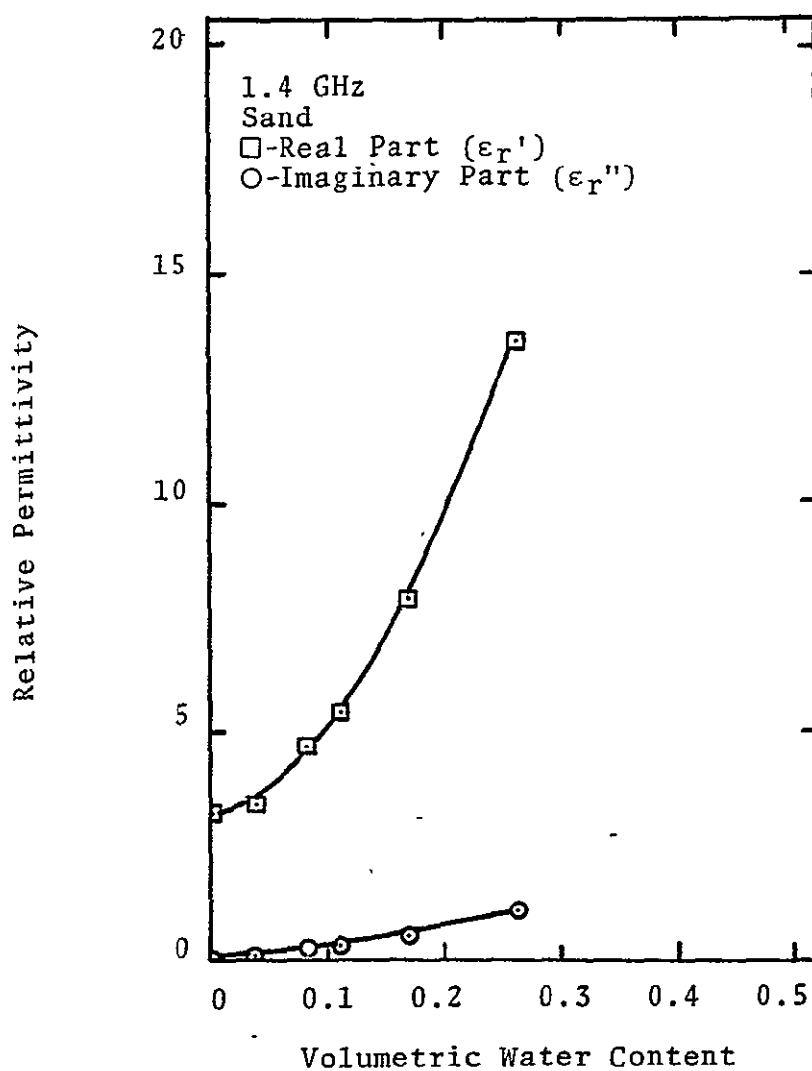


Figure II-18. Relative permittivity of sand as a function of volumetric water content.

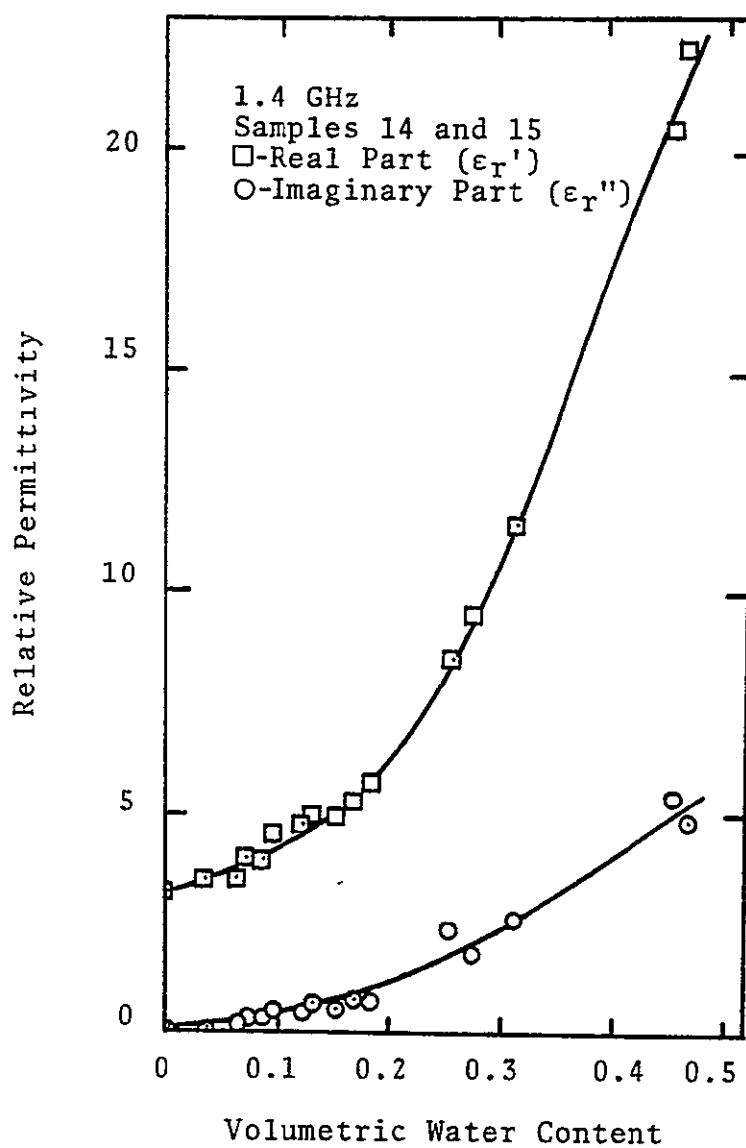


Figure II-19. Relative permittivity of samples 14 and 15 as a function of volumetric water content.

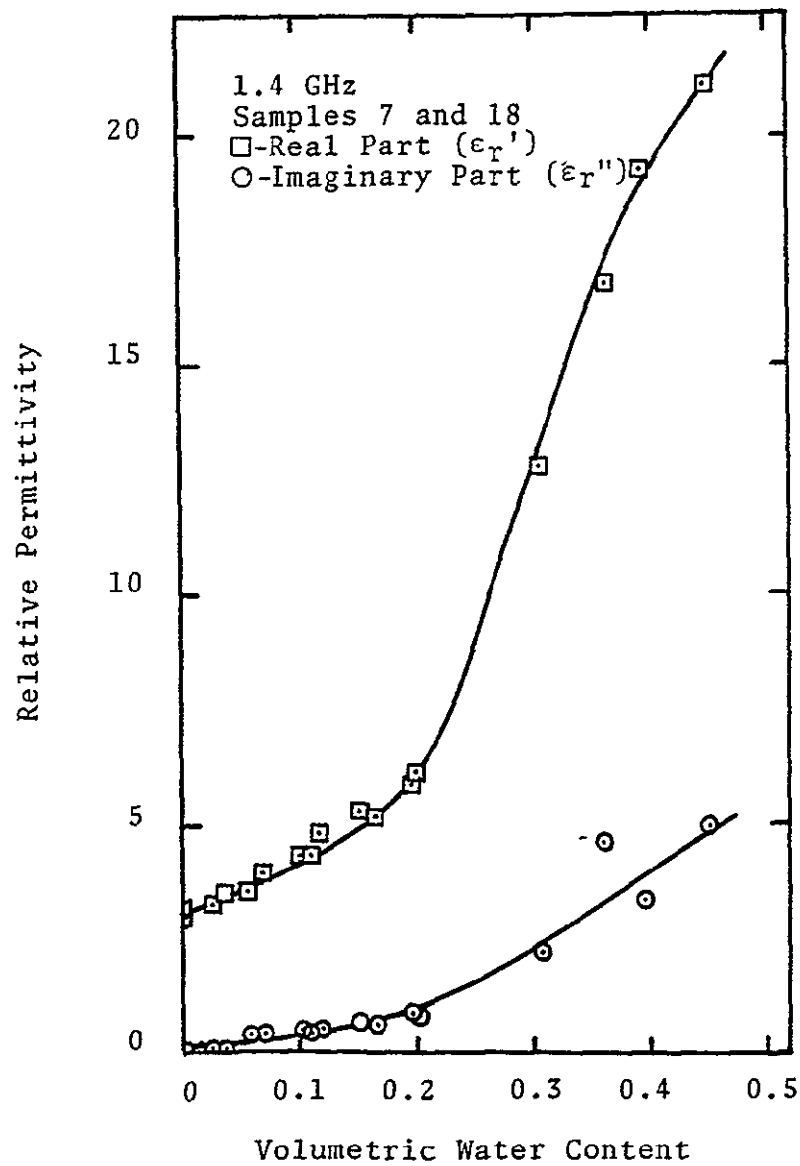


Figure II-20. Relative permittivity of samples 7 and 18 as a function of volumetric water content.

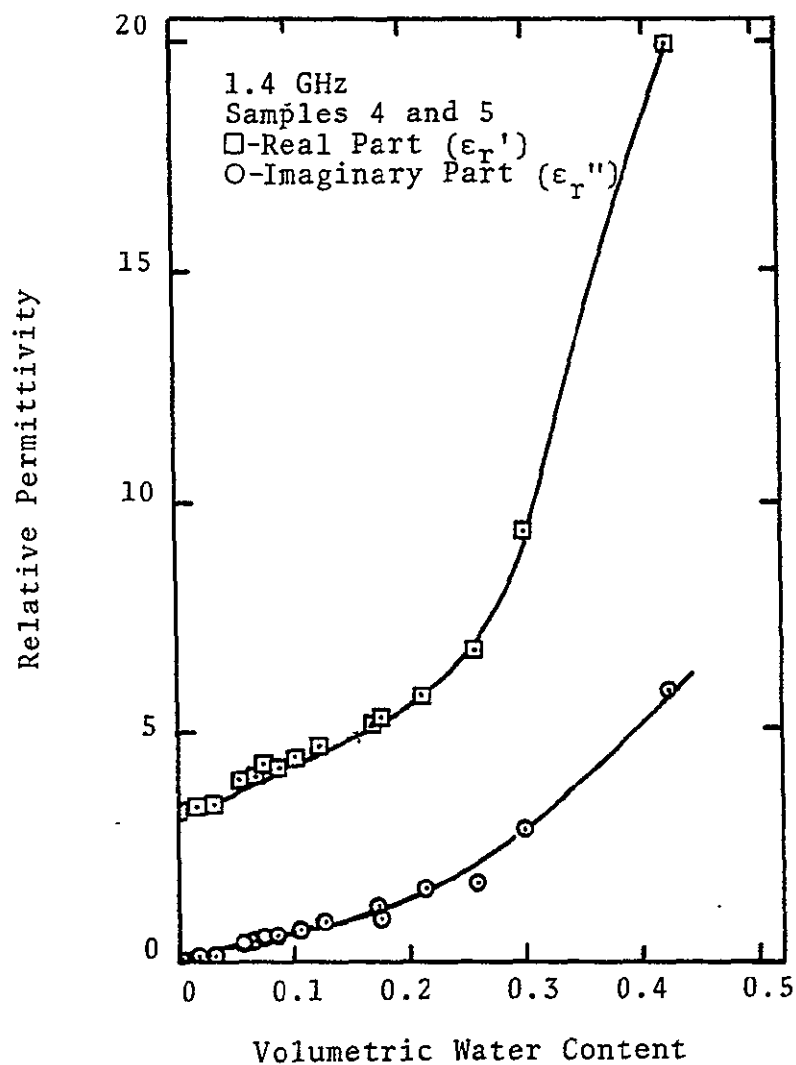


Figure II-21. Relative permittivity of samples 4 and 5 as a function of volumetric water content.

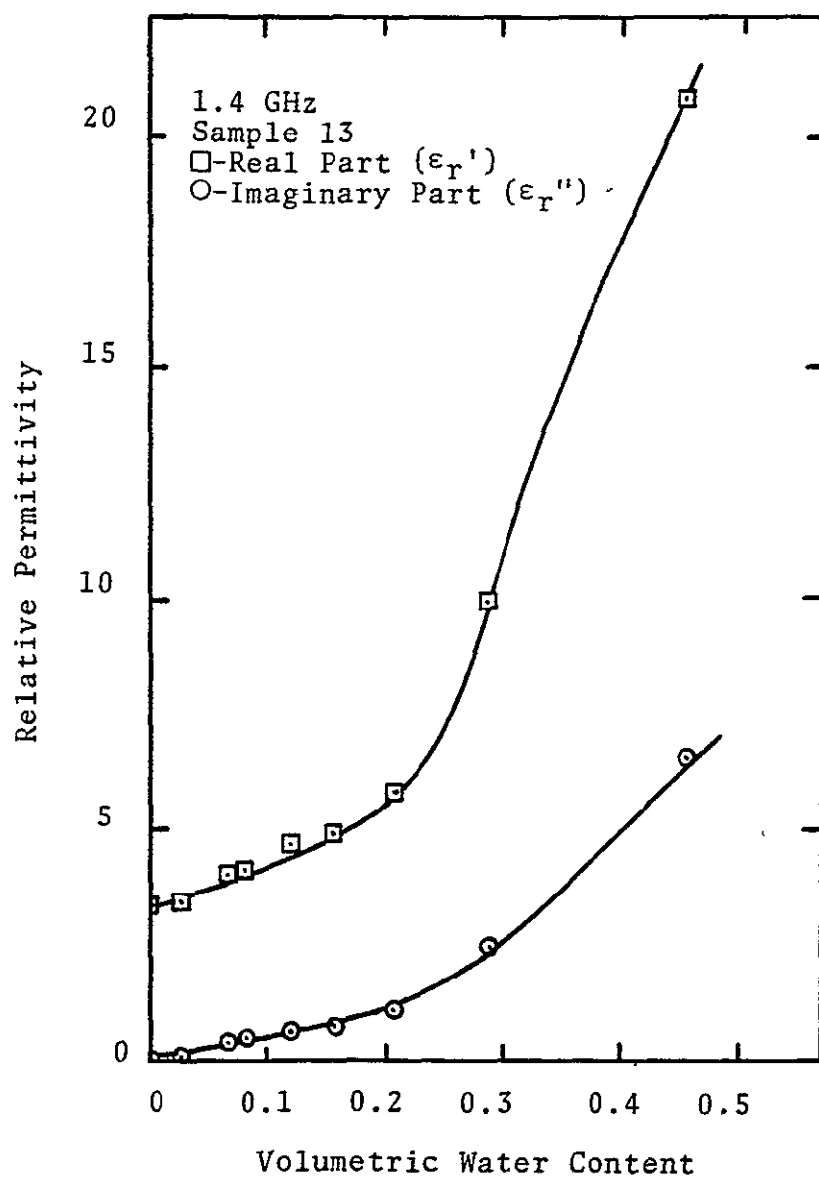


Figure II-22. Relative permittivity of sample 13 as a function of volumetric water content.



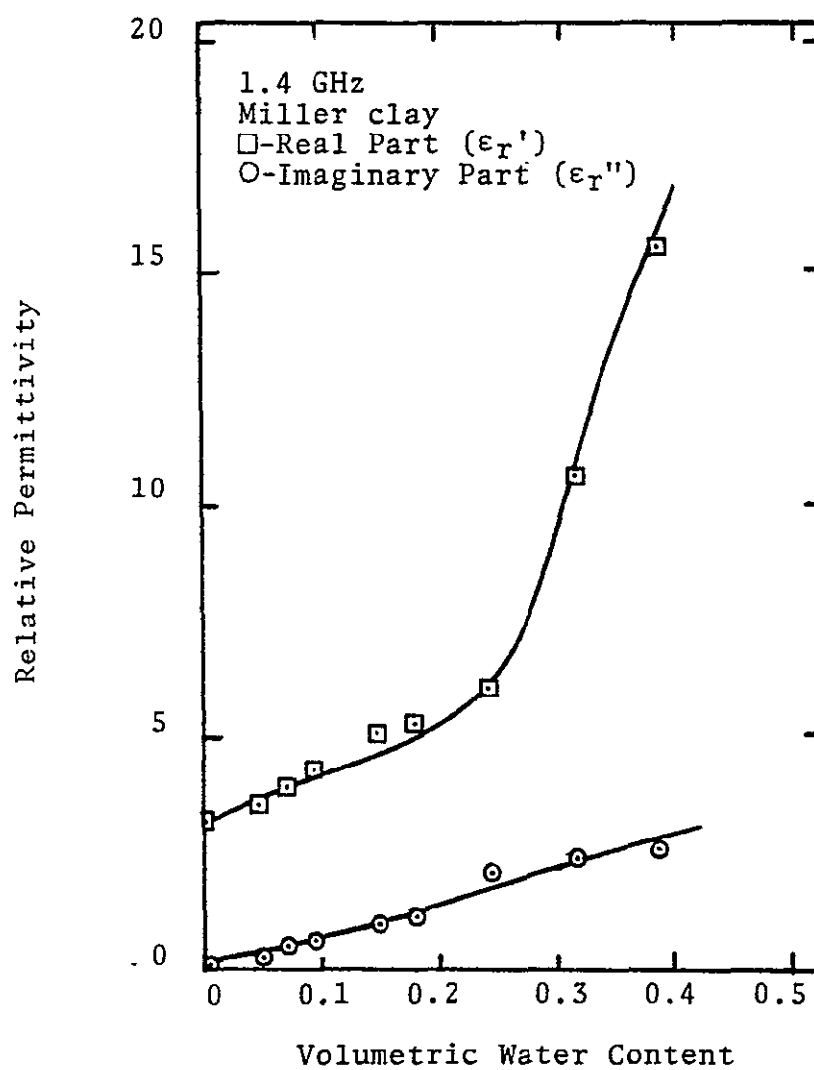


Figure II-23. Relative permittivity of Miller clay as a function of volumetric water content.

which is proportional to the amount of pore water. Volumetric transition moisture is defined by the intersection of two straight lines, one drawn through the points before the transition region and one drawn through the points after the transition region. Table II-4 is a tabulation of the transition moisture defined in this manner and Figure II-24 is a plot of the permittivities above the transition regions.

The analysis described above supports the hypothesis that the basic dependence of permittivity on soil water can be described in terms of the matric potential at which the soil water is held. The permittivity of soil is dependent not only upon the total number of dipole moments (water molecules), but it is also dependent upon the energy state at which they are held to the soil particles. This energy state is defined by the matric potential of the soil. This phenomena could be directly demonstrated by mapping the permittivity measurements as a function of volumetric water content (Figures II-18 through II-23) into the soil's matric potential as a function of volumetric water content. The resulting plot of permittivity versus matric potential should be independent of soil texture. However, reliable measurements of matric potential as a function of volumetric water content are not available for all of the soils for which permittivity measurements were

Table II-4  
Tabulation of Volumetric Transition Moistures  
Graphically Obtained from Figures  
II-18 through II-23

Soil Samples	Volumetric Transition Moisture
Sand	0.106
14 & 15	0.20
7 & 18	0.21
4 & 5	0.24
13	0.22
Miller Clay	0.245

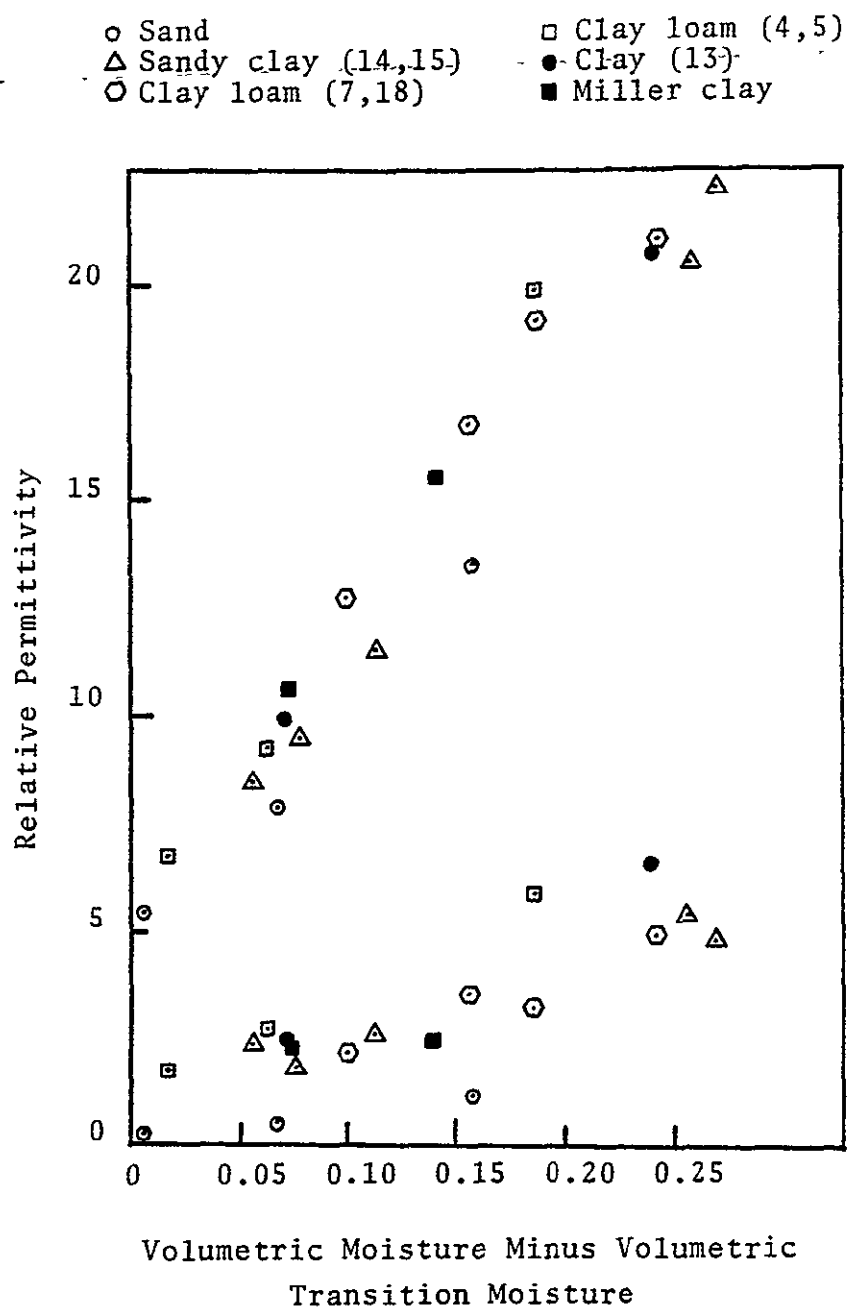


Figure II-24. Permittivity of all soils referenced to the transition moisture.

made. As a result a direct demonstration of the hypothesis is not possible.

Matric potential measurements of Avondale clay loam were obtained from T. Schmugge of the NASA Goddard Space Flight Center. These measurements were made by the U.S. Water Conservation Laboratory in Phoenix, Arizona. Similar measurements for other Phoenix soil textures are reported by Isdo et al. [17]. The soil used by Isdo et al. was obtained from the same general area as samples 1 through 18 listed in Table II-3. Of the soil samples listed in Table II-3, the characteristics of sample 7 and 18 most closely resemble those of Avondale clay loam.

Assuming the matric potential of Avondale clay loam is adequate to describe the matric potential of samples 7 and 18, the hypothesis that permittivity is dependent on the soil matric potential independent of soil texture can be indirectly demonstrated. This will be done by using the matric potential measurements of Avondale clay loam as a reference for calculating matric potential curves for Miller clay and sand using their permittivity measurements. The resulting matric potential versus water content curves can then be compared to the independently reported measurements of matric potential for typical soil textures shown in Figure II-9.

Columns one and two of Table II-5 contain a tabulation of matric potential versus volumetric soil moisture for

Table II-5  
 Matric Potential Versus Soil Moisture for Samples 7 and 18,  
 Miller Clay and Sand

Matric Potential (bars) Avondale Clay Loam	Soil Moisture (cm <sup>3</sup> /cm <sup>3</sup> )	Permittivity Samples 7 and 18	Soil Moisture Miller Clay	Soil Moisture Sand
75.0	0.10	4.35	0.125	0.075
16.5	0.14	5.00	0.175	0.09
9.0	0.158	5.31	0.188	0.10
5.0	0.175	5.63	0.200	0.11
2.3	0.20	6.25	0.22	0.125
1.15	0.22	7.10	0.265	0.155
0.165	0.285	10.00	0.315	0.20
0.08	0.315	12.50	0.34	0.25

T-D

Avondale clay loam. Column three contains the permittivity of samples 7 and 18 for the moisture contents in column two. The moisture contents of Miller clay and the sand sample that correspond to the permittivities of column three are listed in columns four and five. Figure II-25 contains the resulting plots of matric potential versus volumetric soil moisture for the three soil textures of Table II-5. The general characteristics of these plots compare very favorably with the typical plots of Figure II-9. Note that the moisture contents of Figure II-25 are based on volume while the moisture contents of Figure II-9 are based on weight. Although the data of Figure II-25 are only approximate, it does support the hypothesis that soil permittivity is dependent on the matric potential at which water molecules are held to the soil.

The apparent result that soil permittivity is in fact independent of soil texture when it is plotted as a function of matric potential is of vital importance to the understanding of the soil moisture information that is available from microwave measurements. As explained in the last section, it is the matric potential of the soil water that is important in determining the ability of a plant to uptake water, or for that matter in determining the state of saturation of a soil (which is important in soil run-off prediction). This leads to the conclusion that a microwave sensor should yield information directly related to the

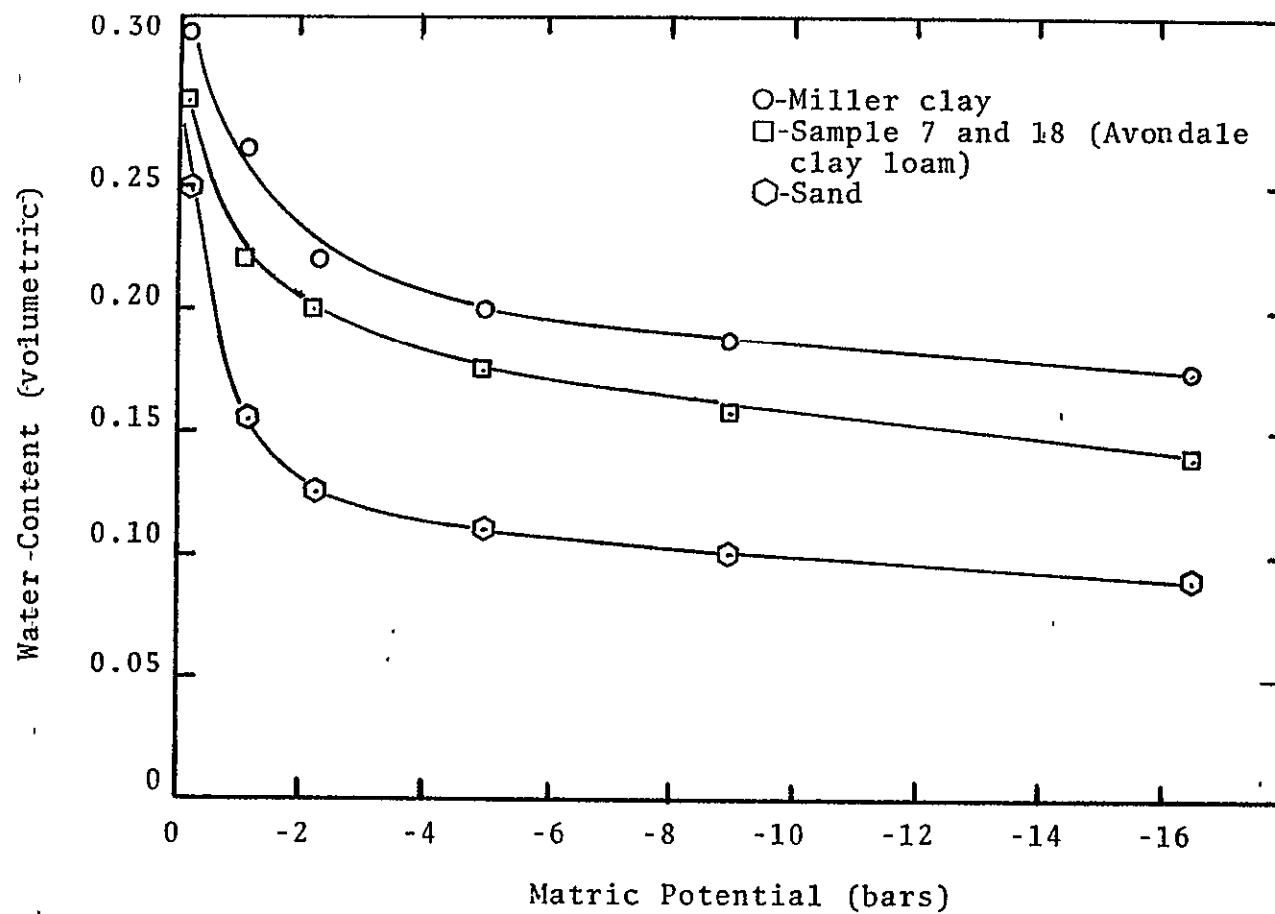


Figure II-25. Matric potential of Miller clay, samples 7 and 18, and sand assuming equivalence of permittivity versus soil moisture for all soil textures.



availability of soil water to vegetation. Further, this information is independent of soil type.

Comparison to other L-band measurements - Hoekstra and Delany [18] measured the permittivity of soil over a wide range of microwave frequencies. Their data show a dielectric relaxation where the real part of the permittivity decreases with frequency and the imaginary part goes through a maximum. This dielectric relaxation is attributed to water in the soil, but its characteristics are different from the dielectric relaxation of bulk water. Hoekstra and Delany have shown that the frequency of maximum dielectric loss (maximum  $\epsilon''$ ) of the relaxation of water in soils is displaced to a lower frequency than that of bulk water. Also, the relaxation occurs over a narrower frequency band than in bulk water.

Experimental results [19]-[21] have shown that the dielectric properties of bulk water and other materials with permanent dipole moments can be predicted using equations of the Debye form. Hoekstra and Delany [18] modeled the real part of the soil permittivity assuming two closely spaced relaxations. They describe each with a modification of the Debye equation by Cole and Cole [22]:

$$\epsilon' = \epsilon_{1s} + \frac{\epsilon'_{1s} - \epsilon'_{1\infty}}{(1 + j\omega\tau_1)^{1-\alpha_1}} + \epsilon'_{2s} + \frac{\epsilon'_{2s} - \epsilon'_{2\infty}}{(1 + j\omega\tau_2)^{1-\alpha_2}} \quad (\text{II-9})$$

where the subscripts 1 and 2 refer to the two separate dispersions. The subscripts  $\infty$  and s refer to the values  $\epsilon'$  at frequencies where  $\omega\tau \gg 1$  and  $\omega\tau \ll 1$ , respectively;  $\tau$  is the relaxation time,  $\alpha$  is a parameter indicating the distribution of relaxation times and  $\omega$  is radian frequency. The characteristic frequency of the dominant dispersion was shown experimentally to range between 1.5 GHz and 4 GHz, while the characteristic frequency of the second dispersion corresponds roughly to that of bulk water.

Hoekstra and Delany [18] found that, within their experimental error, the same relaxation parameters could be used in their model to describe the dielectric relaxation of the four types of soils that they measured at a constant 10% moisture by weight. These soils ranged from fine sand to clay. Since the amounts of adsorbed water differs between sand and clay, Hoekstra and Delany concluded that adsorption effects were not directly responsible for dielectric relaxation of water in soils. This conclusion does not necessarily agree with results of Newton and McClellan [13]. It was shown earlier that permittivity of soil at moistures below the transition moisture is dependent only on the volumetric soil moisture and not on soil texture. The dependence on soil texture is only evident for moistures above the transition moisture and is a result of the fact that the transition moisture is dependent on soil texture. Figures II-18 through II-23 and Figure II-24 demonstrate

that the real part of the measurements reported by Newton and McClellan vary with soil texture only as a result of the fact that the transition moisture varies with soil texture. As noted by Cihlar and Ulaby [14], based on the review of many permittivity measurements, the difference between soils of various textures does appear smaller when the permittivities are plotted as a function of water content by volume. This is true simply because the plots are normalized to equal amounts of water.

Since the permittivity of soil is not only dependent upon volumetric water content, but also upon the matric potential of that water, it is possible for the measurements of Hoekstra and Delany [18] not to show evidence of a texture dependence when plotted as a function of volumetric water content if the water was held at approximately the same matric potential for all of the soils. Since no information is given by Hoekstra and Delany concerning the matric potential of the soil water, there is no way to check this possibility. However, if this were true it would support the hypothesis that the fine sand used as a sample could support at least 15% moisture in adsorbed and solvate water. This would mean that their measurements were made before the transition moisture. If this was the case, the permittivities they had to work with would be independent of soil type. It should also be noted that it takes a large texture difference to

produce a small change in volumetric transition moisture. This leads to the fact that the permittivity of most agricultural soils from the same general area will be independent of soil type when viewed as a function of volumetric moisture content. As a result, soil type should be a minor effect when analyzing microwave data for soil moisture, at least at L-band.

Although the data reported by Hoekstra and Delany [18] have not demonstrated the effects of soil texture as did the data reported by Newton and McClellan [13], other authors have measured effects of texture, although not all at L-band. Lundien [16], Gieger and Williams [23], Hipp [24], Wiebe [25] and Babai [26] have seen textural effects even though the data have not been of sufficient quality to make conclusive statements as to the dependence of permittivity on water in the adsorption complex.

#### Other Effects

Up to this point there has been no mention of the permittivity dependence on frequency, soil temperature, or adsorbed cations. Cihlar and Ulaby [14] provide a good compilation of most of the current literature containing microwave permittivity measurements. It was pointed out that measurements of Gieger and Williams [23] at  $K_a$ -band demonstrate a dependence on soil texture, as well as others including Wiebe [25] and Babai [26] at X-band.

However, it appears that the effect of soil texture is not nearly as great at  $K_a$ -band and X-band as it is at L-band. In fact, for frequencies other than L-band, experimental error in the permittivity measurements and the textural classifications appear to be as great as the true textural effects. As a result, the composite of all X-band measurements that are compiled by Cihlar and Ulaby [14] in Figure 23 of that report (p. 30) will be utilized in this document for all X-band calculations of microwave emission or scattering coefficient, regardless of the soil type being modeled.

Soil permittivity does depend on soil temperature as a result of the water contained in the soil. This has been demonstrated by Lundien [16], Hoekstra and Delany [18], and Poe [27]. However, the dependence on soil temperature is not a significant effect for temperatures over the range of 15°C to 30°C. As a result, effects of soil temperature on soil permittivity will not be considered in this document.

The type of cation adsorbed by the soil particle changes the cation exchange capacity of the soil and as a result has a large effect on the amount of water of hydration that can be held by the soil. Obviously, this affects the soil permittivity-matric potential relationship. In addition, the ion content of the soil water affects the

imaginary part of the soil permittivity. As the soil water ion content is increased, the conductivity of the soil increases. This effect has not been completely verified experimentally, however, calculations of permittivities of water-salt-soil mixtures provide a good approximation of the effect (Figure II-26) [28]. Good agricultural soil will not have salt contents large enough to greatly affect soil permittivity, however, mapping areas of saline soils is an important and difficult task for agricultural planners.

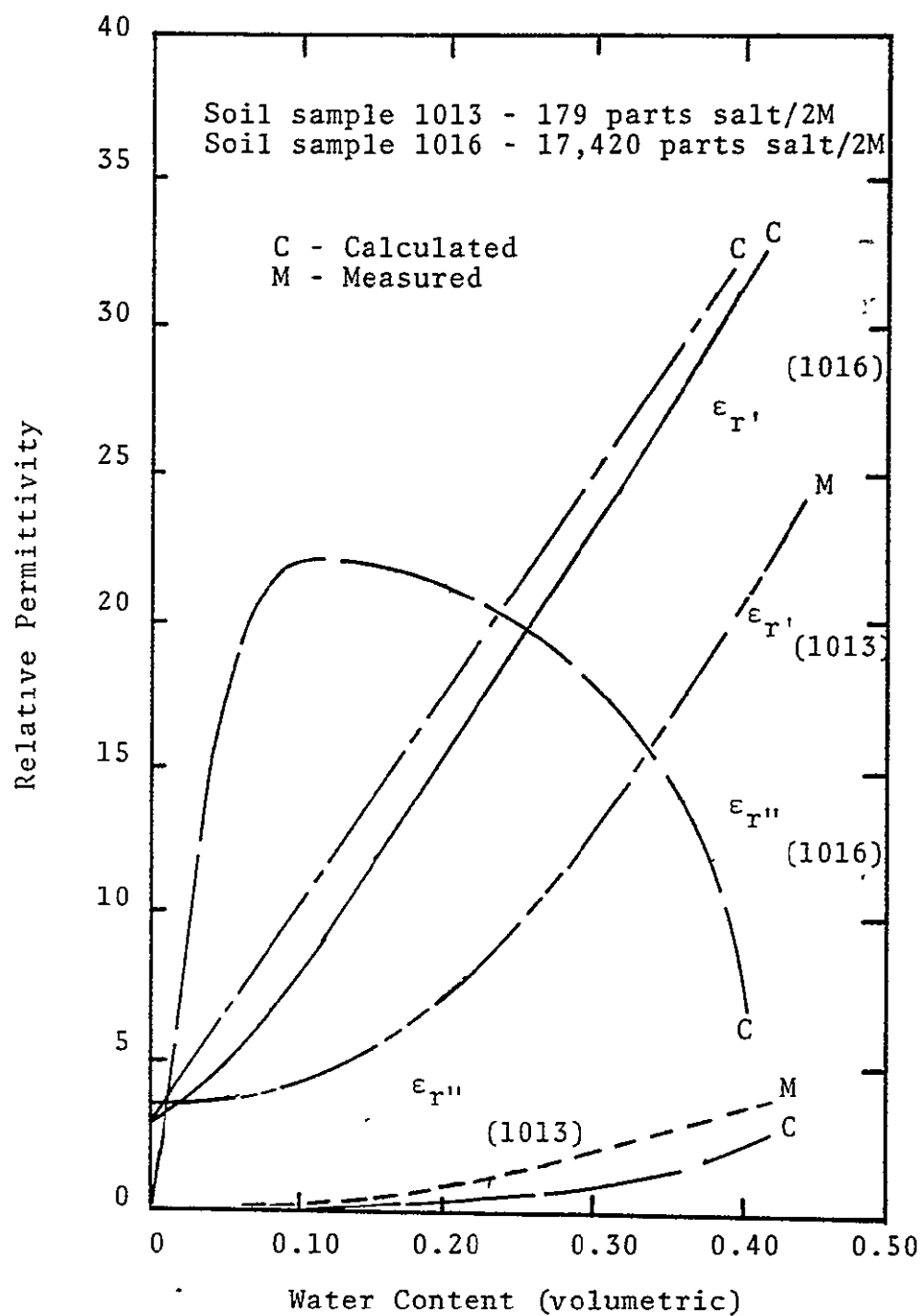


Figure II-26. Results of calculations of relative permittivity for soils of different salt contents (after Carver [28]).

## CHAPTER III

### MICROWAVE EMISSION

In Chapter II it was demonstrated that the electric permittivity of the soil is the driving function behind the dependence of soil emission on soil moisture. It is the purpose of this chapter to review techniques that have been used to model the emission of soil as a function of permittivity, or analogously, soil moisture. This discussion will include the techniques for describing the effects of surface roughness and vegetation cover since these parameters significantly modify the emission of the soil. In addition, previously reported measurements that demonstrate the soil moisture dependence, as well as the surface roughness effects and vegetation effects, will be discussed and their applicability to the study noted.

Before reviewing the techniques that have been used to model the microwave emission of a soil-vegetation complex, it is instructive to point out the various components that contribute to a measurement of the emission of such a scene. Although emission from the soil-vegetation complex is the primary source of energy, there are other contributing sources the importance of which depends on the measurement configuration. These sources include; the intervening atmosphere between the soil-vegetation complex and the antenna, atmospheric radiation reflected from the surface into



the antenna aperture, cosmic point sources such as the sun reflected from the surface into the aperture, and man-made radiation in the frequency band of measurement. Emission of the radiometer system backscattered from the surface into the receiving aperture also contributes to the measured antenna temperature. Figure III-1 graphically illustrates these various components of a passive microwave measurement.

The effects of sources other than the soil will be discussed in Chapter VI. The emission from the soil-vegetation complex is the component that is of primary importance to this work. It is only this component that contains information concerning the soil moisture distribution, and it is the only component that is discussed in this chapter.

### Mathematical Description of Energy Transfer

Since the thermal microwave emission of a soil medium originates in the soil volume and propagates outwardly, it is reasonable to model the emission process within the volume separately from the modifying effects of the surface roughness and vegetation cover. These latter two effects can be modeled separately. In keeping with this line of reasoning, the literature review presented in this chapter is divided into descriptions of literature dealing with the subsurface, surface, and vegetation cover individually.

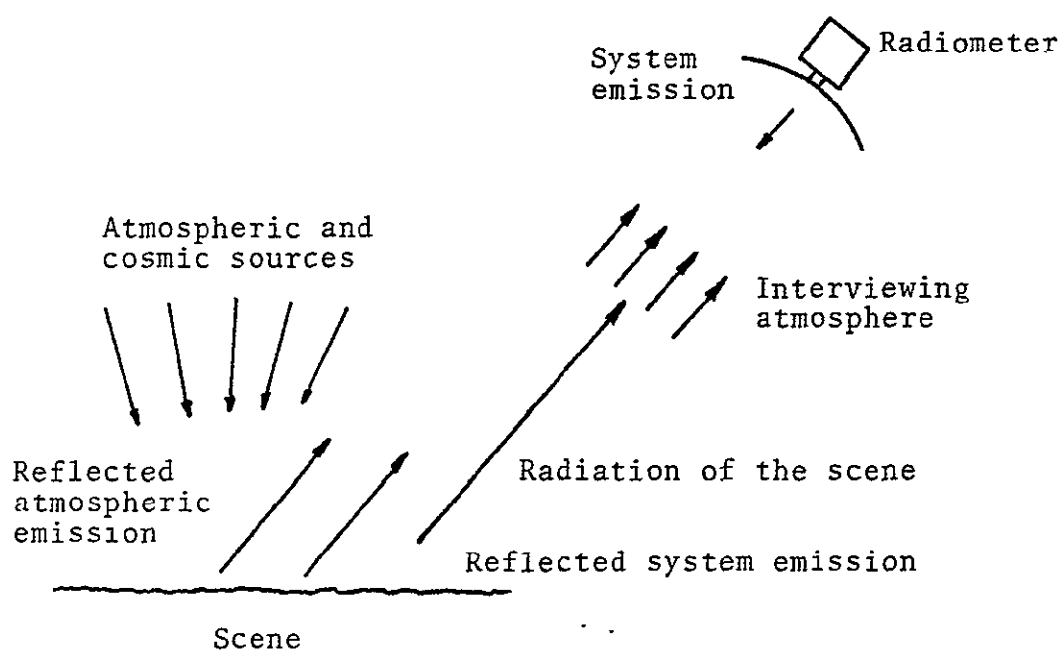


Figure III-1. Graphic illustration of the various contributions to a radiometer measurement.

Emission from the soil volume is discussed first. Peake's [29] classical approach to modeling emission from smooth and rough soil volumes is discussed and its inadequacies pointed out. Following that, the radiative transfer approach to modeling emission from a smooth surface soil volume is presented. Stogryn [30] and Tsang et al. [31] provide general solutions, while Burke and Paris [32] provide a more straightforward, but less rigorous solution. A review of literature describing models of surface roughness are provided next. This literature is subdivided into the four general techniques of modeling rough surface scatter. These techniques are geometrical optics or ray tracing; the Kirchhoff solution (physical optics); small perturbation theory; and the composite surface theory. Subdivision of the discussion in this manner organizes the techniques by their utility in handling specific types of surface roughness. Following the review of literature on surface roughness is a brief discussion of the literature dealing with vegetation effects.

#### Soil Volume

Models of the emission from a soil volume have traditionally been derived for the case of a smooth surface. This is convenient for the purposes of this discussion since the smooth surface can be considered as a reference surface for comparison of the various models of subsurface

emission. Ideally, the surface roughness models can be applied directly to the results of the subsurface emission models to determine the effect of surface roughness. In the following paragraphs two approaches to modeling emission from a non-scattering soil volume will be described. Then, literature dealing with the effects of scattering in the soil volume will be reviewed.

Peake's approach - In modeling the emission of a soil medium, one is concerned with the effects of spatial permittivity and temperature variations, as well as scatterers contained in the volume. The classical approach to modeling the thermal microwave emission was developed by Peake [29] in 1969. In Peake's approach the emissivity of the medium is defined as the ratio of energy emitted by a blackbody at the same temperature as the subject medium. Assuming that a semi-infinite soil medium is in thermodynamic equilibrium with blackbody (isotropic) radiation, Peake demonstrated that emissivity is equal to absorptivity using Kirchhoff's radiation law. For a semi-infinite medium, absorptivity is equal to one minus reflectivity. Reflectivity is the integral of the differential scattering coefficients of the surface. Peake's approach, therefore, relates the emissivity of a surface to its differential scattering coefficients.

Peake's formulation is, however, only rigorously valid for homogeneous soil with uniform moisture and temperature

profiles. This is due to Peake's necessary assumption that the soil medium be in thermodynamic equilibrium with isotropic radiation. The power intensity impinging on the underside of the soil surface due to the soil volume is only isotropic when both the soil moisture and soil temperature distributions are uniform with depth.

The Peake approach is the basis for describing the emissivity of a soil volume bounded by a plane surface in terms of the Fresnel reflection coefficient [33]. The Fresnel reflection coefficient can be used in conjunction with the Peake approach to describe a soil medium containing a uniform soil moisture and soil temperature distribution with depth. This technique can be used to approximate the emission from a nonuniform soil moisture distribution by replacing the Fresnel reflection coefficient with an effective Fresnel reflection coefficient calculated for the nonuniform profile. (This is only an approximation since a basic assumption of the Peake approach is isotropic radiation). Richerson [34] utilized an effective Fresnel reflection coefficient to describe emission from a soil medium composed of horizontally homogeneous layers. In that solution the direction of propagation was taken to be the direction that a ray would be refracted as it crosses the dielectric boundaries.

Another method for solving for the effective reflection coefficient of a plane stratified medium is given

by Casey [35]. Casey solves the equations of propagation in the medium by putting them in the form of Hill's [36] equations for which there are known series solutions. Neither of the techniques presented by Richerson [34] nor that due to Casey can take spatial temperature variations into account, since temperature does not enter into the effective reflection coefficient calculations.

Radiative transfer - The Peake approach describes the emission from a soil volume in terms of the emissivity of the soil. Emissivity, as defined by Peake [29], is computed based on the differential scattering coefficients of the soil. This technique is not directly applicable to the situation of nonconstant soil temperature profiles since the differential scattering coefficients are not temperature dependent. The radiation flux of the soil is emitted from a volume and is dependent on the temperature distribution within that volume. Therefore, models that describe the radiation flux emitted by a soil volume must be dependent on the soil permittivity and soil temperature profiles. Two techniques that meet these requirements are described below; a rigorous solution by Stogryn [30], and an approximate solution by Burke and Paris [32].

Stogryn [30] solves for the specific intensity of radiation from a semi-infinite soil volume with a planar

surface using Maxwell's equations. In his formulation Stogryn makes no simplifying assumptions about the soil temperature or soil permittivity variations. Stogryn characterizes the soil medium by a randomly fluctuating electric current. The random current is due to microscopic fluctuations in the positions of charged particles within the medium. These fluctuations result in a current density whose average is zero, but whose mean square does not vanish. Stogryn uses the fluctuation-dissipation theorem [37], [38] to define the expected value of this current density. Stogryn used Maxwell's equations to relate the average value of this thermally induced current density to the randomly fluctuating electric field in the soil medium. The Fourier components of this field are related to the intensity of emission. Since the Fourier components of the electric field are related to intensity, Stogryn obtained a formulation for the intensity of radiation from a soil volume resulting from a thermally induced current density.

The focal point of Stogryn's [30] formulation is the relationship between the random current density and the soil permittivity and soil temperature. As noted above, this relationship is based on the fluctuation-dissipation theorem [37], [38]. Although Stogryn's formulation is general, the number of problems for which explicit solutions

can be obtained are very limited. The solution of Stogryn's formulation for actual soil permittivity and soil temperature profiles (even assuming two-dimensioned uniformity) requires a large amount of digital computer time.

A formulation for emission from a stratified medium, with arbitrary moisture and temperature profiles is also provided by Tsang et al. [31]. Their approach is very similar to that of Stogryn [30]. However, numerical results are illustrated and compared with closed form analytical solutions and results obtained with the WKB method [39] for simple profiles.

An alternative to the general formulation by Stogryn [30] is provided by Burke and Paris [32] through an application of the radiation transfer equation to emission from soils. This formulation of the radiative transfer process was primarily an offshoot of the formulation by Paris [40] describing the transfer of microwave energy through the atmosphere. The radiative transfer equations derived by Burke and Paris were formulated for incoherent radiation and a plane homogeneously stratified soil medium containing a temperature variation with depth only. The results of this model were shown to compare favorably with airborne radiometric X-band data acquired by NASA over Phoenix, Arizona in 1974. The radiative transfer model is amenable to physical interpretation, is not



computationally difficult, and approaches the general solution of Stogryn as the soil layers are allowed to become infinitely thin. The Burke and Paris model will be described in greater detail in Chapter IV.

Scattering in the soil volume - The formulations given above assume that the soil permittivity varies smoothly without discontinuities. Such discontinuities would cause scattering within the soil volume. However, soil, in its natural state, contains voids, rocks, plant roots, etc., that cause permittivity discontinuities. The effect of scattering within the soil volume has been addressed by Stogryn [41], Wilhelmi et al. [42] and England [43], among others.

Stogryn [41] treats the volume scattering due to small random dielectric fluctuations in a medium bounded by a plane surface. In this formulation, which is an approximate first order perturbation method, Stogryn allows the non-random part of the dielectric constant to vary with depth. Stogryn provides calculations of back-scatter cross section per unit area to demonstrate the effect of the volume scattering. The Peake approach would have to be employed in applying this result to radiometric applications. This immediately indicates that the theory could only be used to predict the emission of a volume containing uniform moisture and temperature profiles.

Wilhelmi et al. [42] described backscatter from rough surfaces using the physical optics approach described in the next section, but included effects of volume scatter due to inhomogeneities in the subsurface. The thrust of their work was to demonstrate volumetric depolarization effects. The rationale of their theoretical technique was that the electromagnetic field crossing the surface and entering the volume experiences multiple scattering and is returned back to the surface where it is transferred across the boundary adding to the backscatter from the surface. This addition of field power is possible since the volume scattering mechanism destroys the coherence of the internal and external fields. The efficiency of the volume scatter mechanism was determined by experimentally determined parameters. Although Wilhelmi et al. developed this technique specifically for scatter of laser light, it was described here as an example of another approach to modeling volume scatter.

The approach used by England [43] was to apply a modified version of scattering theory that has previously been applied to atmospheric radiative transfer or to neutron scattering. England's approach was based on a radiative transfer approach similar to that of Burke and Paris [32]. As a result, England's results are directly applicable to the work reported in this document. In

his development, England assumed a linearly varying temperature profile with depth, homogeneous soil permittivity, and randomly distributed point scatters. England's results demonstrate that the reduction in the intensity of emission due to volume scattering may be tens of degrees, but that this "darkening" is dependent on the dominance of scattering over absorption. It is pointed out that scatterers have a greater effect the lower the real part of the soil permittivity. However, the real part of the permittivity of soil in the microwave frequency range increases significantly with soil moisture, while the imaginary part does not increase as greatly. This led England to conclude that... "The introduction of small amounts of liquid water (to a low loss soil) reduces or even effectively eliminates scatter-induced darkening. Therefore, scatterers tend to play an insignificant role in emission from moist soil or wet snow."

### Surface Roughness

As described in the last section, the classical approach to analytical descriptions of emission from natural scenes was developed by Peake [29]. Stogryn [44] demonstrated the utility of this technique for describing the emissivity of scenes using a variety of surface scattering theories. Peake's approach inherently intertwines

the subsurface and surface effects into one formulation since the scattering coefficients of the scene are functions not only of surface profile, but also of subsurface electrical properties. However, there have been no other approaches to modeling the emission from rough surface<sup>±</sup> except for a formulation by Johnson [45] which has not been validated experimentally. As a result, the various approaches that have been commonly used in the literature to calculate scattering coefficients of rough surfaces will be reviewed. These techniques are the geometrical optics approach, the Kirchhoff solution, the small perturbation approach, and the composite surface theory.

Geometrical and pseudo-physical optics models - The geometrical optics approach to modeling rough surfaces applies when the frequency of the electromagnetic wave is sufficiently high that the finiteness of the wavelength may be neglected [46]. A geometrical optics model can be viewed as a collection of infinitely large plane facets, each of which generate a specular type reradiation pattern. It is assumed that all facets which are not normal to the direction of propagation can be ignored. Although this is a very crude model, it is an effective one since all viable theories of rough surface scatter reduce to this model when the incident wavelength becomes very small compared to the standard deviation and the autocorrelation

of the surface profile [47]. Examples of the geometrical optics technique of modeling rough surfaces are given by Kodis [48] and Barrick [49]. By comparing numerical computations to geometrical optics theory, Fung et al. [50] have shown the range of surface conditions for which the geometrical optics theory is valid. The condition for validity is

$$\lambda K < 0.31 \cos \theta$$

$$\sigma/\lambda \geq 1.0$$
(III-1)

where  $\sigma$  is the rms surface height deviations,  $K$  is the radius of curvature of the surface (for randomly rough surfaces  $K$  is the average curvature),  $\lambda$  is the incident wavelength and  $\theta$  is the incident angle.

Several authors have presented extensions of the basic geometrical optics approach that do not assume specular reflection from infinite size facets. These models can be considered pseudo-physical optics theories. Spetner and Katz [51] and Waite [52] present models that assume a collection of small facets with a uniform pattern and size distribution. Both of these models assume that the radar return is composed of the summation of the returns from a collection of randomly located scatterers, although these authors make different assumptions about the radar cross

cross section and reradiation pattern of individual facets.

Katzin [53] extended the pseudo geometrical optics models further by introducing two size ranges of facets to represent the surface. Katzin assumed a combination of facets large with respect to a wavelength and facets very small with respect to a wavelength. The reradiation pattern of the large facets is highly directive, but with a finite width about the specular return: The pattern of individual large facets was assumed to be proportional to the fourth power of the incident wavelength with a random reradiation pattern. Katzin further assumed that the facets were randomly located around a mean surface so that the backscattered energy from the two types of facets is additive. Katzin's model was extended by Khamsi et al. [54] to include a third facet size between the large and small facets assumed by Katzin. Khamsi et al. demonstrated that three size ranges provide better agreement between theory and measurements.

Kirchhoff solution - The Kirchhoff or physical optics approach to calculating fields scattered from rough surfaces is formulated according to Huygen's principal. The Helmholtz integral expresses the scattered fields in terms of the total field and its normal derivative or their equivalents on the surface [55]. The associated boundary conditions are not generally known and the Kirchhoff method

consists essentially in approximating these values such that the Helmholtz integral can be evaluated [56].

The field at each point on the surface is approximated by assuming that it is the sum of the incident wave and a wave reflected from a smooth plane tangent to the surface at the given point. The tangent plane approximation restricts the method to locally flat surfaces composed of irregularities with small curvatures and incident angles not near grazing. Brekkovskikh [57] has given the surface criterion for the Kirchhoff approach as:

$$4\pi r_c \cos \theta \gg \lambda \quad (\text{III-2})$$

where  $r_c$  is the radius of curvature,  $\theta$  is the local incident angle, and  $\lambda$  is the wavelength. This criterion was based purely on geometrical considerations. Based on a comparison of numerical and theoretical computations, Fung et al. [50] gave the ranges of validity for physical optics theory as:

$$\begin{aligned} \lambda K &\leq 2.92 \cos^3 \theta \quad \text{for } \sigma/\lambda \leq 0.1 \\ \lambda K &\leq 0.31 \cos \theta \quad \text{for } \sigma/\lambda \geq 1.0 \end{aligned} \quad (\text{III-3})$$

where  $K$  is the radius of curvature of the surface,  $\theta$  is the incident angle,  $\sigma$  is the rms surface height deviations, and  $\lambda$  is the wavelength. Although the conditions stated above describe the surface conditions for strict validity of the Kirchhoff approximation, Beckmann and Spizzichino [58] indicate that the technique works reasonably well for many surfaces that do not meet these conditions.

A number of authors have used the Kirchhoff approximation to solve for scatter from rough surfaces. Beckmann and Spizzichino [58] use the Kirchhoff approximation in conjunction with the Scalar Helmholtz integral to solve for scatter from a perfect conductor. Fung [59] formulated the vector solution of fields scattered from rough surfaces using the Stratton-Chu integral, but did not provide an explicit expression for the scattered fields. Stogryn [60] was able to obtain explicit expressions for scatter from normally distributed rough surfaces using the Kirchhoff approximation. Leader [61] generalized Fung's formulation to the case of bidirectional reflectance and was able to provide sample calculations.

Small perturbation - The small perturbation solution can be used to describe the scatter from surface irregularities that are small compared with the wavelength of the incident radiation. In addition, the slope of the surface should be much less than unity. The basic concept of the small perturbation technique is due to the work of Rice [62], who generalized the acoustic method of Rayleigh [63] to a vector wave and a random surface. Fung [55] provides a good summary of this approach.

Rice [62] described the surface by a two-dimensional Fourier series with coefficients that are random variables. The scattered and incident fields are described by an



infinite series. The coefficients of the series describing the fields are determined by using boundary conditions at the surface. Rice did not attempt to arrive at a solution that is directly applicable to a particular situation, his results were general in nature. Rice considered the situation of perfect conductivity, but found that the series solution diverged logarithmically. By allowing the surface to have a large but finite conductivity, Rice showed that the cause of the divergence could be eliminated. Valenzuela [64] applied Rice's theory to the case of scatter from slightly rough sea. For the case of finite conductivity, Valenzuela evaluated the boundary conditions to terms of the second order; one order beyond that evaluated by Rice for infinite conductivity.

The criterion of the surface roughness for validity of the small perturbation technique is so stringent that naturally occurring surfaces generally do not fit the criterion. Based on the Fung et al. [50] numerical-theoretical computational comparison, the range of surface conditions for validity of the small perturbation technique is:

$$\sigma/\lambda \leq 0.053 \quad (\text{III-4})$$

where  $\sigma$  is the rms height deviations and  $\lambda$  is the wavelength of the incident radiation. However, this technique is used

in conjunction with other theories to model more realistic surfaces. This technique is described below.

Composite surface theory - Beckmann [65] pointed out that many rough surfaces encountered in practical applications are superpositions of several scales of roughness. Beckmann attacked this problem by defining the surface as the sum of independent stationary random functions. He solved for the mean square amplitude of the scatter from each surface using the scalar Kirchhoff integral and summed the results to get the overall mean squared scattered amplitude. Using this technique Beckmann demonstrated that the dominant surface roughness component is not the one with the greatest surface roughness, but it is the one with the greatest rms slope. This result indicates the importance of small scale structure since small scale structure can have the greatest rms slope.

Although Beckmann's [65] solution was for composite rough surfaces, it is not what is currently termed the composite surface theory. The composite surface theory as used in the current literature jointly utilizes the Kirchhoff approximation and perturbation techniques to solve for the scatter from surfaces made up of large scale surface deviations upon which very small scale surface deviations are imposed. The criteria of validity of each roughness scale, in order for these techniques to be

applied, are as previously specified. Wright [66] first introduced this technique as a method of predicting scatter from sea surfaces where small scale waves ride on top of large scale swell.

Wright's [66] technique is known as an incoherent model since Wright calculated the scattered power resulting from the small scale surface deviations and simply averaged over the tilt angles resulting from the large scale surface deviations. This assumes that the total scattered power is the sum of two independent contributions, at least to the first order.

Chan and Fung [67] provide a technique for a coherent composite surface theory. Their technique is to solve for the fields at the surface due to the small scale undulations using perturbation techniques and then use this field in the Kirchhoff solution to solve for the scattered power from the composite surface.

An example of using the incoherent composite surface theory to calculate emissivity of the sea is given by Wu and Fung [68]. Wu and Fung simply utilize the Peake approach to convert differential scattering coefficients calculated using the composite surface theory to emissivity.

## Vegetation

### Models of scattering coefficients of vegetation -

There has been some concern with modeling the effects of

vegetation on the propagation of energy in the MegaHertz frequency range as a result of communication problems in forest environments [69] - [71]. However, there are few published theoretical models of scatter or emission from vegetation for the microwave frequency range.

Du [72] modeled the scattering from randomly distributed leaves. He assumed that the leaves were of uniform thickness, arbitrary shape and planar, but much larger than the wavelength of the incident radiation. The scatter from each individual leaf was calculated based on the reflection from an infinite plane of equivalent permittivity. Comparison of calculations based on this model to measurements of backscatter from soybeans at 10 GHz and 35 GHz demonstrate that the general magnitude, angular dependence, and polarization effects were fairly well predicted.

Another model of microwave scattering by vegetation was formulated by Peake [73]. Peake modeled the scatter from vegetation by assuming that the vegetation consisted of long, thin, homogeneous dielectric cylinders arranged in a random fashion, but with a higher probability of vertical orientation. Peake's model required that the diameter of the cylinders be much smaller than a wavelength and that the spacing of the cylinders be large with respect to a wavelength. At  $K_a$ -band, Peake found that this model was adequate to account for the general intensity of radar

return from grass, and that a reasonable change in moisture content and blade density can account for the observed seasonal dependence. Measurements at X-band were not in as good agreement with the model since the grass was not deep enough to provide sufficient attenuation to satisfy the assumptions of the model.

More recently Waite and Cook [74] investigated the volume scatter from low level vegetation. As a result of their measurement program, they concluded that the behavior of grass could best be described not as a scattering volume, but as a homogeneous lossy dielectric. However, in order to get the best agreement between the measurements and model predictions, the measurements had to be corrected for roughness effects. Waite and Cook further noted that Peake's grass model was not entirely applicable to their data set since it assumes an infinite grass layer thickness.

Models of emission of vegetation - The literature cited thus far were concerned with developing models of vegetation applicable to active microwave measurements. Sibley [75] generated a simplistic vegetation model applicable to passive microwave measurements to determine the effect of vegetation on the emission from the underlying soil. Sibley approached the problem from the standpoint of propagation through planar dielectric layers. Thermal

radiation originates in the soil and part is transmitted across the surface of the soil into the vegetation canopy. This radiation propagates through the vegetation and into the atmosphere. The vegetation canopy is considered to be a dielectric layer which is described by its permittivity. Therefore, Sibley's problem reduced to describing the permittivity of the vegetation layer and characterizing its geometrical form mathematically such that effects of propagation through the vegetation medium could be calculated. Sibley considered two geometrical forms for his model; a uniform vegetation cover and vegetation planted in rows.

In describing the permittivity of the vegetation canopy, Sibley postulated that the canopy was a mixture of vegetation (primarily water) and air; therefore, its dielectric properties could be described using the Weiner model for a dielectric mixture as presented by Evans [76]. Peake and Oliver's [77] formulation of the permittivity of vegetation was used in the dielectric mixture calculation.

Although Sibley [75] considered two geometrical forms for his model, only the equations for a uniform vegetation cover are given to demonstrate Sibley's technique. Sibley assumed that the canopy not only attenuates the emission from the soil, but also contributes to the total apparent temperature through thermal emission. The contribution of the canopy is derived from the general expression of the

apparent temperature of the dielectric layer of thickness  $H$ . This requires the assumption that all points within the canopy emit radiation equally. Assuming the temperature, attenuation constant, and emittance are constant within the canopy, the contribution of a uniform canopy is

$$T_{\text{canopy}} = t \left( \frac{\epsilon}{2\alpha} \right) (1 - e^{-2\alpha H \sec \theta}) \quad (\text{III-5})$$

where  $t$  is the thermometric temperature of the canopy and  $\epsilon$  is the differential emission coefficient. Under the assumption of thermal equilibrium, the differential emission coefficient is equal to the absorption coefficient. However, for a plant canopy this does not generally hold; therefore, Sibley defined an energy transfer factor  $f$ .

$$T_{\text{canopy}} = t f (1 - e^{-2\alpha H \sec \theta}) \quad (\text{III-6})$$

where  $f < 1$  represents a gain of energy by the canopy and  $f > 1$  represents a loss of energy by the canopy.

Another approach to modeling vegetation for the passive case is given by Basharinov and Shutko [78]. Their characterization of the vegetation is based primarily on the quantity of water in the vegetation as given by

$$W = p G l S_0 p \quad (\text{III-7})$$

where

$p$  - density of filling of a unit volume

- G - volumetric moisture content of the vegetation
- l - plant cover height
- S<sub>0</sub> - area of plant cover
- ρ - specific gravity of water

Two cases of vegetation cover were considered; sparse plant cover and dense plant cover. The density of filling of a unit volume, p, varies from 0.001 to 0.0001 for sparse cover and from 0.01 to 0.001 for dense cover.

The influence of sparse plant cover was estimated by Basharinov and Shutko [78] based on an estimate of the optical thickness,  $\tau_p$ , of the plant cover using two extreme model approximations. The minimum influence of vegetation was modeled by assuming that the capillary moisture contained in the plant elements is a layer of fog. The optical depth of the fog was determined using the Rayleigh approximation without considering diffraction effects. The maximum influence of vegetation was modeled by assuming that the moisture content of the vegetation is a layer of precipitated water. The value of optical depth in this case was calculated on the basis of the attenuation of water for the given wavelength and the thickness of the assumed water layer.

Increments of radiometric brightness temperature resulting from the vegetation layer was calculated using:

$$\Delta T_p = t_o (1 - K_m) (1 - e^{-2\tau_p}) \quad (\text{III-8})$$



where

$t_o$  - thermodynamic temperature of the soil and vegetation

$K_m$  - radiating capacity of the soil

Note that the term defined as radiating capacity is simply the square of the absolute value of the Fresnel reflection coefficient, so that  $1-K_m$  is the emissivity of the soil (based on the Peake approach). Calculations by Basharinov and Shutko [78] based on this equation, show that the two extreme model approximations for sparse vegetation produce results that differ by two orders of magnitude.

Basharinov and Shutko [78] modeled a dense cover of vegetation as a smooth homogeneous dielectric slab over a smooth soil surface. An effective radiating capacity of the vegetation-soil complex was calculated based on a two-layer Fresnel reflection coefficient model. An increment of radiating capacity resulting from the vegetation cover was calculated by taking the difference between the effective radiating capacity of the vegetation-soil complex and the radiating capacity of the soil:

$$\Delta K = K_{ef} - K_m \quad (III-9)$$

where  $K_{ef}$  is the effective radiating capacity of the vegetation-soil complex. The increment of brightness temperature due to the vegetation is then calculated simply by:

$$\Delta T = t_o \Delta K \quad (III-10)$$

Qualitative comparisons between the models of Basharinov and Shutko [78] and experimental data indicate that the general trends observed in the data are predicted. Their primary results are:

- 1) Sparse vegetation of ten decimeters high has very little influence on emission in the centimeter and decimeter wavelengths,
- 2) As thickness, height and moisture content of the vegetation increase, the emission of the vegetation increases first in the centimeter wavelengths and then extends into the decimeter wavelengths, and
- 3) Dense green vegetation one meter high effectively shields emission of the soil, even in decimeter wavelength range.

#### Microwave Measurements

Individual scientists have acquired measurements of emission and scattering of natural scenes as a function of soil moisture over the last several years. There was little organization to the effort until 1974 when the NASA Johnson Space Center initiated the Joint Soil Moisture Experiment. Due to the lack of organization, measurements reported in the literature prior to that time were generally acquired to answer specific questions of concern to

individual scientists. Measurement programs were not designed to systematically acquire data that could be used to determine the effects of individual scene parameters on the ability to estimate soil moisture with microwave sensors. As a result, data that are adequate to address this study do not currently exist in the literature. However, the available measurements do demonstrate the effects of soil moisture, surface roughness, and vegetation on the emission and scattering of soil.

#### Active Microwave Measurements

Measurements made by researchers at the University of Kansas with ground-based systems during the last two to three years demonstrate the radar response to soil moisture. These measurements are used to illustrate the response of radar signals to soil moisture and vegetation in the discussion below.

Bare soil - The response of radar backscatter to the moisture in soil is demonstrated in Figure III-2 [79]. The data presented in Figure III-2 were acquired from a field with a surface rms height deviation of 2.5 cm at an incident wavelength of 6.4 cm. Figure III-2 indicates that the response of the normalized radar cross section,  $\sigma^0$ , to the effective soil moisture in a skindepth is fairly linear, but with increasing sensitivity to soil moisture for

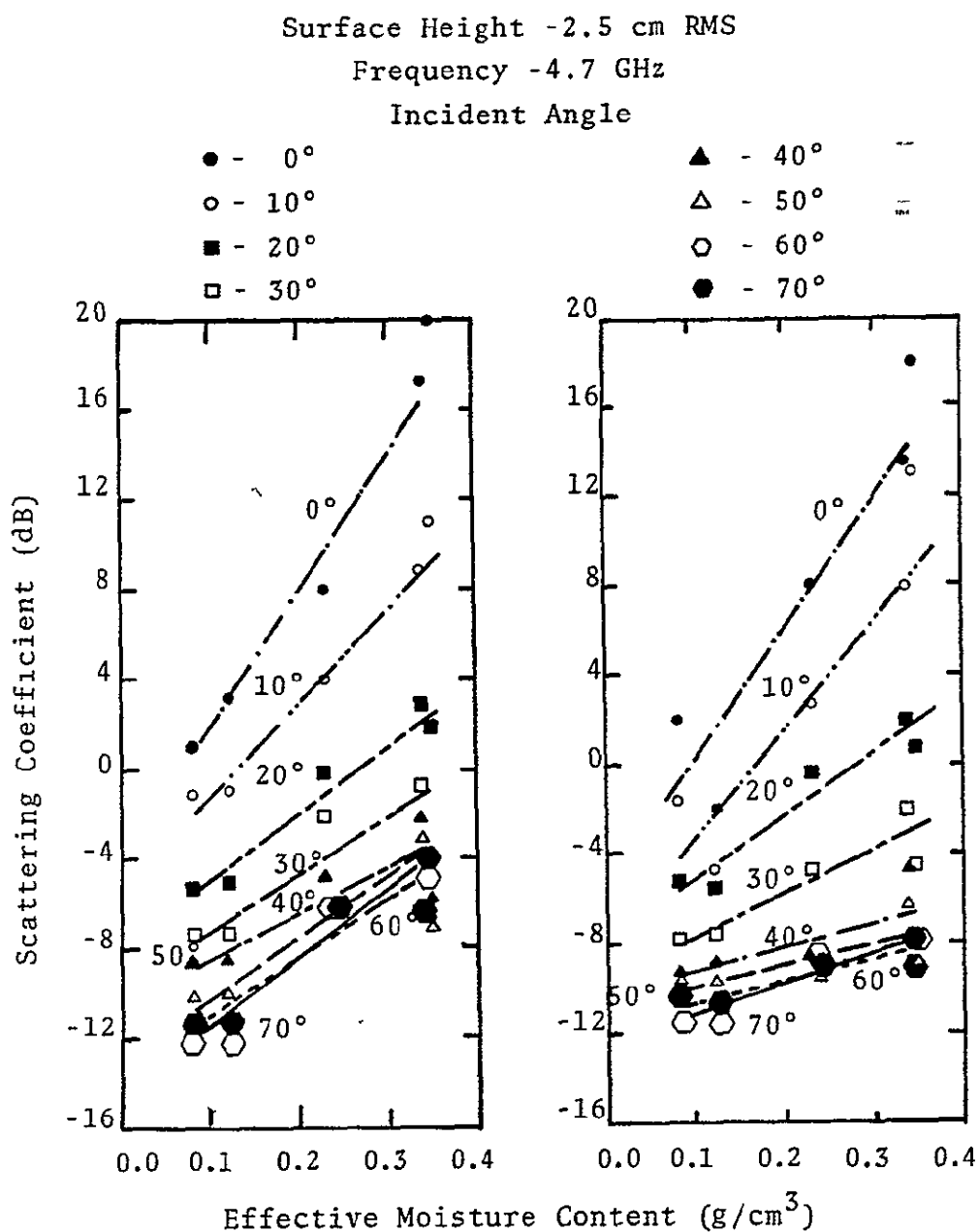


Figure III-2. Scattering coefficient as a function of effective soil moisture content (after Ulaby et al. [79]).

decreasing incident angles. This variation of the sensitivity of  $\sigma^\circ$  to soil moisture with incident angle and frequency is demonstrated in Figure III-3 [79]. From Figure III-3 it is apparent that the sensitivity decreases rapidly between nadir and the  $20^\circ$  incident angle and levels off past  $30^\circ$  or  $40^\circ$ . In addition, the angular dependence is more pronounced at 7.1 GHz as compared to 4.1 GHz. In general, HH polarization exhibits better sensitivity than VV polarization at the same frequency and incident angle.

Although  $\sigma^\circ$  has a good response to soil moisture for a single specific surface roughness, a scene with another surface roughness may demonstrate a different response to soil moisture for the same frequency and incident angle. As surface roughness varies, the magnitude of  $\sigma^\circ$  as well as its sensitivity to soil moisture changes. Figures III-4 and III-5 demonstrate this effect for constant soil moisture at 2.75 GHz and 7.25 GHz as a function of incident angle [80]. Ulaby and Batlivala [80] performed an analysis to determine the optimum radar parameters for soil moisture detection and minimization of surface roughness effects of bare soil. They concluded that the optimum radar parameters are an incident angle range of  $7^\circ$  to  $15^\circ$ , a frequency of about 4 GHz and either HH or VV polarization.

Vegetation - Ulaby [81] reports radar backscatter measurements of corn, milo, soybeans and alfalfa. These crops were planted using standard agricultural practices.

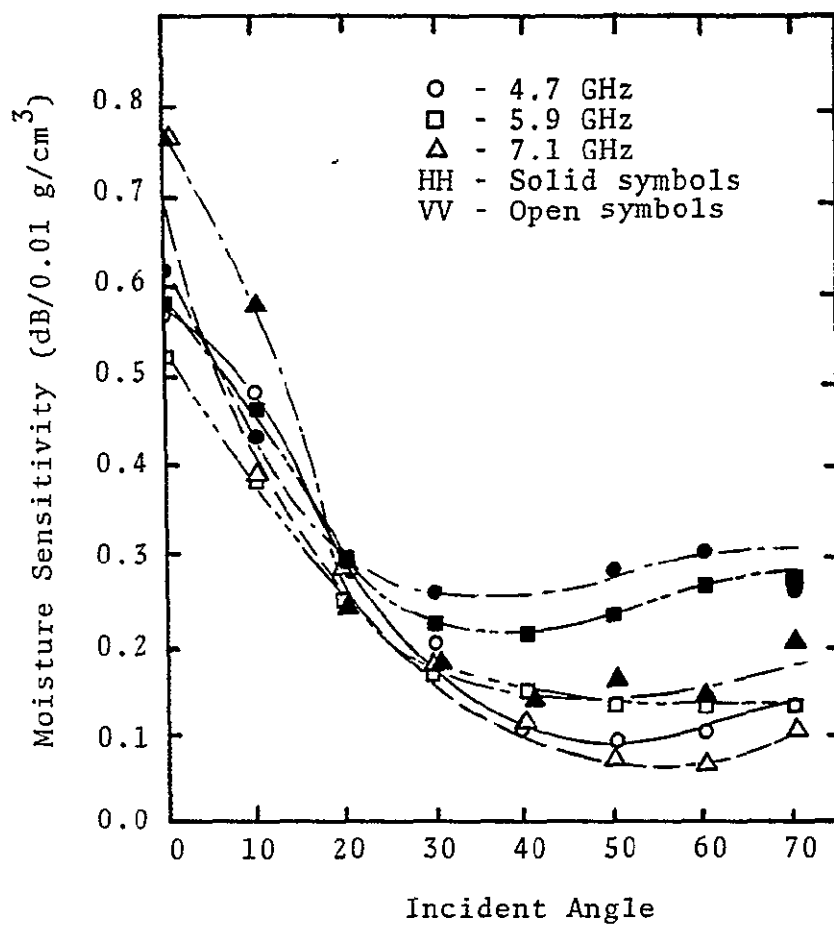


Figure III-3. Moisture sensitivity as a function of incident angle (after Ulaby et al. [79]).

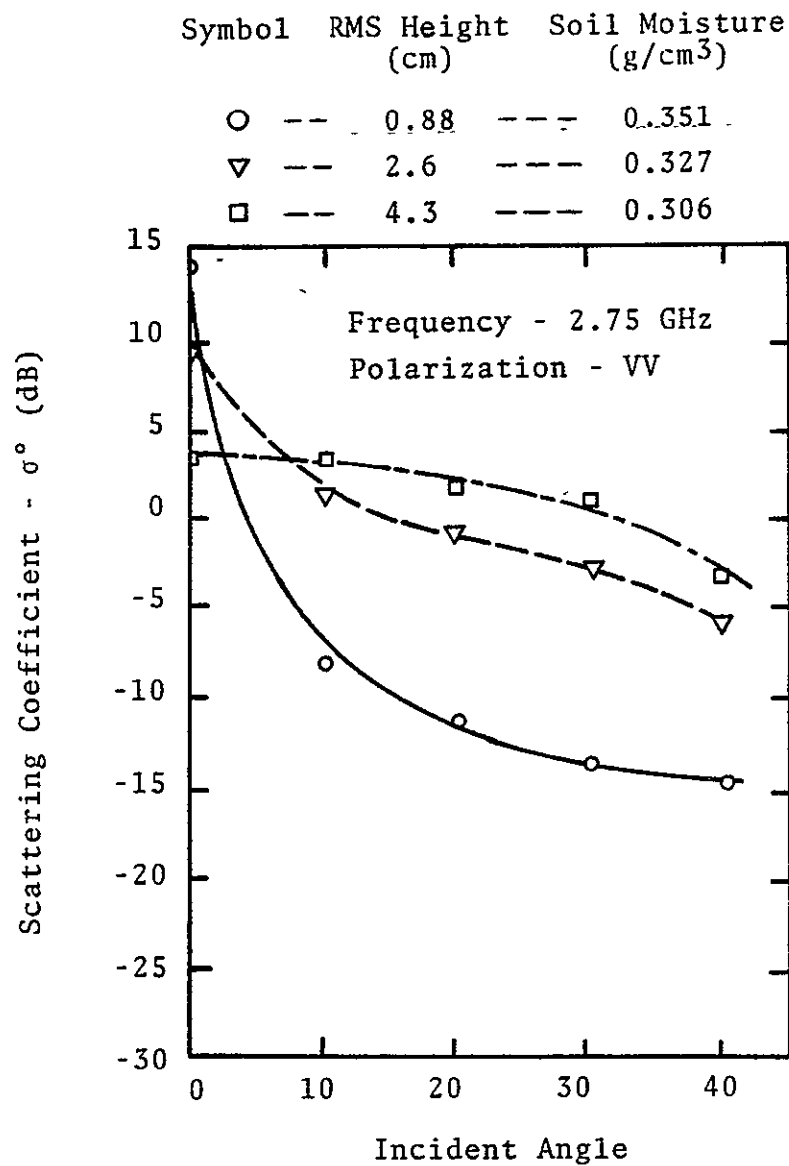


Figure III-4. Angular response for three bare fields with similar soil moisture but different surface roughness (after Ulaby and Batlivala [80]).

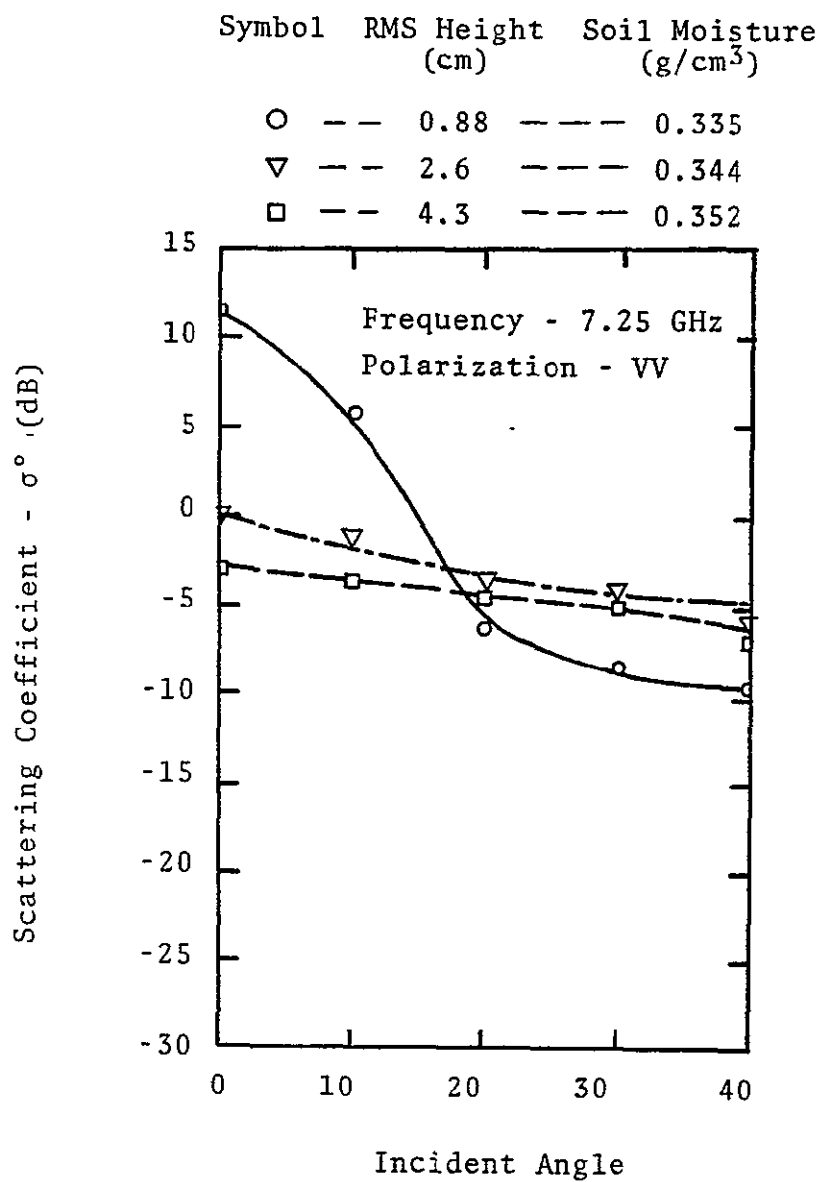


Figure III-5. Angular response for three bare fields with similar soil moisture but different surface roughness (after Ulaby and Batlivala [80]).



Data acquired at 5.9 GHz (Figure III-6) indicates that soil moisture has a measurable effect on backscatter through vegetation. The largest effect is at incident angles near nadir. Ulaby points out that as the frequency is decreased, the sensitivity to soil moisture increases slightly, and as frequency is increased the sensitivity to soil moisture decreases. Measurements of a uniform stand of very dense sorghum indicate no response to soil moisture variations at frequencies above 2.75 GHz [82]. However, the density at which the measured sorghum field was planted was considerably greater than would occur as a result of standard agricultural practices.

#### Passive Airborne Microwave Measurements

Data reported by Jean [83] in 1971 at 1.42 GHz, 2.69 GHz, and 10.69 GHz over bare agricultural fields near Weslaco, Texas demonstrate a definite dependence on the soil moisture contained in the second and third centimeters of soil. The data at 1.42 GHz demonstrated a linear dependence on soil moisture, while the data at 2.69 GHz and 10.69 GHz demonstrated a nonlinear dependence. This nonlinear dependence is characterized by a small change in measured antenna temperature per percent soil moisture for moistures less than 20 percent soil moisture by weight, and a large change in antenna temperature per

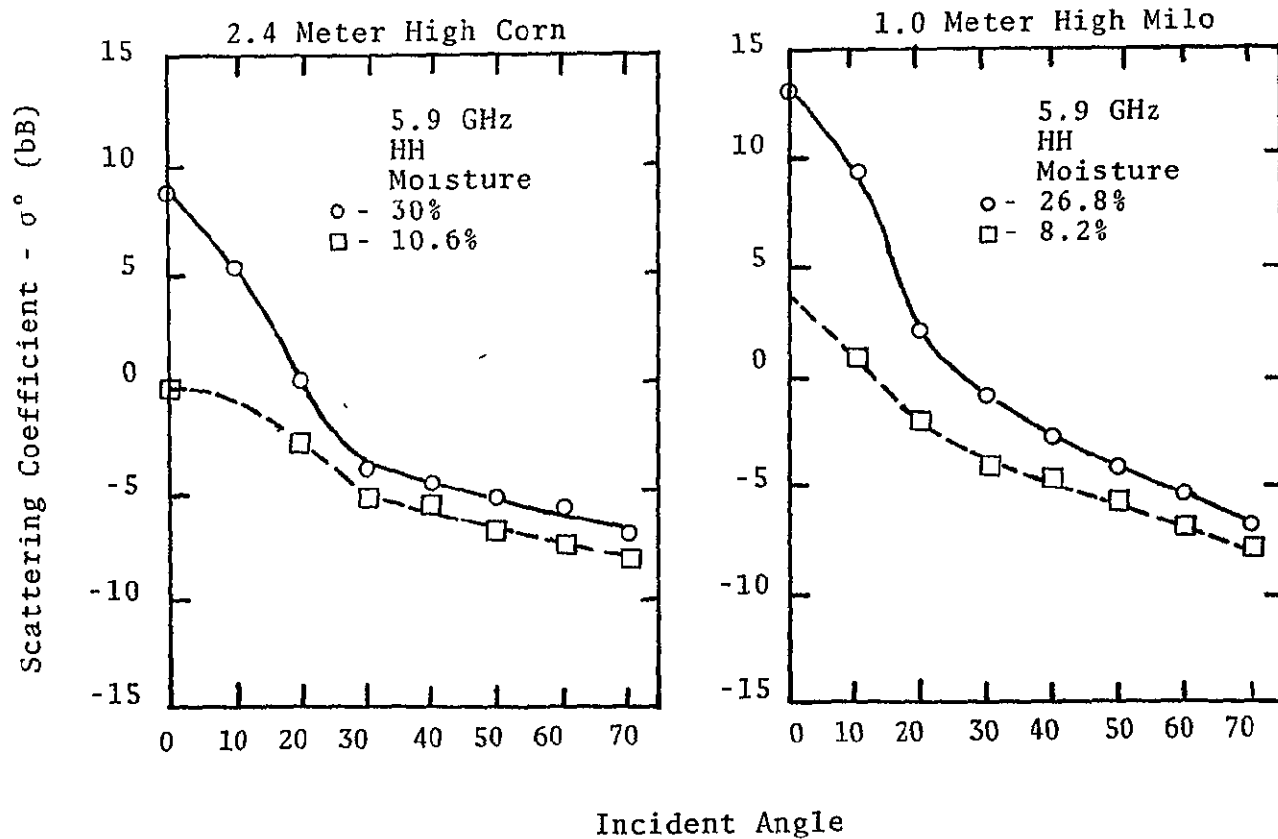


Figure III-6(a). Scattering coefficient measured at 5.9 GHz for low and high soil moisture conditions (after Ulaby [81]).

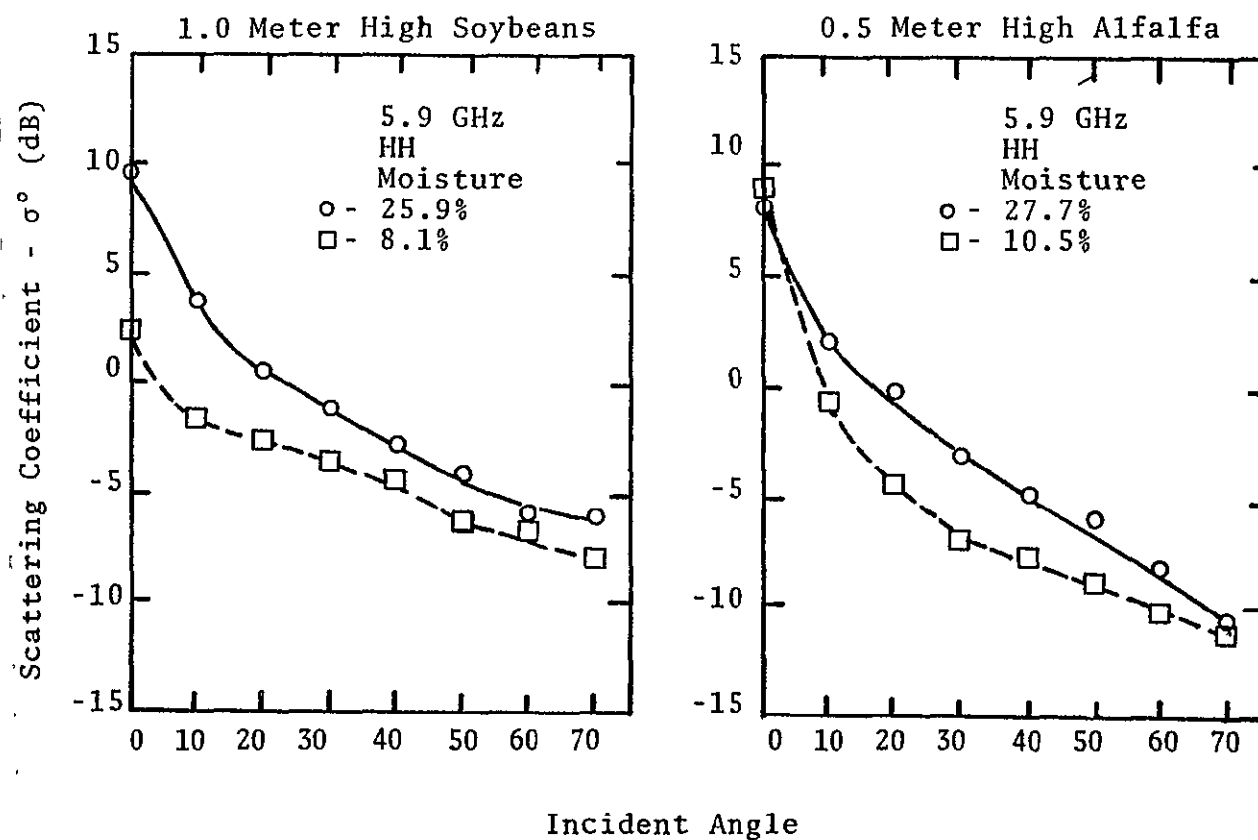


Figure III-6(b). Scattering coefficient measured at 5.9 GHz for low and high soil moisture conditions (after Ulaby [81]).

percent soil moisture for moistures above 20 percent. Although effects of soil texture, soil density, physical temperature differences between fields and surface roughness were not considered in Jean's analysis, he estimated that soil moisture could be measured to an accuracy of 5 to 10 percent by weight under ideal conditions. Kroll [84] compared measurements over Chickasha, Oklahoma and Weslaco, Texas acquired in 1973 to Jean's measurements with comparable results.

Schmugge et al. [85] reports data in 1972 and 1973 acquired at an agricultural test site in Phoenix, Arizona at 19.4 GHz and 1.42 GHz. Figure III-7 compares the response of the 19.4 GHz radiometer to soil moisture in the top centimeter of soil for light soils (sandy loam and loam) and heavy soils (clay loam). Although there is a linear decrease of antenna temperature with soil moisture, the depression of antenna temperature for a given moisture content is less for heavy soils than for the light soils. This is apparently a result of the fact that the clay soils maintain a higher percent soil moisture than the loam soils for the same matric potential. The details of this explanation were contained in Chapter II. Since field capacity is related to matric potential, the difference in the antenna temperature variations between the heavy and light soils can be accounted for by plotting brightness

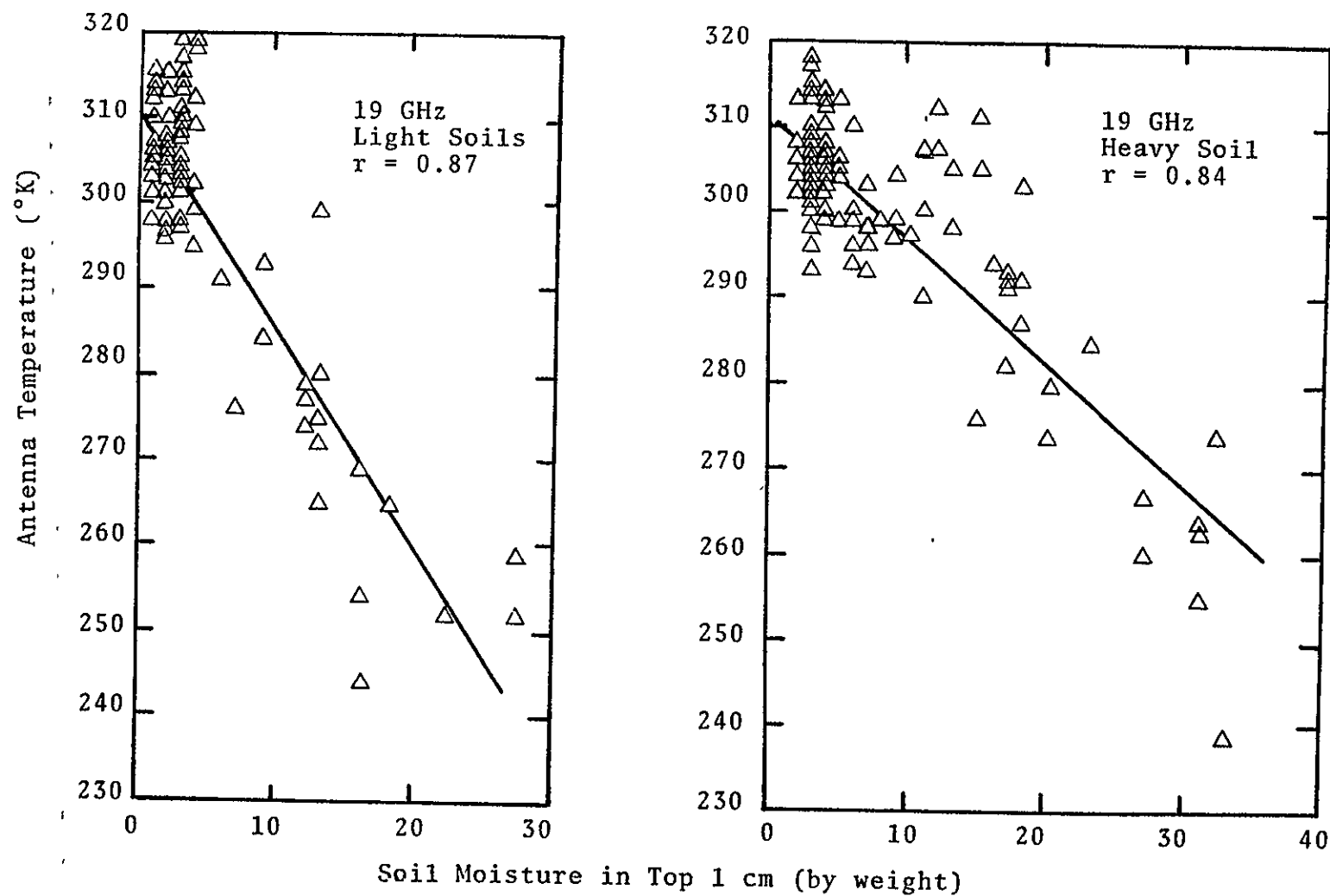


Figure III-7. Plot of 19 GHz measured antenna temperature versus soil moisture for light soils (sandy loam and loam) and heavy soils (clay loam) (after Schmugge et al. [85]).

temperature as a function of percentage field capacity instead of soil moisture (Figure III-8).

Schmugge et al. [85] shows that similar linear behavior is observed for the antenna temperature obtained with the 1.42 GHz radiometer when plotted as a function of percentage field capacity in the top centimeter (Figure III-9). However, when antenna temperature is plotted versus percentage field capacity in the top 2.5 cm layer, there appears to be a "flat region" out to about 50 percent field capacity where the linear decrease begins (Figure III-10). The flat region extends out even further when the antenna temperature is compared to the percentage field capacity of the top 5 cm of soil. These results lead Schmugge et al. to conclude that the 1.42 GHz radiometer was primarily responding to soil moisture in the top 1 to 2 centimeters of soil.

Schmugge et al. [86] reported the results of the first aircraft experiment that was flown as part of the currently on going Joint Soil Moisture Experiment that is being sponsored by the NASA Johnson Space Center. This experiment was flown in April, 1974, at the agricultural test site in Phoenix, Arizona using radiometers operating at 10.69 GHz and 1.4 GHz. The purpose of the experiment was to obtain data to quantify the effects of nonuniform vertical distribution of moisture, surface roughness, and soil type. The radiative transfer model described by Burke and Paris [32] was utilized in the analysis of these data.

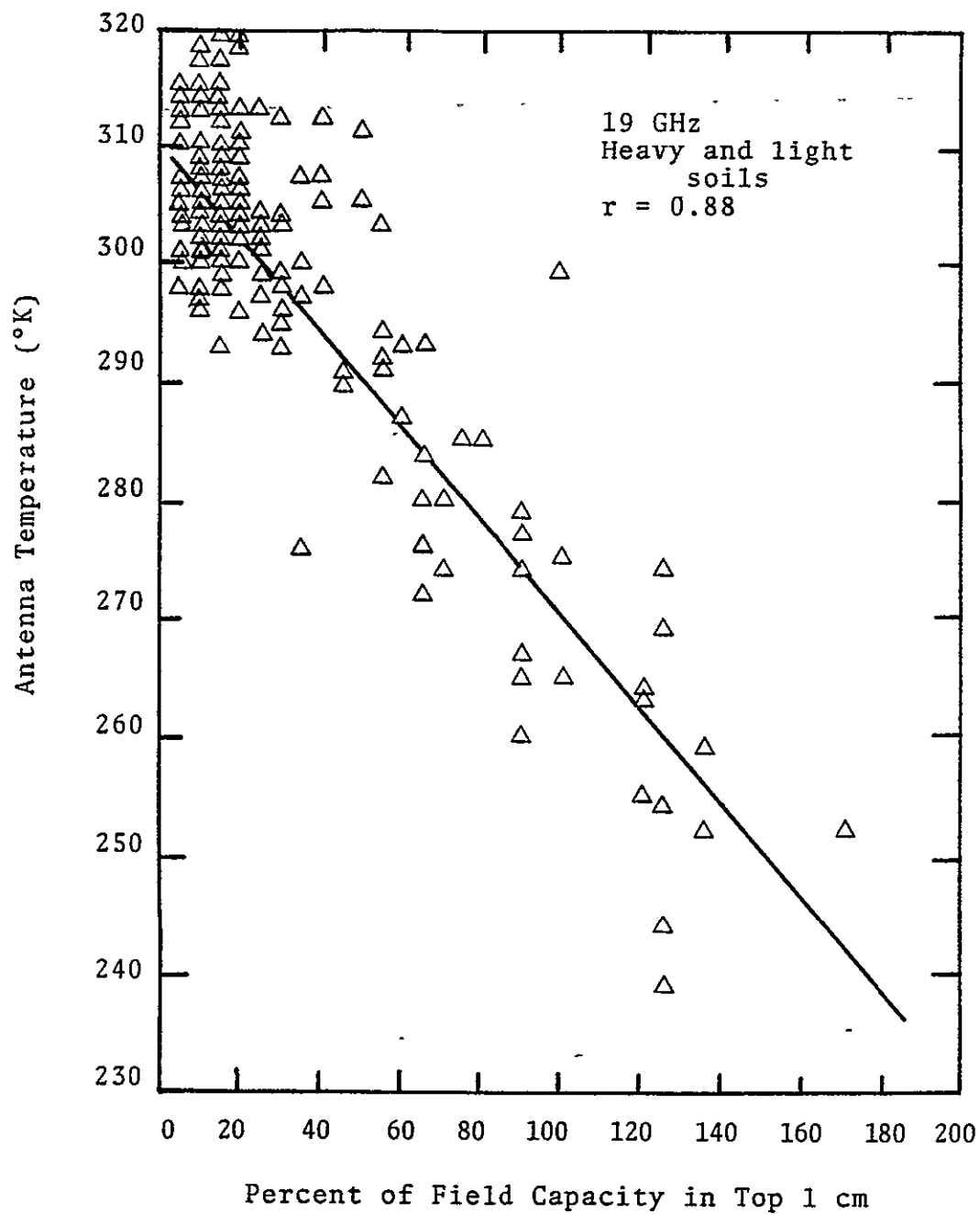


Figure III-8. Plot of 19 GHz measured antenna temperature versus soil moisture in top 1 cm expressed as percent field capacity (after Schmugge et al. [85]).

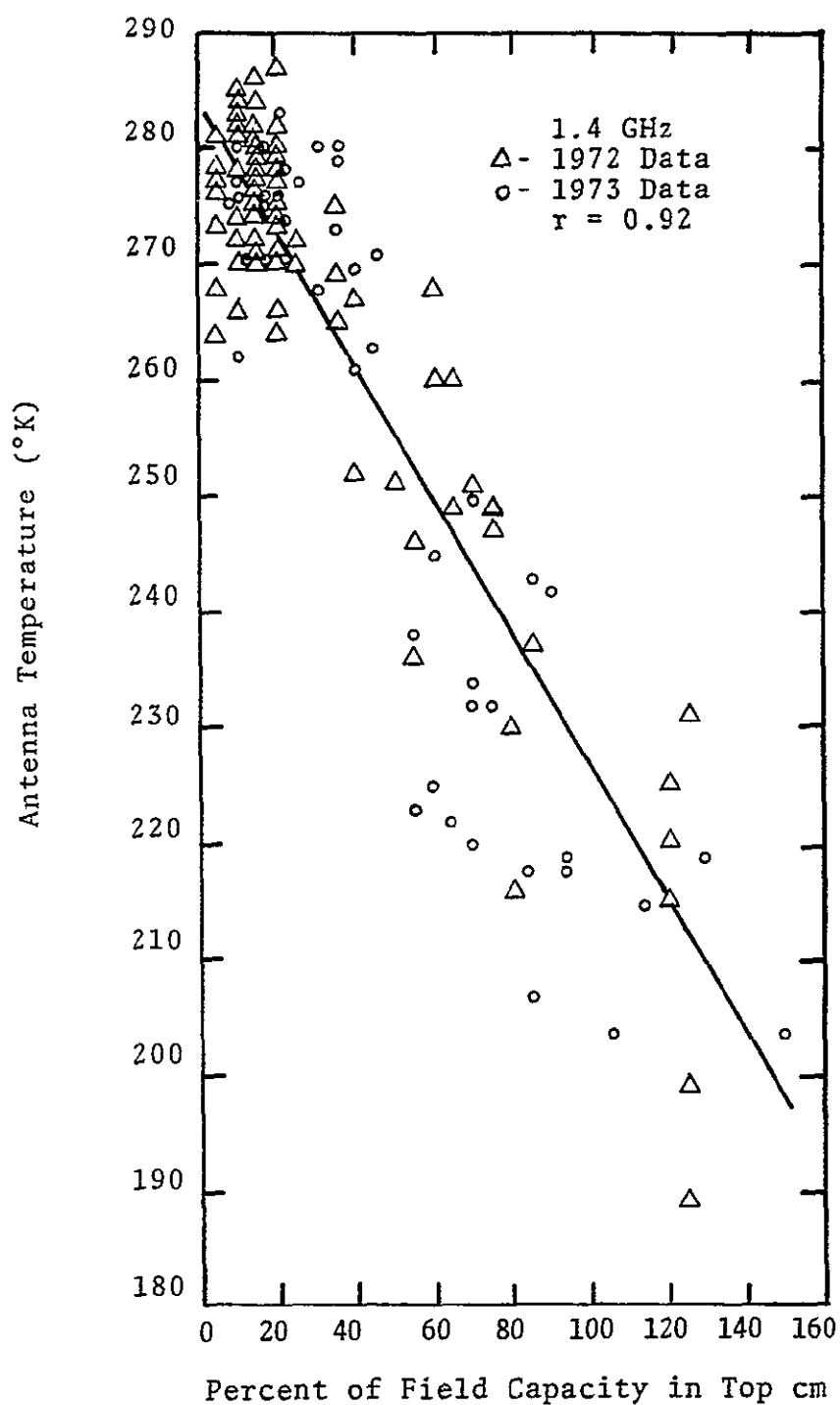


Figure III-9. Plot of 1.4 GHz measured antenna temperature versus soil moisture in top 1 cm expressed as a percent of field capacity (after Schmugge et al. [85]).



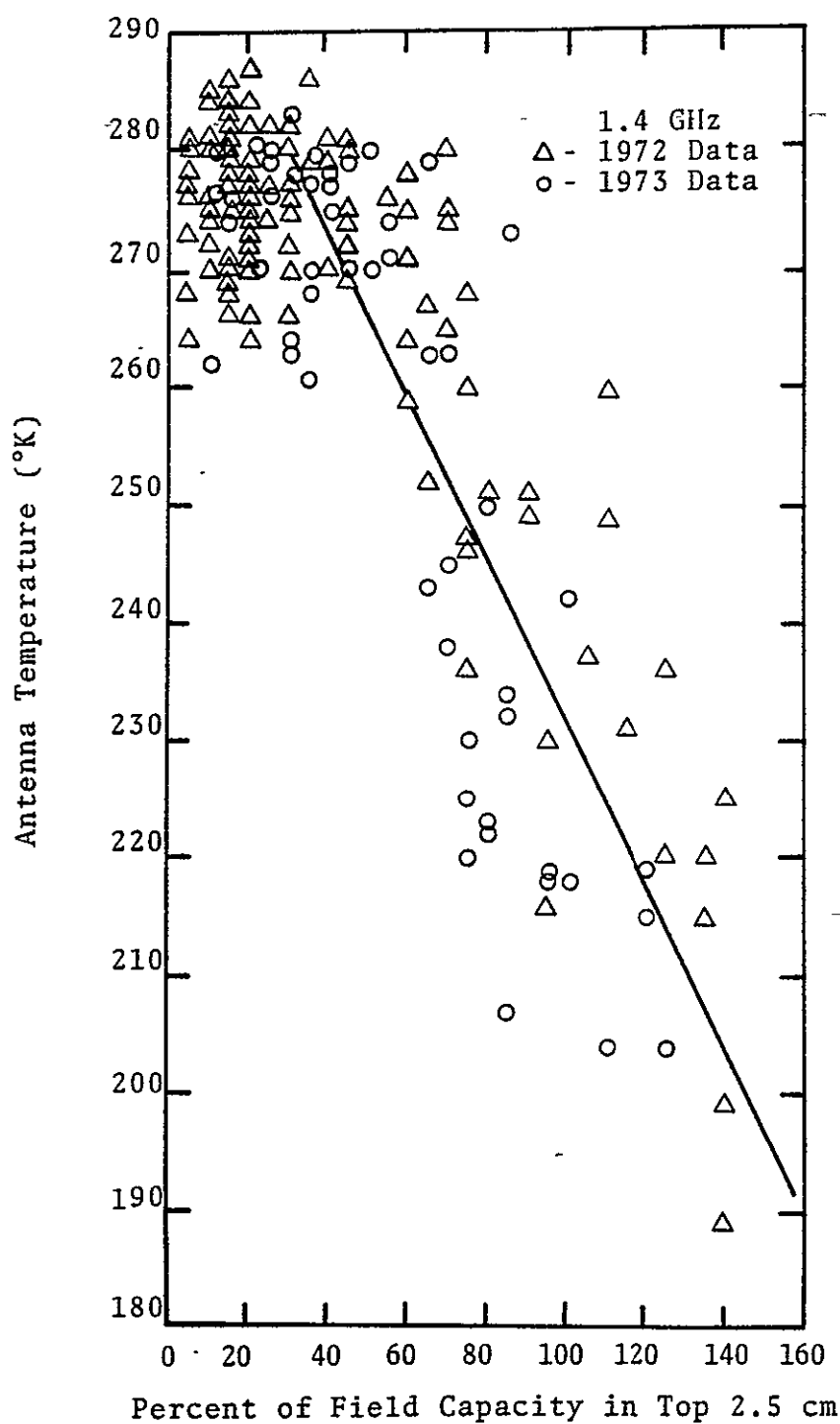


Figure III-10. Plot of 1.4 GHz measured antenna temperature versus soil moisture expressed as a percent of field capacity in the top 2.5 cm (after Schmugge et al. [85]).

X-band data were acquired at an incident angle of  $49^\circ$ . L-band data were acquired at  $40^\circ$  incidence. Since the Burke and Paris [32] radiative transfer model is a smooth surface model, and since most of the Phoenix fields were listed, Schmugge et al. [86] assumed that the primary effect of surface roughness was to change the effective look direction of the antenna. With this assumption, Schmugge et al. concluded that surface roughness effects can be separated by comparing two parameters; a parameter denoted by P which is one-half of the sum of the vertical and horizontal apparent antenna temperatures, and a parameter denoted by Q which is the difference of the vertical and horizontal apparent antenna temperatures. These parameters are the first two Stokes parameters, where P is related to intensity of emission and Q is related to the polarization of the emission. Schmugge et al. also concluded that the microwave signature of the surface rewetting effect described by Jackson [87] is an increase in the polarization of emission. This conclusion was based on the fact that the Q observed at dawn was greater than that observed at midday for the same fields at 10.69 GHz. In addition, they concluded that the L-band radiation comes from much deeper in the soil than the X-band radiation. However, they further concluded that surface soil moisture (0-2 cm) dominates over the subsurface soil moisture gradient at both frequencies.

## Passive Ground-Based Measurements

Measurement programs utilizing ground-based radio-meters have been performed for a number of years for the purpose of basic research in several areas. They include programs executed by researchers at the Aerojet-General Corporation, Jet Propulsion Laboratory, and Texas A&M University, who performed ground-based experiments to acquire data to determine the relationship between radiation from soil and soil moisture. Results of these measurement programs are described below.

Bare soil - Richerson [34] and Jean et al. [88] reported measurement of coarse sand made at 31.4 GHz at Texas A&M University in 1971. Comparison of measurements of smooth sand, made immediately after wetting, to theoretical predications were satisfactory. However, measurements made of the same scene an hour after irrigation had a much less well defined relationship to soil moisture. This problem was a result of the formation of a dry layer above the wet subsurface. Measurements of wet rough sand were less sensitive to soil moisture than measurements of the smooth sand.

Other measurements demonstrating the effect of soil moisture layering are reported by Blinn and Quade [89], and Blinn et al. [90]. Their measurements demonstrate the effect of varying the depth of a very sharply defined dry

layer of sand over a wet layer of sand. It is shown that such a worst case soil layering situation can cause the emission to oscillate as the depth of the layer is varied (Figure III-11). In addition, Blinn and Quade demonstrated the depth of penetration of 1.4 GHz, 10.69 GHz and 31.6 GHz emission for a number of sands and gravels as a function of particle size and moisture content. Figure III-12 shows the penetration depth for sand as a function of moisture and frequency. The depth of emission at 1.4 GHz is shown to be greater than 15 cm for dry sand and from 5 to 7 cm for wet sand (15 percent moisture by weight).

Lee [91] and Newton et al. [92] reported measurements of bare smooth and rough soil surfaces as a function of soil moisture. These measurements were made at 1.4 GHz and 10.6 GHz with the sensor described in Chapter V. Their measurements demonstrate that surface roughness decreases the sensitivity of the emission to soil moisture. As shown in Figure III-13, the emission from dry soil is approximately independent of surface roughness. However, for wet soil the emission is greater from the rough surface. This phenomenon is also evident in measurements made by Blinn and Quade [89] of smooth and raked sand (Figure III-14).

Poe et al. [93] report a series of measurements made at 37 GHz, 13.6 GHz, 5.0 GHz and 1.4 GHz of bare soil in Tempe, Arizona. These measurements further demonstrate

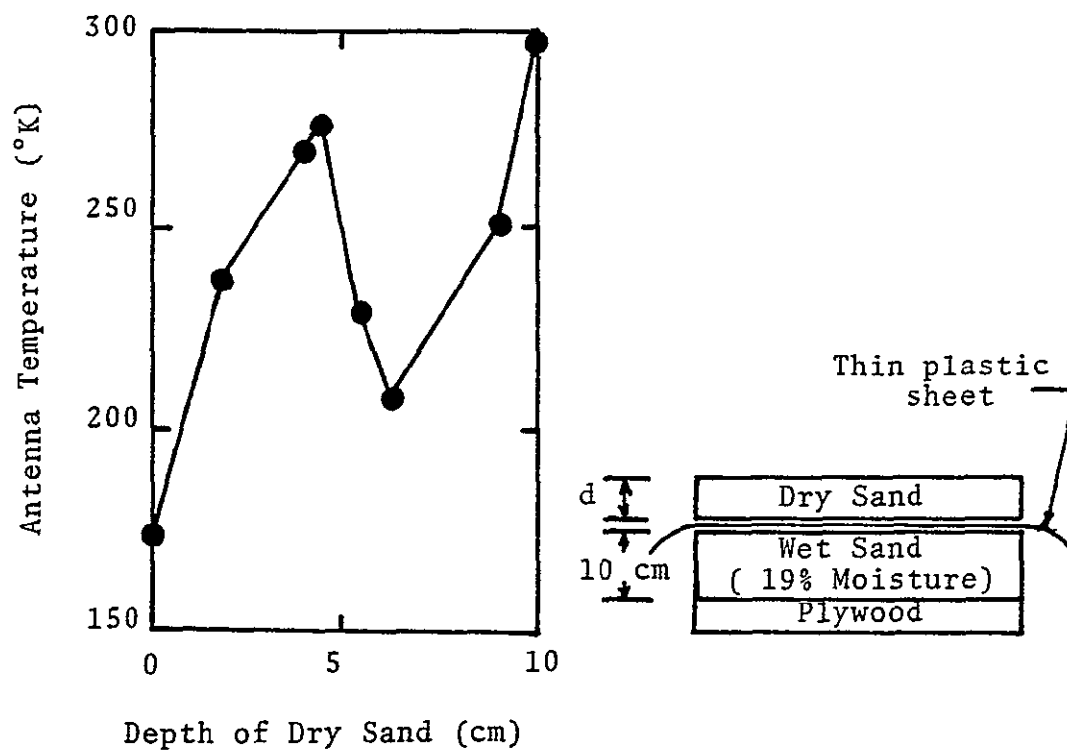


Figure III-11. The 21 cm response for dry and overlying wet sand (after Blinn et al. [90]).

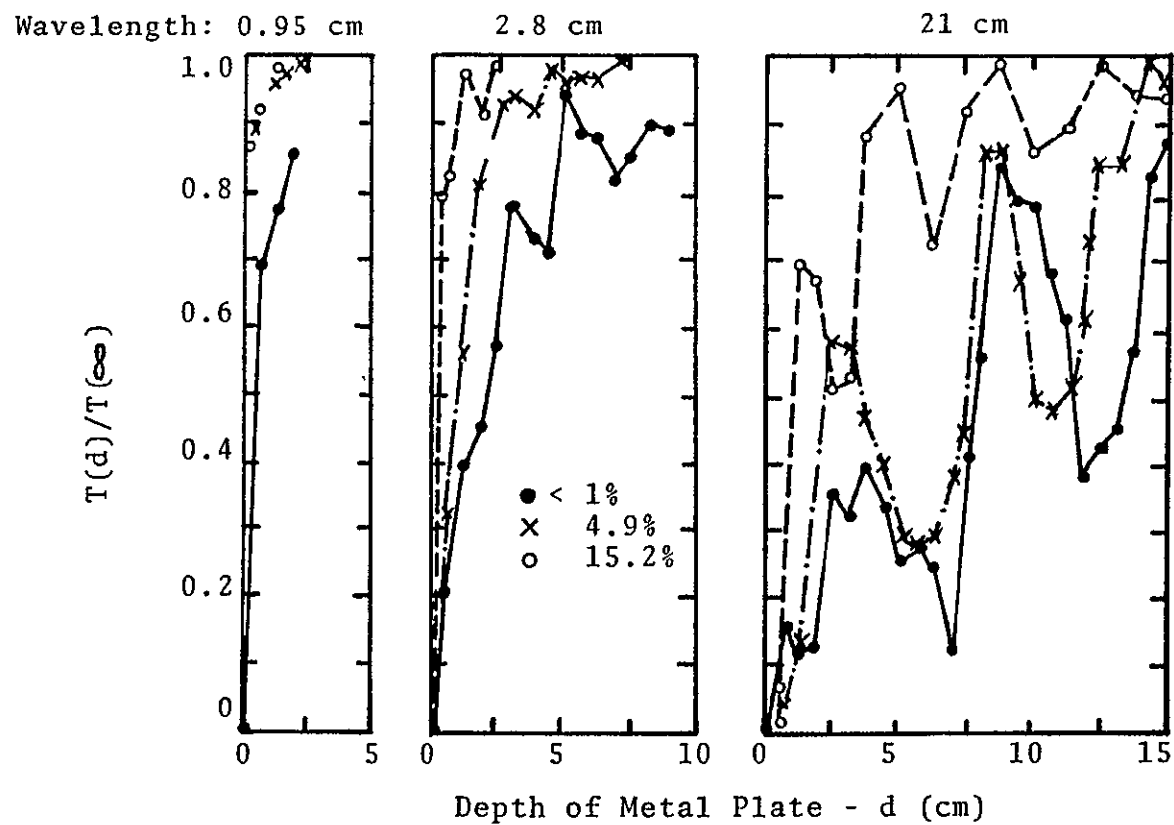


Figure III-12. Plate measurements of moist sand (after Blinn et al. [90]).

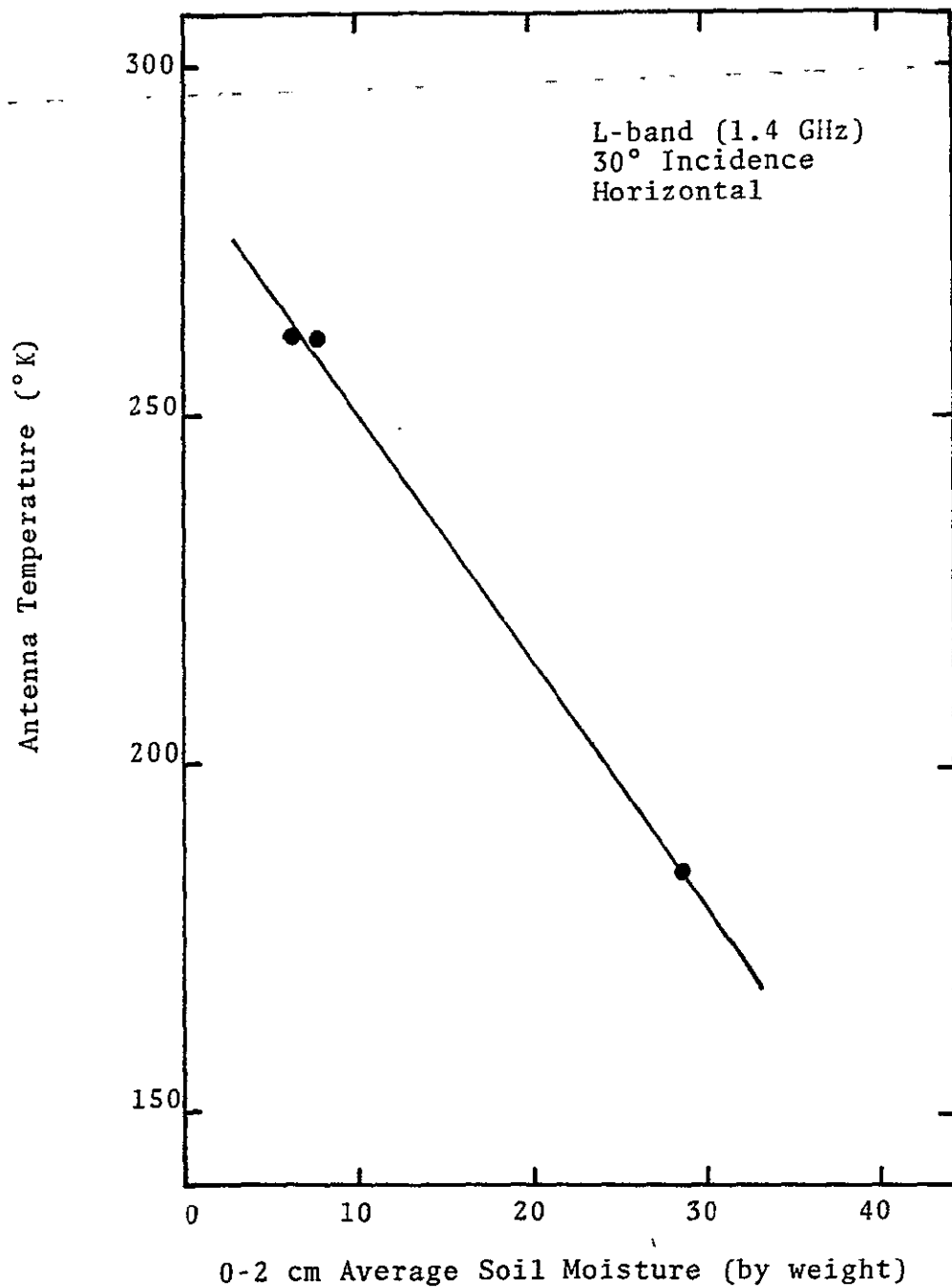


Figure III-13. Antenna temperature versus soil moisture for a smooth bare field (after Lee [91]).

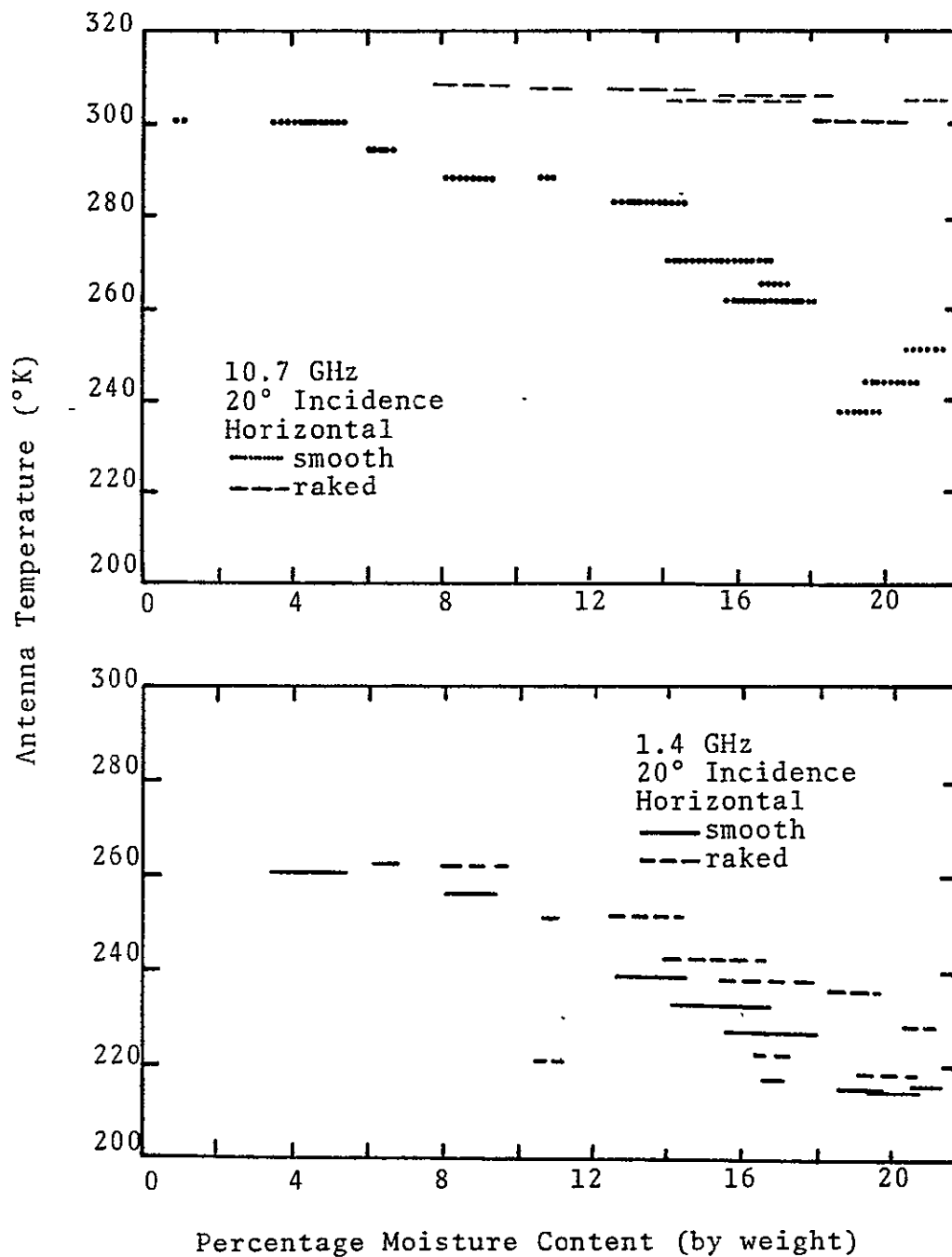


Figure III-14. Moisture effects for smooth and rough junction sand (after Blinn and Quade [89]).



that the lower frequencies have a greater sensitivity to soil moisture than the higher frequencies, and that the sensitivity for horizontal polarization is greater than for vertical polarization. An algorithm is presented which permits a calculation of the vertical profile of the total volume of water per unit area using measured horizontally polarized antenna temperature which have been normalized by the surface soil temperature. The model is based on the intuitive feeling by the authors that it is the total mass of water per unit area lying between the surface and the skindepth which determines the brightness temperature, rather than the specific details of the distribution of moisture. Although the model produced reasonable results for very wet soil conditions, it produced poor results for dry conditions. Generally, soil moisture distribution with depth is fairly uniform for wet conditions. The poor estimates produced by the algorithm for dry conditions indicates that the basic assumption made by Poe et al. that the soil moisture distribution has a minimal effect is invalid.

Vegetated soil - Very few ground-based passive microwave measurements of vegetated soil have been published in the literature. Riegler [94] reports limited measurements of alfalfa, oats and wheat using passive and active microwave systems at X-band. The data are, however, too sparse to

draw any conclusions concerning the effect of vegetation on the ability to remotely measure soil moisture. Lee [91] and Newton et al. [92] also report measurements of vegetated smooth and rough surfaces. The vegetation used in these studies was 0.4 meter high oats planted in a uniform cover. Lee's results show that the vegetation acted as an attenuator at 1.4 GHz, and that it exhibited a masking effect at 10.63 GHz regardless of the surface roughness. Although the vegetation acted as an attenuator at 1.4 GHz, the soil moisture dependence was only slightly affected. In addition, good agreement was found between the vegetation model developed by Sibley [75] and experimental results.

#### Applicability of Published Literature

A considerable number of authors have reported either airborne or ground-based passive microwave measurements, however, a review of these measurements show that they are disjoint in terms of the scenes measured and the frequencies and incident angles utilized. Many of the measurements are useful for comparing the effects of specific combinations of scene and sensor parameters. However, there are too few microwave measurements reported in the literature to be of use in any systematic analysis of soil emission to determine the effects of volume inhomogeneities, surface roughness and vegetative cover.

## CHAPTER IV

### MODELS

#### Introduction

Chapter III contains a review of previously published approaches to modeling the soil-vegetation complex. In that review the scene was decomposed into three categories; the soil volume, the surface and the vegetation cover. This same approach to modeling the soil-vegetation complex will be used in this chapter. The rationale, development and interpretation of the models used to describe each scene component in this study will be given, as well as the rationale for choosing the models.

Only models that describe emission from the soil-vegetation complex are discussed. This radiation will be termed brightness temperature. The total emission from a scene consists not only of the brightness temperature of the scene, but also of emission from several other sources (Figure III-1). These components include thermal microwave emission of the intervening atmosphere between the scene and measurement system, emission of the sky reflected from the scene into the receiving antenna

aperture, manmade sources and reflections of point sources such as the sun into the receiving aperture. The total emission from a scene will be termed the apparent temperature of the scene. A radiometer responds to the apparent temperature of a scene and will be termed antenna temperature. Although most of the components of the apparent temperature of a scene may be considered negligible in many cases, they must sometimes be considered when comparing antenna temperature measurements to model predictions of scene brightness temperature. Such a comparison will be left to Chapter VI.

The model presented to describe the brightness temperature of the soil-vegetation complex is a composite of three individual models. Certain assumptions are required in order to use these individual models in conjunction with one another as a model of the composite soil-vegetation complex. For instance, the soil volume will be modeled by assuming that it is composed of horizontally homogeneous layers. However, this model will be used in conjunction with an independent model of the surface. As a result, an assumption must be made concerning the location of the reference datum that will describe the planar top layer of the soil volume model. The mean surface height will be

used as this reference datum (Figure IV-1). A similar assumption must be made for the interface between the vegetation model and the surface model. In fact, the same reference datum will be used for this interface as shown in Figure IV-1.

### Soil Volume

#### Model Description

Modeling options - It was pointed out in Chapter III that the classical approach to modeling the emission from soil has been the Peake approach [29]. This approach relates the emissivity of a scene to the integral of the differential scattering coefficients defined for the top side of the surface. As a result, the Peake approach results in a composite model of the soil volume and soil surface. It cannot be used to model the soil volume independently of the soil surface. In addition, the Peake approach is a special case of a more general formulation (as is shown in the next section) and is only strictly valid for uniform soil moisture and uniform soil temperature profiles.

Stogryn [30] derived a general formulation for the emitted radiation intensity of a volume. Stogryn's only assumptions were that the volume was horizontally uniform

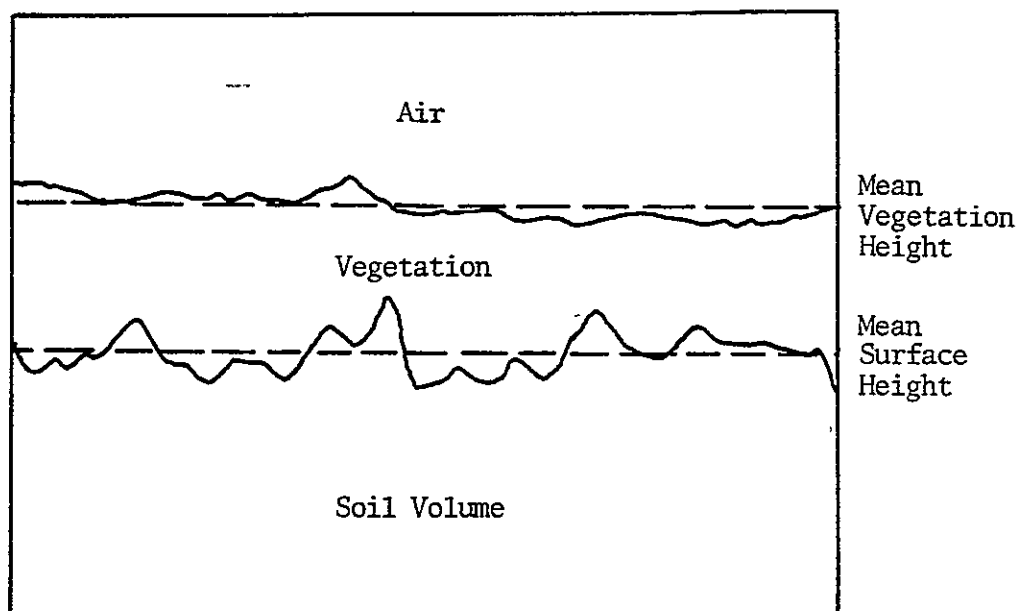


Figure IV-1. Soil surface and vegetation surface reference datums.

and had a smooth surface. Stogryn points out that the number of permittivity profiles for which explicit, exact or even approximate solutions can be obtained using this formulation is very limited. Stogryn outlines a numerical procedure for evaluating his formulation for arbitrary permittivity variations. However, he noted that "this approach requires a considerable amount of computation which is not directly related to the desired results" [30]. In addition, Stogryn states that "such a procedure can be expected to consume a large amount of time on a high speed digital computer when results are required for a number of angles." More importantly this approach does not provide results that can be interpreted in terms of a single parameter related to the soil moisture profile.

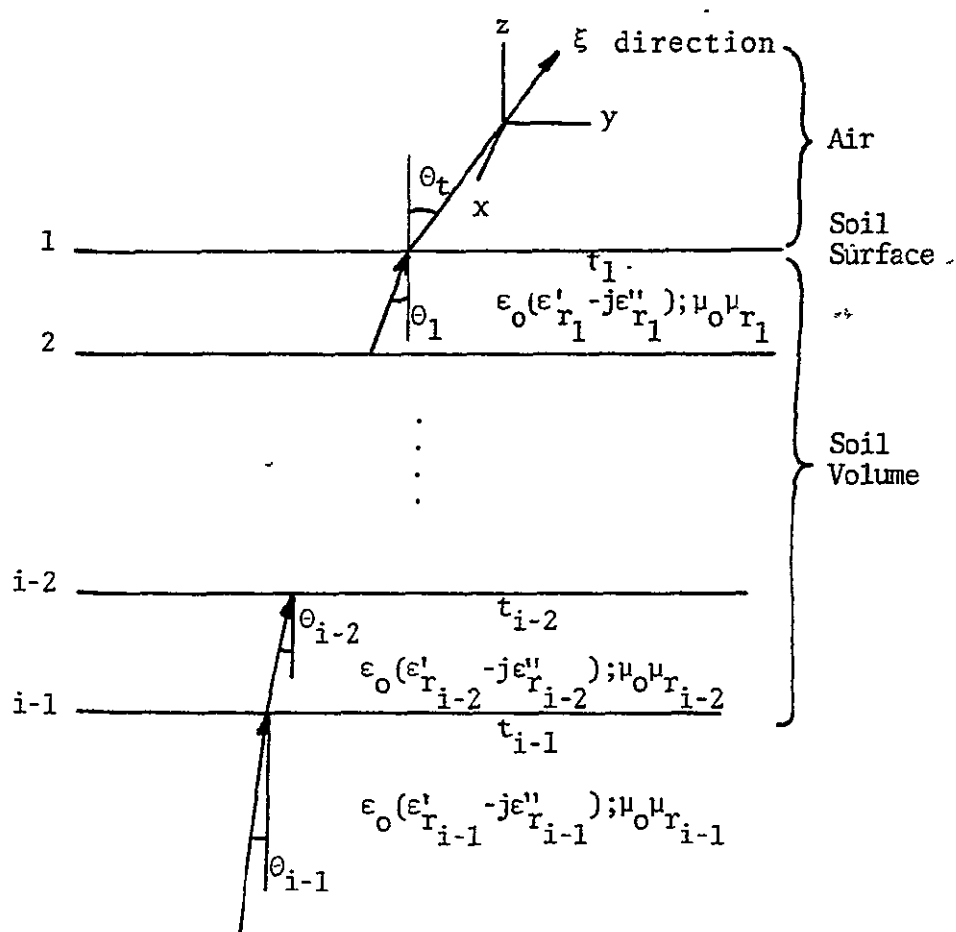
For the case where permittivity varies slowly with depth, Stogryn [30] and Tsang et al. [31] demonstrate that their formulation is identical to the integral radiative transfer equation for a semi-infinite, plane, non-scattering, stratified volume in thermodynamic equilibrium. Further, the radiative transfer approach to modeling the emission from a layered horizontally plane homogeneous soil volume approaches Stogryn's exact solution as the layers become infinitely thin.

Ground data measurements of soil moisture and soil temperature profiles made in support of the microwave emission measurements reported in Chapter V could only be obtained for specific depth increments. As a result, the soil permittivity profiles used in conjunction with a model of emission from a soil volume will be assumed to be piecewise continuous. This assumption eliminates the advantage of using an exact formulation, such as those by Stogryn [30] and Tsang et al. [31], to model the radiation intensity emitted from the soil volume. A radiative transfer approach will be adequate.

Radiative transfer equations - England [43] demonstrated that scattering within the soil volume had negligible effects on the emission of moist soil. As a result the radiative transfer approach of Burke and Paris [32] is adequate to effectively model the radiation intensity emitted by a soil volume.

The basic derivation of the Burke and Paris [32] approach will be reviewed in order to demonstrate the assumptions underlying the model. The soil volume is modeled as a horizontally plane stratified medium with each layer consisting of a non-scattering homogeneous soil (Figure IV-2). Soil permittivity and soil temperature are assumed to be constant across any given layer of soil. The soil surface and the layer interfaces are assumed to be





- $t_i$  - physical soil temperature of each layer  
 $\epsilon_o$  - permittivity of free space  
 $\mu_o$  - permeability of free space  
 $\epsilon'_{r_i} - j\epsilon''_{r_i}$  - relative permittivity of each layer  
 $\mu_{r_1}$  - relative permeability of each layer ( $\approx 1.0$ )

Figure IV-2. Soil volume geometry used in the radiative transfer model of soil emission.

smooth. The power intensity transmitted across each layer interface can be calculated in terms of the Fresnel transmission coefficients.

The transfer of radiation within the soil volume is described by the basic equation of radiative transfer as given by Chandrasekhar [95].

$$\frac{d I_{\omega}(z)}{dz} = -\gamma_{\omega}(z) I_{\omega}(z) + J_{\omega}(z) \quad (\text{IV-1})$$

In (IV-1)  $I_{\omega}(z)$  is the intensity of the radiation propagating upward as denoted in Figure IV-2. It is only dependent on the  $z$  coordinate since each layer is uniform in  $x$  and  $y$ .  $J_{\omega}(z)$  is the radiation source function of the soil. It is constant within each layer and is given by Planck's emission law as noted below. Both  $I_{\omega}(z)$  and  $J_{\omega}(z)$  are power intensities and have units of watts per  $\text{m}^2$  steradian. The subscript  $\omega$  denotes dependence on frequency.

$\gamma_{\omega}(z)$  is the power absorption coefficient of the soil. It is also constant within each layer and is dependent on frequency. Generally,  $\gamma_{\omega}(z)$  is given as the mass absorption coefficient times the density of the medium. For a

non-scattering media, it is

$$\gamma_{\omega}(z) = 2 \alpha(z) \quad (IV-2)$$

where  $\alpha(z)$  is the electric field attenuation coefficient.

Goody [96] has shown that the emission of a body is Planckian if the population of energy levels is due primarily to collisions among molecules. Therefore, even without the restriction of local thermodynamic equilibrium, the source function is given by Planck's emission law:

$$J_{\omega}(t) = \frac{2 h \nu^3}{c^2} \left( \frac{1}{e^{h\nu/k t} - 1} \right) \quad (IV-3)$$

where

$h$  - Planck's constant ( $6.63 \times 10^{-34}$  Joule-second)

$k$  - Boltzman's constant ( $1.38 \times 10^{-23}$  Joule/°K)

$c$  - speed of light

$t$  - temperature

$\nu$  - frequency

For microwave frequencies it can be shown that the source function given by (IV-3) is directly related to the temperature of the medium. At microwave frequencies  $h\nu/kt \ll 1$ . Expanding the second term of (IV-1) and neglecting terms above the first order yields:

$$J_{\omega}(t) = \frac{2h\nu^3}{c^2} \left[ \frac{1}{(1 + \frac{h\nu}{kt}) - 1} \right] \quad (\text{IV-4})$$

or

$$J_{\omega}(t) = \frac{2kt}{\lambda^2}$$

where free space wavelength is given by

$$\lambda = \frac{c}{\nu}$$

The result of (IV-4) is generally known as the Rayleigh-Jeans approximation [95]. Equation (IV-4) describes the total radiation energy. Assuming random polarization, this energy can be divided equally into orthogonal polarization states:

$$J_{\omega}(t)_v = J_{\omega}(t)_h = \frac{kt}{\lambda^2} \quad (\text{IV-5})$$

where

v - vertical polarization

h - horizontal polarization

The source function in (IV-1) is directly related to the temperature of the medium. It is therefore reasonable to define an effective temperature of emission,  $T_e$ , that is directly proportional to  $I_\omega(z)$ .  $I_\omega(z)$  and  $T_e$  are polarization dependent, however.

Subscripts denoting polarization will be suppressed in the following equation development and the energy in each polarization state will be assumed to be uncorrelated. Adopting this terminology and considering a narrow range of frequencies near  $\omega$  and one polarization, (IV-1) can be rewritten as

$$\frac{dT_e(z)}{dz} = -2\alpha(z)T_e(z) + 2\alpha(z)t(z) \quad (IV-6)$$

where

$T_e$  - effective temperature of emission at one polarization

$t$  - temperature of the medium

For the horizontally homogeneous plane stratified medium defined in Figure IV-2;  $\alpha$ ,  $T_e$ , and  $t$  are all constant for a given layer.

Since electrical properties of the soil volume have been defined to be piecewise continuous in depth, (IV-6) can only be evaluated within individual layers. The discontinuities at each interface must be handled separately. The effective temperature of emission within a layer can be obtained by integrating (IV-6) over the layer thickness. For the first layer (IV-6) is integrated from a point just below the surface to a point just above the second interface. This integration results in

$$T_e(1^-) = t_1(1 - e^{-2\alpha_{z_1}\Delta z_1}) + T_e(z^+)e^{-2\alpha_{z_1}\Delta z_1} \quad (\text{IV-7})$$

The argument,  $1^-$ , denotes a point just below the surface (interface 1) and  $2^+$  denotes a point just above the second interface (Figure IV-2). The thickness of the layer between the surface (interface 1) and interface 2 is given by  $\Delta z_1$ . The attenuation constant,  $\alpha$ , is dependent only on the depth  $z$ , hence the notation  $\alpha_{z_1}$ .

In (IV-7) the energy emitted in layer 1 is given by

$$t_1(1 - e^{-2\alpha_{z_1}\Delta z_1})$$

while the upwelling radiation from the soil volume below interface 2 is given by  $T(2^+)$ . The exponential coefficient multiplying  $T(2^+)$  in (IV-7) describes the attenuation that the upwelling energy from below interface 2 experiences as it propagates through layer 1.

The upwelling radiation referenced to a point just above interface 2 is given by

$$T_e(2^+) = \bar{R}_2 t_1 (1 - e^{-2\alpha_1 \Delta z_1}) + T_e(2^-) T_2 \quad (\text{IV-8})$$

The first term on the right of (IV-8) represents that portion of the energy emitted in layer 1 that is reflected from interface 2 back toward the surface.  $\bar{R}_2$  represents the power reflection coefficient in the negative  $z$  direction at interface 2. (Hereafter "bars" over a power transmission or reflection coefficient denotes that they correspond to the negative  $z$  direction). The second term on the right of (IV-8) is simply the upwelling energy from below interface 2 transferred across interface 2 using the power transmission coefficient corresponding to interface 2,  $T_2$ .

The form of the equation defining  $T_e(1^-)$  can be visualized by substituting (IV-8) into (IV-7)

$$T_e(l^-) = t_1 (1 - e^{-2\alpha_{z_1} \Delta z_1}) + e^{-2\alpha_{z_1} \Delta z_1} \cdot$$

$$\left[ \bar{R}_2 t_1 (1 - e^{-2\alpha_{z_1} \Delta z_1}) + T_e(z) T_2 \right]$$

By repeating this procedure for N layers, a series can be defined to represent  $T_e(l^-)$ :

$$BT_{\text{volume}} = T_e(l^-) = T_e (1 + e^{-2\alpha_{z_1} \Delta z_1} \bar{R}_2)$$

$$+ \sum_{i=2}^N T_{e_i} (1 + e^{-2\alpha_{z_i} \Delta z_i} \bar{R}_{i+1}) \cdot \quad (\text{IV-9})$$

$$e^{-2 \sum_{k=1}^{i-1} \alpha_{z_k} \Delta z_k} \prod_{j=2}^i T_j$$

where

$$T_{e_i} = t_i (1 - e^{-2\alpha_{z_i} \Delta z_i})$$

N - number of layers

$$R_N + 1 = 1.0$$

$$\Delta z_N = \text{infinity}$$



Equation (IV-9) defines the effective temperature of emission for the soil volume just below the surface.

$T_e(l^-)$  will be defined as the radiometric brightness temperature of the soil volume,  $BT_{\text{volume}}$ .

$T_e(l^-)$  is dependent on the angle  $\theta_1$  at which the energy is approaching the surface from below (Figure IV-2). This is a result of the dependence of the power transmission coefficients, power reflection coefficients, and attenuation constants on angle. For a uniform soil permittivity profile the transmission coefficients go to unity and the reflection coefficients go to zero, but the attenuation constant is still dependent on angle,  $\theta_1$ .

For the case of a smooth soil surface, the brightness temperature of the soil is given by simply multiplying (IV-9) by the power transmission coefficient for a smooth surface.

$$BT_{\text{soil}} = T_e(l^+) = T_e(l^-) \cdot T_1 = BT_{\text{volume}} \cdot T_1 \quad (\text{IV-10})$$

The technique of handling rough surfaces will be presented in the next section.

To complete the formulation, equations defining  $\alpha_{z_i}$ ,  $T_i$ , and  $\bar{R}_i$  must be provided. A formulation for  $\alpha_{z_i}$  will first be derived, then a technique of obtaining  $T_i$  and  $\bar{R}_i$  will be discussed.

Attenuation constant ( $\alpha_z$ ) - In order to evaluate (IV-9) an expression is needed for the attenuation constant,  $\alpha_z$ . Most electromagnetic textbooks [39], [97], [98] give an expression for the attenuation constant that is independent of the direction of propagation. In using such an expression the direction from which energy is incident on each layer interface is taken into account in the reflection and transmission coefficients at each interface. However, the evaluation of (IV-9) is more convenient (as will be pointed out below) if the direction of propagation is included in the expression for the attenuation constant.

An expression for the  $z$  component of the attenuation constant is derived below. It will be seen that the resulting expression is dependent on the direction of propagation. In deriving  $\alpha_z$  a plane wave harmonic in time traveling in the  $\xi_i$  direction and independent of the  $x$  coordinate will be assumed (Figure IV-2). This wave will have the form:

$$\bar{E}_i(y, z, t) = \bar{E}_i e^{jk_i \xi_i} e^{j\omega t} \quad (\text{IV-11})$$

where

$$\xi_i = \bar{n}_i \cdot \bar{r}$$

$\bar{n}_i$  - unit vector defining the direction of  
propagation in the  $i^{\text{th}}$  layer

$\bar{r}$  - position vector

$t$  - time

For a general medium,  $k_i$  is complex and takes the form:

$$k_i = \beta_i + j\alpha_i \quad (\text{IV-12})$$

Therefore (IV-11) may be written:

$$\bar{E}_L(y, z, t) = \bar{E}_i e^{j(\beta_i + j\alpha_i)\xi_i} e^{j\omega t} \quad (\text{IV-13})$$

The rectangular coordinates of  $\xi_i$  are:

$$\xi_{x_i} = 0$$

$$\xi_{y_i} = y \sin \theta_i$$

$$\xi_{z_i} = z \cos \theta_i$$

(IV-14)

Using these in (IV-13) yields:

$$\begin{aligned} \bar{E}_i(y, z, t) = \bar{E}_i e^{-\alpha_i \Delta \xi_i} \\ e^{j(\beta_i y \sin \theta_i + \beta_i z \cos \theta_i)} e^{j\omega t} \end{aligned} \quad (\text{IV-15})$$

The x, y, and z coordinate components of  $\beta_i$  are given by

$$\begin{aligned} \beta_{x_i} &= 0 \\ \beta_{y_i} &= \beta_i \sin \theta_i \\ \beta_{z_i} &= \beta_i \cos \theta_i \end{aligned} \quad (\text{IV-16})$$

At any interface, Snell's law requires that the phase velocity parallel to the interface must be equal in the two media that define the interface, thus, the y components of the phase velocities must match across the interfaces.

$$\beta_{y_i} = \beta_{y_{i+1}} \quad (\text{IV-17})$$

So

$$\begin{aligned} \beta_{y_i} &= \beta_{y_i} \\ \beta_i \sin \theta_i &= \beta_{y_i} \end{aligned} \quad (\text{IV-18})$$

In addition, the boundary conditions at each interface require that the parallel components of the electric field be equal at the interface. This condition requires that

$$\bar{E}_i \sin \theta_i = \bar{E}_{i+1} \sin \theta_{i+1} \quad (\text{IV-19})$$

be independent of the  $y$  dimension. It is obvious from (IV-15) that this can only occur if

$$\alpha_{y_i} = 0 \quad (\text{IV-20})$$

It is known that [97], [98]

$$k_i^2 = \omega^2 \mu_i (\epsilon'_i - j \epsilon''_i) \quad (\text{IV-21})$$

where

$$\mu_i = \mu_0 \mu_{r_i}$$

$$\epsilon'_i = \epsilon_0 \epsilon'_{r_i}$$

$$\epsilon''_i = \epsilon_0 \epsilon''_{r_i}$$

$\mu_0$  - permeability of free space ( $4\pi \times 10^{-7}$  henrys/  
meter)

$\epsilon_0$  - permittivity of the space ( $8.85 \times 10^{-12}$  farads/  
meter)

From (IV-12)

$$k_i^2 = (\cancel{\beta_{x_i}^2} + \beta_{y_i}^2 + \beta_{z_i}^2) - (\cancel{\alpha_{x_i}^2} + \alpha_{y_i}^2 + \alpha_{z_i}^2) + 2j\beta_i\alpha_i \quad (\text{IV-22})$$

Equating the real and imaginary parts of (IV-21) and  
(IV-22) yields

$$\beta_{y_i}^2 + \beta_{z_i}^2 - \alpha_{z_i}^2 = \omega^2 \mu_0 \mu_{r_i} \epsilon_0 \epsilon'_{r_i} \quad (\text{IV-23a})$$

$$-2\beta_i\alpha_i = \omega^2 \mu_0 \mu_{r_i} \epsilon_0 \epsilon''_{r_i} \quad (\text{IV-23b})$$

Substituting (IV-18) into (IV-23a) yields

$$\beta_{z_i}^2 - \alpha_{z_i}^2 = \omega^2 \mu_0 \epsilon_0 (\epsilon'_{r_i} - (\beta_i \sin \theta_i)^2) \quad (\text{IV-24})$$

where [93]

$$\mu_{r_i} \approx 1.0$$

$$\beta_i = \left[ \frac{\epsilon'_{r_i}}{2} \left( 1 + \sqrt{1 + \left( \frac{\epsilon''_{r_i}}{\epsilon'_{r_i}} \right)^2} \right) \right]^{1/2}$$

while (IV-23b) reduces to

$$-2\beta_{z_i} \alpha_{z_i} = \omega^2 \mu_0 \epsilon_0 \epsilon''_{r_i} \quad (\text{IV-25})$$

Solving (IV-24) and (IV-25) simultaneously

$$\beta_{z_i} = \frac{\omega^2 \mu_0 \epsilon_0 (\epsilon'_{r_i} - (\beta_i \sin \theta_i)^2)}{2} \left[ 1 + \sqrt{1 + \left( \frac{\epsilon''_{r_i}}{\epsilon'_{r_i} - (\beta_i \sin \theta_i)^2} \right)^2} \right] \quad (\text{IV-26})$$

$$\alpha_{z_i} = -(\omega^2 \mu_0 \epsilon_0 \epsilon''_{r_i}) / 2\beta_{z_i}$$

Equation (IV-26) describes the  $z$  component of the electric field attenuation,  $\alpha_z$ , and phase,  $\beta_z$ , constants. Note that these quantities are constant across any given layer. The use of these quantities for calculating the power transmission coefficients is discussed below.

Power transmission and reflection coefficients -

Analytical descriptions of the power transmission and reflection coefficients are also needed in order to evaluate (IV-9). The layer interfaces defined in Figure IV-2 are assumed to be smooth. As a result, the transmission and reflection of electric fields at these interfaces can be described using the Fresnel electric field transmission and reflection coefficients given in most electromagnetic textbooks [39], [97], [98]. Since the derivation of these coefficients is well known, it will not be repeated here. However, the relationship between these coefficients and the power transmission and reflection coefficients required in (IV-9) will be presented.

Given the complex vector electric,  $\vec{E}$ , and magnetic,  $\vec{H}$ , field intensities, the average power density can be computed using Poynting's theorem [97].

$$\bar{P}_{\text{average}} = \frac{1}{2} \text{Real}(\vec{E} \times \vec{H}^*) \quad (\text{IV-27})$$



For the geometrical arrangement shown in Figure IV-3, the power density transmitted across area S is given by

$$P_{t \text{ avg.}} = \frac{1}{2} \text{Real}(E_t H_t^*) \cos \theta_t \quad (\text{IV-28})$$

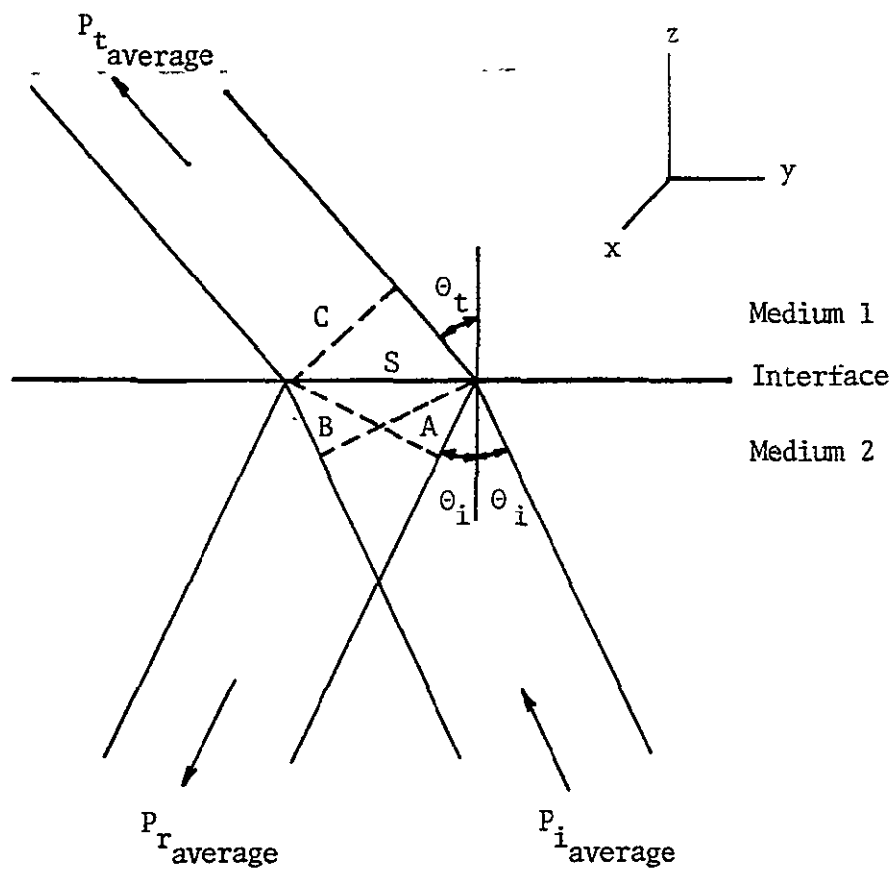
where  $E_t$  and  $H_t$  are the transmitted field intensities. The relationship between the magnetic and electric field intensities is given by

$$H_t = E_t / \eta_1 \quad (\text{IV-29})$$

where  $\eta_1$  is the intrinsic impedance of the medium.

$$\eta_1 = \sqrt{\frac{\mu_0 \mu_{r_1}}{\epsilon_0 (\epsilon'_{r_1} - j \epsilon''_{r_1})}} \quad (\text{IV-30})$$

The Fresnel transmission coefficient for the electric field intensity will be denoted by  $t_e$ . Incorporating this notation into (IV-28) yields



$$\text{area A} = \text{area B}; \quad \frac{\text{area A}}{\text{area S}} = \cos \theta_i; \quad \frac{\text{area C}}{\text{area S}} = \cos \theta_t$$

Figure IV-3. Geometry used to describe the relationship between incident, reflected, and transmitted power density.

$$P_{t_{avg}} = \frac{1}{2} |t_e|^2 |E_i|^2 \text{Real}\left(\frac{1}{\eta_1^*}\right) \cos \theta_t \quad (\text{IV-31})$$

The power transmission coefficient is defined as the ratio of transmitted power density to incident power density. The power density incident on area  $S$  is

$$P_{i_{avg}} = \frac{1}{2} |E_i|^2 \text{Real}\left(\frac{1}{\eta_1^*}\right) \cos \theta_i \quad (\text{IV-32})$$

so that the power transmission coefficient is given by

$$T = |t_e|^2 \frac{\cos \theta_t}{\cos \theta_i} \sqrt{\frac{\epsilon_{r_1}}{\epsilon_{r_2}}} \quad (\text{IV-33})$$

It can similarly be shown that the power reflection coefficient is equivalent to the square of the magnitude of the electric or magnetic field Fresnel reflection coefficient:

$$R = |\rho_e|^2 = |\rho_h|^2 \quad (\text{IV-34})$$

$\rho_e$  is the Fresnel reflection coefficient for the electric field intensity and  $\rho_h$  is for the magnetic field intensity.

Applying the conservation of energy requirement at the interface, an equation relating power transmission to Fresnel reflection coefficients can easily be derived. At the interface the power density transmitted plus the power density reflected must equal the incident power density.

$$P_{i_{avg.}} \cos \theta_i = P_{r_{avg.}} \cos \theta_i + P_{t_{avg.}} \cos \theta_t \quad (IV-35)$$

Substituting (IV-27) and (IV-29) into (IV-35) yields:

$$\frac{|E_t|^2}{|E_i|^2} = \left(1 - \frac{|E_r|^2}{|E_i|^2}\right) \sqrt{\frac{\epsilon'_2}{\epsilon'_1}} \frac{\cos \theta_t}{\cos \theta_i} \quad (IV-36)$$

Since the square of the magnitude of the Fresnel electric field transmission and reflection coefficients is given by

$$|t_e|^2 = \frac{|E_t|^2}{|E_i|^2}$$

and

$$|\rho_e|^2 = \frac{|E_r|^2}{|E_i|^2}$$

then (IV-36) reduces to

$$|t_e|^2 \frac{\cos \theta_t}{\cos \theta_i} \sqrt{\frac{\epsilon'_t}{\epsilon'_i}} = (1 - |\rho_e|^2) \quad (\text{IV-37})$$

Combining (IV-33) and (IV-37), it is seen that the power transmission coefficient is related to the Fresnel electric field reflection coefficient by

$$T = (1 - |\rho_e|^2) \quad (\text{IV-38})$$

Equation interpretation - Equations (IV-9), (IV-26), and (IV-33) or (IV-38) define the radiative transfer model of emission from a soil volume. A note of caution is in order in applying these equations. It was shown that a

plane wave propagating in the soil medium is only attenuated in the  $z$  direction. As a result, the planes of constant amplitude are parallel to the  $xy$  plane, and not parallel to planes of constant phase. The planes of constant phase are perpendicular to the direction of energy flow. Since only the  $z$  component of the attenuation and phase constants are of concern, and the  $z$  direction is perpendicular to the planes defining the interfaces between the layers, the Fresnel reflection coefficients in (IV-34) and (IV-38) must be of the form:

$$\rho_{h_i} = \frac{k_{z_i} - k_{z_{i-1}}}{k_{z_i} + k_{z_{i-1}}}$$

(IV-39)

$$\rho_{v_i} = \frac{\epsilon_{r_{i-1}} k_{z_i} - \epsilon_{r_i} k_{z_{i-1}}}{\epsilon_{r_{i-1}} k_{z_i} + \epsilon_{r_i} k_{z_{i-1}}}$$

where

$$k_{z_i} = \beta_{z_i} + j\alpha_{z_i}$$

$$\epsilon_{r_i} = \epsilon'_{r_i} - j\epsilon''_{r_i}$$

$v$  - vertical polarization

$h$  - horizontal polarization

Note that the angular dependence is contained in  $\beta_{z_i}$  and  $\alpha_{z_i}$  and not in the reflection coefficients.

Since the Fresnel reflection coefficients are calculated using (IV-39), one does not have to contend with complex angles of refraction that occur for imperfect dielectrics. This is the advantage of deriving the radiative transfer model in terms of only the  $z$  components of the attenuation and phase constants.

It can be seen in Figure IV-2 that only medium 0, air, and the  $N^{\text{th}}$  medium are semi-infinite in extent. As a result, the power transmission coefficients for all interfaces except the first must be calculated for a layered media. Likewise the power reflection coefficients in the negative  $z$  direction must be calculated for a layered media, except for the last interface. This can be done by using the impedance matching technique described by Tyrus [39] and Ramo et al. [98] to calculate the Fresnel reflection coefficients used in (IV-34) and (IV-38).

Only small errors are observed, however, if the reflection coefficient for each interface is calculated assuming semi-infinite media on each side of the interface. Under this assumption, the reflection coefficient at any interface is independent of the incident direction, so

$$\overline{R}_i = R_i$$

for all  $i$ , where  $i$  denotes the interface. Since

$$T_i = 1 - R_i$$

(IV-9) reduces to a slightly simpler form. This assumption was used for the calculations in the remainder of this report.

#### Demonstration of the Model

Comparison to accepted procedures - An in-depth derivation and discussion on the applicability of the integral equations describing radiative transfer is given by Chandrasekhar [95]. Further discussion on this approach is provided by Paris [40]. Equation (IV-9) is simply a numerical approximation to the integral equation of radiative transfer. The integral equation is given by

$$T_e(1^-) = \int_{0^-}^{\infty} 2\alpha_z(z) T(z) e^{-\int_z^{0^-} 2\alpha_z(s) ds} dz \quad (\text{IV-40})$$

The limit of the integrals,  $0^-$ , denotes integration from  $0$  to just below the surface. In this case,  $\alpha_z(z)$  is a



smoothly varying function of depth as is  $T(z)$ , which is the source function given by Planck's law of emission. In the limit as the thickness of the individual layers is decreased, (IV-9) approaches (IV-40).

Calculated soil volume brightness temperatures - The effect of moisture and temperature profiles on the radiation emitted from the soil volume can be demonstrated using (IV-9). Note, however, that these calculations do not include effects of the surface-to-air interface, but are calculations of the radiation impinging on the surface from below. The radiation is referenced to the mean surface height reference datum shown in Figure IV-1. There are three cases that are of interest:

- 1) uniform temperature and  
uniform moisture
- 2) nonuniform temperature and  
uniform moisture
- 3) uniform temperature and  
nonuniform moisture

For the case of uniform moisture and temperature profiles, the brightness temperature of the soil volume,  $BT_{\text{volume}}$ , calculated using (IV-9) is simply equivalent to the soil temperature. In addition, it is independent of the angle at which the radiation is impinging on the surface from below, i.e., it is isotropic. This can be seen by

simplifying (IV-9). Under the uniform moisture and uniform temperature assumption (IV-9) reduces to

$$BT_{\text{volume}} = t_z (1 - e^{-2\alpha_z \Delta z_z}) \quad (\text{IV-41})$$

where

$t_z$  - soil temperature

$\alpha_z$  - attenuation constant of the soil

$\Delta z_z$  - depth of soil

Since the soil is semi-infinite in extent,  $\Delta z_z$  is infinity and (IV-41) reduces to

$$BT_{\text{volume}} = t_z \quad (\text{IV-42})$$

This result is interesting since it demonstrates that for uniform moisture and temperature profiles, the dependence of the brightness temperature on soil moisture is controlled totally by the surface boundary effects.

An explanation for the above phenomena can be found by examining (IV-9). Even though the moisture and temperature

profiles are assumed to be uniform, (IV-9) can be evaluated as written. In doing this, the maximum depth below which at least one percent of the total radiation originates can be determined (Figure IV-4). For uniform profiles of 15%, 25% and 35% moisture by volume, this depth for 1.4 GHz is 26 cm, 20 cm, and 16 cm, respectively. Since the emission from each layer decreases as the soil moisture decreases, the maximum depth of emission has to increase to maintain the same brightness temperature. However, it is of interest to note that although the maximum depth of emission increases, the equivalent depth of water for each soil moisture (calculated using (II-8)) is not equal. For 15%, 25%, and 35% soil moistures it is 3.9 cm, 5.0 cm, and 5.6 cm, respectively. This demonstrates that the emission from a soil volume is not dependent on equivalent volumes of soil water for a given frequency.

For a nonuniform temperature profile and uniform soil moisture profile, it can be shown that the radiation impinging on the surface from below is not isotropic. It is a function of the transmission angle,  $\theta_1$  (Figure IV-2), i.e., the direction from which energy is incident on the surface from below. This is a result of the fact that the distance energy must travel from its point of origin to reach the surface increases as the transmission angle,  $\theta_1$ , increases. In effect, the temperature profile along the

Percentage Contribution to Total Volume Emission From Individual Subsurface Layers

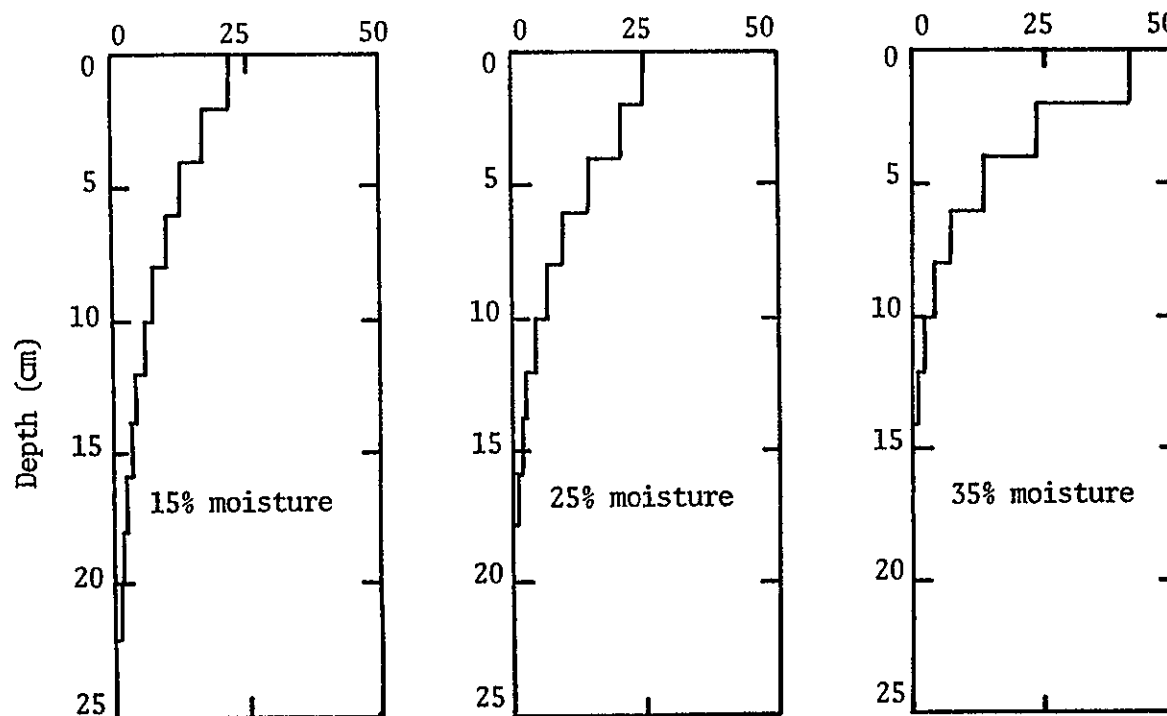


Figure IV-4. Percentage contribution of two centimeter soil layers to the total volume emission calculated at 1.4 GHz for uniform soil moisture and temperature profiles.

ray path changes as the transmission angle is changed.

It is of interest to note that the energy impinging on the surface from below is not polarization dependent as long as the soil moisture profile is uniform. This can be seen in Figure IV-5. Figure IV-5 is the brightness temperature of the volume calculated using (IV-9) for two uniform moisture profiles of 15% and 35%, and the two non-uniform temperature profiles shown in Figure IV-6. The only polarization dependent terms in (IV-9) are the transmission and reflection coefficients. For uniform soil moisture profiles the reflection coefficients are zero for all angles  $\theta_1$  and the transmission coefficients are unity.

Figure IV-5 again demonstrates the effect of moisture on the depth from which the volume emission originates. For a 15% uniform moisture profile and transmission angles less than  $46^\circ$ , it is seen that temperature profile A produces less volume emission than temperature profile B. Figure IV-6 shows that temperature profile B is cooler than profile A near the surface and warmer for depths greater than 3.5 cm. This indicates that for 15% moisture and angles less than  $46^\circ$ , a major percentage of emission is originating below 3.5 cm. Figure IV-7(a) demonstrates this for  $\theta_1$  equal to zero degrees. Since the emission due to temperature profile A is greater than that due to temperature profile B for transmission angles greater than  $46^\circ$ ,

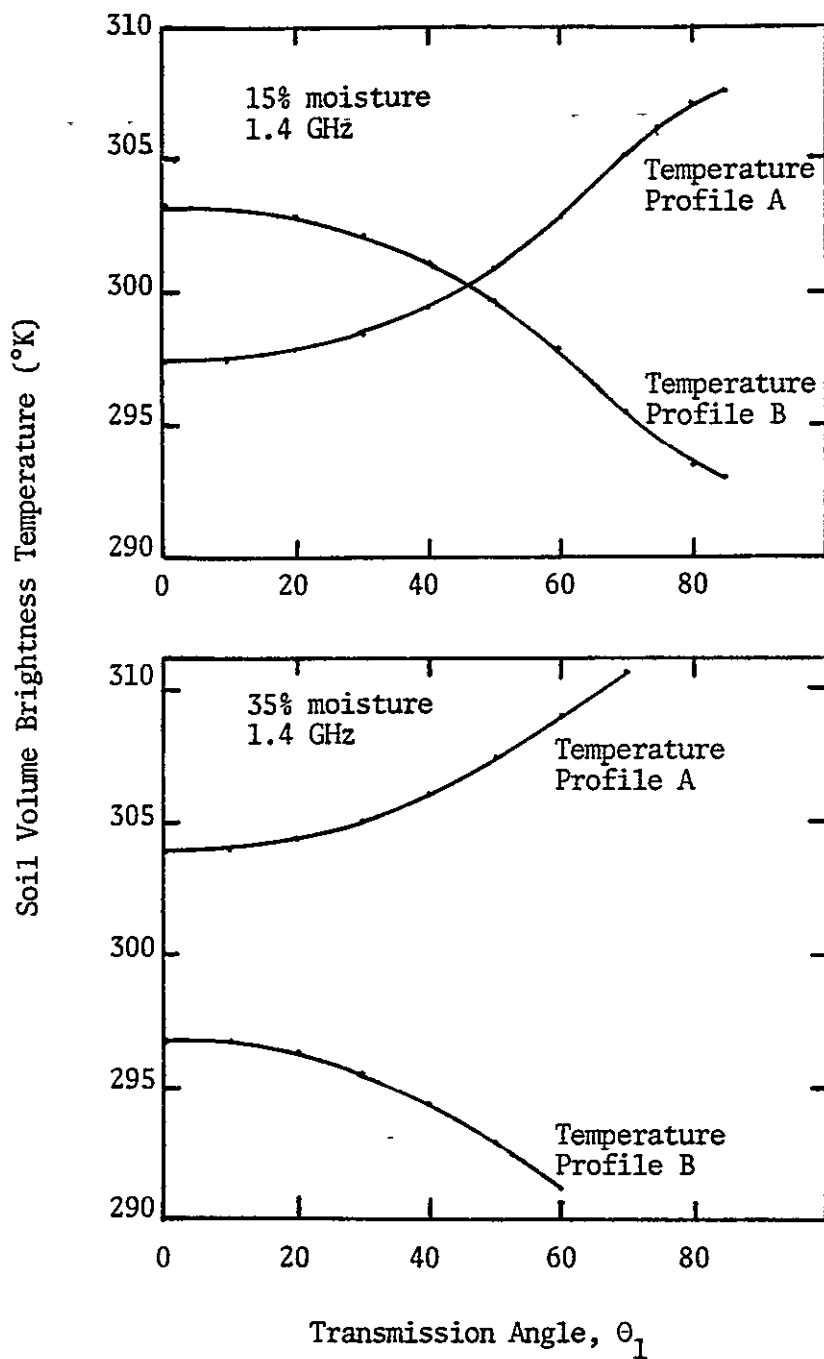


Figure IV-5. Brightness temperature of a soil volume for uniform moisture and nonuniform temperature profiles. Each curve represents both vertical and horizontal polarizations.

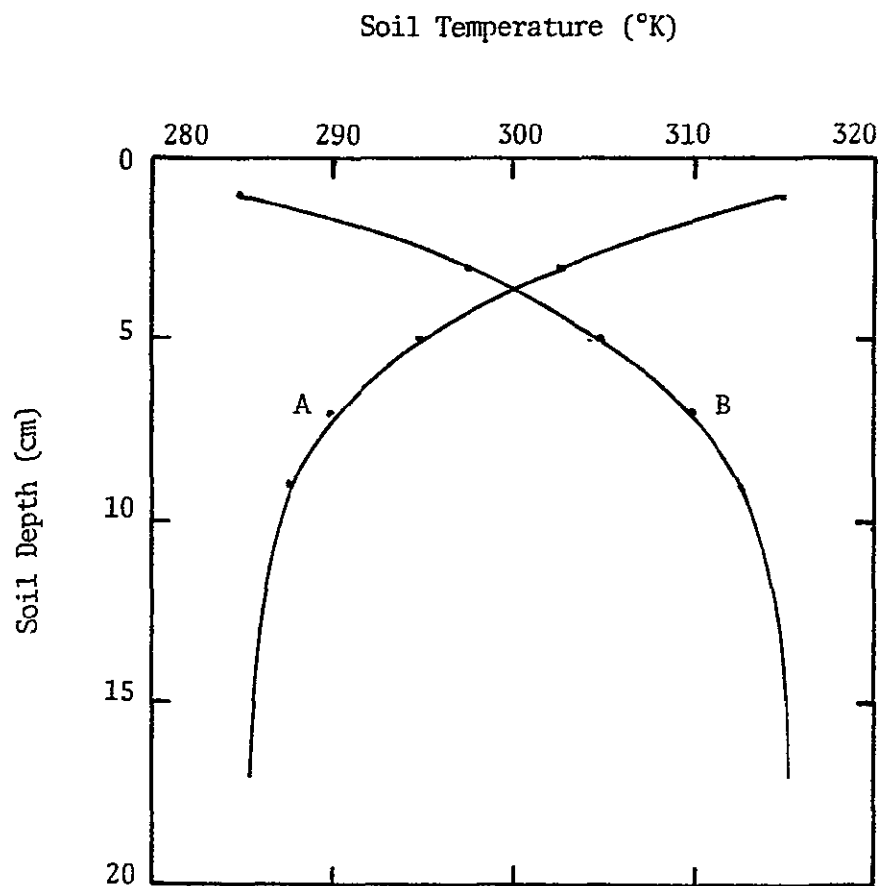


Figure IV-6. Soil temperature profiles used to demonstrate that the emission from a soil volume is not isotropic for nonuniform temperature profiles (Figure IV-5).

C-3

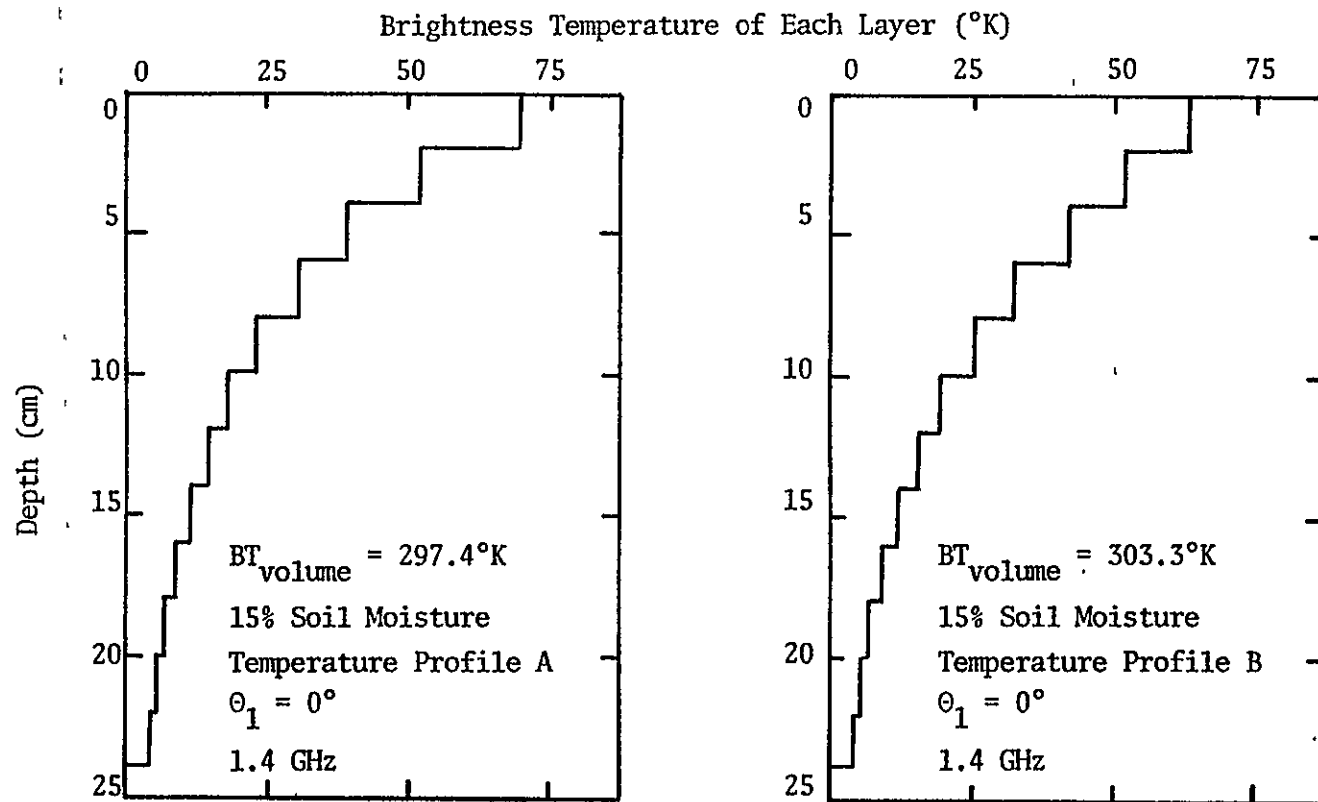


Figure IV-7(a). The contribution of two centimeter soil layers to the total volume brightness temperature for soil temperature profiles A and B of Figure IV-6.



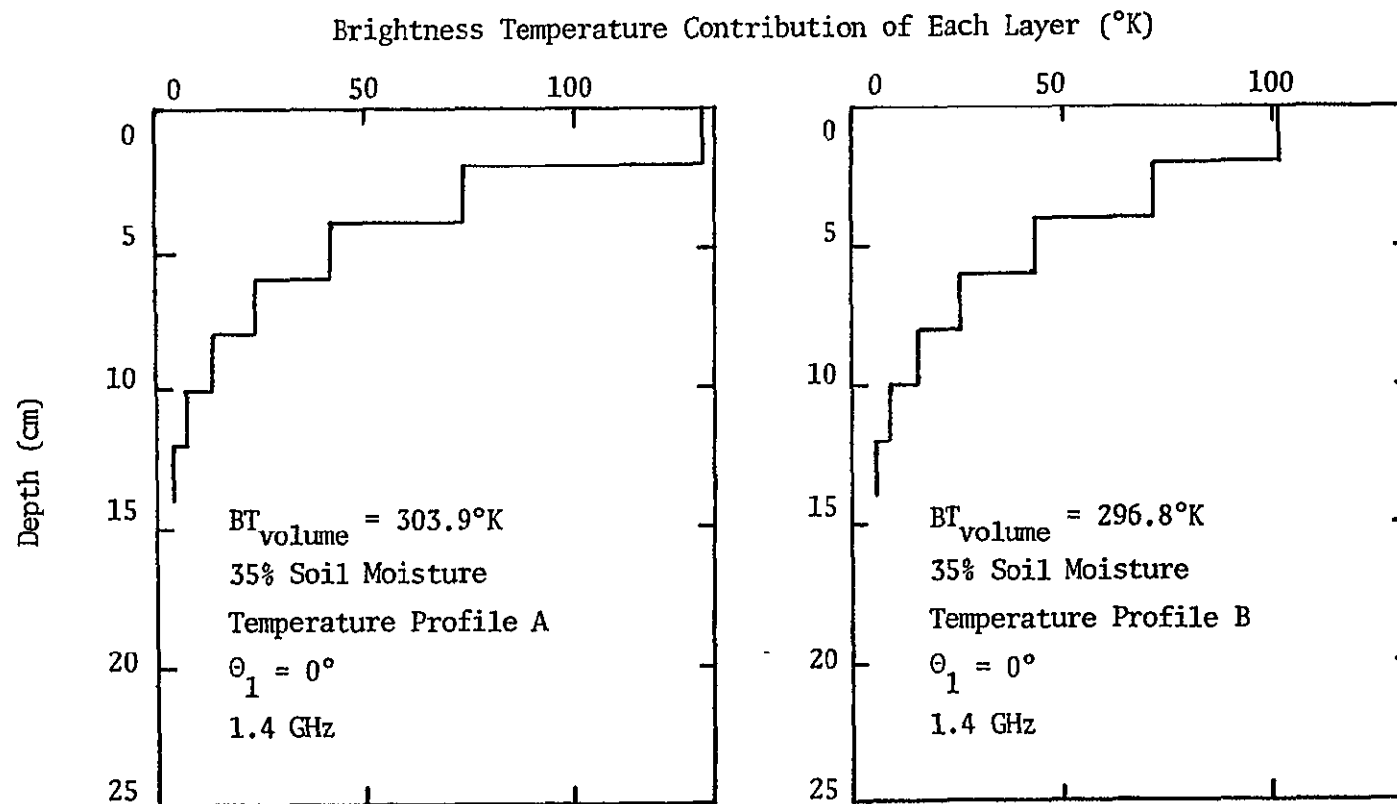


Figure IV-7(b). The contribution of two centimeter soil layers to the total volume brightness temperature for soil temperature profiles A and B of Figure IV-6.

then the depth from which the majority of the emission originates decreases as the transmission angle increases.

At 35% moisture, Figure IV-5 demonstrates that the temperature in the top few centimeters dominates. This is simply due to the fact that the maximum depth of emission is much shallower at 35% moisture than it is at 15% moisture. Figure IV-7(b) demonstrates the contributions of each soil layer to the total emission for a 35% uniform moisture profile at a transmission angle of zero degrees.

The third case of interest is a uniform temperature profile and nonuniform moisture profile. Since the moisture changes between layers, the reflection and transmission coefficients for each layer interface are not zero and one, respectively, as they were for uniform moistures. The reflection and transmission coefficients now depend on the permittivities of the layers forming the boundary, and on the transmission angle  $\theta_1$ . The attenuation constant also depends on the permittivity of the soil and the transmission angle. As a result, the radiation impinging on the surface from below is not isotropic, but varies with angle  $\theta_1$ . In addition, the radiation is polarization dependent.

The statements made above can be demonstrated using the soil moisture profiles of Figure IV-8. Figure IV-9 is the resulting volume brightness temperature,  $BT_{\text{volume}}$ ,

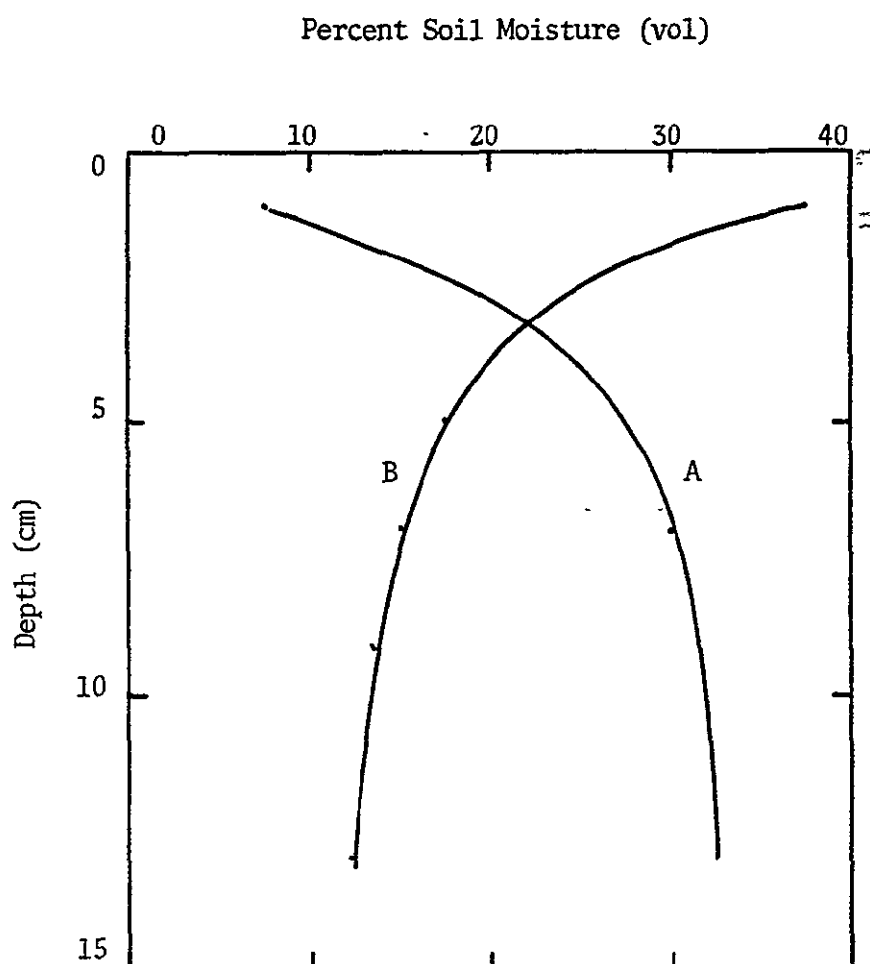


Figure IV-8. Soil moisture profiles used to demonstrate that the emission from a soil volume is not isotropic for nonuniform moisture profiles.

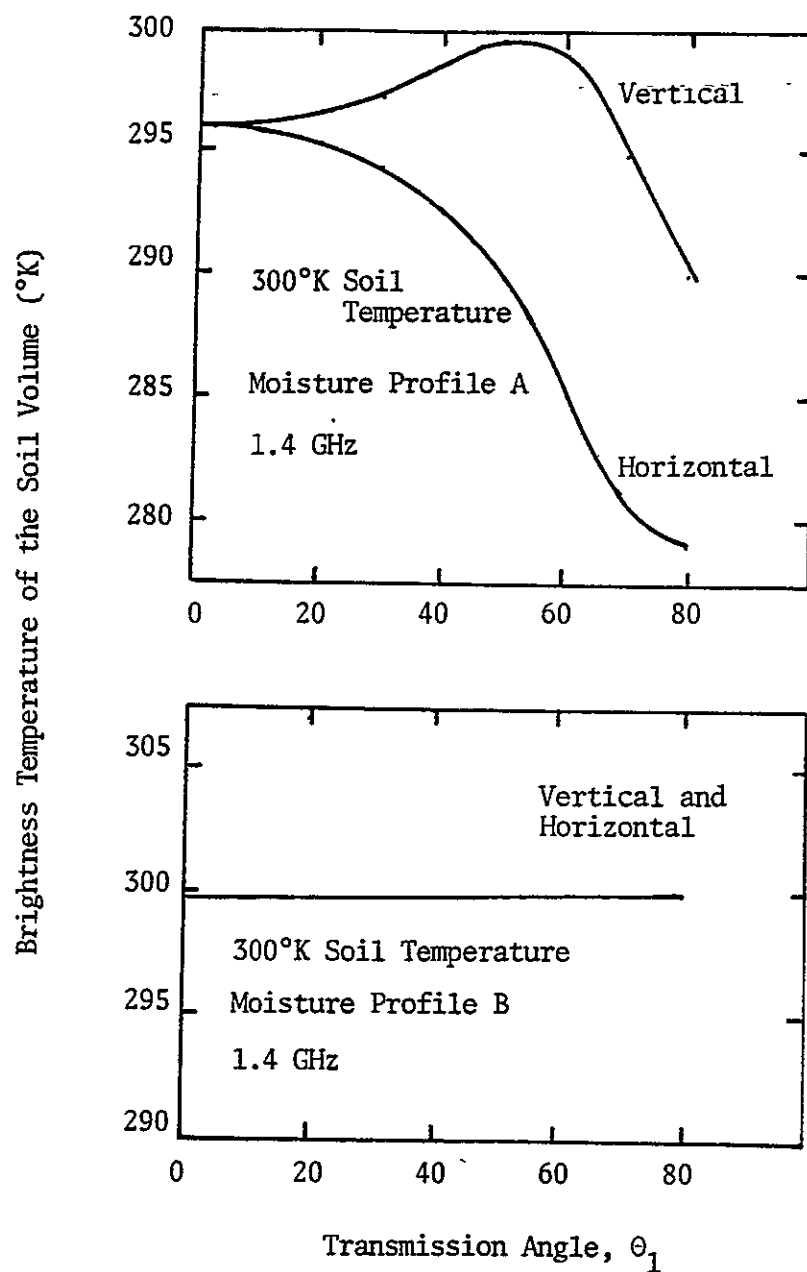


Figure IV-9. Calculated brightness temperatures of the soil volume for nonuniform soil moisture profiles.

calculated for these profiles as a function of  $\theta_1$  using (IV-9) and assuming a uniform soil temperature of 300°K. Moisture profile A produces a volume emission that has a dependence on  $\theta_1$  that is characteristic of the smooth interface power transmission coefficient. However, moisture profile B, which is wetter at the surface than below, does not. This is due to the fact that the greatest percentage of energy originates in the top layer. As seen in (IV-9) the energy originating in this layer is not directly modified by a transmission coefficient.

Figure IV-10 demonstrates the contribution of each soil layer for both profiles at a transmission angle of zero degrees. It is seen that the first layer contributes the majority of energy for moisture profile B. As the transmission angle increases, the percentage contribution of the first layer (for moisture profile B) also increases.

In summary, the effects of moisture and temperature profiles on the brightness temperature of the soil volume have been demonstrated. Uniform soil moisture and soil temperature profiles produce isotropic emission from the soil volume. However, for uniform conditions the maximum depth for which emission is influential depends only on the soil moisture, and the magnitude of the total soil volume emission depends only on the soil temperature. A nonuniform temperature profile causes the emission from

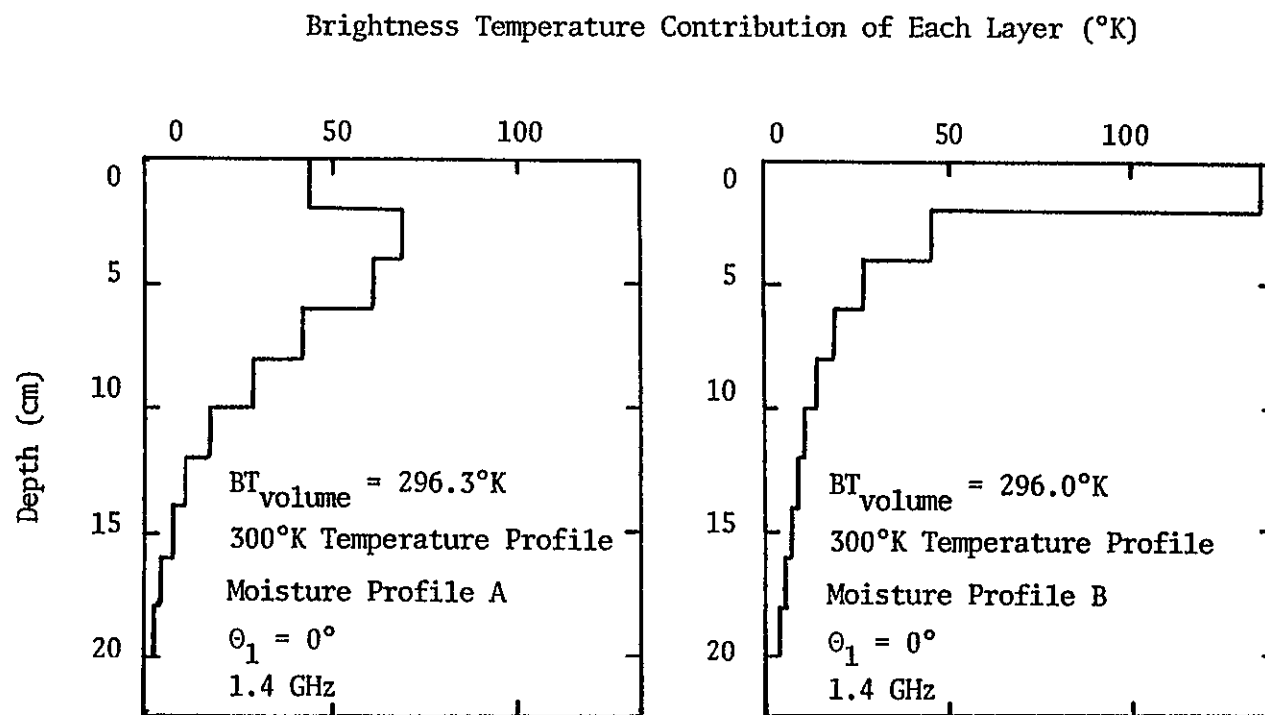


Figure IV-10. The contribution of two centimeter soil layers to the total volume brightness temperature for soil moisture profiles A and B of Figure IV-8.

the soil volume to be nonisotropic, but not polarization dependent. A nonuniform moisture profile causes the emission from the soil volume to be nonisotropic and polarization dependent.

### Surface Roughness

#### Model Development

Peake approach - Most of the approaches to modeling the emission from rough surfaces that are described in the literature stem from the Peake approach. They model the surface emission utilizing bistatic scattering coefficients defined for the top side of the surface. Inherent in this approach is the assumption that the soil is in thermodynamic equilibrium with blackbody (isotropic) radiation impinging on the surface from the hemisphere above the surface. Due to this assumption, the Peake approach is not strictly valid for the cases in which the energy impinging on the surface from below is not isotropic. As was shown in the last section, a nonuniform soil moisture or soil temperature profile produces nonisotropic volume radiation. As a result, the Peake approach is only a special case of a more general solution to emission from soil surfaces.

Transmission scattering - A more general formulation than the Peake approach is required for describing the emission of moist soils. This is due to the fact that the soil moisture and soil temperature profiles are very dynamic and are very seldom uniform with depth, thereby violating the assumption of isotropic radiation. For the purposes of this report, the soil moisture and soil temperature profiles will be assumed to be constant over the area within the antenna footprint. With this assumption, a general formulation for the emission of soil can be obtained by describing the transmission of energy from the soil volume across the soil surface. This formulation does not require that the radiation be isotropic, that is, it does not require the assumption of thermodynamic equilibrium.

The radiation intensity incident on the surface from below as a function of soil permittivity and soil temperature profile is described by the radiative transfer equations. It is now necessary to develop equations that describe transmission of that energy across an arbitrary surface.

It is convenient to describe the effect of the surface in terms of differential transmission coefficients. These differential transmission coefficients describe the power that is transmitted into an increment of solid angle,  $d\Omega_t$ ,



defined above the surface. This transmitted power is due to energy incident on the surface from below through an increment of solid angle,  $d\Omega_1$ , defined below the surface.

The differential transmission coefficients can be described by considering an infinite surface forming, on the average, a plane, although over small regions it may have complexity of structure (Figure IV-11). If a differential element of radiation of intensity  $I_1 d\Omega_1$  impinges on the surface from below at an angle of incidence (transmission angle),  $\theta_1$  and azimuth angle  $\phi_1$ , on an element of surface area  $A$ , and the differential intensity of scattered radiation from  $A$  to a point a distance  $R$  away in the direction  $(\theta_t, \phi_t)$  is  $I_t d\Omega_t$ , then the differential transmission coefficient will be defined by

$$\tau(\theta_1, \phi_1; \theta_t, \phi_t) = \frac{4\pi R^2 I_t}{(I_1 \cos \theta_1) A} \quad (\text{IV-43})$$

Conceptually, energy impinges on the surface from below from all angle pairs  $(\theta_1, \phi_1)$ . The total radiation transmitted into  $d\Omega_t$  in the direction  $(\theta_t, \phi_t)$  results from energy impinging on the surface from all directions  $(\theta_1, \phi_1)$ . The differential energy transmitted into  $d\Omega_t$  in

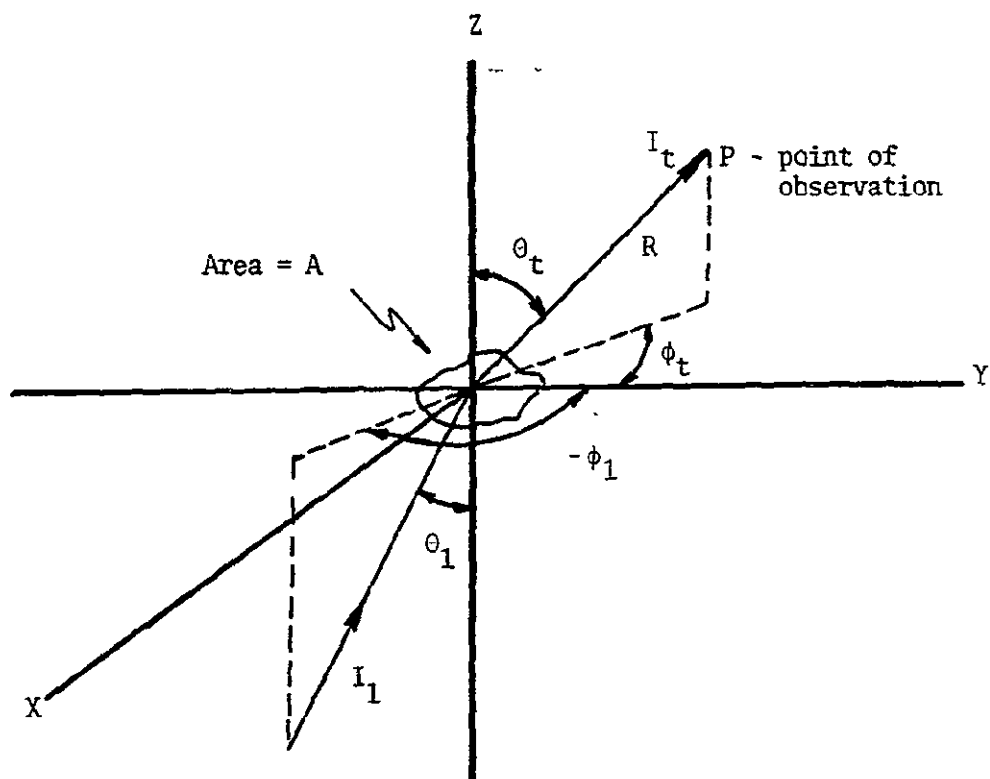


Figure IV-11. Geometry used to describe differential transmission coefficients.

the direction  $(\theta_t, \phi_t)$ , a distance  $R$  from the surface, caused by radiation impinging on the surface from below from  $d\Omega_1$  in the direction  $(\theta_1, \phi_1)$  is

$$P_t(1, t) d\Omega_t d\Omega_1 = \frac{1}{4\pi} \tau(1, t) \left[ I_1(1) A \cos \theta_1 \right] d\Omega_t d\Omega_1 \quad (\text{IV-44})$$

where

$$d\Omega = \sin \theta d\theta d\phi$$

$A$  - area on the surface through which energy is transmitted

Regarding the notation,  $P(1, t)$ , the first letter in parenthesis denotes the angle pair from which radiation is incident  $(\theta_1, \phi_1)$ . The second letter in the parenthesis denotes the angle pair describing the direction into which energy is transmitted  $(\theta_t, \phi_t)$ . Integrating over all angle pairs  $(\theta_1, \phi_1)$  yields

$$P_t(t) d\Omega_t = A d\Omega_t \left[ \frac{1}{4\pi} \int_0^{2\pi} \int_0^{\pi/2} \cos \theta_1 \tau(1, t) I_1(1) d\Omega_1 \right] \quad (\text{IV-45})$$

The differential element of radiation incident on the surface from below and the differential element of transmitted radiation can be at orthogonal polarization states

with respect to one another. Thus, the differential transmission coefficients will be written in the form  $\tau_{ij}(1, t)$ . The first subscript indicates the incident polarization state (vertical or horizontal) and the second indicates the transmitted polarization state. Equation (IV-45) can now be written in the form:

$$\begin{aligned} (P_t(t))_i d\Omega_t &= A d\Omega_t \left[ \frac{1}{4\pi} \int_0^{2\pi} \int_0^{\pi/2} \cos \theta_1 \right. \\ &\quad \left. (\tau_{ii}(1, t) I_{i_i}(1) + \tau_{ji}(1, t) I_{j_j}(1)) d\Omega_1 \right] \quad (\text{IV-46}) \end{aligned}$$

where

$$\tau_{ji}(1, t) = \frac{4\pi R^2 I_{t_i}(\theta_t, \phi_t)}{A \cos \theta_1 I_{j_j}(\theta_1, \phi_1)}$$

The differential element of energy transmitted into the direction  $(\theta_t, \phi_t)$  can also be written:

$$(P_t(t))_i d\Omega_t = A \cos \theta_t I_{t_i}(\theta_t, \phi_t) d\Omega_t \quad (\text{IV-47})$$

Equating (IV-46) and (IV-47) yields:

$$A \cos \theta_z I_{z_k}(z) d\Omega_{z_k} = A d\Omega_{z_k} \left[ \frac{1}{4\pi} \int_0^{2\pi} \int_0^{\pi/2} \right. \quad (IV-48)$$

$$\left. \cos \theta_1 (\tau_{ii}(1,z) I_{i_k}(1) + \tau_{ji}(1,z) I_{j_k}(1)) d\Omega_1 \right]$$

So

$$I_{z_k}(z) = \frac{1}{4\pi} \int_0^{2\pi} \int_0^{\pi/2} \frac{\cos \theta_1}{\cos \theta_z} (\tau_{ii}(1,z) I_{i_k}(1) + \tau_{ji}(1,z) I_{j_k}(1)) d\Omega_1 \quad (IV-49)$$

Equation (IV-49) is a general equation defining the power intensity emitted by a rough medium. Since the radiometric brightness temperature is directly related to radiation intensity, the brightness temperature of the soil is given by

$$BT_{soil} = \frac{1}{4\pi} \int_0^{2\pi} \int_0^{\pi/2} \frac{\cos \theta_1}{\cos \theta_z} \cdot \quad (IV-50)$$

$$(\tau_{ii}(1,z) BT_{volume_i} + \tau_{ji}(1,z) BT_{volume_j}) d\Omega_1$$

Equation (IV-50) can be transformed into:

$$BT_{\text{solid}_i} = \frac{1}{4\pi} \int_0^{2\pi} \int_0^{\pi/2} ( \tau_{ii}(t, 1) BT_{\text{volume}_i} + \tau_{ij}(t, 1) BT_{\text{volume}_j} ) d\Omega, \quad (\text{IV-51})$$

through the use of the reciprocity relations [29]:

$$\cos \theta_i \tau_{ij}(1, t) = \cos \theta_j \tau_{ji}(t, 1) \quad (\text{IV-52})$$

where  $i$  and  $j$  denote either polarization state.

To complete the formulation it is necessary to develop equations that describe the differential transmission coefficients.

Differential transmission coefficients - The various techniques of modeling electromagnetic scatter from rough surfaces were described in Chapter III. In that discussion, the ranges of validity of the various techniques were presented. Geometrical or ray tracing techniques are valid only for surfaces with very large radii of curvature compared to a wavelength. Small perturbation theory is valid only for surfaces with very small rms surface height fluctuations with respect to a wavelength.

Most soil surfaces do not fit either one of these criteria, nor do they strictly fit the criteria of the Kirchhoff approximation. Generally, the criteria for the Kirchhoff approximation is, however, closer to real soil surfaces than the others. In addition, it has been pointed out by Beckmann and Spizzichino [58] that the Kirchhoff approximation works reasonably well for surfaces not strictly fitting its surface criteria.

The Kirchhoff approach was utilized in conjunction with the Stratton-Chu integral as modified by Silver [99] to develop an expression for the differential transmission coefficients. This derivation is presented in Appendix A. However, the results of this derivation did not yield the expected results. There are no other expressions for transmission through a rough surface presented in the literature. Therefore, there were no corresponding derivations with which to check the results of Appendix A.

Since a suitable expression for the differential transmission coefficients was not obtained, it was necessary to develop an equivalent expression to (IV-50). An equivalent expression is developed below in terms of the bistatic scattering coefficients of the underside of the surface.

Conversion to scattering coefficients - Since expressions for bistatic scattering coefficients are available in the literature, it is convenient to write (IV-50) in

terms of scattering coefficients. A transmission function will be defined that describes the energy transmitted across a rough boundary. This function will be defined in terms of the energy incident on the surface from below and the bistatic scattering coefficients of the underside of the surface. It relates the energy transmitted into an increment of solid angle above the surface,  $d\Omega_t$ , in terms of the energy incident on an equivalent smooth surface from an increment of solid angle below the surface,  $d\Omega_1$ .

For a smooth surface, the energy transmitted across the surface can be written in terms of the energy incident on the surface through  $d\Omega_1$ , and the energy reflected from the surface through  $d\Omega_r$  (Figure IV-12). The directions associated with  $d\Omega_1$ ,  $d\Omega_t$ , and  $d\Omega_r$  are related through Snell's law.

$$P_i d\Omega_1 = P_t d\Omega_t + P_r d\Omega_r$$

$$P_t d\Omega_t = P_i d\Omega_1 - P_r d\Omega_r \quad (IV-53)$$

but

$$d\Omega_1 = d\Omega_r \quad (IV-54)$$



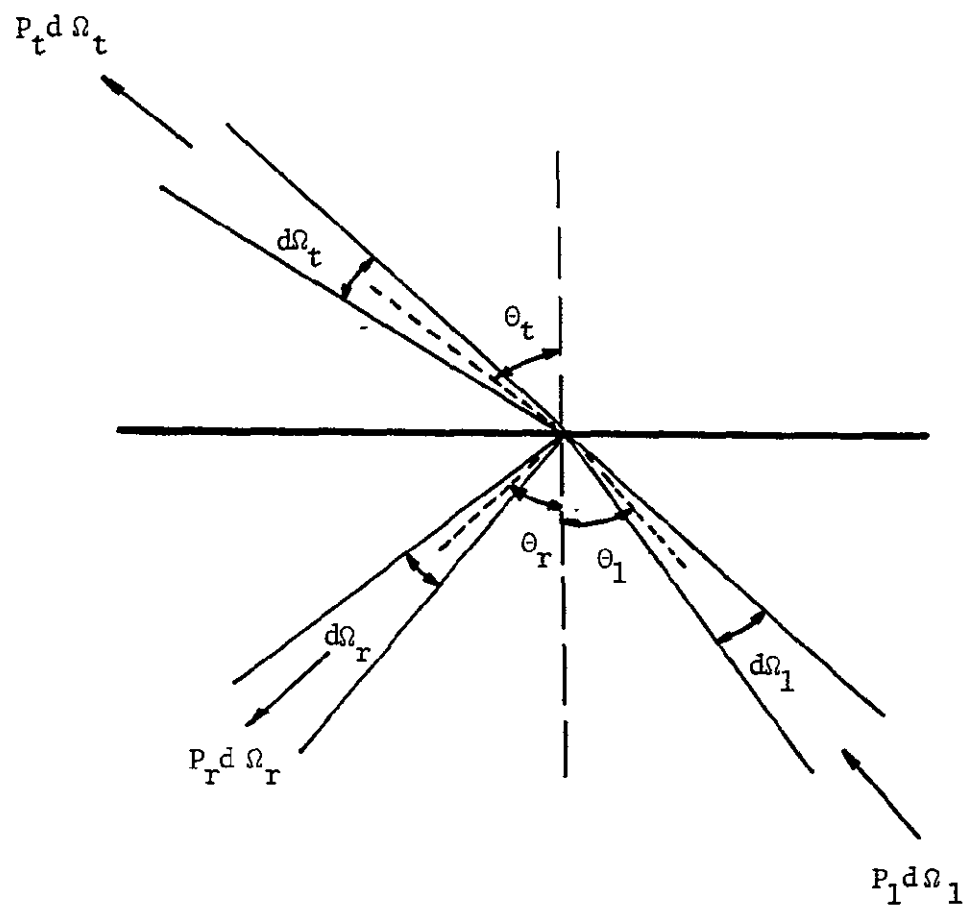


Figure IV-12. Geometry used to describe the transmission and reflection of energy at a smooth interface.

so

$$P_t d\Omega_t = P_i d\Omega_i - P_r d\Omega_r \quad (\text{IV-55})$$

Equation (IV-55) is based on the boundary condition at the surface. The tangential electric fields must be equal on either side of the surface.

Rough surfaces can be modeled as an effective smooth surface. In doing this, (IV-53) is still valid. However, the energy reflected from the rough surface into  $d\Omega_r$  must be substituted into (IV-53) rather than the energy reflected from a smooth surface as done previously. Also, the transmitted energy will be related to the incident energy by a transmission function.

$$P_t d\Omega_t = T(\theta_t, \phi_t) P_i d\Omega_i \quad (\text{IV-56})$$

where

$$P_i d\Omega_i = A \cos \theta_i I_i(\theta_i, \phi_i) d\Omega_i \quad (\text{IV-57})$$

For a rough surface, the energy reflected into  $d\Omega_r$  can be obtained using bistatic scattering coefficients. Energy is reflected into  $d\Omega_r$  as a result of energy incident on the subsurface from all incident angles. The bistatic scattering coefficients,  $\gamma(s,r)$ , describe the energy that is scattered into  $d\Omega_r$  as a result of energy incident on the surface from any arbitrary solid angle increment  $d\Omega_s$  from the direction  $(\theta_s, \phi_s)$ , as shown in Figure IV-13.

$$P_r d\Omega_r d\Omega_s = A \cos \theta_s I_i(s) \frac{\gamma(s,r)}{4\pi} d\Omega_r d\Omega_s \quad (\text{IV-58})$$

where

$$\gamma(s,r) = \frac{4\pi R^2 I_r(\theta_r, \phi_r)}{A \cos \theta_s I_i(\theta_s, \phi_s)}$$

$I_r(\theta_r, \phi_r)$  - intensity reflected into  $d\Omega_r$   
as a result of energy impinging  
on the surface from  $d\Omega_s$

Equation (IV-58) is integrated over all increments of solid angle  $d\Omega_s$  to obtain the total energy reflected into  $d\Omega_r$  as a result of energy incident on the surface from all angle pairs  $(\theta_s, \phi_s)$ .

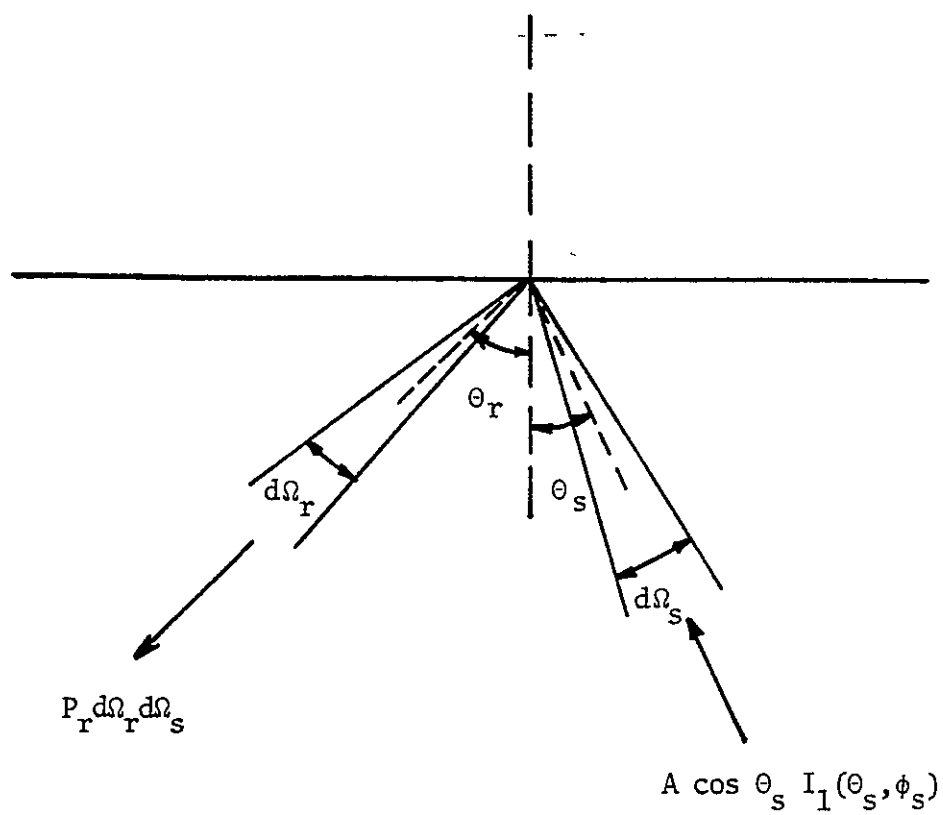


Figure IV-13. Geometry used to describe bistatic scattering coefficients.

$$P_r d\Omega_r = \frac{A d\Omega_r}{4\pi} \int_0^{2\pi} \int_0^{\pi/2} \cos \theta_s \gamma(s, r) I_1(s) d\Omega_s \quad (\text{IV-59})$$

Substituting (IV-56), (IV-57) and (IV-59) into (IV-53) yields the transmission function of the surface.

$$\begin{aligned} T(\theta_t, \phi_t) P_i d\Omega_i &= P_i d\Omega_i - \frac{A d\Omega_r}{4\pi} \int_0^{2\pi} \int_0^{\pi/2} \cos \theta_s \cdot \\ &\quad \gamma(s, r) I_1(s) d\Omega_s \end{aligned} \quad (\text{IV-60})$$

$$T(\theta_t, \phi_t) = 1 - \frac{\frac{d\Omega_r}{4\pi} \int_0^{2\pi} \int_0^{\pi/2} \cos \theta_s \gamma(s, r) I_1(s) d\Omega_s}{\cos \theta_i \cdot I_1(i) d\Omega_i}$$

Since (IV-60) describes an effective smooth surface, then

$$\begin{aligned} d\Omega_i &= d\Omega_r \\ \cos \theta_i &= \cos \theta_r \\ \gamma(s, r) &= \gamma(s, i) \\ \phi_r &= \pi + \phi_i \end{aligned} \quad (\text{IV-61})$$

Substituting (IV-61) into (IV-60) yields:

$$\mathcal{T}(\theta_t, \phi_t) = 1 - \frac{1}{4\pi} \int_0^{2\pi} \int_0^{\pi/2} \frac{\cos \theta_s}{\cos \theta_r} \gamma(s, r) \frac{I_1(s)}{I_1(l)} d\Omega_s \quad (\text{IV-62})$$

Relying on the reciprocity relationships:

$$\cos \theta_s \gamma(s, r) = \cos \theta_r \gamma(r, s) \quad (\text{IV-63})$$

and the fact that  $\cos \theta_l = \cos \theta_r$ , then (IV-61) becomes

$$\mathcal{T}(\theta_t, \phi_t) = 1 - \frac{1}{4\pi} \int_0^{2\pi} \int_0^{\pi/2} \gamma(l, s) \frac{I_1(s)}{I_1(l)} d\Omega_s \quad (\text{IV-64})$$

Equation (IV-64) can now be used to describe the energy transmitted into  $d\Omega_t$  as a result of energy incident on the surface from below from all directions.

$$P_t d\Omega_t = \mathcal{T}(t) P_l d\Omega_l$$

$$A \cos \theta_s I_s(\pm) d\Omega_s = \tau(\pm) A \cos \theta_i I_i(\pm) d\Omega_i$$

$$I_s(\pm) d\Omega_s = \left[ \tau(\pm) I_i(\pm) \frac{\cos \theta_i}{\cos \theta_s} \right] d\Omega_i \quad (\text{IV-65})$$

#### Demonstration of the Model

Comparison to the Peake approach - It was shown that for a uniform soil moisture profile the radiation impinging on the surface from below is isotropic. With this assumption (IV-64) reduces to

$$\tau(\theta_s, \phi_s) = 1 - \frac{1}{4\pi} \int_0^{2\pi} \int_0^{\pi/2} \gamma(l, s) d\Omega_s$$

and

$$I_s(\theta_s, \phi_s) = \frac{\cos \theta_i}{\cos \theta_s} \left[ 1 - \frac{1}{4\pi} \int_0^{2\pi} \int_0^{\pi/2} \gamma(l, s) d\Omega_s \right] I_i(\theta_i, \phi_i) \quad (\text{IV-66})$$

Equation (IV-66) is equivalent to Peake's result which was derived under the assumption of thermodynamic equilibrium. Note that the derivation of (IV-66) did not require the assumption of thermodynamic equilibrium.

The equivalent Peake equation is given by

$$I_t(\theta_t, \phi_t) = \left[ 1 - \frac{1}{4\pi} \int_0^{2\pi} \int_0^{\pi/2} \gamma'(l, s) d\Omega'_s \right] I_i(\theta_i, \phi_i) \quad (\text{IV-67})$$

where  $\gamma'(l, s)$  and  $d\Omega'_s$  are defined in the upper hemisphere. Figure IV-14 demonstrates the definition of the solid angle increments. Equations (IV-66) and (IV-67) describe the relationship between the bistatic scattering coefficients defined in each hemisphere.

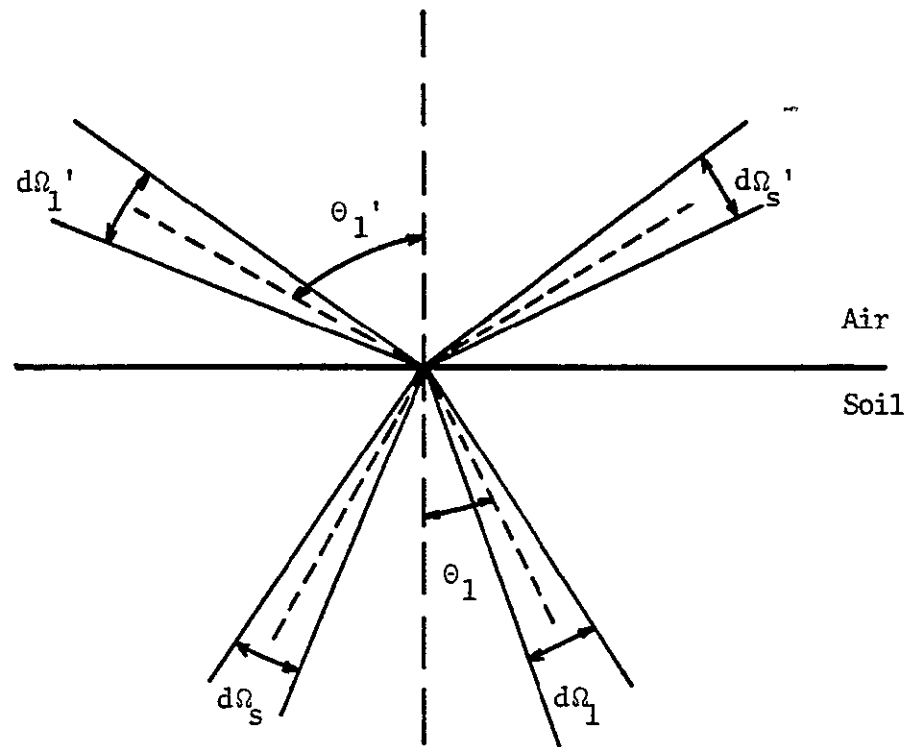
$$1 - \frac{1}{4\pi} \int_0^{2\pi} \int_0^{\pi/2} \gamma'(l, s) d\Omega'_s = \frac{\cos \theta_i}{\cos \theta_t}.$$

or

$$\left[ 1 - \frac{1}{4\pi} \int_0^{2\pi} \int_0^{\pi/2} \gamma(l, s) d\Omega_s \right]$$

$$I'(\theta_t, \phi_t) = \frac{\cos \theta_i}{\cos \theta_t} I(\theta_t, \phi_t) \quad (\text{IV-68})$$





$$\frac{\sin \theta_1}{v_{\text{soil}}} = \frac{\sin \theta_1'}{v_{\text{air}}}$$

$v$  - phase velocity

Figure IV-14. Geometry used to relate the bistatic scattering coefficients in the hemisphere above the soil surface to the bistatic scattering coefficients in the hemisphere below the soil surface.

It is also of interest to note that for a smooth surface and uniform soil moisture profile that

$$\gamma(1,s) = |\rho(1,s)|^2 \delta(\theta_1) \delta(\phi_1)$$

where

$\rho(1,s)$  - Fresnel reflection coefficient

$\delta(\ )$  - Dirac delta function

So that (IV-64) becomes

$$\mathcal{T}(\theta_x, \phi_x) = 1 - \frac{1}{4\pi} \int_0^{2\pi} \int_0^{\pi/2} |\rho(1,s)|^2 \delta(\theta_1) \delta(\phi_1) d\Omega_s$$

(IV-69)

$$\mathcal{T}(\theta_x, \phi_x) = 1 - |\rho(\theta_1, \phi_1; \theta_s, \phi_s)|^2$$

as would be expected based on the Peake approach.

Computed effects of roughness - The soil moisture and surface roughness dependence of energy emitted from a soil surface can be demonstrated using (IV-65). In doing this, analytical expressions for the bistatic scattering coefficients are required. One technique of

obtaining the bistatic scattering coefficients is to use the physical optics approach to determine the scatter from a rough surface.

Leader [61] has solved the Stratton-Chu integral as modified by Silver [99] for the power reflected from a rough surface due to power incident on that surface from a particular direction. Performing an ensemble average over the surface height deviations, Leader found that

$$\frac{I_{r,i}(\theta_r, \phi_r)}{I_{i,i}(\theta_i, \phi_i)} = \left\langle \left( \frac{E_r(\theta_r, \phi_r) E_r^*(\theta_r, \phi_r)}{E_i(\theta_i, \phi_i) E_i^*(\theta_i, \phi_i)} \right) \right\rangle \quad (\text{IV-70})$$

$$= \frac{2\pi A}{(4\pi R)^2} \left( a_i - \frac{m_y}{m_z} a_{y_i} \right)^2 \frac{Q m_z^2}{(m_z^4 + Q m_y^2)^{3/2}}$$

where

$I_r(\theta_r, \phi_r)$  - average power intensity reflected into  $d\Omega_r$  due to energy incident on the surface from  $d\Omega_1$

A - area illuminated

R - distance to the point under consideration

$n_y = \sin \theta_r - \sin \theta_1$

$n_z = \cos \theta_r + \sin \theta_1$

i - vertical or horizontal polarization

And

$$Q_i = -\cos \theta_r (1 + \rho_i(\theta_i, \theta_r) + \cos \theta_i (1 - \rho_i(\theta_i, \theta_r)))$$

$$Q_{y_i} = \sin \theta_i (1 - \rho_i(\theta_i, \theta_r)) + \sin \theta_r (1 + \rho_i(\theta_i, \theta_r)) - (\cos \theta_r + \cos \theta_i) \left. \frac{\partial \rho_i(\theta_i, \theta_r)}{\partial z_j} \right|_{z_x=0, z_y=0} \quad (\text{IV-71})$$

where

$\rho_i(\theta_i, \theta_r)$  - Fresnel reflection coefficient for  
vertical or horizontal polarization

$z_j$  - surface slope in the x or y direction

Equation (IV-70) is dependent on the surface statistics through the roughness parameter  $Q$ .

$$Q = [k C'(\tau_0) \sigma_z^2]^{-2} \quad (\text{IV-72})$$

where

$k$  - wave number

$C'(\tau_0)$  - derivative of the autocorrelation function  
of the surface evaluated at  $\tau_0$

$\tau_0$  - point of expansion of  $C(\tau)$  in deriving (IV-70)

$\sigma_z^2$  - surface height variance

In deriving (IV-70), Leader made the following assumptions

- 1) The incident wave is plane and linearly polarized.
- 2) Multiple interaction of irregularities such as shadowing and multiple scattering may be neglected.
- 3) The observation point is in the far field.
- 4) The Stratton-Chu integral is applied over a finite portion of a closed surface.
- 5) The surface can be approximated at any point as an infinite plane.
- 6) Only energy in the plane of incidence is considered.

Leader's [61] result, (IV-70), can be converted to a differential scattering coefficient in the following manner. The differential scattering coefficients are defined as:

$$Y(\theta_i, \phi_i; \theta_r, \phi_r) = \frac{4\pi R^2 I_r(\theta_r, \phi_r)}{A \cos \theta_i I_i(\theta_i, \phi_i)} \quad (\text{IV-73})$$

Separating (IV-73) into orthogonal polarization state gives:

$$\gamma_{ii}(\theta_i, \phi_i; \theta_r, \phi_r) = \frac{4\pi R^2 I_{r_i}(\theta_r, \phi_r)}{A \cos \theta_i I_{i_i}(\theta_i, \phi_i)} \quad (\text{IV-74})$$

$$\gamma_{ji}(\theta_i, \phi_i; \theta_r, \phi_r) = \frac{4\pi R^2 I_{r_i}(\theta_r, \phi_r)}{A \cos \theta_i I_{i_j}(\theta_i, \phi_i)}$$

However, Leader showed that under his assumptions,

$$\gamma_{ji}(\theta_i, \phi_i; \theta_r, \phi_r) = 0 \quad (\text{IV-75})$$

In addition, since only energy in the plane of incidence is considered,

$$\gamma_{ii}(\theta_i, \phi_i; \theta_r, \phi_r) = \gamma_{ii}(\theta_i; \theta_r) \delta(\phi_i) \quad (\text{IV-76})$$

where  $\delta(\phi_1)$  is the Dirac delta function.

Combining (IV-70), (IV-74), (IV-75), and (IV-76) gives:

$$\gamma_{ii}(\theta_i, \phi_i; \theta_r, \phi_r) = \left[ \frac{4\pi R^2}{A \cos \theta_i} \right] \frac{2\pi A}{(4\pi R)^2} \cdot$$

$$\left( a_i - \frac{m_y}{m_z} a_{y_i} \right)^2 \frac{Q m_z^2}{(m_z^4 + Q m_y^2)^{3/2}} \delta(\phi_i) \quad (\text{IV-77})$$

Noting that (IV-77) is defined for the hemisphere below the soil surface, it can be combined with (IV-64) to yield an expression for the surface transmission function.

$$T_L(\theta_t, \phi_t) = 1 - \frac{1}{4\pi} \int_0^{\pi/2} \left[ \frac{1}{2 \cos \theta_i} \cdot \right.$$

$$\left. \left( a_i - \frac{m_y}{m_z} a_{y_i} \right)^2 \frac{Q m_z^2}{(m_z^4 + Q m_y^2)^{3/2}} \right] \frac{I_{i_i}(s)}{I_{i_i}(1)} d\theta_i \quad (\text{IV-78})$$

Equation (IV-78) defines that fraction of power incident on the surface from  $d\Omega_1$  below the surface that is transmitted across the surface into  $d\Omega_t$ . Combining (IV-78) with (IV-65) provides a description of the energy emitted from the soil at the  $i^{\text{th}}$  polarization into the direction  $(\theta_t, \phi_t)$ ; that is,

$$I_{t_i}(\theta_{t_i}, \phi_{t_i}) = T_i(\theta_{t_i}, \phi_{t_i}) I_{i_i}(\theta_{i_i}, \phi_{i_i}) \frac{\cos \theta_{i_i}}{\cos \theta_{t_i}}$$

$$BT_{soil_i}(\theta_{t_i}, \phi_{t_i}) = T_i(\theta_{t_i}, \phi_{t_i}) BT_{volume_i}(\theta_{i_i}, \phi_{i_i}) \frac{\cos \theta_{i_i}}{\cos \theta_{t_i}} \quad (IV-79)$$

In order to perform example calculations using (IV-78) and (IV-79), appropriate values of the roughness parameter,  $Q$ , must be defined. The point,  $\tau_0$ , about which the derivative of the autocorrelation function is expanded increases with transmission angle,  $\theta_t$ . Therefore, as seen in (IV-77),  $Q$  decreases with transmission angle,  $\theta_t$ . The distribution of  $Q$  changes as the surface roughness changes. It is therefore necessary to define a  $Q$  distribution that is appropriate for each surface roughness of interest. The  $Q$  distributions that correspond to the smooth, medium and rough surfaces described in Chapter V are determined in Chapter VII (Table VII-6). These distributions are used below to demonstrate the effects of surface roughness.

Assuming uniform soil moisture and soil temperature profiles, the radiation impinging on the surface from below is isotropic. Under this condition (IV-78)



reduces to

$$T_i(\theta_t, \phi_t) = 1 - \frac{1}{4\pi} \int_0^{\pi/2} \left[ \frac{1}{2 \cos \theta_i} \cdot \left( a_i - \frac{m_y}{m_z} a_{yi} \right)^2 \frac{Q m_z^2}{(m_z^4 + Q m_y^2)^{3/2}} d\theta_s \right] \quad (\text{IV-80})$$

Using (IV-80) and (IV-79), a normalized brightness temperature can be defined as

$$\text{NBT}_i = \frac{I_{t_i}(\theta_t, \phi_t)}{I_{t_i}(\theta_i, \phi_i)} = T_i(\theta_t, \phi_t) \frac{\cos \theta_i}{\cos \theta_t} \quad (\text{IV-81})$$

This normalized brightness temperature corresponds to emissivity as defined by Peake [29] for the special case of uniform soil moisture and soil temperature profiles.

The effect of soil moisture for uniform profiles will be demonstrated with (IV-80) and (IV-81) or (IV-79) using the Q distributions defined in Chapter VII. Figures IV-15 and IV-16 show the emitted radiation intensity for a smooth surface at 1.4 GHz as a function of transmission angle and soil moisture. These calculations were performed assuming uniform moisture and temperature profiles. Note that transmission angle is equivalent to the definition of incident angle that is normally used to describe radar

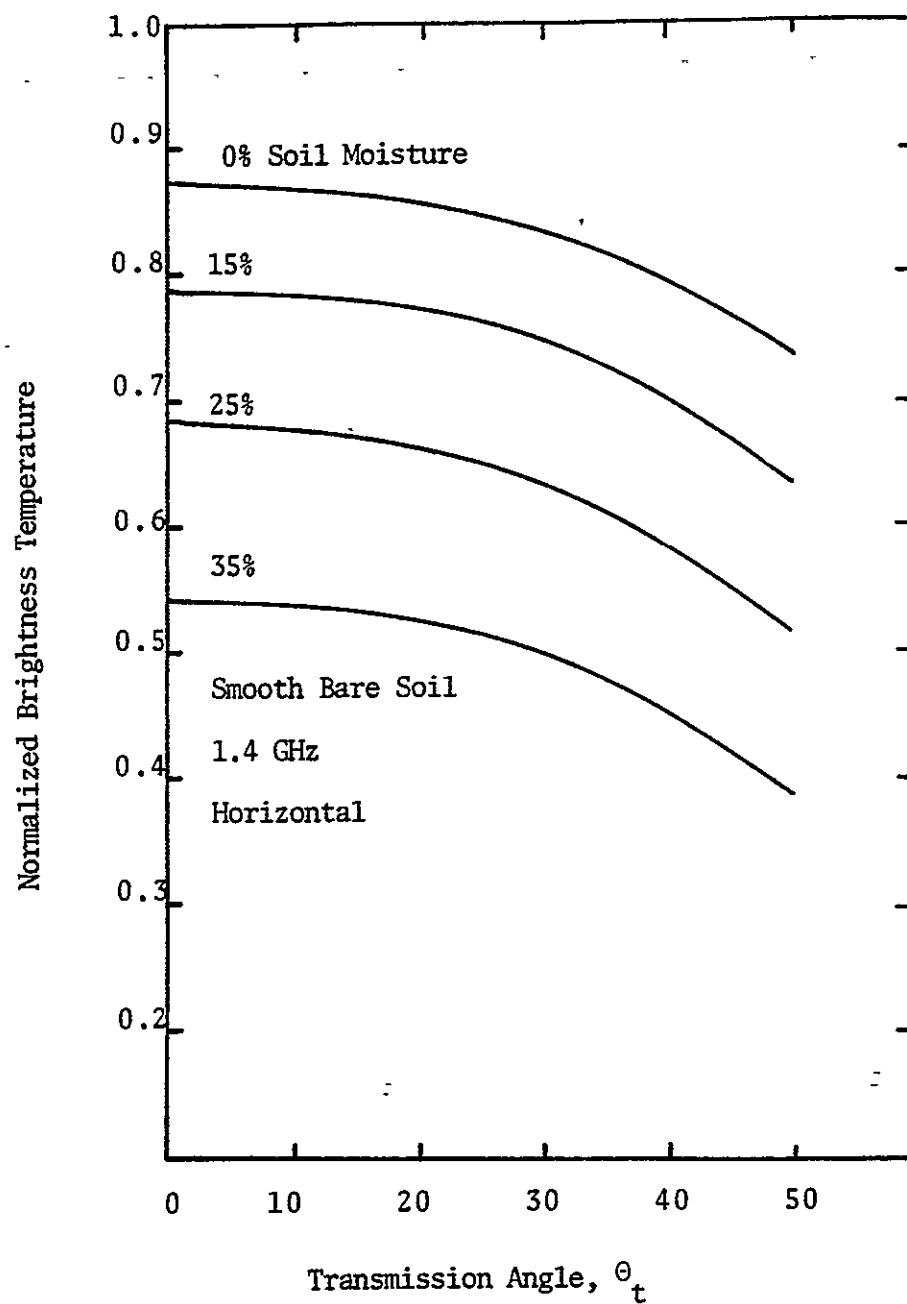


Figure IV-15. Calculated horizontally polarized emission of smooth bare soil as a function of volumetric soil moisture and transmission angle.

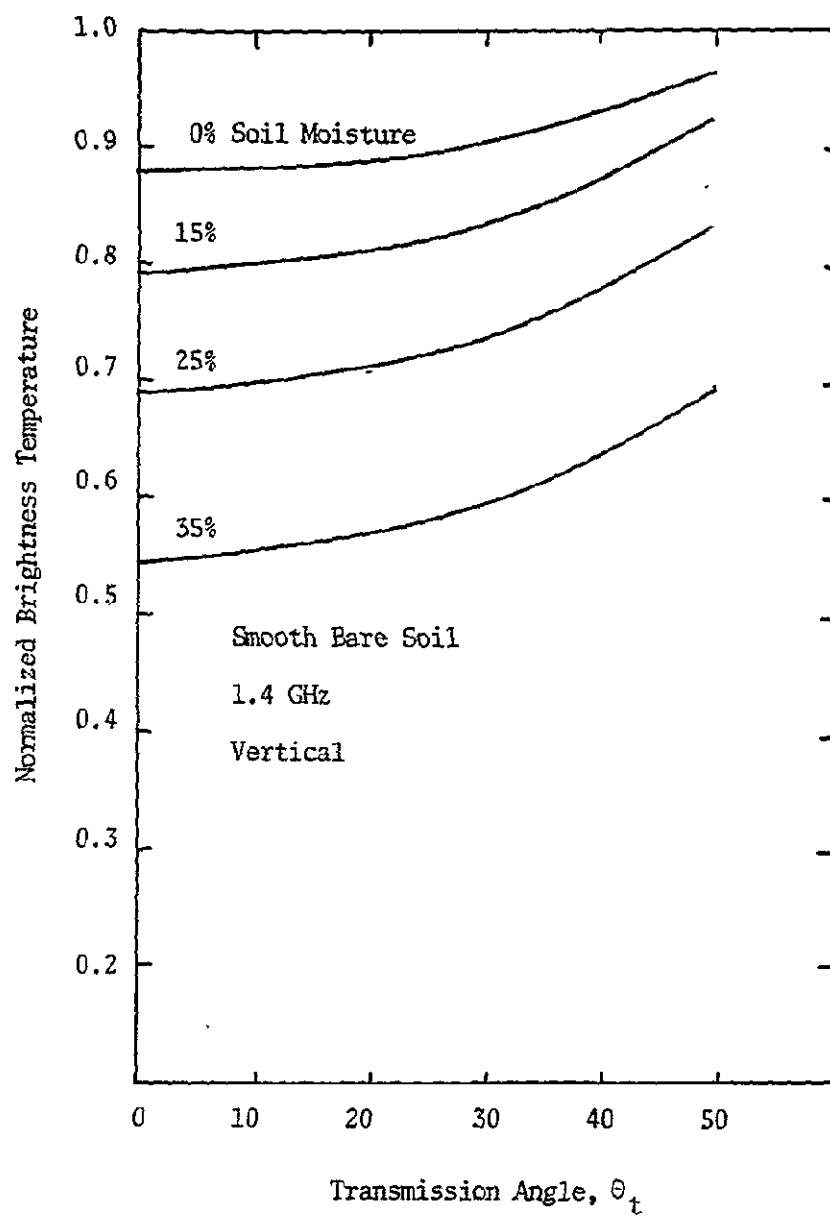


Figure IV-16. Calculated vertically polarized emission of smooth bare soil as a function of volumetric soil moisture and transmission angle.

backscatter. The change in emission as a function of soil moisture for a smooth surface at nadir can be more clearly seen in Figure IV-17. It is seen that on the average, the emitted radiation intensity at nadir changes approximately  $2.8^{\circ}\text{K}$  per percent volumetric moisture for a smooth surface, assuming a soil temperature of  $300^{\circ}\text{K}$ . As the angle of transmission is increased, this slope will decrease for vertical polarization and slightly increase for horizontal polarization (Figure IV-18).

The effect of surface roughness can now be demonstrated and compared to the soil moisture and soil temperature response of a smooth surface. For uniform soil moisture and uniform soil temperature profiles, the emitted radiation intensity is directly proportional to the soil temperature. Since the transmission function  $T_i(\theta_t, \phi_t)$  is not dependent on soil temperature, the effect of surface roughness on the soil emission is unchanged for different soil temperatures. However, the effect of surface roughness does change with soil moisture. Figures IV-19 and IV-20 show calculations of soil brightness temperature as a function of the transmission angle and roughness for both polarizations, a uniform soil temperature of  $300^{\circ}\text{K}$  and a uniform soil moisture of 35 percent.

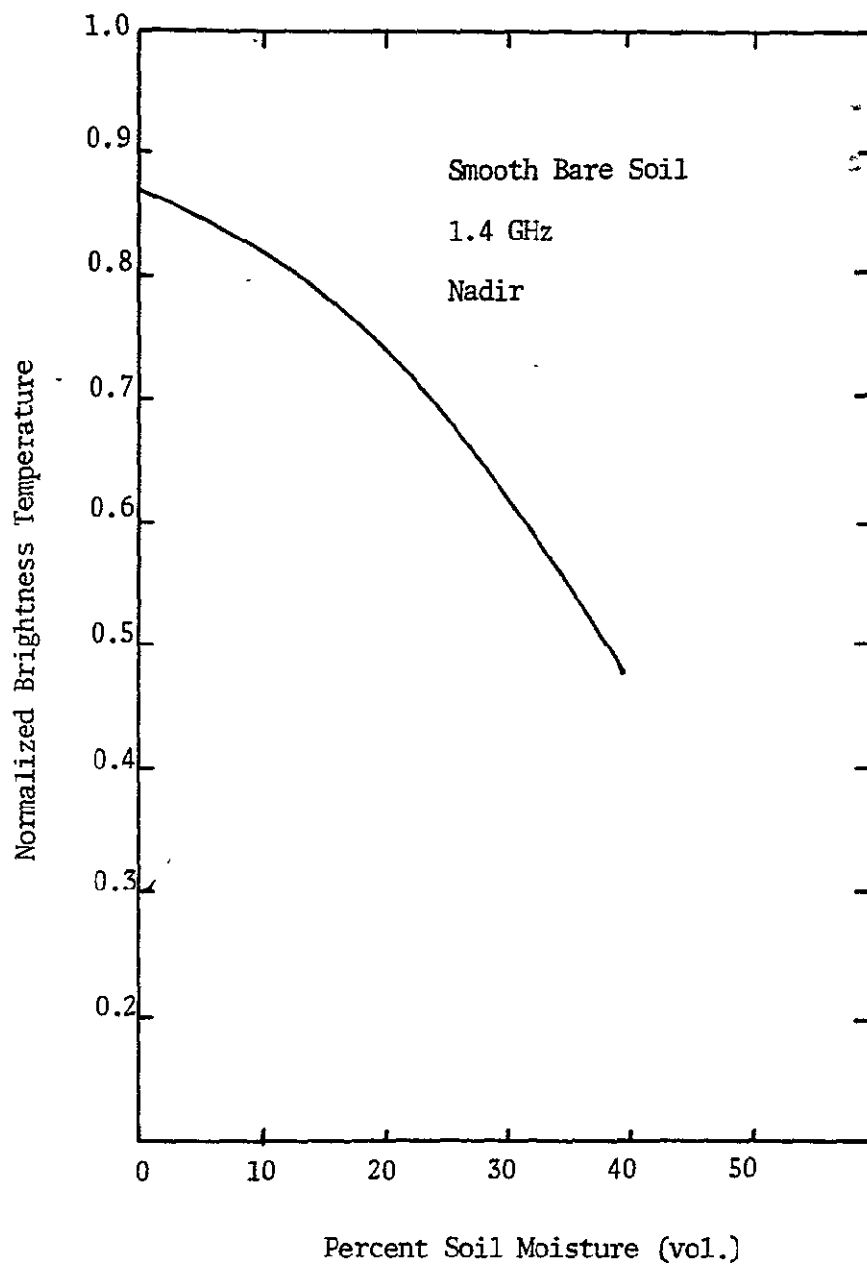


Figure IV-17. Calculated change in emission of smooth bare soil as a function of volumetric soil moisture.

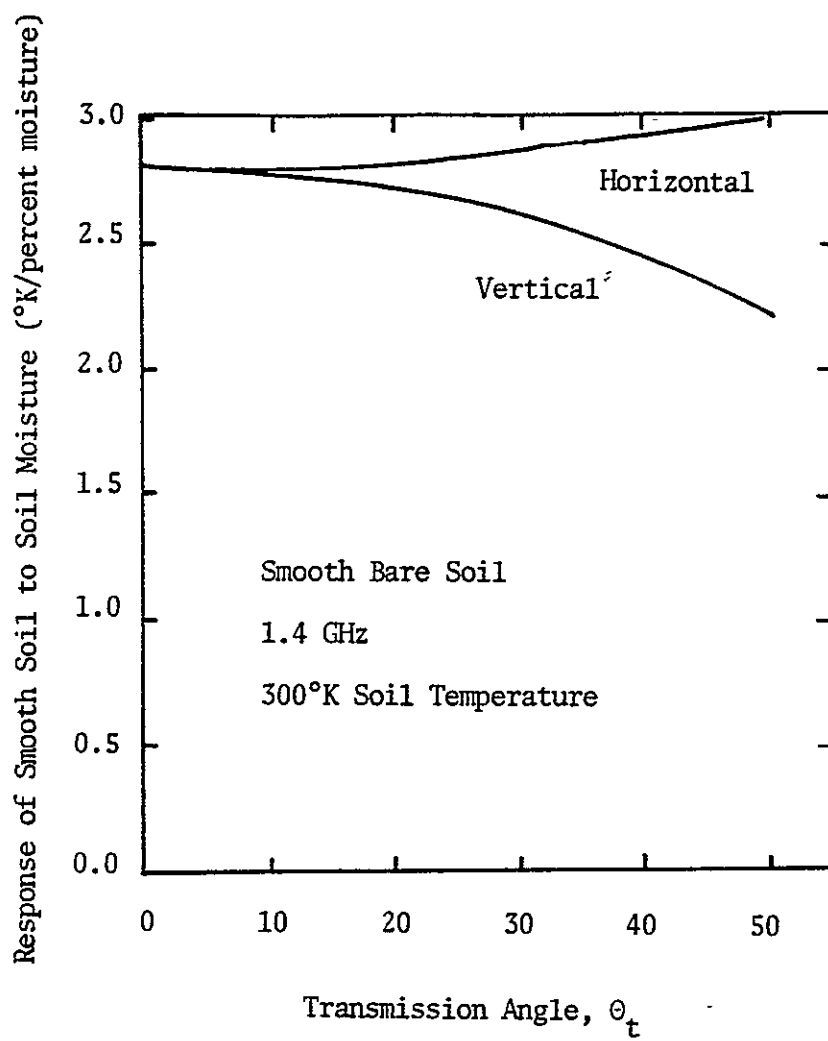


Figure IV-18. Calculated response of smooth bare soil to volumetric soil moisture as a function of transmission angle.

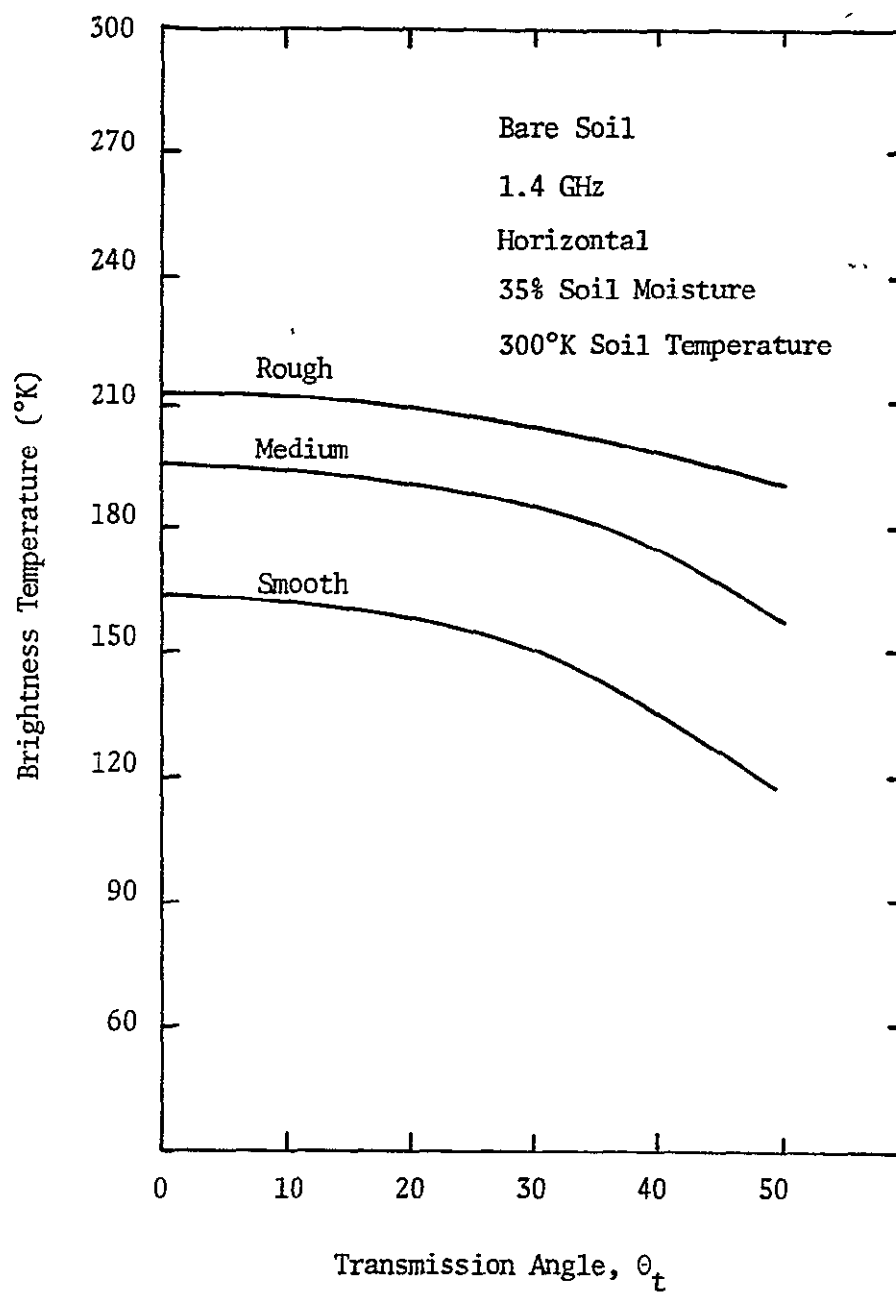


Figure IV-19. Calculated horizontal brightness temperature of bare soil as a function of roughness and transmission angle.

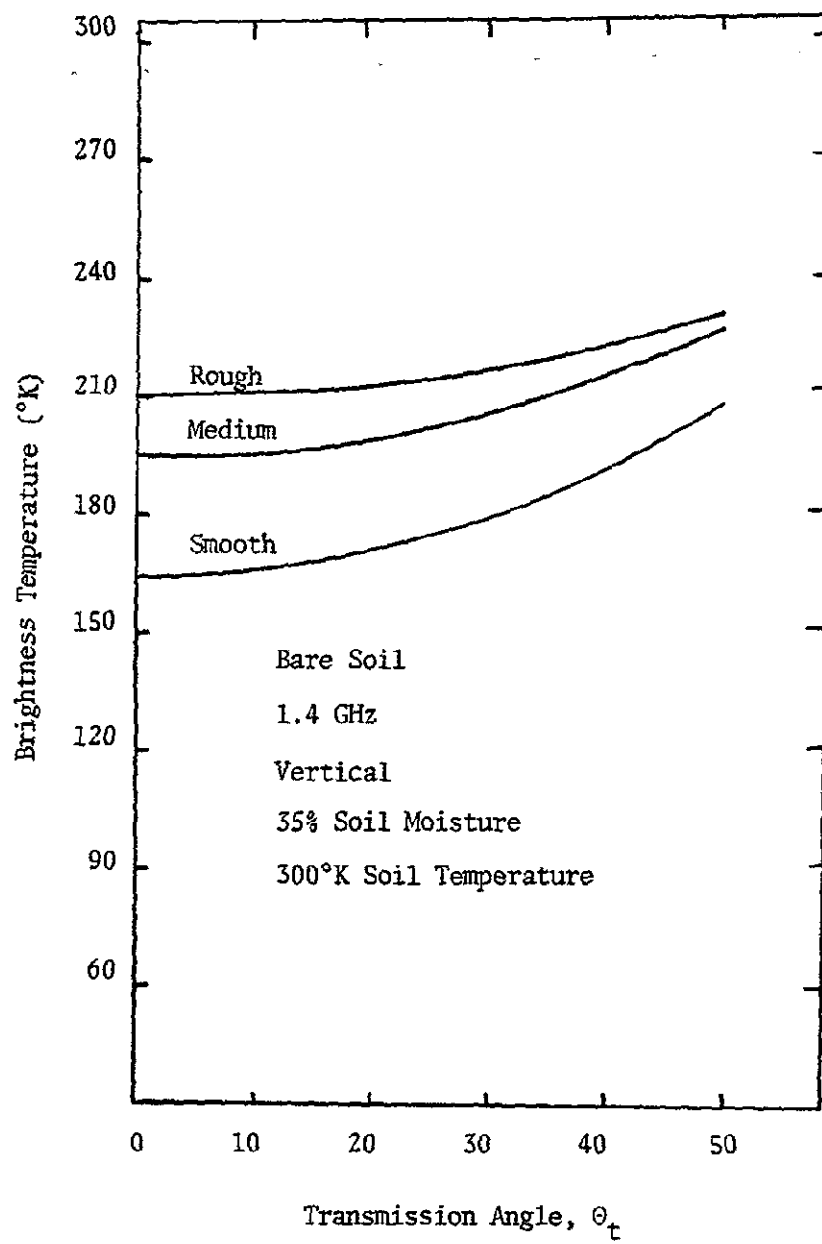


Figure IV-20. Calculated vertical brightness temperature of bare soil as a function of roughness and transmission angle.



The effect of soil moisture can be seen more clearly by plotting brightness temperature versus soil moisture at one transmission angle. Figure IV-21 is such a plot at nadir. Note that the effect of roughness is not simply a shift in brightness temperature, as is the case for soil temperature, but the roughness actually changes the response to soil moisture. As surface roughness increases, the brightness temperature increase is greater the higher the soil moisture. So, as the surface gets rougher, the response to soil moisture decreases. This is demonstrated at nadir in Figure IV-22. Figure IV-22 is a plot of the average slopes of the curves in Figure IV-21 as a function of rms surface height.

## Vegetation

### Model Description

Two models describing emission from vegetation were briefly presented in Chapter III, one by Sibley [75] and one by Basharinov and Shutko [78]. Each modeled the vegetation as a planar dielectric slab overlying the soil surface. Sibley modeled the transmission through the slab and Basharinov and Shutko modeled the emissivity of the slab based on the effective reflection coefficient. The main difference between the two approaches lies in their

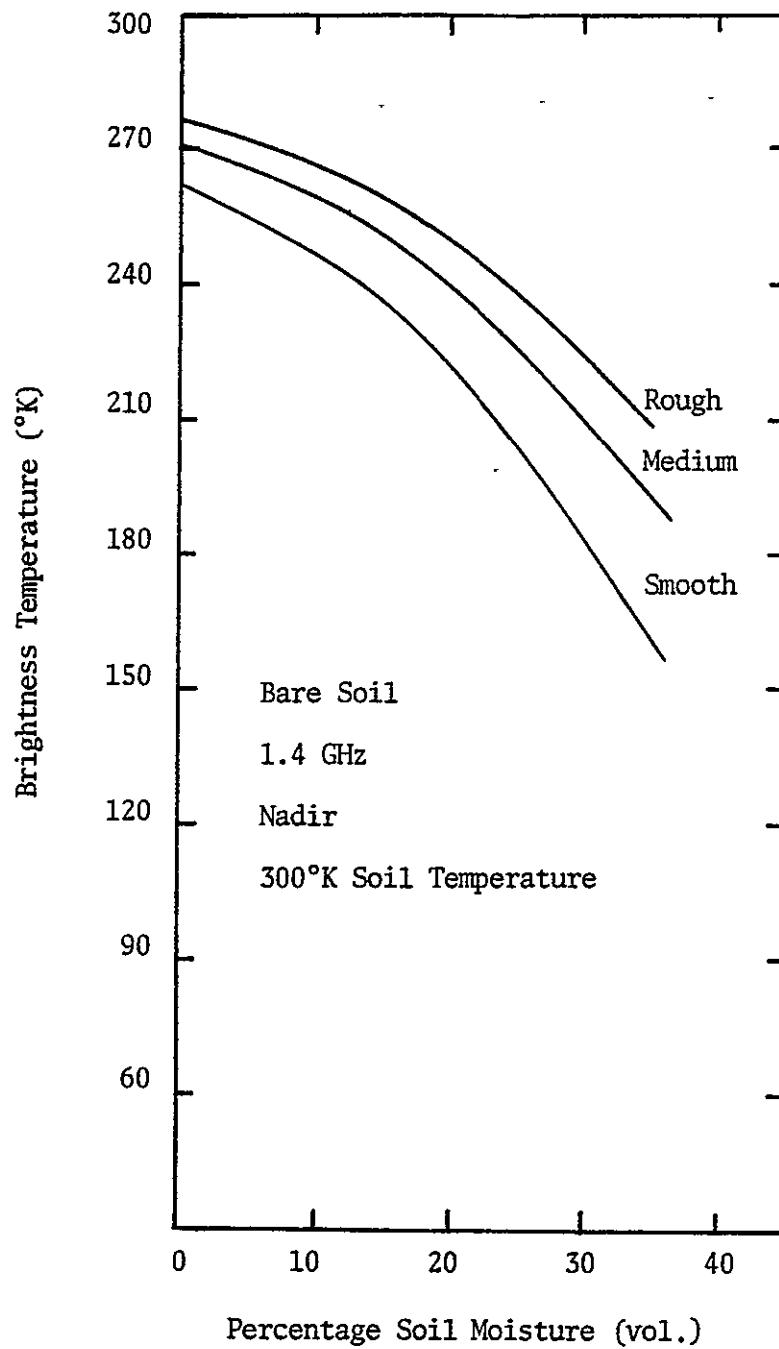


Figure IV-21. Calculated brightness temperature of bare soil as a function of roughness and soil moisture.

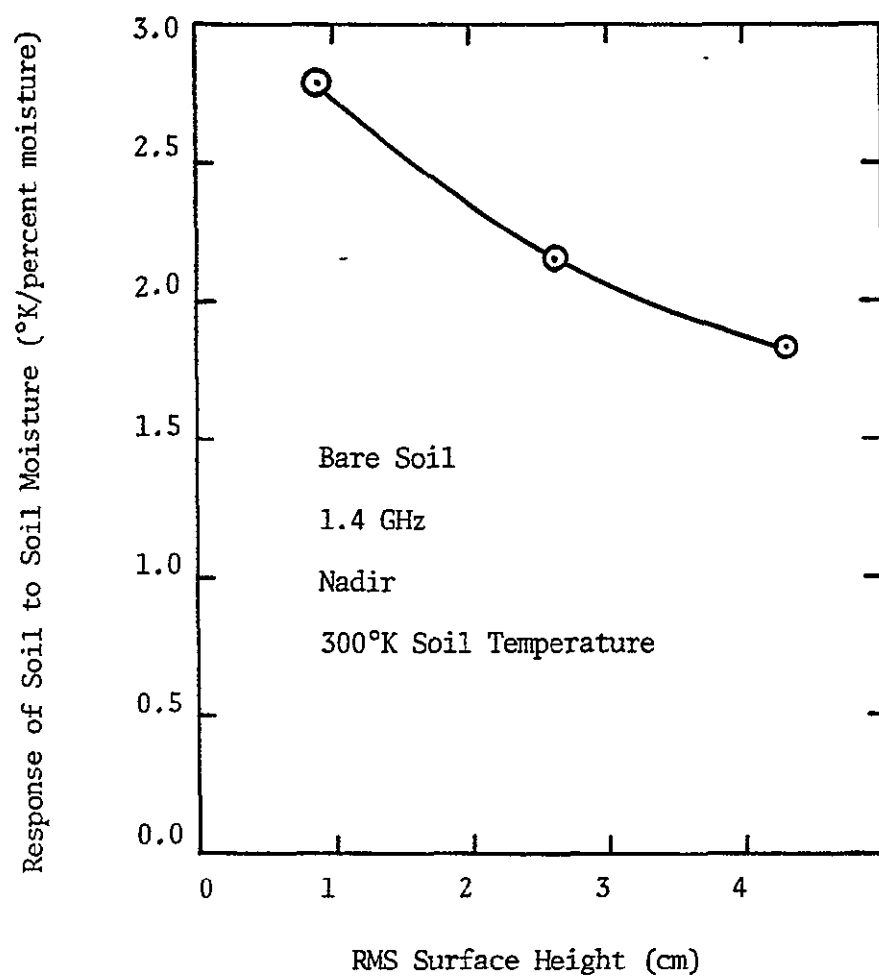


Figure IV-22. Change in the response of bare soil emission to soil moisture as a function of surface roughness.

respective techniques of determining the propagation properties of the slab.

Basharinov and Shutko [78] modeled the optical depth of the vegetation slab by assuming that the water in the plant volume was either a fog or precipitated water. Sibley [75] calculated the permittivity of the vegetation based on a mixing formula. He then used this permittivity to calculate the attenuation of energy emitted from the soil as it propagated through the vegetation, and to calculate the emission of the vegetation.

It has been shown by Lee [91] and Newton et al. [92] that Sibley's approach is sufficient to describe the general effects of vegetation. In addition, Waite and Cook [74] concluded that scattering within the vegetation canopy could be neglected. As a result, Sibley's approach will be utilized in this document.

Sibley's [75] vegetation model is based on the fact that energy is radiated from a soil volume, across the surface boundary and through the vegetation canopy. The radiative transfer model describes the emission from the soil volume, and the surface model presented in the previous section describes the effects of the surface. These two models together describe the brightness temperature of the soil.

For vegetated surfaces the brightness temperature of the soil is simply modified to account for propagation through the vegetation layer. This requires calculating the attenuation coefficient of the planar vegetation slab. Only the permittivity of the vegetation slab must be specified in order to calculate this coefficient.

Sibley [75] used the Weiner model for a dielectric mixture as presented by Evans [76] to calculate the permittivity of the vegetation slab. In doing this, Sibley postulated that the vegetation was a mixture of vegetation (primarily water) and air. The resulting equation for the permittivity of the vegetation canopy is:

$$\epsilon_m = \frac{\epsilon_v(1+p\mu) + \mu(1-p)}{\epsilon_v(1-p) + p + \mu} \quad (\text{IV-82})$$

where  $\epsilon_v$  is the relative permittivity of the vegetation,  $p$  is the fraction of the canopy volume which is occupied by vegetation, and  $\mu$  is a parameter called the Formzhal which describes the dispersion of one medium within the other.

The selection of  $u$  is not critical and is generally assumed to be in the range of 10 to 25. Peake and Oliver's [77] formulation of the permittivity of vegetation was used in the dielectric mixture calculation. It is given as

$$\epsilon_v = \frac{F}{2} \text{Real}(\epsilon_w) + j \frac{F}{2} \text{Imaginary}(\epsilon_w) \quad (\text{IV-83})$$

where  $F$  is the fraction of water by weight in the plant and  $\epsilon_w$  is the relative permittivity of water. The Debye form of the permittivity of water was used and is given by [100], [101].

$$\epsilon_w = \epsilon_\infty + \frac{\epsilon_s - \epsilon_\infty}{1 + j(f/f_0)} \quad (\text{IV-84})$$

The parameter  $\epsilon_\infty$  is generally chosen to be 5.5 while

$$\epsilon_s = 87.7 - 0.4(t - 273) \quad (\text{IV-85})$$

and

$$f_0 = 9.0 + 0.405(t - 273)$$

$t$  is the temperature of the canopy in degrees Kelvin and  $f$  is frequency.

Uniformly vegetated surface - It will first be assumed that the soil is covered by a homogeneous dielectric layer with permittivity described by (IV-82). Neglecting atmospheric effects, there are two processes through which the emission of bare ground is modified by a vegetation layer. The emission from the bare ground, described by (IV-79) is attenuated as it propagates through the canopy. Also, thermal radiation from the canopy augments the radiation from the soil surface.

The magnitude of a field having propagated a distance  $H$  through a lossy dielectric is

$$E = E_0 e^{-\alpha H \sec \theta_t} \quad (\text{IV-87})$$

where  $E_0$  is the initial field strength,  $\theta_t$  is the transmission angle, and  $\alpha$  is the attenuation constant given by

$$\alpha = \left[ \frac{\mu_0 \mu_{r_v} \epsilon_0 \epsilon_{r_v}}{2} \sqrt{1 + \left( \frac{\epsilon_{r_v}''}{\epsilon_{r_v}'} \right)^2} - 1 \right]^{1/2} \quad (\text{IV-88})$$

where

- $\mu_{r_v}$  - relative permeability of the vegetation ( $\approx 1.0$ )
- $\epsilon'_{r_v}$  - real part of the relative permittivity of the vegetation
- $\epsilon''_{r_v}$  - imaginary part of the relative permittivity of the vegetation

Average power density is proportional to the square of the magnitude of the electric field, and the brightness temperature of the soil is proportional to emitted power density. As a result, the component of the brightness temperature of the soil-vegetation complex that is due to the brightness temperature of the soil passing through the vegetation is

$$\left( BT_{\text{soil-vegetation}} \right)_{\text{soil component}} = BT_{\text{soil}} e^{-2\alpha H \sec \theta_t} \quad (\text{IV-89})$$

In addition to the attenuation of the emission from the soil, the vegetation layer also contributes to the total brightness temperature of the soil-vegetation complex. Assuming that all points within the canopy emit radiation



equally, the canopy contribution can be derived from the general expression for the radiation intensity of a dielectric layer of thickness H.

$$BT_v = \int_0^H B(h) e^{-\int_h^H a(z) \sec \theta_t dz} \sec \theta_t dh \quad (\text{IV-90})$$

where

$BT_v$  - brightness temperature of the vegetation

$B(h)$  - differential source function

$a(z)$  - power attenuation constant at height  $z$ ;

$$a(z) = 2 \alpha(z)$$

Sibley [75] assumed that the source function in the vegetation is equal to

$$B(h) = \epsilon(h) \epsilon_g(h) \quad (\text{IV-91})$$

where

$t(h)$  - temperature of the canopy at height  $h$

$\epsilon_\delta(h)$  - differential emission coefficient at height  
 $h$  (radiation per unit length)

Assuming that the temperature, attenuation constant, and source function are constant with the canopy, (IV-90) reduces to

$$BT_v = t_v \left( \frac{\epsilon_s}{2\alpha} \right) (1 - e^{-2\alpha H \sec \theta_z}) \quad (\text{IV-92})$$

Sibley [75] points out that if the system is in thermal equilibrium, the differential emission coefficient is equal to the absorption coefficient,  $2\alpha$ . Since the condition is often violated in a plant canopy, Sibley assumes that the emission coefficient is equal to

$$\epsilon_\delta = f 2\alpha \quad (\text{IV-93})$$

where  $f$  is an energy transfer factor. Thus,

$$BT_v = t_v f (1 - e^{-2\alpha H \sec \theta_z}) \quad (\text{IV-94})$$

If  $f < 1$  the canopy is gaining energy, and if  $f > 1$  the canopy is losing energy.

The total brightness temperature of the soil-vegetation complex (for a uniform cover of vegetation) can now be written as

$$BT_{\text{soil-vegetation}} = BT_{\text{soil}} e^{-2\alpha H \sec \theta_t} + BT_v \quad (\text{IV-95})$$

Calculations based on these equations will be given below.

Row crops - Sibley [75] also developed the equations that describe the effect of row planted vegetation on the emission of soil. The equations describing the emission and attenuation characteristics of uniform vegetation were simply modified to account for the geometry of the rows. The rows are assumed to consist of uniform vegetation with a rectangular cross section. Figure IV-23 denotes the geometry of the situation. The direction from which the scene is observed is denoted by  $\theta_t$ , the incident angle, and  $\phi_t$ , the azimuth angle. Both  $\theta_t$  and  $\phi_t$  can only assume values less than or equal to  $\pi/2$ . The direction  $\theta_t = 0^\circ$  is normal to the surface, and  $\phi_t = 0^\circ$  is perpendicular to the rows.

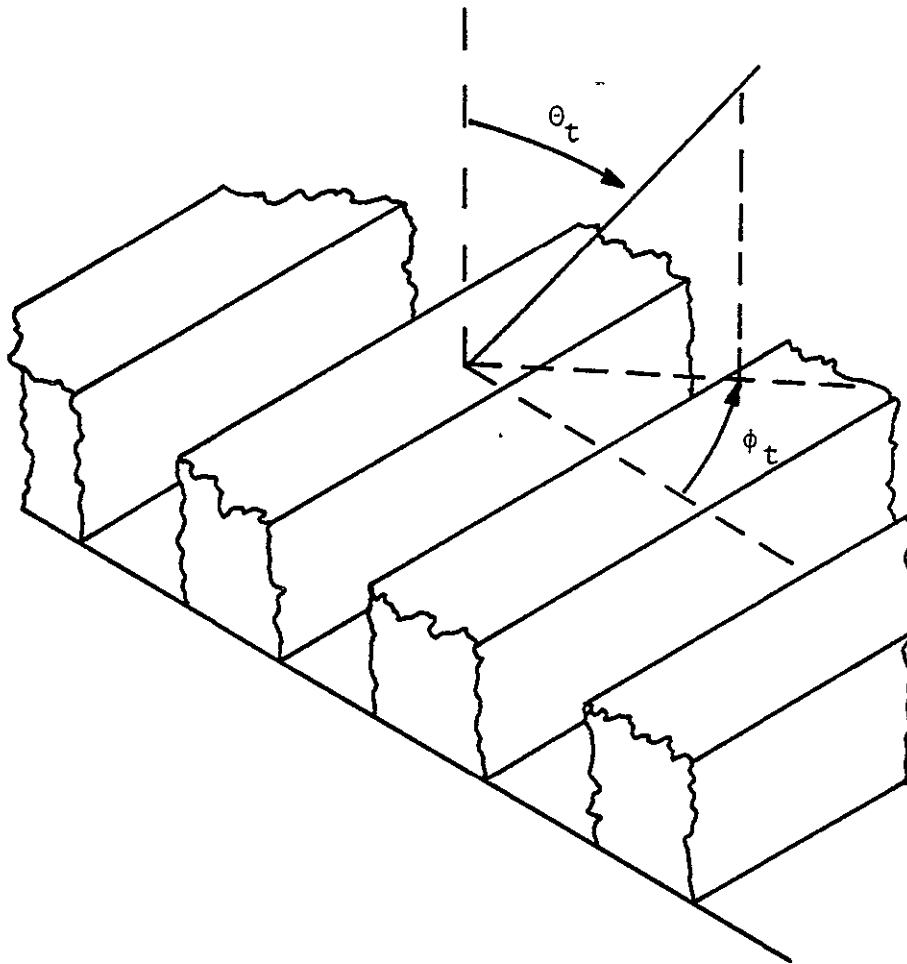


Figure IV-23. Geometry for radiation from row vegetation (after Sibley [75]).

A cross-sectional view of the rows is given in Figure IV-24. The height and width of the rows are denoted by  $H$  and  $W$ , respectively. The width of the non-vegetated space between the rows is denoted by  $A$ . The dimension  $B$  is denoted on Figure IV-24 and also on Figure IV-25. It is given as

$$B = H \tan \theta_t \cos \phi_t \quad (\text{IV-96})$$

Note that the length  $(A + W)$ , the row period, may be considered a unit length. The power radiated into direction  $(\theta_t, \phi_t)$  by any region of length  $(A + W)$  is the same. As a result, the brightness temperature of an entire field with uniform row spacing is given by the average power radiated from any region  $(A + W)$  long.

If  $B < A$  only a portion of the power radiated from the soil experiences attenuation. The average length of path the energy must traverse through the vegetation canopy is used as the length over which the radiation experiences attenuation. This average distance is determined by first projecting the cross sectional area of the canopy into the plane of incidence as shown in Figure IV-26(a). This projected cross sectional area is

$$H W \sec \theta_t \quad (\text{IV-97})$$

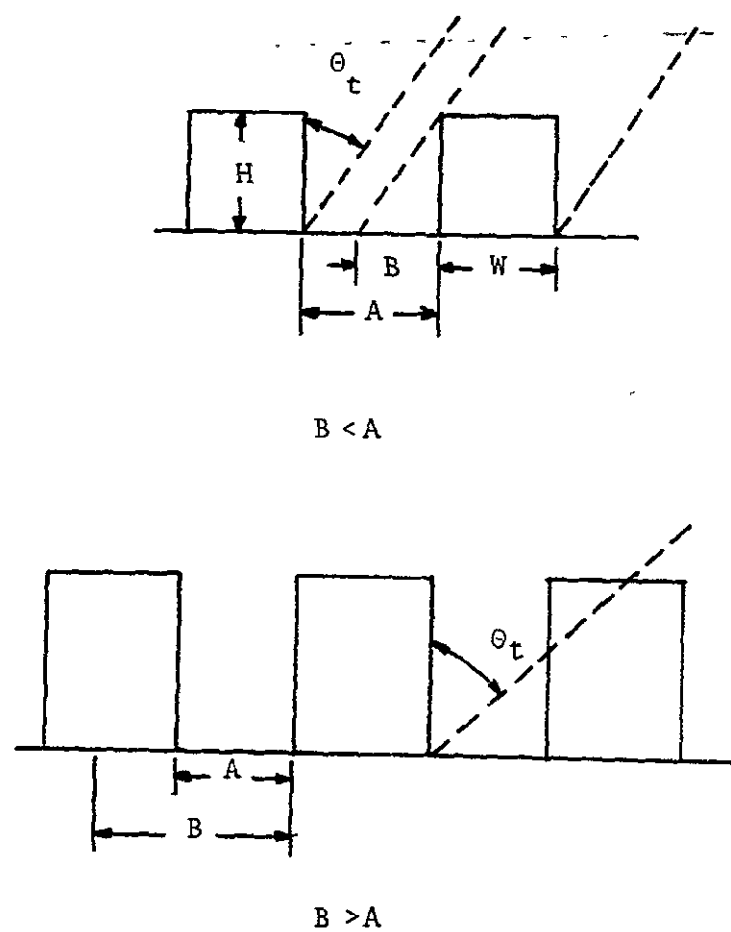


Figure IV-24. Geometry for emission perpendicular to rows (after Sibley [75]).

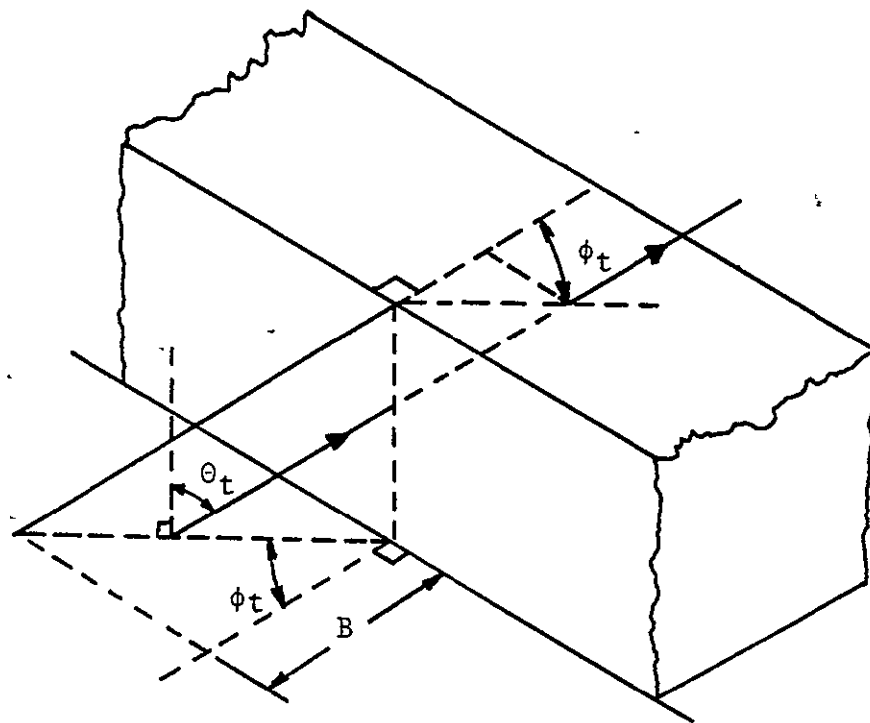


Figure IV-25. Geometry for propagation through a row canopy at an arbitrary azimuth angle (after Sibley [75]).

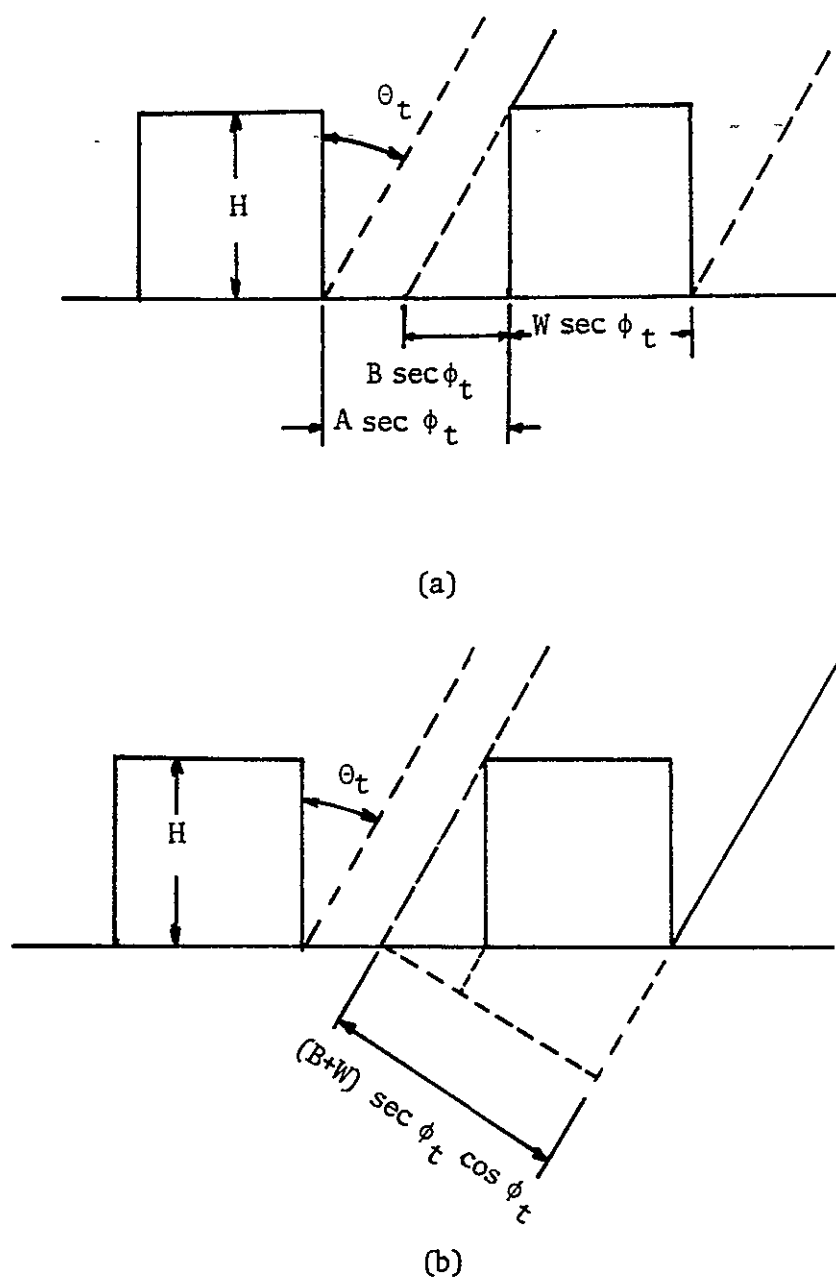


Figure IV-26. Geometry used to aid in the explanation of the average distance the soil emission must traverse through a row canopy for arbitrary azimuth and transmission angles.



Secondly, the projection of  $(B+W)$  onto the plane of incidence,

$$(B+W) \sec \phi_t \quad (\text{IV-98})$$

is projected onto the plane perpendicular to the direction of propagation (Figure IV-26(b)). This projection is

$$(B+W) \sec \phi_t \cos \theta_t \quad (\text{IV-99})$$

Dividing (IV-97) by (IV-99) results in the average distance the radiation must traverse through the vegetation for the case  $B < A$ .

$$d = \frac{H W \sec \phi_t}{(B+W) \sec \phi_t \cos \theta_t} \quad (\text{IV-100})$$

If  $B > A$  all of the soil is either covered or shadowed by vegetation. For this case the average attenuation distance is

$$d = \frac{H W}{(A+W) \cos \theta_t} \quad (\text{IV-101})$$

For simplicity, a special function will be defined to account for the differences in the two cases,  $B > A$  and  $B < A$ .

$$L(A,B) = B \quad \text{when } B < A$$

(IV-102)

$$L(A,B) = A \quad \text{when } B \geq A$$

Utilizing this function, the apparent temperature of row crops is given by

$$BT_{row} = \frac{[A - L(A,B)] BT_{soil} + [L(A,B) + W] BT_{soil-vegetation}}{A + W} \quad (IV-103)$$

where  $BT_{soil}$  is defined by (IV-79), and  $BT_{soil-vegetation}$  is defined by (IV-95). However, the average attenuation distance is now given by

$$d = \frac{HW}{(L(A,B) + W) \cos \theta_k} \quad (IV-104)$$

## Model Demonstration

Uniform vegetation - Sibley's [75] formulation for a uniform cover of vegetation over smooth soil (with uniform temperature and moisture profile) is demonstrated in Figure IV-27. These data show that as vegetation density is increased, the apparent temperature also increases until eventually the dependence of the apparent temperature on soil moisture is completely masked. This effect is also apparent if vegetation density is held constant and frequency is increased (Figure IV-28). Therefore, as the frequency of the measurement is increased, the ability to detect soil moisture deteriorates. Figure IV-28 also demonstrates the effect of a temperature difference between the soil and vegetation canopy.

As evidenced by Figures IV-27 and IV-28, computations based on Sibley's [75] formulation indicate that the sensitivity of apparent temperature to variations in moisture content depend on several parameters. For a uniform canopy of 100% coverage over a smooth surface, the vegetation volumetric density, vegetation height, frequency, and transmission angle affect the sensitivity to moisture. Since there are several parameters that affect the sensitivity in the same manner, there are numerous equivalent states. However, it was determined

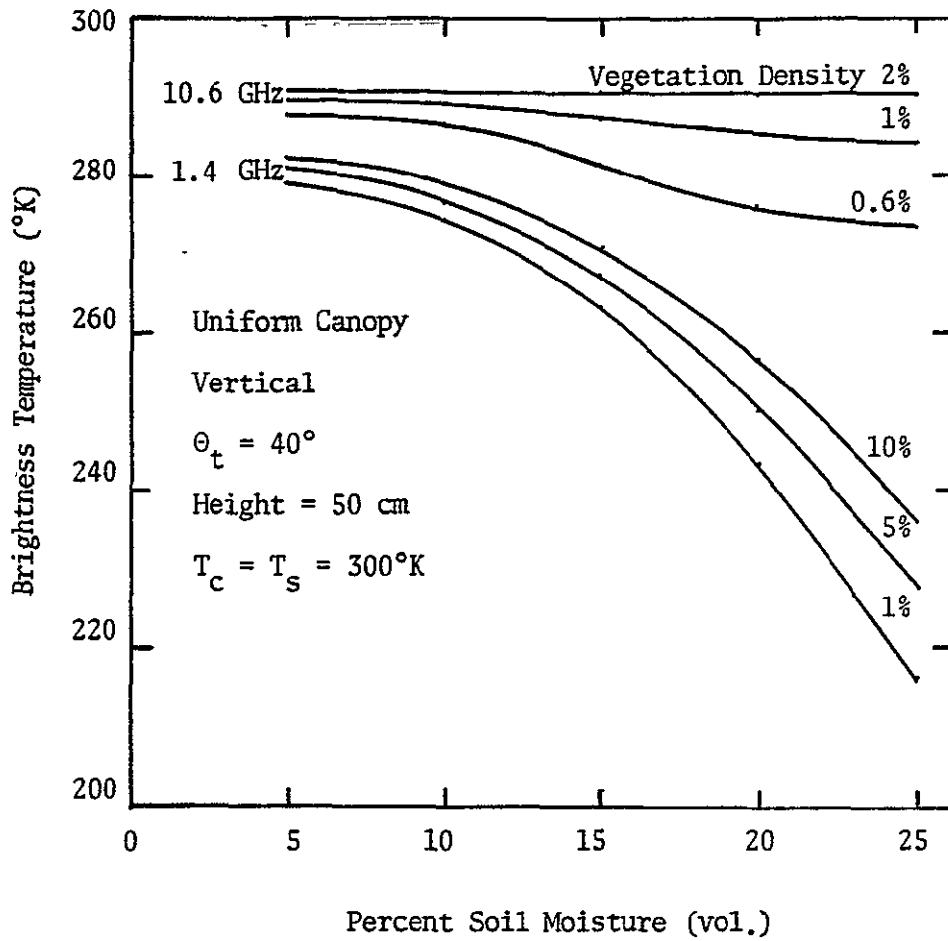


Figure IV-27. Vertically polarized brightness temperature of a uniform canopy as a function of soil moisture and vegetation density.

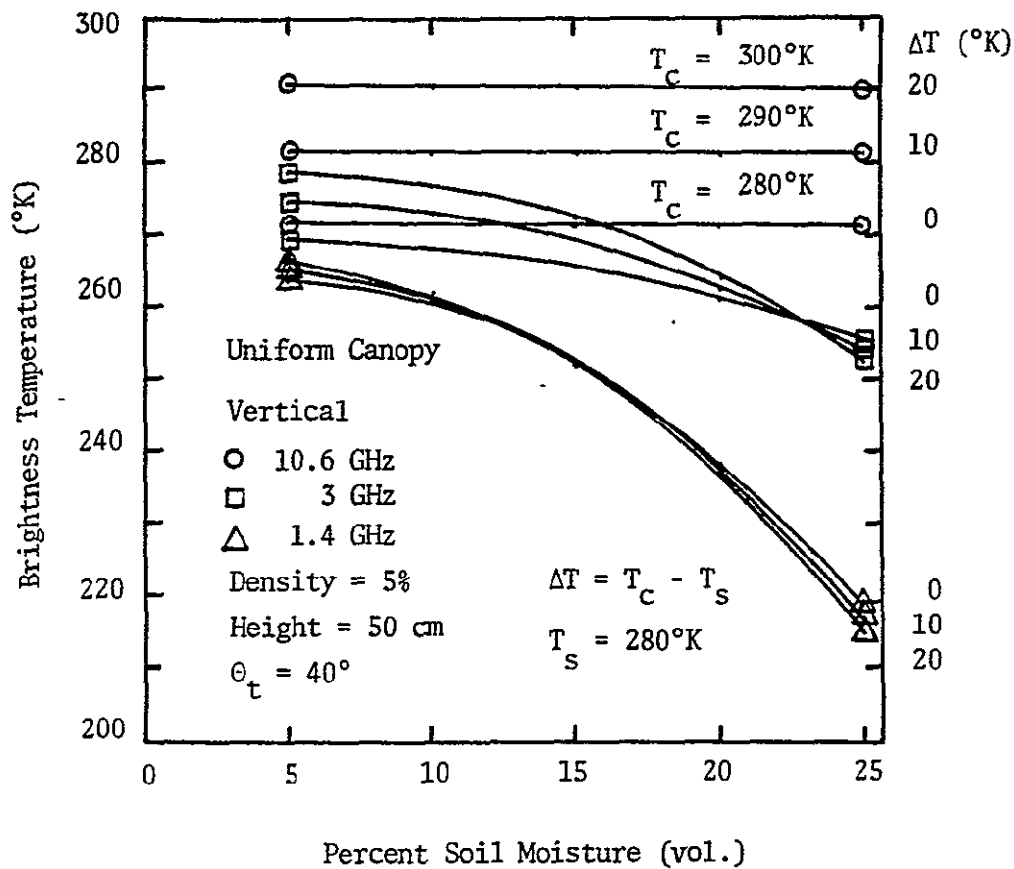


Figure IV-28. Vertically polarized brightness temperature of a uniform canopy as a function of soil moisture for three combinations of vegetation and soil temperatures.

that equivalent states have approximately equal vegetation height-density products. It was also determined that equivalent states were independent of transmission angle.

Figure IV-29 is a plot of measured soil moisture content (based on Sibley's formulation) against height-density product. As the height-density product increases, the apparent soil moisture that could be measured using an airborne radiometer decreases. In addition, the rate of decrease is higher as the frequency of the measurement increases. However, it is of significance to note that in the L-band frequency region it appears that there is a potential of measuring soil moisture in the presence of normal vegetation.

Row vegetation - Calculations based on the equation for row crops (Figures IV-30 and IV-31) show that the sensitivity to changes in moisture are highly dependent on the azimuth angle as would be expected. Figures IV-32 and IV-33 illustrate this dependence for uniform soil moisture of 20% and several transmission angles. As expected, the lower the transmission angle the smaller the effect of the azimuth angle. As a result, the optimum transmission angle for remote sensing soil moisture through vegetation is nadir for both uniform and row planted vegetation.

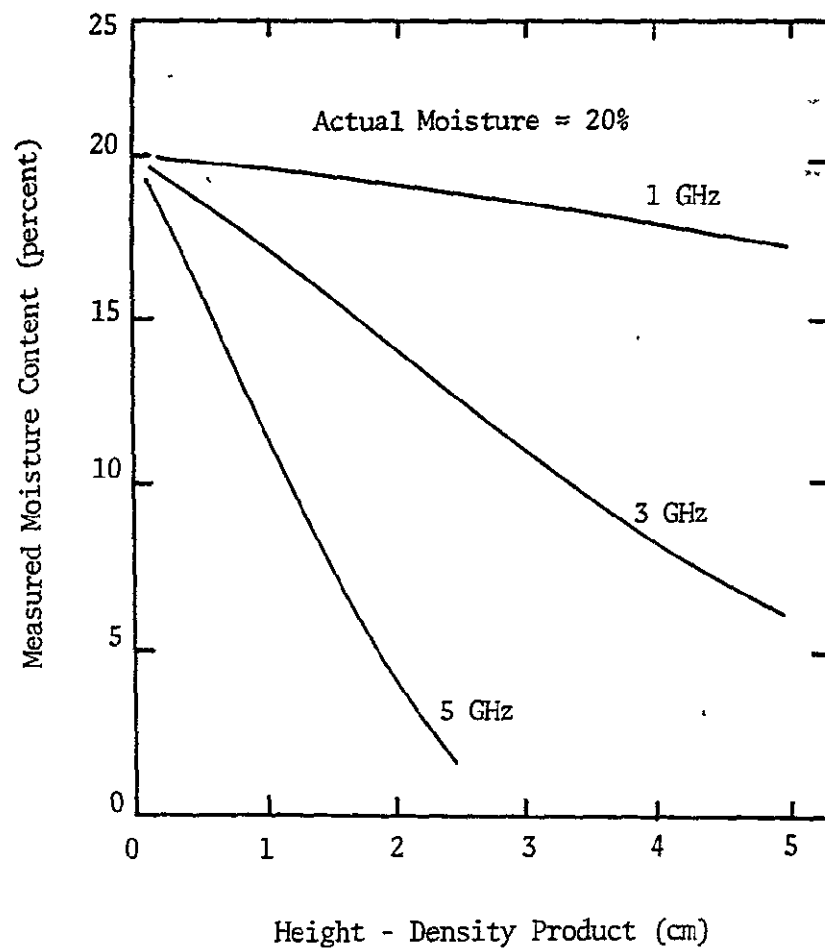


Figure IV-29. Moisture content determined from apparent temperature of vegetated soil (after Sibley [75]).

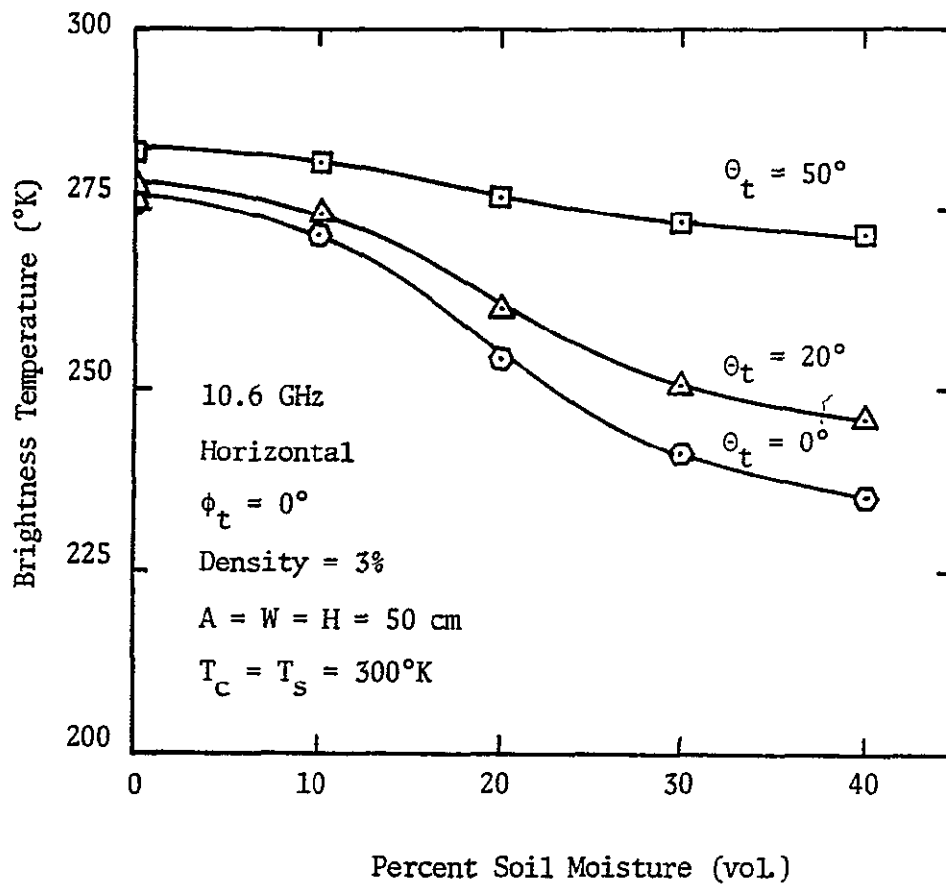


Figure IV-30. Brightness temperature of row vegetation at 10.6 GHz as a function of soil moisture and transmission angle looking perpendicular to the rows.



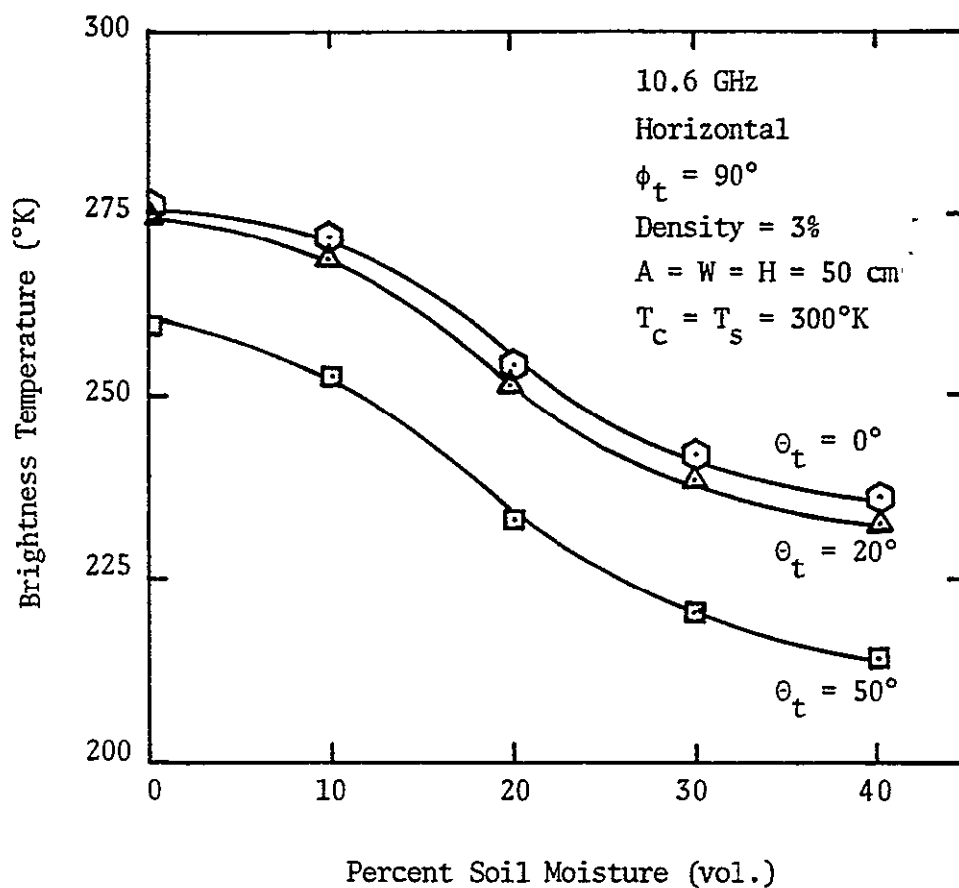


Figure IV-31. Brightness temperature of row vegetation at 10.6 GHz as a function of soil moisture and transmission angle looking parallel to the rows.

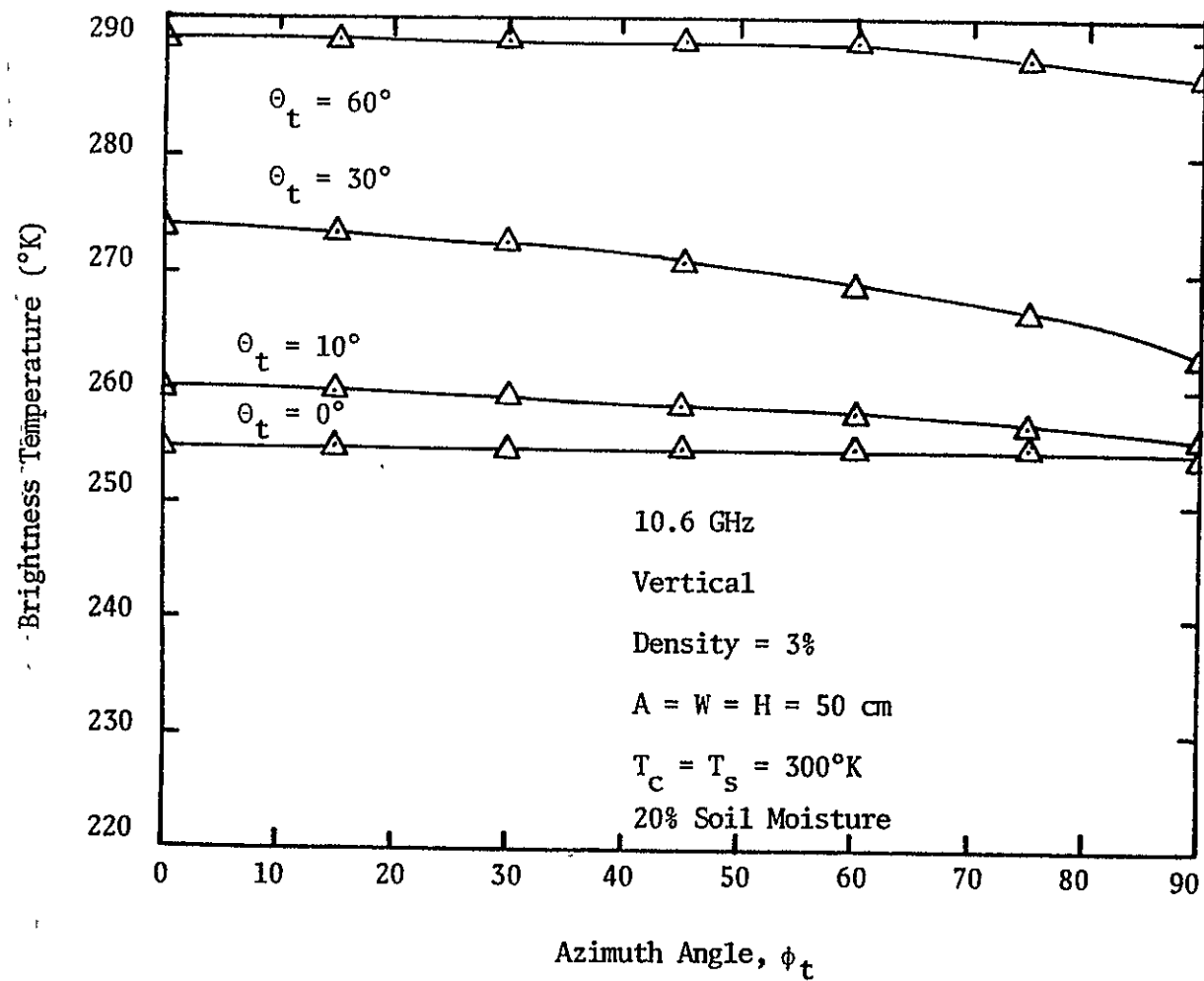


Figure IV-32. Vertical brightness temperature of row vegetation as a function of transmission and azimuth angles.

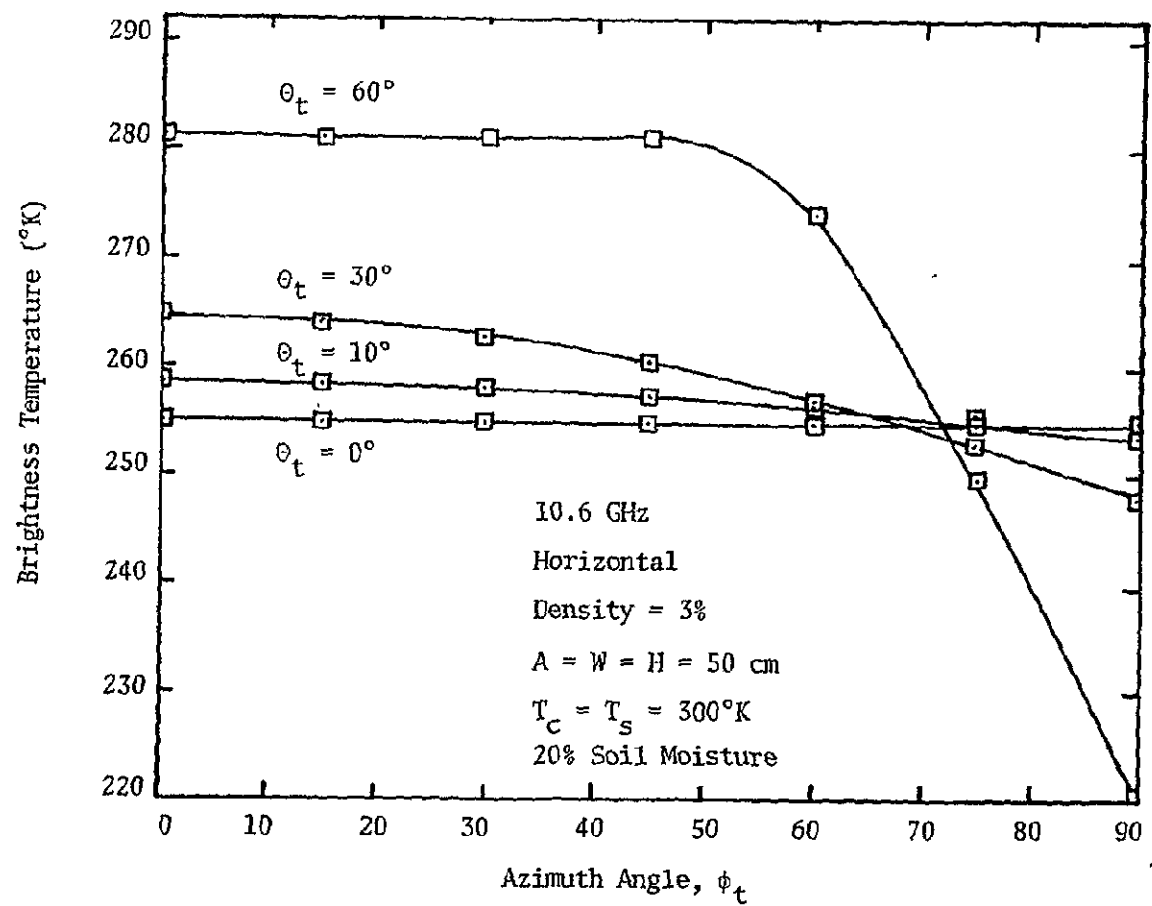


Figure IV-33. Horizontal brightness temperature of row vegetation as a function of transmission and azimuth angles.

## CHAPTER V

### MEASUREMENT PROGRAM

An on-going systematic measurement program designed to measure the effects of scene parameters such as soil moisture, soil temperature, surface roughness and vegetation cover on the microwave emission of soil was initiated by Texas A&M University (TAMU) in 1973. This program has been funded by the NASA Johnson Space Center (JSC) as part of the NASA Johnson Space Center Joint Soil Moisture Experiment (JSME). The objective of the JSME is to verify that a useful measure of soil moisture can be obtained remotely using active and/or passive microwave sensors.

The measurements reported in this document were acquired by Texas A&M University as part of the JSME. In acquiring these data, the NASA/JSC two frequency truck mounted radiometer system was utilized. This system is described in the following section. The individual experiments involving the use of this system are described after the system description, and general comments are made concerning microwave data reduction and accuracy.

#### Microwave Signature Acquisition System

##### Background

In 1971 the Earth Observation Division of the NASA Johnson Space Center wrote specifications for procurement

of a five frequency radiometer system. AIL, a division of Cutler Hammer received the contract to build the system. Due to funding restrictions, only two of the original five frequencies were constructed by AIL, 1.4 GHz and 10.6 GHz. The resulting system, termed the Microwave Signature Acquisition System (MSAS) by NASA, was subsequently delivered to NASA in late 1972 and mounted on two vehicles in the spring of 1973. The receiver and RF hardware were mounted on a hydraulic boom capable of obtaining a height of 65 feet (Figure V-1). The controller, tape drive, and minicomputer were mounted in an air-conditioned van (Figure V-2). The antenna mount is configured such that the incident angle can be varied from nadir to zenith. The antennas can also be rotated about their major axis to change the receiver polarization with respect to the plane of incidence.

#### MSAS Description

The MSAS consists of basically three subsystems as detailed in Figure V-3:

- 1) RF Subsystem
- 2) Receiver Subsystem
- 3) Data Processing Subsystem

The L-band RF and receiver subsystems are essentially the same as the S194 radiometer that was flown aboard Skylab.

ORIGINAL PAGE IS  
OF POOR QUALITY

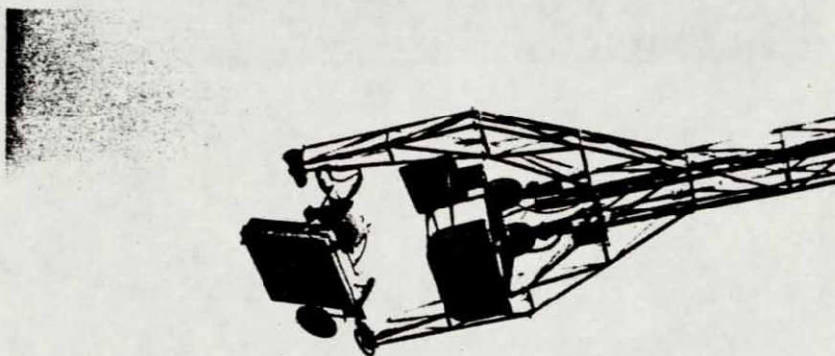
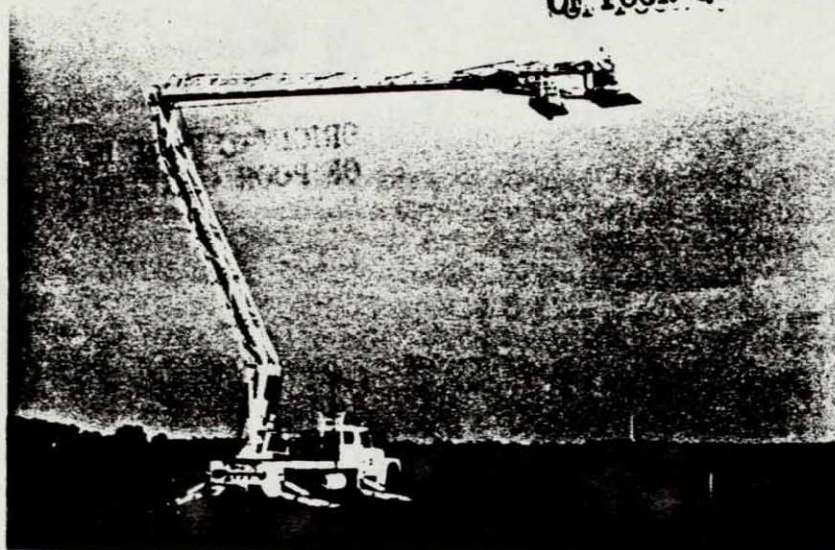


Figure V-1. Boom truck with the radiometer mounted at the end of the boom (top). Close-up showing details of the radiometer antennas and truss structure (bottom).

ORIGINAL PAGE IS  
OF POOR QUALITY



Figure V-2. Van that houses the radiometer control and data processing electronics.





These radiometers are of the "Dicke" type which modulates the incoming power against a stable reference source.

In a standard Dicke type receiver, a Dicke switch, driven by a reference oscillator, alternately connects the output of the antenna port and a reference source to the input of the RF amplifier. If the antenna temperature differs from the temperature of the reference source, a square wave modulated signal is produced. The modulated signal is then processed to yield a dc voltage proportional to the temperature difference of the known reference and the equivalent antenna temperature.

The MSAS is constructed such that the gain of the receiver is also modulated in synchronism with the Dicke switch rate. This modulation is accomplished through the use of a digital attenuator that forces the receiver output corresponding to the reference source input to be equal to the receiver output corresponding to the antenna input. The attenuator value is directly related to the radiometric antenna temperature. Since the Dicke switch rate is 105 Hz, it is assumed that the system gain does not fluctuate within one cycle of the switch.

For internal calibration purposes, the MSAS has two internal reference noise generators. One has an equivalent noise temperature of approximately 383°K and the other has an equivalent noise temperature of 272°K. These sources

provide a means of periodically measuring the equivalent noise temperature of the receiver.

RF subsystem - As presently configured, the RF subsystem consists of a modular X-band RF head built in a separate temperature controlled enclosure with a waveguide connection to the 10.6 GHz antenna. It has already been noted that the L-band RF hardware is contained within the receiver enclosure. The L-band frequencies of operation are within the 1 to 2 GHz passband of the receiver, therefore, it is essentially a tuned radio frequency amplifier and, hence, does not use a mixer or local oscillator. The L-band RF hardware performs the switching operation between the antenna and the reference noise generators (RNG's), protection filtering and preamplification.

In contrast, the X-band output must be down-converted from a center frequency of 10.63 GHz to a center frequency of 1.5 GHz in order to be within the receiver passband. The X-band RF head performs the RF switching between the antenna and the RNG's, filtering, down-conversion, and IF preamplification.

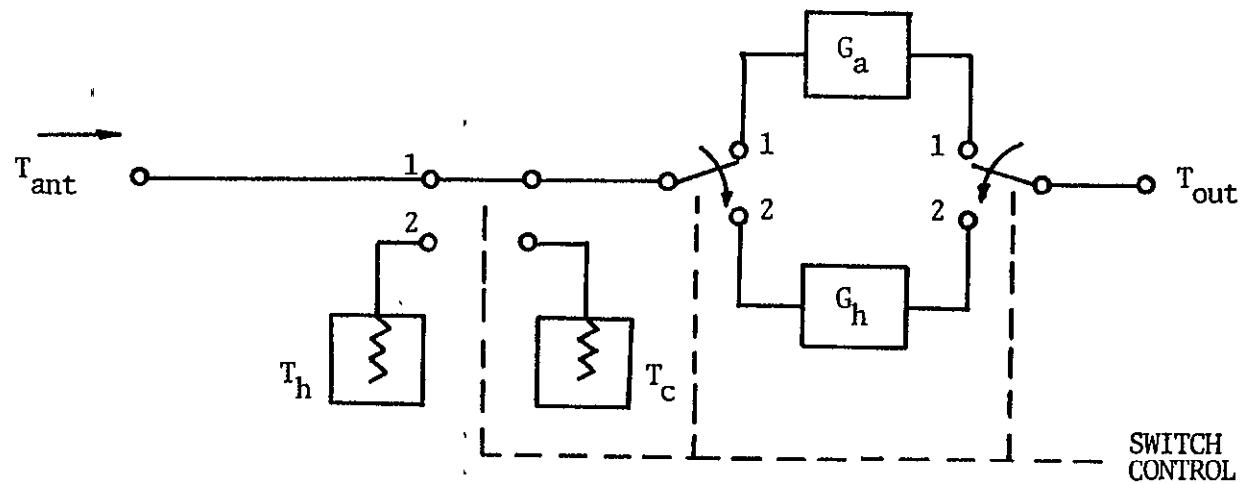
Contained within the RF hardware of the X-band head and the L-band RF hardware are the two RNG's, each set of which were specifically designed for a particular frequency band of operation. The warmer RNG is used as the reference for comparison to the antenna output port; both are used for internal calibration. The stability and the uncertainty

in measuring the temperature of the RNG's has a major effect on the ultimate accuracy of the radiometer. The design and construction of these RNG's are discussed in detail by Hornbostel [102].

Receiver subsystem - The receiver subsystem consists of a broadband IF input square law detector, low noise and low offset dc amplifier, Y-factor measurement circuitry, timing and control circuitry for Dicke switch operation and synchronism, alarm and band selector logic, and the data multiplexer. The essential part of the receiver subsystem is the Y-measurement circuitry. This circuitry performs the digital attenuation that enables the radiometer to act as a form of gain-modulated switched radiometer.

The Y-measurement system can be simply depicted as in the block diagram of Figure V-4. As previously stated, it uses a gain modulation technique that automatically changes the gain of the radiometer system in synchronism with the switching between the antenna and the hot RNG. The gain is automatically adjusted to satisfy the equality

$$G_a(T_{ant} + T_e) = G_h(T_h + T_e) \quad (V-1)$$



Switch Position	$T_{out}$
1	$G_a (T_{ant} + T_e)$
2	$G_a (T_h + T_e)$

Figure V-4. Block diagram descriptive of the gain modulation technique.

where

$G_a$  - gain of the receiver when looking at the antenna

$G_h$  - gain of the receiver when looking at the hot RNG

$T_{ant}$  - radiometric antenna temperature

$T_e$  - noise temperature of the receiver

$T_h$  - noise temperature of the hot RNG

$T_c$  - noise temperature of the cold RNG

The gain adjustment is accomplished through the use of a digital attenuator that forces the receiver output voltage that corresponds to the hot RNG to be equal to the dc voltage out of the receiver when the input is from the antenna. The setting of the attenuator is termed a Y-factor and is defined as:

$$G_a = Y G_h \quad (V-2)$$

therefore,

$$Y = \frac{G_a}{G_h} = \frac{T_h + T_e}{T_{ant} + T_e} \quad (V-3)$$

and

$$T_{ant} = \frac{T_h + T_e(1 + Y)}{Y} \quad (V-4)$$

Equation (V-4) demonstrates that the system output,  $T_{ant}$ , is independent of gain.

$T_e$  is the equivalent noise temperature of the receiver and is measured periodically through the use of both the hot and cold RNG's. This is accomplished by replacing the antenna input by that of the cold RNG. Equation (V-4) then becomes:

$$T_e = \frac{T_c Y - T_h}{1 - Y} \quad (V-5)$$

Since the radiometer output is independent of gain variations, the gain stability of the system need only be sufficient to prevent loss of signal below the sensitivity threshold of the detector. About 10 dB of automatic gain control (AGC) is included in the receiver to compensate for long-term aging effects, thus assuring near optimum gain.

Data Processing Subsystem - The data processing subsystem performs the functions of radiometer control, input data formatting, system performance monitoring, and furnishes malfunction alarms for the radiometer system. The hardware for this includes a ruggedized Rohm minicomputer, a teletype with paper punch and reader, a magnetic tape unit, and a system control panel.

The minicomputer is used for system performance monitoring, data formatting, and as the teletype and magnetic tape interface. It was also designed to be used for real-time data reduction, however, this function was inoperative until recently. Data reduction techniques were implemented on Texas A&M University computers and are described in detail by Newton [103] and Newton and Tesch [104]. Modifications to the MSAS software for real-time data reduction are described by Clark and Newton [105].

Radiometer alarms are activated and displayed directly at the control panel by the data processing subsystem if any system malfunctions are detected. The radiometer receiver is controlled through the teletype or manual operator inputs selectable at the control panel.

Radiometric data in the form of a serial digital data train is formatted in the receiver and output to the computer in 16-bit parallel data transfers. Simultaneously, the computer accepts 16 channels of analog input via an

input multiplexer and 10-bit AD converter. These analog channels are for supplemental or auxiliary data and are formatted together with the radiometric data and output to a seven track computer compatible (Univac 1108) magnetic tape. In addition, these analog signals may be selected in groups of four for real-time analog strip chart recording.

### Experiments

A series of three experiments have been performed with the MSAS at Texas A&M University. The first of this series was completed in 1973 and was a joint effort between NASA Johnson Space Center, Texas A&M University, and Lockheed Electronics Co., Inc. The results of this experiment are reported by Lee [91] and Newton et al. [92]. Data tabulations are contained in the document by Lee [91] and will not be presented in this document. Experiments were also performed in 1974 and 1975 at Texas A&M University. The data from these experiments are largely the basis for this work. Both of these experiments are described below.

#### Measurement Program in 1974

The 1974 experiment was conducted at the Texas A&M University Research Farm from June 26 through July 21. University of Kansas, NASA/JSC, and Lockheed Electronics Co., Inc. personnel also participated in the experiment.



The purpose of the experiment was to obtain simultaneous active and passive microwave data of well controlled bare and vegetated soil as a function of soil moisture and uniform surface roughness similar to flat tilled agricultural fields. The NASA/JSC L-band (1.4 GHz) and X-band (10.6 GHz) radiometer (MSAS) and the University of Kansas-2-8 GHz radar spectrometer were used to obtain the microwave data. Tabulated passive microwave data and summary tabulations of corresponding ground truth data were documented by Newton [103] and will not be duplicated here. Details of the raw data reduction of the passive microwave data are also presented by Newton [103]. The corresponding active microwave data are reported by Batlivala and Cihlar [106], and a complete listing of ground truth data are reported by Newton and Lee [107].

Ground truth and microwave data were obtained from ten plots of land in the TAMU Research Farm in Burleson County, Texas. Figure V-5 shows the field layout. It should be pointed out that Newton and Lee [107] describe the soil within the test field as 16% sand, 35% silt and 49% clay. However, those numbers were based on one textural analysis. Several later textural analyses revealed that a closer estimate of the average field texture is 3% sand, 35% silt and 62% clay. The soil was uniform across the test fields and is classified as Miller clay.

ORIGINAL PAGE IS  
OF POOR QUALITY

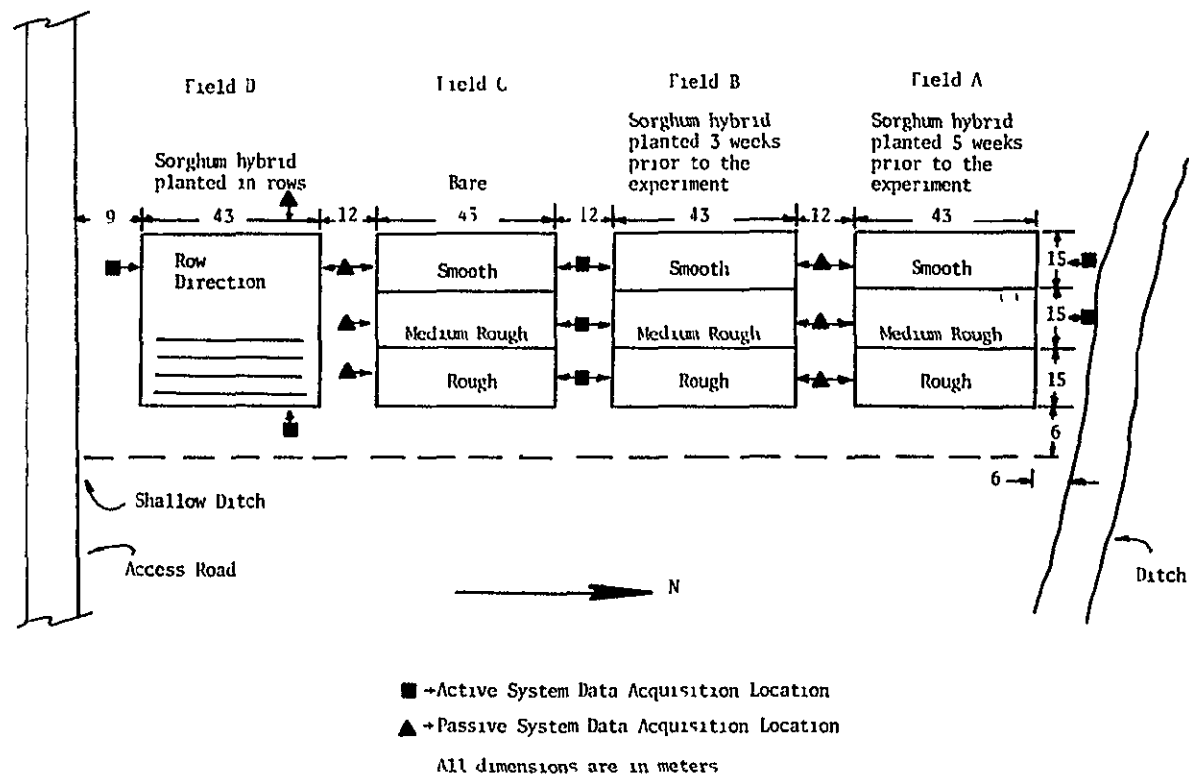


Figure V-5. Layout of the 1974 experimental plots.

Nine of the ten plots shown in Figure V-5 were 15 m by 46 m (sets A, B, C) and one was 46 m square (plot D). The nine smaller plots were in sets of three with each set having one plot prepared with a smooth surface, one with a medium rough surface, and one with a rough surface. Set C was bare while sets A and B were uniformly planted in a sorghum hybrid. Set A was planted approximately five weeks prior to the field measurements and set B was planted three weeks before. Two densities of vegetation were thereby available for the experiment. However, the vegetation did not grow well on the rough fields of sets A and B. Consequently, the vegetation densities on these fields were different from the density of vegetation on the corresponding smooth and medium rough fields. Plot D was also planted in sorghum hybrid approximately six weeks before the experiment, but in rows running north and south.

Figure V-6 through V-8 show the three magnitudes of surface roughness. The smooth had an rms surface height of 0.88 cm, the medium 2.6 cm, and the rough 4.3 cm. Figure V-9 shows an example of the uniform vegetation. The vegetation in set B was approximately 125 cm high, while in set A it was approximately 188 cm high. Figure V-10 shows the vegetation planted in rows. It averaged 252 cm in height.

Each of the field sets were consecutively sprinkle irrigated until they were saturated (12-14 hours). Active



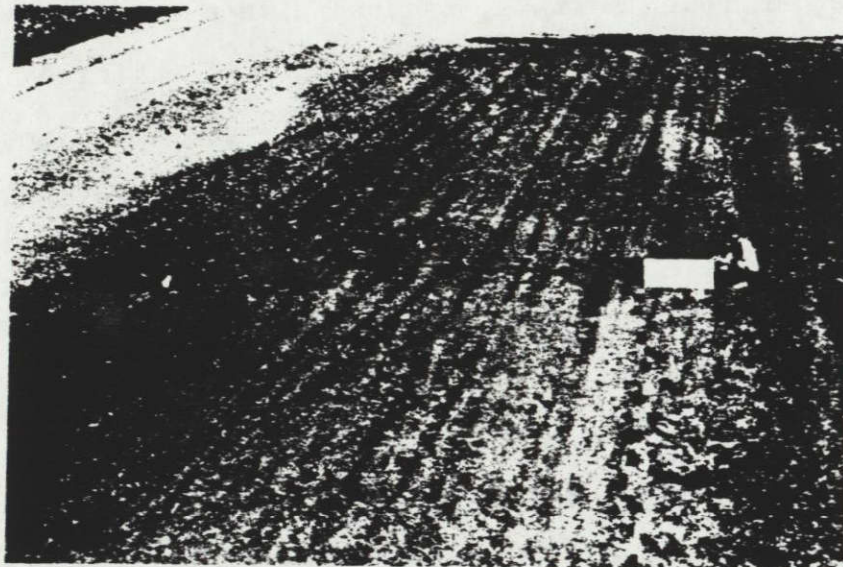


Figure V-6. Smooth field used in the 1974 measurements program.

ORIGINAL PAGE IS  
OF POOR QUALITY

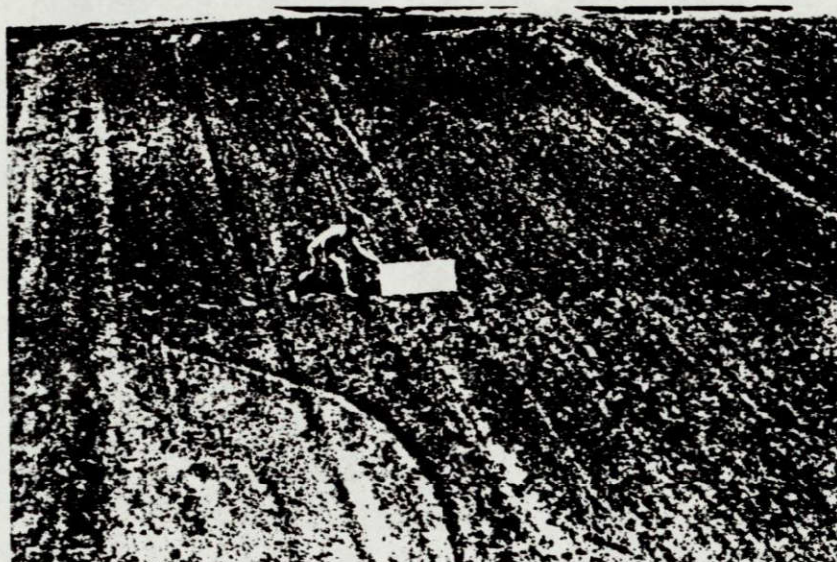


Figure V-7. Medium rough field used in  
the 1974 measurements program.





Figure V-8. Rough field used in the 1974 measurements program.



ORIGINAL PAGE IS  
OF POOR QUALITY

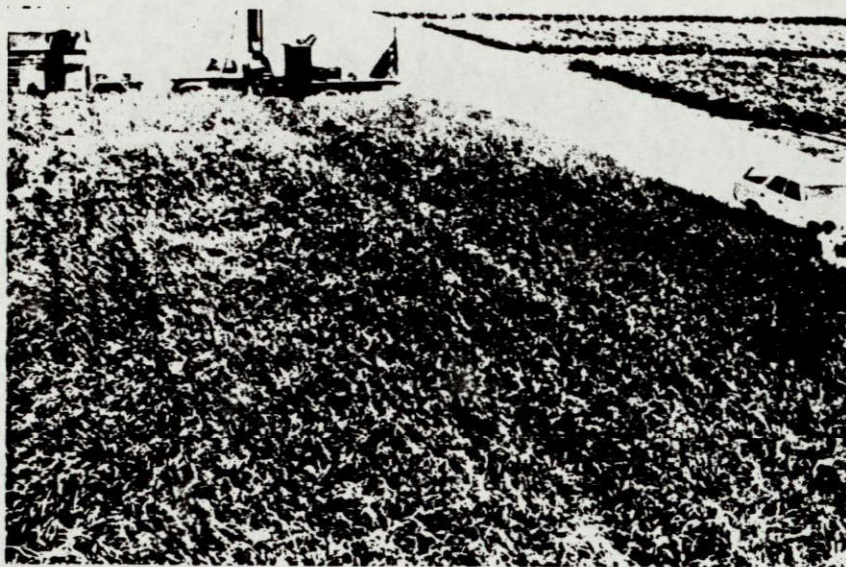


Figure V-9. Example of the uniform vegetation covers used in the 1974 measurements program.



Figure V-10. Row planted vegetation used in the 1974 measurements program.



and passive data were recorded simultaneously at each plot (except for plots A and B rough) as a function of soil moisture, transmission angle, polarization, and frequency. Measurements of plot D were made both parallel and perpendicular to the rows. Figure V-5 indicates the relative positions of the active and passive systems during data acquisition. Passive data were acquired at  $0^\circ$ ,  $20^\circ$ ,  $35^\circ$ , and  $50^\circ$  transmission (i.e. incident) angles for both horizontal and vertical polarizations at 1.4 GHz and 10.6 GHz. Sky temperature measurements were also made at zenith periodically during data acquisition. Data were taken on a twenty-four hour schedule, therefore, both day and night measurements were acquired.

Soil moisture and soil temperature profile measurements were made simultaneously with the microwave measurements. Soil moisture samples were obtained from 0-1 cm, 1-2 cm, 2-5 cm, 5-9 cm, and 9-15 cm layers. Soil temperature measurements were made with probes at the mid-point of each of these layers. These measurements were made at four locations equally spaced along both edges of each field, since the ground truth personnel had to remain out of the antenna field of view. Soil bulk density profiles, surface roughness, and vegetation height and density were obtained at numerous locations throughout the experiment.



### Measurement Program in 1975

The 1975 experiment was conducted at the TAMU Research Farm from July 13 through July 25, very near the site of the 1973 and 1974 experiments. The purpose of the experiment was to obtain passive microwave data of well-controlled row tilled bare and vegetated soil to demonstrate the effects of soil moisture and row direction. The NASA/JSC L-band and X-band MSAS was used to acquire the microwave data. Tabulations of the microwave data and corresponding ground truth data are reported by Newton and Tesch [104]. Newton and Tesch also provide detailed ground truth and experiment descriptions.

Two adjacent fields each approximately 45 m by 41 m were used as test fields. The soil within these fields was Miller clay. A drawing of the two field layouts and ground truth sampling sites is shown in Figure V-11. Field A was bare soil and field B was cotton that had an average height of 61 cm and an average width of 60 cm at the start of the measurements. Both fields were plowed with rows running east-west and separated with a zone of cotton approximately 3.05 meters in width. Average height and width for a row in field A was 20 cm and 95 cm, respectively. For a row in field B the typical height and width were 13 cm and 90 cm, respectively.

ORIGINAL PAGE IS  
OF POOR QUALITY

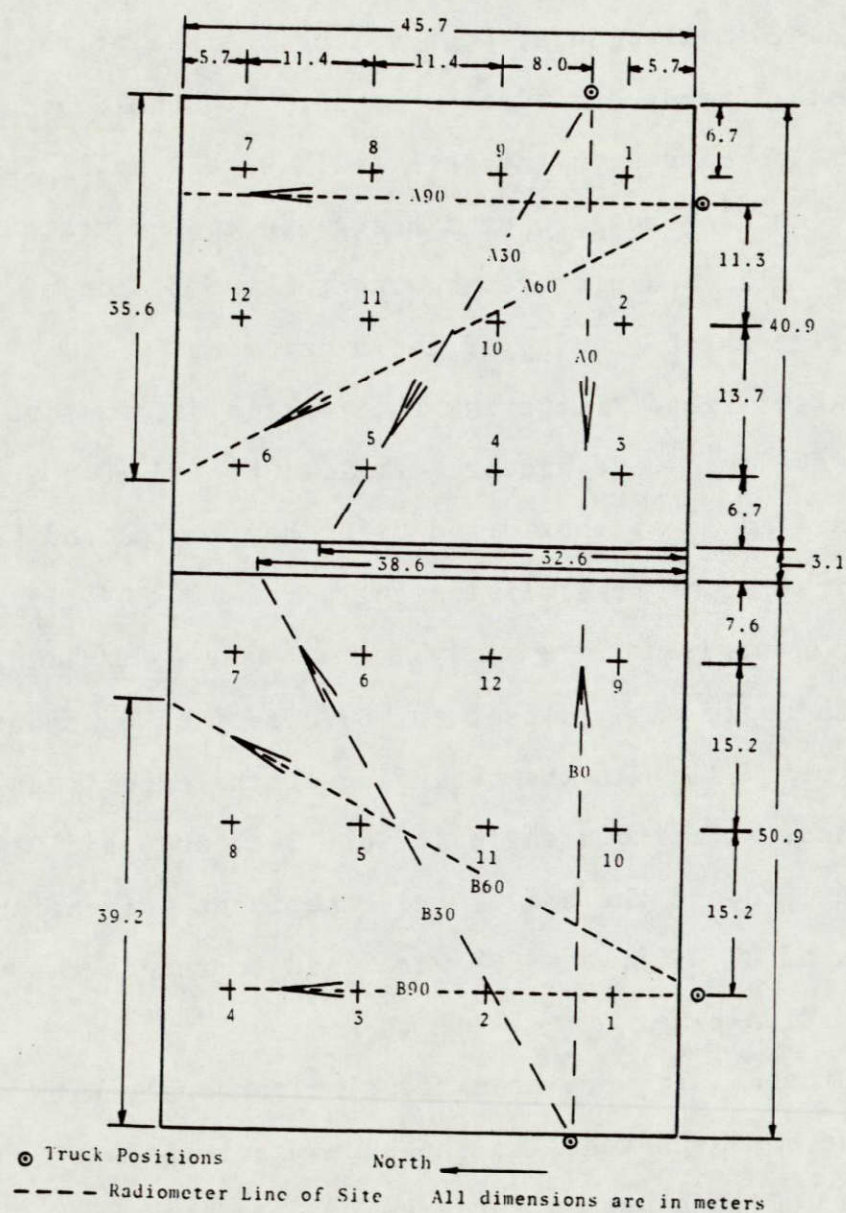


Figure V-11. Layout of the 1975 experimental plots.



The cotton in field B was planted approximately 7 1/2 weeks before the measurements were started. At the time of the measurements the cotton was in good health. Before the measurements were started, the bare field was weeded of small plants, however, by the end of the experiment small weeds had again emerged. It should be noted that measurements of the bare field were usually taken in the morning because of a heavy dew on the cotton plants. Figure V-12 is a picture showing the two fields as they looked at the beginning of the experiment.

After flood irrigating the two fields, passive microwave data were acquired at 1.4 GHz and 10.6 GHz for fields A and B as they dried using horizontal and vertical polarization at transmission angles of  $0^\circ$ ,  $20^\circ$ ,  $35^\circ$ , and  $50^\circ$ . Transmission angle scans were made as a function of azimuth angle with respect to row direction as denoted in Figure V-11. At the beginning of the experiment scans were made at azimuth angles of  $0^\circ$ ,  $30^\circ$ ,  $60^\circ$ , and  $90^\circ$ . However, toward the end of the experiment only azimuth angles of  $0^\circ$ ,  $45^\circ$ , and  $90^\circ$  were used to reduce the data acquisition time.

Ground data were acquired simultaneously with the microwave measurements in the same manner as was done in the 1974 measurement program.

ORIGINAL PAGE IS  
OF POOR QUALITY

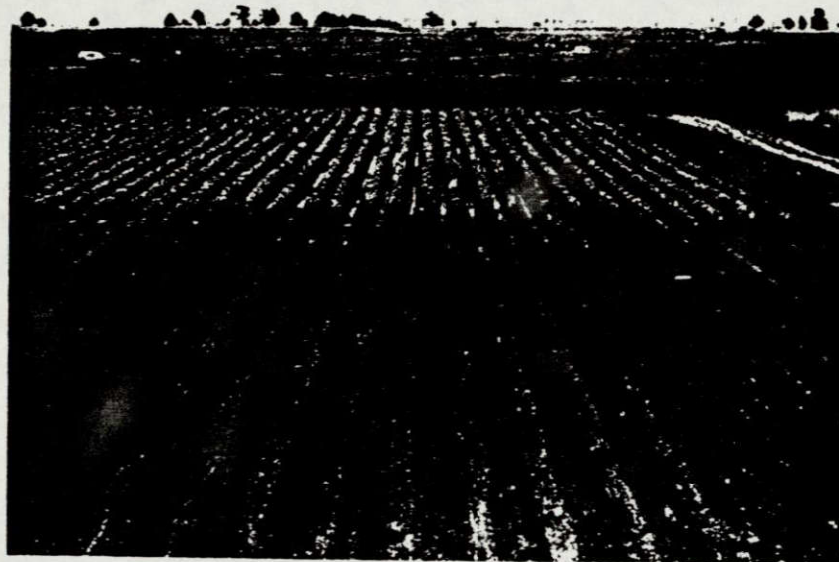


Figure V-12. Field layout used in the 1975 measurements program.



## Microwave Data Reduction

The techniques of reducing raw radiometer data to apparent antenna temperature in degrees Kelvin is fully explained by Newton [103]. The derivation of the equations used to reduce the raw data is provided by Paris [108]. Only a summary of data reduction equations and calibration constants will be given here. Figure V-13 is a functional block diagram of the MSAS. Figure V-13 is useful in understanding the data reduction equations that are given by Newton. A summary of these equations is provided below:

$$\overline{T}_m = \frac{T_{AA} - (1 - L_{AA}) t_{AA}}{L_{AA}} \quad (V-6)$$

$$T_{AA} = \frac{T_{SA} - r(t_d L_{CAA} + (1 - L_{CAA}) t_{CAA})}{1 - r} \quad (V-7)$$

$$T_{SA} = C_3 T_{SH} + (C_2 - C_3) t_d + (1 - C_2) t_{CAA} \\ - \frac{A_H - A_A}{A_H' - A_C'} \left[ C_3 T_{SH}' - C_1 T_{SC}' + (C_1 - C_3) t_d' \right] \quad (V-8)$$

$$r = \left[ \frac{R_A - 1}{R_A + 1} \right]^2$$

$$C_1 = \frac{L_{CC}}{L_{CAA} L_{CAB}}$$

where

$\bar{T}_m$  - mean weighted radiometric temperature of the scene (antenna temperature).

$T_{AA}$  - radiometric temperature at the output of the antenna.

$L_{AA}$  - transmittance of the antenna.

$t_{AA}$  - physical temperature of the antenna.

$T_{SA}$  - radiometric temperature on the receiver side of the impedance mismatch at the antenna input port.

$L_{CAA}$  - transmittance of the cable connecting the antenna to the receiver enclosure.

$t_{CAA}$  - physical temperature of the antenna-receiver cable.

$t_d$  - physical temperature of the receiver enclosure.

$r$  - power reflection coefficient of the antenna-cable mismatch.

- $R_A$  - voltage standing wave ratio of the antenna-cable mismatch.
- $L_{CH}$  - transmittance of the cable connecting the Dicke switch to the hot reference noise generator (RNG).
- $L_{CC}$  - transmittance of the cable connecting the Dicke switch to the cold reference noise generator (RNG).
- $L_{CAB}$  - transmittance of the cable inside the receiver enclosure connecting the Dicke switch to the external antenna cable.
- $T_{SH}$  - radiometric temperature of the hot RNG.
- $T_{SC}$  - radiometric temperature of the cold RNG.
- $A_H$  - attenuator setting in counts when the input to the receiver is the hot RNG.
- $A_C$  - attenuator setting in counts when the input to the receiver is the cold RNG.
- $A_A$  - attenuator setting in counts when the input to the receiver is from the antenna.

The quantities that are primed denote measurements that are made during the internal calibration sequence.

Equations(V-1)through(V-3)are used to reduce the MSAS attenuator setting,  $A_A$ , to the measured antenna temperature of the scene. The system constants that must be determined in order to use these equations



are  $L_{AA}$ ,  $r$ ,  $C_1$ ,  $C_2$ , and  $C_3$ . Values for constants  $L_{AA}$ ,  $r$ , and  $C_2$  (which are the antenna transmittance, the power reflection coefficient between the antenna and the cable connecting the antenna to the receiver or RF head enclosure, and the loss factor of that cable) as given by Newton [103] were used to reduce both the 1974 and 1975 data sets. Constants  $C_1$  and  $C_3$  were estimated individually for each data set.

The constants  $C_1$  and  $C_3$  were estimated by comparing MSAS measurements of uniform scenes to theoretical calculations of the brightness temperature of those scenes. As a result, the absolute calibration of the reduced measurements is only as good as the theoretical models used to estimate the emission of the scene. Measurements of the atmosphere at zenith, of smooth water, and smooth soil (for 1974 data) were used to calculate  $C_1$  and  $C_3$ . These targets were chosen since a very accurate model of atmosphere emission was available from Paris [108], and smooth surfaces can be accurately modeled using Fresnel equations. However, at the 10.6 GHz wavelength, the surfaces assumed to be smooth were not ideally smooth.

Although the absolute accuracy of the measurements may not be precise, the precision of the measurements is good. At 1.4 GHz the standard deviation of the measurements based on a one second integration time was typically  $0.6^\circ\text{K}$ ,

while at 10.6 GHz it was 1.7°K. Each data points used in the following chapters are averages of 60 to 90 one second measurements.

Other errors to be aware of arise from the pointing accuracy of the antennas. The antenna positioning mechanism was not optimum and pointing accuracies are estimated to be  $\pm 5^\circ$  in incident and polarization angle. Periodically higher inaccuracies occurred, but these measurements were generally deleted.

## CHAPTER VI

COMPARISON BETWEEN ANTENNA TEMPERATURE  
AND BRIGHTNESS TEMPERATURE

The models described in Chapter IV will be used to aid in the analysis of the antenna temperature measurements described in Chapter V. As a result, it will be necessary to compare radiometer antenna temperature measurements to theoretical calculations of the brightness temperature of the scene. The measured antenna temperature is not a pure measurement of the brightness temperature of a scene, but it is degraded by two phenomena. First, the apparent radiation impinging on the antenna does not only consist of the brightness radiation of the scene. It has components due to sources other than the scene of interest as described in the introductions to Chapter III and Chapter IV. Secondly, the antenna beamwidth further degrades the measurement.

Because of these non-ideal conditions, care must be exercised when comparing theoretical calculations to antenna measurements. Therefore, a discussion of the response of an antenna to the brightness temperature of a scene is provided before analyzing the antenna measurements that were described in Chapter V. In this discussion the relationships describing the measured antenna

temperature in terms of the apparent radiation incident on the antenna will be provided. Following that, the effects of the antenna beamwidth will be presented. Finally, the contribution of atmospheric radiation to the apparent temperature of a scene will be described.

### Measured Antenna Temperature

#### Power Output of An Antenna

The purpose of this section is to describe the relationships between the apparent intensity impinging on an antenna and the output power of the antenna. In doing this the relationship between the apparent intensity and the brightness temperature of the scene as calculated using the models of Chapter IV will also be pointed out.

The apparent radiation intensity leaving a scene is the sum of several components as described in Chapters III and IV. The apparent radiation intensity leaving a scene can be described in terms of these components in the following manner

$$I_A = I_B + I_{R_s} + I_{SE} + I_{TA} + I_P \quad (VI-1)$$

where

- $I_A$  - apparent radiation intensity
- $I_B$  - brightness intensity (described analytically by the models in Chapter IV)
- $I_{RS}$  - reflected sky radiation
- $I_{SE}$  - radiation emitted by the system and reflected from the surface back into the antenna aperture
- $I_{IA}$  - radiation emitted by the intervening atmosphere between the scene and the antenna
- $I_P$  - point source radiation directed toward the antenna aperture

Only the reflected sky radiation and the self emitted radiation need be seriously considered as degrading factors in measuring the brightness temperature using a ground-based system.

In the microwave region of the spectrum the emitted radiation intensity of a scene is proportional to the temperature of the scene. However, intensity is defined as electromagnetic energy leaving or approaching a differential element of area on an imaginary plane within the time interval  $t + dt$  and having a direction of propagation contained in a differential solid angle  $d\Omega$  whose central direction is normal to the imaginary plane [109].

Intensity has dimensions

$$\text{Intensity} \Rightarrow I \Rightarrow \frac{\text{energy}}{\text{area time steradian}} \Rightarrow \frac{\text{watts}}{\text{m}^2 \text{ Hz rad}^2 \text{ sec}^2}$$

It is extremely important to note that intensity is invariant along its propagation path. That is, the radiation leaving a surface will be characterized by the same value of intensity at any distance from its origin.

Flux is the radiant energy leaving or approaching an imaginary plane within a time interval  $t + dt$  in all directions in a hemispherical solid angle bounded by the imaginary plane [109]. Flux is the total rate of energy flow and has dimensions

$$\text{Flux} \Rightarrow q \Rightarrow \frac{\text{energy}}{\text{area time}} = \frac{\text{watts}}{\text{m}^2 \text{ Hz sec}}$$

The intensity vector describes the flux in any direction. The integration of intensity over the hemisphere will give flux, if a suitable correction is included to account for the projected area (Figure VI-1).

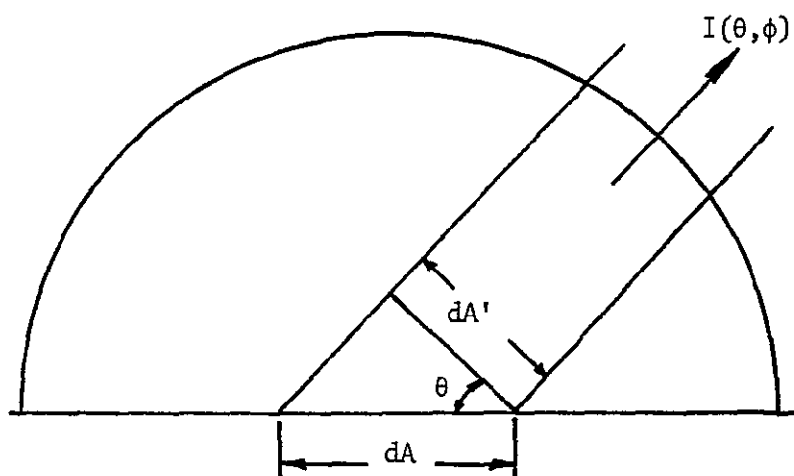
$$q = \int_0^{2\pi} \int_0^{\pi/2} I(\theta, \phi) \frac{dA'}{r^2} = \int_0^{2\pi} \int_0^{\pi/2} I(\theta, \phi) \cos \theta d\Omega \quad (\text{VI-2})$$

where

$q$  - flux

$I(\theta, \phi)$  - intensity

$dA' = \cos \theta dA$



$$d\Omega = r^2 dA = r^2 \sin \theta d\theta d\phi$$

$$dA' = \cos \theta dA$$

Figure VI-1. Geometry used to demonstrate the proper integration of intensity to obtain flux.

$dA'$  - element of area perpendicular to the direction  
of intensity (Figure VI-1)

$dA$  - element of area on the plane bounding the  
hemisphere through which the flux is passing

So, given the intensity of emission from a scene, the flux can be computed for a given direction. Knowing the area over which this flux crosses allows one to calculate the total power emitted from the area.

A review of the equations that define the power output of an antenna is required in order to relate intensity of emission to the measurements made by a radiometer. The apparent intensity impinging on the antenna is  $I_A$  (watts/m<sup>2</sup> steradian), assuming that the system is integrating over some finite time and bandwidth. This intensity is interpreted as watts per unit antenna aperture area per steradian. For an area extensive homogeneous scene within  $d\Omega$ ,  $I_A$  is that intensity passing through  $dA'$  which is associated with  $d\Omega$  (Figure VI-2). Since  $d\Omega$  is independent of distance, the same power density (i.e.,  $I_A d\Omega$  watts/Hz m<sup>2</sup>) is observed at the antenna aperture as is observed at  $dA'$ . The power received by an antenna is

$$W_k = \iint_{4\pi} \iint_{\substack{\text{Antenna} \\ \text{Aperture}}} (I_A(\theta, \phi))_k d\Omega dA_e \quad (\text{VI-3})$$



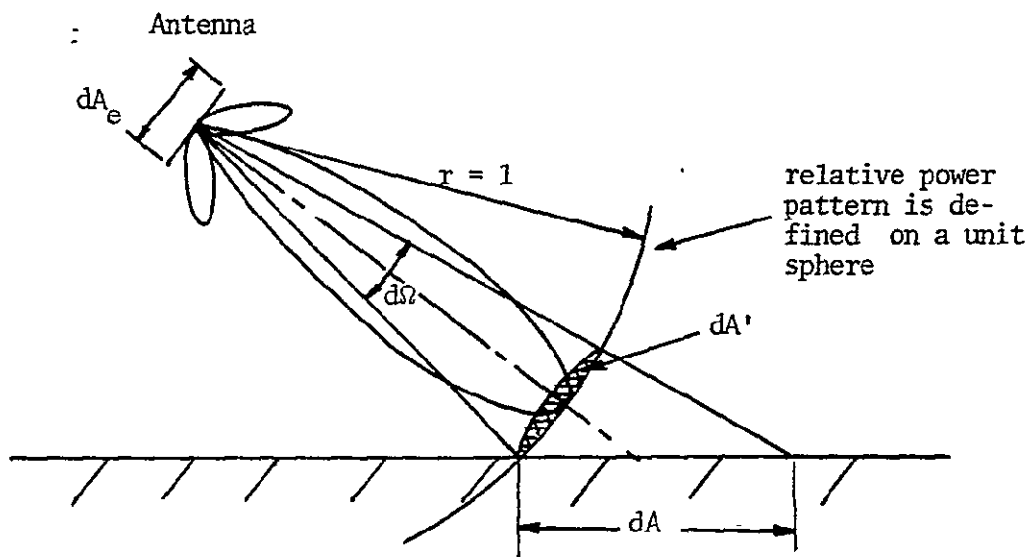


Figure VI-2. Representation of an antenna beamwidth.

where

$W_k$  - power output (watts), where subscript  $k$  denotes polarization relative to the antenna coordinate system

$(I_A(\theta, \phi))_k$  - apparent intensity of radiation (watts/m<sup>2</sup> ster Hz) in the direction  $(\theta, \phi)$  at the  $k^{\text{th}}$  polarization with respect to the antenna coordinate system

$$d\Omega = \sin\theta d\theta d\phi$$

$dA_e$  - effective antenna aperture in the direction  $(\theta, \phi)$  with respect to the antenna major axis

Assuming that the cross polarized antenna power pattern is negligible, then

$$dA_e = dA_{e_k}$$

Equation VI-2 can be integrated over the antenna aperture to yield

$$W_k = \iint_{4\pi} (I_A(\theta, \phi))_k A_{e_k}(\theta, \phi) d\Omega \quad (\text{VI-4})$$

The effective aperture of an antenna is given by

$$A_{e_k}(\theta, \phi) = \frac{\lambda^2}{4\pi} g_{d_k}(\theta, \phi) \quad (\text{VI-5})$$

where

$A_{e_k}$  - effective antenna aperture for the  $k^{\text{th}}$  polarization

$g_{d_k}$  - directive gain for the  $k^{\text{th}}$  polarization (for a lossless antenna directive gain is equal to power gain [110])

$\lambda$  - wavelength

and

$$g_{d_k}(\theta, \phi) = \frac{4\pi P_k(\theta, \phi)}{\iint_{4\pi} P_k(\theta, \phi) d\Omega} \quad (\text{VI-6})$$

where

$$\frac{P_k(\theta, \phi)}{\iint_{4\pi} P_k(\theta, \phi) d\Omega}$$

is the one way relative power pattern of the antenna. So

$$A_{e_k}(\theta, \phi) = \frac{\lambda^2 P_k(\theta, \phi)}{\iint_{4\pi} P_k(\theta, \phi) d\Omega} \quad (\text{VI-7})$$

Substituting (VI-7) into (VI-4) yields:

$$W_k = \iint_{4\pi} (I_A(\theta, \phi))_k \left[ \frac{\lambda^2 P_k(\theta, \phi)}{\iint_{4\pi} P_k(\theta, \phi) d\Omega} \right] d\Omega \quad (\text{VI-8})$$

Since one is generally only interested (or only able to compute) energy impinging on the antenna through its main lobe, (VI-8) can be written

$$W_k = \frac{\lambda^2}{\iint_{4\pi} P_k(\theta, \phi) d\Omega} \left[ \iint_{\substack{\text{main} \\ \text{lobe}}} (I_A(\theta, \phi))_k P_k(\theta, \phi) d\Omega \right. \\ \left. + \iint_{\substack{\text{remaining} \\ \Omega}} (I_A(\theta, \phi))_k P_k(\theta, \phi) d\Omega \right] \quad (\text{VI-9})$$

Assuming that the side lobes and back lobes are negligible, (VI-9) reduces to

$$W_k = \frac{\lambda^2}{\iint_{4\pi} P_k(\theta, \phi) d\Omega} \iint_{\substack{\text{main} \\ \text{lobe}}} (\bar{I}_A(\theta, \phi))_k P_k(\theta, \phi) d\Omega \quad (\text{VI-10})$$

The assumptions involved in deriving (VI-10) were that the cross polarized antenna power pattern is negligible and that the side lobes and back lobes of the like polarized power pattern are also negligible. Under these assumptions, (VI-10) describes the power output of an antenna at the  $k^{\text{th}}$  polarization with respect to the antenna coordinate system due to a polarized intensity  $I_A$  incident on its aperture. However, the models in Chapter IV describe the polarization of emission from the scene with respect to the plane of transmission rather than the antenna coordinate system. This problem of inconsistency in polarization definition is discussed later in the chapter.

#### Apparent Antenna Temperature

It is now of interest to convert the power measured by the antenna to antenna temperature. By doing this the relationship between measured antenna temperature and scene brightness temperature can be illustrated.

The power measured by a radiometer is related to temperature based on the equation describing the thermal noise power in a resistive element.

$$W = kTB \quad (VI-11)$$

where

k - Boltzman's constant

B - Bandwidth

T - Temperature of the resistive element in degrees Kelvin

If W represents the power output of a radiometer antenna, T will be termed the measured antenna temperature and will be denoted  $T_m$ .

In the microwave region the Rayleigh Jean's approximation to Planck's emission law [95] can be used to relate the apparent intensity of emission from a scene to the apparent temperature of the scene. In this case the apparent temperature contains the polarization dependence. Note that this polarization dependence is with respect to the plane of incidence and is denoted by i. The apparent temperature is defined as the temperature a blackbody would have to be in order to emit radiation equal to the polarized apparent radiation of the scene.

$$I_{A_i} = \frac{kT_{A_i}}{\lambda^2} \quad (VI-12)$$

where

$T_{A_i}$  - apparent temperature of the scene at the  $i^{\text{th}}$  polarization

$\lambda$  - wavelength

Letting  $k$  denote a polarization state with respect to the antenna coordinate system (IV-10) becomes

$$W_k = k T_{m_k} B$$

$$= \frac{\lambda^2}{\iint_{4\pi} P_k(\theta, \phi) d\Omega} \iint_{\substack{\text{main} \\ \text{lobe}}} \left[ \int_{\nu_1}^{\nu_2} \frac{k T_A}{\lambda^2} d\nu \right] P_k(\theta, \phi) d\Omega \quad (\text{VI-13})$$

where

$\nu$  - frequency ( $\nu_2 - \nu_1$  defines the bandwidth of interest)

Assuming that the radiation intensity is constant over the bandwidth

$$T_{m_k} = \frac{1}{\iint_{4\pi} P_k(\theta, \phi) d\Omega} \iint_{\substack{\text{main} \\ \text{lobe}}} (T_A(\theta, \phi))_k P_k(\theta, \phi) d\Omega \quad (\text{VI-14})$$

Equation IV-14 describes the relationship between the measured antenna temperature and the apparent temperature of the scene. Utilizing (VI-1), the apparent scene temperature in (VI-14) can be broken down into its respective components to demonstrate the effect of its various components on the measured antenna temperature. Equation VI-14 expands to

$$T_{mk} = \frac{1}{\iint_{4\pi} P_k(\theta, \phi) d\Omega} \left[ \iint_{\substack{\text{main} \\ \text{lobe}}} (T_B + T_{RS} + T_{SE} + T_{IA} + T_P) P_k(\theta, \phi) d\Omega \right] \quad (\text{VI-15})$$

where

- $T_B$  - brightness temperature of the scene
- $T_{RS}$  - reflected sky temperature
- $T_{SE}$  - self emitted temperature reflected from the surface back into the antenna aperture
- $T_{IA}$  - temperature of the intervening atmosphere
- $T_P$  - point source radiation incident on the antenna aperture

Note that since each of the components are additive, their contributions can be calculated independently. Only the contributions due to the reflected sky temperature and the



self emission will be discussed further in this report. The reflected sky radiation is discussed later in this chapter and the self emission is discussed in Appendix D. The other contributions are insignificant as far as this work is concerned.

#### Effects of Beamwidth

Theoretical models like those described in Chapter IV provide estimates of emitted radiation in terms of power density per unit angle. However, antenna temperature measurements are actually averages over some finite range of angles due to the antenna beamwidth. An idealized antenna with an infinitely narrow beamwidth would be required to measure an apparent scene temperature without averaging over a range of transmission angles.

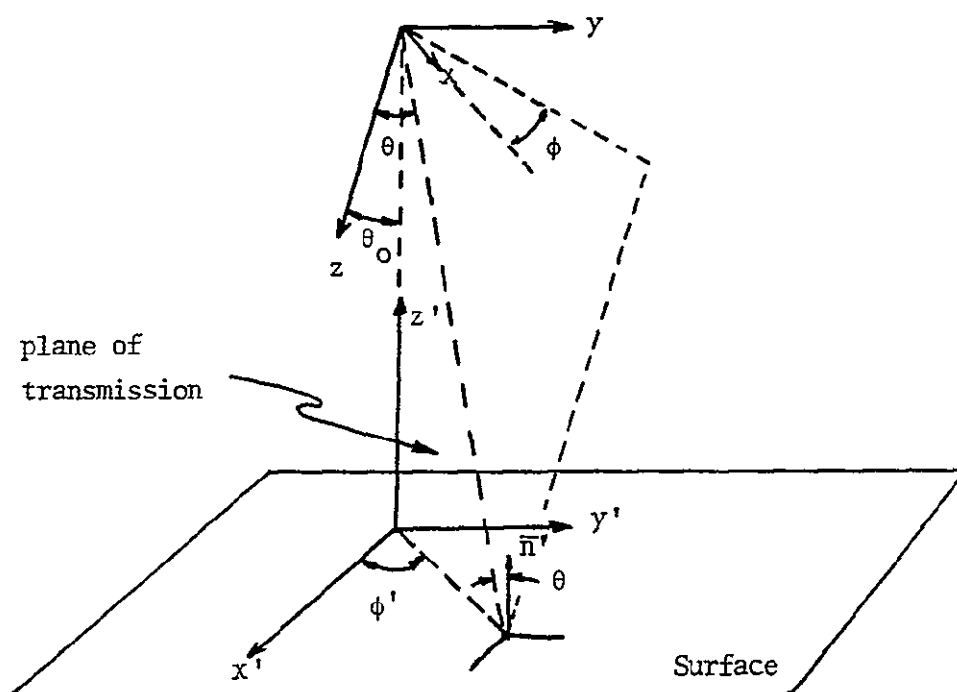
In addition to this averaging effect, the polarization of calculated brightness temperatures is defined with respect to the plane of transmission while the antenna power pattern is defined for each of two orthogonal polarization states with respect to the antenna reference frame. Since the antenna receives energy from a finite beamwidth, an antenna temperature measured at one of the antenna polarizations actually consists of components of both of the surface polarizations.

Peake [111], Claassen and Fung [112], and Grody [113] discuss in detail the problem associated with inverting a measured antenna temperature to the apparent temperature of a scene. Such a detailed discussion will not be provided here, but examples of the amount of degradation that can be expected due to the averaging effects and the polarization mixing effect will be presented.

#### Polarization Mixing

Equation (VI-14) describes the measured antenna temperature in terms of the apparent temperature of the scene. In this equation, the subscript  $k$  denotes that polarization is defined with respect to the antenna coordinate system. However, the models developed in Chapter IV were developed such that polarization was defined with respect to the plane of transmission of radiation from the surface toward the antenna. This polarization state was denoted by  $i$ . Figure VI-3 denotes the antenna and ground coordinate systems.

As a result of the inconsistency in defining polarization, the measured antenna temperature at polarization  $k$  is actually a mixture of the two surface polarization states defined with respect to the plane of transmission. Dropping the assumptions made in deriving (VI-14), a general expression describing this polarization mixing



$\theta_0$  - transmission angle at which the major axis of the antenna is viewing the surface

Figure VI-3. Relationship between the antenna and surface coordinate systems.

can be obtained by expanding (VI-14). In expanding (VI-14), a linearly polarized antenna is assumed. The two polarization states will be denoted by "v" for vertical and "h" for horizontal (Figure VI-4). With the aid of the geometry shown in Figure VI-4 the antenna temperature can be written in terms of the two surface polarizations.

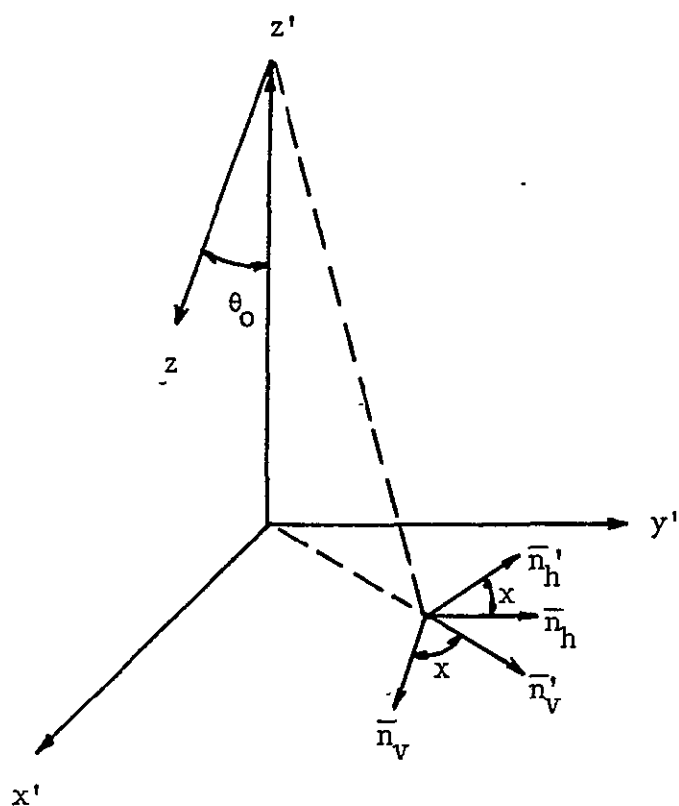
$$T_{A_v} = \sin^2 \psi T_{A_h}' + \cos^2 \psi T_{A_v}'$$

(VI-16)

$$T_{A_h} = \cos^2 \psi T_{A_h}' + \sin^2 \psi T_{A_v}'$$

The prime denotes polarization defined with respect to the plane of transmission. The general form of (VI-14) for a horizontally polarized antenna is [112]:

$$\begin{aligned} T_{m_h}(\theta_o) = \frac{1}{D} \iint_{4\pi} & \left[ P_v(\theta, \phi) (\sin^2 \psi T_{A_h}' + \cos^2 \psi T_{A_v}') \right. \\ & + P_h(\theta, \phi) (\cos^2 \psi T_{A_h}' + \sin^2 \psi T_{A_v}') \\ & \left. + (T_{A_v}' - T_{A_h}') P_v(\theta, \phi) P_h(\theta, \phi) \sin 2\psi \cos \beta \right] d\Omega \end{aligned} \quad \text{(VI-17)}$$



$\bar{n}'_h$  and  $\bar{n}'_v$  - projections of the unit vectors defining the surface polarization onto the surface plane

$\bar{n}_h$  and  $\bar{n}_v$  - projections of the unit vectors defining the antenna polarizations onto the surface plane

Figure VI-4. Relationship between the surface and antenna polarization vectors.

where

$$D = \iint_{4\pi} (P_v(\theta, \phi) + P_h(\theta, \phi)) d\Omega$$

$P_v(\theta, \phi)$  - cross polarized antenna power pattern  
 $P_h(\theta, \phi)$  - like polarized antenna power pattern  
 $\beta$  - relative phase between the antenna polarization components [112]

The angle  $\psi$  is denoted in Figure VI-4 and is defined in the surface coordinate system. Its dependence on  $\theta$  and  $\phi$  in the antenna coordinate system must be taken into account when (VI-17) is integrated.

Equation (VI-17) can be used to demonstrate the effect of polarization mixing of the like polarized components and the cross polarized components.

Like polarization - To demonstrate the degradation due to only the like polarized antenna pattern, the cross polarized pattern will be neglected. It will also be assumed that the apparent temperature impinging on the antenna is constant over the beamwidth of the antenna. With the above assumptions and neglecting side and back lobes, (VI-17) reduces to

$$T_{m_h}(\theta_0) = \frac{1}{D} \left[ T'_{A_h} \iint_{\text{main lobe}} P_h(\theta, \phi) \cos^2 \psi d\Omega + T'_{A_v} \iint_{\text{main lobe}} P_h(\theta, \phi) \sin^2 \psi d\Omega \right] \quad (\text{VI-18})$$

The terms  $H$  and  $V$  defined by

$$H = \frac{1}{D} \iint_{\substack{\text{main} \\ \text{lobe}}} P_h(\theta, \phi) \cos^2 \psi d\Omega$$

\*

(VI-19)

$$V = \frac{1}{D} \iint_{\substack{\text{main} \\ \text{lobe}}} P_h(\theta, \phi) \sin^2 \psi d\Omega$$

are measures of the relative amount of energy received by the antenna from the surface horizontal and vertical polarizations, respectively.

$$T_{m_h} = H T_{A_h}' + V T_{A_v}'$$

(VI-20)

The terms  $H$  and  $V$  describe the polarization mixing due to the antenna beamwidth. Note that the sum of  $H$  and  $V$  must always equal unity.

For a linear vertically polarized antenna,  $H$  describes that fraction of the horizontally polarized (surface coordinate system) energy that is being measured by the antenna. The worst case condition within the framework of the above assumptions can be illustrated by assuming that the antenna has a uniform unity power pattern over the main

lobe. With this assumption, the terms H and V can be calculated for different antenna beamwidths and the transmission angle at which the antenna is viewing the surface. Figure VI-5 are the results of these computations [113]. Note that the degradation is most severe at nadir, and it gets worse as the beamwidth gets larger.

The beamwidth between half-power points for the 1.4 GHz antenna is approximately  $20^\circ$  while for the 10.6 GHz antenna it is approximately  $6^\circ$ . Figure VI-5 and calculations of the brightness temperature of a smooth surface (Figures IV-19 and IV-20) were used to calculate the degradation that can be expected in the 1.4 GHz radiometer measurements (Figure VI-6). Since the 1.4 GHz system has the largest beamwidth, Figure VI-6 is the worst case condition that should be observed with the MSAS. Although the beamwidth of the antenna is large, the degradation in the measurement is small since the vertical and horizontal brightness temperatures approach each other as the transmission angle gets near zero.

Cross polarization - Following Grody [113], the effects due to cross polarization can be demonstrated by assuming that the cross polarized power pattern of the antenna is related to the like polarized power pattern by a constant factor.



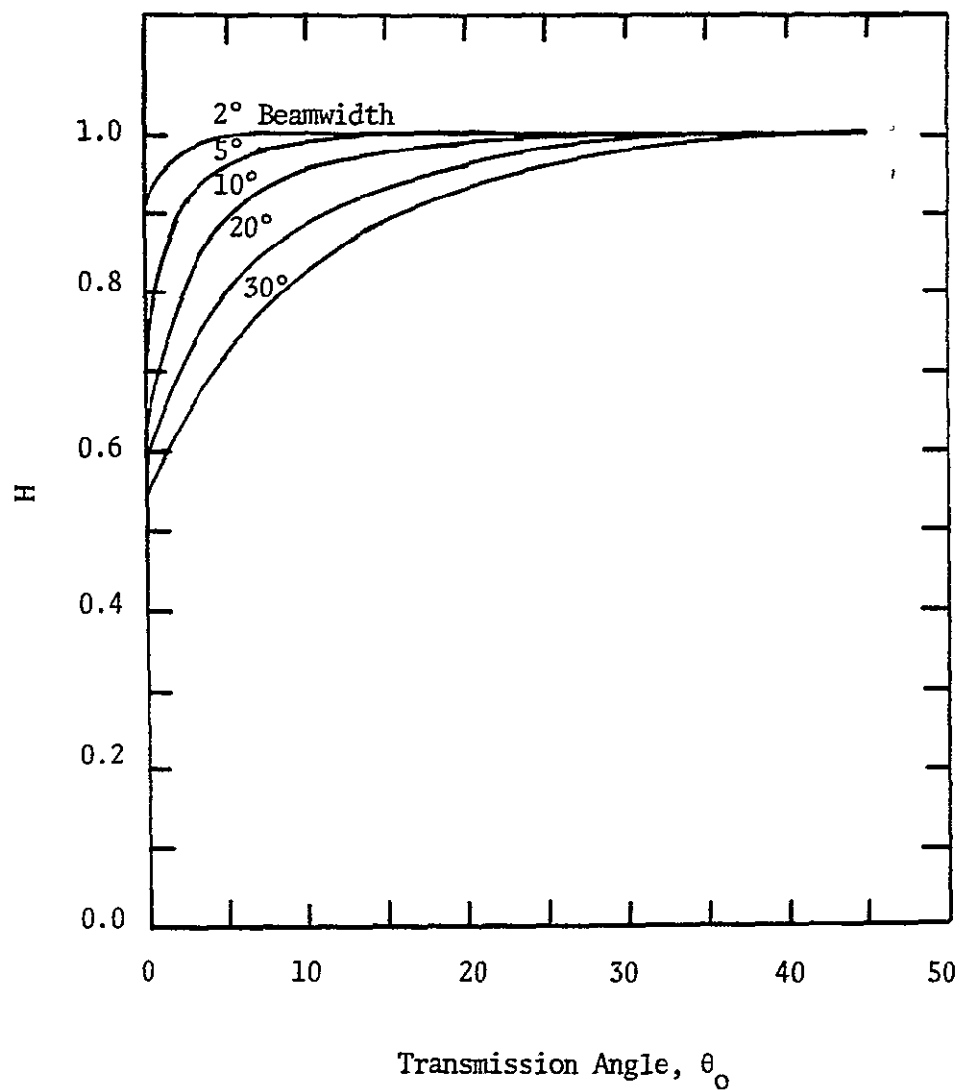


Figure VI-5. Normalized power received in horizontal polarization as a function of transmission angle,  $\theta_0$ , for different beamwidths (after Grody [113]).

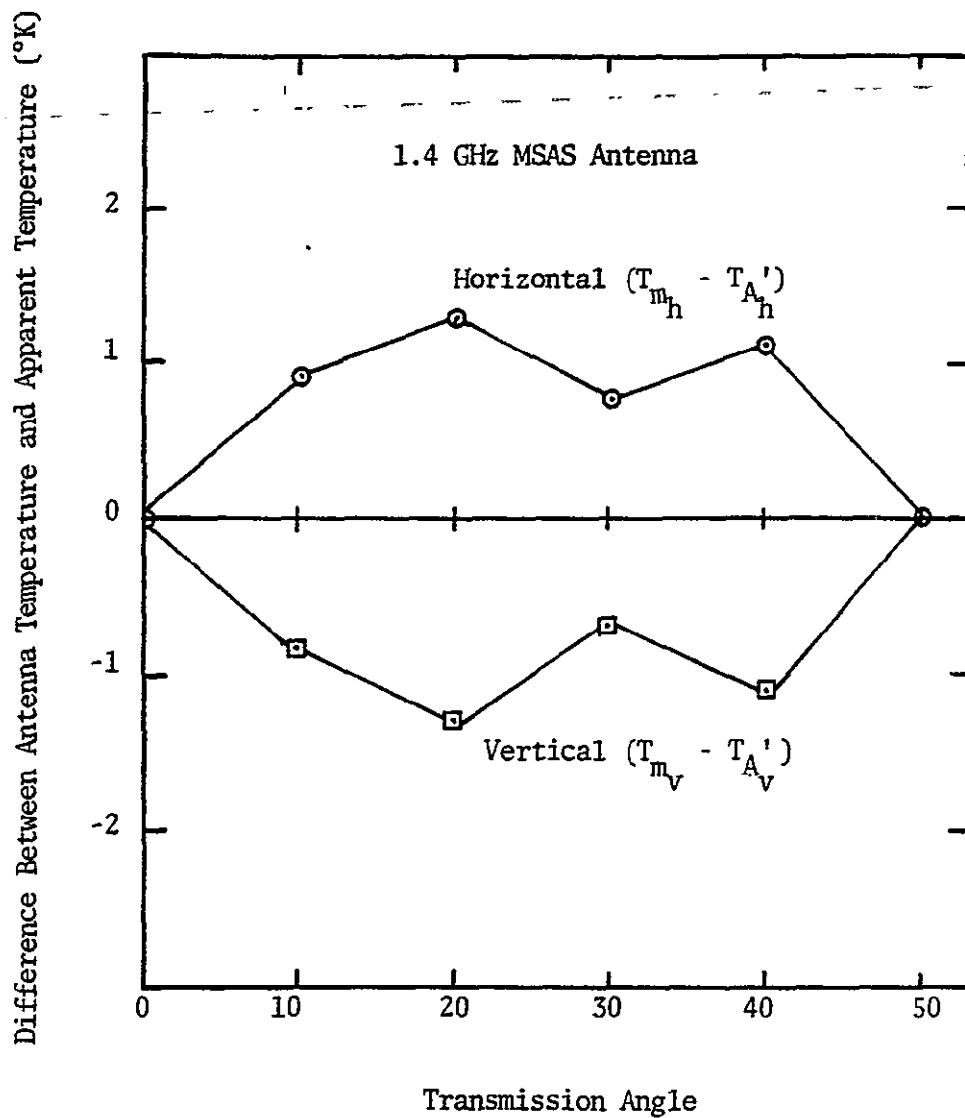


Figure VI-6. Comparison of measured antenna temperature to the corresponding apparent temperature.

$$P_v(\theta, \phi) = \frac{P}{1-p} P_h(\theta, \phi) \quad (\text{VI-21})$$

As before a linear horizontally polarized antenna has been assumed. Substituting (VI-21) into (VI-17) and neglecting the third term in the integral of (VI-17)

$$H_{\text{cross}} = p + (1-2p) H \quad (\text{VI-22})$$

Assuming a uniform unity like and cross polarized antenna power pattern across the main lobe only,  $H$  is given by (VI-19).

For angles larger than the beamwidth, it is observed from Figure VI-5 that  $H$  is approximately unity. For this condition

$$H_{\text{cross}} \approx 1-p \quad (\text{VI-23})$$

$$V_{\text{cross}} \approx p$$

For this case  $H_{\text{cross}}$  and  $V_{\text{cross}}$  replace  $H$  and  $V$  in (VI-20).

However, both of the MSAS antennas have cross polarized power patterns greater than 25 dB down from the like polarized pattern. This corresponds to a  $p$  of less than 0.01. As a result, the cross polarized degradation is negligible even at scan angles less than the antenna beamwidth.

#### Transmission Angle Averaging

In the above discussion on polarization mixing the apparent temperature of the scene was assumed to be constant over the beamwidth of the antenna. This was assumed so that the effects polarization mixing could be discussed independently of the antenna averaging effect. Averaging occurs over a finite range of transmission angles defined by the antenna beamwidth and look direction of the antenna.

The effects of transmission angle averaging will now be discussed independently of polarization mixing. To do this the beamwidth of the antenna will have to be assumed very narrow in the dimension perpendicular to the plane of transmission. This assumption, although unrealistic in terms of the real antenna beamwidths of the MSAS, will provide estimates of the worst case condition.

Again neglecting side and back lobes, the cross polarized antenna power pattern, and assuming a linear

horizontally polarized antenna with the like polarized antenna power pattern described above, (VI-18) becomes

$$T_{m_h} = \frac{1}{D} \int_{\theta_1}^{\theta_2} T_{A_h}' P_h(\theta, \phi) \sin \theta d\theta \quad (\text{VI-24})$$

where  $\theta_1$  and  $\theta_2$  define the beamwidth in the plane of transmission. The apparent scene temperature is no longer assumed constant over transmission angle. Equation (VI-24) is used to demonstrate the degradation of the brightness temperature resulting from antenna averaging. All components to the apparent temperature except the brightness temperature are neglected, and the antenna power pattern is assumed to be unity and uniform over the main lobe. Figure VI-7 is the resulting calculations of the measured antenna temperature as a function of beamwidth and the corresponding brightness temperature. The degradation increases as the beamwidth gets larger. The half-power beamwidth of the 1.4 GHz antenna MSAS is approximately  $30^\circ$ , while the half-power beamwidth of the 10.6 GHz antenna is approximately  $12^\circ$ .

#### Atmospheric Radiation

It was stated earlier that, for a ground-based radiometer system viewing the earth, the sky radiation and the

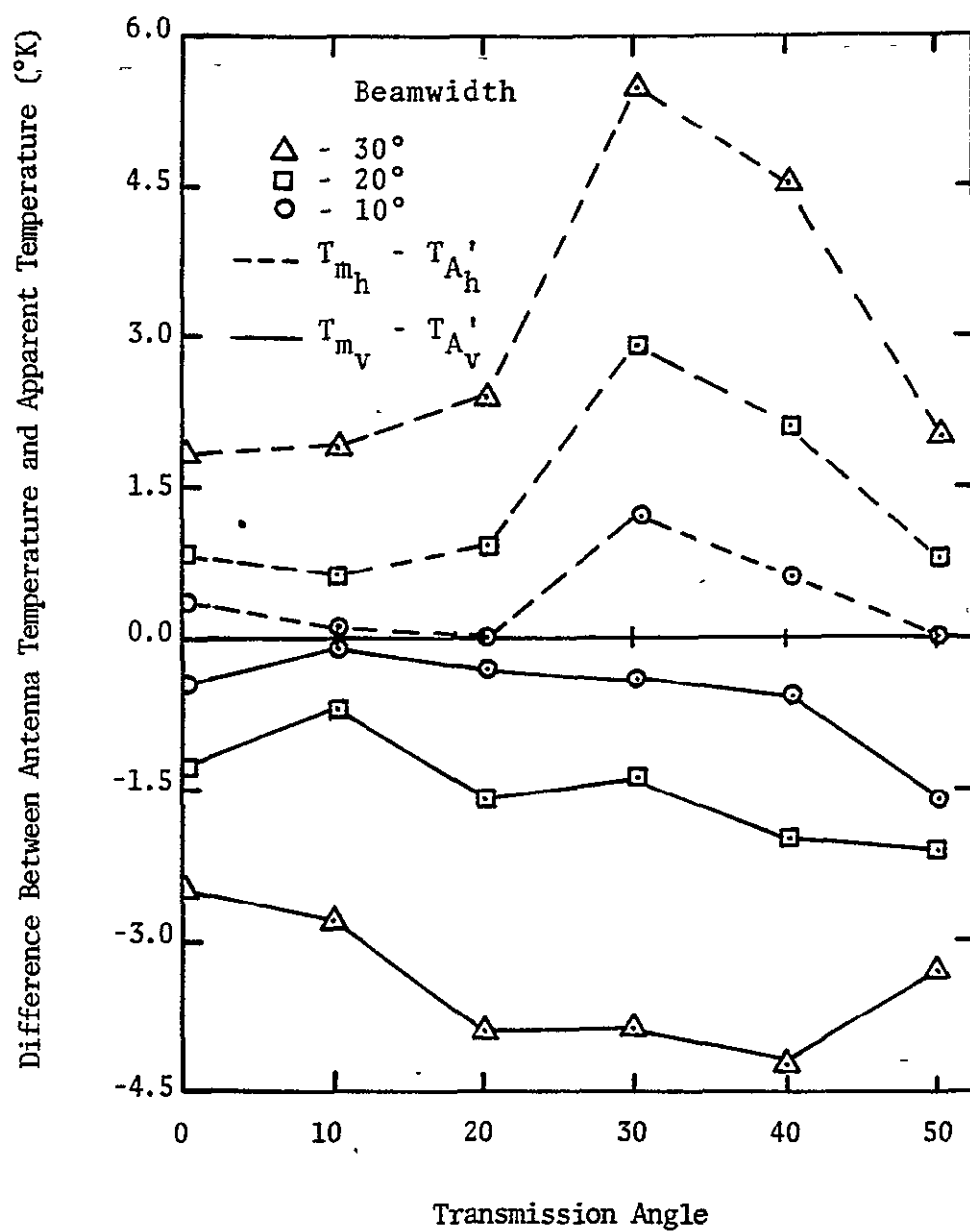


Figure VI-7. Degradation of measured antenna temperature due to transmission angle averaging.

self emitted radiation reflected from the surface were the only potential contributions of any consequence to the apparent temperature of the scene. A scheme for correcting near-nadir antenna measurements for self emission is described in Appendix B. The potential effects of reflected sky radiation is discussed below.

Paris [40] provides a good discussion on the origin and transfer of thermal microwave energy in the atmosphere. Figure VI-8 is a plot of sky brightness temperature as a function of zenith angle for both of the MSAS frequencies assuming a standard atmosphere. These sky brightness temperatures were calculated by Paris [114]. They are used below to demonstrate the contribution of the atmosphere to the apparent temperature of a scene.

Paris [40] also provides calculations to demonstrate the extremes of the sky brightness temperature under various conditions. The results of these calculations are provided in Table VI-1 and Table VI-2. It is seen that the sky brightness temperature at 1.4 GHz is affected little by adverse conditions, however, at 10.6 GHz the sky brightness temperature can change dramatically.

The bistatic scattering coefficients developed by Leader [61] and presented in Chapter IV can be used to calculate the sky radiation that is reflected into the antenna aperture. The radiation from the atmosphere is

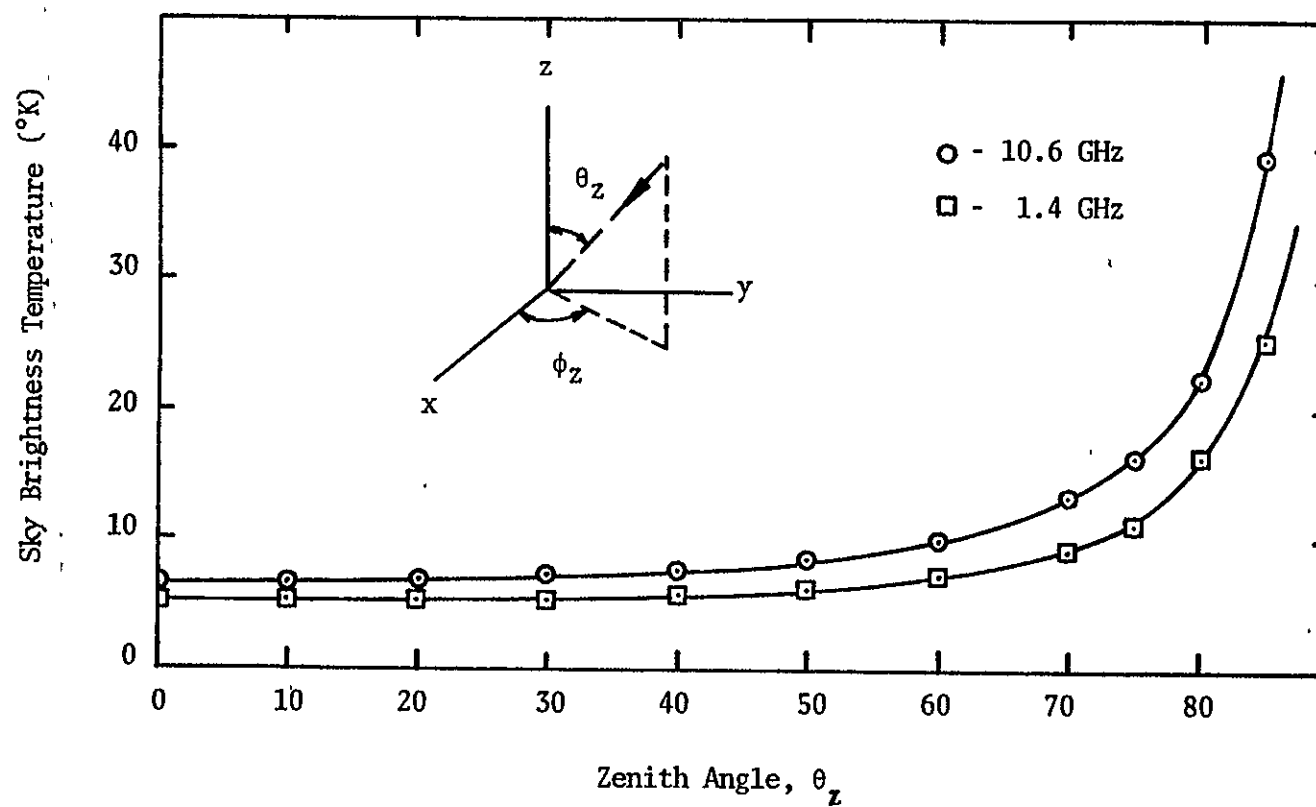


Figure VI-8. Sky brightness temperature for a standard atmosphere as computed by Paris [114].



TABLE VI-1

Ranges of Sky Brightness Temperature of the Atmosphere:  $\theta_z = 0$  deg. (after Paris [40])

Frequency (GHz)	Sky Brightness-temperature ( $^{\circ}\text{K}$ )					
	Clear Sky		Clouds (No Rain)		Clouds and Rain	
1.42	2.1	( 2.1)	2.2*	2.1 ( 2.2)	3.7	2.1 ( 2.3) 5.5
2.695	2.3	( 2.3)	2.4	2.3 ( 2.7)	8.0	2.3 ( 3.1) 17.6
4.805	2.5	( 2.6)	3.1	2.5 ( 3.7)	20.2	2.5 ( 5.4) 84.9
5.81	2.6	( 2.8)	3.4	2.6 ( 4.4)	28.1	2.6 ( 7.1) 151.6
8.0	2.8	( 3.2)	4.6	2.8 ( 6.3)	49.3	2.8 ( 13.4) 263.3
10.69	3.1	( 4.1)	6.8	3.1 ( 9.7)	80.8	3.1 ( 26.3) 293.7
15.375	4.4	( 7.6)	15.4	4.4 ( 19.5)	142.4	4.4 ( 57.9) 299.6
19.35	8.8	( 20.7)	48.5	8.8 ( 43.2)	202.2	8.8 ( 88.5) 300.6
31.4	10.7	( 20.9)	44.8	10.7 ( 62.0)	267.3	10.7 (164.0) 301.5
33.2	11.4	( 21.6)	45.4	11.4 ( 66.0)	272.2	11.4 (173.0) 301.6
37.0	14.3	( 25.0)	50.2	14.3 ( 76.7)	279.8	14.3 (191.3) 301.7
53.8	233.3	(252.0)	267.2	233.3 (264.0)	295.7	233.3 (282.6) 302.2

\*The data are presented in the following format: Minimum Value (Value for Average Atmosphere, Cloud Condition, or Rain Condition) Maximum Value.

TABLE VI-2

Ranges of Sky Brightness Temperature of the Atmosphere:  $\theta_z = 55$  deg. (after Paris [40])

Frequency (GHz)	Sky Brightness-temperature ( $^{\circ}\text{K}$ )							
	Clear Sky		Clouds (No Rain)			Clouds and Rain		
1.42	3.7	( 3.7)	3.8*	3.7	( 3.9)	6.4	3.7	( 4.1) 9.5
2.695	4.0	( 4.0)	4.2	4.0	( 4.7)	13.7	4.0	( 5.4) 30.0
4.805	4.4	( 4.5)	5.2	4.4	( 6.5)	34.3	4.4	( 9.3) 130.9
5.81	4.5	( 4.8)	5.9	4.5	( 7.6)	47.2	4.5	( 12.3) 210.7
8.0	4.8	( 5.6)	7.9	4.8	( 11.0)	80.3	4.8	( 23.0) 290.6
10.69	5.4	( 7.1)	11.7	5.4	( 16.7)	125.6	5.4	( 44.3) 299.6
15.375	7.6	( 13.0)	26.4	7.6	( 33.1)	200.0	7.6	( 93.3) 301.3
19.35	15.2	( 35.1)	79.3	15.2	( 71.1)	252.1	15.2	(148.5) 301.7
31.4	18.3	( 35.5)	73.7	18.3	( 99.2)	286.6	18.3	(221.8) 302.1
33.2	19.6	( 36.6)	74.6	19.6	(104.9)	222.9	19.6	(230.0) 302.2
37.0	24.4	( 42.2)	82.0	24.4	(120.0)	290.2	24.4	(245.3) 302.2
53.8	261.8	(280.5)	292.3	261.8	(284.8)	298.5	261.8	(290.2) 302.2

\*The data are presented in the following format: Minimum Value (Value for Average Atmosphere, Cloud Condition, or Rain Condition) Maximum Value.

incident on the surface from all zenith angle pairs  $(\theta_z, \phi_z)$ . The radiation reflected from the surface into a particular direction is given by

$$T_{Rs}(\theta_t) = \int_0^{2\pi} \int_0^{\pi/2} \gamma_i(\theta_z, \phi_z; \theta_t, \phi_t) BT_{sky} d\Omega \quad (VI-25)$$

where

$\gamma_i$  - bistatic scattering coefficient of the surface at the  $i^{th}$  polarization

$BT_{sky}$  - sky brightness temperature

The bistatic scattering coefficients developed by Leader are only defined for the plane of transmission. In addition, the sky brightness temperature is assumed to be independent of the azimuth angle,  $\phi_z$ .

Figures VI-9 through VI-12 are results of calculations using (VI-25) and the 1.4 GHz brightness temperature in Figure VI-8. It can be seen that the soil moisture has a considerable effect on the reflected sky radiation. The wetter the soil the higher the reflection. It can also be seen that the surface roughness affects the amount of radiation that is reflected. As the surface gets wetter the effects of surface roughness is exaggerated. Another observation that can be made is that as expected, more energy is reflected in horizontal polarization.

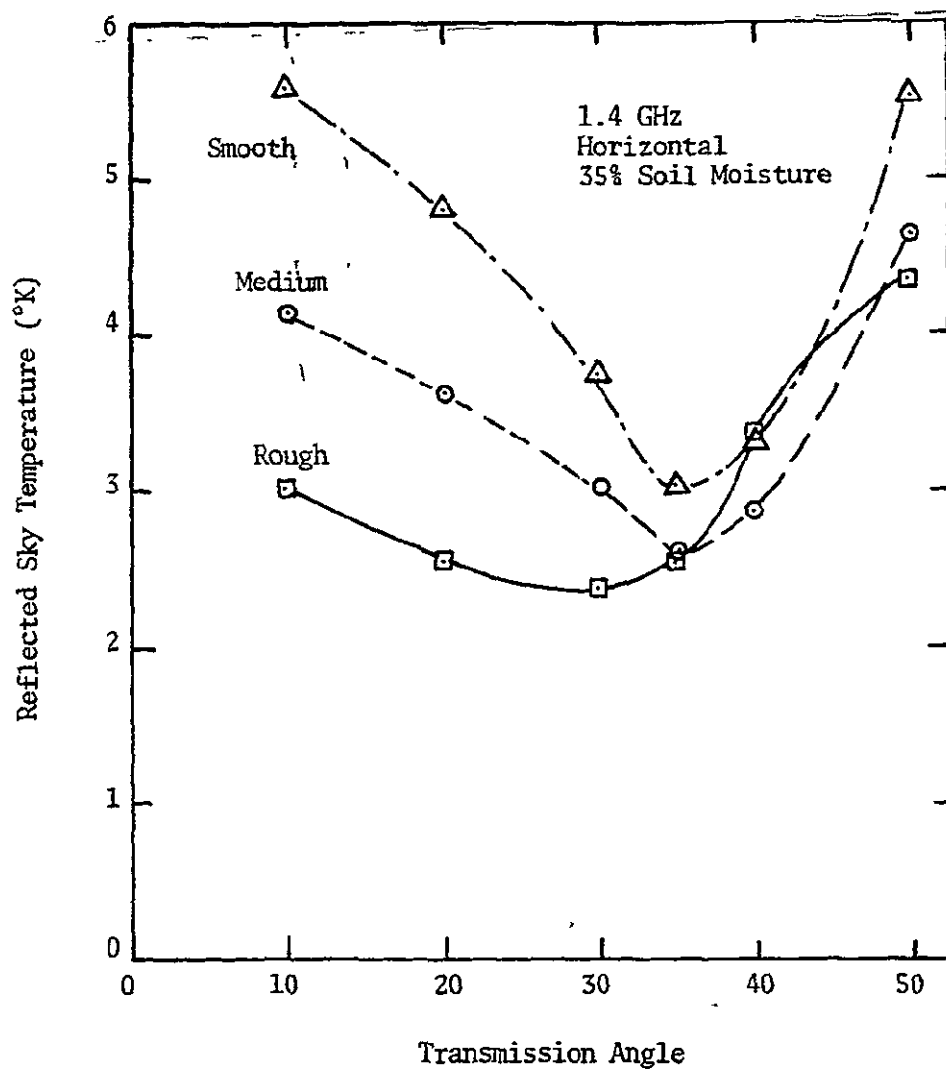


Figure VI-9. Reflected horizontally polarized sky brightness temperature for 35% soil moisture.

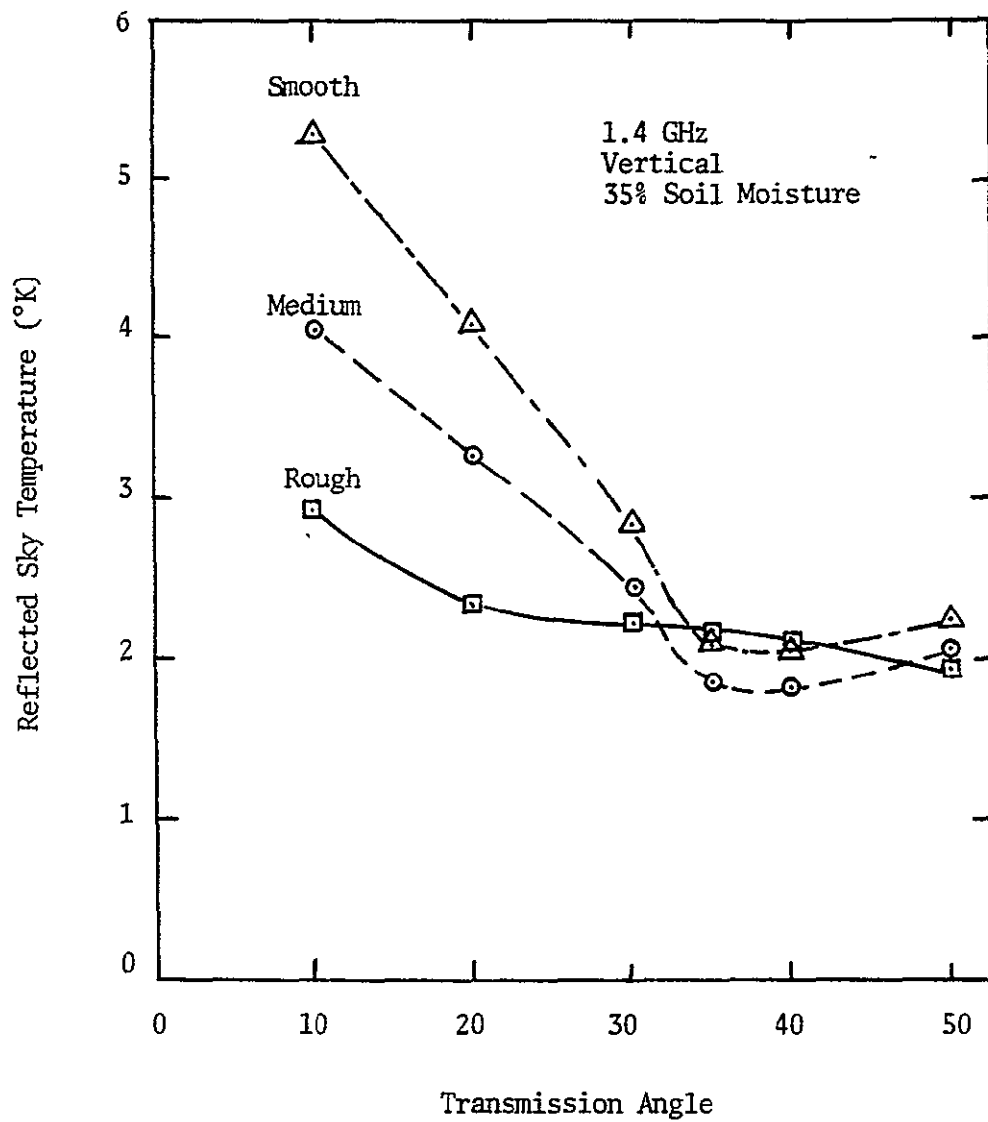


Figure VI-10. Reflected vertically polarized sky brightness temperature for 35% soil moisture.

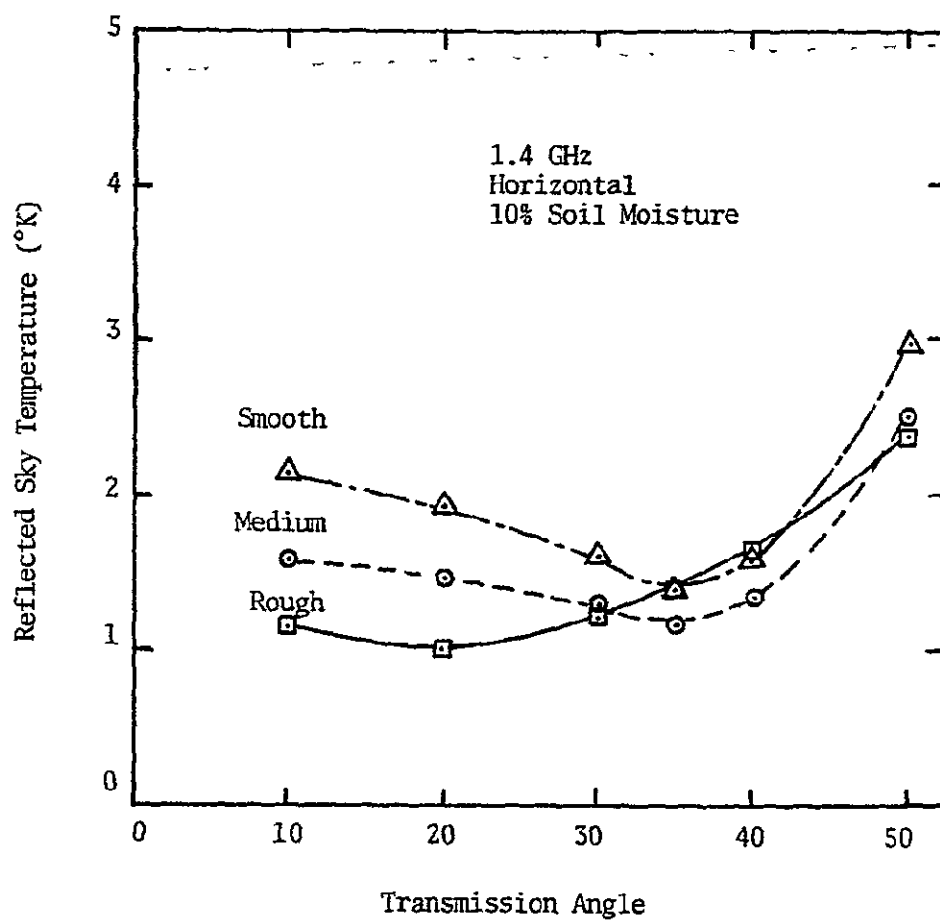


Figure VI-11. Reflected horizontally polarized sky brightness temperature for 10% soil moisture.

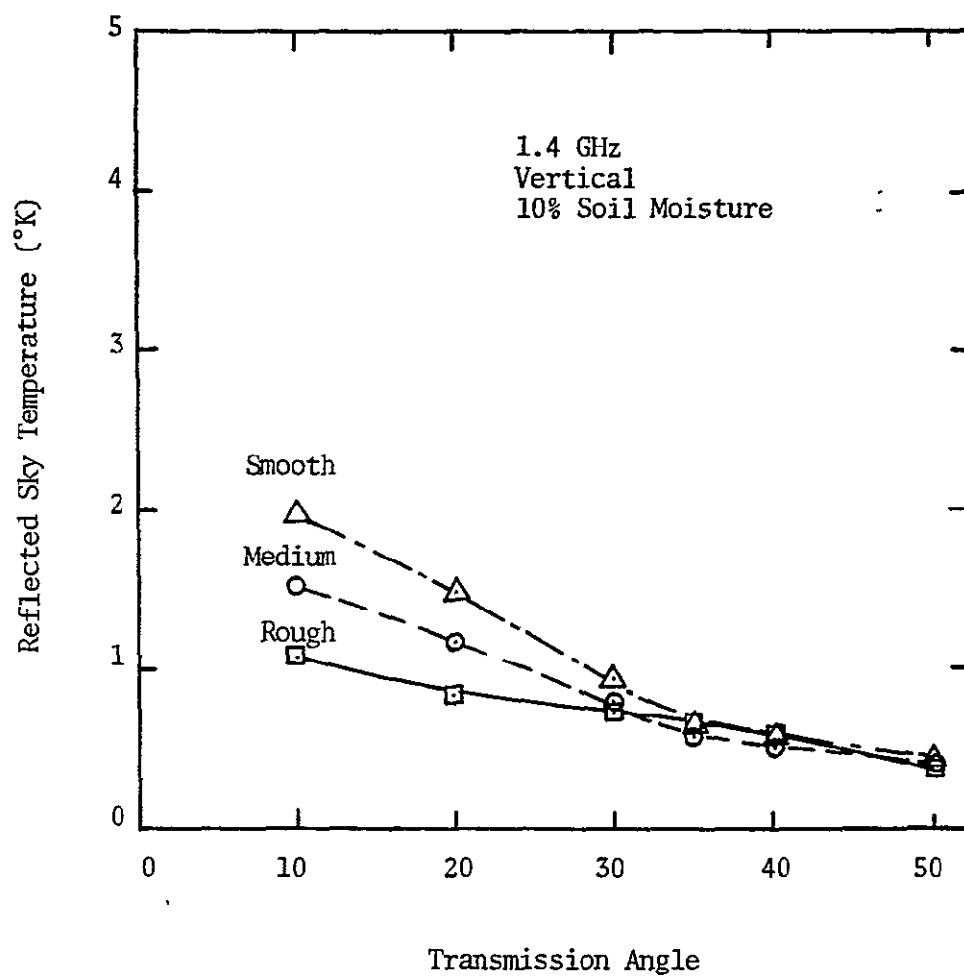


Figure VI-12. Reflected vertically polarized sky brightness temperature for 10% soil moisture.

## CHAPTER VII

### ANALYSIS OF MEASUREMENTS

#### Introduction

The ground based measurements of soil emission described in Chapter V will be analyzed in this chapter to determine the effects of soil moisture, surface roughness and vegetative cover. The theme of this analysis will be to determine the soil moisture information that can be obtained from microwave radiometer measurements. The analysis will involve comparisons between model predictions and measured results. In addition, the models will be used as tools in explaining the dependence of the measurements on scene parameters.

All of the measurements that are analyzed in this chapter were obtained at the Texas A&M Research Farms. The experimental plots within this research farm area consist of the same soil type (Miller clay). It was pointed out in Chapter II that the permittivity of soil was a function of soil matric potential, independent of soil texture. However, since all of the measurements analyzed in this chapter correspond to the same soil texture, the conclusions that pertain to soil moisture will apply equally to soil matric potential. As a result,



on a matric potential basis, the conclusions of this chapter will apply to all soil textures.

The chapter is organized so that each scene parameter can be addressed separately. First, the effects of soil moisture and soil temperature profiles are discussed. Following that, the effects of surface roughness are addressed for both flat tilled and row tilled bare soil surfaces. The effects of a vegetation cover over the soil surfaces are then investigated. In the final section of the chapter a procedure for estimating soil moisture information using radiometer measurements is presented, and the potential accuracy of this technique is discussed.

#### Quantification of Moisture and Temperature Profiles

It is clear that the microwave emission of a soil is governed by the temperature of the soil and by the permittivity of the soil, which is in turn governed by the soil moisture, (or, more correctly, matric potential). However, since the soil moisture and soil temperature are not uniform with depth, the problem of estimating soil moisture information from microwave data is greatly complicated. Even after roughness effects are eliminated there is a problem of interpreting the moisture information that is obtained from the microwave data. Microwave energy

is emitted from some soil volume, not just a single layer. As a result, the sensor is responding to a range of soil moistures depending on the soil moisture profile and the maximum depth from which radiation is emitted. In addition, the temperature of the soil also affects the magnitude of the radiation emitted from the soil. In order to interpret microwave emission for soil moisture information, it is necessary to; 1) determine a technique of compensating the antenna temperature measurements for the effects of soil temperature variations, 2) determine the effect of the shape of the soil moisture profile on the sensor response, 3) determine a single parameter that will describe this effect, and 4) determine the soil depth over which the parameter describes the soil moisture. The microwave data can then be interpreted in terms of this descriptive parameter. Such a parameter will be developed and interpreted below. A technique of normalizing antenna measurements to soil temperature will also be presented.

#### Soil Moisture Profile

Description of soil moisture parameters - There are many techniques of defining a parameter that describes the soil moisture distribution with depth. However, it is difficult to develop a parameter that uniquely describes the effect of each profile individually since the same

emission may be produced by more than one profile shape. One of the earliest attempts at obtaining a single parameter to describe a soil moisture profile was by Lee [91]. Lee's technique was to calculate the electromagnetic attenuation profile of the soil based on the permittivity profile, integrate the profile to determine the skindepth and determine the equivalent uniform soil moisture profile that would produce the same skindepth. This parameter is termed the equivalent skindepth moisture content and is denoted by  $m_s$ . It was subsequently compared by Batlivala and Ulaby [115] along with two other parameters termed the equivalent incoherent reflection coefficient moisture content and the equivalent coherent reflection coefficient moisture content, to the moisture at fixed depth increments.

The equivalent coherent reflection coefficient moisture content was defined by Batlivala and Ulaby [115] as the moisture content of a uniform soil medium whose power reflection coefficient at the surface is equal to the power reflection coefficient of a soil medium with the nonuniform soil moisture profile. They defined the equivalent incoherent reflection coefficient moisture content as the moisture content of a uniform soil medium whose power reflection coefficient is equal to

$$R = 1 - E \quad (VII-1)$$

where  $R$  is the power reflection coefficient of the non-uniform soil. The term denoted by  $E$  is an effective emissivity at nadir based on the relationship:

$$E = (1 - R_0) \left[ \Gamma_1 P_1 + \sum_{i=2}^{m-1} (\Gamma_i P_i \prod_{j=1}^{i-1} Q_j) + \prod_{j=1}^{m-1} Q_j \right] \quad (VII-2)$$

where

$R_0$  - power reflection coefficient at the air soil interface

$i$  - layer index ( $i = 1$  is the surface layer and  $i = n$  is a semi-infinite homogeneous layer)

$$\Gamma_i = 1 - 1/L_i$$

$$P_i = 1 + R_i/L_i$$

$$Q_i = (1 - R_i)L_i$$

$$L_i = \exp(\alpha_i d_i)$$

$R_i$  = power reflection coefficient at the interface between the  $i$  and  $i + 1$  layers

$\alpha_i$  - attenuation coefficient of layer  $i$  (nepers/cm)

$d_i$  - width of  $i^{\text{th}}$  layer (cm)

Based on a comparison of the linear correlation coefficients calculated for  $\sigma^\circ$  and each of these equivalent moisture definitions, Batlivala and Ulaby [115] concluded that the equivalent incoherent reflection coefficient moisture content was the most appropriate in terms of the radar response to soil moisture. However, Batlivala and Ulaby grouped all the measurements of  $\sigma^\circ$  from the 1974 smooth, medium rough and rough fields (see Chapter V) together when calculating the correlation coefficients. The data should have been grouped by surface preparation. As a result, their correlation coefficient calculations are questionable.

For the passive case, the idea of equivalent moisture contents based on reflection coefficients is not advantageous since these do not generally conform to the physical phenomenon of the emission process. Such definitions of equivalent moisture content rely on the Peake [29] development of emissivity which is ambiguous for nonuniform temperature profiles. Even the equivalent incoherent reflection coefficient model described above is independent of the soil temperature profile, although the formulation of the effective emissivity, (VII-2), was adopted from the Burke and Paris [32] radiative transfer model.

A technique that is more soundly based on physical phenomenon is to calculate an equivalent incoherent soil moisture based on the percentage energy contribution of arbitrarily defined soil layers to the total emitted energy at the surface. In this case the percentage contribution of each layer is based on the emitted energy of each layer referenced to the soil surface. The equivalent incoherent soil moisture is then determined by summing the soil moisture of each layer, weighted by the percentage energy contribution of that layer at the soil surface. This summation is shown in (VII-3).

$$m_I = \sum_{l=1}^N \frac{SM(l) \cdot \Delta BT_{\text{volume}}(l)}{BT_{\text{volume}}} \quad (\text{VII-3})$$

where

$m_I$  - equivalent incoherent soil moisture content  
(either volumetric or gravimetric)

$SM(i)$  - soil moisture in each layer

$\Delta BT_{\text{volume}}(i)$  - brightness temperature contribution of each  
layer referenced to the soil surface

$BT_{\text{volume}}$  - total brightness temperature of the soil  
volume

$N$  - number of layers

It should be noted that  $m_I$  will be affected to a certain extent by the soil temperature profile since  $BT(i)$  depends on the respective temperature of the  $i^{th}$  layer.

Another parameter that has been used to describe an equivalent soil moisture is the attenuated soil moisture in a skindepth. This parameter is calculated by performing a weighted average of soil moisture down to a skindepth. In this case the weighting function is the attenuation constant of the soil from the  $i^{th}$  layer to the surface. This summation is shown in (VII-4).

$$m_A = \sum_{i=1}^N \frac{SM(i) \cdot \exp(-\sum_{j=1}^i \alpha(j))}{\text{Skindepth}} \quad (\text{VII-4})$$

where

$m_A$  - attenuated soil moisture in a skindepth

$\alpha(j)$  - attenuation constant at each layer

$SM(i)$  - soil moisture in each layer

For off-nadir angles,  $m_A$  is calculated by assuming that the energy travels along a ray path determined by Snell's law of refraction. As in the case of the equivalent skindepth moisture content, the temperature profile has no effect on this parameter.

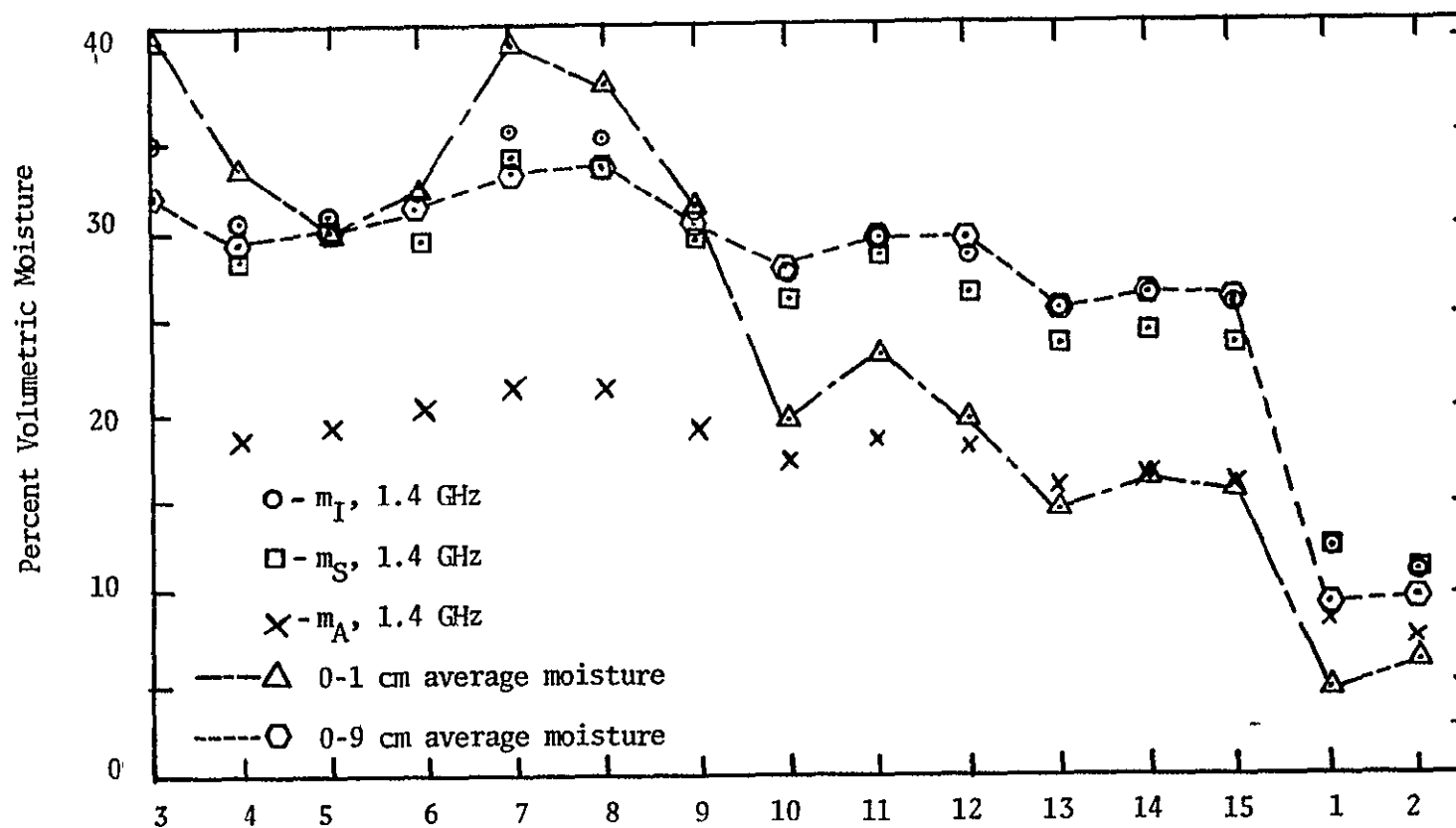
Optimization of the soil moisture description -

Several parameters have been set forth as descriptions of the moisture in a soil volume. It is necessary to choose only one of these parameters for the remaining analysis. The chosen parameter should be the one that best meets the needs of the applications of concern and that is soundly based on physical reasoning. Physical reasoning tends to direct the choice toward the equivalent incoherent soil moisture,  $m_I$ . This statement is made because  $m_I$  is based on the radiative transfer model which is the best description to date of the actual emission process from a soil volume.

Simple statistical methods and direct comparisons between all of the parameters and the actual measured soil moisture profiles will provide clues as to the best choice for application purposes. Figure VII-1 is a plot comparing the soil moisture profiles averaged over specific depth increments for all of the profiles measured in field CS (the 1974 smooth bare field, Figure V-5) to each of the previously described parameters calculated for 1.4 GHz. Only 1.4 GHz results are shown in Figure VII-1 since at 10.6 GHz the emission originates from very shallow skin-depths and is of little utility in providing moisture at depths below 2 cm. This will be demonstrated later.

It is obvious from Figure VII-1 that the attenuated water content in a skindepth,  $m_A$ , is not directly related





Ground Data Measurement Set - 1974 Smooth Bare Field (CS)

Figure VII-1. Comparison of calculated soil moisture parameters to the measured soil moisture averaged over depth.

to the measured soil moisture in any depth increment. As a result, this parameter appears to be of little utility at the present time. However, the equivalent incoherent soil moisture and the equivalent skindepth soil moisture does correspond to the measured moisture averaged over some finite depth increment. As a result these parameters contain information concerning the soil moisture profile and will be of utility for certain applications.

More quantitative facts that are useful in determining the optimum parameter to use in the subsequent analysis of the microwave data are the correlation coefficient and the covariance between the normalized antenna temperature and each of the parameters.  $T_N$  is the normalized antenna temperature. It is calculated by dividing the measured antenna temperature in degrees Kelvin by the surface soil temperature in degrees Kelvin. Table VII-1 contains a tabulation of the normalized antenna temperature and the three parameters of concern for field CS. The correlation coefficient is defined in the standard manner [116]:

$$r = \frac{S_{xy}}{S_x S_y} \quad (\text{VII-5})$$

TABLE VII-1

Data Used to Calculate Correlation Coefficients (Field CS)

Profile	Normalized Antenna Temperature (1.4 GHz, 20°, vertical) $T_{N_v}$	Equivalent Incoherent Soil Moisture; $m_I$ (percent <u>grams</u> ) $\text{cm}^3$	Equivalent Skindepth Soil Moisture; $m_S$ (percent <u>grams</u> ) $\text{cm}^3$	Attenuated Soil Moisture in a Skindepth, $m_A$ (percent <u>grams</u> ) $\text{cm}^3$
CS 1	0.90	12.9	12.8	8.6
CS 2	0.92	11.3	11.7	7.4
CS 3	0.60	34.7	34.9	24.0
CS 4	0.72	30.4	28.5	18.9
CS 5	0.63	31.0	30.0	19.5
CS 6	0.62	32.2	29.6	20.2
CS 7	0.56	35.4	34.1	21.4
CS 8	0.60	35.2	33.8	21.6
CS 9	0.61	31.2	29.7	19.6
CS 10	0.69	27.3	26.1	17.4
CS 11	0.68	29.2	28.6	18.6
CS 12	0.78	28.6	26.4	18.1

TABLE VII-1 (Continued)

Profile	Normalized Antenna Temperature (1.4 GHz, 20°, vertical) $T_{N_v}$	Equivalent Incoherent Soil Moisture; $m_I$ (percent $\frac{\text{grams}}{\text{cm}^3}$ )	Equivalent Skindepth Soil Moisture; $m_S$ (percent $\frac{\text{grams}}{\text{cm}^3}$ )	Attenuated Soil Moisture in a Skindepth, $m_A$ (percent $\frac{\text{grams}}{\text{cm}^3}$ )
CS 13	0.79	25.3	23.8	16.1
CS 14	0.79	26.2	24.4	16.7
CS 15	0.81	25.7	23.9	16.3

where

$S_{xy}$  - covariance between the given data points  $x$  and  $y$

$S_x$  - sample standard deviation of  $x$

$S_y$  - sample standard deviation of  $y$

$x$  - normalized antenna temperature

$y$  - soil moisture parameter

Table VII-2 tabulates the results of the calculations.

Note that the correlation coefficient is approximately the same for all three soil moisture parameters. Since  $S_x$  is the same for all cases, it is more instructive to compare the covariance calculations. If  $S_{xy}$  is zero then the two variables are uncorrelated. As expected,  $S_{xy}$  is largest for the equivalent incoherent soil moisture and smallest for the attenuated soil moisture in a skin-depth. These results coupled with physical intuition indicate that  $m_I$ , the equivalent incoherent soil moisture, should be used throughout the remainder of the analysis as the parameter with which to correlate antenna temperature measurements.

Interpretation of the equivalent incoherent soil moisture - It is now instructive to interpret the parameter  $m_I$  in terms of a measured soil moisture quantity. In other words, assuming that this parameter could be estimated without error from microwave antenna temperature measurements. What soil moisture information does it provide?

TABLE VII-2

## Results of the Correlation Analysis

Data Group	$S_{xy}$	$r$
$T_{N_V}$ and $m_I$	-0.794	-0.912
$T_{N_V}$ and $m_S$	-0.771	-0.914
$T_{N_V}$ and $m_A$	-0.461	-0.911

This can most easily be seen in Figures VII-2 and VII-3 which are plots of soil moisture averaged to various depths for all of the soil profiles observed for the 1974 smooth bare field. Figure VII-2 contains a plot of  $m_I$  calculated for 10.6 GHz. Figure VII-3 contains a plot of  $m_I$  calculated for 1.4 GHz.

The parameter  $m_I$  for 10.6 GHz corresponds nearly exactly with the average soil moisture in the 0-1 cm layer for soil moistures above 25 percent. For soil moistures below 25 percent, it corresponds to a layer slightly deeper than 1 cm, although this depth is still closer to 1 cm than it is to 2 cm. It is evident that  $m_I$  corresponds to deeper layers the drier the soil moisture profile, although at 10.6 GHz these layers are very shallow.

At 1.4 GHz the same general trend occurs between  $m_I$  and the depth of the bottom of the layer containing the corresponding average soil moisture content. It is, however, much more pronounced and occurs at deeper layers, as would be expected. Figure VII-3 demonstrates that  $m_I$  calculated for 1.4 GHz generally corresponds to a layer between 0-5 cm and 0-15 cm, except for very wet conditions, above 35 percent soil moisture where it corresponds to a shallower layer.

It should be noted for interpretation purposes that the smooth bare field was irrigated just prior to acquiring

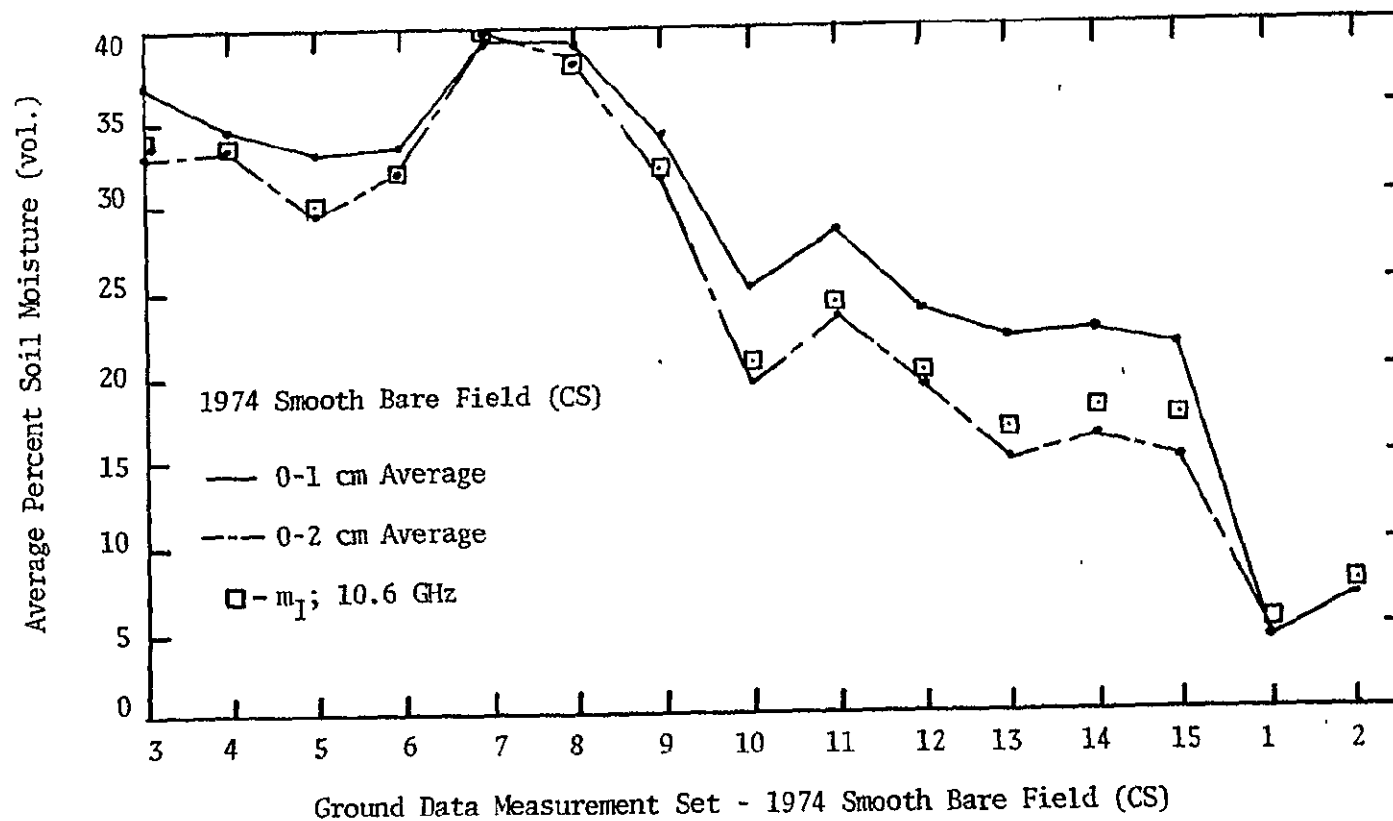


Figure VII-2. Comparison of equivalent incoherent soil moisture calculated at 10.6 GHz to measured soil moisture averaged over depth.



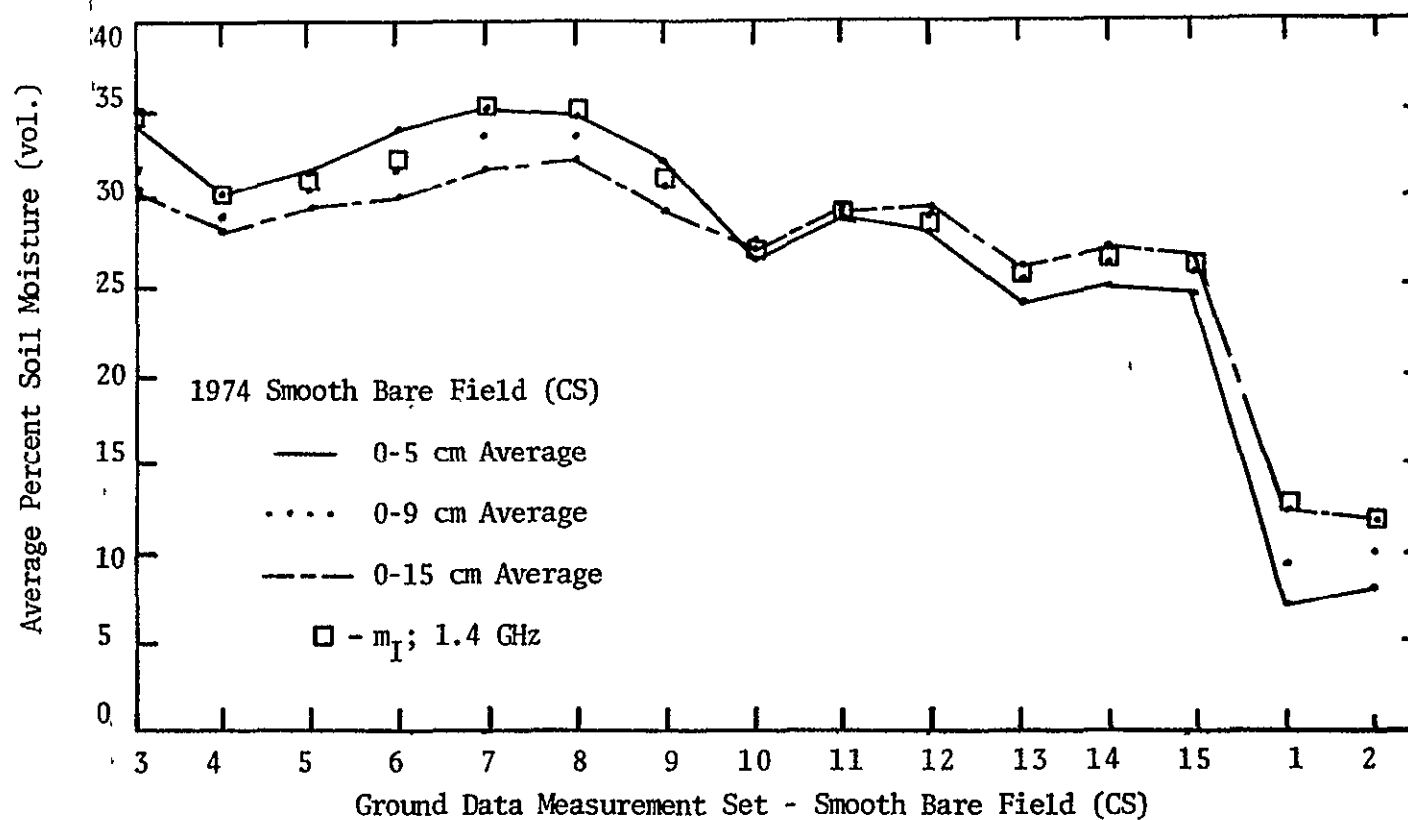


Figure VII-3. Comparison of equivalent incoherent soil moisture calculated at 1.4 GHz to measured soil moisture averaged over depth.

profile three. As a result, the surface 0-1 cm layer was wetter than the 0-2 cm layer from the time ground data measurement three was acquired until ground data measurement set seven was acquired. This is evident in Figure VII-2. Also, the 0-5 cm layer was wetter than the 0-9 cm layer which was wetter than the 0-15 cm layer between ground data set three and ground data set ten, when the order reversed. This can be seen in Figure VII-2. When the upper layers are wetter than the lower layers, the profile is said to be inverted. This condition occurs just after irrigation or a rain. Under this condition  $m_I$  corresponds to a shallower layer than when the profile is not inverted. However, the degree to which this is true still depends on the moisture in the lower 0-5 cm and 0-9 cm levels.

Since the  $m_I$  calculated for 10.6 GHz corresponds to the moisture in depths less than two centimeters for all profile situations, it will be assumed that 10.6 GHz only responds to 0-2 cm moisture hereafter. However, it is necessary to define the soil depth which corresponds to the  $m_I$  calculated for 1.4 GHz. The layer with which each  $m_I$  corresponds was calculated by linearly interpolating the average moisture contents. Figure VII-4 is the result of these calculations. They were done for the profiles of all three 1974 fields, CS, CM, and CR.

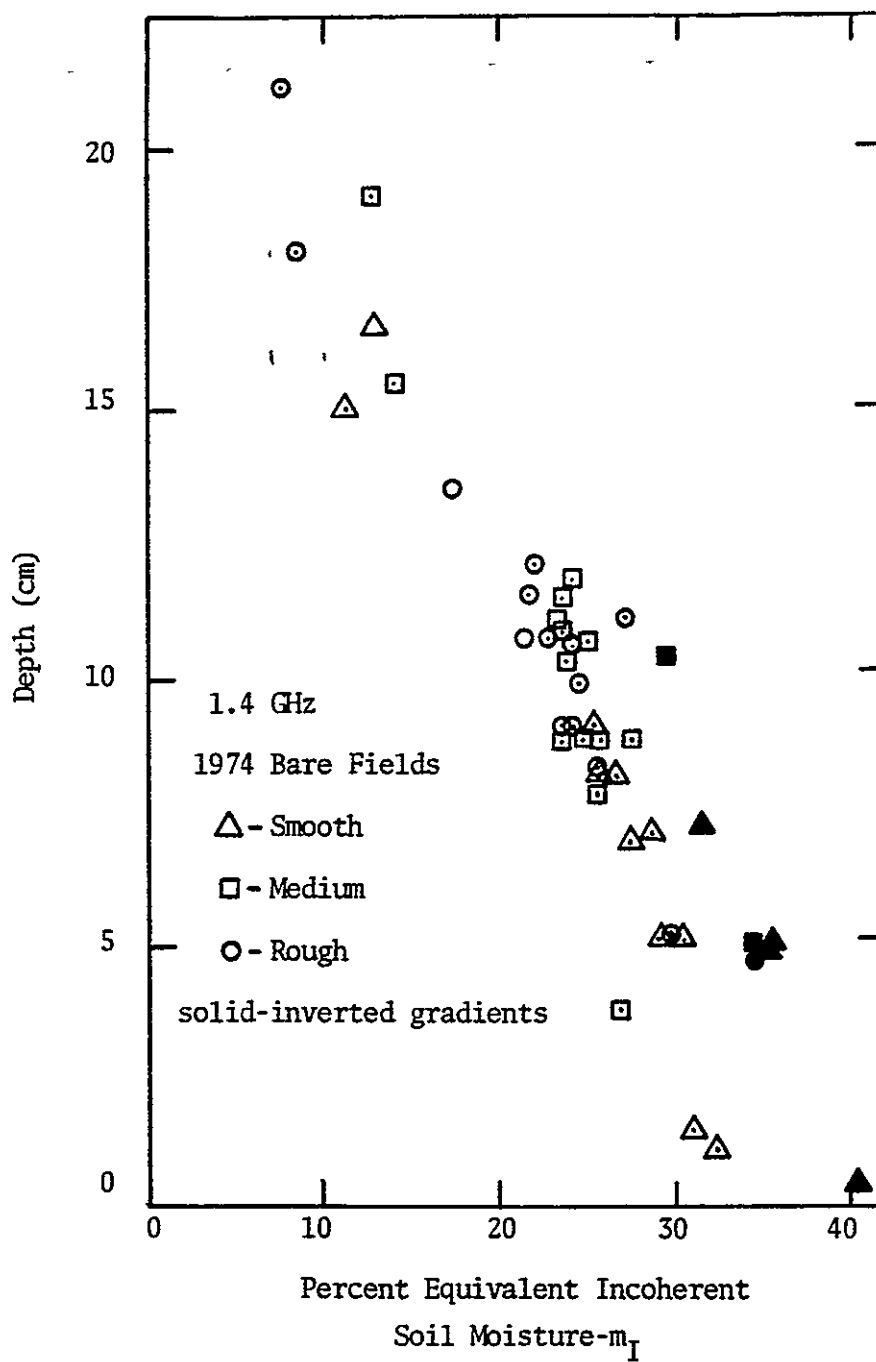


Figure VII-4. Comparison of equivalent incoherent soil moisture ( $m_I$ ) calculated at 1.4 GHz to the depth that corresponds to an average soil moisture equal to  $m_I$ .

It is obvious from Figure VII-4 that there is a linear relationship between the equivalent incoherent soil moisture and the depth to the bottom of the corresponding soil layer, at least for  $m_I$ 's below 25 percent. The apparent nonlinearity above 25 percent is a result of the actual soil moisture profile shape. There are three types of soil moisture profiles as depicted in Figure VII-5. Note that it is profile type B that generally causes the departure from a linear correlation with depth for  $m_I$ 's above 25 percent (Figure VII-4). However, a linear least squares straight line fit to all of the data in Figure VII-4 yields a correlation coefficient of 0.92 and the following linear regression equation:

$$D = -0.58 m_I + 23.64 \quad (\text{VII-6})$$

where  $D$  is the depth to the bottom of the layer in centimeters to which  $m_I$  corresponds.

A better estimate of the corresponding depth of measurement can be made by grouping the data of Figure VII-4 into three categories as denoted in Table VII-3. Table VII-3 inherently assumes that profile type A, an inverted profile, can be distinguished from the others.

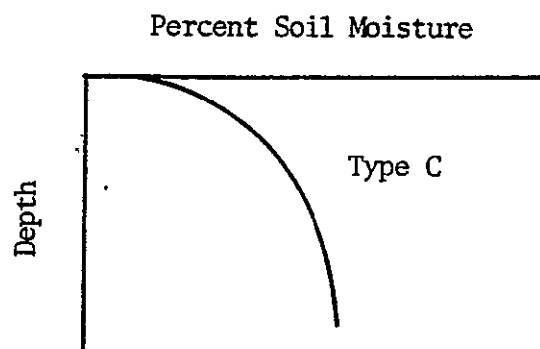
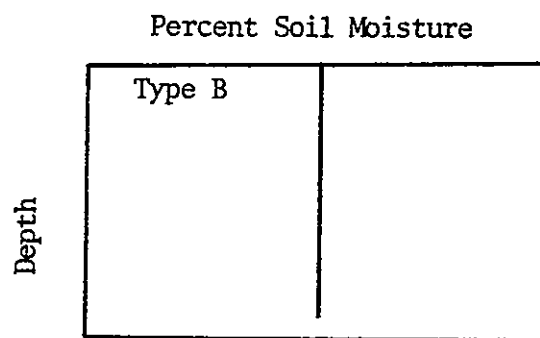
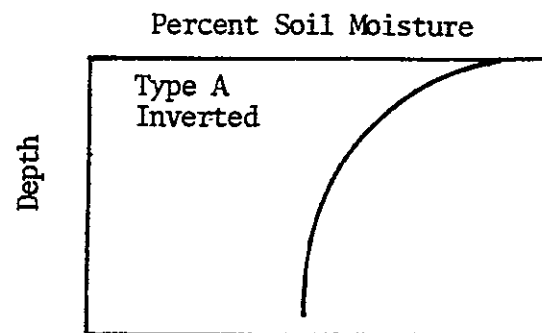


Figure VII-5. Definition of soil moisture profile type.

TABLE VII-3

## Separation of Profiles for Regression Analysis

Category	Definition
I	$m_I < 0.25$
II	$m_I > 0.25$ profile type A
III	$m_I > 0.25$ profile type B and C

It is felt that a soil moisture profile can be classified as type A simply by comparing the 10.6 GHz estimate of  $m_I$  to the 1.4 GHz estimate. If the 10.6 GHz estimate is larger, then the surface is wetter than the immediate subsurface and the profile is inverted. This result is of vital importance since the ability to distinguish inverted profiles from non-inverted profiles provides information on the recent history of water input to the soil system.

A linear least squares regression fit to the equivalent incoherent soil moisture categories given in Table VII-3 produce the results contained in Table VII-4. Figure VII-6 is a plot of these regression fits along with the 70 percent confidence intervals for each of the fits. In this linear regression analysis the basic assumptions are that the depths being estimated are normal uncorrelated random variables with equal variance and zero mean. Assuming that the equivalent incoherent soil moisture is measured without error, the 70 percent confidence intervals define the range of depths that will include the true mean depth with a 70 percent confidence.

The equivalent incoherent soil moisture,  $m_I$ , will be used in the remainder of this document to describe the soil moisture to which the antenna measurements are responsive. For convenience, it will be denoted by the acronym EQSM.

TABLE VII-4  
 Linear Regression Equations for Soil Profile  
 Categories I, II, and III

Category	Regression Line	Correlation Coefficient
I	$D = -0.569 m_I + 23.77$	0.94
II	$D = -0.635 m_I + 27.405$	0.92
III	$D = -1.055 m_I + 35.79$	0.81



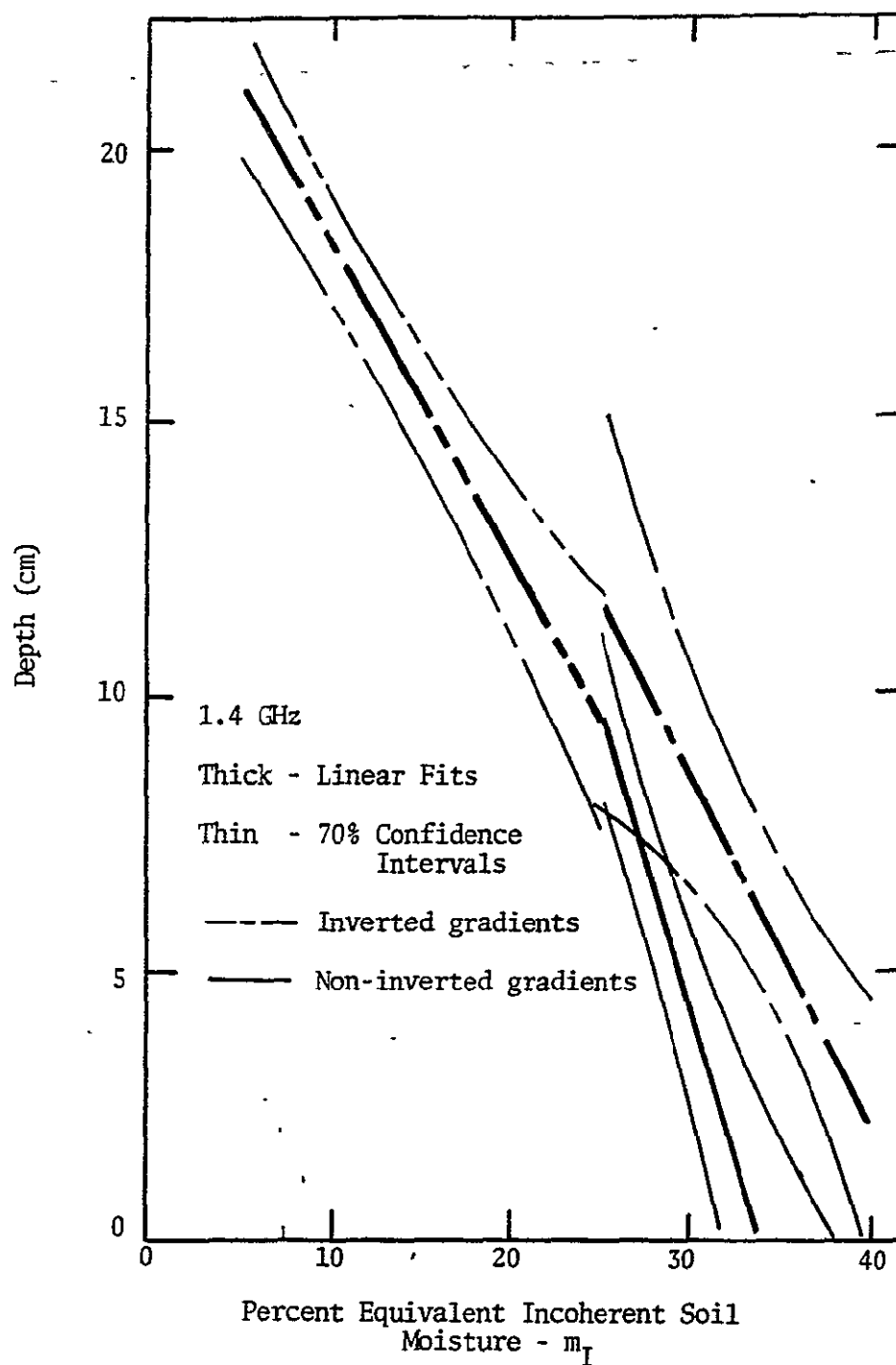


Figure VII-6. Linear regression fits and confidence intervals for the data in Figure VII-4.

Appendix C contains calculations of EQSM for all of the soil moisture profiles measured during the 1974 and 1975 measurement programs.

### Soil Temperature Profile

The effect of the soil temperature profile was demonstrated in Chapter IV. It was shown that emission from the soil is dependent on the soil temperature magnitude and the shape of the temperature profile. In order to analyze antenna measurements for soil moisture information without being biased by differences in soil emission due to differences in the soil temperature profile, it is necessary to normalize the antenna temperature measurement to a soil temperature parameter.

Physical reasoning indicates that the best parameter with which to normalize antenna temperature measurements to eliminate differences due to the soil temperature would be an equivalent incoherent soil temperature, calculated using the same technique as is used to calculate  $m_I$ , the equivalent incoherent soil moisture. However, such a parameter cannot be utilized in a system designed to remotely measure soil moisture since the soil temperature profile is an unknown quantity. Surface soil temperature is a remotely measurable quantity, however, and can be used in such a system if required.

Therefore, as a compromise, the surface soil temperature will be used in the following analysis to normalize the measured antenna temperatures.

Normalized antenna temperatures calculated using surface soil temperatures compare very favorably with antenna temperatures normalized using an equivalent incoherent soil temperature,  $t_I$ .

$$t_I = \sum_{i=1}^N \frac{t(i) \cdot \Delta BT_{\text{volume}}(i)}{BT_{\text{volume}}} \quad (\text{VII-7})$$

where

$t_I$  - equivalent incoherent soil temperature

$t(i)$  - soil temperature of each layer

$\Delta BT_{\text{volume}}(i)$  - brightness temperature of each layer  
referenced to the soil surface

$BT_{\text{volume}}$  - total brightness temperature of the  
soil volume

For at least 97 percent of the 1974 measurements the antenna temperature normalized using the surface soil temperature is within 0.01 of the antenna temperature normalized using  $t_I$ . None differ by more than 0.02.

As with the equivalent incoherent soil moisture, the equivalent incoherent soil temperature will be

denoted by an acronym, EQST, in the remainder of this report. It will not be used to normalize antenna temperatures for analysis purposes, but it will be used to describe the measured soil temperature. Appendix C also contains tabulations of EQST for the soil temperature profiles measured during the 1974 and 1975 measurement programs.

#### Data Interpretation and Soil Moisture Correlation

Antenna temperature measurements will be analyzed in this section to demonstrate the soil moisture dependence, and the effects of surface roughness and vegetation cover on this dependence. The measured antenna temperatures are not corrected for antenna beamwidth or reflected sky temperature. It is doubtful that these measurement deficiencies can easily be corrected in any system designed for the purpose of making a usable estimate of soil moisture. Rather, the system will have to be designed to minimize such effects. The corrections were not made for these particular deficiencies in order to demonstrate that usable soil moisture information is contained in the degraded soil brightness temperature measurement. However, the reflected self emission component is a serious effect for angles near nadir. Since this effect only

occurs as a serious problem in ground-based system measurements, all of the data measured at nadir have been corrected for this self emission component. Appendix B provides a detailed discussion of the self-emission effect and the scheme used to correct the measurements.

In the discussion that follows, the soil moisture dependence is first demonstrated using smooth bare soil measurements. Then, the effects of other scene parameters on this dependence are presented. The effects of surface roughness are presented first, then the effects of vegetation cover are discussed.

#### Smooth Surface Moisture and Angle Dependence

The effect of soil moisture is the largest for smooth bare soil surfaces. Surface roughness and vegetation cover tend to degrade this dependence. As a result, the soil moisture dependence will be presented first for a smooth bare soil surface. The effect of surface roughness and vegetation will be demonstrated later.

The experimental plots used in the 1974 measurement program contained a smooth bare field. Only 1.4 GHz data are used since the bare smooth field, field CS, did not appear smooth at the 10.6 GHz wavelength. The effect of transmission angle for a surface smooth at 10.6 GHz will be the same as will be demonstrated for the smooth surface at 1.4 GHz.

Normalized antenna temperature is plotted as a function of transmission angle for four soil moisture profiles in Figure VII-7. The measured antenna temperatures were normalized using the 0-1 cm soil temperature to eliminate effects of surface temperature variation. It can be seen (Figure VII-7) that the change in the vertical normalized antenna temperature with soil moisture decreases as the transmission angle is increased (i.e., the response to soil moisture decreases as transmission angle increases). It is not as obvious, but the response to soil moisture for horizontal polarization increases slightly with transmission angle.

Both of these phenomena are demonstrated in Figure VII-8 through VII-14. These figures contain plots of normalized antenna temperature as a function of soil moisture for each transmission angle. A best fit straight line has also been drawn through the points on each plot. The slopes of the straight lines describe the average sensitivity to soil moisture. The slope for horizontal polarization shows a slightly increasing trend with transmission angle while for vertical polarization it shows a decreasing trend (Figure VII-15). In Figure VII-15 the slopes are referenced to a ground temperature of 300°K such that sensitivity in degrees Kelvin per percent moisture can be plotted. The trends in Figure VII-15

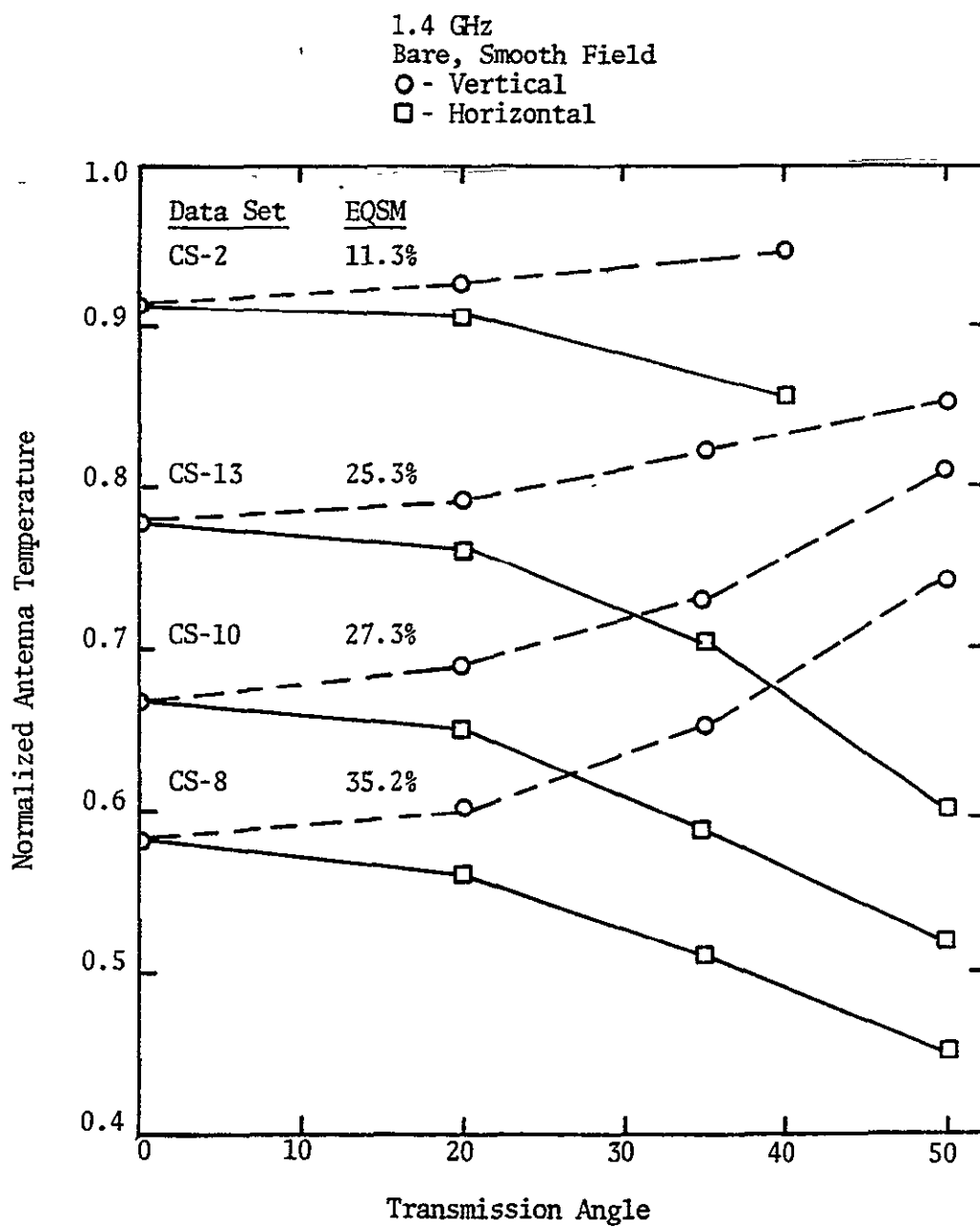


Figure VII-7. Measured 1.4 GHz emission as a function of soil moisture and transmission angle.

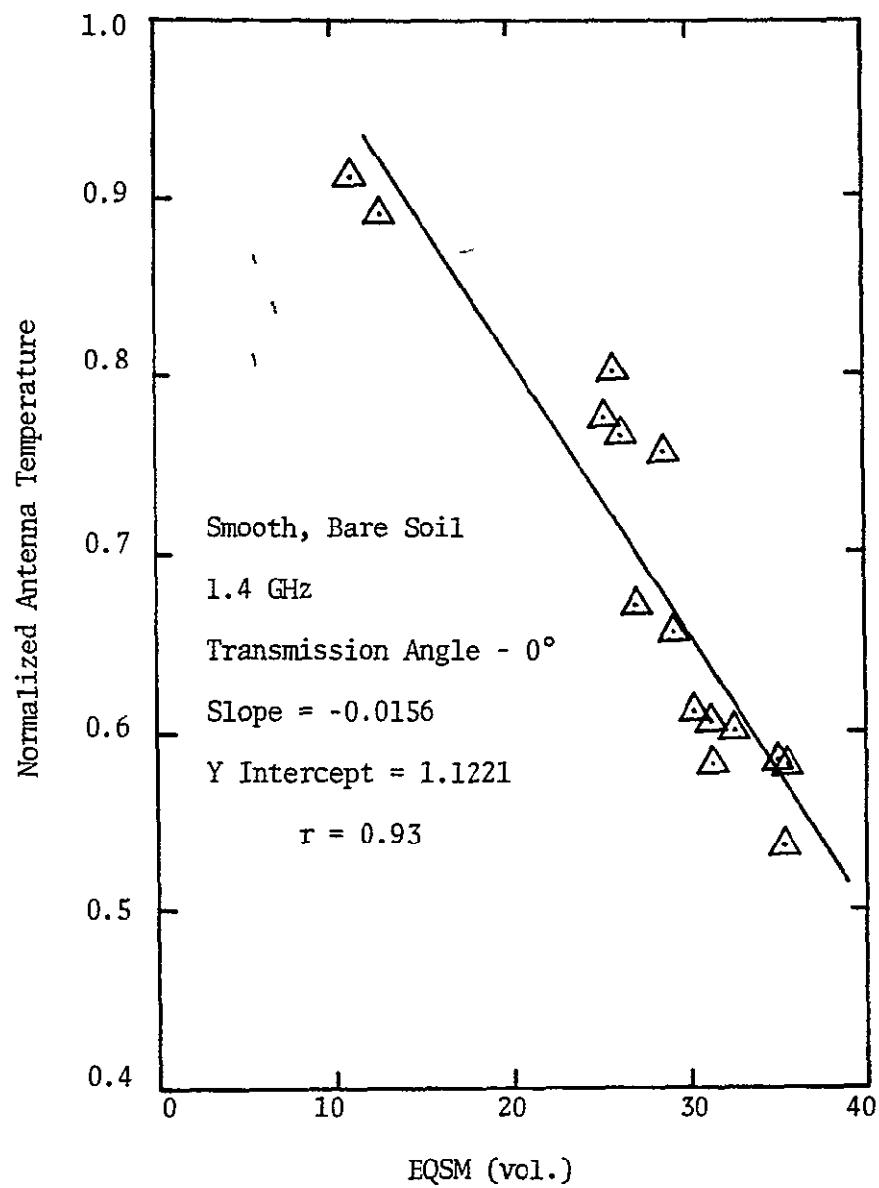


Figure VII-8. 1.4 GHz antenna temperature measurements of smooth, bare soil at nadir as a function of equivalent incoherent soil moisture.



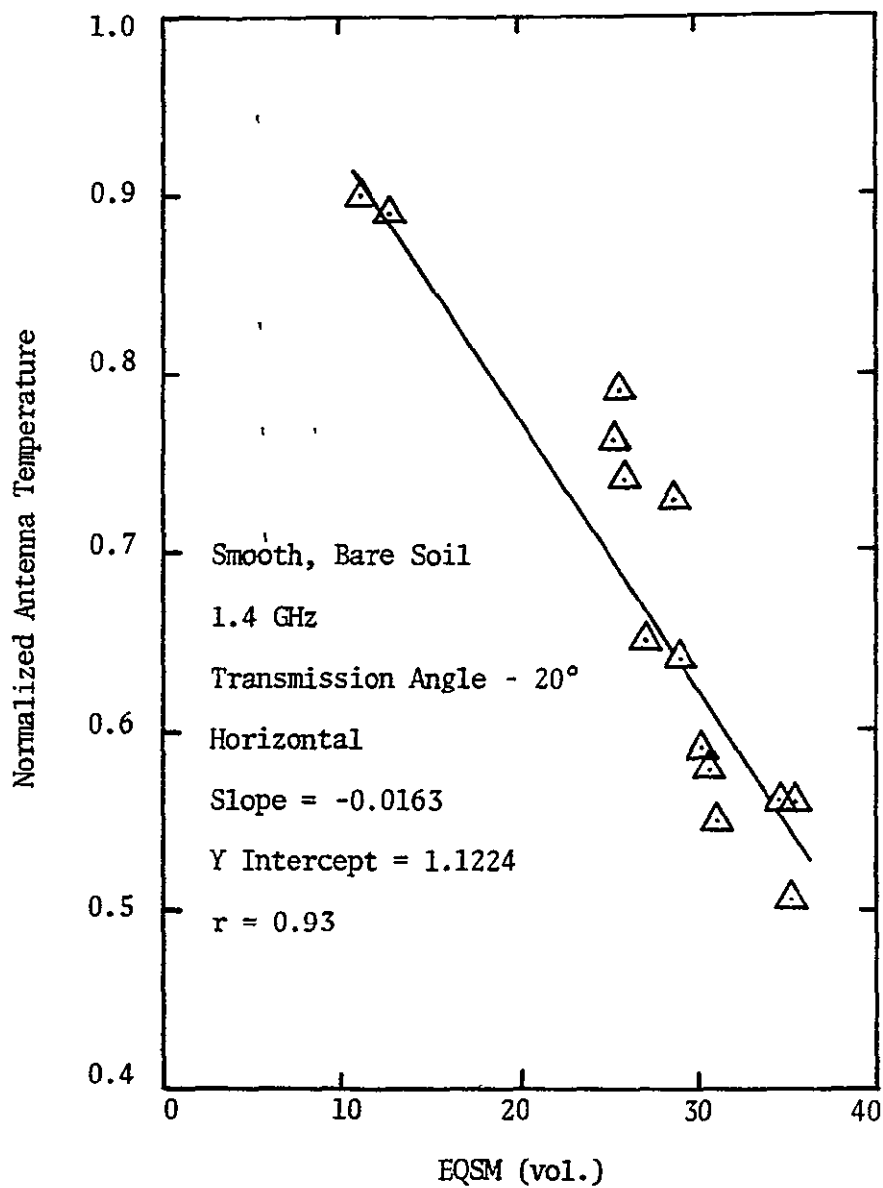


Figure VII-9. Horizontal 1.4 GHz antenna temperature measurements of smooth, bare soil at 20° as a function of equivalent incoherent soil moisture.

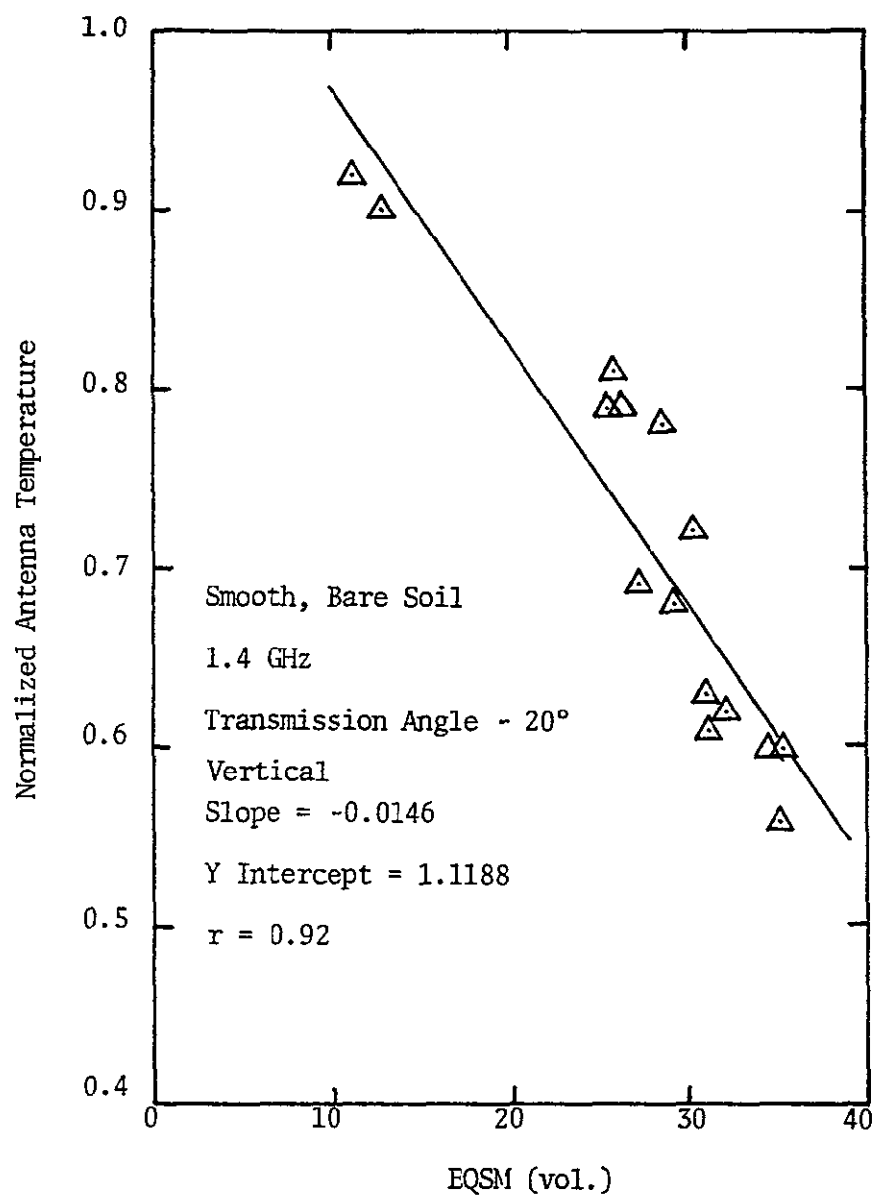


Figure VII-10. Vertical 1.4 GHz antenna temperature measurements of smooth, bare soil at  $20^\circ$  as a function of equivalent incoherent soil moisture.

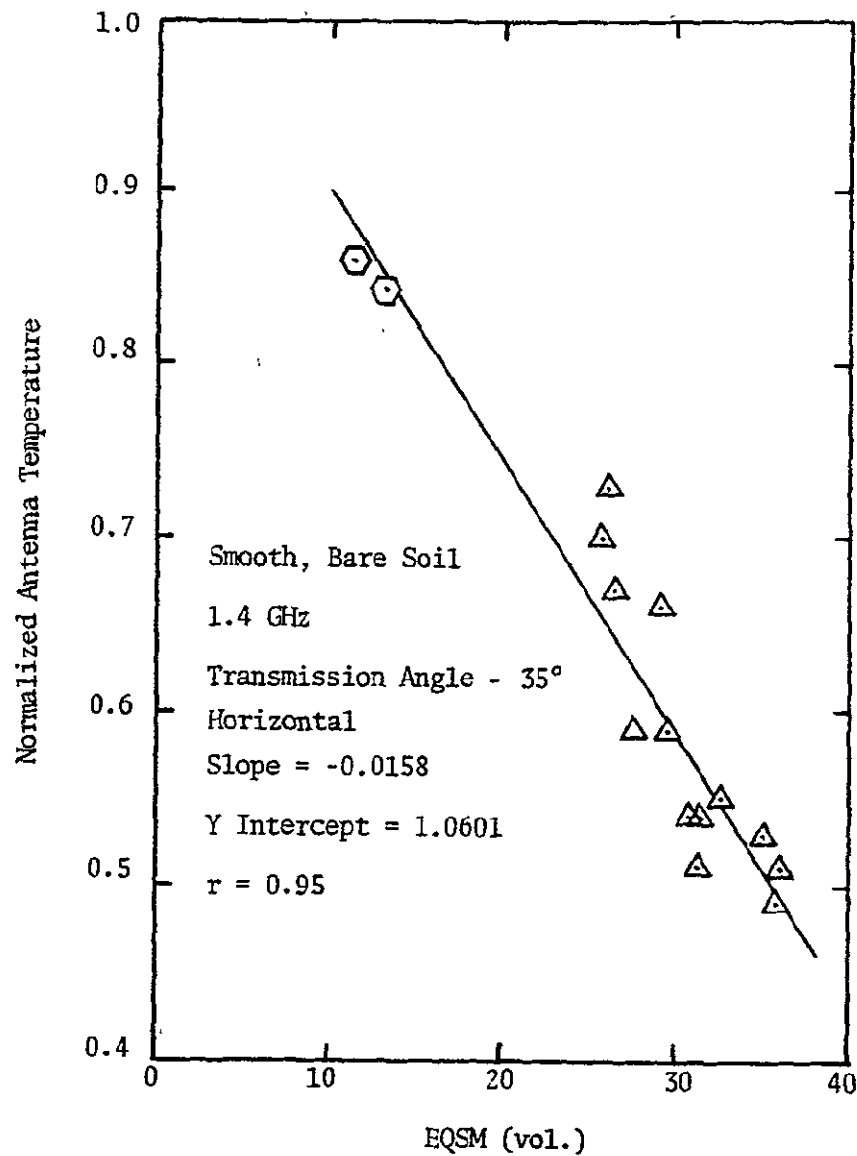


Figure VII-11. Horizontal 1.4 GHz antenna temperature measurements of smooth, bare soil at  $35^\circ$  as a function of equivalent incoherent soil moisture.

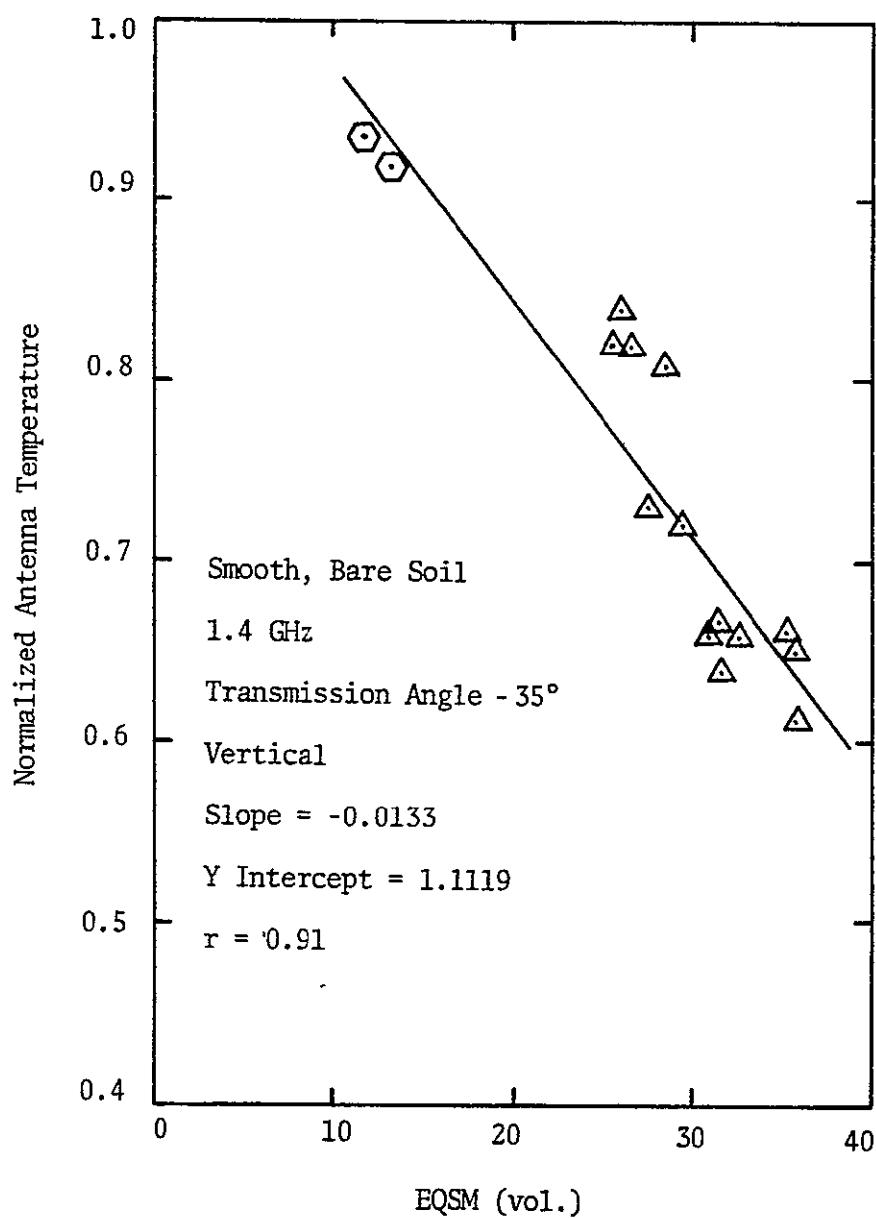


Figure VII-12. Vertical 1.4 GHz antenna temperature measurements of smooth, bare soil at 35° as a function of equivalent incoherent soil moisture.

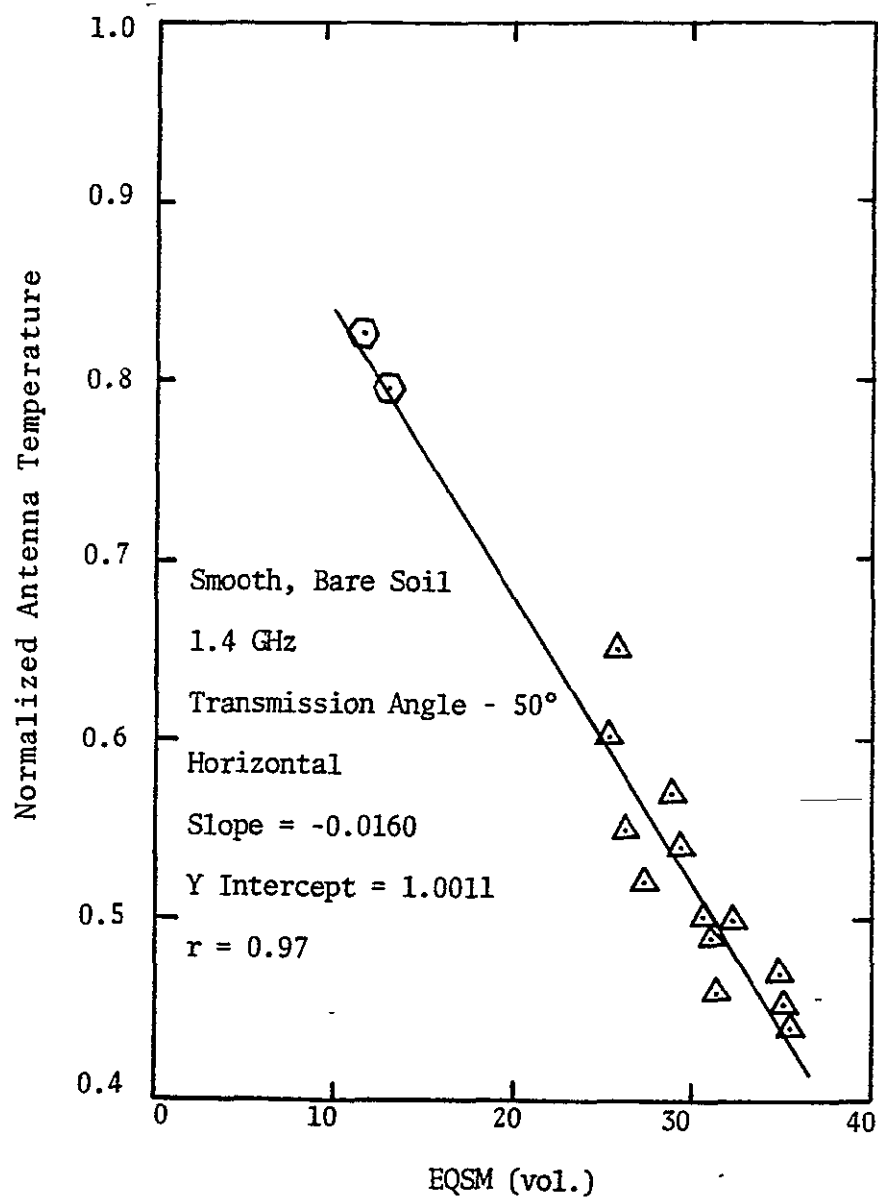


Figure VII-13. Horizontal 1.4 GHz antenna temperature measurements of smooth, bare soil at 50° as a function of equivalent incoherent soil moisture.

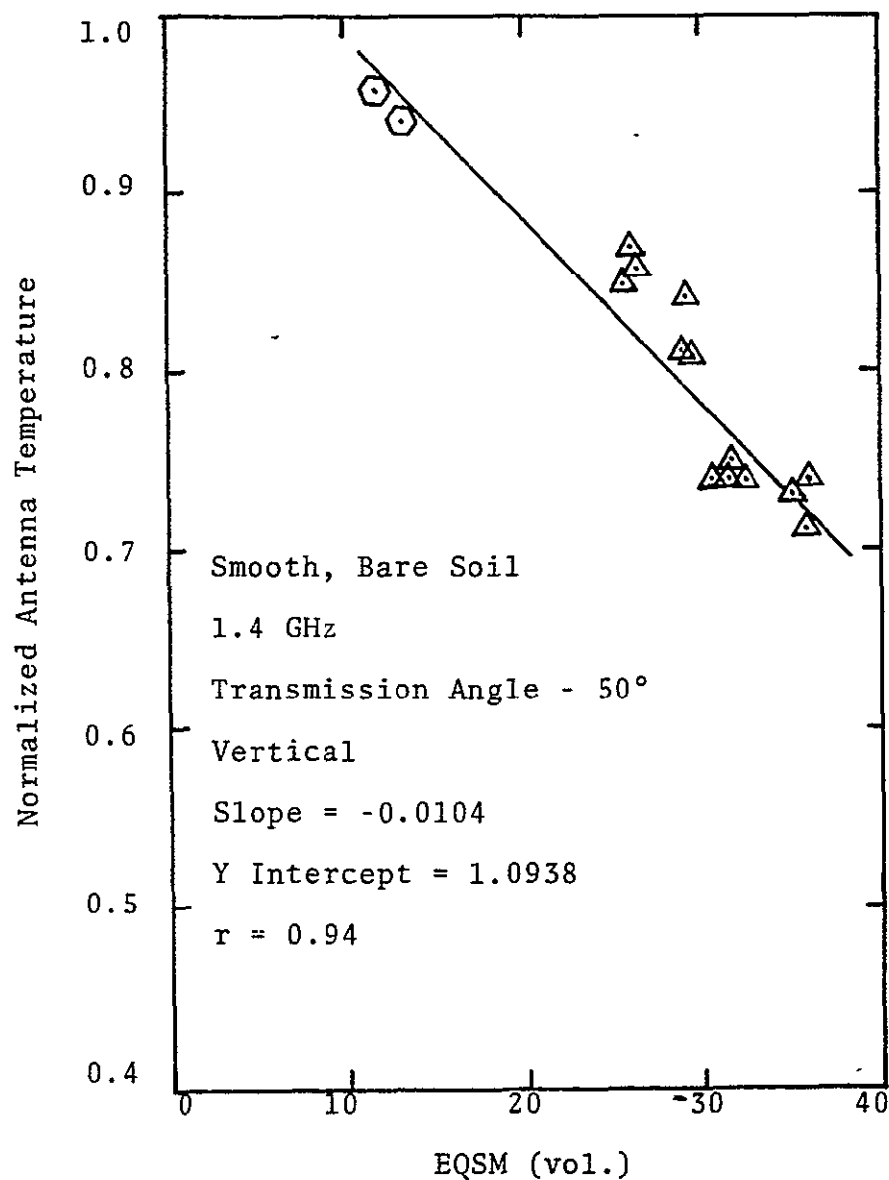


Figure VII-14. Vertical 1.4 GHz antenna temperature measurements of smooth, bare soil at  $50^\circ$  as a function of equivalent incoherent soil moisture.

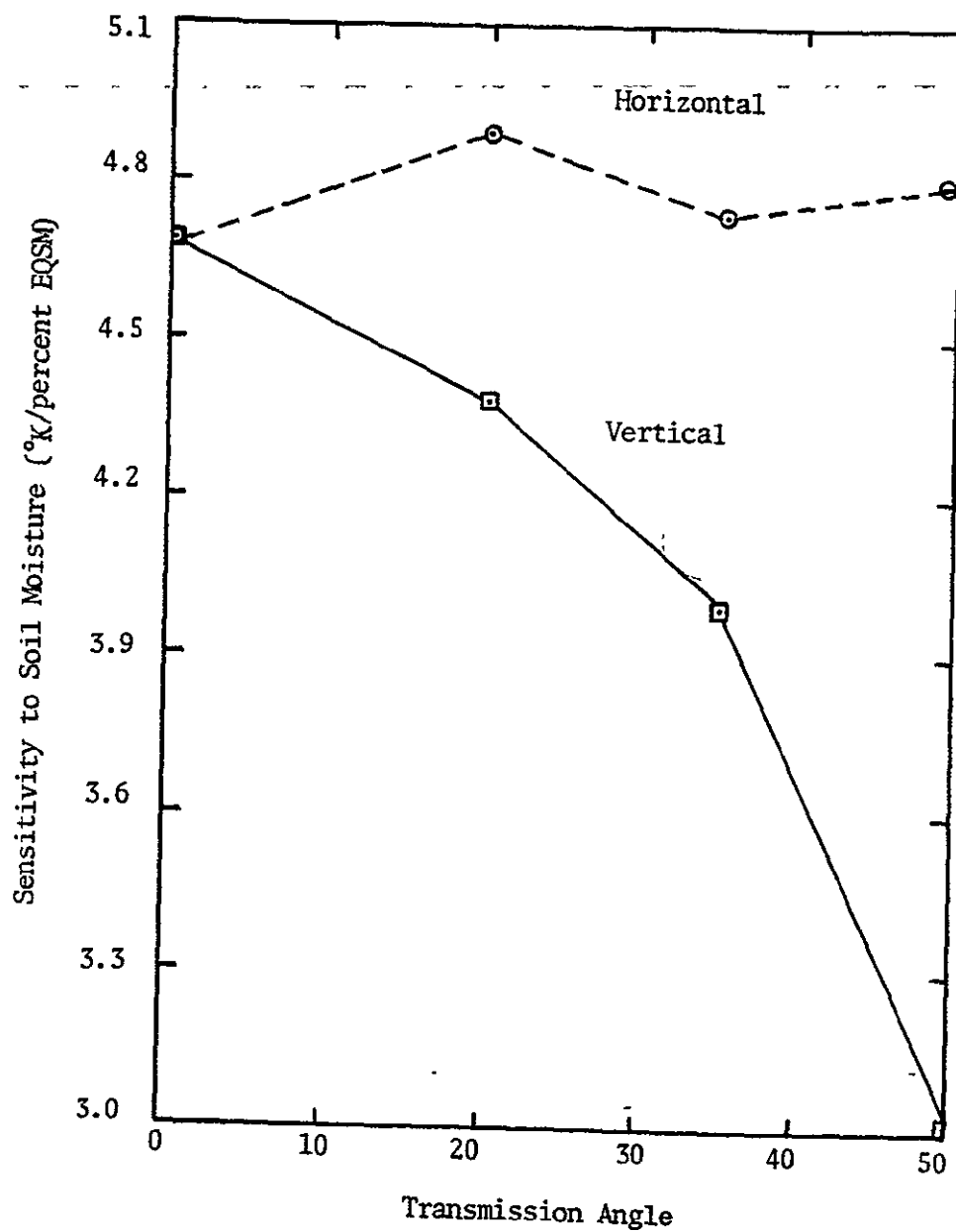


Figure VII-15. Sensitivity of 1.4 GHz antenna temperature measurements to soil moisture of smooth, bare soil based on linear regression fits.

were predicted in Chapter IV (Figure IV-18) using the model for the emission from a smooth soil.

The predictions of this model indicate the rationale behind the phenomenon. The sensitivity to vertically polarized emission to soil moisture decreases with transmission angle. This is due to the fact that the natural angular response causes the vertical emission to increase as the transmission angle increases. However, the brightness temperature of emission can never exceed the physical temperature of the soil. Thus, the allowable range over which the vertical emission can change with soil moisture decreases as the transmission angle increases. For horizontal polarization the natural angular response causes the emission to decrease with angle. Thus, as transmission angle is increased the allowable range over which the emission can change with soil moisture is virtually unchanged.

In the discussion above, straight lines were fit to the measurements in Figures VII-8 through VII-14 to demonstrate the overall response to soil moisture. However, the energy emitted from the soil is directly dependent on the permittivity of the soil. This means that normalized antenna temperature plotted versus soil moisture should have a curvature that is the inverse of the permittivity curve of Miller clay (Figure II-23). Calculations based on the models presented in Chapter IV



demonstrate this phenomenon (Figure IV-17). The curvature of the plot in Figure IV-17 is inverse to the curvature of the plot of permittivity versus soil moisture for Miller clay (Figure II-23). The permittivity curve of Miller clay breaks at approximately 24 percent moisture. Although there are no antenna temperature measurements for moistures between 15 percent and 25 percent, the data plotted in Figures VII-8 through VII-14 indicate that 24 to 25 percent is the breakpoint.

In view of the discussion above, it is obvious that the points plotted in Figures VII-8 through VII-14 could be fitted with two straight lines. One for equivalent soil moistures ranging from 0 to 25 percent, and one for moistures ranging from 25 percent to saturation. Such a fit is demonstrated in Figure VII-16 using the predictions of the model.

It is interesting to compare the slopes of the best fit lines through the measurements presented in Figures VII-8 through VII-14 for moistures above 25 percent to the slopes of the lines through all of the points. This can be done by converting the slopes to sensitivity in degrees Kelvin per percent moisture. The slopes of the linear regression lines fitted to all of the points were converted to a soil moisture sensitivity by multiplying them by a reference ground temperature of 300°K. The

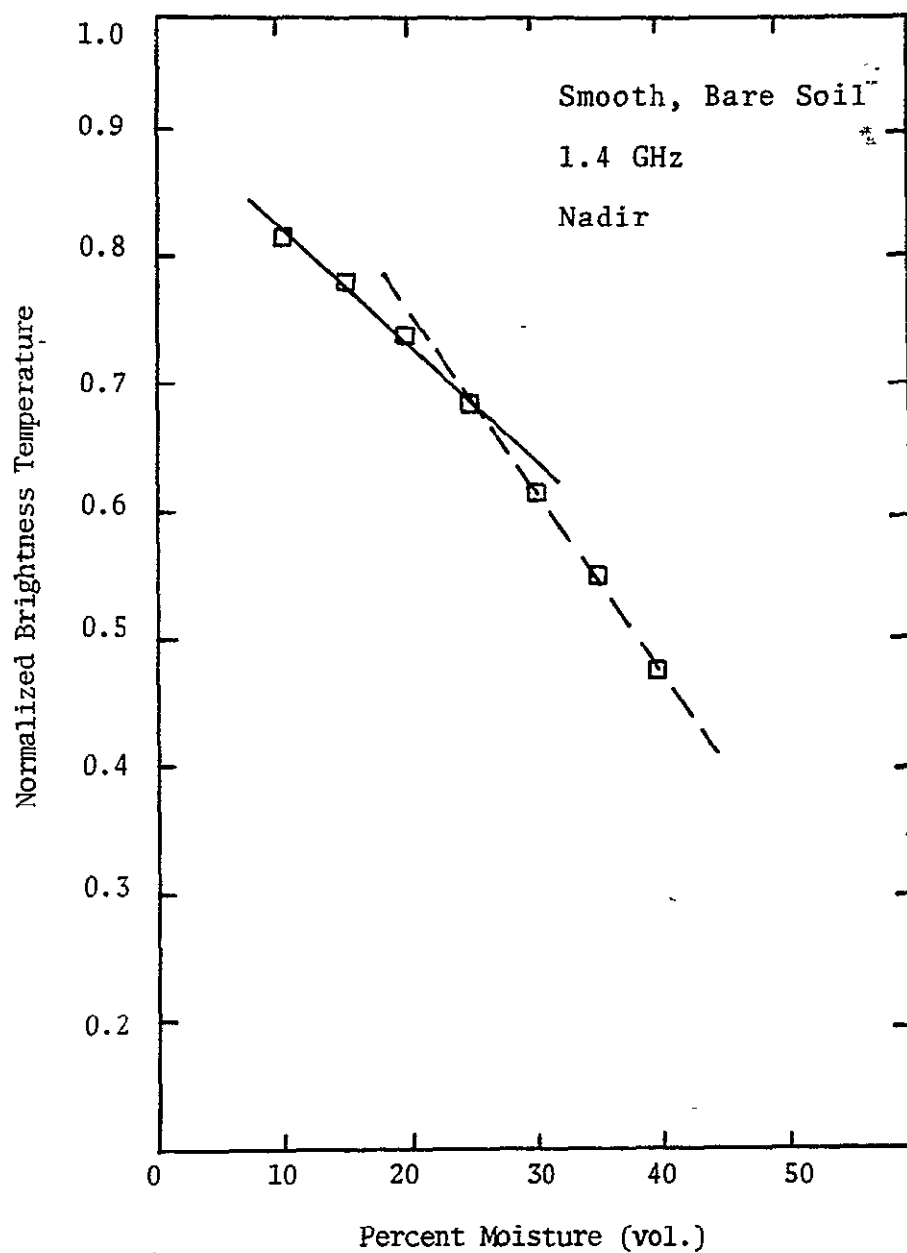


Figure VII-16. Calculated brightness temperature of a smooth, bare soil as a function of uniform soil moisture.

results are presented in Figure VII-15. The slopes of the linear regression lines fitted to the points above 25 percent soil moisture were converted to sensitivity in the same manner and plotted in Figure VII-17. A comparison of Figure VII-15 and Figure VII-17 demonstrate that the true response of antenna temperature measurements to variations in soil moisture for moistures above 25 percent is greater than the average response observed over the entire moisture range from dry to saturated.

#### Effects of Roughness

Antenna temperature measurements were made on two types of surface roughness during the 1974 and 1975 measurement programs. In 1974 the experimental plots were roughened as uniformly across the fields as possible. However, in 1975 the experimental plot was prepared in rows similar to the tillage practices used in the area near Phoenix, Arizona. This was done so that the effects of row direction could be investigated. As a result the discussion on roughness effects is divided into two parts; one on uniform roughness and one on the effects of row tillage.

Uniform roughness - It has been demonstrated that the emission from bare smooth soil is sensitive to changes in the shape and overall magnitude of the soil moisture

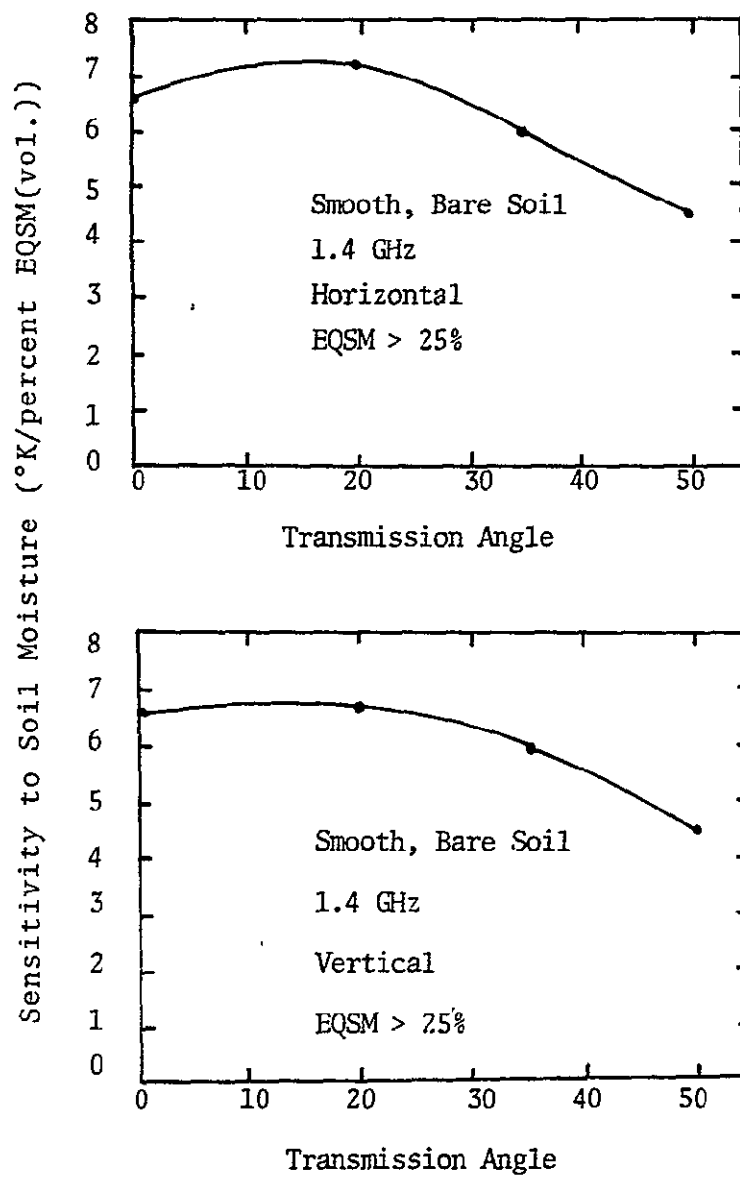


Figure VII-17, Sensitivity of antenna temperature measurements to soil moisture for average moistures greater than 25%.

profile. However, as the soil surface is roughened the sensitivity to soil moisture decreases. Naturally, the effect of a given surface roughness is dependent on the wavelength of the radiation. For 1.4 GHz at a transmission angle of  $20^\circ$ , Figure VII-18 demonstrates the reduction in the sensitivity of the emission to soil moisture due to the uniform roughness of the 1974 experimental plots. The smooth field (CS) had a rms surface height deviation of 0.88 cm, the medium rough (CM), 2.6 cm, and the rough (CR), 4.3 cm.

The fact that the response to soil moisture actually decreased with surface roughness was not expected at first. It was only after the model in Chapter IV was developed that a clear understanding of the emission phenomenon for rough surfaces was understood. In order to describe the emission from a rough surface using the model developed in Chapter IV, it was necessary to determine the values of  $Q$ , the roughness parameter distribution with transmission angle, that describe each of the surface preparations. The technique of obtaining the  $Q$  distributions for 1.4 GHz will be described, then a simple physical interpretation of the model predictions will be made.

Although the roughness parameter,  $Q$ , is defined in terms of the surface autocorrelation function and variance

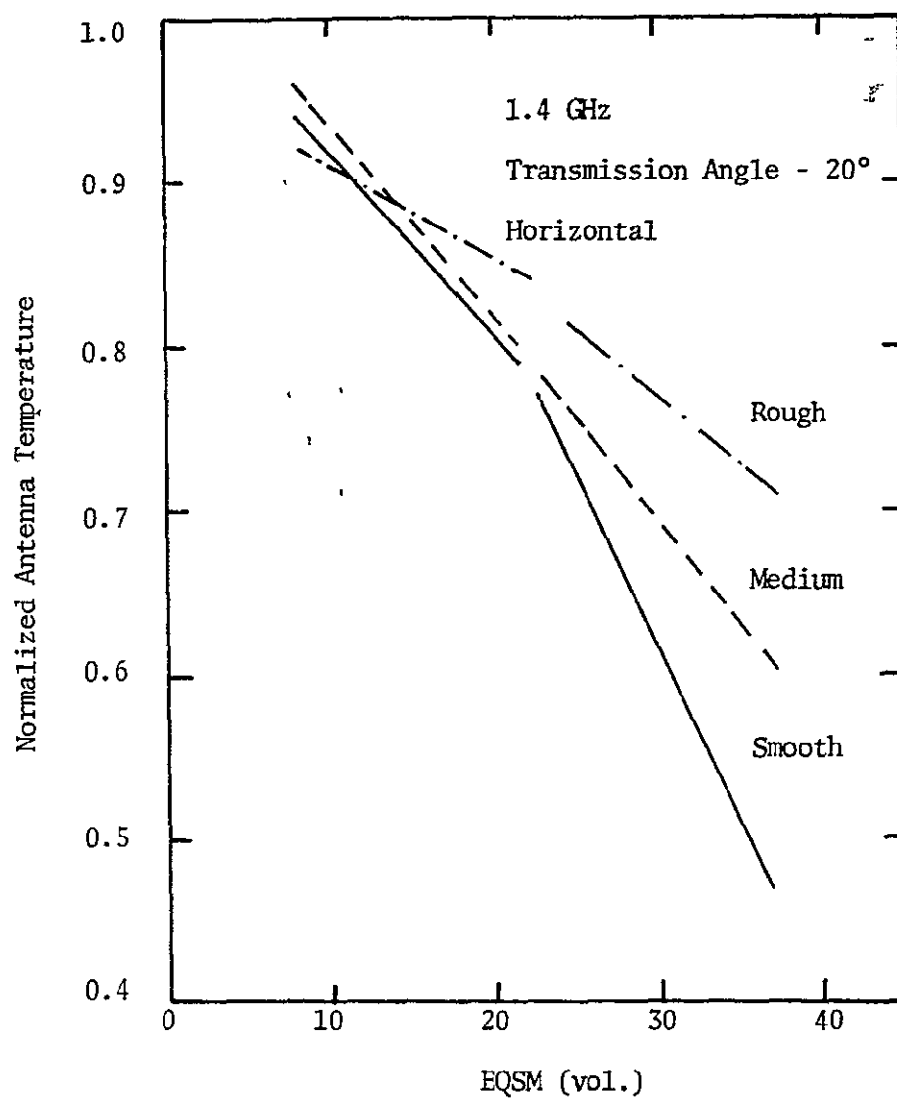


Figure VII-18. Normalized 1.4 GHz antenna temperature measurements as a function of soil moisture for three surface roughness conditions.

of the surface height distribution, (IV-72), it cannot easily be obtained from a measurement of the surface profile. Part of this problem arises from the difficulty in properly choosing  $\tau_0$ , the point about which the derivative of the surface autocorrelation function is evaluated. In order to get around this difficulty, the Q distributions that define each of the surface preparations were obtained directly from the antenna temperature measurements. However, this comparison was made at only one soil moisture content. By forcing the antenna temperature measurements to fit the model predictions at only one moisture content, the model prediction of the response of the brightness temperature to soil moisture was left unbiased.

The distributions of Q with transmission angle were obtained by overlaying antenna temperature measurements made at an EQSM of 35 percent with model calculations of brightness temperature as a function of transmission angle. In order to obtain antenna temperature measurements of all three surfaces at 35 percent equivalent moisture, it was necessary to perform a linear regression fit to the antenna temperature measurements as a function of EQSM. Table VII-5 contains the results of these fits. These fits were then used to obtain the antenna temperatures that correspond to 35 percent EQSM. Figure VII-19 is a

TABLE VII-5

Linear Regression Fits to the 1974 1.4 GHz Measurements

Field	Transmission Angle	Polarization	EQSM < 25			EQSM > 25		
			Slope	Intercept	r <sup>2</sup>	Slope	Intercept	r <sup>2</sup>
CS*	20	Hor	-0.011	1.025	0.99	-0.024	1.346	0.82
		Vert	-0.009	1.015	0.99	-0.022	1.358	0.83
	35	Hor	-0.012	1.001	1.00	-0.020	1.189	0.79
		Vert	-0.008	1.023	1.00	-0.020	1.328	0.80
	50	Hor	-0.017	1.019	1.00	-0.015	0.984	0.77
		Vert	-0.007	1.035	0.99	-0.015	1.230	0.84
CM	20	Hor	-0.014	1.116	0.90	-0.013	1.087	0.61
		Vert	-0.012	1.088	0.77	-0.011	1.054	0.52
	35	Hor	-0.015	1.106	0.86	-0.012	1.028	0.57
		Vert	-0.009	1.057	0.72	-0.011	1.087	0.61
	50	Hor	-0.019	1.142	0.83	-0.012	0.945	0.57
		Vert	-0.008	1.050	0.60	-0.009	1.076	0.72



Table VII-5 (Continued)

Field	Transmission Angle	Polarization	EQSM < 25			EQSM > 25		
			Slope	Intercept	r <sup>2</sup>	Slope	Intercept	r <sup>2</sup>
CR	20	Hor	-0.005	0.965	0.77	-0.009	1.057	0.84
		Vert	-0.005	0.960	0.64	-0.009	1.060	0.80
	35	Hor	-0.0053	0.940	0.57	-0.016	1.227	0.80
		Vert	-0.0045	0.957	0.62	-0.011	1.1165	0.88
	50	Hor	-0.007	0.942	0.61	-0.013	1.088	0.82
		Vert	-0.0037	0.9545	0.54	-0.010	1.118	0.95

\*A point at 25% EQSM calculated using the regression for EQSM > 25% was used in determining the regression fit for EQSM < 25%

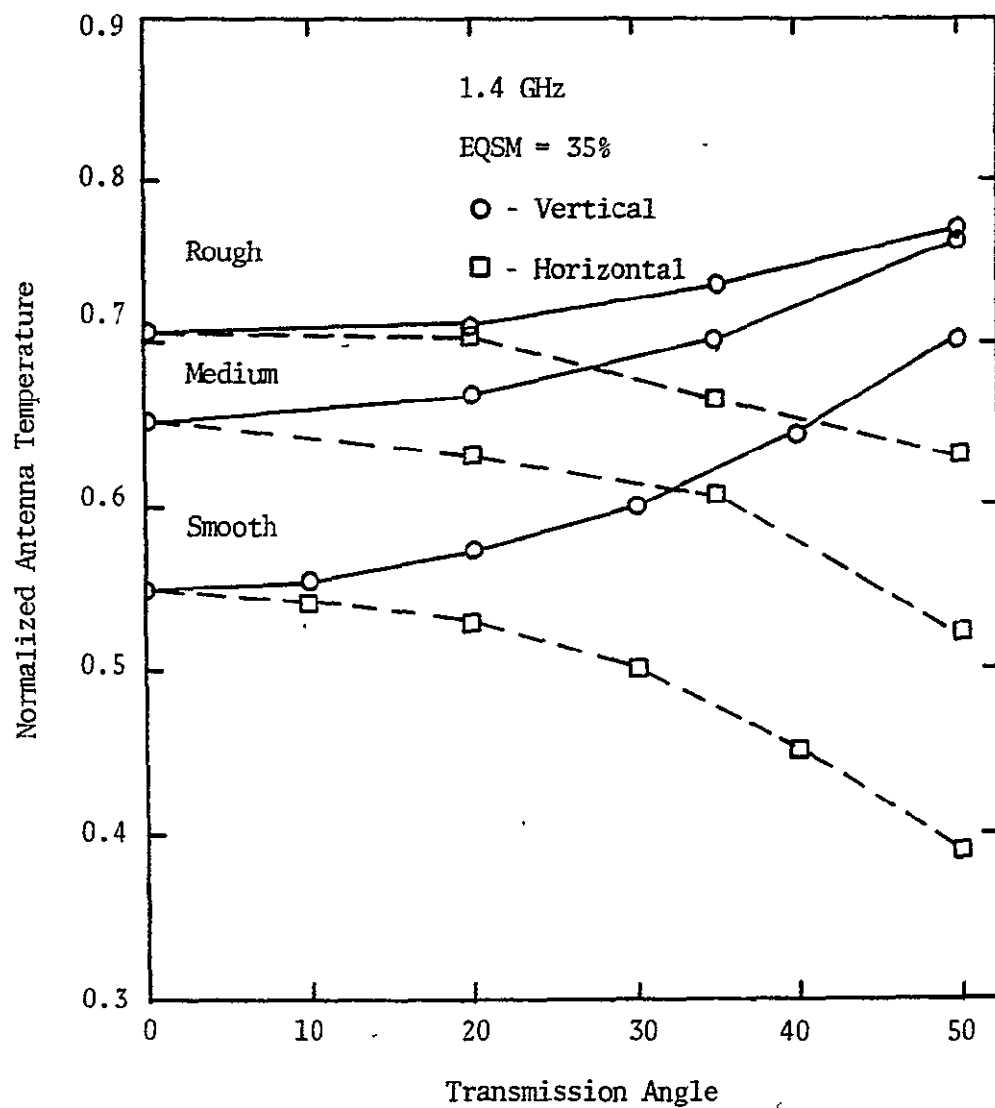


Figure VII-19. Normalized antenna temperatures corresponding to a 35% EQSM. These data were used in conjunction with Figures VII-20 and VII-21 to obtain the Q distributions for each surface.

plot of these antenna temperatures for each surface roughness. Actually the smooth surface in Figure VII-19 is described by a Fresnel surface rather than the antenna measurements. This was done to insure that the surface roughness model matched the Fresnel smooth surface model for the smooth surface Q distribution.

The data plotted in Figure VII-19 were simply overlaid on the model predictions contained in Figures VII-20 and VII-21 in order to obtain the Q distributions that describe each surface roughness. The proper Q for each transmission angle was determined by the intersection of the antenna measurements and the model predictions. Table VII-6 contains the resulting Q distributions for all three surfaces.

The Q distributions contained in Table VII-6 were used to generate the plots in Chapter IV relating to surface roughness. Figure IV-21 describes the predicted response of the brightness temperature of soil to soil moisture for the three surface preparations. The general trend of decreasing soil moisture response with increasing roughness that is evident in Figure VII-18 is predicted. This can be explained in physical terms by simply interpreting the surface roughness model. For a perfectly smooth surface only energy that is incident on the surface from below at a particular angle is transmitted across

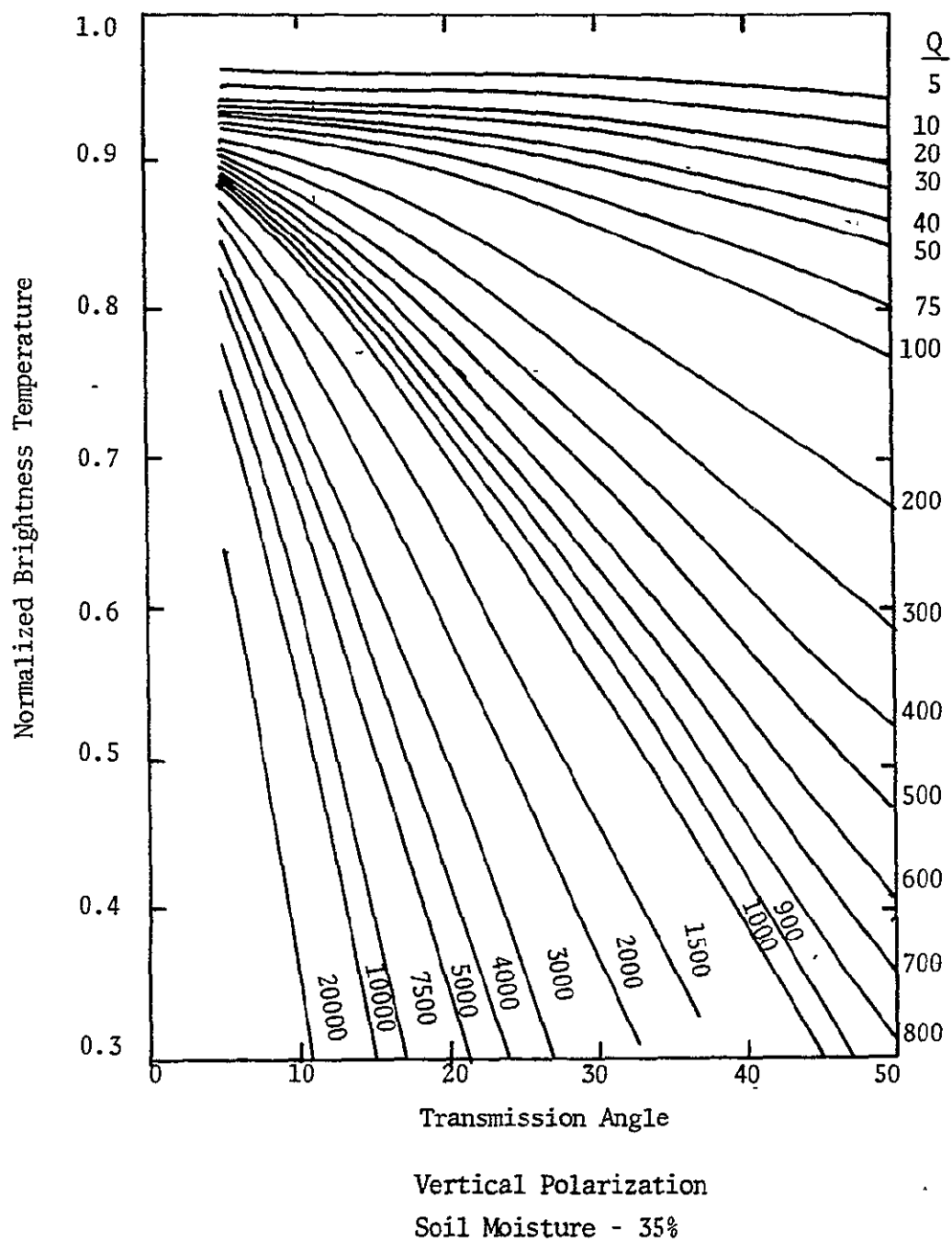
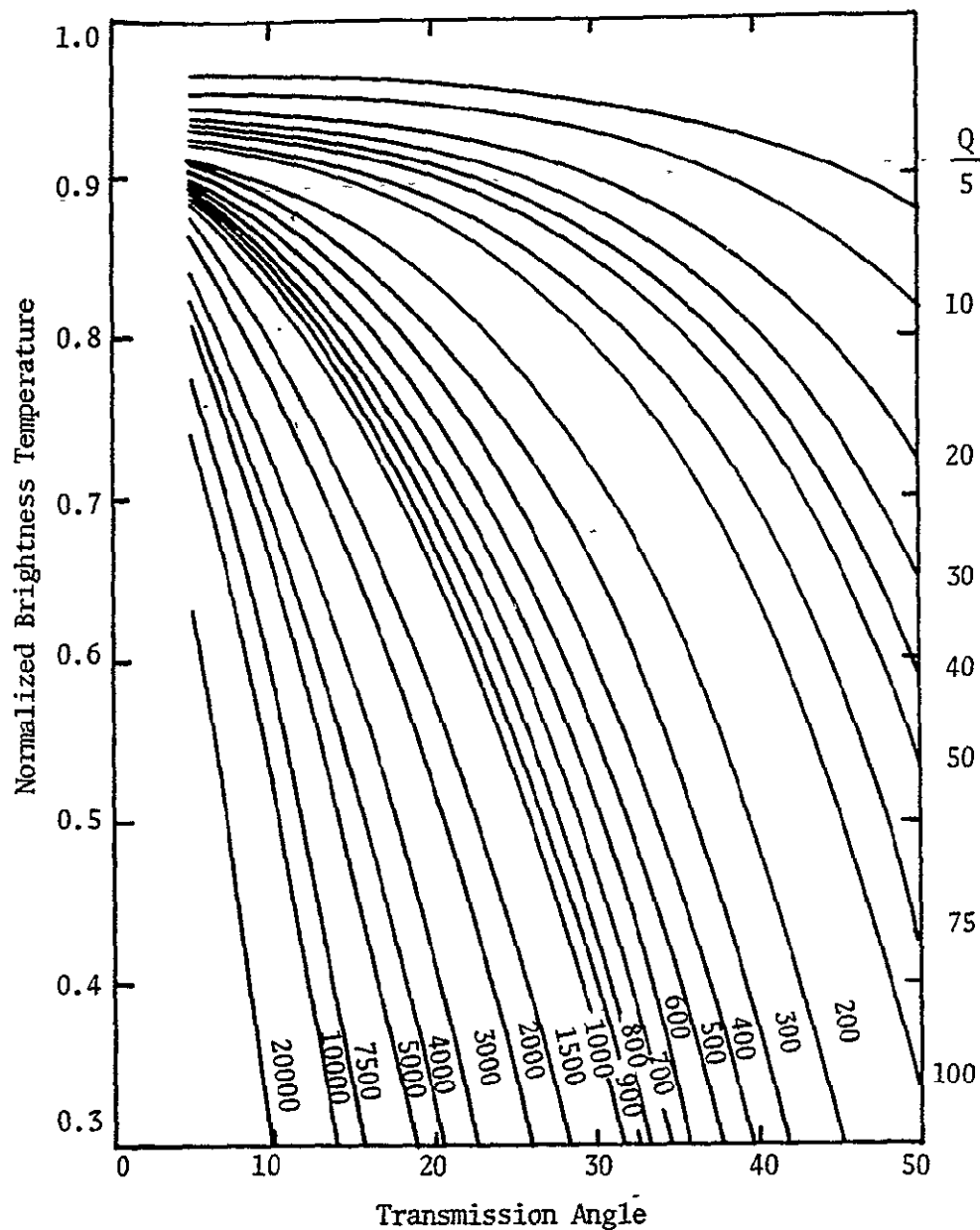


Figure VII-20. Vertically polarized normalized brightness temperature as a function of transmission angle and  $Q$ , calculated for 35% soil moisture.



Horizontal Polarization

Soil Moisture - 35%

Figure VII-21. Horizontally polarized normalized brightness temperature as a function of transmission angle and  $Q$ , calculated for 35% soil moisture.

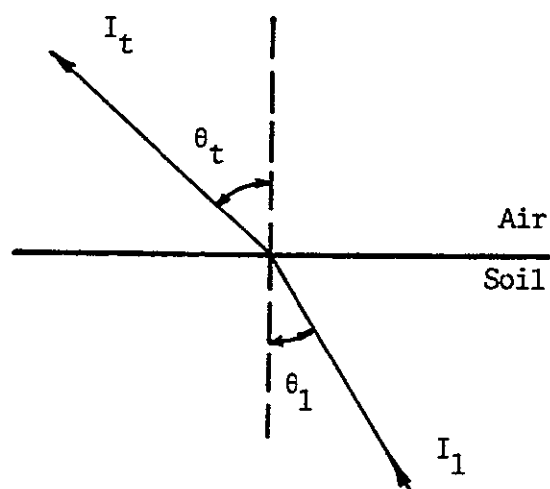
TABLE VII-6  
Roughness Parameter, Q, for Each Surface

Transmission Angle	Preparation					
	Smooth (Field CS)		Medium (Field CM)		Rough (Field CR)	
	Hor	Vert	Hor	Vert	Hor	Vert
5	-	-	19,524.0	19,000.0	13,774.0	13,923.0
10	9,375.0	9,375.0	5,642.0	5,486.0	3,680.0	3,900.0
20	1,942.0	2,166.0	1,166.0	1,313.0	738.0	980.0
30	638.0	820.0	380.0	494.0	265.0	381.0
35	386.0	529.0	224.0	336.0	164.0	266.0
40	239.0	355.0	143.0	222.0	97.0	188.0
50	84.0	166.0	54.2	108.0	34.0	100.0

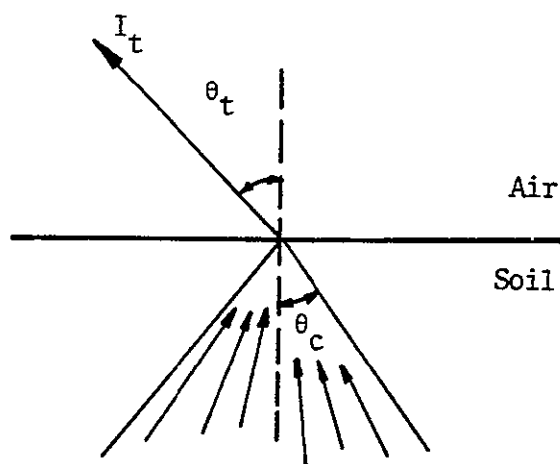
the surface. This is due to Snell's law of refraction. However, as the surface is roughened, the allowable cone of angles from which energy can be transmitted across the surface boundary widens. This is illustrated in Figure VII-22. The larger the cone below the surface, the more energy is available to go across the surface. Thus, as the surface gets rougher, the brightness temperature increases.

This effect is more pronounced for wet soil than for dry soil due to the shape of the brightness temperature curve as a function of transmission angle. This can be explained in terms of the transmission across a smooth surface. Figure VII-23 depicts the vertical brightness temperature of a smooth surface for various soil moistures. Any point on Figure VII-23 describes the brightness temperature of a perfectly smooth surface. For a rough surface a weighted integration must be performed over transmission angle from nadir to the angle defining the cone described above. Note that performing such an integration over the curves in Figure VII-23 from nadir to  $\theta_c$  will yield results that are proportionately larger than the smooth surface brightness temperature for very wet soil than for very dry soil. This is due to the compression of brightness temperature as a function of soil moisture at the higher transmission angles.

CS



(a) Smooth



Volume Radiation

(b) Rough

Figure VII-22. Graphical illustration of a physical interpretation of the effect of roughness on the emission from a soil surface.



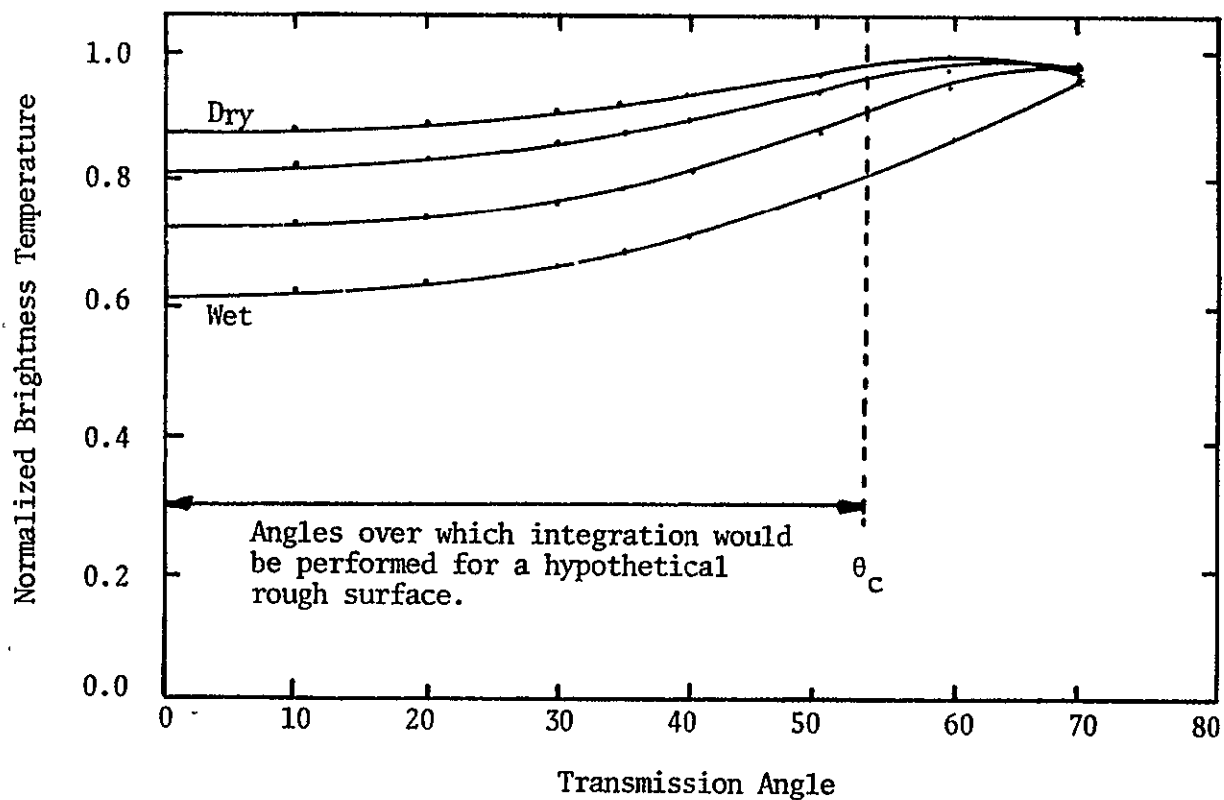


Figure VII-23. Illustration of the compression in the result of the integration effect (Figure VII-22) of a rough surface as the soil moisture changes from wet to dry.

At 10.6 GHz the "smooth" field (CS) appeared rough. As a result there is no smooth surface measurement for this frequency. This is demonstrated in Figure VII-24 for a transmission angle of  $20^\circ$ . The smooth and medium rough measurements group together while the rough measurements form a cluster with a slightly higher magnitude.

The scatter in the 10.6 GHz measurements in Figure VII-24 is not due entirely to system noise. The nominal standard deviation of the 10.6 GHz measurements was  $1.7^\circ\text{K}$  while for 1.4 GHz it was  $0.6^\circ\text{K}$ . Much of the scatter is due to inaccuracies in measuring the 0-1 cm soil moisture. This problem is addressed in more detail in the last section of this chapter where a soil moisture estimation procedure is discussed.

In the above discussion measurements at only  $20^\circ$  were presented. The soil moisture response for all three surface preparations at nadir is very similar to the response at  $20^\circ$ . However, as the transmission angle is increased beyond  $20^\circ$  to  $35^\circ$  and  $50^\circ$ , the emission tends to generally increase for all moistures and surfaces at vertical polarization, and generally decrease for horizontal polarization. However, the general effect of surface roughness is maintained. Figures VII-25 through VII-27 are plots of the linear regressions in Table VII-5. They demonstrate these effects at  $20^\circ$ ,  $35^\circ$  and  $50^\circ$ .

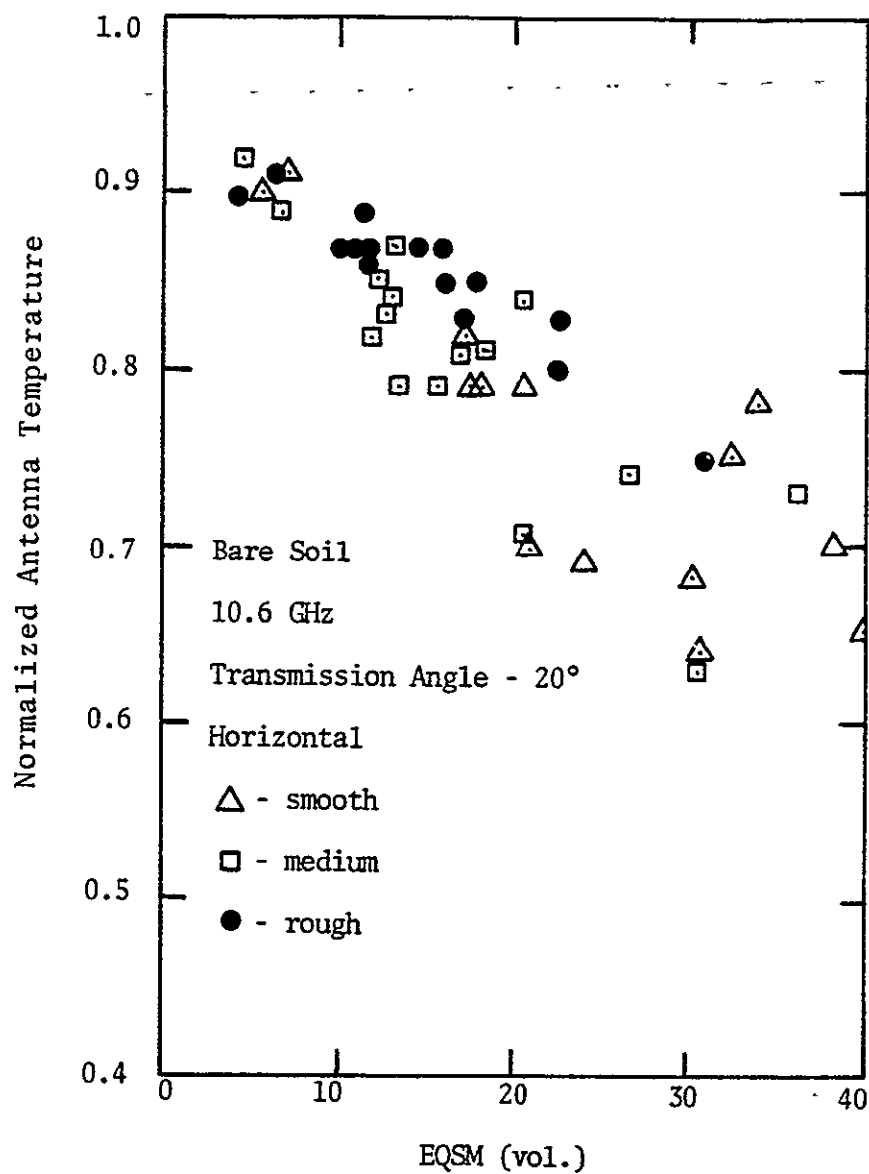
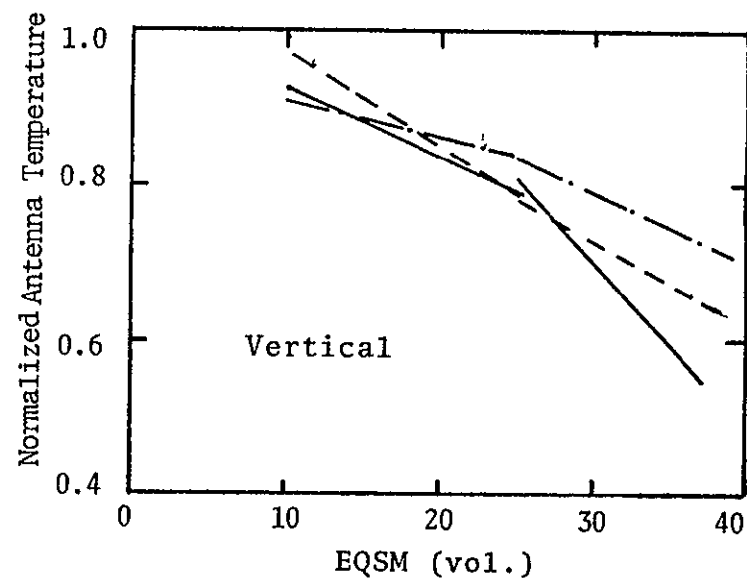
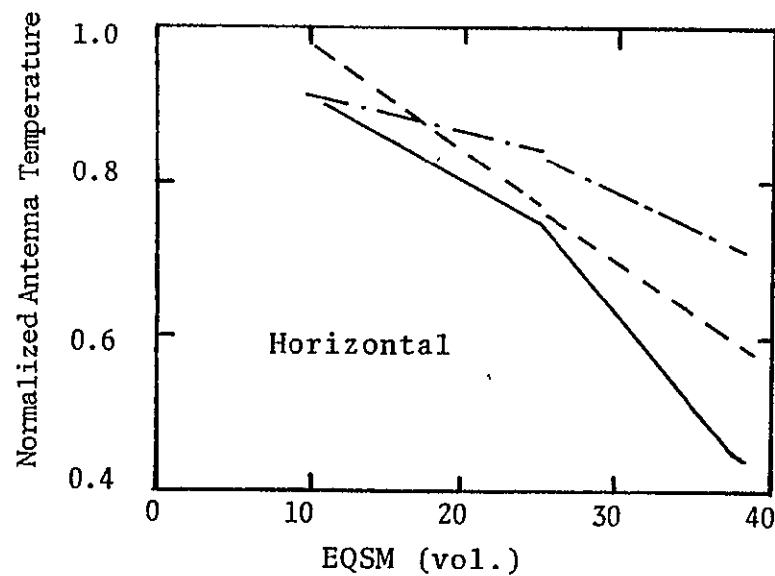


Figure VII-24. Horizontal 10.6 GHz antenna temperature measurements as a function of soil moisture for three surface conditions.



1.4 GHz

Transmission Angle -  $20^\circ$

— smooth

---- medium

-.- rough

Figure VII-25. Linear regression fits to 1.4 GHz antenna temperature measurements of bare soil as a function of soil moisture for three surface preparations.

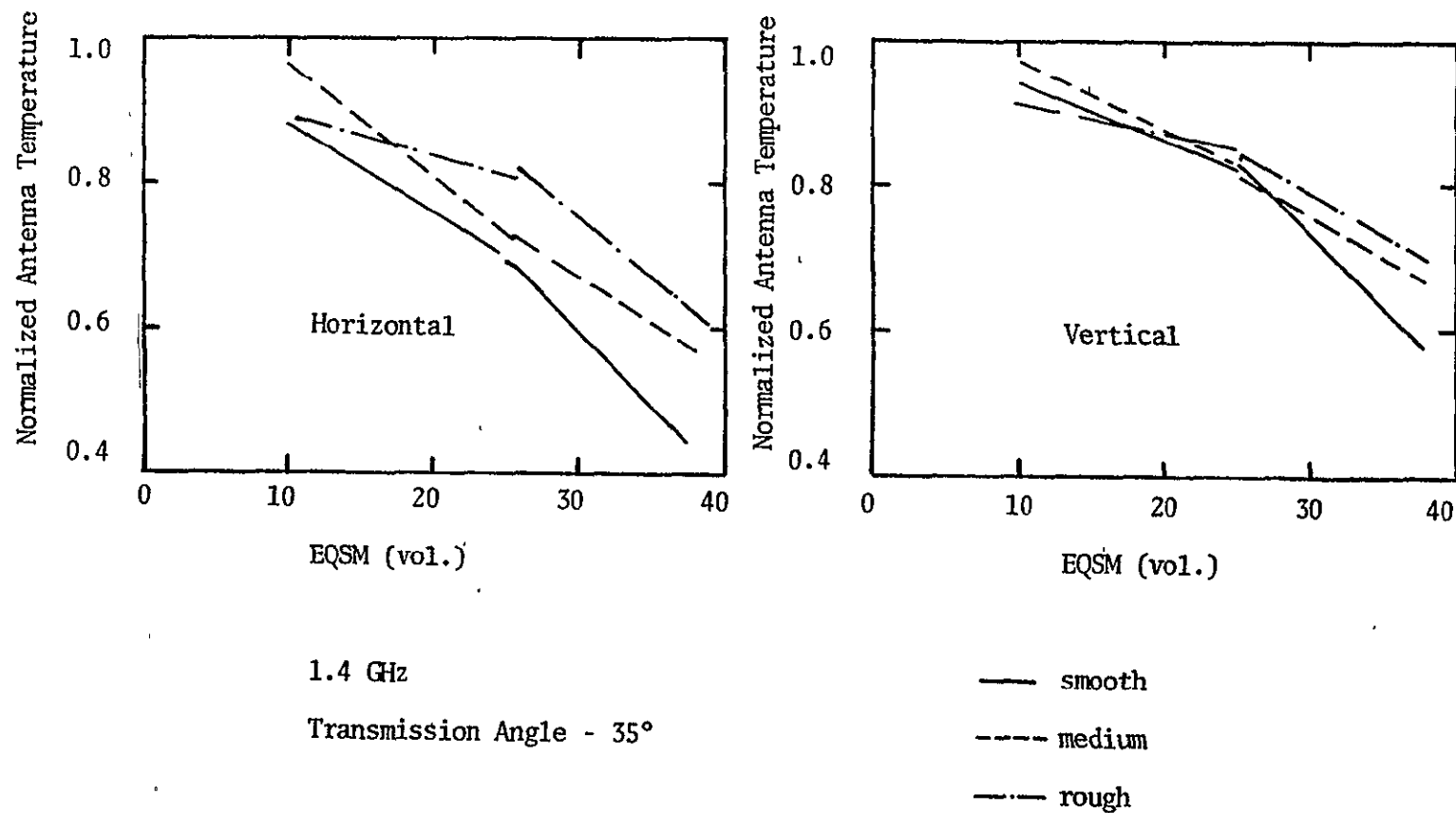
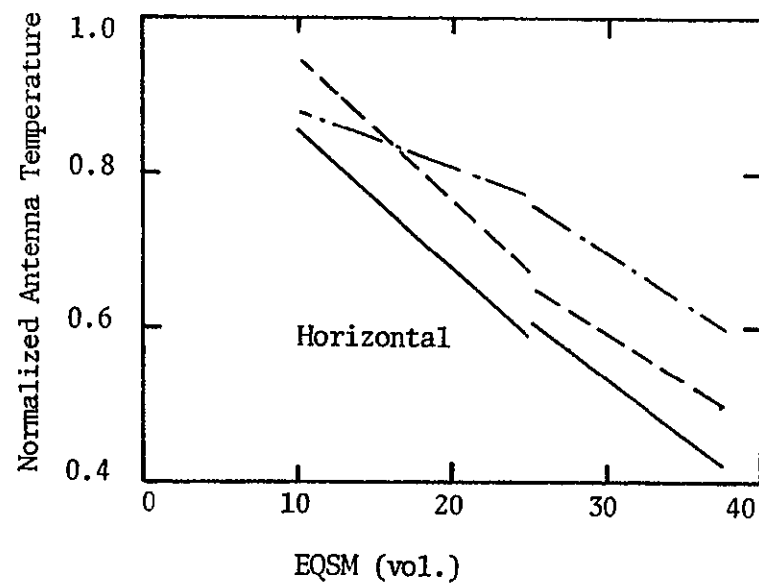
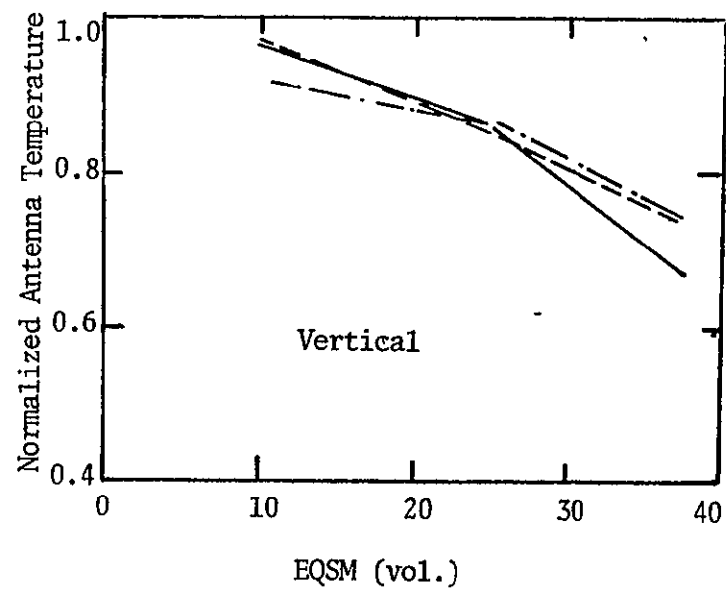


Figure VII-26. Linear regression fits to 1.4 GHz antenna temperature measurements of bare soil as a function of soil moisture for three surface preparations.



1.4 GHz

Transmission Angle -  $50^\circ$



— smooth

--- medium

-.- rough

Figure VII-27. Linear regression fits to 1.4 GHz antenna temperature measurements of bare soil as a function of soil moisture for three surface preparations.

Effect of row direction - It was seen in the paragraphs above that the effect of uniform roughness was to decrease the sensitivity of the antenna temperature measurements to soil moisture. The effects of row tillage on this response will now be addressed. Only the bare field is discussed at this time. The effects of vegetation are discussed in the next section.

The 1975 experimental plots were prepared using standard agricultural practices normally used in Phoenix, Arizona. As a result, the surface was actually a composite rough surface. The periodic row structure formed the large scale surface roughness. The average height and width of this row structure in field A, the bare field, was 20 cm and 95 cm, respectively.

The rms surface height deviations were not measured for the overlying small scale roughness. However, another parameter, the effective surface area per unit planar surface area [107] was measured. This value is a unitless quantity and was, on the average, 1.26 on the ridges and 1.15 in the furrows. This compares to an average of 1.85 for the bare medium rough 1974 field, CM, and an estimated value of between 1.0 and 1.2 for the smooth 1974 field, CS. The furrows were quite smooth in field A since the field was flood irrigated and the water ran in the furrows. As a result, one would expect the small scale

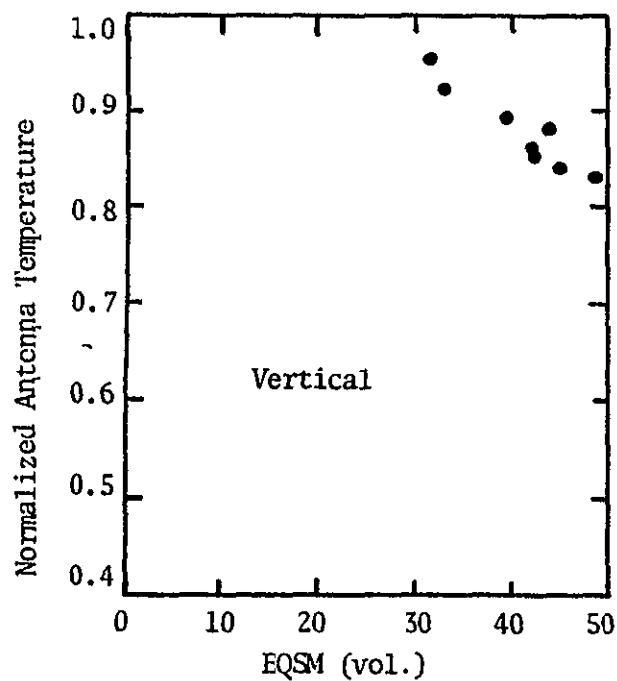
structure to have a rms surface height deviation that was somewhere in between the values for the 1974 smooth and medium rough fields.

A theoretical model for the emission from a composite surface is not discussed in this report. However, the results that were obtained with the uniform roughness model are very enlightening with respect to the 1975 row roughness measurements. The 1975 measurement set will not be analyzed in great detail, but the effect of the row structure on the change in emitted radiation due to changes in soil moisture will be pointed out. A general comparison will also be made between the 1974 and 1975 measurements sets. Measurements made at 1.4 GHz will be described first, then measurements made at 10.6 GHz will be briefly presented.

It was demonstrated for uniformly rough soil that the best response to soil moisture was obtained at low transmission angles. As a result, measurements at a transmission angle of  $20^\circ$  will be used to demonstrate the effects of row direction on the moisture dependence of antenna temperature measurements. Figures VII-28 through VII-32 demonstrate this effect at 1.4 GHz and a  $20^\circ$  transmission angle.

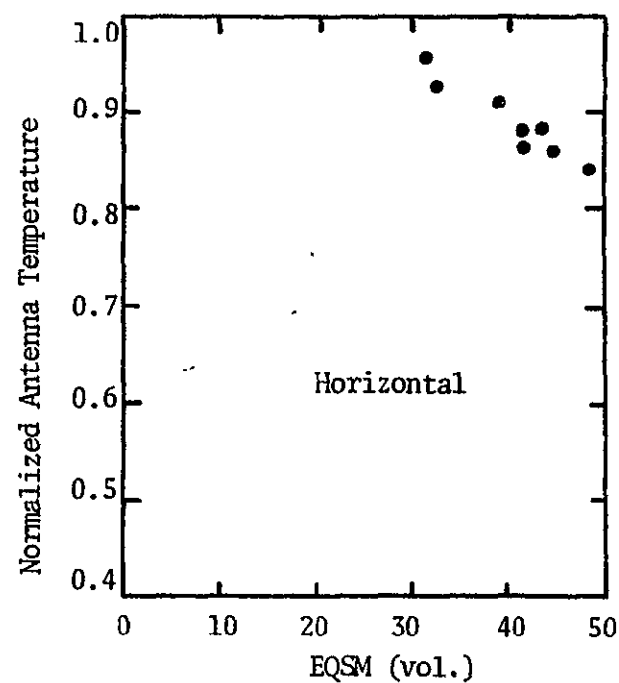
A moisture dependence is obviously retained for bare row tilled terrain, however, it is modified to a certain





1.4 GHz

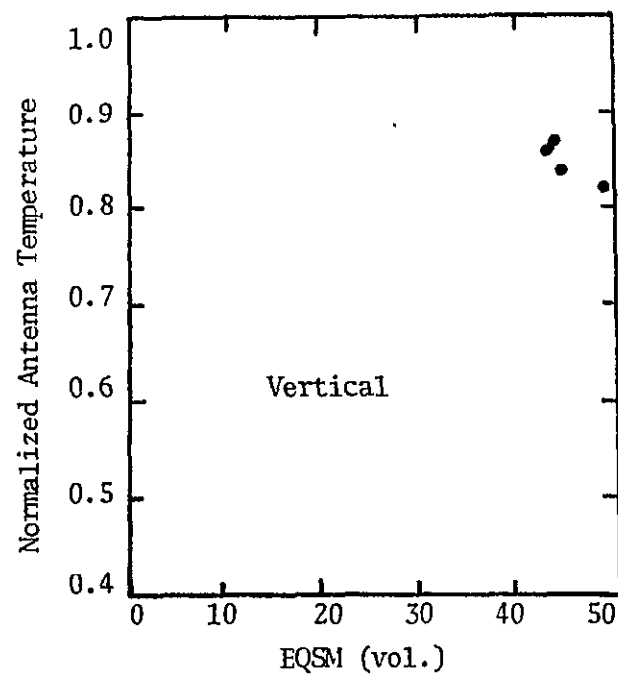
Field A - Bare



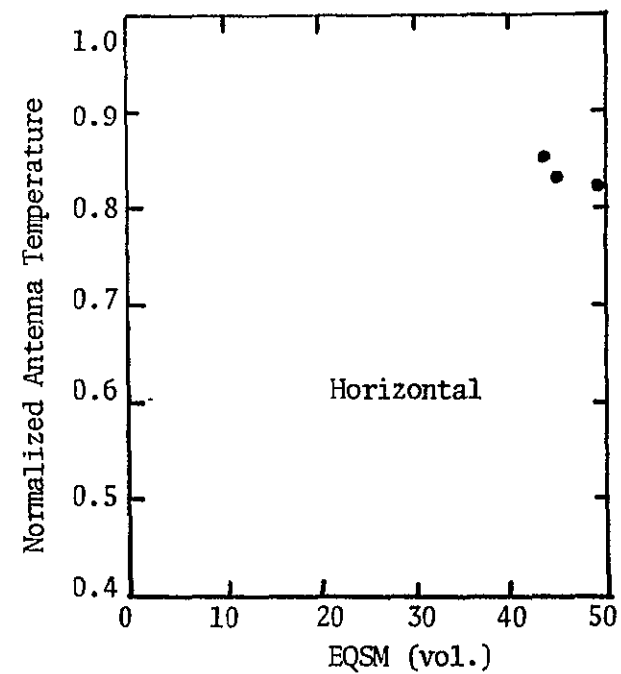
Transmission Angle -  $20^\circ$

Azimuth Angle -  $0^\circ$

Figure VII-28. 1.4 GHz antenna temperature measurements made at an azimuth angle of  $0^\circ$  with respect to the row direction, as a function of soil moisture.



1.4 GHz  
Field A - Bare



Transmission Angle -  $20^\circ$   
Azimuth Angle -  $30^\circ$

Figure VII-29. 1.4 GHz antenna temperature measurements made at an azimuth angle of  $30^\circ$  with respect to the row direction, as a function of soil moisture.

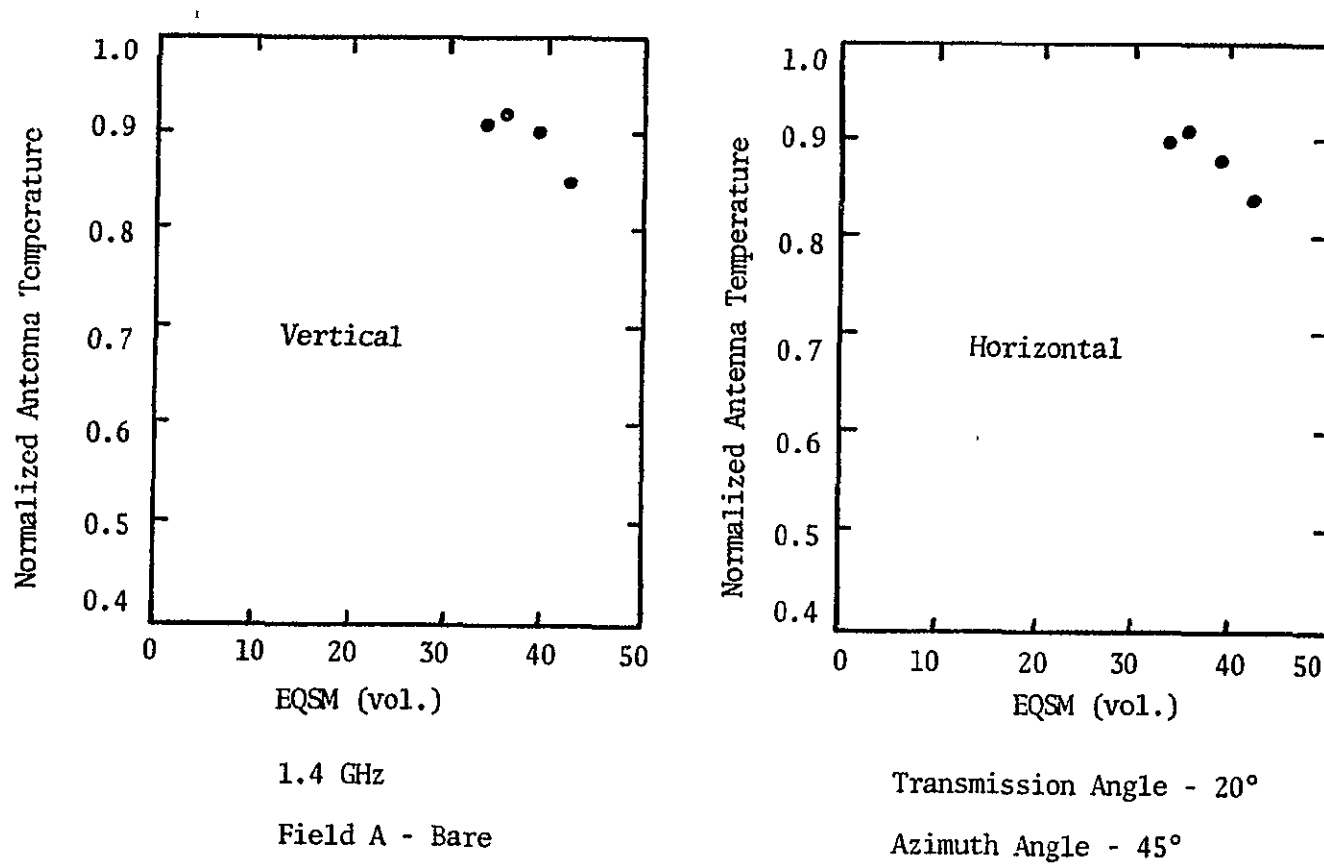
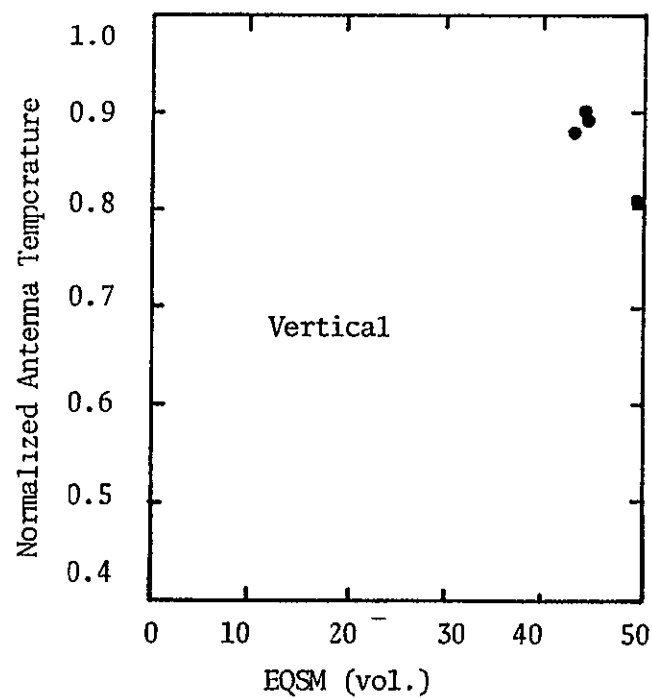
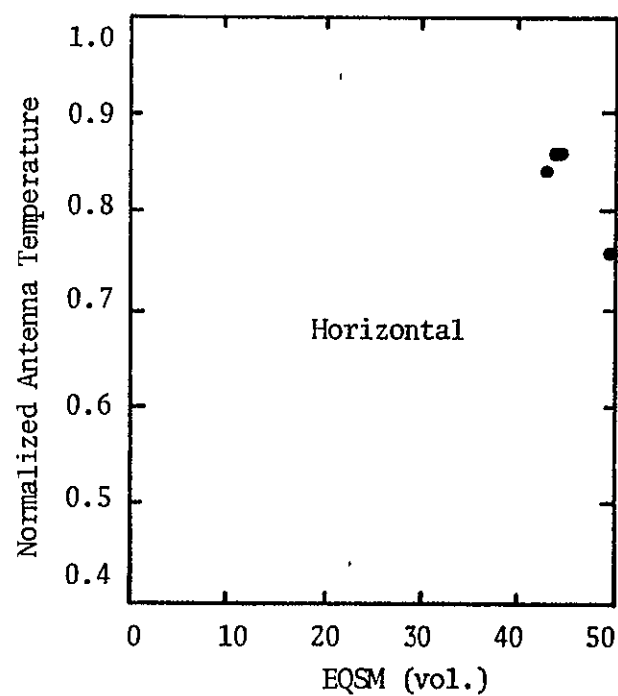


Figure VII-30. 1.4 GHz antenna temperature measurements made at an azimuth angle of 45° with respect to the row direction, as a function of soil moisture.



1.4 GHz

Field A - Bare



Transmission Angle -  $20^\circ$

Azimuth Angle -  $60^\circ$

Figure VII-31. 1.4 GHz antenna temperature measurements made at an azimuth angle of  $60^\circ$  with respect to the row direction as a function of soil moisture.

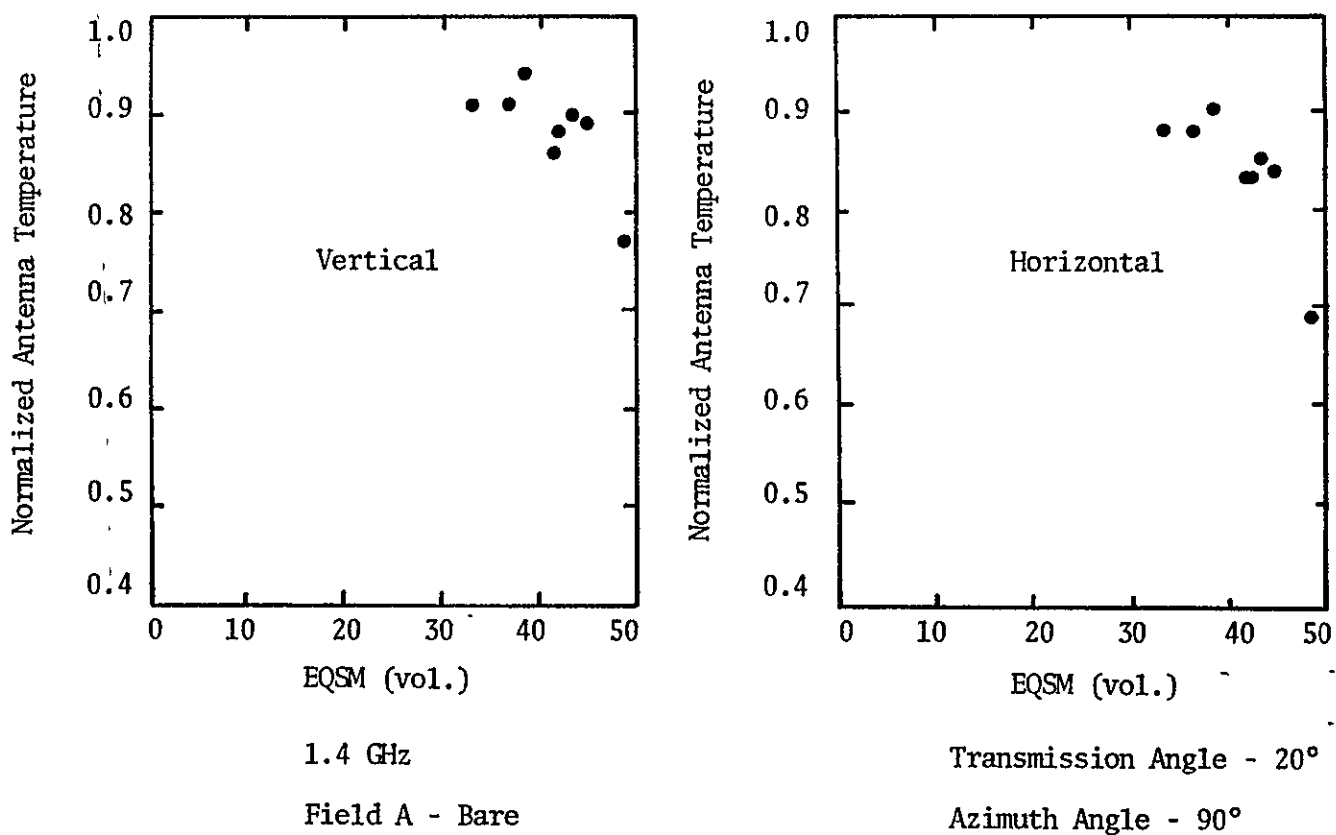


Figure VII-32. 1.4 GHz antenna temperature measurements made perpendicular to the row direction as a function of soil moisture.

degree from the response seen for a uniformly rough field. Before discussing this modification, the difference in the magnitude of the soil moisture parameter between the 1974 and 1975 measurements will be explained. It is obvious from Figures VII-28 through VII-32 that the volumetric equivalent soil moistures for the 1975 data set are much larger than those of the 1974 data set. This was not expected since both data sets are acquired over the same soil type, Miller clay. The difference is a result of the soil bulk density measurements. Table VII-7 demonstrates that the bulk density measurements made in 1975 were considerably larger than those made in 1974. The bulk density measurements differ most likely as a result of the difficulty in making the measurement and inconsistencies in the measurement techniques used in 1974 and 1975.

Soil moisture was initially measured on a weight basis. It was converted to a volumetric basis using (II-7) and the bulk density measurements contained in Table VII-7. Since the bulk density measurements do not compare from year to year, then the volumetric soil moisture calculations do not compare. The gravimetric soil moisture measurements, however, do compare between the 1974 and 1975 measurements. This can be demonstrated by comparing antenna temperature measured during each of the two experiments on a soil moisture by weight basis. This is reasonable since the experimental plots consisted

TABLE VII-7

## Soil Bulk Density Measurements

Depth (cm)	1974 Experiment							1975 Experiment
	Fields A and B			Field C			Field D	Fields A and B
	Smooth	Medium	Rough	Smooth	Medium	Rough		
0-2	1.15	1.06	1.05	1.55	1.27	1.32	1.06	1.64
2-5	1.22	1.11	1.07	1.28	1.12	1.07	1.11	1.65
5-9	1.34	1.22	1.07	1.26	1.17	1.07	1.22	1.63
9-15	1.38	1.33	1.06	1.23	1.20	1.06	1.33	1.77

of the same soil type during both years. Figure VII-33 contains measurements from both 1974 and 1975. By removing the inconsistency due to the bulk density measurements the equivalent soil moisture axis becomes consistent between measurement sets.

It can be seen in Figure VII-33 that the measurements acquired in 1975 over the row tilled field are considerably higher than those acquired over the uniformly rough field. This magnitude increase cannot be explained at the present time. However, since the 1975 data plotted in Figure VII-33 were measured parallel to the rows, the soil moisture response was expected to be comparable to the response obtained for a uniformly rough field. This can be confirmed by comparing the slope of a best fit straight line drawn through the 1975 measurements to the slopes of lines drawn through the 1974 bare field measurements. Table VII-8 contains the results of linear least squares regression fits to these data. Comparing slopes it can be seen that the bare row tilled field does respond to moisture in the same manner as would a uniformly rough field with a rms surface height deviation somewhere between the 1974 medium rough field (2.6 cm) and the 1975 rough field (4.3 cm).

Neglecting the overall magnitude shift between the 1974 and 1975 measurements, the effects of row direction



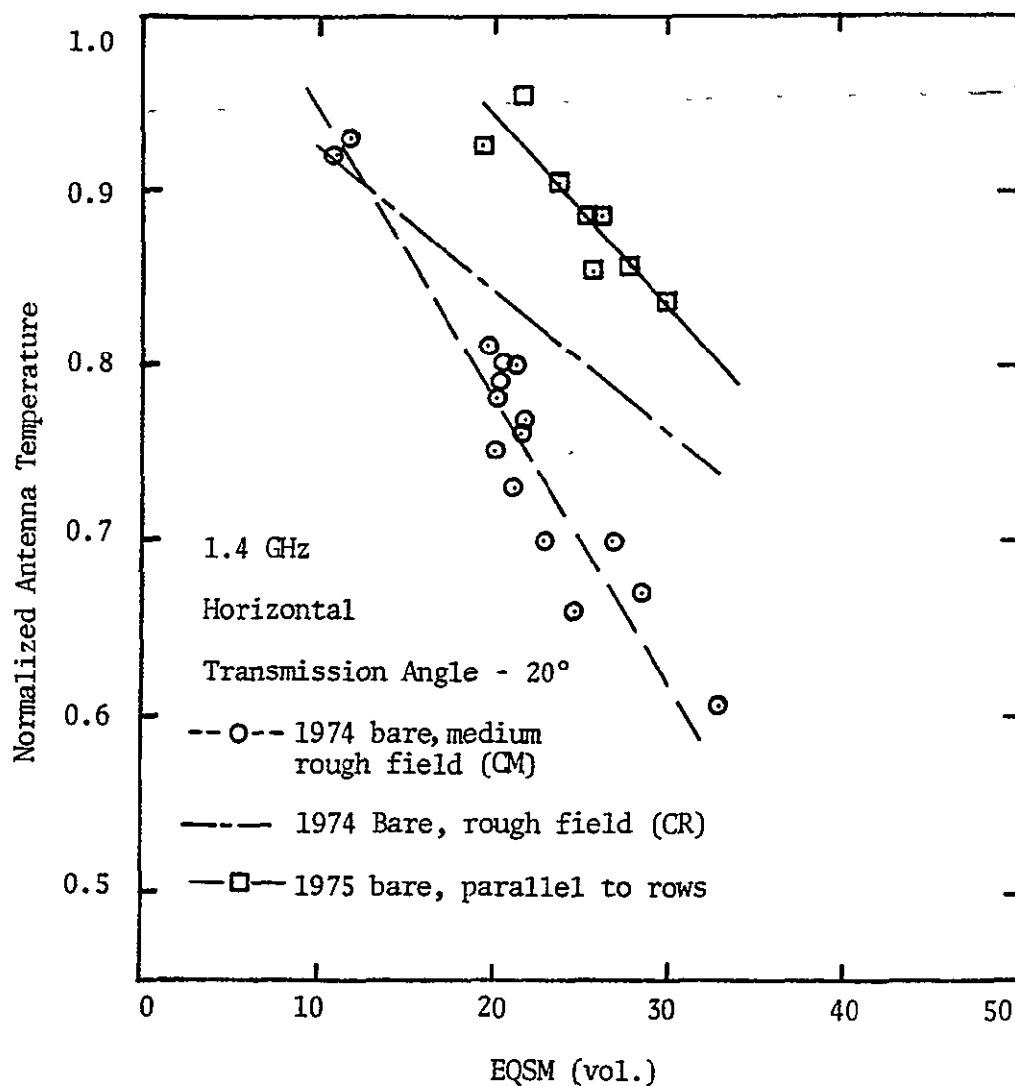


Figure VII-33. Comparison of linear regression fits to 1974 measurements of uniformly rough, bare surfaces to 1975 measurements of row tilled bare surfaces.

TABLE VII-8

Comparison Between 1974 and 1975 Measured Response to  
Soil Moisture by Weight at a Transmission Angle of 20°

Field	Slope* m	Y Intercept* b	Regression Coefficient* r
(1975) A Parallel to rows	-0.0111	1.161	0.88
(1974) CS Smooth			
EQSM (WT) < 20	-0.0162	1.0527	0.89
EQSM (WT) > 20	-0.0174	0.9992	0.64
(1974) CM Medium Rough	-0.0168	1.116	0.93
(1974) CR Rough	-0.0084	1.0088	0.88

\*Normalized Antenna Temperature (NAT) =  $m \cdot \text{EQSM}(\text{WT}) + b$

on the response to moisture changes will now be discussed. By comparing Figures VII-28 through VII-32 it can be seen that at 1.4 GHz a dependence on soil moisture is maintained for all azimuth angles with respect to the row direction, but that as the azimuth angle increases to  $90^\circ$  the scatter in the measurements increases considerably. In addition, the row tillage causes the effects of antenna beamwidth to become much more severe.

In Chapter VI two effects of beamwidth were considered, polarization mixing and transmission angle averaging. In the analysis in which the effects of transmission angle averaging were discussed, the surface was assumed to be such that the average mean surface height formed a horizontal plane. In this case the range of transmission angles over which the antenna collected energy was simply defined by the antenna beamwidth. However, for a surface containing large scale periodic undulations, the transmission angles over which the antenna collects energy is defined by the surface undulations and the direction from which the antenna "views" these undulations. When measurements are made parallel to the rows the transmission angles over which the antenna averaging occurs are the same as for a horizontally plane surface. However, as the azimuth angle is increased, the range of transmission angles over which averaging occurs increases. In addition,

.

beamwidth averaging is not uniform across these angles, but is weighted by the distribution of surface slopes that falls within the antenna beamwidth.

This can be visualized by intersecting the surface with a vertical plane and plotting the distribution of surface slopes that would occur on this intersection. As the plane is rotated with respect to the surface row direction, the surface slope distribution changes from no slope, to distributions that become more heavily weighted at larger slopes. This is demonstrated in Figure VII-34. These slope distributions define the distribution of transmission angles over which the antenna averages. The effect of this phenomenon can be demonstrated using the measurements contained in Figures VII-28 through VII-32 by comparing the general characteristics of these plots to the characteristics of the measurements made over the uniform surfaces.

It was demonstrated in Figures VII-25 through VII-27 that for a uniformly rough field the vertical antenna temperature measurements generally increase as the transmission angle is increased and the horizontal measurements generally decrease. This same phenomena occurs for the row tilled surface as the azimuth angle, with respect to the row direction, is increased. Increasing the azimuth angle effectively increases the transmission angle at which the surface slope distribution peaks. In Figure

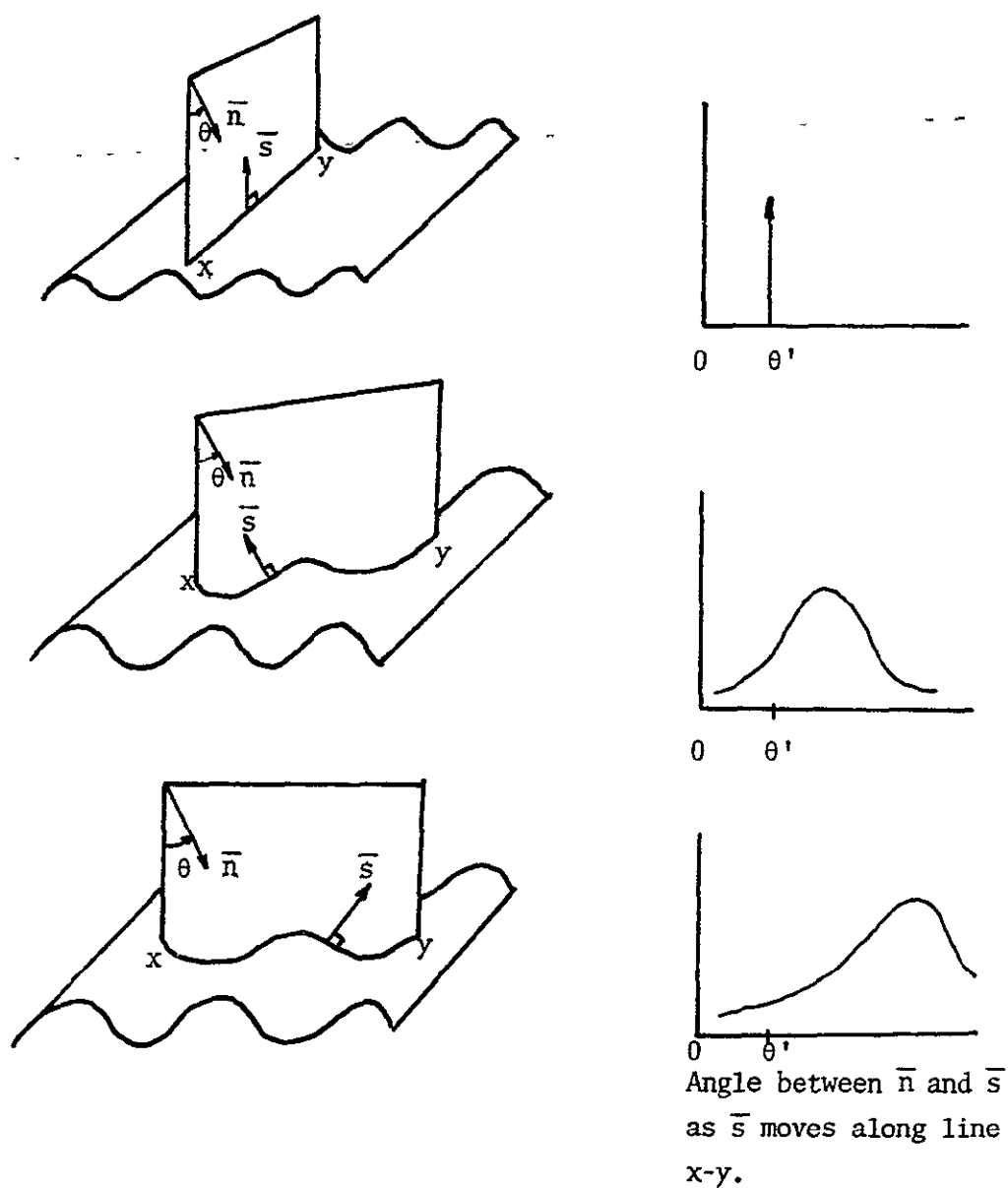
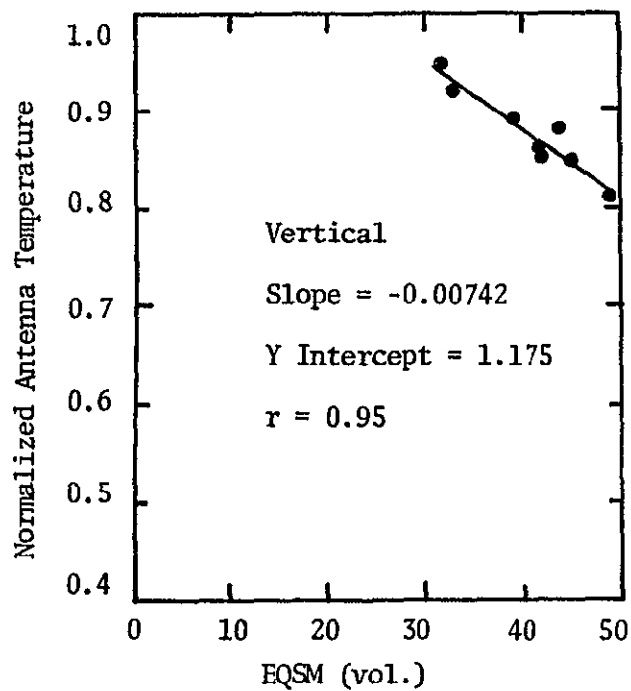


Figure VII-34. Illustration of how the distribution of transmission angles from which an antenna receives radiation changes as the azimuth angle between the plane of transmission and row direction is varied.

VII-28 the vertical and horizontal measurements are very nearly the same magnitude. However, as the azimuth angle increases, the vertically polarized measurements become increasingly larger than the horizontally polarized measurements (Figure VII-32).

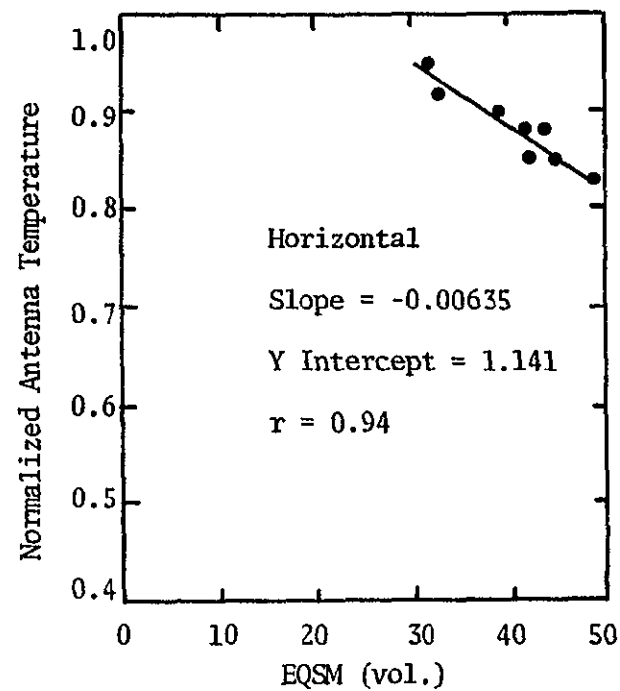
The phenomenon described above can be used to demonstrate that viewing a row tilled field parallel to the rows is approximately the same as viewing a uniformly roughened field with the same rms surface height deviations as is superimposed on the row structure. Figures VII-35 through VII-37 are plots of normalized antenna measurements of the bare field made parallel to the rows at three different transmission angles. They behave in the same manner as the corresponding measurements of the uniformly roughened fields (Figures VII-25 through VII-27). As the transmission angle is increased, the vertical measurements generally increase and the horizontal measurements generally decrease. Also, the sensitivity to moisture decreases with transmission angle for vertical polarization and increases for horizontal polarizations as demonstrated for uniform rough fields in Figure VII-15. This is evidenced by the slope of linear least squares regression lines.

In the discussion above the effects of transmission angle averaging due to the antenna beamwidth were discussed, but the effect of polarization mixing was not considered.



1.4 GHz

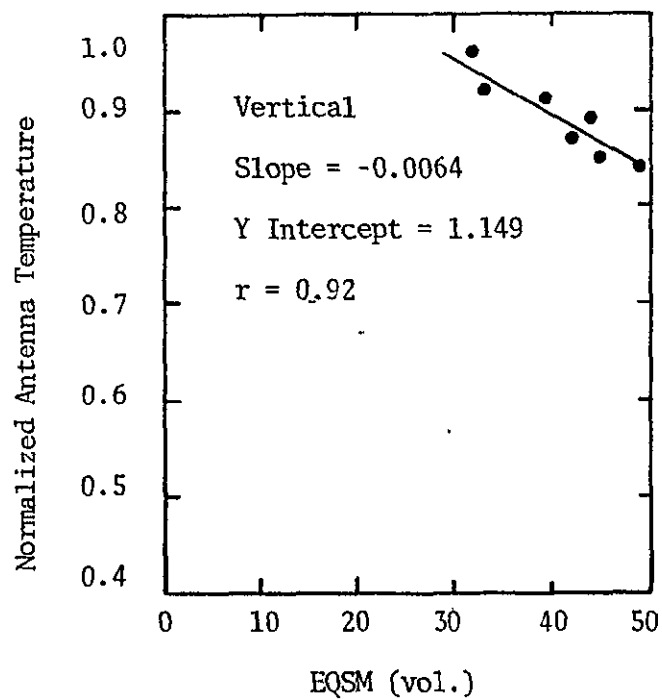
Field A - Bare



Transmission Angle -  $20^\circ$

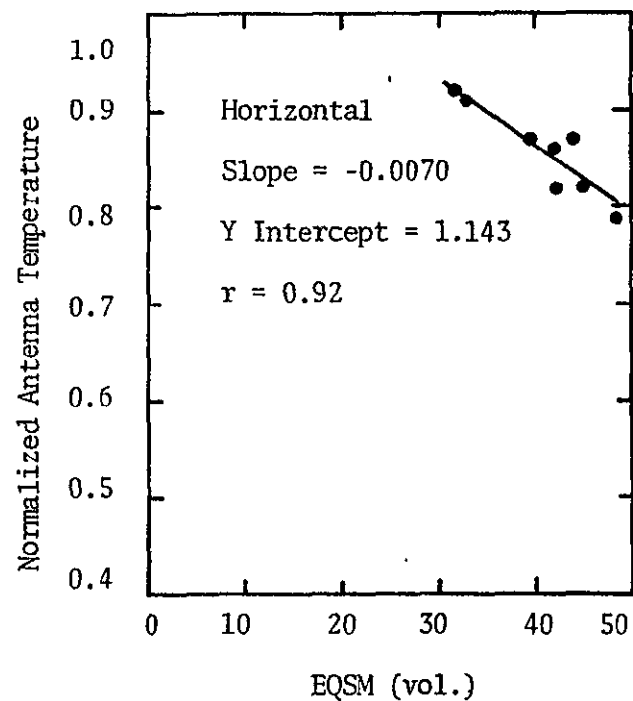
Parallel to Rows

Figure VII-35. 1.4 GHz antenna temperature measurements made parallel to the row direction at  $20^\circ$  as a function of soil moisture.



1.4 GHz

Field A - Bare

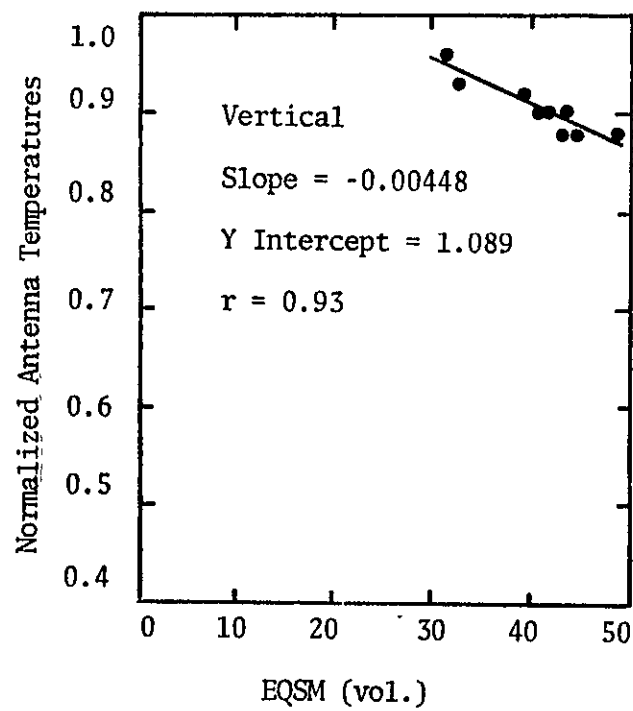


Transmission Angle -  $35^\circ$

Parallel to Rows

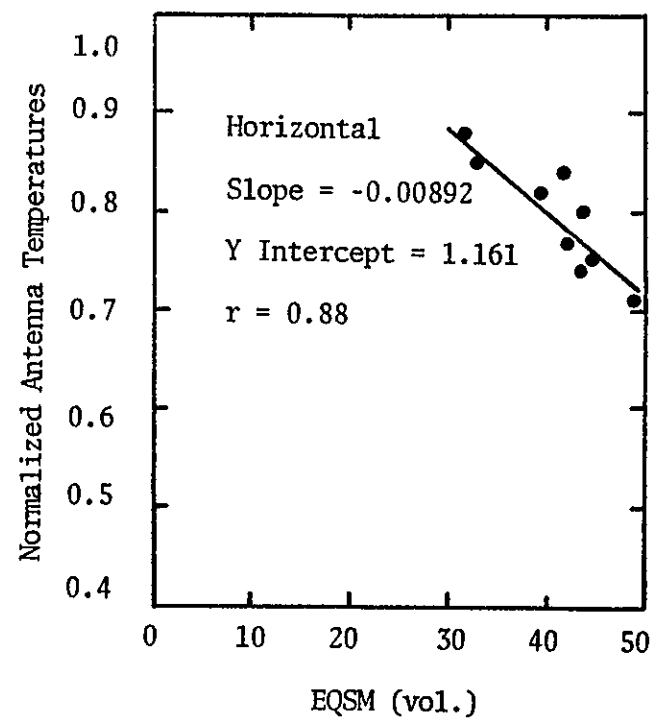
Figure VII-36. 1.4 GHz antenna temperature measurements made parallel to the row direction at  $35^\circ$  as a function of soil moisture.





1.4 GHz

Field A - Bare

Transmission Angle -  $50^\circ$ 

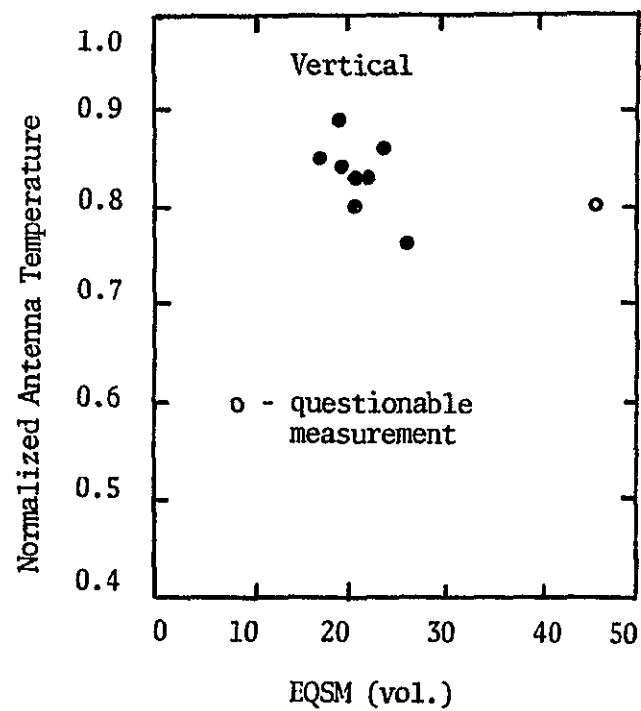
Parallel to Rows

Figure VII-37. 1.4 GHz antenna temperature measurements made parallel to the row direction at  $50^\circ$  as a function of soil moisture.

For a row tilled field the effects of polarization mixing due to the antenna beamwidth can be much more severe than would occur for a generally flat surface.

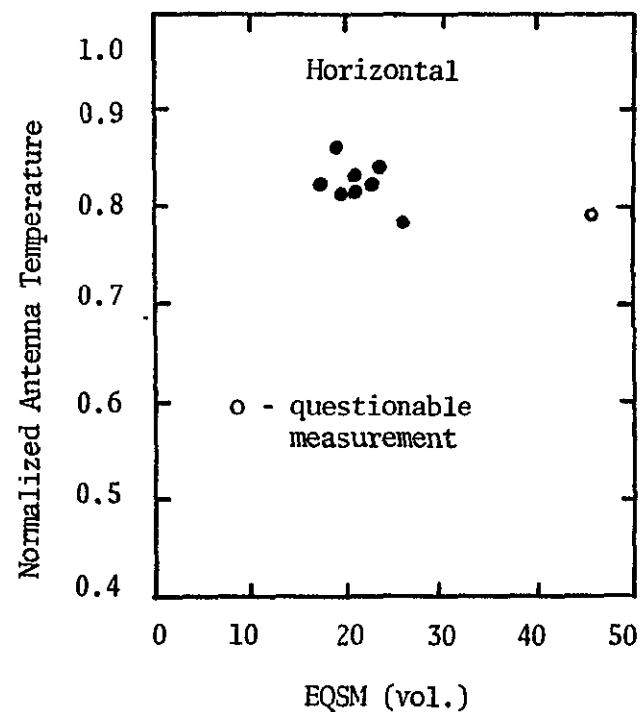
In analyzing the effects of polarization mixing in Chapter VI, the emission from the surface was assumed to be constant across the surface area viewed by the antenna. For a surface with no large scale surface undulations this assumption is not too unreasonable since the emission across the area viewed by the antenna only changes as a result of the angular variations over the angle range defined by the antenna beamwidth. However, for a surface with large scale undulations, the radiation emitted from the area viewed by the antenna is modulated as a result of angular variations due to the surface slope distribution within the antenna footprint. Since this angular variation will generally be much greater than the angular variation that results from the antenna beamwidth, the effects of polarization mixing can be severe and will depend on the orientation of the antenna with respect to the row direction, even when the antenna is viewing the surface at nadir.

Measurements made at 10.6 GHz have not been discussed thus far. However, the comments made in the discussion above also apply to the 10.6 GHz measurements, except that the small scale surface height variations appear much rougher at the 10.6 GHz wavelength. Figures VII-38 and VII-39 are plots of 10.6 GHz measurements made in



10.6 GHz

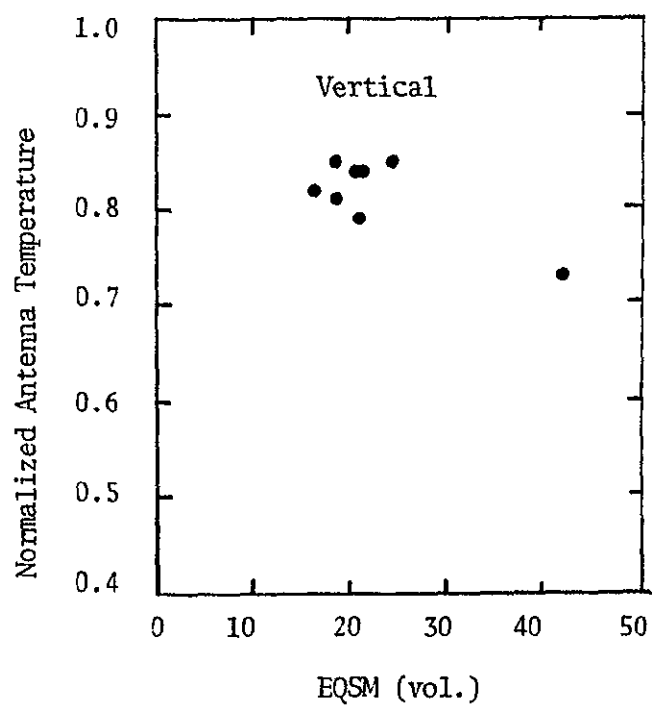
Field A - Bare



Transmission Angle -  $20^\circ$

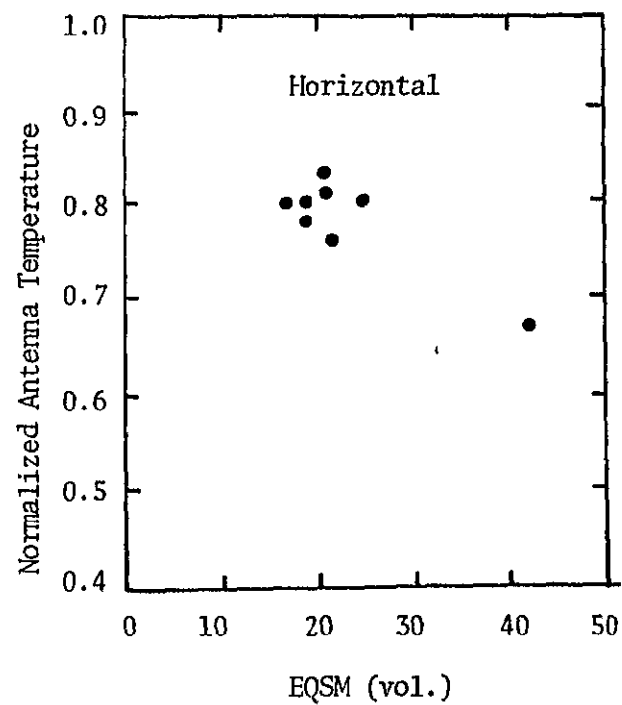
Parallel to Rows

Figure VII-38. 10.6 GHz antenna temperature measurements made parallel to the row direction as a function of soil moisture.



10.6 GHz

Field A - Bare



Transmission Angle - 20°

Perpendicular to Rows

Figure VII-39. 10.6 GHz antenna temperature measurements made perpendicular to the row direction as a function of soil moisture.

1975. As with the 1.4 GHz measurements, the moisture sensitivity demonstrated in Figure VII-38 (measurements parallel to the rows) is approximately the same as that exhibited in Figure VII-24 for the smooth and medium rough fields of 1974. Also the magnitude of the vertical and horizontal measurements made parallel to the rows at a  $20^\circ$  transmission angle are about the same (Figure VII-38). In Figure VII-39 (measurements perpendicular to the rows), the vertical measurements are higher than the horizontal measurements. This was expected since the antenna is averaging over predominately larger transmission angles when viewing the rows at an azimuth angle of  $90^\circ$ . In addition, the moisture sensitivity is reduced as would be expected.

It should be noted that some of the scatter in the 1975 10.6 GHz measurements is due to a hardware problem. The standard deviations of these measurements ranged from  $1.7^\circ\text{K}$  to  $3.5^\circ\text{K}$ . The lower value of  $1.7^\circ\text{K}$  is the standard deviation that is normally observed when the system is operating properly.

#### Effect of Vegetation

Measurements of vegetation canopies were made during both the 1974 and 1975 measurements program. A uniform cover of vegetation was planted in 1974, while a row

canopy was planted in 1975. The effect of uniform and row planted vegetation will be described below.

Uniform vegetation cover - In 1974 vegetation was uniformly planted in fields A and B. The average height of the vegetation in the smooth section of field A was 188 cm, and in the smooth section of field B it was 125 cm. The average plant moisture in both fields was approximately 63 percent. Since the average volumetric density [107] of the vegetation (a unitless quantity) in each of these fields was approximately one percent, the vegetation height-density products were 1.88 cm and 1.25 cm in fields A and B respectively. As expected from the results of the vegetation model presented in Figure IV-27, the vegetation effectively masks the soil emission at 10.6 GHz for these two fields. This is demonstrated in Figure VII-40.

Figures VII-41 and VII-42 demonstrate the effect of the vegetation in field B on the soil emission at 1.4 GHz for transmission angles of 20° and 35°. There is only a small effect. It appears that the emission is attenuated slightly for moistures below 20 percent EQSM and amplified slightly for moistures above 20 percent EQSM. This cannot be fully confirmed since there is only one measurement above 20 percent EQSM. However, at a transmission angle of 50° all of the 1.4 GHz measurements are increased. This is demonstrated in Figure VII-43.

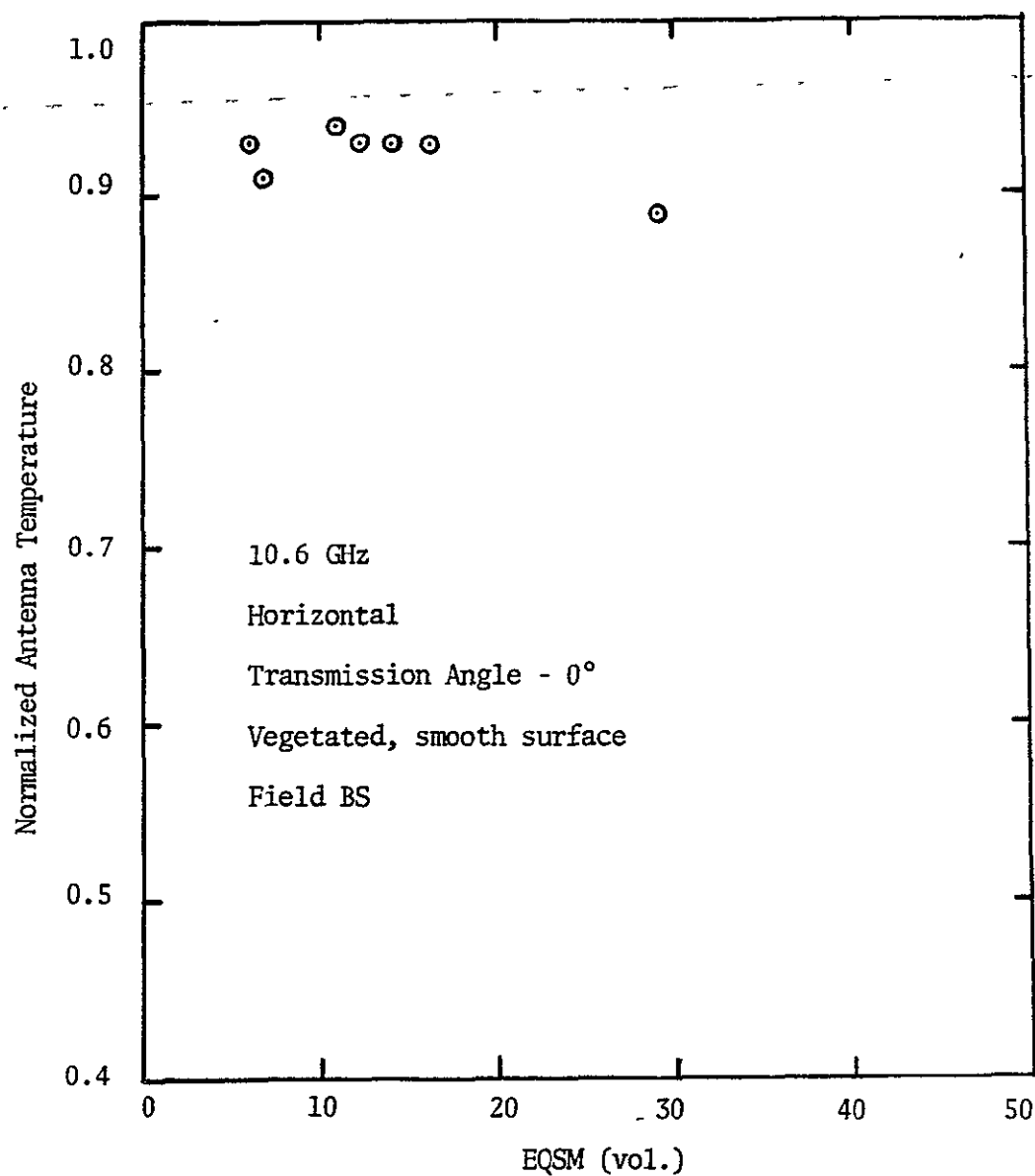


Figure VII-40. Horizontal 10.6 GHz antenna temperature measurements of a vegetated smooth surface as a function of soil moisture.

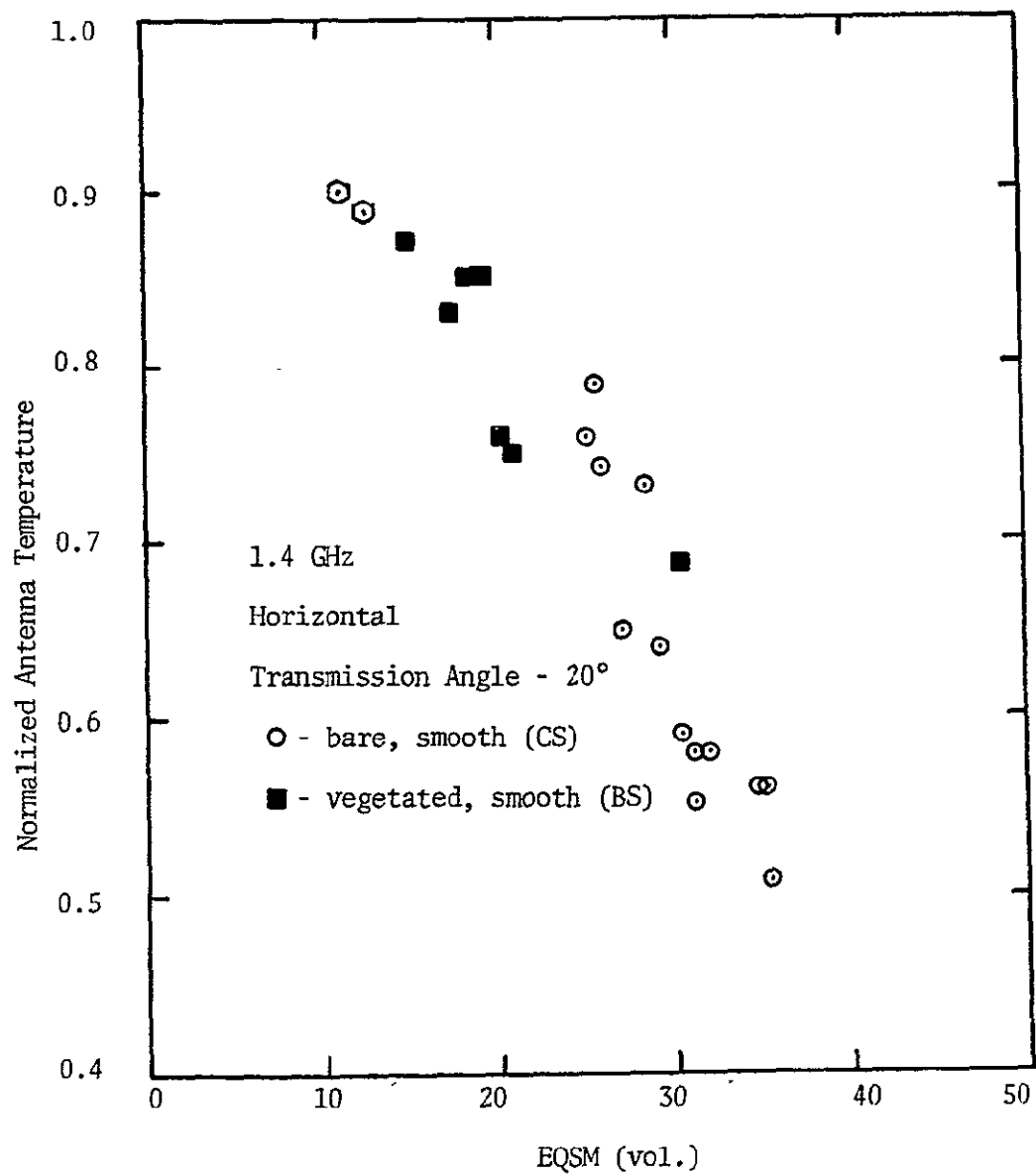


Figure VII-41. Comparison of bare and vegetated 1.4 GHz measurements made as a function of soil moisture at a 20° transmission angle.



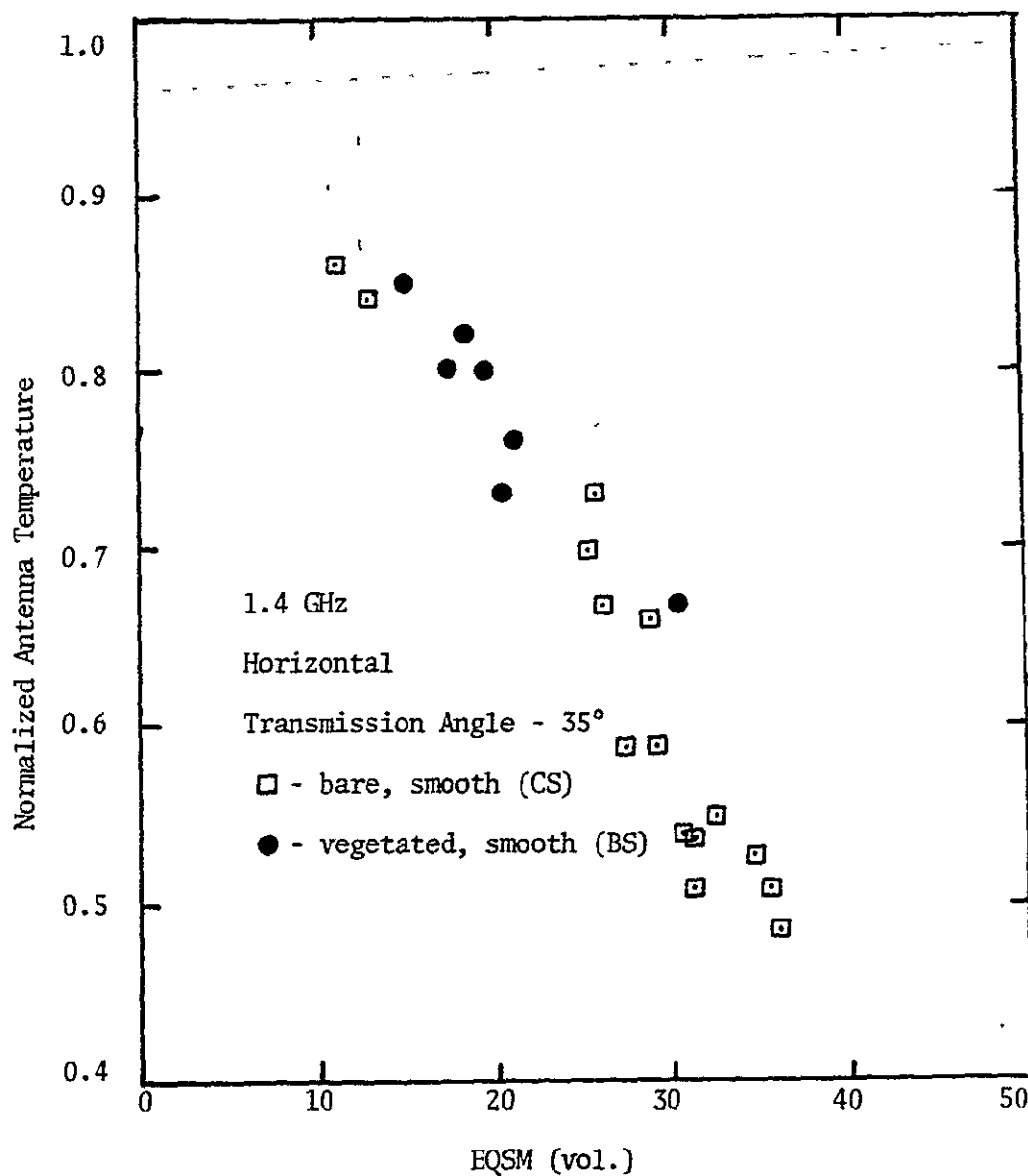


Figure VII-42. Comparison of bare and vegetated 1.4 GHz measurements made as a function of soil moisture at a 35° transmission angle.

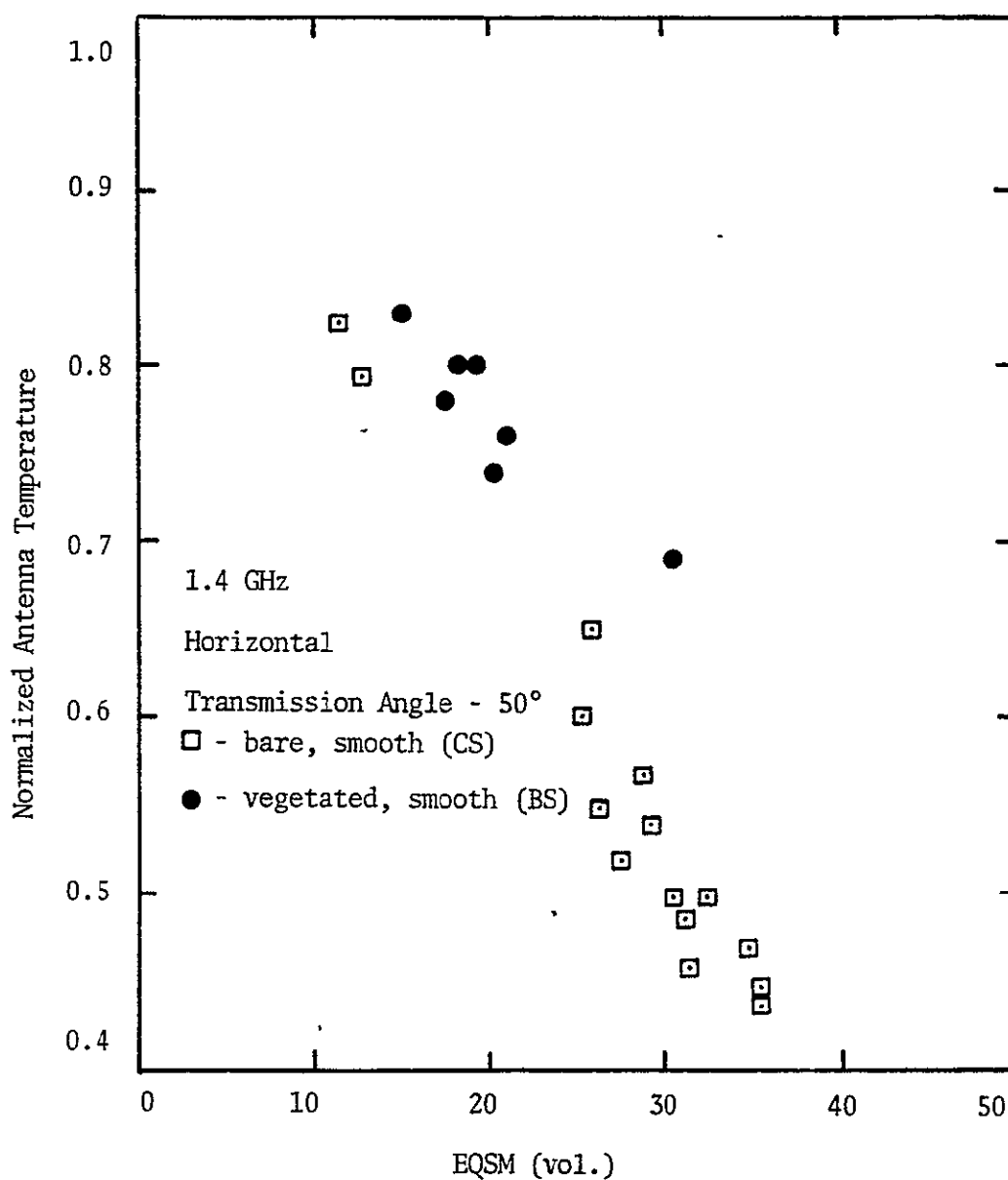


Figure VII-43. Comparison of bare and vegetated 1.4 GHz measurements made as a function of soil moisture at a 50° transmission angle.

The above result indicates that as the vegetation height-density product is increased, the emission from the soil vegetation scene at 1.4 GHz increases. This is confirmed by comparing 1.4 GHz measurements of the smooth section of field A to the smooth section of field B. Figure VII-44 and VII-45 demonstrate that even at a transmission angle of  $20^\circ$ , a vegetation height-density product increase from 1.25 cm to 1.88 cm increases the emission at both vertical and horizontal polarizations.

Row vegetation cover - Field B of the 1975 experimental plot was row planted in cotton that had an average height of 61 cm, an average plant moisture content of 73 percent, and an average volumetric density of 0.23 percent. As a result, the vegetation height-density product was 0.14 cm.

Figures VII-46 and VII-47 demonstrate the effect of this vegetation cover for measurements made parallel and perpendicular to the rows at 10.6 GHz. These figures demonstrate that the soil moisture dependence is greatly reduced from the bare soil dependence. A comparison of these figures demonstrate that the measurements made parallel to the rows are larger than those made perpendicular to the rows. The row vegetation model predicted that the emission should be reduced in going from parallel to the rows to perpendicular to the rows. However, this model did not take into account the row structure

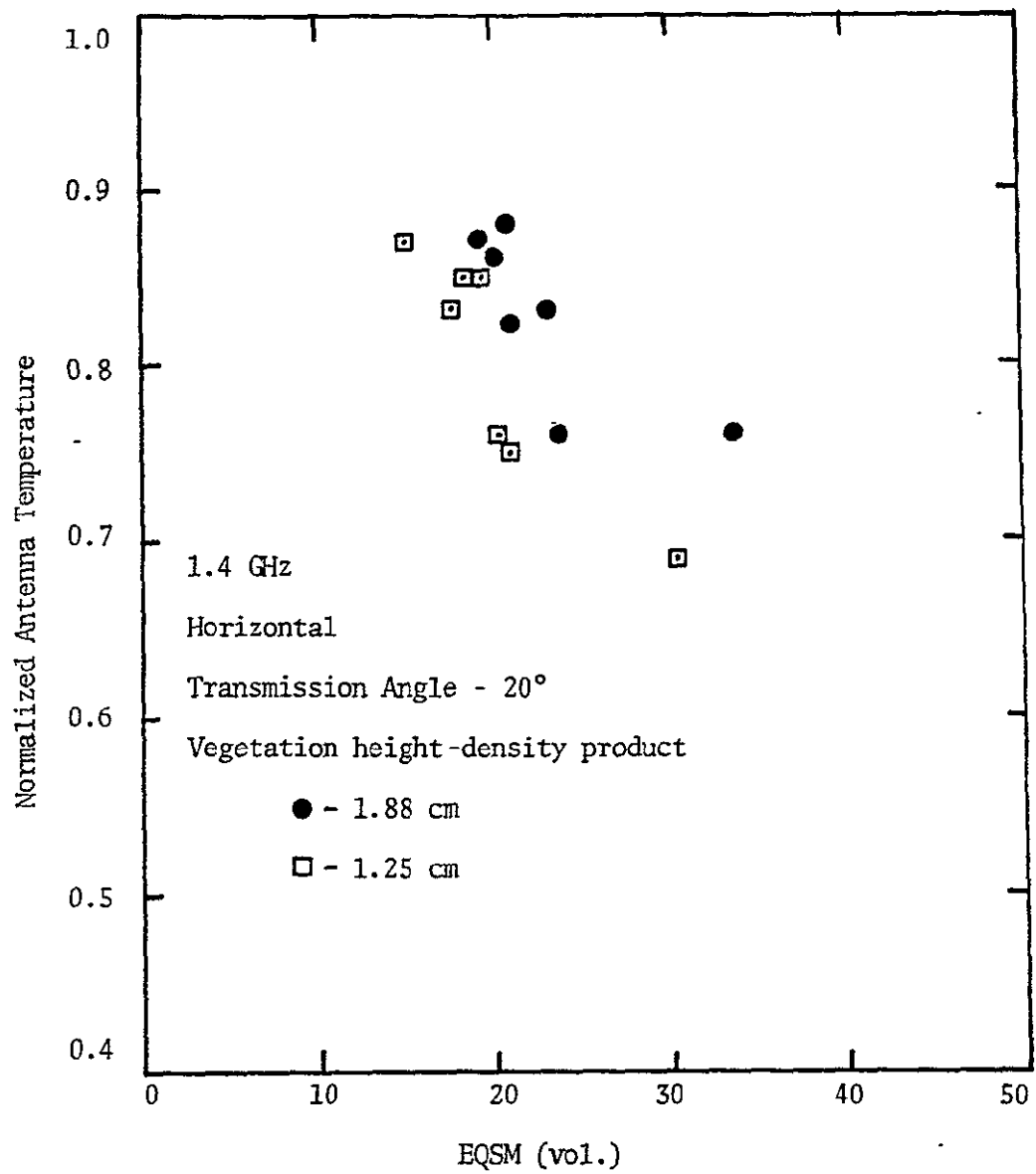


Figure VII-44. Comparison of horizontal 1.4 GHz measurements of two uniform vegetation densities.

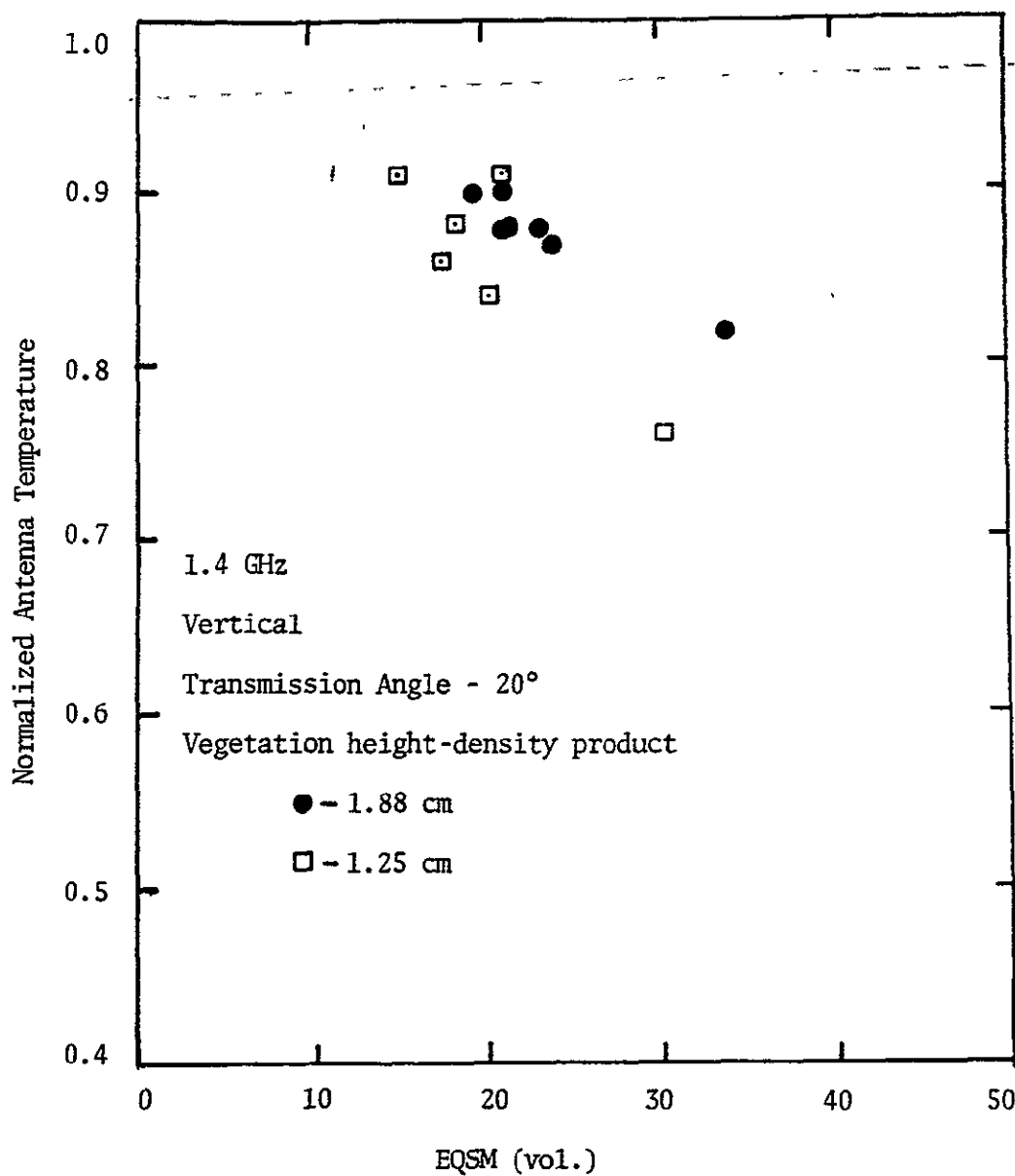
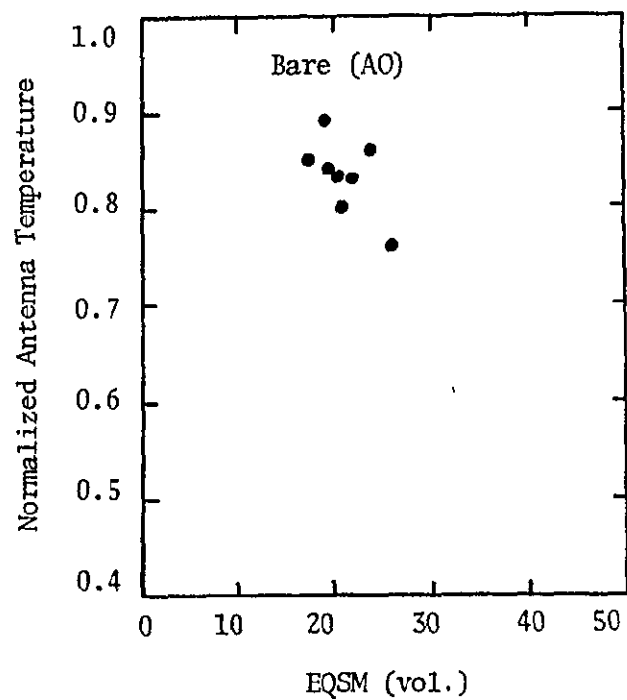
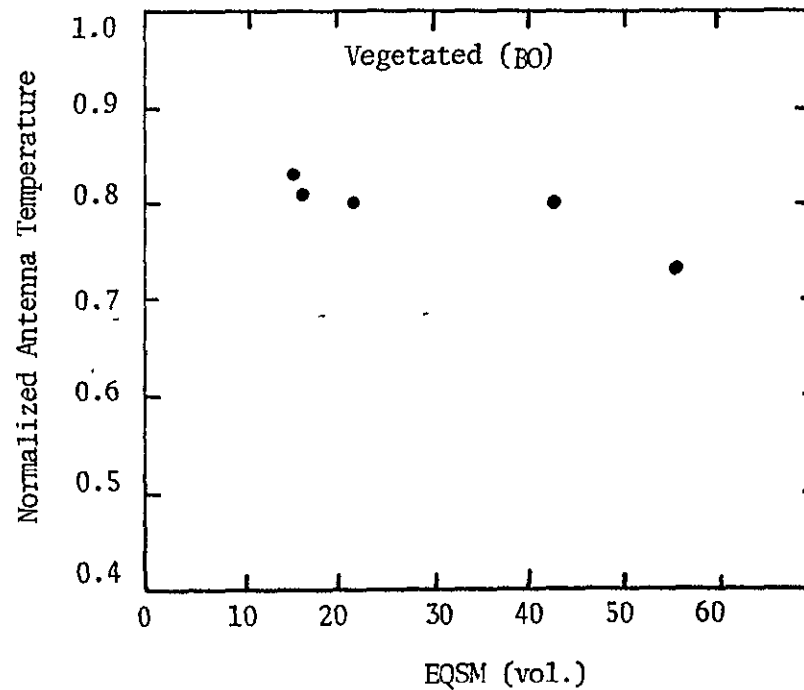


Figure VII-45. Comparison of vertical 1.4 GHz measurements of two uniform vegetation densities.



10.6 GHz

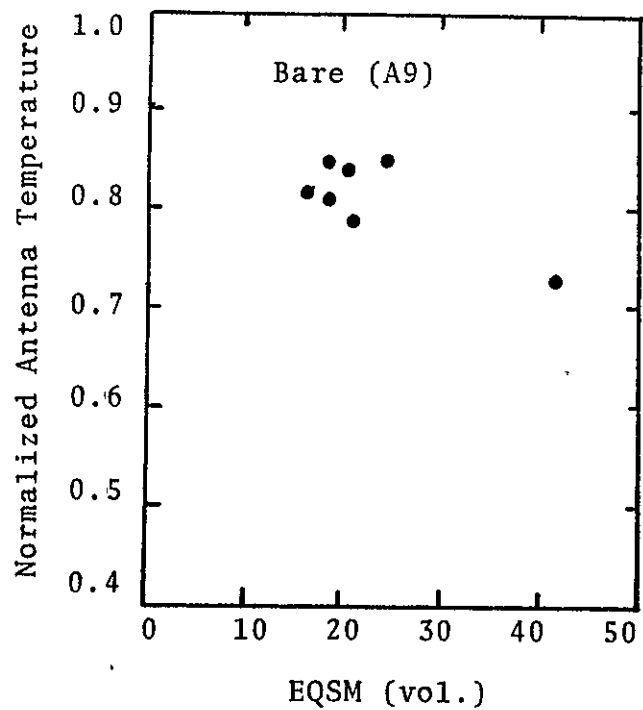
Vertical Polarization



Transmission Angle - 20°

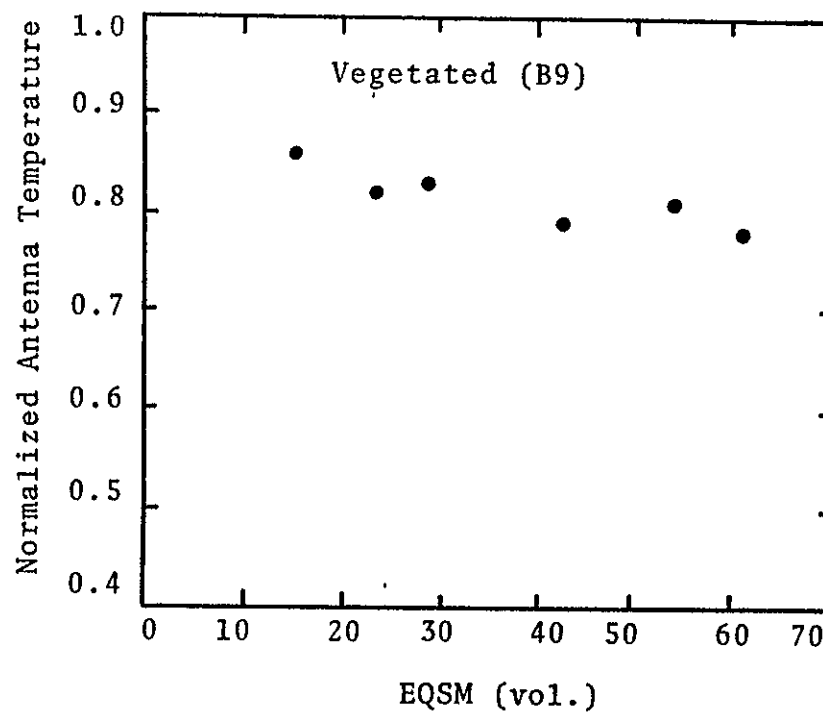
Parallel to Rows

Figure VII-46. Comparison between bare and vegetated 10.6 GHz antenna temperature measurements made parallel to the row direction.



10.6 GHz

Vertical Polarization

Transmission Angle -  $20^\circ$ 

Perpendicular to Rows

Figure VII-47. Comparison between bare and vegetated 10.6 GHz antenna temperature measurements made perpendicular to the row direction.

of the soil. It was previously shown in the bare soil measurements that the soil row structure will cause the vertically polarized antenna temperature measurements made perpendicular to the rows to be larger than those made parallel to the rows. This indicates that the soil row structure should be incorporated into the row vegetation model.

At 1.4 GHz Figure VII-48 demonstrates that the soil radiation effectively penetrates the vegetation cover when viewing the field parallel to the rows. The moisture response is retained without modification in measurements made parallel to the rows. Figure VII-49 shows evidence that the soil moisture dependence is affected when viewing the fields perpendicular to the rows. However, this statement is made as a result of the two points denoted by special symbols. If these two measurements are in error, then the soil moisture dependence is affected only by increased measurement scatter, as for the bare soil case.

### Soil Moisture Estimation

#### Scope

The effect of soil moisture on the thermal microwave emission of bare and vegetated soil has been shown both theoretically and experimentally. Although the shape of



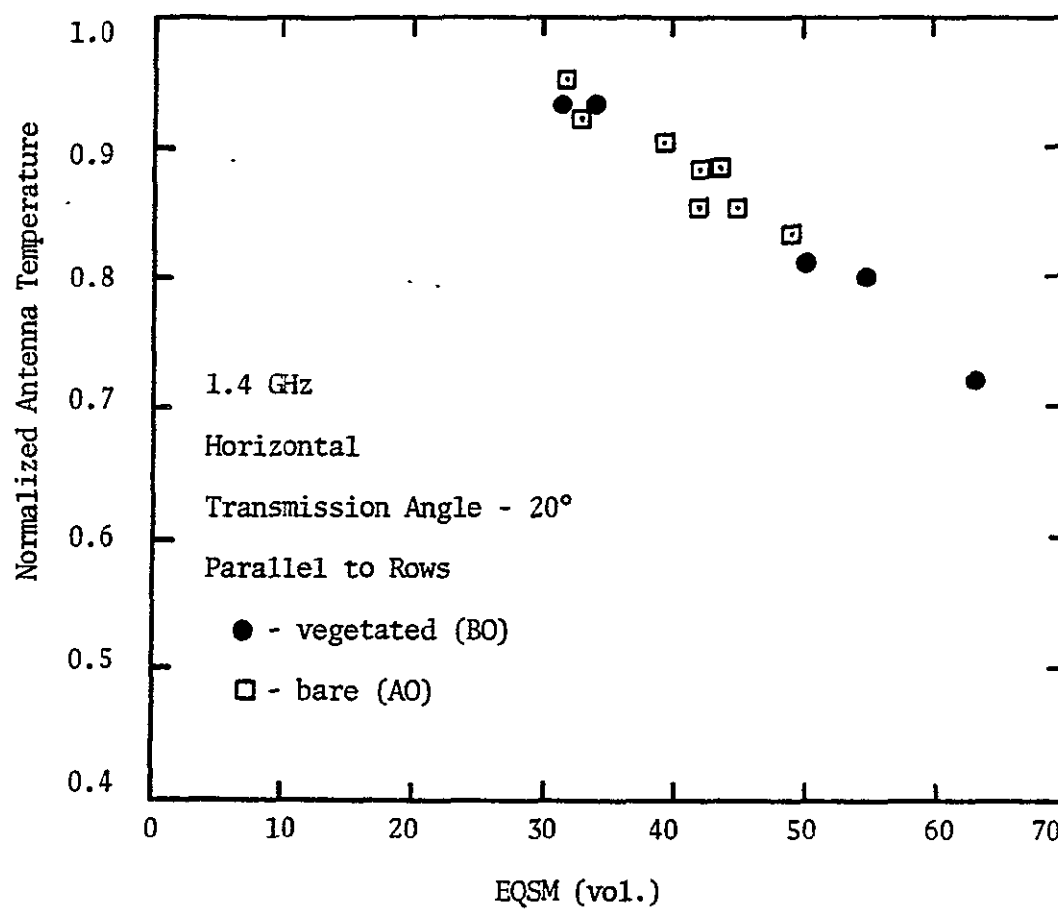


Figure VII-48. Comparison of bare and vegetated 1.4 GHz measurements of row tilled surfaces made parallel to the rows as a function of soil moisture.

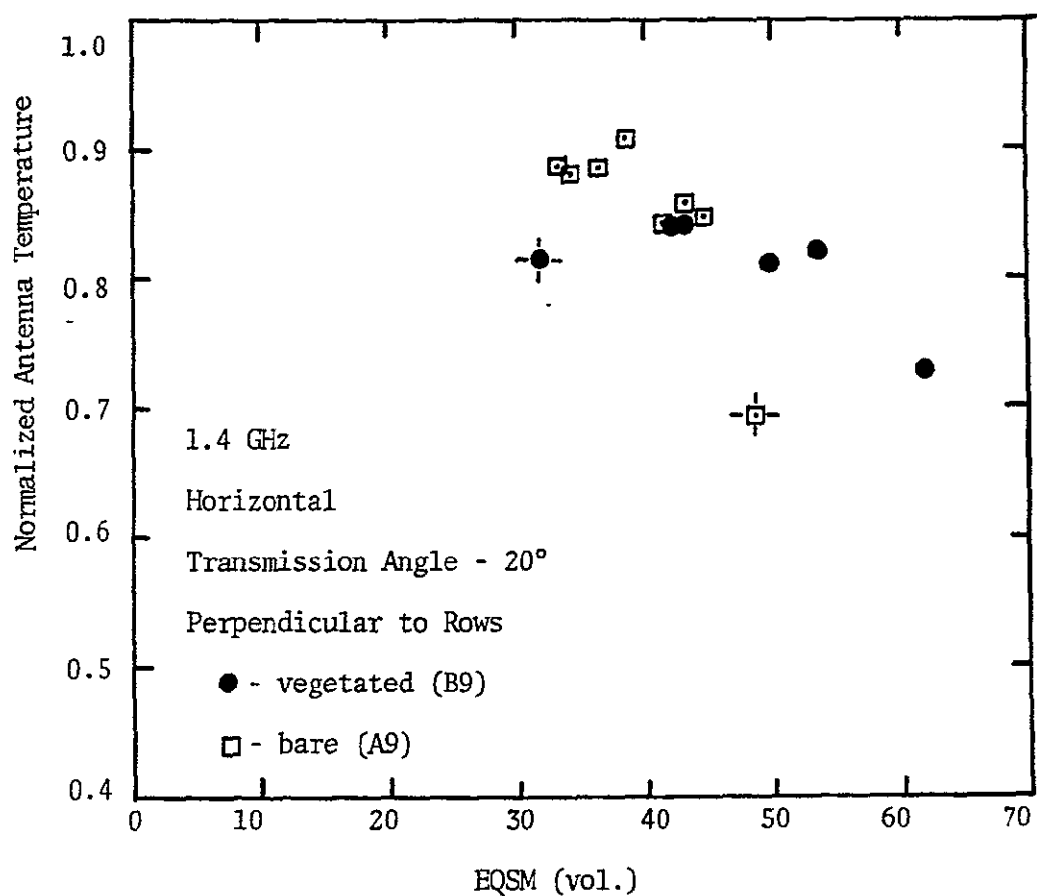


Figure VII-49. Comparison of bare and vegetated 1.4 GHz measurements of row tilled surfaces made perpendicular to the rows as a function of soil moisture.

the soil moisture profile affects the magnitude of the emission from the soil volume, it was shown that the soil moisture profile can be quantified by a parameter termed the equivalent incoherent soil moisture. This parameter is denoted by EQSM. It was further shown that the parameter can be interpreted as the average soil moisture in the soil moisture profile for some surface layer of soil. The depth of this layer is directly related to the magnitude of the EQSM, or average soil moisture, for 1.4 GHz measurements. At 10.6 GHz the layer is always between one and two centimeters thick.

The analysis summarized above and the antenna temperature measurements discussed earlier in this chapter demonstrate that soil moisture information and the depth with which that soil moisture corresponds can be measured remotely with passive microwave sensors. There are, however, scene parameters such as vegetation cover and surface roughness that modify the response of the soil emission to soil moisture. A technique of estimating the equivalent soil moisture parameter, EQSM, for uniformly smooth or rough soil will be illustrated below. The effect of a vegetation cover on this estimation technique will also be discussed.

The analysis presented below is structured around estimating the average volumetric soil moisture, EQSM. Soil moisture is estimated rather than matric potential

simply because the measurements reported in this document were acquired from experimental plots consisting of the same soil texture, and the matric potential versus soil moisture curves were not available for this soil. Due to the results presented in Chapter II, the analysis presented below should apply equally well to soil matric potential which could be converted to available plant water (depending on the plant of interest) for agricultural applications, or degree of soil saturation for hydrologic applications. Such an analysis would be independent of soil texture.

#### Uniform Roughness

It has been demonstrated that the emission from bare, smooth soil is sensitive to changes in the shape and overall magnitude of the soil moisture profile. However, as the soil surface is roughened the sensitivity to soil moisture decreases. Naturally, the effect of a given roughness is dependent on the wavelength of the radiation. For 1.4 GHz Figure VII-50 is a plot of 1.4 GHz antenna temperature measurements made at a 20° transmission angle. These data demonstrate the sensitivity reduction due to uniform roughness that is similar to flat tilled agricultural fields. At the 10.6 GHz wavelength the bare "smooth" field appeared rough. As a result there is no smooth surface measurements at 10.6 GHz. This was demonstrated in Figure VII-24.

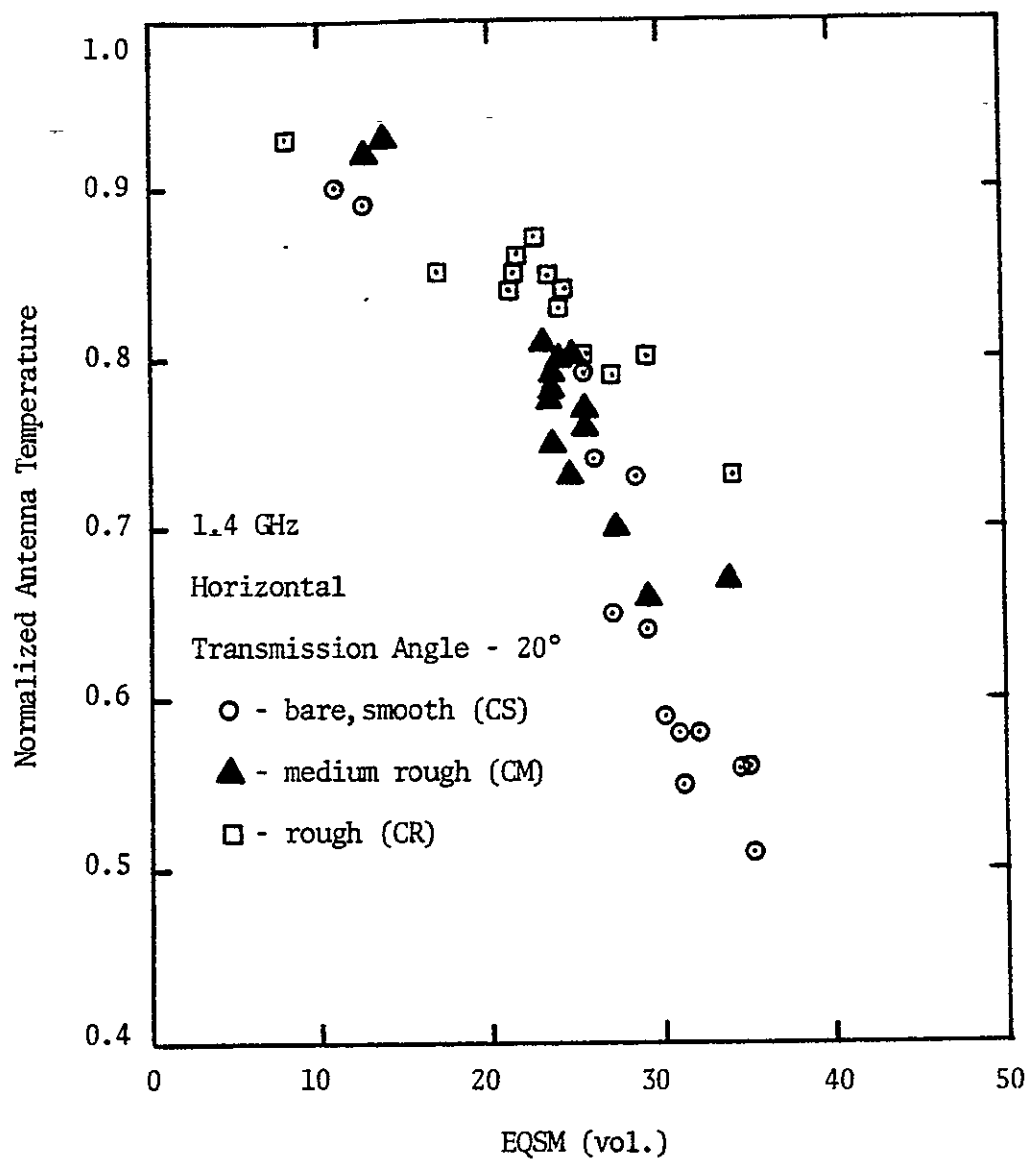


Figure VII-50. Horizontal 1.4 GHz antenna temperature measurements as a function of soil moisture for three surface conditions.

The individual antenna temperature measurements were plotted in Figures VII-24 and VII-50 to demonstrate the apparent scatter of the measurements. This scatter is not due entirely to the noise of the radiometer system. Much of the scatter is a result of the inaccuracies in measuring the soil moisture. This is especially true at 10.6 GHz since the EQSM plotted in Figure VII-24 is derived from surface (0-1 cm) soil moisture measurements. Figure VII-51 is a plot of the standard deviation versus the mean of the zero to one centimeter soil moisture measurements for the smooth and medium rough bare fields used in 1974. The magnitude of the standard deviation is seen to be quite large in comparison with the mean surface moisture, except for very dry conditions. These data indicate the uncertainty in measuring soil moisture.

Figure VII-51 demonstrates that although ground measurements are taken to be the standard to which the microwave measurements are compared, the error bars on the "ground truth" measurements can be extremely large. However, in the analysis below the ground soil moisture measurements to which the microwave measurements are compared are assumed to be exact quantities and not random variables. As a result, the estimates of the accuracy to which soil moisture can be remotely measured based on this analysis should be conservative estimates.

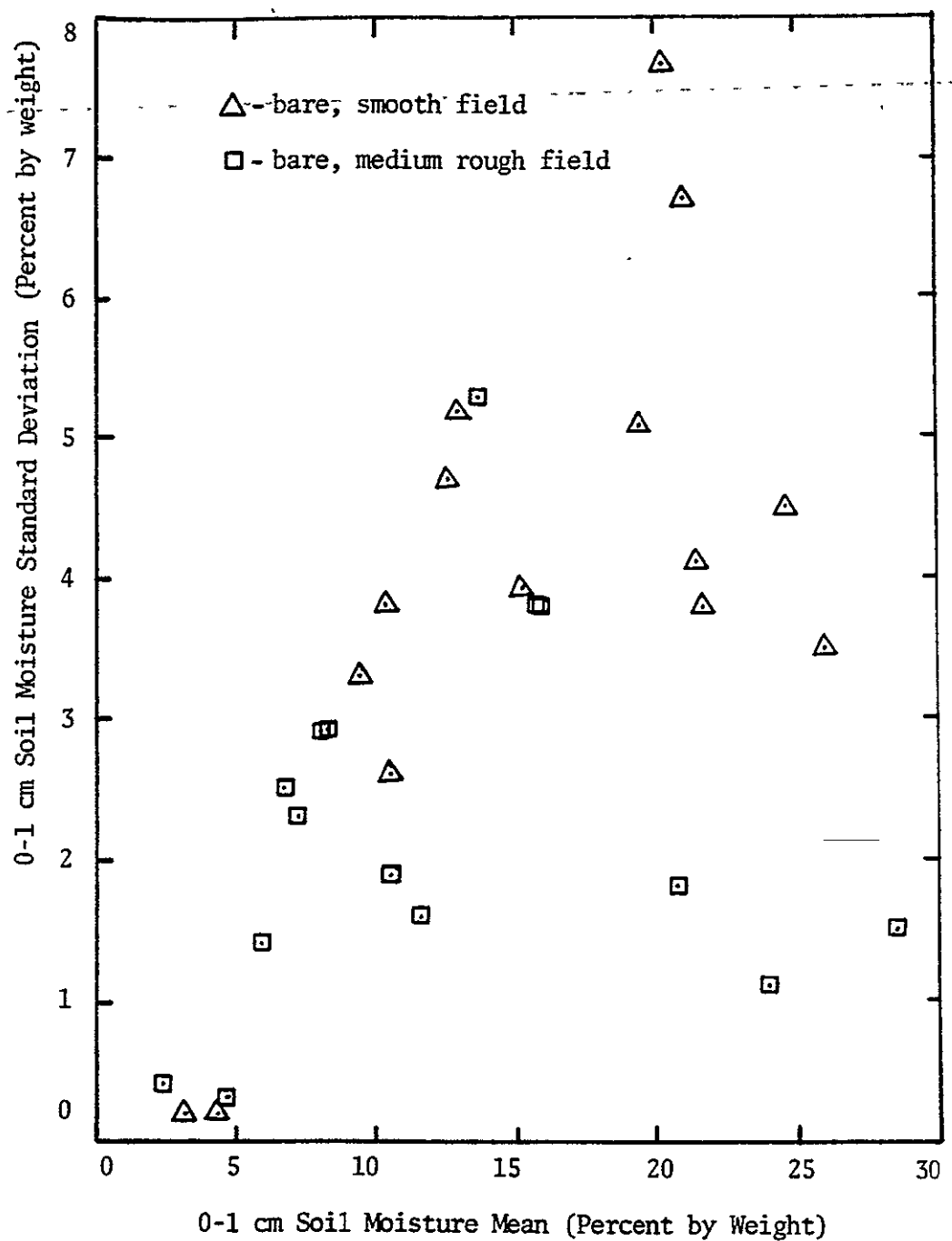


Figure VII-51. Comparison of the mean and standard deviation of the 0-1 cm soil moisture measured in fields CS and CM.

Surface roughness prediction - In order to utilize passive microwave antenna temperature measurements for estimating soil moisture for unknown terrain, it will be necessary to remove the effects of surface roughness from the measurements, or at least quantify the surface roughness over which the measurements were made. If the effects of roughness could be removed then a soil moisture estimate could be made based on an effective smooth surface soil moisture response. If the surface roughness was only quantified, a soil moisture estimate could be made based on the soil moisture response for that roughness. In either case it is necessary to determine if surface roughness can be quantified using only the antenna temperature measurements.

A plot of 1.4 GHz normalized antenna temperature versus transmission angle is shown in Figure VII-52 as a function of surface roughness for a specific soil moisture condition. Note that as the surface gets rougher the overall emission increases. In addition, the vertical and horizontal emission tends to get closer for off nadir angles as the roughness increases. As a result, the difference in the vertical and horizontal antenna temperatures is a function of surface roughness. It must now be determined if this correlation can be used to estimate roughness with reasonable accuracy, and for which transmission angle this correlation is optimum.



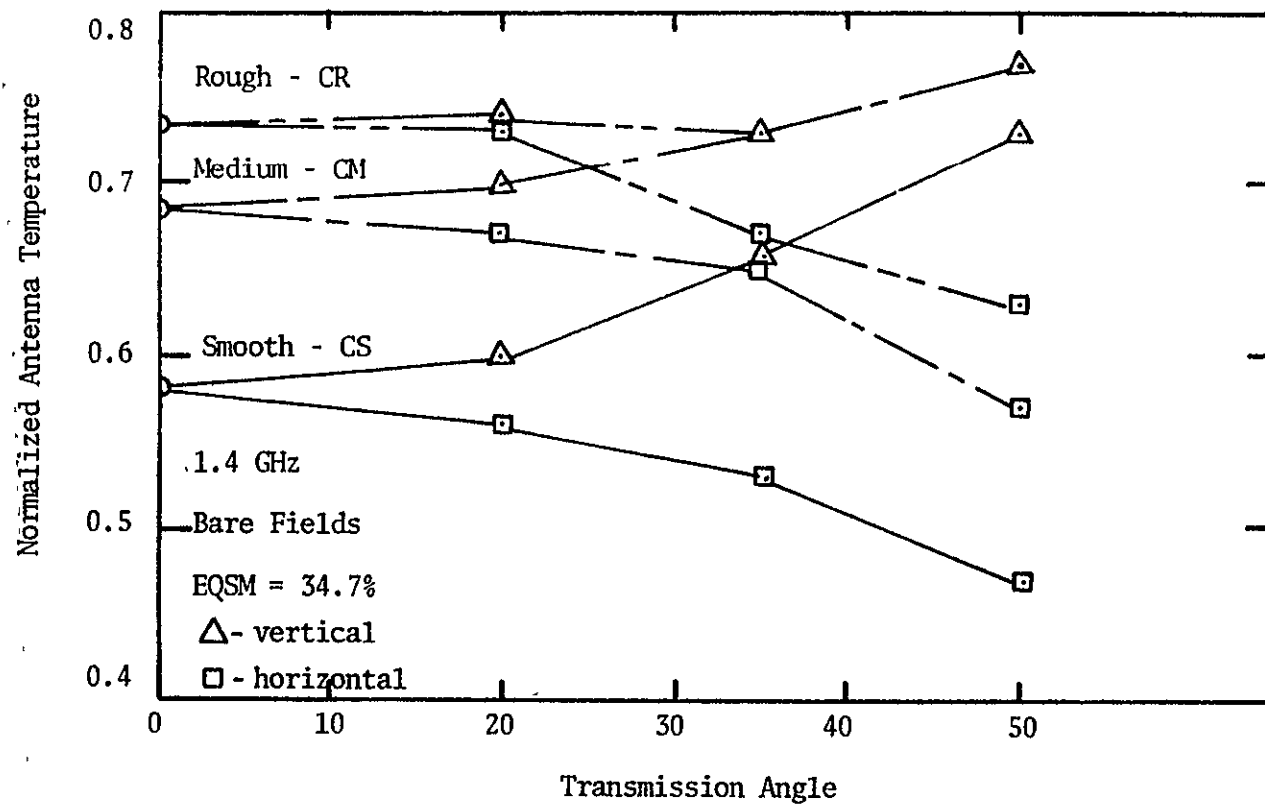


Figure VII-52. 1.4 GHz antenna temperature measurements made as a function of transmission angle for three surface preparations.

The relationship between the difference in the vertical and horizontal 1.4 GHz normalized antenna temperatures and surface roughness is shown in Figures VII-53 through VII-55. These plots are based on the linear regression equations generated for the normalized antenna temperature versus EQSM (Table VII-5). Note that the difference between the vertical and horizontal normalized antenna temperatures not only changes with roughness, but that it also changes with moisture.

At a transmission angle of  $20^\circ$  the difference between the vertical and horizontal normalized antenna temperatures is very small. As a result, the relative sensitivity of this difference to changes in moisture is very large, at least for the smooth and medium rough fields. At the  $50^\circ$  transmission angle the difference between the vertical and horizontal measurements is large, but the relative change in this difference with moisture is also large. However, the dependence of this difference on soil moisture is not consistent between rms surface height deviations. That is, the difference between the vertical and horizontal normalized antenna temperatures change 54% as the moisture changes from 15% to 35% for the smooth field (Field CS). For the same soil moisture change, this difference changes 66% for the medium rough field, and only 30% for the rough field. However, at a  $35^\circ$  transmission angle the difference

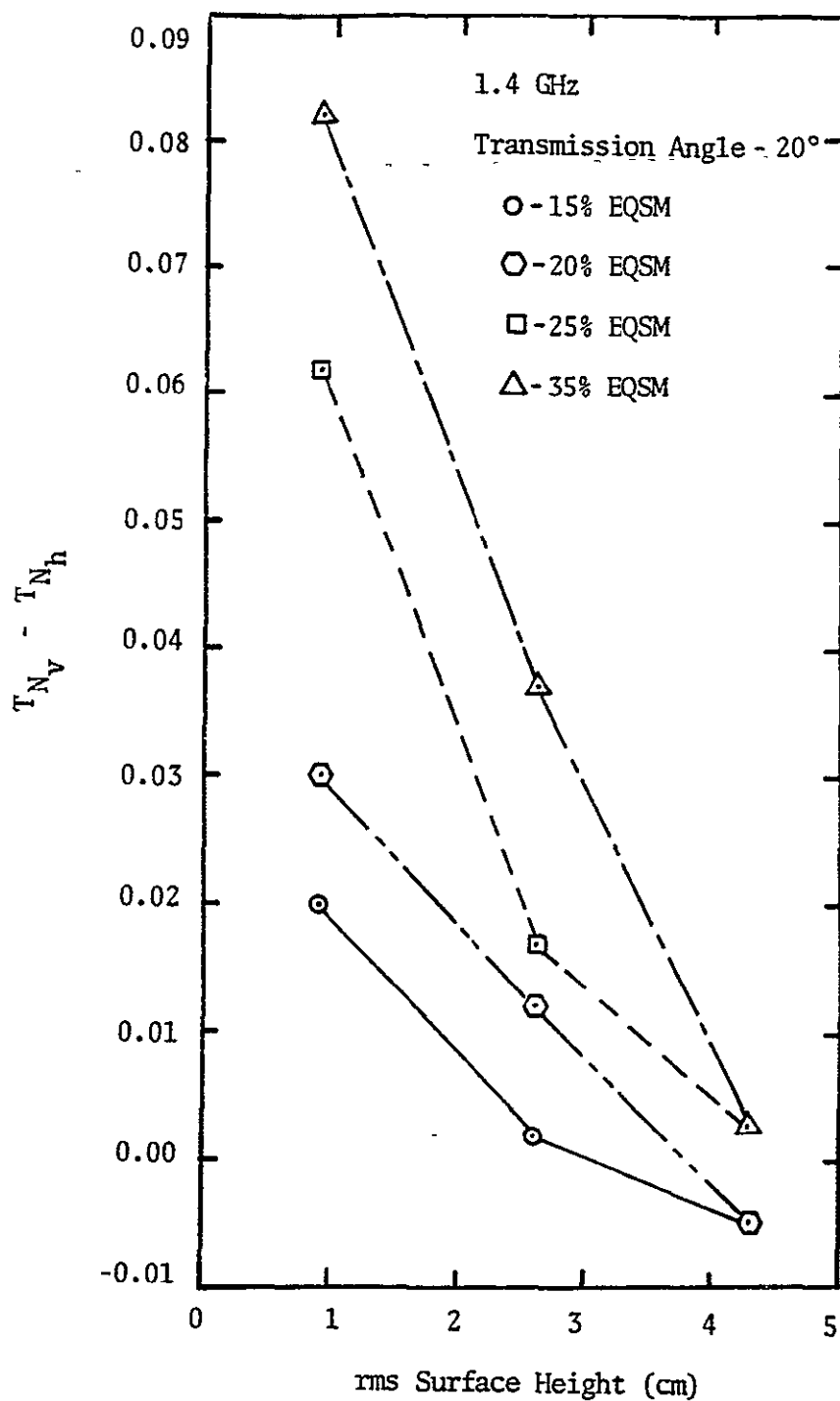


Figure VII-53. Comparison of the effect of soil moisture on the difference between vertical and horizontal normalized antenna temperatures measured at 20° for three rms surface heights.

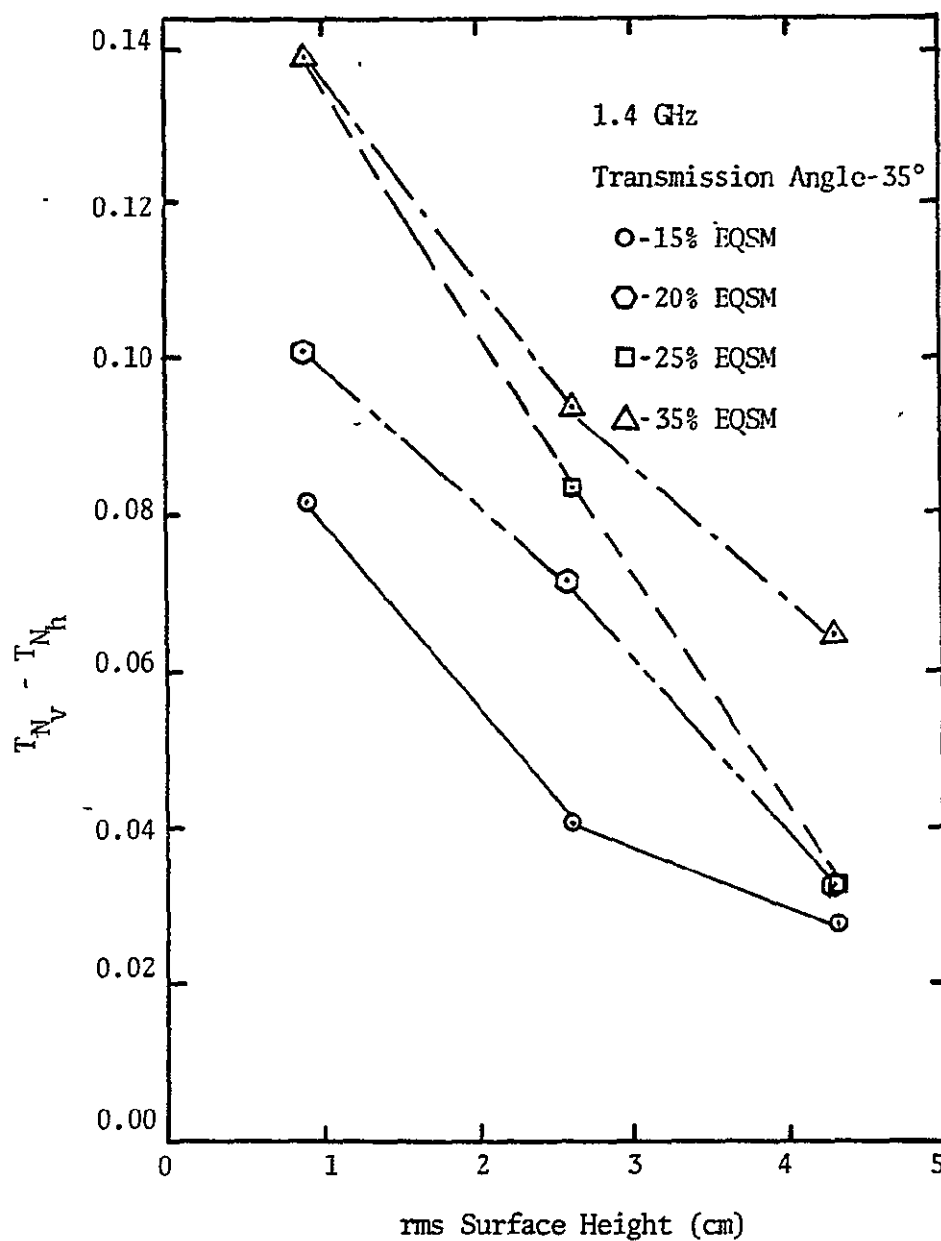


Figure VII-54. Comparison of the effect of soil moisture on the difference between vertical and horizontal normalized antenna temperatures measured at 35° for three rms surface heights.

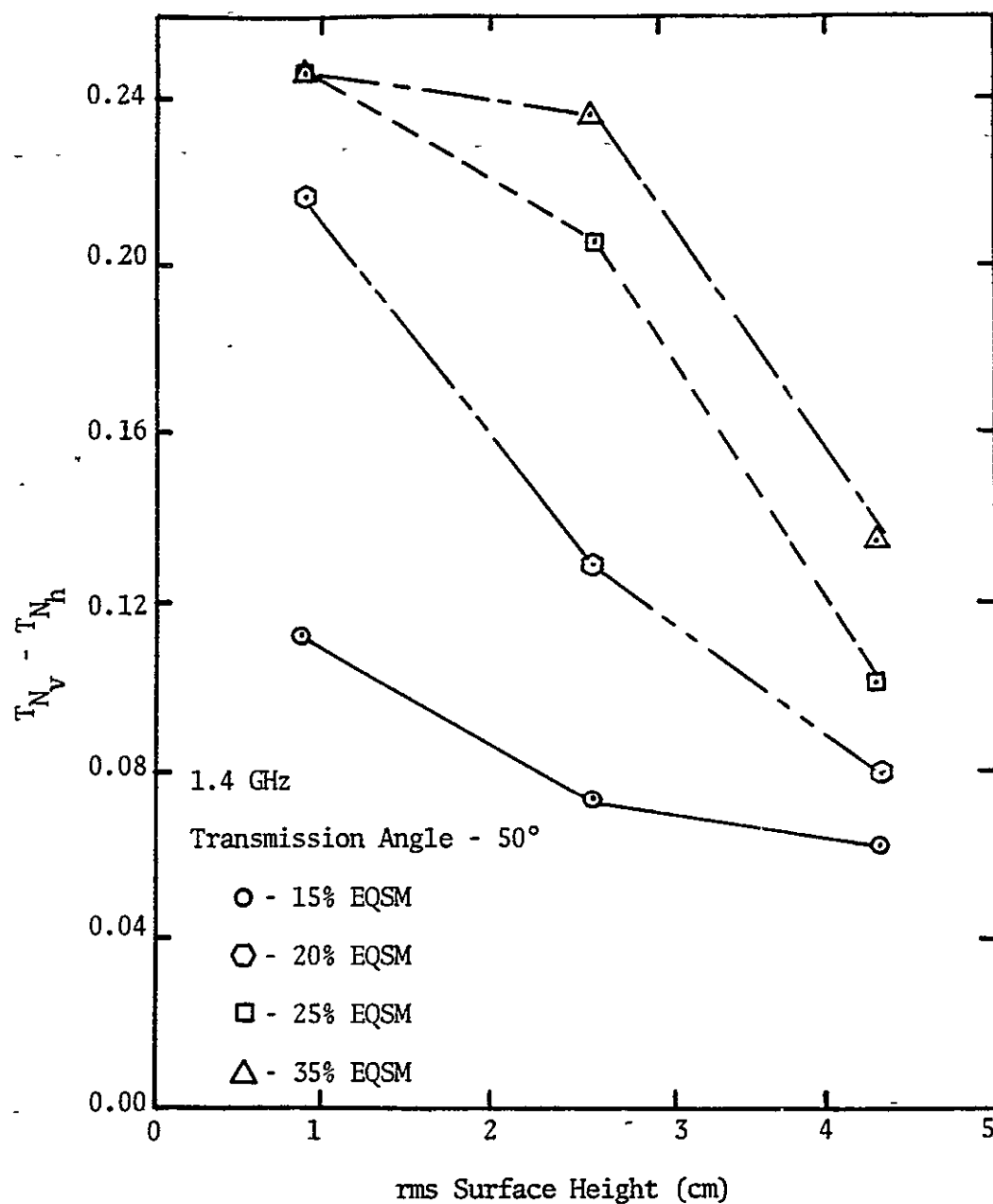


Figure VII-55. Comparison of the effect of soil moisture on the difference between vertical and horizontal normalized antenna temperatures measured at 50° for three rms surface heights.

between the vertical and horizontal normalized antenna temperatures change 41% for field CS, 38% for field CM and 27% for field CR as the moisture changes from 15% to 35%. In addition, the differences are large enough to be measurable. As a result, it appears from this crude analysis that the 35° transmission angle, of the three angles that were investigated, would yield the best results for estimating surface roughness for unknown moisture conditions.

It is possible that the effect of soil moisture on the difference between the vertical and horizontal normalized antenna temperature is not as large as is indicated by Figure VII-54. Plotting all of the points that are available at 35° (Figure VII-56), there are five points that are separated from the others. These points are denoted by the solid triangles. These particular points correspond to two measurement sets that were acquired before irrigation and while the soil was very dry. There is no way of knowing whether or not these points fall below the other points because of the low soil moisture condition, or whether or not all of the other points are higher than these points due to the surface smoothing effect of the irrigation.

Soil moisture measurement - Now that a parameter has been identified that is dependent on surface roughness,

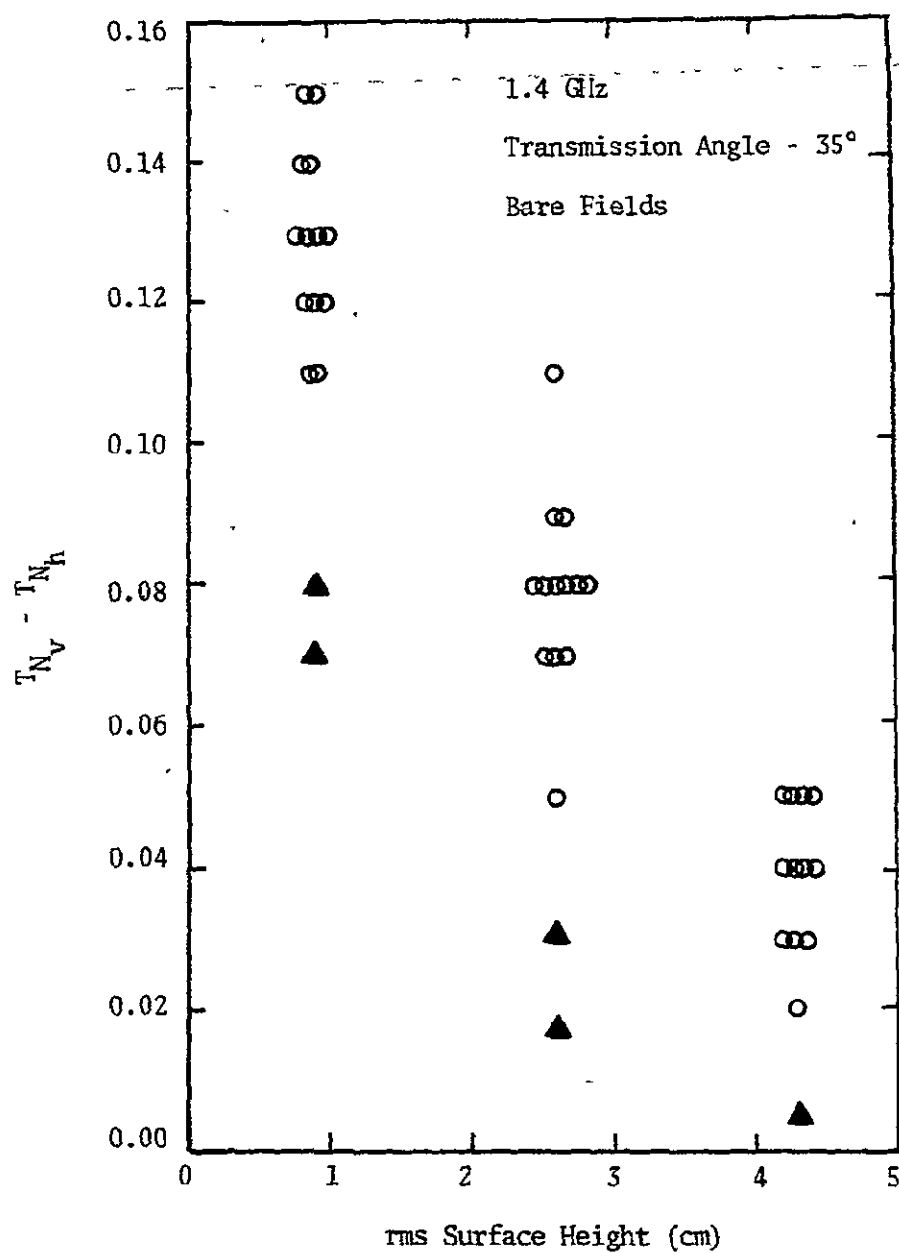


Figure VII-56. The difference between vertical and horizontal antenna temperatures measured at 35° for three rms surface heights.

this parameter can be used in conjunction with horizontal or vertical antenna temperature measurements to estimate soil moisture. It has been shown above that a transmission angle of  $35^\circ$  is probably the best transmission angle (of the three angles investigated) to use to estimate the roughness condition. A choice must now be made as to which polarization and which transmission angle will be used to estimate the soil moisture. It was demonstrated earlier that the highest sensitivity to soil moisture was obtained at a transmission angle of  $20^\circ$ , although measurements at the other angles also have a useable moisture sensitivity. At the  $20^\circ$  transmission angle horizontal and vertical antenna temperature measurements have about equal sensitivity to moisture. For purposes of illustration, horizontal antenna temperature measurements made at  $20^\circ$  will be used in conjunction with the difference between the vertical and horizontal antenna temperature measurements made at  $35^\circ$  to demonstrate a technique of estimating EQSM, the average soil moisture in a surface soil layer.

Using the difference between the vertical and horizontal antenna temperature measurements at  $35^\circ$  and the horizontal antenna temperature measurements at  $20^\circ$ , an algorithm can be devised that estimates both the surface roughness and average soil moisture (EQSM) simultaneously. A graphical representation of such an algorithm is



presented in Figure VII-57. The horizontal axis is the normalized horizontal antenna temperature measured at  $20^\circ$ , and the vertical axis is the difference between the vertical and horizontal normalized antenna temperatures measured at  $35^\circ$ . Note that both rms surface roughness and soil moisture information is displayed in this plot. The solid lines in the plot define the rms surface roughness. The dashed lines are EQSM contours. These contours are plotted in Figure VII-58 without the individual measurements.

Figure VII-58 can be utilized to estimate moisture and surface roughness by simply plotting the unknown measurements and determining which partition the measurements fall within. In order to get an estimate of the expected accuracy of an algorithm based on such an approach, 80% confidence intervals were calculated for the horizontal axis of Figure VII-58. It is obvious that these confidence intervals will depend on the surface roughness, with the estimation accuracy decreasing with roughness.

Table VII-9 contains the confidence intervals calculated at 35% EQSM for the normalized horizontal antenna temperature measurement at  $20^\circ$  for each surface roughness. These are confidence intervals on the mean of a population and not on individual measurements. By comparing these

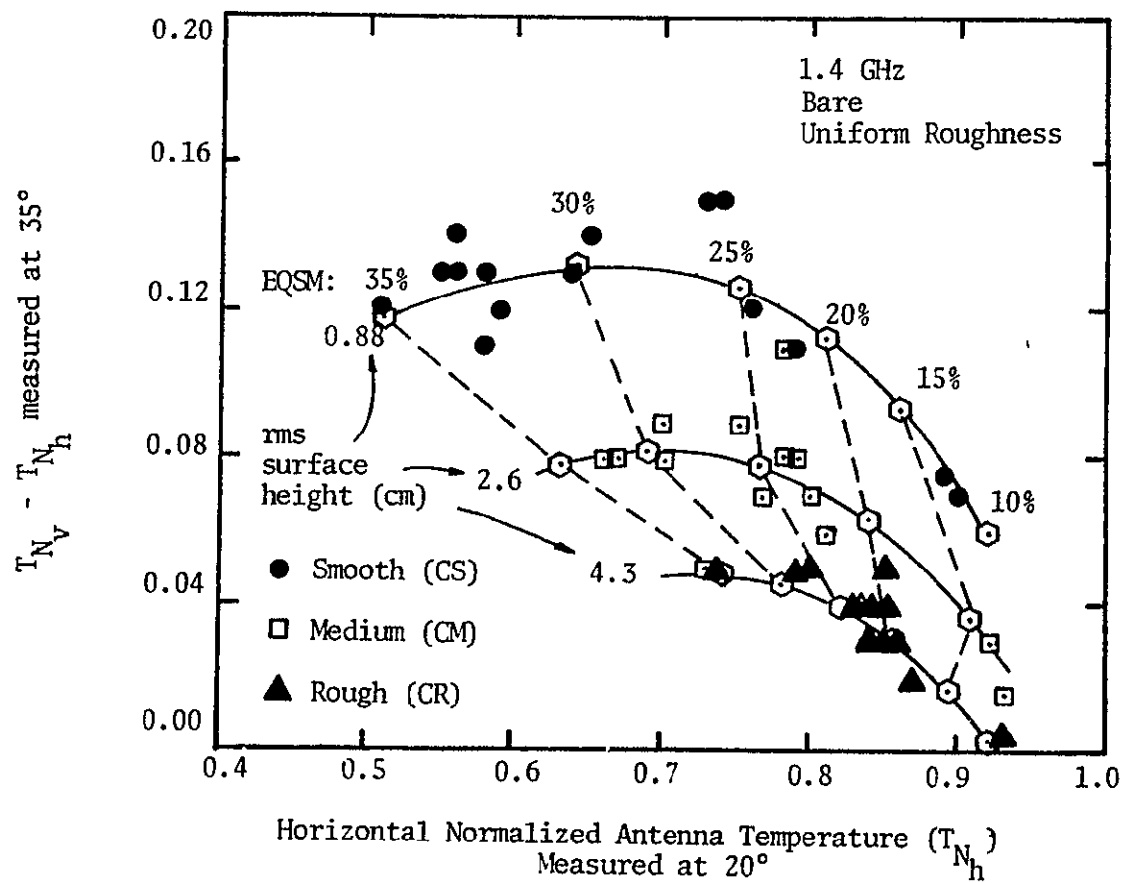


Figure VII-57. Demonstration of the separability of 1.4 GHz antenna temperature measurements into soil moisture and surface roughness classes.

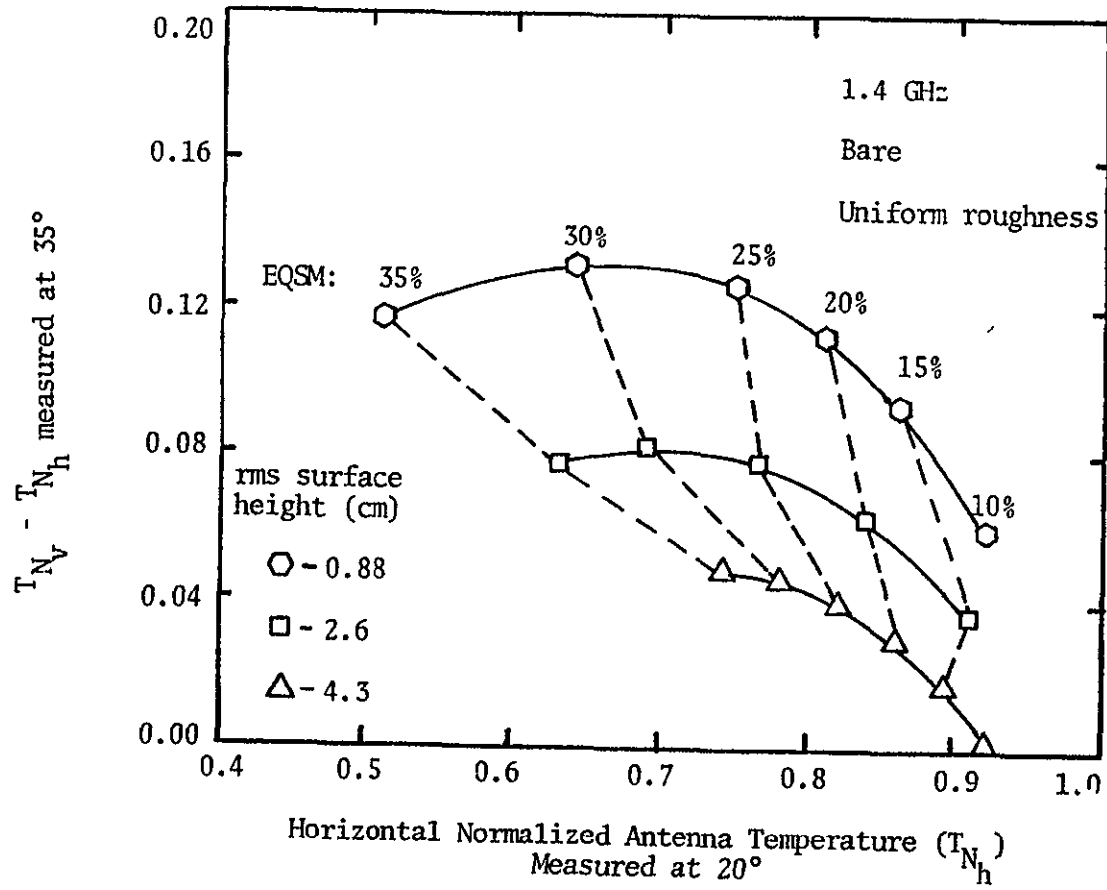


Figure VII-58. Soil moisture and surface roughness partitions obtained from Figure VII-57 for 1.4 GHz measurements.

TABLE VII-9  
 80% Confidence Intervals on the Population Mean at 25% EQSM  
 for  $T_{N_h}$  Measured at 1.4 GHz

Field	Surface Roughness	EQSM	$T_{N_h}$	Degree of Confidence
CS	0.88	25%	$0.75 \pm 0.064$	80%
CM	2.6	25%	$0.76 \pm 0.058$	80%
CR	4.3	25%	$0.822 \pm 0.043$	80%

confidence intervals to the EQSM contours in Figure VII-58, it can be seen that the soil moisture estimation accuracy - assuming the surface roughness is known is approximately +3% and -6% EQSM for the smooth field, +4% and -5% EQSM for the medium rough field, and +5.5% and -6% EQSM for the rough field. These are only approximate estimates obtained graphically from Figure VII-58 using the data of Table VII-8. However, the estimates should be reasonably conservative since the ground data were taken to be exact quantities when in reality the error in making "ground truth" measurements is at least as large as the error in the radiometer measurements. At any rate, these approximations indicate that at 1.4 GHz for bare uniformly rough soil, the average soil moisture in some surface layer can be estimated with an 80% degree of confidence to fall within a 9% EQSM window for smooth and medium rough surfaces, and to within a 11% to 12% EQSM window for a rough surface.

A technique capable of estimating EQSM using 1.4 GHz measurements has been illustrated above. The depth for which that average moisture corresponds can be estimated from Figure VII-6. In Figure VII-6 a distinction was made between inverted soil moisture gradients and non-inverted soil moisture gradients. In order to make this distinction, the EQSM measured at 1.4 GHz can be compared

with the EQSM measured at 10.6 GHz. Recall that at 10.6 GHz the EQSM estimate will always correspond to the 0-1 cm to 0-2 cm surface layer. Thus, if the 10.0 GHz EQSM estimate is greater than the 1.4 GHz EQSM estimate, then the soil moisture profile can be assumed to be inverted.

It was earlier demonstrated that antenna temperature measurements at 10.6 GHz are sensitive to smaller scales of roughness than are 1.4 GHz measurements. As a result, it is to be expected that the estimation accuracy of EQSM using 10.6 GHz will not be as good as it is for 1.4 GHz. Figure VII-59 is the 10.6 GHz measurements plotted in the same manner as the 1.4 GHz data are plotted in Figure VII-57. Although the measurements from the three surfaces generally cluster and do appear separable, the clusters are much closer and less well defined than for the 1.4 GHz measurements. This was expected. No effort was made to draw moisture and surface roughness contours on Figure VII-59, however, the estimation accuracy calculated for the measurements of the smooth and medium rough fields were no better than  $\pm 10\%$  EQSM. For the rough field it was approximately  $\pm 6\%$  EQSM. Although the moisture sensitivity of the rough field was smaller, there was less scatter in the antenna temperature measurements than there was for the smooth and medium rough fields (Figure VII-24). Again, these approximations are based on 80% confidence

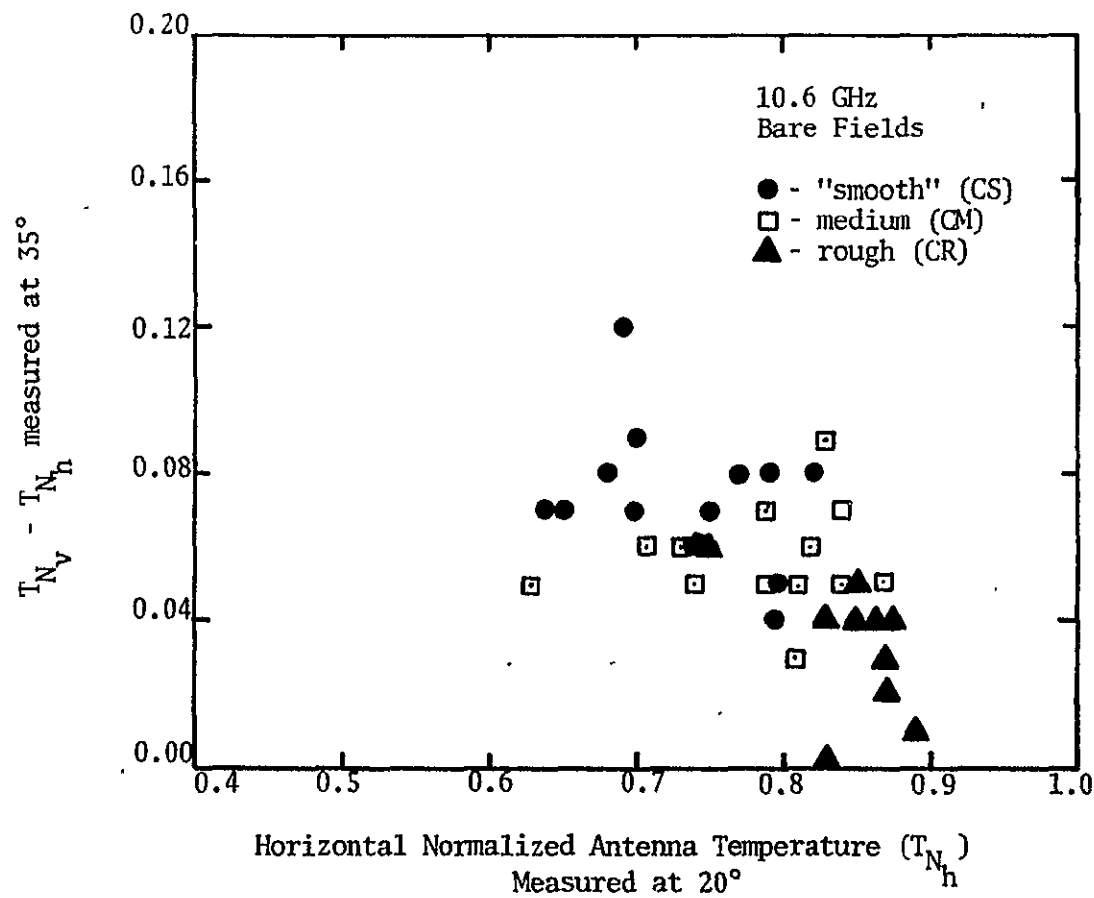


Figure VII-59. 10.6 GHz measurements plotted in a manner that demonstrates the separability of soil moisture and surface roughness (as in Figure VII-57).

limits of the population mean assuming the surface roughness is known. Although this accuracy seems poor, it is probably reasonable considering the scatter in the ground surface moisture measurements illustrated in Figure VII-51.

The two frequency approach described above for estimating the near surface soil moisture gradient can be implemented at 1.4 GHz and 10.6 GHz frequencies with promising results. However, the sensitivity to surface roughness at 10.6 GHz and resulting decrease in response to soil moisture indicate that for a two frequency system a slightly lower frequency than 10.6 GHz would increase the accuracy of the near surface estimate. In addition, the ability to estimate moisture at different depths by using different wavelengths indicate that the soil moisture profile could be estimated with increased accuracy simply by adding additional frequencies to the measurement system.

#### Row Structure

It was demonstrated in Figure VII-28 through VII-32 that 1.4 GHz measurements of bare row tilled terrain retain a reasonable moisture sensitivity. It was shown, however, that the moisture sensitivity was better when the measurements were made parallel to the rows. In fact, a soil moisture estimation accuracy similar to that obtained above for the medium rough field should be obtainable



from measurements made parallel to the rows. The measurement accuracy will no doubt be reduced for measurements made at larger azimuth angles with respect to the rows.

At 10.6 GHz, although there were very little data available at high soil moistures, Figures VII-38 and VII-39 indicate that there is a usable soil moisture sensitivity in measurements made both parallel and perpendicular to the row direction. Burke and Paris [32] demonstrated the potential of measuring the surface soil moisture of row tilled fields at 10.6 GHz (Figure VII-60). Although no ground samples were obtained from fields 313 and 296, irrigation had been partially completed on these fields. In Figure VII-60 the measurements from fields 313 and 296 fall in higher moisture partitions indicating that the 10.6 GHz measurements are sensitive to soil moisture. The significance of Figure VII-60 lies in the fact that the antenna temperature measurements were made at a range of azimuth angles and not just parallel or perpendicular to the rows.

Burke and Paris [32] used a smooth surface model to generate Figure VII-60. Because of this they concluded that the surface roughness effectively changed the look direction from  $50^\circ$  to approximately  $30^\circ$ . This conclusion was based on the fact that the difference in the vertical and horizontal measurements was smaller than the smooth surface model predicted (Figure VII-61). However, it was

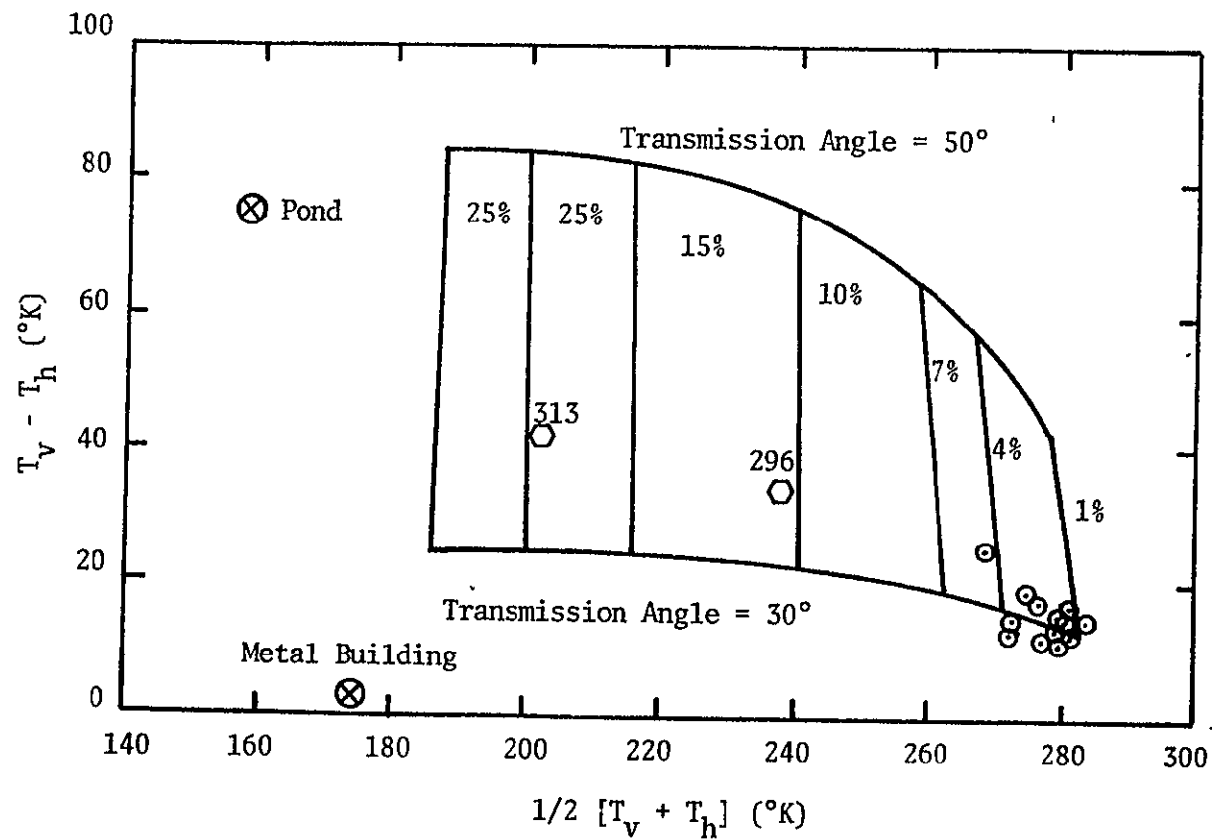


Figure VII-60. The difference between predicted brightness temperatures at vertical and horizontal polarization as a function of their average for transmission angles of 30° and 50°. The straight lines are lines of constant moisture in the top layer (after Burke and Paris [32]).

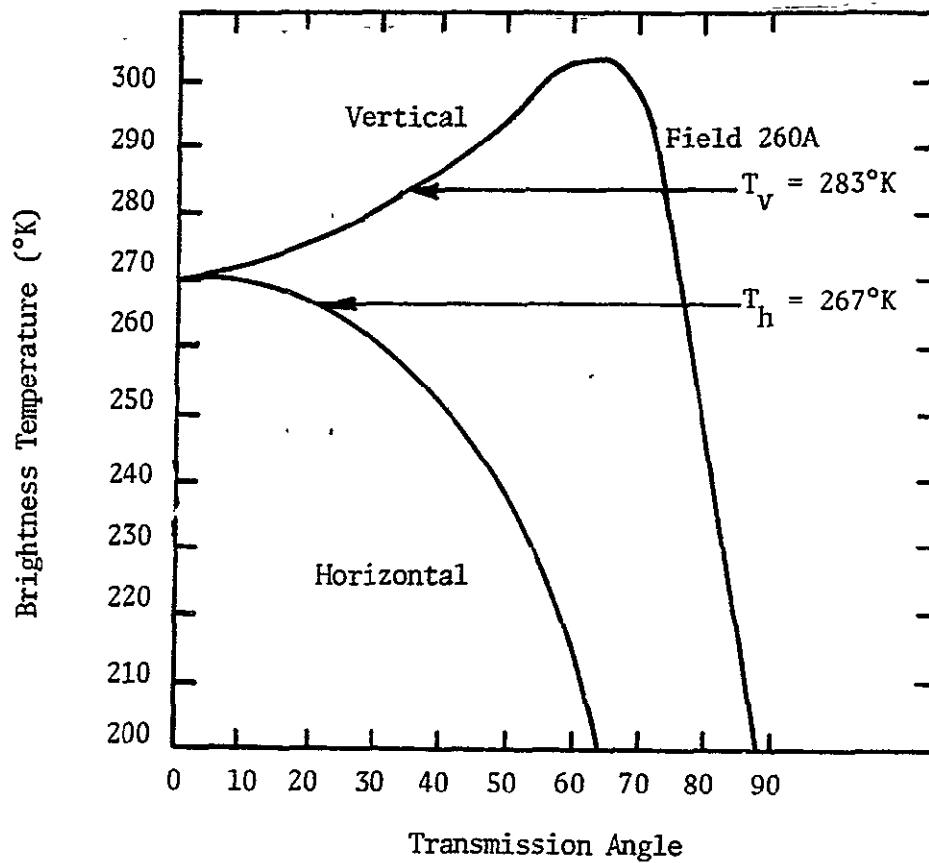


Figure VII-61. Brightness temperature predictions for field 260A. Arrows mark the vertical and horizontal 10.6 GHz antenna temperature measurements (after Burke and Paris [32]).

demonstrated in this report that the small scale surface roughness superimposed on top of the row structure is responsible for the reduction in the difference between the vertical and horizontal antenna temperatures. Since the moisture partitions in Figure VII-60 are based on a smooth surface model and since it was shown earlier that surface roughness decreases the moisture response, then the moisture partitions drawn by Burke and Paris in Figure VII-60 are probably incorrect. They would tend to indicate a better moisture sensitivity than is actually observable.

#### Effect of Vegetation

Figures VII-40 through 42 demonstrate that a uniform cover of vegetation 125 cm tall has a minimal effect on the sensitivity of 1.4 GHz antenna temperature measurements to soil moisture. However, at 10.6 GHz such a vegetation cover completely masks the soil moisture dependence.

Figure VII-48 demonstrates that when viewing row planted vegetation 61 cm tall parallel to the rows at 1.4 GHz, the soil moisture dependence is unchanged from the bare soil situation. However, there is evidence that the same vegetation reduces the soil moisture dependence when the measurements are made perpendicular to the rows. Figures VII-46 and VII-47 show that the soil moisture sensitivity is greatly reduced at 10.6 GHz for measurements made both parallel and perpendicular to the rows.

It can be concluded that 1.4 GHz can be used to measure soil moisture through uniform vegetation up to 125 cm tall with approximately the same estimation accuracy that was demonstrated for the bare soil condition. No conclusions can be drawn about the amount of vegetation 10.6 GHz measurements can effectively "penetrate" except that it will be considerably less than the vegetation densities that were reported in this document.

## CHAPTER VIII

### CONCLUSION

#### Summary of Results

The work documented in this report consisted of a theoretical development of the physical phenomenon of thermal microwave emission from moist soil, and an experimental investigation to verify the phenomenon. The theoretical development was undertaken to provide a better understanding of: 1) the interaction of water with soil and its affect on soil permittivity, 2) the interaction of electromagnetic energy emitted from the soil volume with the surface boundary, and 3) the relationship between the thermal microwave energy emitted from the soil surface and the soil moisture. The purpose of the experimental investigation was to verify the theoretical predictions and to demonstrate the feasibility of estimating soil moisture remotely using passive microwave sensors.

The experimental measurements were utilized to demonstrate a procedure for estimating soil moisture using a passive microwave sensor. An understanding of the physical phenomenon of thermal microwave emission was provided by the theoretical development, and aided in the analysis of the microwave radiometer measurements. It was shown that the average moisture within a surface layer

can be estimated remotely. The depth to which the average moisture corresponds can also be predicted. The depth of measurement and the accuracy of the soil moisture prediction is a function of the frequency of the emitted radiation. The experimental measurements show that average moisture can be measured to depths up to 20 cm at 1.4 GHz for relatively dry soil, but that at 10.6 GHz only moisture in the 0-2 cm surface layer can be estimated regardless of soil moisture.

The experimental investigation showed that 1.4 GHz and 10.6 GHz can be used to estimate the average soil moisture within two depths; however, it appears that a frequency less than 10.6 GHz would be preferable for the surface measurement. Average soil moisture within two depths would provide information on the slope of the soil moisture gradient near the surface. This information is of considerable importance since it indicates the occurrence of a recent water input event. Such information is vital to soil water budget models used to predict the soil moisture profile to depth. The ability to estimate average moisture at different depths indicates that a multifrequency system could be used to estimate the near surface soil moisture profile. For instance, measurements of 500 MHz would provide average soil moisture estimates for a layer from the surface to below 20 cm, and 5 GHz should provide average soil moisture in a layer between 2 cm and 20 cm.

The theoretical development and the experimental measurements demonstrated that a uniform surface roughness similar to flat tilled fields reduces the sensitivity of the microwave emission to soil moisture changes. However, a technique of estimating surface roughness and soil moisture simultaneously was illustrated. Assuming that the surface roughness is known, the approximate soil moisture estimation accuracy at 1.4 GHz calculated for a 25% average soil moisture and a 80% degree of confidence, is +3% and -6% for a smooth bare surface, +4% and -5% for a medium rough surface, and +5.5% and -6% for a rough surface. At 10.6 GHz it was estimated that the surface soil moisture could be measured to within  $\pm 10\%$  for smooth and medium rough surfaces, and to within  $\pm 6\%$  for a rough surface. These approximate soil moisture estimation accuracies are considered to be conservative estimates since no error was assumed in the "ground truth" measurements.

The effect of row tillage on the ability to estimate soil moisture was also investigated experimentally. This investigation demonstrated that microwave emission measurements made parallel to the row direction have approximately the same response to soil moisture as would measurements made of a flat tilled field that had a surface roughness comparable to the small scale roughness superimposed on the



periodic row structure. Measurements made perpendicular to the row structure demonstrated that the moisture sensitivity is reduced. However, there were not enough experimental measurements to determine conclusively the degree of this reduction.

Measurements of vegetation canopies showed that the response to soil moisture at 1.4 GHz was not affected by uniformly planted sorghum 125 cm tall. An affect was evident on measurements of 188 cm tall sorghum, but a definite soil moisture response was still discernible. Row planted cotton 61 cm tall had no effect on 1.4 GHz measurements made parallel to the rows. All of the vegetation canopies used during the experimental investigation greatly reduced the soil moisture sensitivity of the 10.6 GHz measurements. No conclusive statements can be made concerning the amount of vegetation 10.6 GHz radiation can effectively penetrate.

The theme of the analysis of the experimental measurements was to determine the ability to estimate soil moisture remotely. However, this was done simply because the necessary information was not available to convert the ground measurements of soil moisture to soil water matric potential. The investigation of the soil water interaction and its effect on soil permittivity showed that soil permittivity is dependent on soil water matric potential

and that soil water matric potential is independent of soil texture. As a result, microwave sensors can be used to estimate soil water matric potential and, in fact, these estimates will be independent of soil texture. This point is extremely significant since it is soil matric potential that is the desired parameter in agricultural or hydrological applications requiring soil water information.

#### Recommendations

There are three recommendations that are considered to be most important in terms of initiating activities that will ultimately lead to the implementation of remote microwave soil moisture estimation systems for agricultural or hydrological applications. These recommendations call for:

1. The development of a water budget model that uses as its primary input the remote estimates of average soil moisture for at least two depths. The purpose of such a model would be to extend the near surface measurements of soil moisture that are obtainable with passive microwave sensors, to depths that are of concern to agriculturalists and hydrologists. The primary input to this model should be only remotely sensed information. No other soil moisture information should be used; however, other parameters

that are readily available from geologic maps etc. could be incorporated. It is only through such a model that the ability to remotely sense soil moisture using microwave sensors can be utilized to its full advantage for applications that will exist in the foreseeable future.

2. A study to identify applications that could benefit by remote measurements of soil water parameters, and the accuracy, depth of measurement, and resolution requirements of these applications.

3. An evaluation of optimum sensor parameters and the engineering considerations involved in implementing such parameters to obtain the required accuracy and repeatability of soil moisture estimates. A study of the optimum sensor parameters should include an investigation of frequencies other than 1.4 GHz and 10.6 GHz to determine other depths for which soil moisture can be measured. Such a study would also provide information to determine if surface moisture can be measured more accurately than at 10.6 GHz using a slightly lower frequency, perhaps 5 GHz, as a result of the decrease in the surface roughness effects. To decrease the complexity of implementing a system for estimating soil moisture, an estimation algorithm should be investigated using measurements at only one transmission angle (probably  $35^\circ$ ) rather than from two as was done in the illustration of Chapter VII.

The primary engineering considerations that will have to be addressed in order to implement a usable system will be related to the antenna. This is primarily a result of the low frequency and relatively high resolution requirements that will most likely be specified for particular applications. The effect of beamwidth averaging and polarization mixing should be investigated further, especially for row tilled surfaces.

In addition to the recommendations made above, there are several investigations that should be initiated in order to provide a better understanding of the physical process of thermal microwave emission from soil and vegetation, and its interrelationship with soil moisture.

1. The model development presented in Appendix A should be pursued and the discrepancies indicated in that development resolved. The basic formulation and approach appear to be promising although the equations derived did not provide adequate results. It is believed that such a formulation will provide additional insight into the physical phenomenon of microwave emission from uniformly rough surfaces.

2. A model should be developed for the emission from a composite rough surface so that the effects of row direction on the soil moisture sensitivity of microwave emission can be better understood. Additional experimental

measurements should also be obtained to better demonstrate the effects and to validate the model.

3. A more rigorous vegetation model than was presented in Chapter IV should be developed. Specifically, this model should include effects of scattering in the vegetation canopy to determine the importance of this effect.

4. Additional vegetation measurements should be made to determine the effects of vegetation at 10.6 GHz and a frequency between 10.6 GHz and 1.4 GHz. No conclusions have yet been drawn concerning the amount of vegetation through which soil moisture estimates can be made at these frequencies.

## REFERENCES

- [1] Baver, L. D., W. H. Gardner, and W. R. Gardner, Soil Physics, John Wiley and Sons, Inc., New York, 1972.
- [2] Kezdi, Arpad, Handbook of Soil Physics, Vol. I, Elsevier Scientific Publishing Company, New York, 1974.
- [3] Spangler, M. G., Soil Engineering, International Textbook Company, 1963.
- [4] Atterberg, A., "Die Mechanische Bodenanalyse und die Klassifikation der Mineralböden Schwedens," Intern Mitt. Bodenk, Vol. 2, 1912, pp. 312-342.
- [5] Black, C. A. (editor in chief), Methods of Soil Analysis-Part 1, American Society of Agronomy, Inc., Madison, Wisconsin, 1965, p. 86.
- [6] Kezdi, A., op. cit., pp. 47-48.
- [7] Algee, B. B., J. C. Callaghan and A. E. Creelman, "Rapid Determination of Moisture Content in Soil Samples Using High Power Microwaves," IEEE Transactions On Geoscience Electronics, Vol. GE-7, No. 1, January 1969, pp. 41-43.
- [8] Baver, L. D., W. H. Gardner, and W. R. Gardner, op. cit., p. 290.
- [9] Miller, R. J., R. B. Smith and J. W. Biggar, "Soil Water Content: Microwave Oven Method," Soil Science Society of America Proceedings, Vol. 38, No. 3, May-June 1974, pp. 535-537.
- [10] Taylor, S. A. and G. L. Ashcroft, Physical Edaphology, W. H. Freeman and Company, San Francisco, 1972.
- [11] Baver, L. D., W. H. Gardner and W. R. Gardner, op. cit., pp. 381-383.
- [12] Baver, L. D., W. H. Gardner and W. R. Gardner, op. cit., p. 400.
- [13] Newton, R. W., and W. R. McClellan, "Permittivity Measurements of Soils at L-band," Technical Report RSC-58, Remote Sensing Center, Texas A&M University, College Station, Texas, June 1975.

- [14] Cihlar, J. and F. T. Ulaby, "Dielectric Properties of Soils as a Function of Moisture Content," RSC Technical Report 177-97, Remote Sensing Laboratory, The University of Kansas Center for Research, Inc., Lawrence, Kansas, November 1974.
- [15] Wiebe, M. L., "Various Techniques of Dielectric Constant Measurements as Applied to the Relative Dielectric Constant of Sand as a Function of Moisture Content," Technical Memorandum RSC-22, Remote Sensing Center, Texas A&M University, College Station, Texas, May 1971.
- [16] Lundien, J. R., "Terrain Analysis by Electromagnetic Means," Technical Report No. 3-693, Report 5, U.S. Army Engineer Waterways Experiment Station, Vicksburg, Mississippi, 1971.
- [17] Idso, S. B., et al., "The Utility of Surface Temperature Measurements for the Remote Sensing of Surface Soil Water Status," Journal of Geophysical Research, Vol. 80, No. 21, July 20, 1975, pp. 3044-3049.
- [18] Hoekstra, P. and A. Delany, "Dielectric Properties of Soils at UHF and Microwave Frequencies," Journal of Geophysical Research, Volume 79, Number 11, April 10, 1974.
- [19] Haggis, G. H., J. B. Hasted, and T. J. Buchanan, "Dielectric Behavior of Water in Solutions," Journal of Chemical Physics, Volume 20, Number 9, September 1952.
- [20] Grant, E. H., T. J. Buchanan, and H. F. Cook, "Dielectric Behavior of Water at Microwave Frequencies," Journal of Chemical Physics, Volume 26, Number 1, January 1957.
- [21] Lane, J. A. and J. A. Saxton, "Dielectric Dispersion in Pure Polar Liquids at Very High Radio Frequencies, (Part I)," Proc. Roy. Soc., Volume A, Number 213, 1952.
- [22] Cole, K. S. and R. H. Cole, "Dispersion and Adsorption in Dielectrics; I. Alternating Current Characteristics," Journal of Chemical Physics, Volume 9, Number 341, 1971.
- [23] Geiger, F. E., and D. Williams, "Dielectric Constants of Soils at Microwave Frequencies," Goddard Space Flight Center, Greenbelt, Maryland, 1972.

- [24] Hipp, J. E., "Soil Electromagnetic Parameters as a Function of Frequency, Soil Density, and Soil Moisture," Proceedings of the IEEE, Vol. 62, No. 1, 1974, pp. 98-103.
- [25] Wiebe, M. L. "Laboratory Measurement of the Complex Dielectric Constant of Soils," Technical Report RSC-23, Remote Sensing Center, Texas A&M University, College Station, Texas, June 1971.
- [26] Babai, P., "Measurement of Complex Dielectric Constant of Soil Types in X-band," Technical Memorandum RSC-95, Remote Sensing Center, Texas A&M University, College Station, Texas, June 1974.
- [27] Poe, G. A., A. Stogryn, and A. T. Edgerton, "Determination of Soil Moisture Content Using Microwave Radiometry," Final Technical Report 1684-1, Aerojet General Corporation, El Monte, California, 1971.
- [28] Carver, K. R., (Personal Communication).
- [29] Peake, W. H., "Interaction of Electromagnetic Waves With Some Natural Surfaces," IRE Transactions on Antennas and Propagation, Vol. AP-7, December 1959, pp. 5324-5329.
- [30] Stogryn, A., "The Brightness Temperature of a Vertically Structured Medium," Radio Science, Vol. 5, No. 12, December 1970, pp. 1397-1406.
- [31] Tsang, L., E. Njoku, and J. A. Kong, "Microwave Thermal Emission From a Stratified Medium with Nonuniform Temperature Distribution," Journal of Applied Physics, Vol. 46, No. 2, December 1975, pp. 5127-5133.
- [32] Burke, W. J. and J. F. Paris, "A Radiative Transfer Model for Microwave Emission from Bare Agricultural Soils," NASA Technical Memorandum TM X-58166, National Aeronautics and Space Administration, Lyndon B. Johnson Space Center, Houston, Texas, August 1975.
- [33] Chen, S. N. L. and W. H. Peake, "Apparent Temperatures of Smooth and Rough Terrain," IRE Transactions On Antennas and Propagation, Vol. AP-9, December 1961, pp. 567-572.
- [34] Richerson, J. A., "An Experimental Evaluation of A Theoretical Model of the Microwave Emission of a Natural Surface," Technical Report RSC-27, Remote Sensing Center, Texas A&M University, College Station, Texas, August 1971.



- [35] Casey, K. F., "Application of Hill's Functions to Problems of Propagation in Stratified Media," IEEE Transactions on Antennas and Propagation, Vol. AP-20 No. 3, May 1972, pp. 368-374.
- [36] Whittaker, E. T. and G. N. Watson, A Course of Modern Analysis, Cambridge University Press, New York, 1963, pp. 413-417.
- [37] Landau, L., and E. Lifshitz, Electrodynamics of Continuous Media, Pergamon Press, London, 1960.
- [38] Bekefi, G., Radiation Processes in Plasmas, John Wiley, New York, 1966.
- [39] Tyrus, G., Radiation and Propagation of Electromagnetic Waves, Academic Press, New York, 1969.
- [40] Paris, J. F., "Transfer of Thermal Microwaves in the Atmosphere," Ph.D. Dissertation, Department of Meteorology, Texas A&M University, College Station, Texas, May 1971.
- [41] Stogryn, A., "Electromagnetic Scattering by Random Dielectric Constant Fluctuations in a Bounded Medium," Radio Science, Vol. 9, No. 5, May 1974, pp. 509-518.
- [42] Wilhelmi, G. J., J. W. Rouse, Jr., and A. J. Blanchard, "Depolarization of Light Backscattered from Rough Surfaces," Journal of the Optical Society of America, Vol. 65, No. 9, September 1975, pp. 1036-1042.
- [43] England, A. W., "Thermal Microwave Emission From a Halfspace Containing Scatterers," Radio Science, Vol. 9, No. 4, April 1974, pp. 447-454.
- [44] Stogryn, A., "The Apparent Temperature of the Sea at Microwave Frequencies," IEEE Transactions on Antennas and Propagation, Vol. AP-15, pp. 278-286, March 1967.
- [45] Johnson, L. F., "On the Performance of Infrared Sensors in Earth Observations," Technical Report RSC-37, Remote Sensing Center, Texas A&M University, College Station, Texas, August 1972.
- [46] Tyras, G., op. cit., p. 88.

- [47] Beckmann, P., "Modeling of Rough Surfaces," AGARD, 20th EWPP Meeting on Electromagnetic Wave Propagation Involving Irregular Surfaces and Inhomogeneous Media, The Hague, Netherlands, March 25-29, 1974.
- [48] Kodis, R., "A Note On the Theory of Scattering From an Irregular Surface," IEEE Transactions on Antennas and Propagation, Vol. AP-14, No. 1, January 1966, pp. 77-82.
- [49] Barrick, D. E., "Rough Surface Scattering Based on the Specular Point Theory," IEEE Transactions on Antennas and Propagation, Vol. AP-16, No. 4, July 1968, pp. 449-454.
- [50] Fung, A. K., R. M. Axline, and H. L. Chan, "Exact Scattering From a Known Randomly Rough Surface," Proceedings of the URSI, Commission II Microwave Scattering and Emission from the Earth, Berne, Switzerland, September 23-26, 1974.
- [51] Spetner, L. and I. Katz, "Two Statistical Models for Radar Terrain Return," IRE Transactions on Antennas and Propagation, Vol. 8, May 1960, pp. 242-246.
- [52] Waite, W. P., "Broad-Spectrum Electromagnetic Backscatter," CRES Technical Report 133-17, University of Kansas Center for Research, Inc., Lawrence, August 1970.
- [53] Katzin, M., "On the Mechanisms of Radar Sea Clutter," Proceedings of the IRE, Vol. 44, January 1957, pp. 44-54.
- [54] Khamsi, H. R., A. K. Fung and F. T. Ulaby, "Rough Surface Scattering Based on Facet Model," RSL Technical Report 177-52, The University of Kansas Center for Research, Inc., Lawrence, Kansas, November 1974.
- [55] Fung, A. K., "Scattering Theories and Radar Return," CRES Report No. 48-3, University of Kansas Center for Research, Inc., 1966.
- [56] Beckmann, P. and A. Spizzichino, The Scattering of Electromagnetic Waves From Rough Surfaces, The MacMillan Company, New York, 1963, p. 20.

- [57] Brekkovskikh, L. M., "The Diffraction of Waves by a Rough Surface," Part I and Part II, Zh. Eksper. i Teor. Fiz., Vol. 23, 1952, pp. 275-304
- [58] Beckmann, P. and A. Spizzichino, op.cit., p. 66.
- [59] Fung, A. K., "On Depolarization of Electromagnetic Waves Backscattered From a Rough Surface," Planetary Space Sciences, Vol. 14, 1966, pp. 563-568.
- [60] Stogryn, A., "Electromagnetic Scattering From Rough, Finitely Conducting Surfaces," Radio Science, Vol. 2 (New Series), No. 4, April 1967, pp. 415-428.
- [61] Leader, J. C., "Bidirectional Scattering of Electromagnetic Waves From Rough Surfaces," Presented at the Spring meeting of the USNC/URSI of the IEEE, Washington, D.C., April 16, 1970.
- [62] Rice, S. O., "Reflection of Electromagnetic Waves From Slightly Rough Surfaces," Communications of Pure and Applied Mathematics, Vol. 4, 1951, pp. 351-378.
- [63] Lord Rayleigh, Theory of Sound, Vol. II, MacMillan Company, London, England, 1929, pp. 89-96.
- [64] Valenzuela, G. R., "Depolarization of EM Waves By Slightly Rough Surfaces," IEEE Transactions on Antennas and Propagation, Vol. AP-15, No. 4, July 1967, pp. 552-557.
- [65] Beckmann P., "Scattering by Composite Rough Surfaces," Proceedings of the IEEE, Vol. 53, August 1965, pp. 1012-1015.
- [66] Wright, J. W., "A New Model for Sea Clutter," IEEE Transactions on Antennas and Propagation, Vol. AP-16, No. 2, March 1968, pp. 217-223.
- [67] Chan, H. L. and A. K. Fung, "Backscattering From a Two-Scale Rough Surface with Application to Radar Sea Return," NASA Contract Report CR-2327, NASA Langley Research Center, November 1973.
- [68] Wu, S. T. and A. K. Fung, "A Noncoherent Model for Microwave Emissions and Backscattering from the Sea Surface," Journal of Geophysical Research, Vol. 77, No. 30, October 20, 1972.

- [69] Rosenbaum, S. and L. W. Bowles, "Clutter Return From Vegetated Areas," IEEE Transactions on Antennas and Propagation, Vol. AP-22, No. 2, March 1974, pp. 227-236.
- [70] Sachs, D. L. and P. L. Wyatt, "A Conducting-Slab Model for Electromagnetic Propagation Within a Jungle Medium," Radio Science, Vol. 3 (New Series), No. 2, February 1968, pp. 125-134.
- [71] Tamir, T., "On Radio-Wave Propagation in Forest Environments," IEEE Transactions on Antennas and Propagation, Vol. AP-15, No. 6, November 1967, pp. 806-817.
- [72] Du, Li-Jen, "Scattering and Absorption by Large Leaves at Microwave Frequencies," Technical Report 2440-6, Electro Science Laboratory, Ohio State University, Columbus, Ohio, January 1969.
- [73] Peake, W. H., "Theory of Radar Return from Terrain," IRE International Convention Record, Vol. 7, Part 1: 27, 1959.
- [74] Waite, W. P. and K. R. Cook, "Broad Spectrum Microwave Systems for Remotely Measuring Ecological Parameters," Final Report Project NSF 31515, Department of Electrical Engineering, University of Arkansas, Fayetteville, Arkansas, December 1974.
- [75] Sibley, R., "Microwave Emission and Scattering from Vegetated Terrain," Technical Report RSC-44, Remote Sensing Center, Texas A&M University, College Station, Texas, August 1973.
- [76] Evans, S., "Dielectric Properties of Ice and Snow," Journal of Glaciology, Vol. 5, No. 42, October 1965, pp. 773-792.
- [77] Peake, W. H., and T. L. Oliver, "The Response of Terrestrial Surfaces at Microwave Frequencies," Technical Report AFAL-TR-70-301, Electro Science Laboratory, Ohio State University, Columbus, Ohio, May 1971.
- [78] Basharinov, A. Ye, and A. M. Shutko, "Simulation Studies of SHF Radiation Characteristics of Soils Under Moist Conditions," Academy of Sciences USSR, Institute of Radio Engineering and Electronics (unpublished report), NASA Technical Translation, NASA TT F-16, 489, August 1975.

- [79] Ulaby, F. T., J. Cihlar and R. K. Moore, "Active Microwave Measurements of Soil Water Content," Remote Sensing of Environment, Vol. 3, 1974, pp. 185-203.
- [80] Ulaby, F. T. and P. P. Batlivala, "Optimum Parameters For Mapping Soil Moisture," IEEE Transactions on Geoscience Electronics, Vol. GE-14, No. 2, April 1976, pp. 81-93.
- [81] Ulaby, F. T., "Radar Response to Vegetation," IEEE Transactions on Antennas and Propagation, Vol. AP-23, No. 1, January 1975.
- [82] Ulaby, F. T. and P. P. Batlivala, "Diurnal Variations of Radar Backscatter From a Vegetation Canopy," IEEE Transactions on Antennas and Propagation, Vol. AP-24, No. 1, January 1976.
- [83] Jean, B. R., "Selected Applications of Microwave Radiometer Techniques," Technical Report RSC-30, Remote Sensing Center, Texas A&M University, College Station, Texas, August 1971.
- [84] Kroll, C. L., "Remote Monitoring of Soil Moisture Using Airborne Microwave Radiometers," Technical Report RSC-43, Remote Sensing Center, Texas A&M University, College Station, Texas, June 1973.
- [85] Schmugge, T., T. Wilheit, W. Webster and P. Gloersen, "Remote Sensing of Soil Moisture with Microwave-Radiometers-II," Technical Note G-76114, Goddard Space Flight Center, Greenbelt, Maryland, June 1976.
- [86] Schmugge, T., et al., "Results of Soil Moisture Flights During April 1974," NASA Technical Note TN D-8199, NASA Goddard Space Flight Center, Greenbelt, Maryland, May 1976.
- [87] Jackson, R. D., "Diurnal Changes in Soil Water Content During Drying," Field Soil Water Regime, Soil Society of America, Madison, Wisconsin, 1973, pp. 37-51.
- [88] Jean, B. R., J. A. Richerson and J. W. Rouse, Jr., "Experimental Microwave Measurements of Controlled Surfaces," Seventh International Symposium on Remote Sensing of Environment, University of Michigan, Ann Arbor, Michigan, May 17-21, 1971.

- [89] Blinn, J. C. and J. G. Quade, "Microwave Properties of Geologic Materials: Studies of Penetration Depth and Moisture Effects," 4th Annual Earth Resources Program Review, NASA Manned Spacecraft Center, Houston, Texas, January 17-21, 1972, pp. 53-1 to 53-12.
- [90] Blinn, J. C., J. E. Conel and J. G. Quade, "Microwave Emission From Geologic Materials: Observations of Interference Effects," Journal of Geophysical Research, Vol. 77, No. 23, August 10, 1972, pp. 4366-4378.
- [91] Lee, S. L., "Dual Frequency Microwave Radiometer Measurements of Soil Moisture for Bare and Vegetated Rough Surfaces, Technical Report RSC-56, Remote Sensing Center, Texas A&M University, August 1974.
- [92] Newton, R. W. et al., "On the Feasibility of Remote Monitoring of Soil Moisture with Microwave Sensors," Ninth International Symposium on Remote Sensing of Environment, University of Michigan, Ann Arbor, Michigan, April 15-19, 1974.
- [93] Poe, G., A. Stogryn and A. T. Edgerton, "Determination of Soil Moisture Content Using Microwave Radiometry," Summary Report 1684R-2, Aerojet General Corporation, El Monte, California, June 1971.
- [94] Riegler, R. L., "Radar and Microwave Radiometric Techniques for Geoscience Experiments," Report 1903-2, The Ohio State University Research Foundation, Columbus, Ohio, June 1966.
- [95] Chandrasekhar, S., Radiative Transfer, Dover Publications, Inc., New York, 1960.
- [96] Goody, R. M., Atmospheric Radiation; I. Theoretical Basis, Clarendon Press, Oxford, 1964.
- [97] Stratton, J. A., Electromagnetic Theory, McGraw-Hill Book Company, Inc., New York, 1941.
- [98] Ramo, S., J. R. Whinnery, and T. V. Van Duzer, Fields and Waves in Communication Electronics, John Wiley and Sons, Inc., 1965.
- [99] Silver, S., Microwave Antenna Theory and Design, MIT Radiation Laboratory Series, Vol. 12, McGraw-Hill, New York, 1947.

- [100] Hasted, J. B., "The Dielectric Properties of Water," Progress in Dielectrics, Vol. 3, John Wiley and Sons, Inc., New York, 1961, pp. 101-149.
- [101] Cole, R. H., "Theories of Dielectric Polarization and Relaxation," Progress in Dielectrics, Vol. 3, John Wiley and Sons, Inc., New York, 1961, pp. 47-99.
- [102] Hornbostel, D., "Hot and Cold Body Reference Noise Generators From 0 to 40 GHz," (work supported under NASA/MSO contracts NAS 9-11275 and NAS 9-12045), AIL, a division of Cutler Hammer, Commack, New York, December 1972.
- [103] Newton, R. W., "Passive Microwave Data Report: Joint Soil Moisture Experiment at Texas A&M University; June 26-July 21, 1974", Technical Report RSC-65, Remote Sensing Center, Texas A&M University, College Station, Texas, January 1975.
- [104] Newton, R. W. and E. A. Tesch, "Joint Soil Moisture Experiment: Ground Based Measurements at Texas A&M University; July 13-July 25, 1975," Technical Report RSC-71, Remote Sensing Center, Texas A&M University, College Station, Texas, January 1976.
- [105] Clark, B. V. and R. W. Newton, "Revision to Operating System Software for Microwave Signature Acquisition System," Technical Report RSC-75, Remote Sensing Center, Texas A&M University, College Station, Texas, July 1976.
- [106] Battivala, P. P. and J. Cihlar, "Joint Soil Moisture Experiment (Texas): Documentation of Radar Backscatter and Ground Truth Data," RSL Technical Report 264-1, Remote Sensing Laboratory, University of Kansas, Lawrence, Kansas, April 1975.
- [107] Newton, R. W. and S. L. Lee, "Ground Data Report: Joint Soil Moisture Experiment at Texas A&M University; June 26-July 21, 1974," Technical Report RSC-61, Remote Sensing Center, Texas A&M University, College Station, Texas, October 1974.
- [108] Paris, J. F., "Data Processing Equations for the Microwave Signature Acquisition System (MSAS)," LEC/ASD 640-TR, A.D. 63-0497-3435-07, Lockheed Electronics Company, Inc., Aerospace Systems Division, Houston, Texas, December 1974.

- [109] Love, T. J., Radiative Heat Transfer, Charles E. Merrill Publishing Company, Columbus, Ohio, 1968.
- [110] Jordan, E. C., and K. G. Balmain, Electromagnetic Waves and Radiating Systems, Printice-Hall Inc., Englewood Cliffs, New Jersey, 1968.
- [111] Peake, W. H., R. L. Riegler and C. H. Schultz, "The Mutual Interpretation of Active and Passive Microwave Sensor Outputs," Proceedings of the Fourth Symposium on Remote Sensing of Environment, Willow Run Laboratories, the University of Michigan, Ann Arbor, Michigan, December 1966, pp. 771-777.
- [112] Claassen, J. P. and A. K. Fung, "The Recovery of Polarized Apparent Temperature Distributions of Flat Scenes From Antenna Temperature Measurements," IEEE Transactions on Antennas and Propagation, Vol. AP-22, No. 3, May 1974, pp. 433-442.
- [113] Grody, N. C., "Antenna Temperature for a Scanning Microwave Radiometer," IEEE Transactions on Antennas and Propagation (communication), Vol. AP-23, No. 1, January 1975, pp. 141-144.
- [114] Paris, J. F., "MAODAP - Microwave Atmospheric and Oceanic Data Analysis Program," LEC/HASD Document No. 640-TR-078, Lockheed Electronics Company, Inc., Houston Aerospace Systems Division, Houston, Texas, December 1971.
- [115] Batlivala, P. P., and F. T. Ulaby, "Effects of Roughness on the Radar Response to Soil Moisture of Bare Ground," RSL Technical Report 264-5, Remote Sensing Laboratory, University of Kansas, Lawrence, Kansas, September 1975.
- [116] Ostle, B., and R. W. Mensing, Statistics in Research, The Iowa State University Press, Ames, Iowa, 1975.



## APPENDIX A

## DIFFERENTIAL TRANSMISSION COEFFICIENTS

An attempt was made to develop an expression for differential transmission coefficients using the Kirchhoff approximation in conjunction with the Stratton-Chu integral as modified by Silver [99]. In utilizing this approach the following assumptions were made:

- 1) The incident wave is plane and linearly polarized.
- 2) Multiple interaction and irregularities such as shadowing and multiple scattering may be neglected.
- 3) The observation point is in the far zone.
- 4) The integral is applied over a finite portion of a closed surface.
- 5) The surface can be approximated at any point as an infinite plane.
- 6) Only energy in the plane of incidence is considered.

The expression for the far field reradiation electric field,  $E_s$ , at a point P (Figure A-1) with the time variation understood is given by [99]:

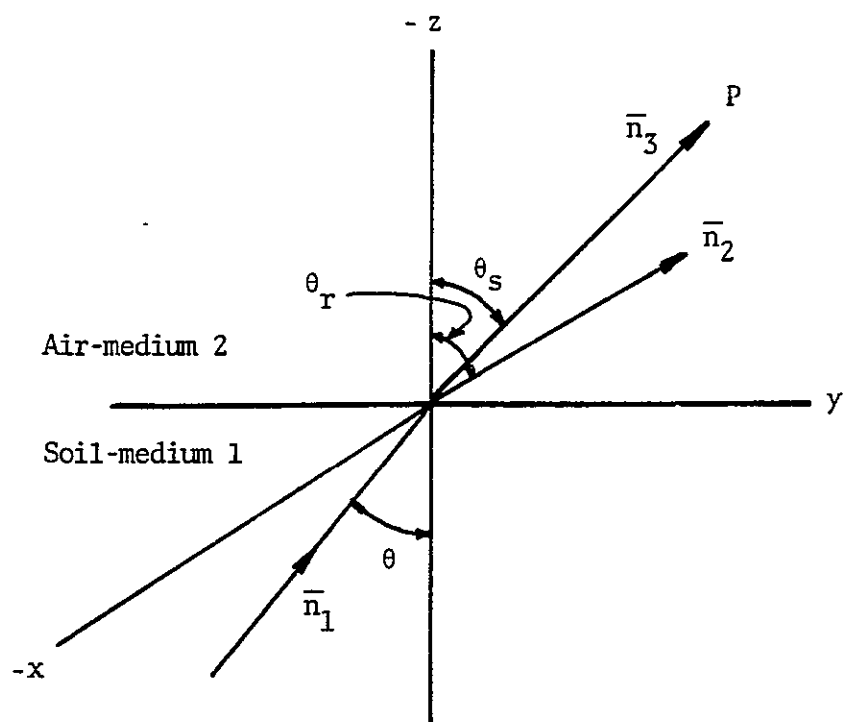


Figure A-1. Geometry used in describing the differential transmission coefficients.

$$E_s(P) = K \bar{m}_3 \times \iint_{\text{Area}} \left[ -\bar{n} \times E_s - \eta_1 \bar{m}_3 \times (-\bar{n} \times \bar{H}_s) \right] \cdot \exp(j k_2 \bar{r} \cdot \bar{m}_3) dS \quad (\text{A-1})$$

where

$$K = (-j k_2 \exp(-j k_2 R)) (4\pi R)^{-1}$$

$\bar{r}$  - position vector from the origin of the coordinate system to the surface element  $dS$

$\bar{n}_3$  - a unit vector in the direction of observation (to point P)

$\eta_1$  - intrinsic impedance of the soil

$\bar{n}$  - unit local surface normal

$k_2$  - wave number in air

$R$  - distance from the origin to the point of observation (point P)

$\bar{E}_s$  - total transmitted electric field at the surface due to the radiation from the soil volume

$\bar{H}_s$  - total transmitted magnetic field at the surface due to the radiation from the soil volume

Propagation of the incident energy is along the vector  $\bar{n}_1$ . The transmitted energy is propagated along  $\bar{n}_3$ . The

unit vector  $\bar{n}_2$  defines the smooth surface angle of refraction. Note that  $-\bar{n} \times \bar{E}_s$  and  $-\bar{n} \times \bar{H}_s$  are the currents on the surface that cause radiation into the upper hemisphere. These currents are due to the radiation impinging on the surface from the soil volume. Equation (A-1) therefore defines the electric field at point P due to the surface currents within the area of illumination that are a result of radiation from the soil volume.

Adapting the notation of Fung [55], two local orthonormal coordinate systems are constructed,  $\bar{n}_1$ ,  $\bar{t}_1$  and  $\bar{d}_1$  in the subsurface and  $\bar{n}_2$ ,  $\bar{t}_2$  and  $\bar{d}_2$  above the surface.

$$\bar{t}_1 = (\bar{m}_1 \times \bar{m})(1 - \bar{m}_2 \cdot \bar{m})^{-1/2}$$

$$\bar{d}_1 = (\bar{m}_1 \times \bar{t}_1)$$

(A-2)

$$\bar{t}_2 = (\bar{m}_2 \times (-\bar{m}))(1 + \bar{m}_2 \cdot \bar{m})^{-1/2}$$

$$\bar{d}_2 = (\bar{m}_2 \times \bar{t}_2)$$

In order to determine the values of  $(-\bar{n} \times \bar{E}_s)$  and  $(-\bar{n} \times \bar{H}_s)$  at each point on the surface, the incident fields from the soil volume are resolved into local polarization components parallel and normal to the local plane of incidence, and multiplied by the corresponding transmission coefficient.

The incident electric and magnetic fields, with the time variations understood, can be defined as

$$\bar{E}_o = \bar{a}_1 [E_o \exp(-jk_1 \bar{m}_1 \cdot \bar{r})]$$

(A-3)

$$\bar{H}_o = (\bar{m}_1 \times \bar{a}_1) E_o / \eta_1$$

where

$\eta_1$  - intrinsic impedance of the soil

$k_1$  - wave number in the soil

Components of the transmitted fields normal to the plane of incidence (horizontal polarization) are given by:

$$E_s^h = [((\bar{a}_1 \cdot \bar{t}_1) \bar{E}_o) t_h] \bar{t}_2$$

(A-4)

$$H_s^h = [((\bar{a}_1 \cdot \bar{t}_1) \bar{E}_o / \eta_1) t_h] \bar{d}_2$$

The components parallel to the plane of incidence (vertical polarization) are given by

$$E_s^v = [((\bar{a}_1 \cdot \bar{d}_1) \bar{E}_0) t_v] \bar{d}_2$$

(A-5)

$$H_s^v = [(-(a_1 \cdot d_1) \bar{E}_0 / \eta_1) t_v] \bar{t}_2$$

The local surface currents can now be expressed as

$$-\bar{m} \times \bar{E}_s = [t_h(\bar{a}_1 \cdot \bar{t}_1)(-\bar{m} \times \bar{t}_2) + t_v(\bar{a}_1 \cdot \bar{d}_1)(-\bar{m} \times \bar{d}_2)] \bar{E}_0$$

$$-\bar{m} \times \bar{H}_s = [t_h(\bar{a}_1 \cdot \bar{t}_1)(-\bar{m} \times \bar{d}_2) + t_v(\bar{a}_1 \cdot \bar{d}_1)(-\bar{m} \times \bar{t}_2)] \bar{E}_0 / \eta_1$$

where

$t_h$  - horizontal electric field transmission coefficient

$t_v$  - vertical electric field transmission coefficient

The integral defining the electric field at point P and polarization i, (A-1), can now be written in the form

$$\begin{aligned}
E_{s_x}(P) = K \iint & \left[ t_h(\bar{a}_1 \cdot \bar{e}_1) \bar{m}_3 \times (-\bar{m} \times \bar{e}_1) \right. \\
& + t_v(\bar{a}_1 \cdot \bar{d}_1) \bar{m}_3 \times (-\bar{m} \times \bar{d}_2) - \bar{m}_3 \times \\
& \left. \left[ t_h(\bar{a}_1 \cdot \bar{e}_1) \bar{m}_3 \times (-\bar{m} \times \bar{d}_2) - t_v(\bar{a}_1 \cdot \bar{d}_1) \bar{m}_3 \times \right. \right. \\
& \left. \left. (-\bar{m} \times \bar{e}_2) \right] \right] E_0 \exp(j\bar{r} \cdot (k_2 \bar{m}_3 - k_1 \bar{m}_1)) dS
\end{aligned} \tag{A-6}$$

where

$$\begin{aligned}
\bar{n} &= (-\bar{i} z_x - \bar{j} z_y + \bar{k}) (z_x^2 + z_y^2 + 1)^{-1/2} \\
z_x &- \text{local surface slope in } x \text{ direction} \\
z_y &- \text{local surface slope in } y \text{ direction} \\
\bar{n}_1 &= \bar{j} \sin \theta_0 - \bar{k} \cos \theta_0 \\
\bar{n}_2 &= \bar{a}_d \sin \theta_r - \bar{n} \cos \theta_r \\
\bar{a}_{d2} &= (-\bar{n} \times \bar{t}_2) \\
\bar{a}_1 &= \bar{i}, \text{ horizontal polarization} \\
\bar{a}_1 &= \bar{j} \cos \theta_0 + \bar{k} \sin \theta_0; \text{ vertical polarization}
\end{aligned}$$

Equation (A-6) is evaluated by converting the cross products to dot products using vector identities, then expanding the result in a Taylor series with respect to surface slopes  $z_x$  and  $z_y$ , and integrating. The expansion of (A-6) results in

$$E_{s_i}(P) = K E_o \iint [a_i + z_y a_{y_i}] \exp(j \vec{r} \cdot (k_2 \vec{m}_3 - k_1 \vec{m}_1)) dS \quad (A-7)$$

For horizontal polarization

$$a_h = -\bar{L} (t_h \cos \theta_s + t_h \cos \theta_r) \Big|_{z_x = z_y = 0}$$

$$a_{y_h} = -\bar{L} \left( \cos \theta_s \frac{\partial t_h}{\partial z_y} + t_h + \cos \theta_r \frac{\partial t_h}{\partial z_y} + t_h \frac{\sin^2 \theta_r \cos \theta_o}{\sin \theta_o \cos \theta_r} \right) \Big|_{z_x = z_y = 0} \quad (A-8)$$

and for vertical polarization

$$a_v = \bar{J} (-t_v + t_v \sin^2 \theta_s - t_v \cos \theta_r \cos \theta_s) \Big|_{z_x = z_y = 0}$$

$$+ \bar{K} (-t_v \sin \theta_s \cos \theta_r - t_v \cos \theta_s \sin \theta_r) \Big|_{z_x = z_y = 0} \quad (A-9)$$

C-4



$$a_{y_v} = \bar{j} \left( -t_v \frac{\cos \theta_s \cos \theta_o \sin^2 \theta_r}{\cos \theta_r \sin \theta_o} - t_v \cos \theta_s \sin \theta_o \right. \\ \left. + \frac{\partial t_v}{\partial z_y} \sin^2 \theta_s - \frac{\partial t_v}{\partial z_y} \cos \theta_s \cos \theta_r - \frac{\partial t_v}{\partial z_y} \right) \Big|_{z_x = z_y = 0}$$

$$+ \bar{k} \left( \cos \theta_s \cos \theta_o \sin \theta_r - \cos \theta_s \cos \theta_r \right. \\ \left. - t_v \frac{\sin \theta_s \sin^2 \theta_r \cos \theta_o}{\sin \theta_o \cos \theta_r} + t_v \cos \theta_s \cos \theta_o \right. \\ \left. - t_v \cos \theta_s \cos \theta_r - \frac{\partial t_v}{\partial z_y} \sin \theta_s \cos \theta_r \right) \Big|_{z_x = z_y = 0}$$

Note that there are no "edge effect" terms (i.e., there is no dependence on  $\partial t_i / \partial z_x$ ). This is a result of the fact that the radiation incident on the surface from below is not depolarized by the surface. There are no terms involving  $t_v$  for horizontal polarization and no terms involving  $t_h$  for vertical polarization.

Leader [61] has evaluated the corresponding integral to (A-7) for the bistatic scattering case. An analogous integration of (A-7) results in

$$I_{s_{ii}} = \frac{\langle E_{s_i}(P) E_{s_i}^*(P) \rangle}{\text{Real}(\eta_{\text{air}})}$$

$$= \frac{2\pi A}{(4\pi R)^2} \left| E_{o_i} \left( a - \frac{m_y}{m_z} a_y \right) \right|^2 \frac{Q m_z^2}{(m_z^2 + m_y^2 Q)^{3/2}} \quad (\text{A-10})$$

where

$$\bar{n}_y = \sin \theta_s - \sin \theta_r$$

$$\bar{n}_z = -\cos \theta_s + \frac{\beta_1}{\beta_2} \cos \theta_r$$

$\beta_1$  - phase constant in the soil

$\beta_2$  - phase constant in the air (1.0)

$Q$  - parameter related to surface roughness

Again, the first subscript on  $I_s$  indicates the polarization of the incident radiation and the second indicates the polarization of the transmitted radiation.

Note that the surface roughness is defined by the parameter  $Q$ . Leader [61] relates  $Q$  to the autocorrelation of the surface. For the case under consideration,

$$Q = [k_1 C'(\tau_0) \sigma_z^2]^{-2} \quad (A-11)$$

where

$k_1$  - wave number in the soil

$C'(\tau_0)$  - derivative of the autocorrelation function of the surface evaluated at a point

$\tau_0$  - point of expansion of  $C(\tau)$  in the evaluation of the integral (A-7)

$\sigma_z^2$  - surface height variance

The point of expansion increases with angle  $\theta_0$ . Since  $C'(\tau)$  increases with  $\tau$ ,  $Q$  decreases with increasing angle  $\theta_0$  [61].

The differential transmission coefficients are defined by

$$\begin{aligned}
 \tau_i(\theta_o, \phi_o; \theta_s, \phi_s) &= \tau_i(0, s) = \frac{4\pi R^2 I_{s,ii}}{(I_o \cos \theta_o) A} + \frac{4\pi R^2 I_{s,ji}}{(I_o \cos \theta_o) A} \\
 &= \tau_{ii}(0, s) + \tau_{ji}(0, s)
 \end{aligned}
 \tag{A-12}$$

It was shown above that

$$I_{s,ji} = 0$$

so

$$\tau_{ij}(0, s) = \tau_{ji}(0, s) = 0$$

Noting that

$$I_{o,i} = \frac{|E_{o,i}|^2}{\text{Reol}(\eta_i)}$$

then the differential scattering coefficient is

$$\tau_i(0,s) = \tau_{ii}(0,s) = \frac{4\pi R^2}{\cos \theta_0 A} \frac{2\pi A}{(4\pi R)^2} \frac{\text{Real}(\eta_1)}{\text{Real}(\eta_2)}.$$

$$\left| a - \frac{m_y}{m_z} a_y \right|^2 \frac{Q m_z^2}{(m_z^4 + Q m_y^2)^{3/2}} \quad (\text{A-13})$$

$$\tau_i(0,s) = \frac{1}{2 \cos \theta \sqrt{\epsilon'_{r1}}} \left| a - \frac{m_y}{m_z} a_y \right|^2 \frac{Q m_z^2}{(m_z^4 + Q m_y^2)^{3/2}}$$

where

$\epsilon'_{r1}$  - real part of the relative soil permittivity

Equation (A-10) is only a function of angle  $\theta_0$  in the plane of incidence,  $\phi = 0^\circ$ . It was assumed at the beginning of the derivation that the contribution to the electric field at point P due to radiation incident on the surface outside the plane of incidence would be neglected. Equation (A-13) can therefore be written

$$\tau_i(\theta_0, \theta_s) = \frac{1}{2 \cos \theta_0 \sqrt{\epsilon'_{r1}}} \left| a - \frac{m_y}{m_z} a_y \right|^2. \quad (\text{A-14})$$

$$\frac{Q m_z^2}{(m_z^4 + Q m_y^2)^{3/2}} \delta(\phi_0 = 0^\circ)$$

where  $\delta(\phi_0 = 0^\circ)$  is the direct delta function evaluated at  $\phi_0 = 0^\circ$ . This allows (A-14) to be integrated over  $\phi_0$  to yield

$$BT_{\text{soil}_i}(\theta_s) = \frac{1}{4\pi} \int_{\theta_0} \tau_{ii}(\theta_0, \theta_s) BT_{\text{volume}_i}(\theta_0) \sin \theta_0 d\theta_0 \quad (\text{A-15})$$

since  $\tau_{ji}(\theta_0, \theta_s)$  is zero.

Although the derivation of (A-14) is based on sound physical principles, calculations based on (A-15) did not adequately match antenna measurements. Currently, it is uncertain as to whether or not the poor results were due to improper implementation of (A-14) and A-15), or an error in the derivation. The calculations demonstrated that the change in magnitude of the term

$$\frac{Q m_z^2}{(m_z^4 + Q m_y^2)^{3/2}}$$

with soil moisture was too large. It caused an unrealistic dependence of soil brightness temperature (as defined by (A-15)) on soil moisture.

## APPENDIX B

## CORRECTION OF DATA FOR SELF EMISSION

## The Self Emission Contribution

Inspection of data acquired over Easterwood Pond (Figures B-1 and B-2) reveals anomalously high radiometric antenna temperatures for angles near nadir. This effect will be demonstrated to be a result of noise emission from the MSAS being reflected off of the water surface back into the MSAS receiving aperture. As expected this effect is also apparent in the bare soil measurements, but to a lesser degree because of the smaller soil permittivity. This effect is a function of the backscattering coefficient of the scene which depends on permittivity and surface roughness. As a result, the noise contribution to the measured antenna temperature resulting from self emission will vary with moisture content, surface roughness, and incident angle. The 1974 measurement set will be used below to demonstrate the magnitude of the self emission component.

The theoretical variation of the brightness temperature of a smooth surface as a function of transmission angle and polarization is given in Figure B-3. Note that the brightness temperature varies little between nadir and  $20^\circ$ . Also, the brightness temperature at nadir is

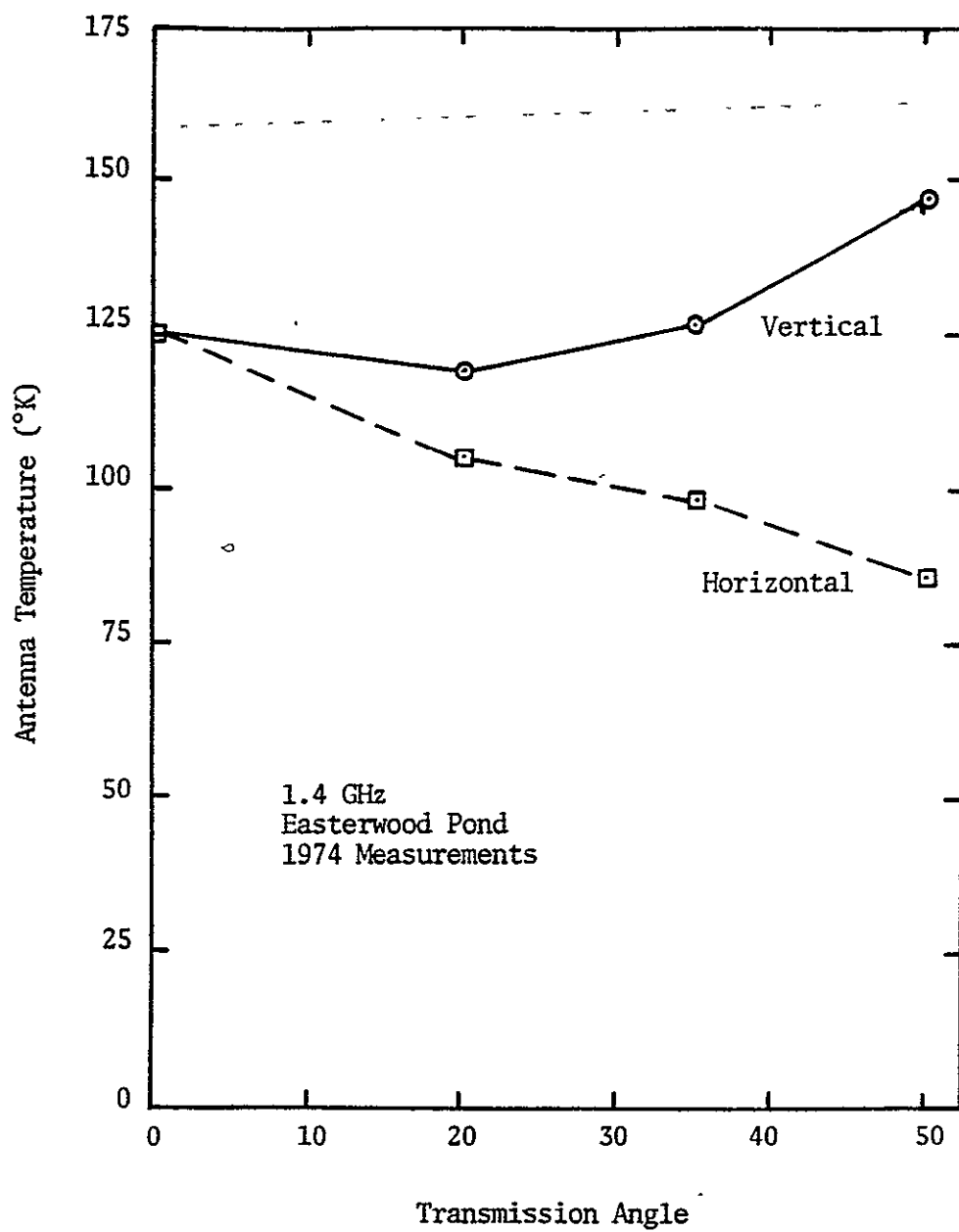


Figure B-1. 1.4 GHz fresh water measurements that demonstrate the effect of self emission near nadir.



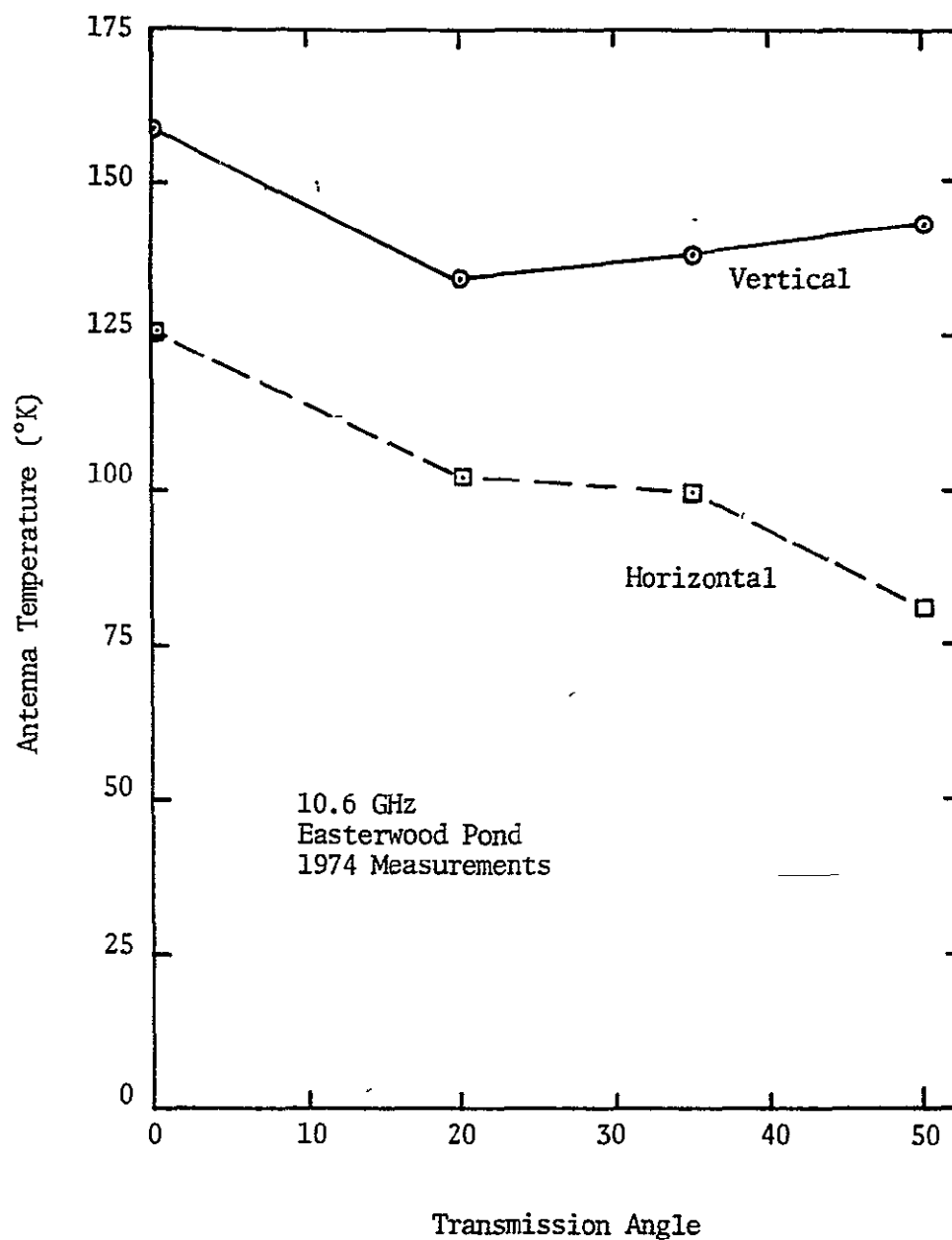


Figure B-2. 10.6 GHz fresh water measurements that demonstrate the effect of self emission near nadir.

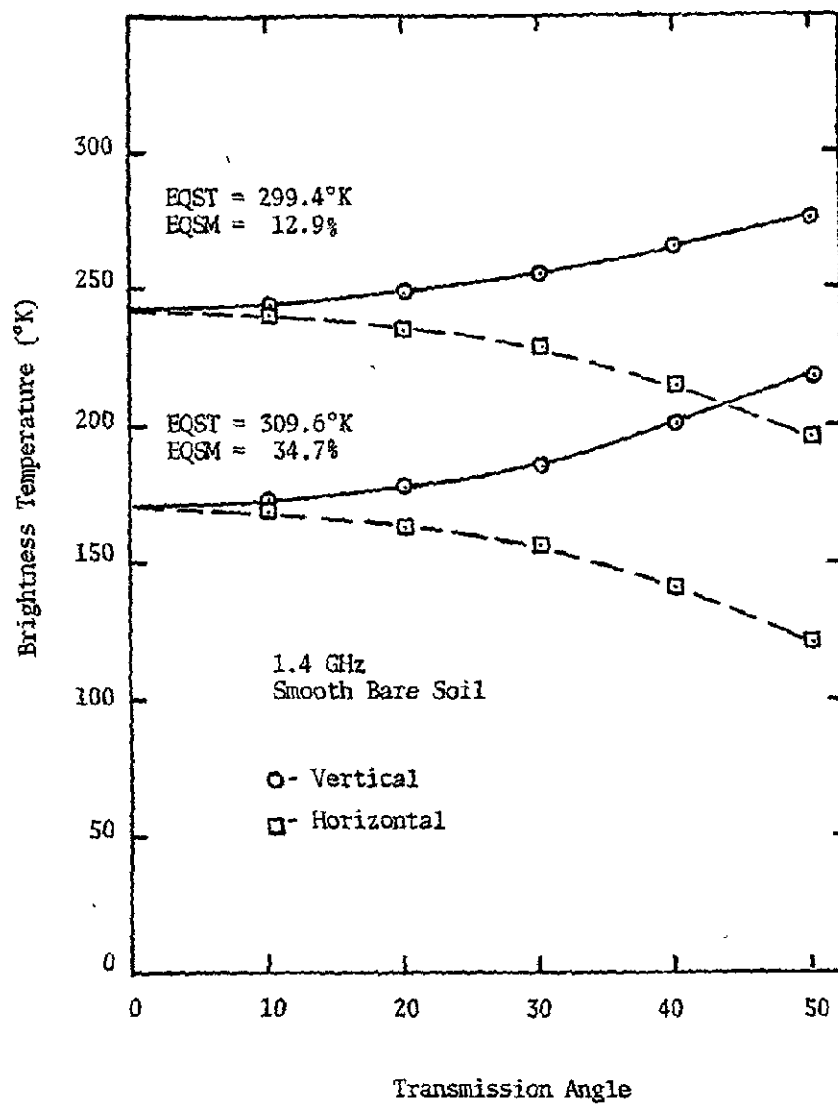


Figure B-3. Calculations of the brightness temperature of smooth bare soil for two extreme moisture conditions.

approximately equal to the horizontal brightness temperature at  $20^\circ$  plus one half of the difference between vertical and horizontal brightness temperatures at  $20^\circ$ . A similar relationship can also be expected for the brightness temperatures of rough surfaces between nadir and  $20^\circ$ . With this in mind, the effect of self emission is apparent in the data of Figures B-4 through B-6. The dotted lines in these figures show the expected normalized antenna temperatures approximated as described above. Note that the self emission at nadir decreases as the surface roughness increases and as the soil moisture decreases.

#### Correction Scheme Using Radar Data

The self emission component to the measured antenna temperature does not only occur at nadir, but is present for all transmission angles. However, the magnitude of this component is a direct function of the backscattering coefficient at each transmission angle (note that transmission angle and incident angle are equivalent). For most surfaces, except perhaps the very rough surface, the magnitude of the backscattering coefficient decreases rapidly with transmission angle. As a result, the self emitted noise energy reflected back to the receiving aperture is a very small component of the total apparent radiation received by the antenna at angles greater than about  $20^\circ$ .

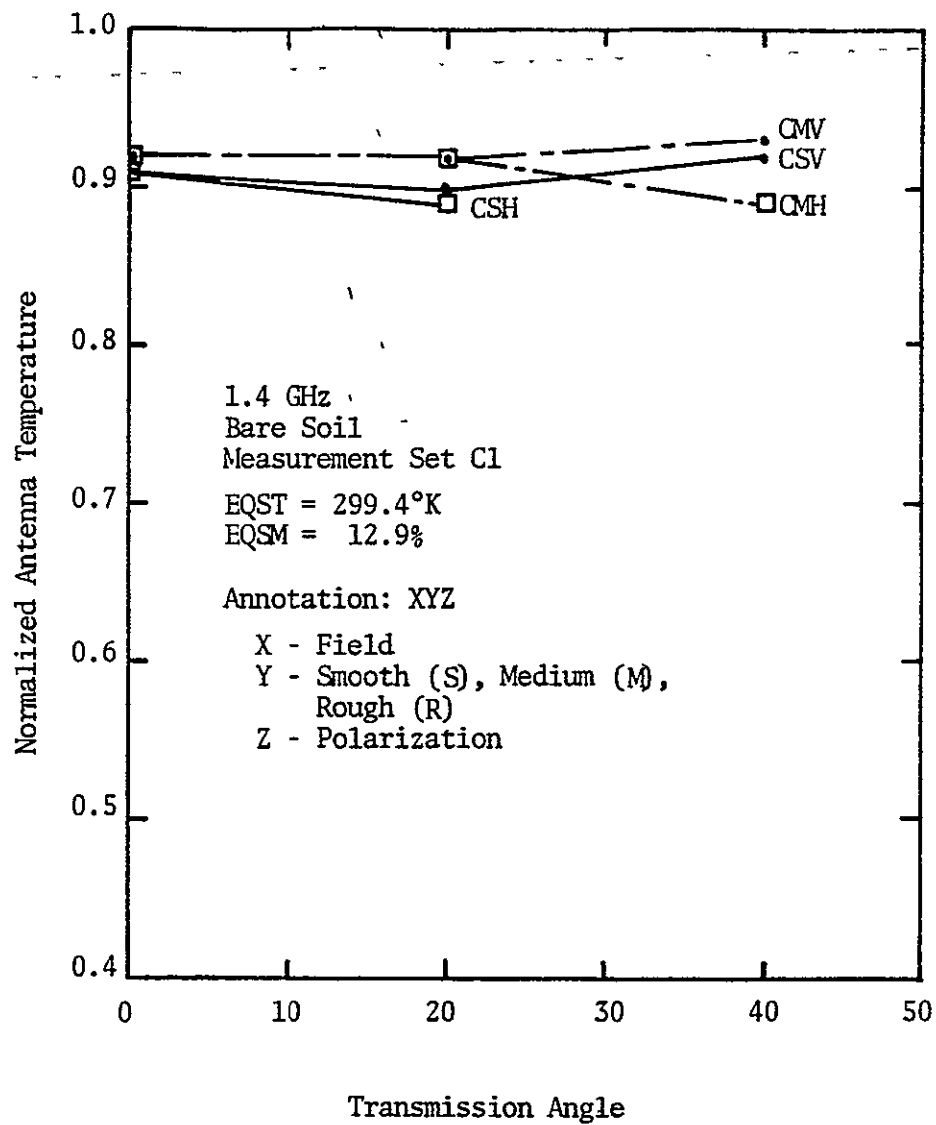


Figure B-4. Measurements of emission from dry bare soil at 1.4 GHz.

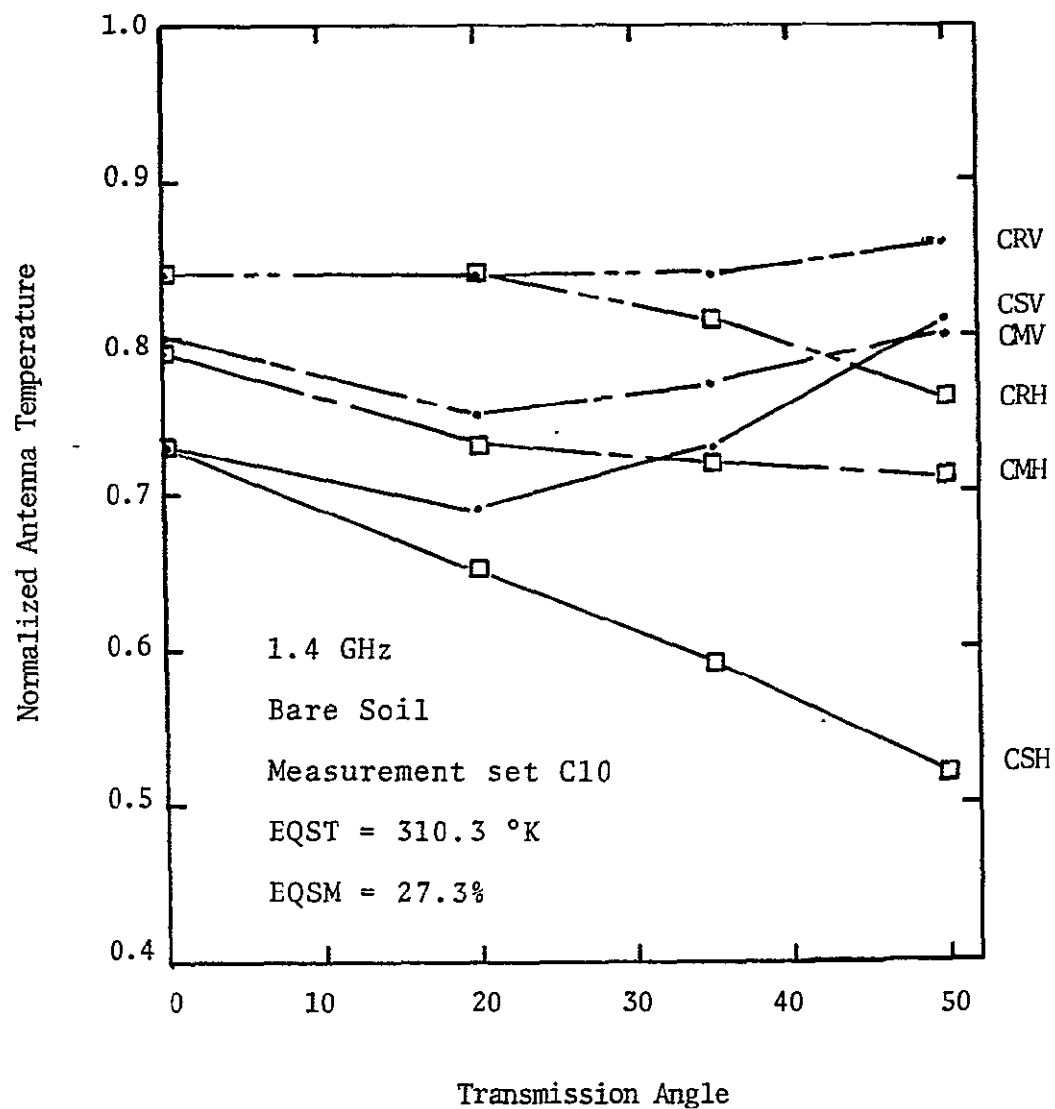


Figure B-5. Measurements of emission from moist bare soil at 1.4 GHz.

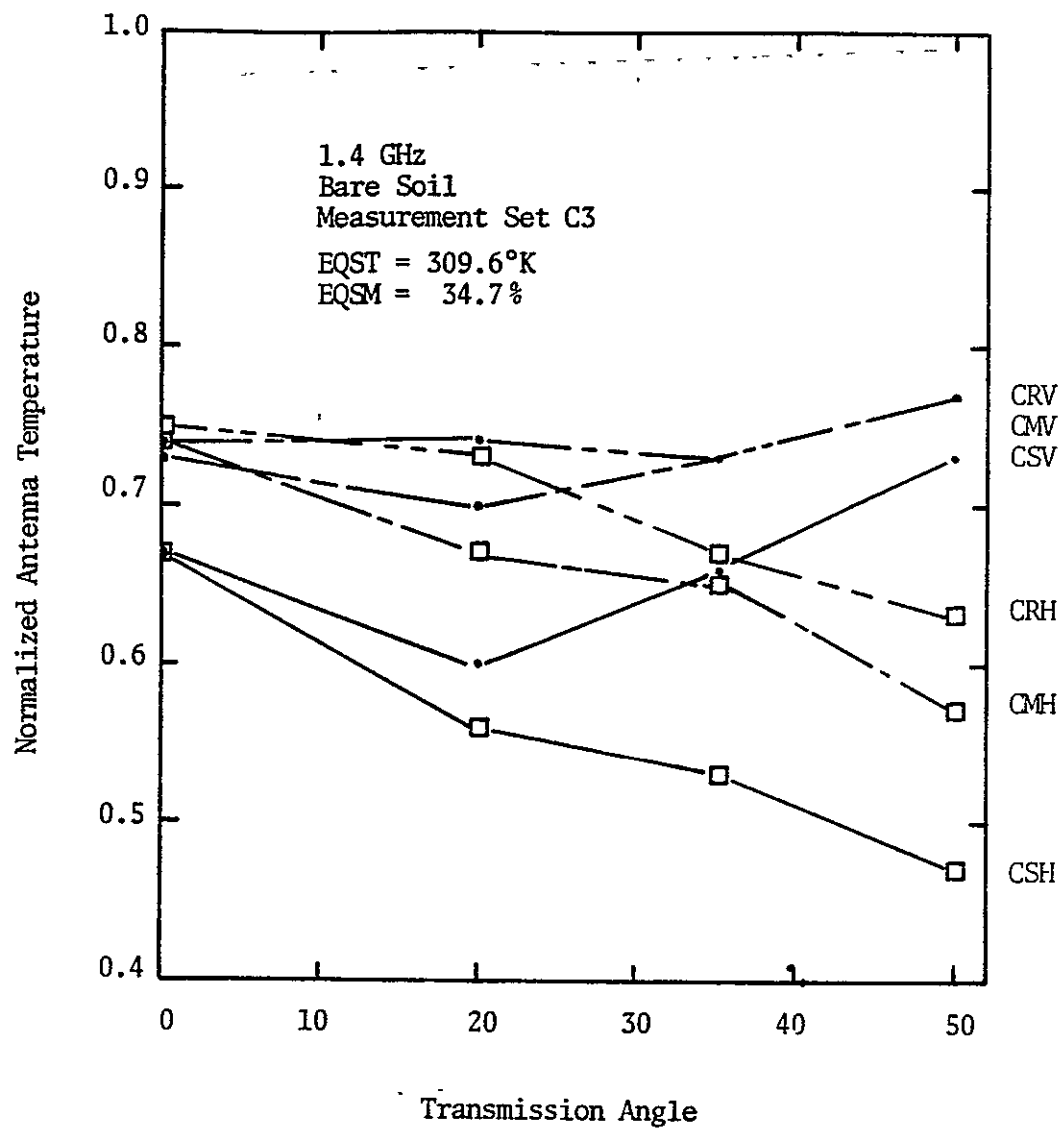


Figure B-6. Measurements of emission from wet bare soil at 1.4 GHz.

Since the self emitted component of the measured antenna temperature is a function of the backscattering coefficient, it is possible to calculate the self emitted component using the radar backscatter measurements reported by Batlivala and Cihlar [106]. The bare fields were irrigated just prior to measurement set number three. As a result, measurement set three has the highest self emission component of all of the 1974 measurements. For this reason this measurement set will be used to demonstrate the magnitude of the self emission component.

Neglecting atmospheric effects and antenna beamwidth effects, the measured antenna temperature can be decomposed into two components.

$$T_m = T_s + T_{se} \quad (B-1)$$

$T_m$  is the measured apparent antenna temperature,  $T_s$  is the contribution of the soil and  $T_{se}$  is the component of the noise power emitted by system that is reflected from the surface back into the antenna aperture.  $T_{se}$  is related to the noise power emitted by the system through the backscatter radar cross section of the surface. Measurements of normalized radar cross section were reported by Batlivala

and Cihlar [106]. Since these measurements were obtained simultaneously with the passive measurements, they can be used in conjunction with the radar equation to calculate the noise emission of the system. Batlivala and Cihlar only reported measurements between 2 GHz and 8 GHz, so their data had to be extrapolated to 1.0 GHz and 10 GHz. Table B-1 contains the results of this extrapolation as a function of incident angle.

#### Self Emission at 1.4 GHz

In order to use the radar equation to calculate the power emitted by the system, one must first determine  $T_{se}$ , the backscattered component of the self emitted power.  $T_{se}$  can be determined by comparing theoretical calculations of the brightness temperature of the soil to the measured antenna temperature. Figure V-7 is a comparison of the measured antenna temperature of the smooth surface to the calculated brightness temperature of smooth soil at 1.4 GHz. In Figure V-7 the theoretical calculations were purposely shifted so that they matched the measurements at  $20^\circ$ . This was done to again demonstrate that the measurements at nadir should fall approximately halfway between the measurements at  $20^\circ$ . Using this criterion, the brightness temperature of the smooth surface at nadir will be assumed to be  $173.5^\circ\text{K}$ . The measurement was  $201.5^\circ\text{K}$ . Using (B-1), the backscattered self emitted component is  $28^\circ\text{K}$ .



TABLE B-1

Values of  $\sigma^0$  Extrapolated from Measurements

Reported by Batlivala and Cihlar [106]

Field*	Angle	Normalized Radar Cross Section			
		1.0 GHz	(VV&HH)	10.0 GHz	(VV&HH)
CS-2	0	19.5 dB	89.13	13.0 dB	19.95
	20	- 4.5 dB	0.35	- 2.0 dB	0.63
	35	-10.0 dB	0.10	- 6.0 dB	0.25
	50	-12.5 dB	0.06	- 8.0 dB	0.16
CM-2	0	13.0 dB	19.95	0.0 dB	1.00
	20	5.5 dB	3.55	- 0.5 dB	0.89
	35	2.0 dB	1.58	- 0.5 dB	0.89
	50	- 1.5 dB	0.71	- 1.0 dB	0.79
CR-2	0	6.6 dB	4.57	- 1.0 dB	0.79
	20	5.2 dB	3.31	- 2.0 dB	0.63
	35	3.7 dB	2.34	- 3.0 dB	0.50
	50	2.2 dB	1.66	- 3.7 dB	0.43

\*Measurement set two reported by Batlivala and Cihlar [106]  
correspond to measurement set three reported by Newton [103]

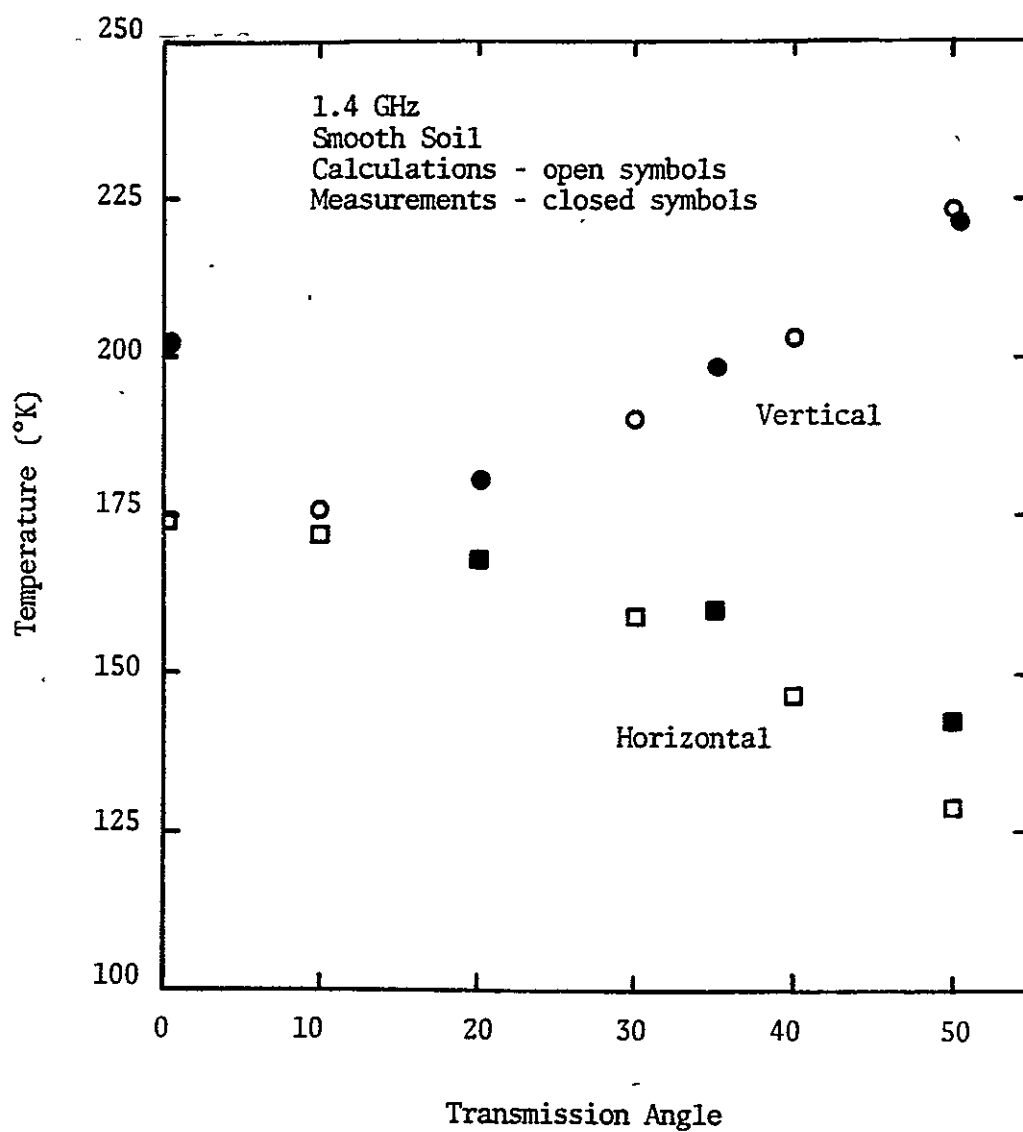


Figure B-7. Comparison of measurements to calculations of emission from smooth soil.

The radar equation can now be used to calculate the self emitted noise power of the 1.4 GHz system using a  $T_{se}$  of 28°K and the radar cross section measured at nadir in Table B-2. The radar equation is

$$P_r = \frac{G_t P_t}{4\pi r^2} \frac{\sigma}{4\pi r^2} \frac{G_r \lambda^2}{4\pi} \quad (B-2)$$

where:

$P_r$  - power received (watts)

$P_t$  - power transmitted (watts)

$G_t$  - maximum gain of the transmitting antenna

$G_r$  - maximum gain of the receiving antenna

$\lambda$  - wavelength (m)

$\sigma$  - radar cross section ( $m^2$ )

$r$  - distance from the scene to the antennas (m)

Batlivala and Cihlar [106] report normalized radar cross section,  $\sigma^\circ$ , which is related to  $\sigma$  by

$$\sigma^\circ = \frac{\sigma}{A} = \sigma \frac{\cos \theta}{r^2 \Delta \Omega} \quad (B-3)$$

TABLE B-2  
Parameters used to Calculate the Self Emitted  
Noise Power of the L-band System

Parameter	Value Used
$P_r$ @ nadir	$9.299 \times 10^{-15}$ watts
$G_r^*$	183.35
$G_t^*$	183.35
$\Delta\theta; \Delta\phi$	$15^\circ$
$\lambda$	0.212 meter
$r$	12.3 meter
$\sigma^\circ$ @ nadir	89.13
$P_t$ @ nadir	$8.13 \times 10^{-14}$ watts

\*Based on the approximate equation

$$G = \frac{41,253}{\Delta\theta\Delta\phi}$$

where  $\Delta\theta$  and  $\Delta\phi$  are beamwidths in degrees

where  $A$  is the area of the scene subtended by the beam width,  $\Delta\Omega$ , of the transmitting and receiving antennas (Figure B-8).  $T_{se}$  can be converted to watts using

$$P = kTB \quad (B-4)$$

where:

$k$  - Boltzman's constant ( $1.23 \times 10^{-23} \frac{\text{watts}}{\text{sec}^\circ\text{K}}$ )

$B$  - bandwidth (27 MHz @ 1.4 GHz)

$T$  - temperature ( $^\circ\text{K}$ )

Table B-2 contains a list of the parameters used in (B-2) through (B-4) to calculate the self emitted power of the 1.4 GHz system. The self emitted power is approximately  $8.12 \times 10^{-14}$  watts. This converts to a noise temperature of  $244.8^\circ\text{K}$ .

This system noise emission can be related back to system parameters using the relationship describing the noise emission of passive components.

$$T_{\text{emitted}} = T_o(1-L) \quad (B-5)$$

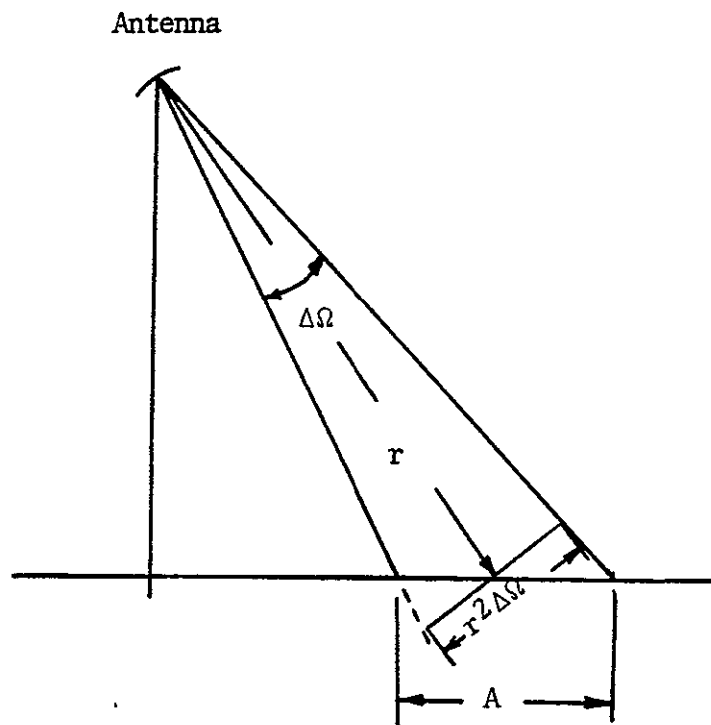


Figure B-8. Relationship between the area "viewed" by an antenna and its beamwidth.

where  $t_0$  is the physical temperature of the component and  $L$  is the transmittance of the component. Since the emission of a passive component is dependent upon its temperature, the self emission of the 1.4 GHz system can be viewed as consisting of two components. The receiver section which is temperature controlled at 55°C, and the antenna and cable connecting the receiver and antenna which is at ambient temperature. Thus

$$T_{se} = T_{\text{receiver emission}} + t_{\text{antenna}}(1 - L_{\text{antenna}}) + t_{\text{cable}}(1 - L_{\text{cable}}) \quad (\text{B-6})$$

Newton [103] gives  $L_{\text{cable}}$  as 0.934 and  $L_{\text{antenna}}$  as 0.86. Assuming that the antenna and cable temperatures are 300°K, then  $L_{\text{receiver}}$  can be calculated using (B-7).

$$L_{\text{receiver}} = 1 - \frac{T_{se} - T_{\text{antenna}}(1 - L_{\text{antenna}}) - T_{\text{cable}}(1 - L_{\text{cable}})}{T_{\text{receiver emission}}} \quad (\text{B-7})$$

The effective receiver transmittance calculated in this fashion is 0.442. The reciprocal of  $L_{\text{receiver}}$  converts to 3.55 dB. This can be interpreted to mean that the 1.4 GHz receiver section has a lumped "insertion loss" of 3.55 dB.

It is now of interest to determine how large a contribution this self emitted power makes to the measured antenna temperature as a function of angle and surface roughness. This can be done using the radar equation and the normalized radar cross sections contained in Table B-1. Table B-3 contains the results of such calculations for 1.4 GHz. Measurement set three is considered to be the worst case condition since the measured radar cross sections were the largest for this set due to the very wet soil conditions. It is clear from Table B-3 that the self emission component is only significant at angles near nadir.

#### Self Emission at 10.6 GHz

The effect of self emission on the 10.6 GHz measurements has not been discussed. This is a result of the fact that the "smooth" field actually appears as a relatively rough field at 10.6 GHz. This is demonstrated by Figure B-9 which is a plot of 10.6 GHz measurements for the "smooth" bare field. These data do not have the characteristics of the emission of a smooth field. Also, the vertical measurement at 20° appears to be invalid. As a result, it was not possible to assume a value at nadir based on the 20° measurements. However, an



TABLE B-3  
 Calculations of the L-band Self Emitted Component;  
 Measurement Set Three

Field	Angle	Self Emitted Component	
		Power (watts)	Noise Temperature (°K)
CS	0	$9.30 \times 10^{-15}$	28.00
	20	$3.90 \times 10^{-17}$	0.12
	35	$1.28 \times 10^{-17}$	0.04
	50	$9.79 \times 10^{-18}$	0.03
CM	0	$2.09 \times 10^{-15}$	6.29
	20	$3.96 \times 10^{-16}$	1.19
	35	$2.02 \times 10^{-16}$	0.61
	50	$1.16 \times 10^{-16}$	0.35
CR	0	$4.79 \times 10^{-16}$	1.44
	20	$3.69 \times 10^{-16}$	1.11
	35	$2.99 \times 10^{-16}$	0.90
	50	$2.71 \times 10^{-16}$	0.82

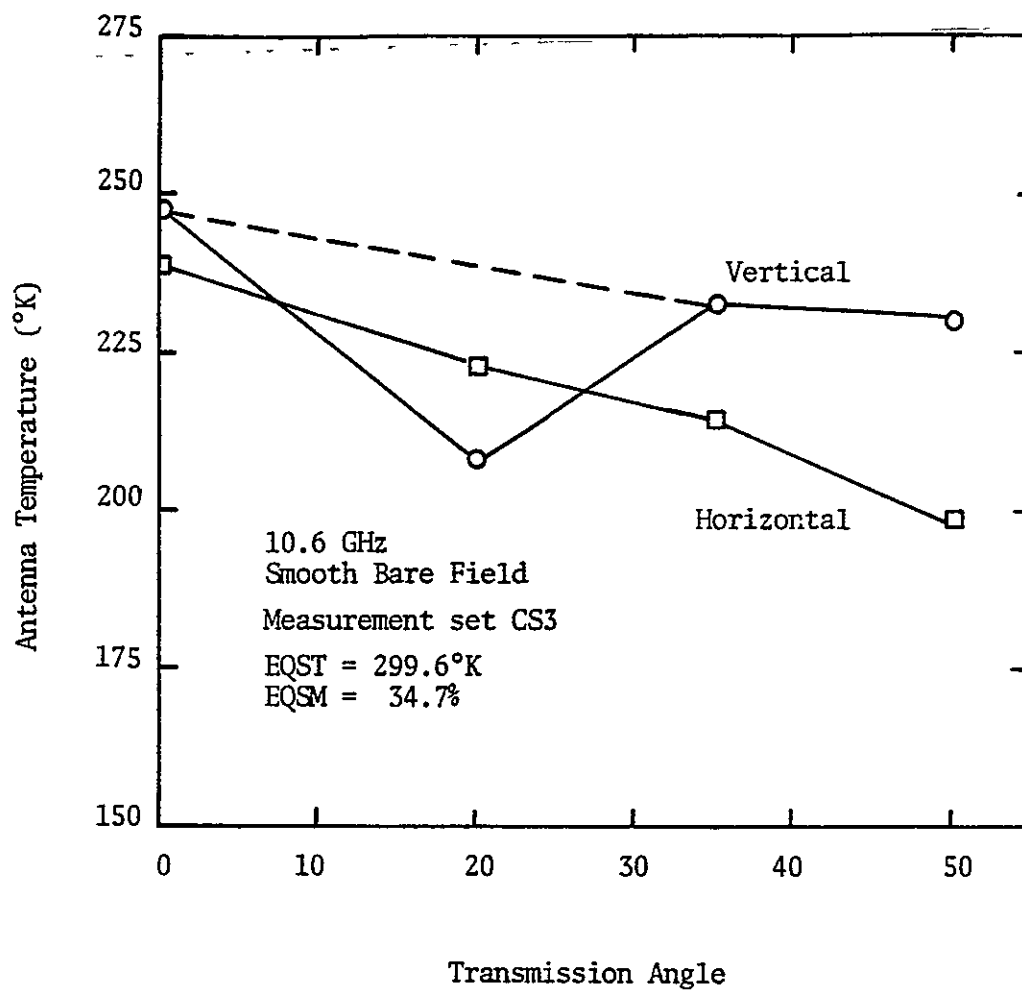


Figure B-9. 10.6 GHz measurements of a wet smooth bare field.

estimate of the X-band self emission for the 10.6 GHz system can be made by considering the design of the 10.6 GHz front end.

Figure B-10 is a block diagram representation of the 10.6 GHz front end. During normal operation, circulator two is in a position to pass energy from the hot reference load to circulator one. Circulator one switches with a duty cycle of one-half, alternately passing energy to the receiver from the hot reference load and the antenna. When circulator one is in a position to pass energy from the antenna to the receiver, it inherently allows energy to pass from the hot reference load out the antenna. Likewise, when it is in a position to pass energy from the hot reference load toward the receiver, it also passes noise energy from the receiver out the antenna.

Neglecting circulator losses, the average noise energy transmitted out of the 10.6 GHz antenna is

$$T_{se} = \left[ \frac{1}{2} T_{generator} + \frac{1}{2} T_{receiver} \right] L_{CA} L_A \quad (B-8)$$

$$+ L_A (t_{CA} (1 - L_{CA})) + t_A (1 - L_A)$$

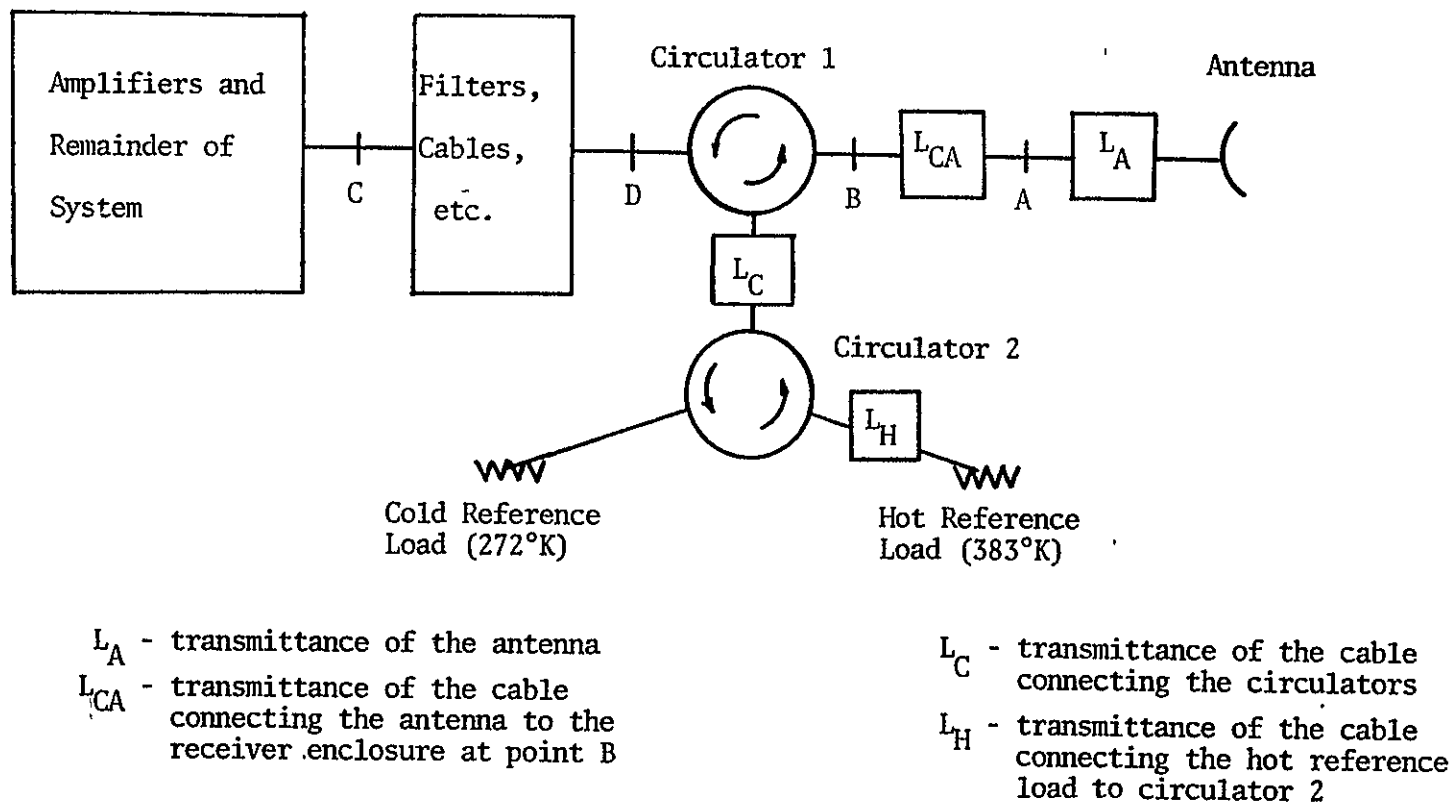


Figure B-10. Simplified block diagram of the 10.6 GHz front end.

$$T_{\text{generator}} = 383(L_H L_C) + L_C(t_H(1-L_H)) + t_C(1-L_C) \quad (\text{B-9})$$

$$T_{\text{receiver}} = t_{\text{receiver}}(1-L_{\text{receiver}}) \quad (\text{B-10})$$

The transmittances are defined in Figure B-10. The lower case  $t$ 's stand for physical temperatures of the respective components. As mentioned before, the receiver is temperature controlled at 55°C, so  $t_{\text{receiver}}$ ,  $t_H$ , and  $t_C$  are 328°K. The "lumped" insertion loss of the receiver is given by the sum of the losses of circulator one, the isolator, the filter, the mixer and the cables. Assuming each of these are 0.5 dB, the lumped insertion loss of the X-band receiver is 2.5 dB. This corresponds to an  $L_{\text{receiver}}$  of 0.56 and a  $T_{\text{receiver}}$  of 143.6°K. Assuming  $L_H$  and  $L_C$  are both 0.97, then  $T_{\text{generator}}$  is 379.75°K. Newton [103] gives  $L_{CA}$  as 0.97 and  $L_A$  as 0.86. Assuming that  $t_{CA}$  and  $t_A$  were 300°K, the self emission of the 10.6 GHz system is calculated to be 268°K using (B-8).

The worst case self emitted contribution to the 10.6 GHz measurements can be estimated as a function of angle and roughness using the computed value of 268°K as the self emission of the X-band system, and the normalized radar cross section measurements of data set three. The radar measurements are tabulated in Table B-1, and Table B-4 contains the values of the 10.6 GHz parameters used in the radar equation. Table B-5 contains the results of the calculations. These calculations follow the trend that would be expected based on the 1.4 GHz results. Only the measurements of the "smooth" field near nadir have a significant self emission component. It is also obvious from these calculations that, at 10.6 GHz, the "smooth" field appears to be a relatively rough field.

TABLE B-4  
Parameters Used to Calculate the Self Emitted  
Component of the X-band System

Parameter	Value Used
$P_t$	$6.59 \times 10^{-13}$ watts
$G_r^*$	1145.92
$G_t^*$	1145.92
$\lambda$	0.028 meters
$r$	12.3 meters
$\Delta\theta; \Delta\phi$	$6^\circ$

\*approximated by

$$G = \frac{41,253}{\Delta\theta\Delta\phi}$$

where  $\Delta\theta$  and  $\Delta\phi$  are beamwidths in degrees

TABLE B-5  
 Calculations of the X-band Self Emitted Component  
 for Measurement Set Three

Field	Angle	Self Emitted Component	
		Power (watts)	Noise Temperature ( $^{\circ}$ K)
CS	0	$5.19 \times 10^{-15}$	2.11
	20	$1.72 \times 10^{-16}$	0.07
	35	$7.62 \times 10^{-17}$	0.03
	50	$5.89 \times 10^{-17}$	0.02
CM	0	$2.60 \times 10^{-16}$	0.11
	20	$2.44 \times 10^{-16}$	0.10
	35	$2.72 \times 10^{-16}$	0.11
	50	$2.91 \times 10^{-16}$	0.12
CR	0	$2.06 \times 10^{-16}$	0.08
	20	$1.72 \times 10^{-16}$	0.07
	35	$1.53 \times 10^{-16}$	0.06
	50	$1.58 \times 10^{-16}$	0.06



## APPENDIX C

EQUIVALENT SOIL MOISTURE AND SOIL  
TEMPERATURE TABULATIONS

This appendix contains tabulations of equivalent incoherent soil moisture and soil temperature calculated using the soil moisture and soil temperature profiles from the 1974 and 1975 experiments. Equation (VII-3) was used to calculate the equivalent incoherent soil moisture. An analogous equation was used to calculate the equivalent incoherent soil temperature.

Table C-1 contains equivalent soil moistures and soil temperatures for the 1974 experiment. In 1974 ground data were normally acquired simultaneously with the microwave measurements at four locations along each side of the experimental plots. The entries in Table C-1 were calculated using the average of these eight soil moisture and soil temperature profiles.

Table C-2 contains equivalent soil moistures and soil temperatures for the 1975 experiment. In 1975 ground data were acquired at 12 locations within each field as shown in Figure V-11. Only those profiles that fell within the antenna footprint during each transmission angle scan were used to calculate average soil moisture and soil temperature profiles used in developing Table C-2.

Table C-3 lists those ground measurement locations from which ground data were averaged for each scan direction. Soil temperature profiles obtained from the row ridges and row furrows were averaged with equal weighting.

TABLE C-1

## Equivalent Soil Moisture and Soil Temperature

## Calculations for the 1974 Experiment

Measurement Set	1.4 GHz			10.6 GHz		
	EQST (°K)	EQSM (Percent)		EQST (°K)	EQSM (Percent)	
		Weight	Volume		Weight	Volume
AS 1	293.1	27.6	33.9	292.6	29.0	33.4
AS 2	297.2	18.2	23.2	294.3	14.8	17.0
AS 3	300.3	18.8	23.9	302.3	13.1	15.1
AS 4	302.7	16.3	21.0	302.3	9.9	11.5
AS 5	300.3	16.3	21.1	298.3	8.8	10.2
AS 6	302.8	15.5	20.1	302.6	8.6	9.9
AS 7	305.2	14.8	19.4	308.2	7.3	8.5
AM 1	295.8	31.6	35.4	294.9	36.2	38.3
AM 2	299.1	28.6	32.3	302.3	29.2	30.9
AM 3	296.2	21.7	25.2	294.9	21.2	22.5
AM 4	300.2	21.2	24.9	302.0	15.0	15.9
AM 5	299.4	20.3	23.9	298.1	15.1	16.0
AM 6	298.6	18.1	21.6	296.7	11.3	12.0
AM 7	302.9	16.7	20.0	303.6	9.7	10.4
AM 8	308.0	15.6	18.9	312.5	9.2	9.8
AR 2	294.5	26.5	28.1	291.4	27.2	28.5
AR 3	294.3	28.1	29.9	291.3	29.1	30.5

Table C-1 (Continued)

Measurement Set	1.4 GHz			10.6 GHz		
	EQST (°K)	EQSM (Percent)		EQST (°K)	EQSM (Percent)	
		Weight	Volume		Weight	Volume
AR 4	300.8	21.0	22.3	301.6	24.1	25.3
AR 5	298.8	22.0	23.4	299.3	22.3	23.4
AR 6	299.0	19.9	21.1	299.5	17.1	17.9
BS 1	292.7	24.6	30.5	292.1	25.3	29.1
BS 2	295.1	16.6	21.1	291.4	14.2	16.3
BS 3	301.9	16.0	20.5	303.7	12.3	14.2
BS 4	300.7	15.1	19.5	300.1	10.9	12.5
BS 5	301.7	13.7	17.7	301.5	9.5	11.0
BS 6	306.2	14.0	18.5	309.1	5.9	6.9
BS 7	303.0	11.3	15.1	301.7	5.3	6.2
BM 1	300.7	25.9	26.6	303.0	26.3	27.9
BM 2	291.8	24.7	28.4	291.3	26.1	27.6
BM 3	293.0	19.2	22.5	290.2	18.3	19.4
BM 4	300.8	18.0	21.3	301.4	13.2	14.0
BM 5	301.4	16.4	19.6	301.5	12.7	13.5
BM 6	300.9	16.3	19.4	302.3	11.4	12.1
BM 7	300.9	16.2	19.3	302.3	13.1	13.9
BM 8	304.3	13.2	16.2	304.5	8.0	8.5
BM 9	304.8	12.5	15.4	307.9	6.7	7.2

Table C-1 (Continued)

Measurement Set	1.4 GHz			10.6 GHz		
	EQST (°K)	EQSM (Percent)		EQST (°K)	EQSM (Percent)	
		Weight	Volume		Weight	Volume
BR 1	302.6	22.2	23.6	305.3	17.2	18.0
BR 2	292.8	18.6	19.8	290.9	14.2	14.9
BR 3	294.1	15.8	16.8	291.7	8.6	9.1
CS 1	309.6	10.3	12.9	312.5	3.8	5.5
CS 2	295.7	8.9	11.3	289.5	4.7	7.0
CS 3	299.4	28.2	40.2	300.5	27.2	42.2
CS 4	301.4	22.0	30.4	304.5	21.8	33.8
CS 5	296.1	22.7	31.0	296.0	19.4	30.1
CS 6	299.3	23.5	32.2	300.5	20.8	32.3
CS 7	302.0	25.1	35.4	304.9	25.9	40.1
CS 8	299.8	25.2	35.2	298.9	24.5	38.0
CS 9	303.2	22.7	31.2	305.8	20.3	31.5
CS 10	301.3	20.4	27.3	299.9	13.5	20.8
CS 11	300.6	21.6	29.2	302.1	15.5	24.0
CS 12	300.6	21.5	28.6	299.5	13.2	20.4
CS 13	301.0	19.1	25.3	302.3	10.9	16.9
CS 14	301.3	19.7	26.2	302.3	11.6	18.0
CS 15	300.8	19.5	25.7	300.5	11.3	17.5
CM 1	305.5	10.8	12.8	308.0	3.6	4.3
CM 2	293.8	11.8	14.0	290.1	5.2	6.4

Table C-1 (Continued)

Measurement Set	1.4 GHz			10.6 GHz		
	EQST (°K)	EQSM (Percent)		EQST (°K)	EQSM (Percent)	
		Weight	Volume		Weight	Volume
CM 3	296.1	28.4	34.1	296.0	28.4	36.1
CM 4	299.1	22.5	26.9	302.8	20.8	26.4
CM 5	299.6	20.0	23.7	299.0	14.2	18.0
CM 6	296.3	21.6	25.5	295.9	16.0	20.4
CM 7	302.6	21.8	25.7	305.8	13.1	16.6
CM 8	304.0	24.5	29.3	307.1	24.0	30.5
CM 9	297.8	23.0	27.3	296.6	16.2	20.6
CM 10	305.7	21.1	24.8	308.6	12.1	15.4
CM 11	300.9	20.1	23.7	299.6	10.6	13.4
CM 12	303.8	20.3	23.8	307.3	9.8	12.3
CM 13	301.7	21.3	25.0	300.5	10.2	12.9
CM 14	304.1	20.6	24.2	306.8	10.2	12.9
CM 15	302.3	20.2	23.7	304.4	9.9	12.5
CM 16	303.5	19.9	23.3	305.0	9.5	11.9
CR 1	304.5	7.3	7.9	308.8	3.5	4.3
CR 2	294.8	7.7	8.4	290.6	5.0	6.3
CR 3	311.3	29.0	34.4	315.8	28.8	30.8
CR 4	298.6	26.0	29.5	303.1	12.8	16.8
CR 5	298.9	15.7	17.3	301.8	8.6	11.2
CR 6	300.0	21.9	24.3	299.2	12.0	15.7

Table C-1 (Continued)

Measurement Set	1.4 GHz			10.6 GHz		
	EQST (°K)	EQSM (Percent)		EQST (°K)	EQSM (Percent)	
		Weight	Volume		Weight	Volume
CR 7	300.8	21.8	24.3	304.1	11.8	15.5
CR 8	305.3	23.7	27.1	307.1	16.9	22.3
CR 9	297.0	22.8	25.7	296.0	17.6	22.2
CR 10	306.8	19.6	21.4	310.8	8.9	11.5
CR 11	299.1	21.9	24.6	298.0	13.4	17.6
CR 12	309.0	20.2	21.9	313.9	7.8	10.0
CR 13	301.7	21.3	23.6	300.6	10.8	14.2
CR 14	306.7	19.9	21.7	311.7	8.2	10.6
CR 15	305.4	20.8	22.8	308.5	8.9	11.5
DO 1	302.3	15.8	18.7	305.2	12.9	13.7
DO 2	301.0	33.8	37.7	301.9	36.3	38.5
DO 3	304.2	31.6	35.6	304.6	33.3	35.3
DO 4	304.3	29.4	33.3	305.1	28.0	29.7
D9 1	303.1	16.2	19.2	304.0	11.3	12.0
D9 2	298.7	34.4	38.4	298.7	35.9	38.0
D9 3	303.6	29.7	33.6	304.9	30.4	32.2
D9 4	303.6	26.4	30.3	304.2	22.2	23.5

TABLE C-2  
Equivalent Soil Moisture and Soil Temperature  
Calculations for the 1975 Experiment

Measurement Set	1.4 GHz			10.6 GHz		
	EQST (°K)	EQSM (Percent)		EQST (°K)	EQSM (Percent)	
		Weight	Volume		Weight	Volume
A0 1	307.6	26.4	43.5	308.7	12.7	20.9
A0 2	300.2	29.8	48.9	301.3	27.9	45.8
A0 3	298.0	27.3	44.9	298.8	15.9	26.0
A0 4	304.9	26.6	43.8	302.5	13.9	22.9
A0 5	300.9	25.5	42.0	302.2	11.9	19.5
A0 6	300.6	25.4	41.9	302.3	14.5	23.8
A0 7	299.4	23.8	39.3	299.1	12.8	21.0
A0 8	300.9	21.9	36.1	301.3	11.7	19.2
A0 9	305.1	19.8	32.8	309.6	10.5	17.2
A3 1	309.7	26.5	43.7	312.3	12.4	20.3
A3 2	300.7	30.0	49.3	302.0	27.1	44.5
A3 3	300.8	27.2	44.8	301.8	15.4	25.2
A3 4	305.2	26.7	44.0	303.5	12.5	20.5
A3 5	300.1	26.4	43.5	300.2	11.6	19.0
A3 6	303.4	25.7	42.4	306.2	13.8	22.6
A3 7	300.5	23.9	39.4	301.2	12.7	20.8
A3 8	299.8	21.6	35.7	301.2	11.6	19.1
A3 9	305.2	20.6	34.0	308.2	10.2	16.6



Table C-2 (Continued)

Measurement Set	1.4 GHz			10.6 GHz		
	EQST (°K)	EQSM (Percent)		EQST (°K)	EQSM (Percent)	
		Weight	Volume		Weight	Volume
A4 1	309.7	26.4	43.5	312.4	13.5	22.2
A4 2	300.7	29.8	49.0	302.0	26.5	43.5
A4 3	300.8	27.1	44.5	301.8	15.2	24.9
A4 4	305.2	26.8	44.1	303.5	14.5	20.5
A4 5	300.1	26.4	43.4	300.2	11.5	18.8
A4 6	303.4	25.7	42.3	306.1	13.3	21.8
A4 7	300.5	23.8	39.3	301.2	12.6	20.7
A4 8	299.8	21.6	35.7	301.2	11.5	18.8
A4 9	305.3	20.4	33.8	308.1	10.1	16.5
A6 1	309.8	26.9	44.3	312.4	14.1	23.1
A6 2	300.8	30.3	49.8	302.0	27.7	45.5
A6 3	300.6	27.1	44.6	301.9	15.9	26.1
A6 4	305.1	26.9	44.3	303.5	13.7	22.5
A6 5	300.1	26.1	43.0	300.2	11.5	18.9
A6 6	303.4	25.9	42.8	306.2	14.2	23.2
A6 7	300.5	23.7	39.0	301.2	12.8	21.0
A6 8	299.8	22.2	36.7	301.2	11.7	19.3
A6 9	305.2	20.3	33.6	308.2	10.2	16.8
A9 1	308.0	26.9	44.2	309.6	13.9	22.7
A9 2	299.8	29.5	48.5	300.9	25.5	41.9

Table C-2 (Continued)

Measurement Set	1.4 GHz			10.6 GHz		
	EQST (°K)	EQSM (Percent)		EQST (°K)	EQSM (Percent)	
		Weight	Volume		Weight	Volume
A9 3	301.1	27.1	44.6	302.2	15.0	24.5
A9 4	305.6	26.2	43.1	303.9	12.4	20.4
A9 5	303.3	25.4	41.9	302.9	11.4	18.8
A9 6	301.7	25.1	41.3	304.0	12.9	21.1
A9 7	300.9	23.4	38.5	301.4	12.6	20.6
A9 8	302.9	21.6	35.6	304.6	11.3	18.6
A9 9	306.1	20.1	33.2	309.2	10.0	16.5
B0 1	305.8	38.5	63.2	306.7	38.8	63.6
B0 2	302.8	30.6	50.3	303.2	26.1	42.9
B0 3	306.3	27.5	45.3	308.0	19.2	31.6
B0 4	305.0	33.3	54.7	306.1	34.0	55.8
B0 5	307.5	25.6	42.1	309.6	13.5	22.1
B0 6	302.9	20.4	33.7	302.1	9.5	15.5
B0 7	310.1	18.8	31.1	310.6	10.1	16.6
B3 1	305.3	40.1	65.8	306.3	40.2	65.9
B3 2	301.3	31.8	52.3	301.4	29.4	48.3
B3 3	306.7	27.6	45.4	308.2	18.9	31.0
B3 4	302.4	31.9	52.4	303.6	28.9	47.4
B3 5	307.8	26.0	42.8	310.1	14.3	23.5

Table C-2 (Continued)

Measurement Set	1.4 GHz			10.6 GHz		
	EQST (°K)	EQSM (Percent)		EQST (°K)	EQSM (Percent)	
		Weight	Volume		Weight	Volume
B3 6	304.1	20.0	33.2	304.2	9.3	15.3
B3 7	309.3	18.7	31.0	312.1	9.8	16.1
B4 1	305.3	40.0	65.7	306.3	40.0	65.6
B4 2	301.3	31.6	51.9	301.4	28.1	46.1
B4 3	306.7	27.4	45.1	308.2	19.0	31.1
B4 4	302.4	31.4	51.6	303.6	28.2	46.3
B4 5	307.7	25.5	42.1	310.1	13.0	21.4
B4 6	303.9	19.9	33.0	304.2	9.3	15.2
B4 7	309.3	18.8	31.3	312.1	10.0	16.4
B6 1	305.3	39.9	65.5	306.3	40.3	66.1
B6 2	301.3	31.6	51.9	301.4	29.0	47.6
B6 3	306.7	27.7	45.5	308.2	19.5	32.0
B6 4	302.5	31.8	52.3	303.6	30.4	49.9
B6 5	307.8	25.8	42.5	310.1	41.1	23.2
B6 6	304.0	20.6	34.1	304.2	9.25	15.2
B6 7	309.3	18.6	30.9	312.1	9.7	15.9
B9 1	305.2	37.7	62.0	306.2	37.2	61.0
B9 2	302.2	30.4	50.0	302.5	25.9	42.5

Table C-2 (Continued)

Measurement Set	1.4 GHz			10.6 GHz		
	EQST (°K)	EQSM (Percent)		EQST (°K)	EQSM (Percent)	
		Weight	Volume		Weight	Volume
B9 3	306.7	26.3	43.3	308.1	14.5	23.8
B9 4	301.9	32.3	53.6	302.6	32.9	54.0
B9 5	307.1	26.0	42.7	308.9	17.4	28.6
B9 6	304.5	19.4	32.1	305.1	9.2	15.1
B9 7	309.6	18.0	29.9	311.7	10.0	16.4

TABLE C-3

Ground Sampling Locations that Correspond to the Antenna  
Temperature Measurement Sets Made at Each Azimuth Angle

Field	Azimuth Angle with Respect to Row Direction	Ground Sampling Location
A	0°	1, 2, 3, 4, 9, 10
	30°	1, 4, 5, 6, 9, 10, 11
	45°	1, 5, 6, 9, 10, 11
	60°	1, 2, 5, 6, 10, 11
	90°	1, 2, 7, 8, 9, 10, 11, 12
B	0°	1, 2, 9, 10, 11, 12
	30°	1, 2, 3, 5, 6, 7, 8, 11
	45°	1, 2, 5, 6, 7, 11
	60°	1, 2, 5, 7, 8, 10, 11
	90°	1, 2, 3, 4